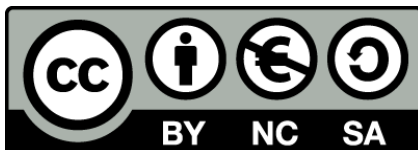




UNIVERSITAT_{DE}
BARCELONA

Velocitat de desplaçament de la falla d'Alhama de Murcia (Bètiques Orientals); implicacions en el seu potencial sísmic

Marta Ferrater Gómez



Aquesta tesi doctoral està subjecta a la llicència **Reconeixement- NoComercial – Compartirlqual 4.0. Espanya de Creative Commons.**

Esta tesis doctoral está sujeta a la licencia **Reconocimiento - NoComercial – Compartirlqual 4.0. España de Creative Commons.**

This doctoral thesis is licensed under the **Creative Commons Attribution-NonCommercial-ShareAlike 4.0. Spain License.**

**Annex 1. Publicacions en revistes
indexades el contingut de les quals
s'ha inclòs en la memòria**

- Ferrater, M., Arrowsmith, R., Masana, E. (2015). **Lateral offset quality rating along low slip rate faults: application to Alhama de Murcia fault (SE Iberian Peninsula)**. Remote Sensing, 7, 14827-14852. Doi: 10.3390/rs71114827
- Ferrater, M., Echeverría, A., Masana, E., Martínez-Díaz, J.J., Sharp, W.D. (2016). **A 3D measurement of the offset in paleoseismological studies**. Computers & Geosciences, 9, 156-163, doi.org/10.1016/j.cageo.2016.02.024.
- Ferrater, M., Ortuño M., Masana, E., Pallàs, R., Perea, H., Baize, S., García-Meléndez, E., Martínez-Díaz, J.J., Echeverría, A., Rockwell, T., Sharp, W.D. (2016). **Refining seismic parameters in low seismicity areas by 3D trenching: the not so slow Alhama de Murcia fault, SE Iberia**. Tectonophysics, 680, 122-128. Doi: 10.1016/j.tecto.2016.05.020
- Ferrater, M., Ortuño M., Masana, E., Martínez-Díaz, J.J., Pallàs, R., Perea, H., Baize, S., García-Meléndez, E., Echeverría, A., Rockwell, T., Sharp, W.D., Medialdea, A., Rhodes, E. (major revision Quaternary International). **Slip-rate estimation along a slow-moving fault combining paleoseismological 3D trenching and morphotectonic analysis: the strike-slip Alhama de Murcia fault (SE Iberian Peninsula)**

Article

Lateral Offset Quality Rating along Low Slip Rate Faults: Application to the Alhama de Murcia Fault (SE Iberian Peninsula)

Marta Ferrater ^{1,*}, Ramon Arrowsmith ² and Eulàlia Masana ¹

¹ RISK-NAT Group, GEOMODELS, Departament de Geodinàmica i Geofísica, Facultat de Geologia, Universitat de Barcelona, c/Martí i Franquès, s/n, Barcelona 08028, Spain;

E-Mail: eulalia.masana@ub.edu

² School of Earth and Space Exploration, Arizona State University, Tempe, AZ 85287-6004, USA;

E-Mail: ramon.arrowsmith@asu.edu

* Author to whom correspondence should be addressed; E-Mail: marta.ferrater@ub.edu;

Tel.: +34-934-034-029.

Academic Editors: Antonio Abellan, Marc-Henri Derron, Michel Jaboyedoff, Zhong Lu and Prasad S. Thenkabail

Received: 28 May 2015 / Accepted: 29 October 2015 / Published: 6 November 2015

Abstract: Seismic hazard assessment of strike-slip faults is based partly on the identification and mapping of landforms laterally offset due to fault activity. The characterization of these features affected by slow-moving faults is challenging relative to studies emphasizing rapidly slipping faults. We propose a methodology for scoring fault offsets based on subjective and objective qualities. We apply this methodology to the Alhama de Murcia fault (SE Iberian Peninsula) where we identify 138 offset features that we mapped on a high-resolution (0.5×0.5 m pixel size) Digital Elevation Model (DEM). The amount of offset, the uncertainty of the measurement, the subjective and objective qualities, and the parameters that affect objective quality are independent variables, suggesting that our methodological scoring approach is good. Based on the offset measurements and qualifications we calculate the Cumulative Offset Probability Density (COPD) for the entire fault and for each fault segment. The COPD for the segments differ from each other. Tentative interpretation of the COPDs implies that the slip rate varies from one segment to the other (we assume that channels with the same amount of offset were incised synchronously). We compare the COPD with climate proxy curves (aligning using the very limited age control) to test if entrenchment events are coincident with climatic

changes. Channel incision along one of the traces in Lorca-Totana segment may be related to transitions from glacial to interglacial periods.

Keywords: high-resolution DEM; strike-slip fault; offset scoring; Alhama de Murcia fault

1. Introduction

Morphotectonic analyses (especially channel offsets) along active strike slip faults are powerful tools to infer parameters such as segmentation, slip-rate, slip per event, and recurrence of earthquakes. Hazard assessment depends on this information and its uncertainty. Research activity on this topic has focused on (1) slip per event along fast-moving faults (e.g., [1–5]); and (2) long-term slip-rates along lower slip rate faults [6–14]. The distinction between them largely comes from the potential for separating the contributions of individual earthquakes to the measured offset, which is higher in the case of rapid slip and recurrence rate and low surface process rates.

The first group of studies shows an along-fault distribution of offsets including quality ratings. Recent surface fault ruptures leave their imprint in the geomorphic record thus individual fault rupturing events may be identified (e.g., [1,2,4,5]). In the second group, studies typically have measured offset terrace risers (e.g., [11,15]) or channels on alluvial fan surfaces (e.g., [9]) with numerical age control to determine slip rates at the 10^3 – 10^4 year timescale. One example of this second group is [6], which systematically analyzes the distribution of 300 measured offsets along the Kunlun (China) fault. The secondary aim of the long-term slip-rates studies for slow faults is to relate the formation age of the measured features with known regional or global climatic events. The long-term slip rate studies typically do not characterize offsets according to the quality of the measurement, with some exceptions [10]. In general, measurement uncertainties are expressed as a range in the plausible retrodeformation [7,11].

It is necessary to make a distinction between the measurement uncertainty and its quality. Aleatory uncertainty is that associated with the measurement process itself, whereas the epistemic uncertainty describes the degree of ambiguity in the interpretation of the offset history of the feature [16,17]. There is no standard methodology to rate the quality of offset landforms (largely ascribed to epistemic uncertainty). Most approaches (all of them developed for fast-moving faults) define a subjective, qualitative rating (*i.e.*, excellent, good, fair, poor) based on landform projections and fault trace delineations as controlling the offset reconstruction (e.g., [2,17]). For example, [5] score between 0 and 1 according to the degradation of the landform and the obliquity between the fault and the channel. This range (0 to 1) allows them to weight the Probability Density Function (PDF) of the individual offset measurement. After that, they sum the individual weighted PDFs along a specified fault reach to obtain the Cumulative Offset Probability Density (COPD; [18]). The COPD may be used to identify the offset sequences tied to successive earthquake ruptures (e.g., [2–5,18,19]). Van der Woerd *et al.*, [6] also obtain a COPD for longer offsets, and they compare it to climatically driven geomorphic events, as climate variations modulate surface process rates and transitions [20].

It is challenging to adapt this methodology to a slow- or moderate-moving fault. Single rupture events usually cannot be identified in the geomorphic record because they have been smoothed by surface

processes. Although the measured offsets are in general large (tens of meters; being the accumulation of several small offsets along time), the ability to identify them decreases with the dimensions of the offset [1,3,6]. This is obvious in offset histograms which show an exponential decrease of the number of identified elements with larger offset magnitudes [3,8,19]. Despite these obstacles associated with the potentially ambiguous landscape record of the superficial effects of slow-moving faults, their hazard assessment is essential [21,22].

In this paper, we adapt some of the approaches applied to small and few-event offsets along rapidly slipping faults to characterize the activity of low slip rate faults. We thus present a new methodology for scoring offsets and we apply it to a slow-moving strike-slip fault (the Alhama de Murcia fault, SE Iberian Peninsula) to refine our understanding of the hazard it poses and to illustrate our approach. We apply the scoring to the 138 offsets we identified as part of this study along the Alhama de Murcia fault. In the proposed methodology, we differentiate between subjective and objective scoring of quality and analyze effectiveness of the quality metrics. From the summary scoring, its distribution along the fault zone, and the distribution of these offsets, we calculate COPDs along strike of the Alhama de Murcia fault and evaluate potential segment boundaries and variations in slip rate. Additionally, we explore possible associations of entrenchment periods with the climatic cycles.

2. Geological Setting

The Alhama de Murcia fault (AMF) is a left-reverse strike slip fault [23]. It is one of the structures in the Eastern Betics Shear Zone (Figure 1; together with Carboneras, Palomares, Carrascoy and Bajo Segura faults), which absorbs the convergence between Eurasian and African plates (Figure 1; [24–26]). The most significant historical earthquakes (intensity \geq VII EMS) in the study area were in 1907 in Totana and in 1579, 1674 (VIII EMS) and 1818 in Lorca [27]. The largest instrumentally recorded earthquake occurred in Lorca on 11 May 2011, had a moment magnitude of 5.2, and VII EMS intensity [28]. The foreshock of this earthquake had a moment magnitude of 4.5 and the focal mechanism of the event shows oblique reverse faulting [28]. No surface rupture in this seismic event has been identified.

The AMF has been segmented based on fault trace geometry, orientation (it varies N45–65E), trace complexity, seismicity, and geological history (Figure 1; [29]). From south to north, the segments are: (1) Huercal Overa-Lorca, ending in the south in a horse-tail (formed by two subsegments whose subdivision is in Rambla de los Pintados); (2) Lorca-Totana, where the fault splits into several sub-parallel fault traces; (3) Totana-Alhama de Murcia; and (4) Alhama de Murcia-Alcantarilla, where the geomorphic manifestation of the fault is diffuse. The southern ending of the fault is in a tiny district belonging to Huercal Overa, named Goñar, but we will refer to it as Huercal Overa (Figure 1).

Although the main sense of motion along the fault is considered to be left-lateral, details of its slip sense are not well known. Morphotectonic studies describe left-lateral channel offsets [30,31] and infer a left-lateral slip-rate of 0.21 mm/year with undetermined uncertainty [32]. GPS velocities from the region [33] show that these values might be minimal, as they imply up to 1.5 mm/year horizontal slip-rate along the Alhama de Murcia and Palomares faults. Paleoseismic studies suggest a component of dip-slip at 0.04–0.35 mm/year for the upper Pleistocene in the Lorca-Totana segment [25,32], and 0.16–0.22 mm/year for the horse-tail termination in Huercal Overa-Lorca segment [34]. Preliminary

results from 3D excavations and subsurface restorations along the Lorca-Totana segment suggest larger left-lateral slip-rate values, higher than 0.62 mm/year and probably around 1 mm/year [35].

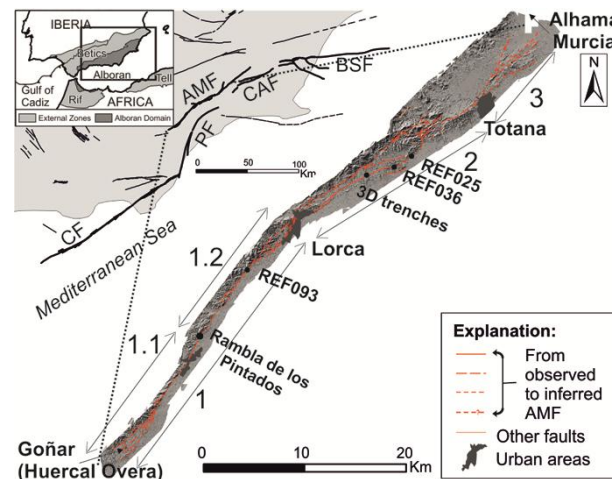


Figure 1. Geological setting of the Alhama de Murcia fault (AMF). Explanation: CF, Carboneras fault; PF, Palomares fault; CAF, Carrascoy fault; BSF, Bajo Segura fault. Inset modified from [36]. Southern segments of AMF and 3D excavation site [25,32] are highlighted. The studied area is covered by the lidar topography-derived DEMs (hillshade basemap). AMF segmentation: (1) Huercal Overa-Lorca segment, (1.1) Huercal Overa-Rambla de los Pintados subsegment; (1.2) Rambla de los Pintados-Lorca subsegment; (2) Lorca-Totana; and (3) Totana-Alhama de Murcia. Segment 4 (Alhama de Murcia-Alcantarilla; not shown) is beyond the limit of the lidar to the northeast of Segment 3. Locations of offset examples are presented by the points REF025, REF036 and REF093.

3. Data Sets Analyzed in this Study

To map offset features along the fault, we have used a 0.5×0.5 m pixel size Digital Elevation Model (DEM) and orthophotography created from 1956 aerial photographs (1:33,000 scale). We have created the DEM from a point cloud acquired in 2013 by airborne light detection and ranging (lidar). The area spans the southwestern termination of the AMF to Alhama de Murcia town to the northeast, and was delimited according to the geomorphology of the fault zone (Figure 1). The lidar data were acquired using a Leica ALS60 SN 6115 in a Cessna 404 aircraft flying at 1500 m altitude with a 150 kHz pulse rate, 18° scan angle and a width per pass of 975 m. The minimum return density in every pass is 4 points/m² with a mean separation between points of 0.5 m, and there are areas where the density reaches 8 points/m² due to pass overlap. The classified data allow the computation of Digital Surface Models (DSM, using both ground and non-ground points) and Digital Elevation Models (DEM, using just ground points) at 0.5 m per pixel (*cf.*, [37]). The orthophotos allowed us to examine sites that have suffered significant anthropogenic alteration since 1956. The orthophotography is available in a Web Map Service belonging to IDERM (Infraestructuras de Datos Espaciales de la Región de Murcia).

4. Proposed Methodology for Assessment of Cumulative Offset Markers

Inspired by existing scoring criteria for offsets along rapidly slipping faults [2,5], here we propose a more detailed way to rate offsets along low slip rate structures such as the AMF. We have divided the presentation into three parts. The first is the measurement *versus* uncertainty relationship, well expressed in the Probability Density Function (PDF) of each offset. We then propose differentiation of the quality scoring in two parts: (A) the subjective quality, which expresses the general confidence of the offset in terms of general geological knowledge; and (B) the objective quality, which is described in terms of three measureable geomorphic parameters (lithological changes, associated morphotectonics and shape). Both qualities have values between 0 and 1 and thus can be used for relative weighting of offset PDFs.

We apply this methodology to AMF along which we have identified and measured 138 left lateral offset features (.kmz file in the Supplementary Material), mainly stream channels (three ridge lines; from now on, we will refer to all features as channels, in general). The measurements and quality ratings were made by the first author, with cursory review from the other two authors. This rich and consistently measured and rated dataset has value for characterizing the Quaternary activity of the AMF (e.g., [25,36]), but also serves as a validation test of our proposed methodology.

4.1. Measurement and Uncertainty Relationship

Measuring the offset of a feature requires an estimate of its pre-deformation morphology [19]. In general, more than one piercing line can be defined (near and full channel projections; [10]). For the AMF offset dataset, we measured all possible combinations of piercing lines of landform elements (including channel rims, Figure 2). We compute mean and mean standard deviation for all the measurements (from two to nine measurements) obtained for the given feature. Mean and mean standard deviation define the Gaussian probability density functions (PDF). Mean standard deviation is 68.3% or 1σ of the PDF.

The relationship between the amount of displacement and the horizontal uncertainty in our AMF dataset do not follow the same proportionality for all features (Figure 3; that is, big offsets do not necessarily have big uncertainties and small offsets, small uncertainties) [17]. Extrapolate a logarithmic relation for uncertainty and offset.

4.2. Subjective Quality

The subjective quality score represents the individual confidence of the geologist when considering each offset. Inspired by [5], its values range between 0 and 1, where 0 is very low quality, 0.25 is low quality, 0.5 is medium quality, 0.75 high quality and 1 very high subjective quality. The experience of the geologist influences the rating [17]. Bond *et al.* [38] and Bond *et al.* [39] show that experience may be a big bias (availability, anchoring, and confirmation) when measuring. Incorrect geological interpretations may result if the conceptual model does not agree with reality. In that sense, experts tend to interpret geological data according to their expertise and previous knowledge (conceptual uncertainty) and they may not show a high confidence about their interpretations. Salisbury *et al.* [4], Scharer *et al.* [16], Salisbury *et al.* [17] and Bond *et al.* [38] propose that the results are better when

more techniques are used to approach the problem (multiple approaches to measurement both remotely and in the field in the offset landform case).

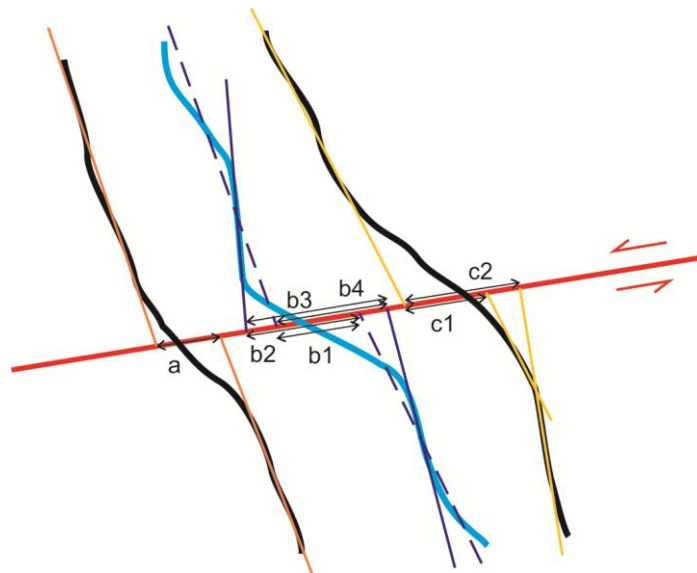


Figure 2. Schema used to define piercing lines (elements) and measure the offset of a channel crossing a sinistral fault (red line with arrows). Black lines are the rims of the channel and blue line is the channel thalweg. Piercing lines are defined for rims and thalweg separately and we consider near and longer length feature projections (solid and dashed). Letters indicate the channel feature taken into consideration and numbers refer to the number of measurements done with all possible combinations of piercing lines for each channel feature (rims and thalweg).

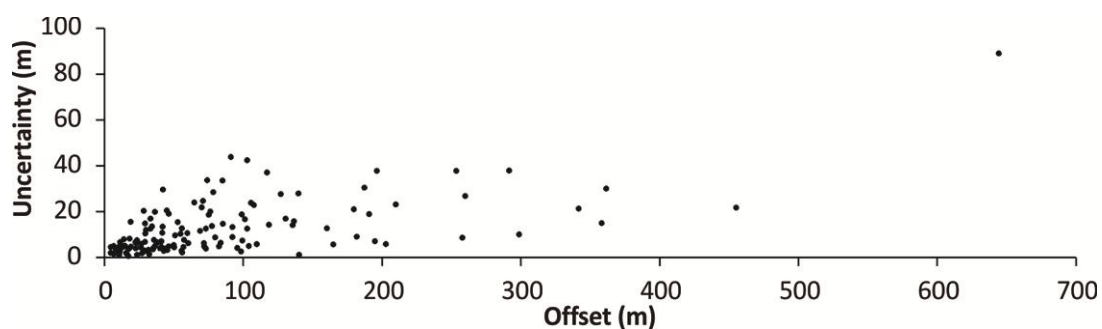


Figure 3. Relationship between offset and uncertainty for the 138 offsets measured along the Alhama de Murcia fault. Horizontal axis is the mean offset value for each feature (PDF mode), vertical axis is the mean standard deviation.

4.3. Objective Quality

The aim of this section is to suggest a scoring approach for geomorphic and geologic aspects of the offset feature, which influence our ability to reconstruct it. We name it “objective quality” because its rating relies on objective (but potentially arbitrary) repeatable metrics to minimize the inherent bias in the subjective quality. However, a minimum knowledge of geology is required.

Six parameters can describe an offset: (1) type (if the channel is entrenched in the basement or in an alluvial fan surface, or we are measuring a ridge line); (2) present-day preservation of the feature; (3) associated age control (absolute, relative or none); (4) lithological changes (if the fault coincides with a rock type change); (5) associated morphotectonics (the number of morphotectonic features spatially related with the analyzed feature); and (6) shape, which depends on three sub-parameters (fault zone width, difference in orientation between the two segments of the channel, and sinuosity; Table 1). The first three shape parameters cannot be easily and consistently scored in terms of objective quality. Nevertheless, they are useful for initial characterization during field or remote fault trace investigation. We move forward with the latter three parameters (objective quality metric parameters; Table 1) as contributors to an index of objective quality ranging from 0 to 1.

Table 1. Objective quality metric parameters (lithological changes, associated morphotectonics and shape) summary description.

Parameter Name	Description
Lithological changes	Fault coincides with a rock type change which controls resistance to erosion
Associated morphotectonics	Morphotectonic elements spatially related (Figure 4)
Shape	Depending on 3 sub-parameters: fault width, orientation of the channel, and sinuosity (Figure 5)

4.3.1. Lithological Changes

The feature receives one point if the rock

type where the channel is entrenched is homogeneous and 0.5 points if the fault coincides with a lithological change. Where the fault puts in contact two different rock types, it is easier to map the fault line scarp. The purpose of this parameter is to represent the possibility of a stream changing its direction because of differences in resistance to erosion of the geologic material rather than active faulting.

4.3.2. Associated Morphotectonics

This parameter reflects the number of other spatially-related morphotectonic features in the vicinity of an offset feature. The significance of an offset feature increases with the presence of others nearby to indicate the consistency of the assignment of fault activity to any given feature. Klinger *et al.* [3] use a similar approach in which they count the number of elements reconstructed using a certain amount of back-slip within 100 m of a specific offset feature. The rating they give to every feature is the number of coinciding elements.

Inspired by [3], our goal here is to score the feature between 0 and 1 by considering the presence of associated morphotectonic features. Thus, we propose a modification of their methodology. For each feature, the region for identifying spatially-related morphotectonic elements is defined by the intersection between (1) the approximate mean width of the fault trace zone along the entire fault; and (2) a circle around the central point of the feature that has a radius of half of the offset measurement plus 200 m (Figure 4). This modification is appropriate for more geometrically complex fault traces such as those

along the AMF. For the AMF, we chose 40 m for the fault zone width because it is an intermediate value between the approx. 20 m of fault zone width observed in the 3D trenches [35] and the approx. 100 m of fault gouge in a geophysical borehole [40].

The specification of the search radius around every feature was defined after comparing the values obtained for four different lengths (Figure S1). The candidate radii were: (1) ten times the offset; (2) the mean offset plus 100 m; (3) the mean offset plus 200 m; and (4) half of the mean offset plus 200 m (Figure S1). For the three first cases, the radius depends too much on the offset, especially for the first one, whose dimensions for big offsets do not match any geological criteria. Although it is the search radius used by [3], the 100 m search radius for Alhama de Murcia fault is too small. The fourth option (half of the mean offset plus 200 m) is our final choice because the influence of the offset measurement on it is lower and the addition of 200 m to the radius makes sense along a slow moving fault given the interplay between surface processes and fault activity.

Each offset feature receives 10 points if its deformation occurs within the fault zone, and one extra point for every morphotectonic feature set inside the area of intersection. The considered morphotectonic elements are: (1) another offset channel; (2) fault parallel valleys; (3) scarps; (4) triangular facets; and (5) shutter ridges. The related feature need not be completely within the intersection zone to score (Figure 4). In places where the fault is comprised of more than a single fault trace, the search area takes into account just those elements related to the fault trace that offsets the considered feature (Figure 4). The maximum points we obtained for the AMF offsets are 16. As it is required that the associated morphotectonics score ranges between 0 and 1, we thus divided the points obtained for every feature by 16.

We are aware of the arbitrariness of this parameter. In fact, the final scoring depends basically on how many morphotectonic features are mapped. This mapping is subjective, especially along slow or moderately-moving faults where the geomorphology related to the fault activity may be weakly evident. Nevertheless, we use this parameter in the objective quality because the consideration of a feature to be analyzed also must take into account the associated mapping uncertainty.

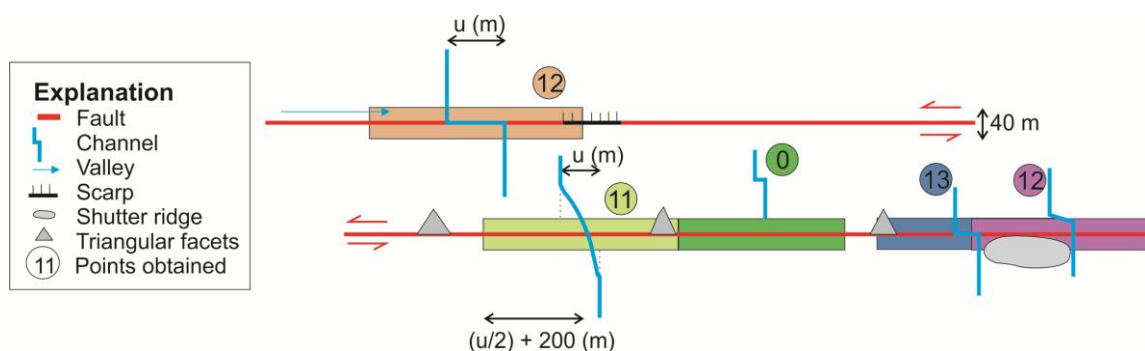


Figure 4. Illustration of the associated morphotectonics scoring for the AMF. The defined boxes are the intersection area between the width of the AMF fault zone (40 m) and the search radius circle around the central point of the feature of half of the offset measurement (u) plus 200 m. Each offset is indicated by the different colored boxes and circled point score. For example, the uppermost (orange) feature has 12 points because the deformation occurs within the fault zone and there are two morphotectonic features (fault parallel valley and scarp) spatially related with it.

4.3.3. Shape

The shape parameter can be decomposed into three sub-parameters: (1) fault zone width; (2) angular difference in orientation between the two parts of the considered feature (on either side of the fault); and (3) sinuosity of the channels. Figure 5 illustrates the rating according to the three sub-parameters (modified significantly from [17]). Every time one sub-parameter decreases one step along its axis, the value of the final shape scoring decreases 0.15 (Figure 5). The three sub-parameters can be considered separately, as well. In this case, every step of increase sub-parameter represents 0.45 points of decrease in the value of its scoring. For example, sinuosity would take ratings 1, 0.55 and 0.1 as it increases. The shape scoring would be the same when considering them (fault zone width, sinuosity and difference in orientation) separately, as values and decrements are proportional.

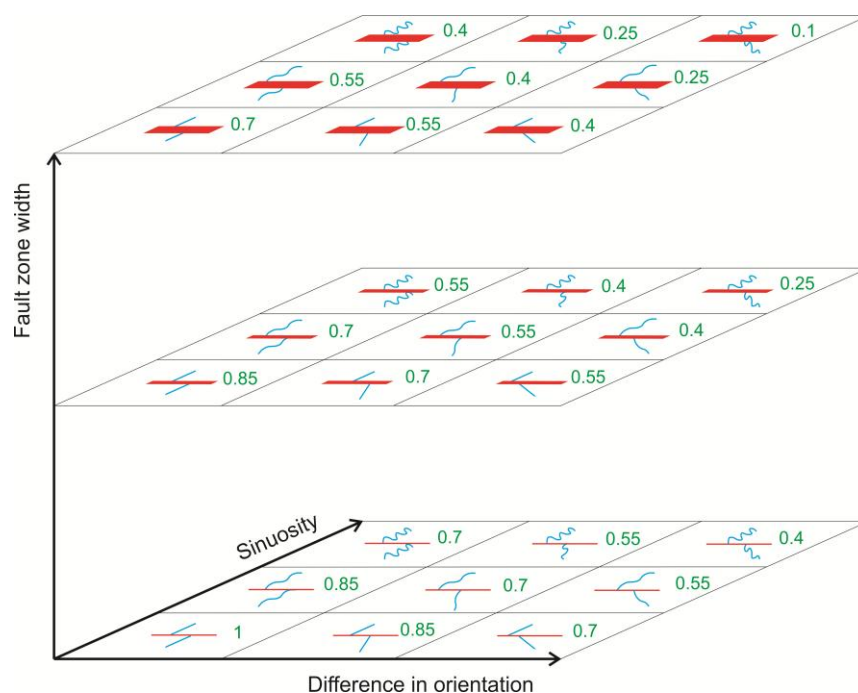


Figure 5. Offset shape rating. Three axes represent shape sub-parameters: fault zone width, difference of orientation of the two segments on each side of the fault and sinuosity. Blue lines are the channels, red lines are the fault zones (thickening with width), and green numbers are the shape scoring for every combination of the sub-parameters. Keeping two of the axes constant, shape rating decreases 0.15 points every step in the other axis, making it possible to have values between 1 and 0.1.

4.4. Final Scoring of Objective Quality

The final score of objective quality is an average of the three parameters, taking into account that “shape” is composed by three sub-parameters, where a is lithological changes, b is associated morphotectonics and c is shape (Equation (1)). The shape parameter is multiplied by three because in fact it is made of three sub-parameters. This way, we weigh the real contribution of the three sub-parameters composing “shape”.

$$\text{Objective quality} = \frac{a + b + 3 * c}{5} \quad (1)$$

5. Application of the Proposed Method to the Alhama de Murcia Fault

We have applied the proposed methodology to the 138 left lateral identified offsets caused by Alhama de Murcia fault (AMF), specifically between Huercal Overa and Alhama de Murcia. Segment 4 (Alhama de Murcia-Alcantarilla) is not evaluated in this study due its diffuse geomorphic manifestation. Along with the measurement of the offset and its uncertainty, quality for every feature is determined. Determination of all objective parameters enabled calculation of the objective quality. Figures 6–8 show examples of the measured features (including qualities and some piercing lines). Values of subjective quality and objective quality can be very different and independent from the mean offset and uncertainty. The same analysis for the rest of the features can be found in the Supplementary Material (.kmz file).

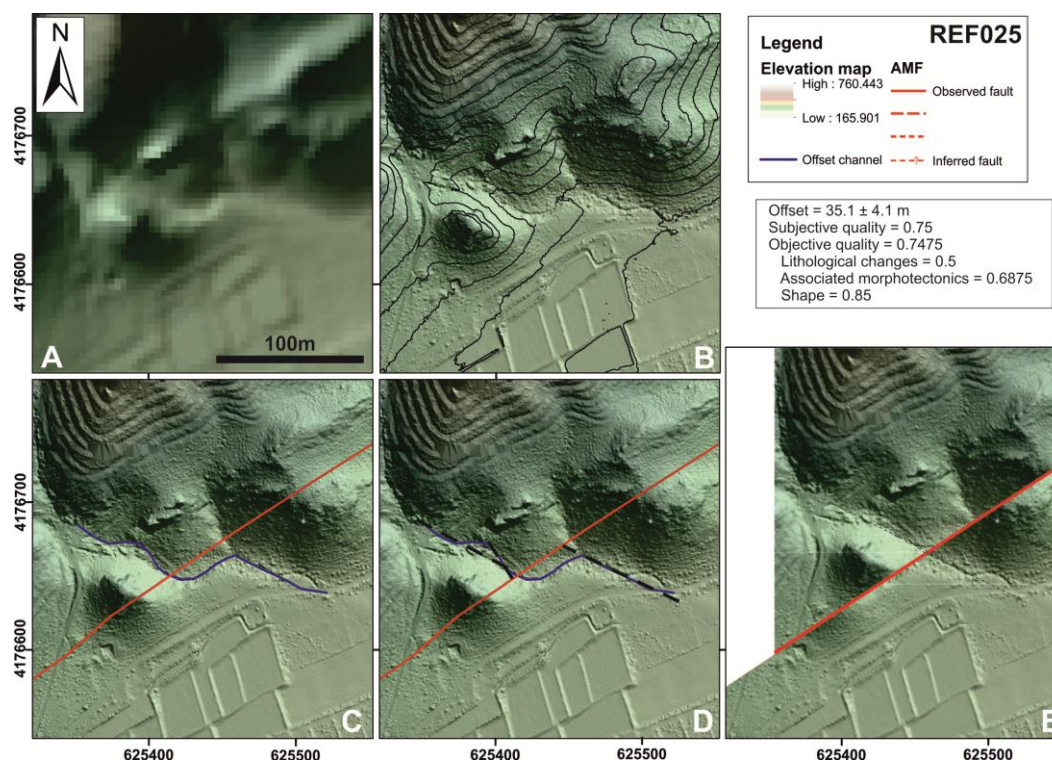


Figure 6. Interpretation of offset REF025—An example where two types of qualities (subjective and objective) are the same: (A) old Digital Elevation Model (DEM) with a resolution of 4 m; (B) new lidar derived hillshade and 5 m contour map; (C) new lidar derived hillshade showing the location of the fault and the offset stream; (D) lidar derived hillshade showing some projected piercing lines (**black dashed lines**); and (E) back slip model of the offset. Offset in meters. See location on Figure 1.

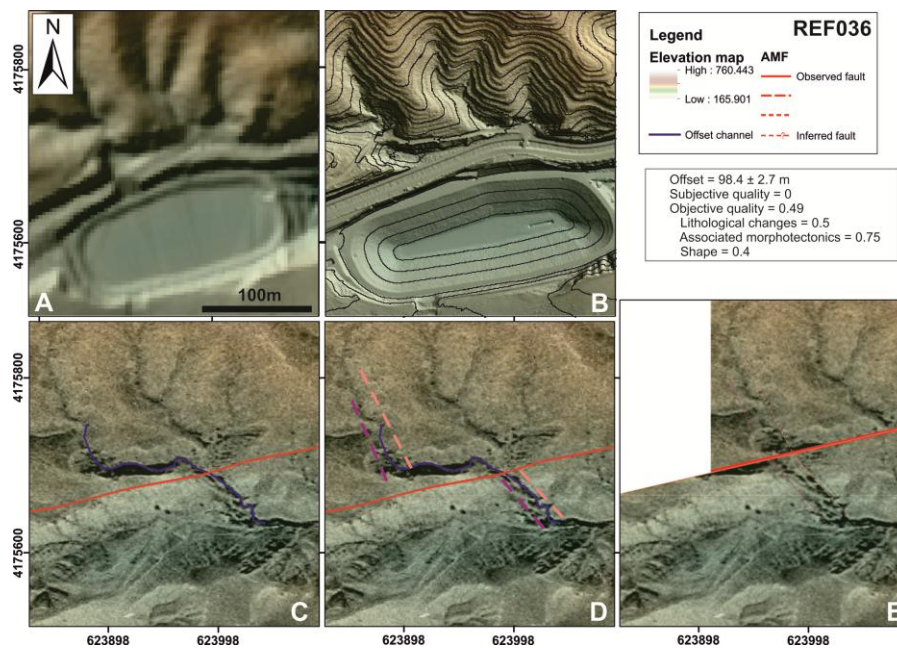


Figure 7. Interpretation of offset REF036—In this example, objective quality is larger than subjective quality: (A) old Digital Elevation Model (DEM) with a resolution of 4 m; (B) new lidar derived hillshade and 5 m contour map; (C) 1956 ortophoto showing the location of the fault and the offset stream; (D) 1956 ortophoto showing some projected piercing lines (**pink dashed lines** represent the left bank of the channel, and purple lines the right bank looking downstream); and (E) back slip model of the offset.

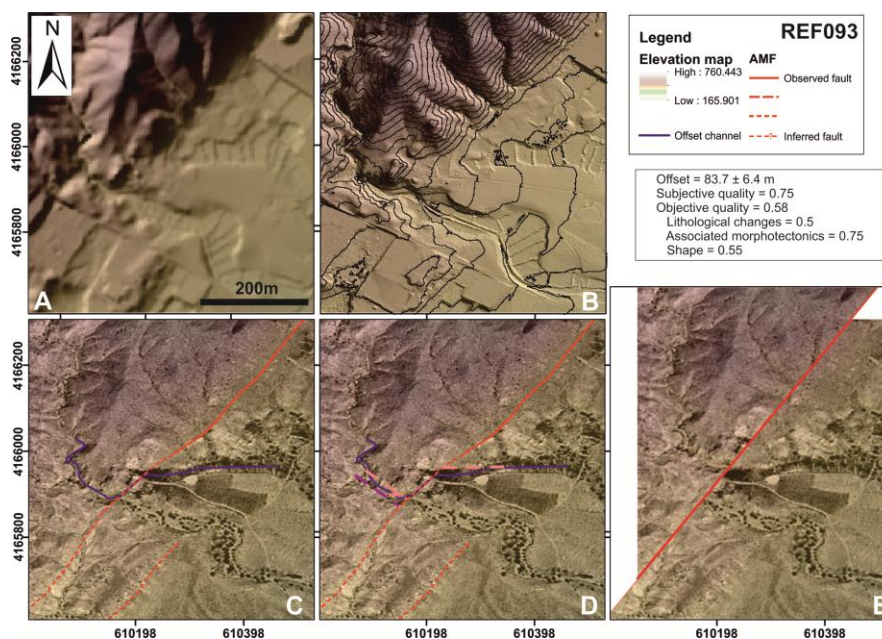


Figure 8. Interpretation of offset REF093—Subjective quality is larger than objective: (A) old Digital Elevation Model (DEM) with a resolution of 4 m; (B) new lidar derived hillshade and 5 m contour map; (C) 1956 ortophoto showing the location of the fault and the offset stream; (D) 1956 ortophoto showing some projected piercing lines (**pink dashed lines** represent the left bank of the channel, and purple lines the right bank looking downstream); and (E) back slip model of the offset.

6. Methodological Discussion

In this section, we present the methodological results as applied to the AMF dataset and discuss prospects for future application of the method. We focus on the differences between the two types of proposed quality types (subjective and objective) and on the chosen objective parameters.

6.1. Types of Quality

The first comparison is between the subjective and objective qualities in general. To do that, we consider both qualities as equally valid in scoring the offsets. The objective quality values are in general larger than the subjective ones (Figure 9). The visual correlation between both values is not strong. The residual differences between the values range between -0.27 and 0.53 (objective quality minus subjective quality). These differences suggest the need to score subjective and objective values separately as they do reflect different aspects of the rating. The fact that the subjective values are lower than the corresponding objective ones probably reflects the confidence of the geologist who is analyzing the offset features.

Another comparison is between both qualities and the offset (Figure 10A). There is no correlation between the amount of offset and its scoring qualities. The resulting subjective and objective contours are displaced 0.1 to 0.3 points vertically. This indicates that in general all features have better objective scoring than subjective scoring (e.g., Figure 9).

There is no correlation between any of the proposed qualities and the mean standard deviation of the measurements (uncertainties) (Figure 10B). As there is no dependency between uncertainty and either quality scoring, we suggest the necessity of including these types of scoring in offset analysis. These values can be used in weighting individual PDFs before the calculation of the COPD ([5] and others). That way, we can include subjective and objective quality criteria in the final analysis.

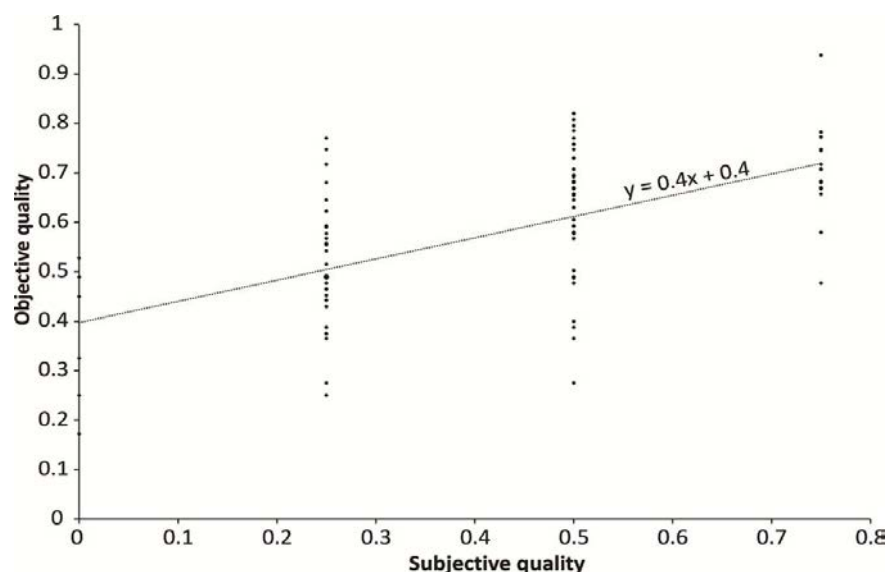


Figure 9. Plot of subjective *versus* objective quality. The equation of the correlation line was added as a reference.

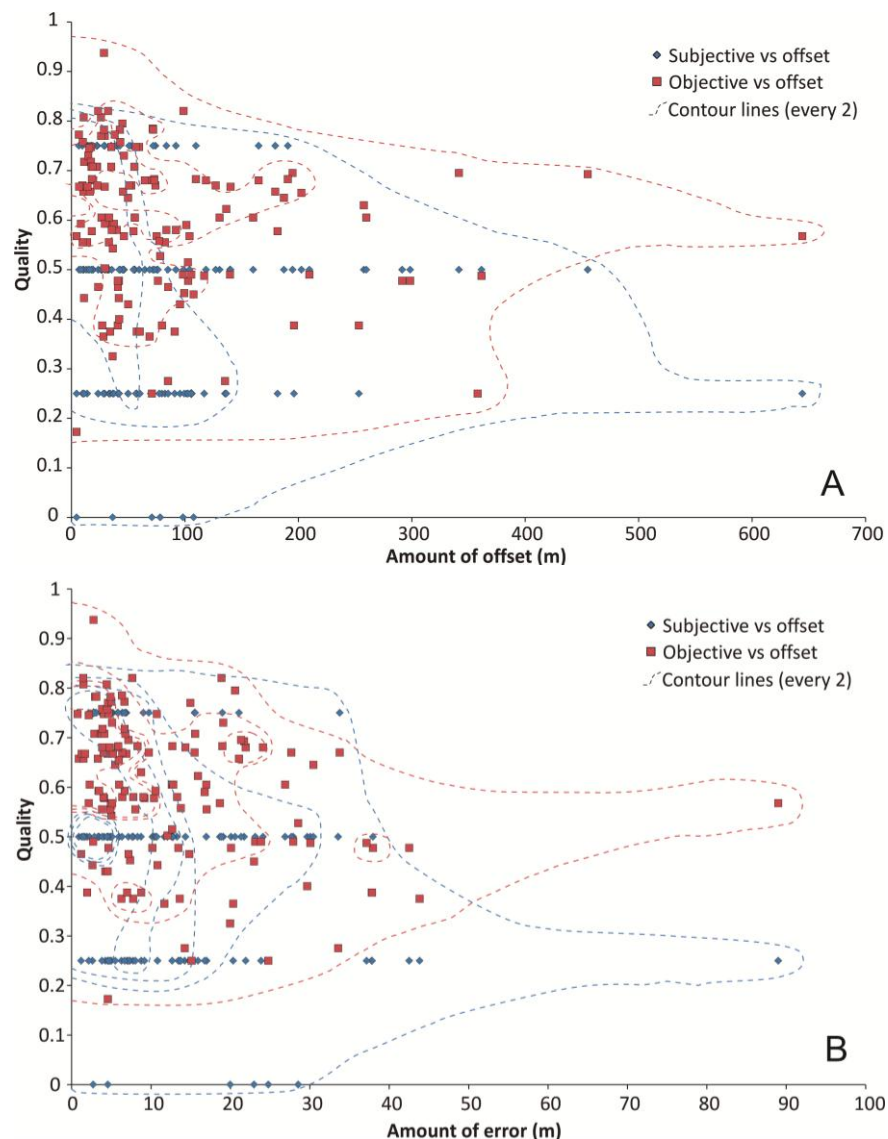


Figure 10. (A) Relation between quality and amount of offset. Objective quality scoring is red and subjective quality scoring is blue. Density contour lines represent the number of measurements in a grid of offset *versus* quality. In general, objective scores are higher than subjective ones. (B) Relation between quality and uncertainty. Objective quality scoring is red and subjective quality scorings is blue. Density contour lines representing the number of measurements in a grid of error *versus* quality. There is no correlation between qualities and the error magnitude.

6.2. Objective Quality Parameters

Objective quality ratings range between 0.18 and 0.94 (Figure 11), and 99 out of 138 offsets score more than 0.5 in objective quality. This implies that almost 75% of the measured offsets along the Alhama de Murcia fault have moderate-high to high given the framework of this study.

In general, objective quality correlates with shape (Figure 11A), thus shape increases when objective quality increases. Although shape contributes 3/5 (60%) to the objective scoring (Equation (1)), the contribution of the shape in the relative contribution plot (Figure 11B) is constant (about 50% of the total objective scoring). This constant contribution is a significant difference compared to the other

objective parameters (lithological changes and associated morphotectonics). Additionally, the average differences between the shape scoring and the objective quality tend to zero (exceptional cases range between -0.25 and 0.25 ; Figure 11B).

These small differences, together with the fact that its contribution to the objective score is constant, suggest that the shape rating by itself can be indicative of the whole objective quality. The objective scoring approximation based just on the shape parameter may be useful in those cases where “associated morphotectonics” parameter cannot (or the geologist does not want to) be used, for instance, when few morphotectonic features are evident.

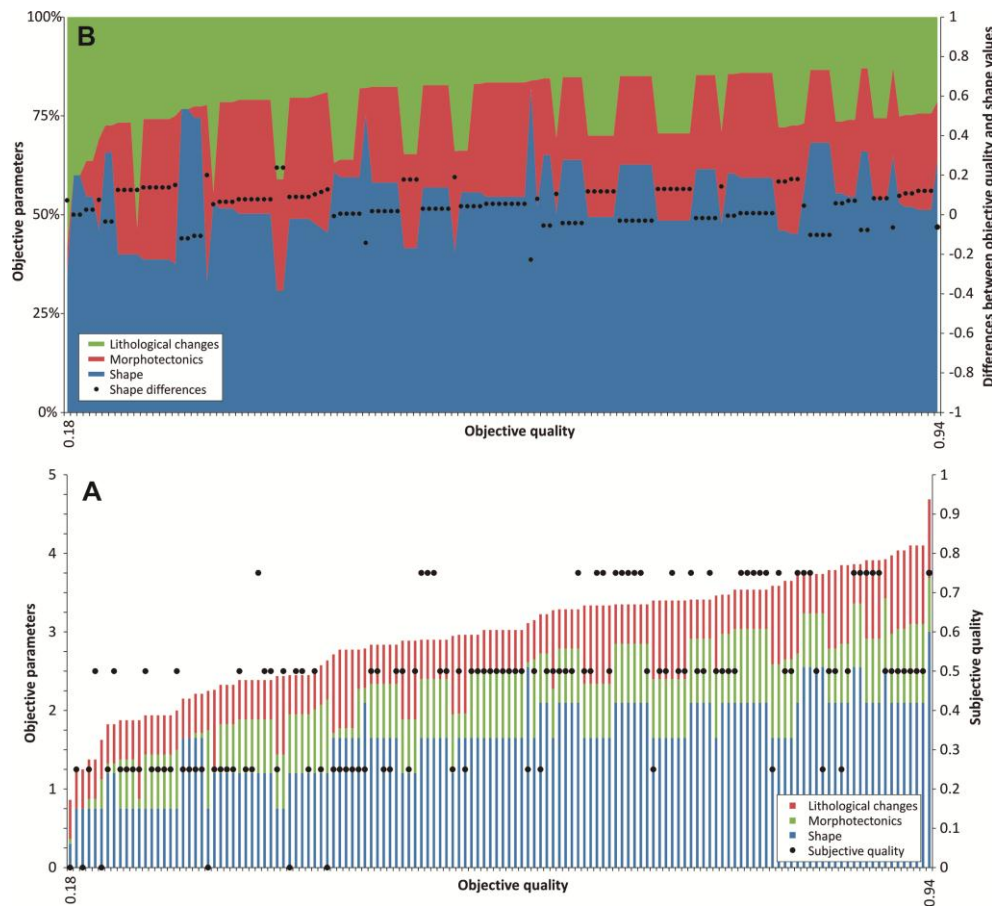


Figure 11. (A) Plot of individual offset objective parameters *versus* total objective quality (left axis). Each parameter’s contribution is shown in a different color. The right axis scales the corresponding subjective scoring (dots) for comparison. The shape score evidently scales the total objective score. (B) Plot of normalized objective parameters (left axis *versus* total objective quality). Every parameter is shown in a different color to make easier to identify the relative contribution of it to the whole objective score. Right axis is the difference between objective quality score and shape rating (objective quality minus shape scoring). The values of this difference range between -0.23 and 0.24 . The relative contribution of shape parameter to the objective quality is constant.

On the other hand, there is not a clear correlation between the subjective quality rating and any objective parameter (Figure 11A). Given that the shape parameter contributes $\sim 50\%$ of the total objective quality, the correlation between shape parameter and subjective quality is similar to the

correlation between both qualities (Figure 9). As argued before, this correlation is not strong enough to be used, and thus we do not use the correlation between shape parameter and subjective quality either.

6.3. Qualities and Parameters Correlation—Summary

As expected, the best correlation occurs between objective quality and the shape parameter (see Table 2 for a summary of correlations of qualities and parameters). Even the “shape” itself represents the 60% of the objective scoring (Equation (1)), this correlation is close to 0.9 and has a 100% level of confidence, confirming that shape is the best indicator of objective quality (Table 2, green cell). This high value supports the validity of the correlation despite the fact that Equation (1) favors it, and thus the correlation strengthens. Likewise, minor correlation between objective and subjective qualities is evident (orange cells with value of 0.6; Table 2). On the other hand, minor and unexpected correlations exist between objective quality and associated morphotectonic parameters and between the amount of measurement and its uncertainty.

Table 2. Multivariable correlation moment Pearson product values between qualities and parameter pairs. Values between -1 and 1 indicates the goodness of the linear relationship (values closer to -1 and 1 are better). The lower value is the confidence value of the correlation; values under 0.05 indicate confidence levels of more than 95%. Green indicates good values; orange are fair values; and red cells are poor correlations. The best correlation is between objective quality and shape. There is a fair correlation between measurement and uncertainty, subjective and objective qualities, and between objective quality and associated morphotectonics.

	Shape	Associated Morphotectonics	Lithologic Changes	Objective Quality	Subjective Quality	Uncertainty	Measurement
Measurement	−0.19	0.01	−0.10	−0.17	−0.11	0.63	1
	0.03	0.93	0.23	0.05	0.22	0	0
Uncertainty	−0.33	−0.01	−0.19	−0.30	−0.25	1	
	0	0.90	0.03	0	0	0	
Subjective Quality	0.57	0.46	0.07	0.61	1		
	0	0	0.42	0	0		
Objective Quality	0.88	0.60	0.41	1			
	0	0	0	0			
Lithologic Changes	0.10	0.02	1				
	0.26	0.79	0				
Associated Morphotectonics	0.31	1					
	0	0					
Shape	1						
	0						

7. Implications for Active Tectonics Investigations

In this section, we examine the distribution and degree of offset clustering of the measured offsets along the AMF to infer fault segmentation and slip rate. The measured offsets (with their uncertainty) along the fault show no evidence of offset clustering (Figure 12). There is no evident relationship between any type of quality and the location along the fault. The histogram in Figure 13A displays no clustering, but it shows the previously suggested offset identification decay with the length of the offsets (e.g., [1,3,6]). This histogram accounts for measurement uncertainty for each offset. In order to obtain clear clusters of amount of offset, we follow the methodology developed by [5] (originally demonstrated by [18]). We sum the individual PDFs (Figure 13B) to produce a COPD with several peaks (Figure 13C). These peaks represent amounts of offset measured with more frequency along the stacking reach (Figure 13C). No clear regularities in the peak position and in the distance between peaks are observed. As expected, we cannot identify individual seismic events, in contrast to what is possible along fast-slipping faults [2,5]. Moreover, accounting for objective and subjective qualities, two additional weighted COPDs are produced (Figure 13D). We weighed the area of every individual PDF with the subjective and objective qualities (Figure S2). This results in two curves with lower and missing peaks compared to the initial COPD (Figure 13D).

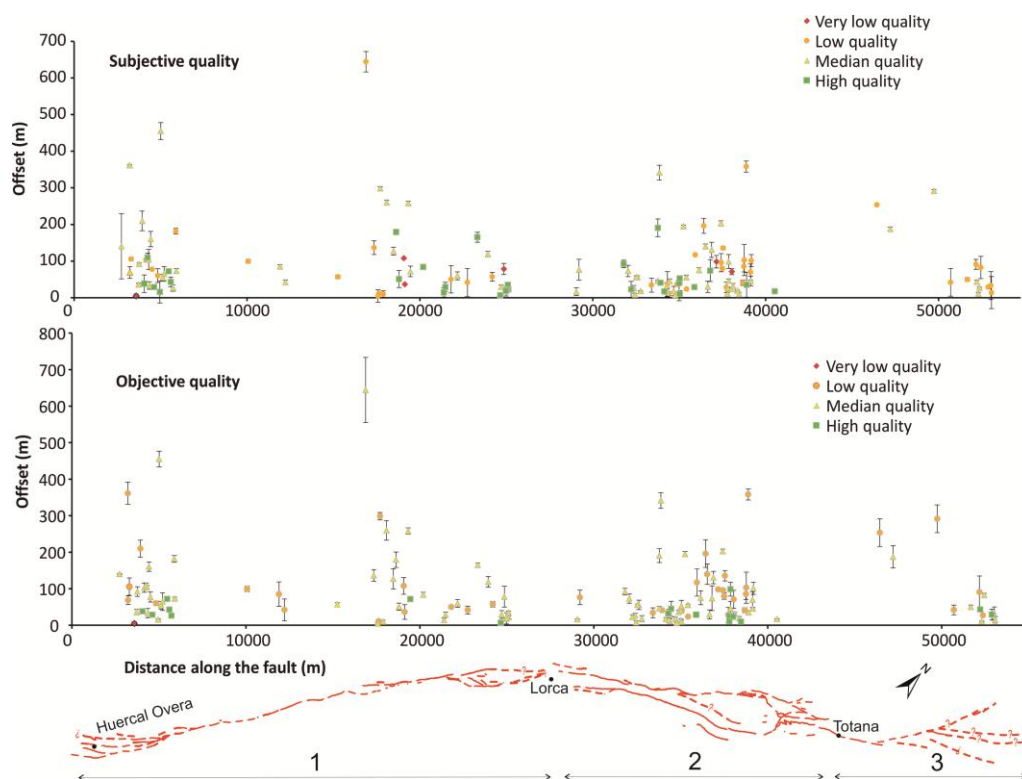


Figure 12. Offset geomorphic features along the Alhama de Murcia fault. Error bars represent uncertainties (mean standard deviation values, 1σ). Scoring for both subjective (**upper plot**) and objective (**lower plot**) quality are represented with different symbols. Objective or subjective quality legend: [0–0.25), very low quality; [0.25–0.5), low quality; [0.5–0.75), median quality; [0.75–1], high quality. No clusters on the amount of offset are evident in these plots. The AMF trace and its segmentation (see Figure 1 for numbers explanation) are shown at the bottom of the figure.

The COPD of all of the data (Figure 13C,D) does not take into account the characteristics of the individual fault segments (Figure 1). Even if we assume that all the fault segments have the same characteristics (e.g., slip-rate), where the fault is composed of several fault traces, the individual parameters will vary. Therefore, we do the same analysis considering individual segments and individual fault traces (Figure 14). COPDs are computed for Segments 1.1 (Huercal Overa-Rambla de los Pintados), 1.2 (Rambla de los Pintados-Lorca) and 3 (Totana-Alhama de Murcia) where the fault is a single trace; and for segments where the fault splays: (a) three fault traces in the horse-tail termination; (b) the sub-parallel traces in Segment 2 (Lorca-Totana); and (c) for two traces in the Totana-Alhama de Murcia segment (Segment 3).

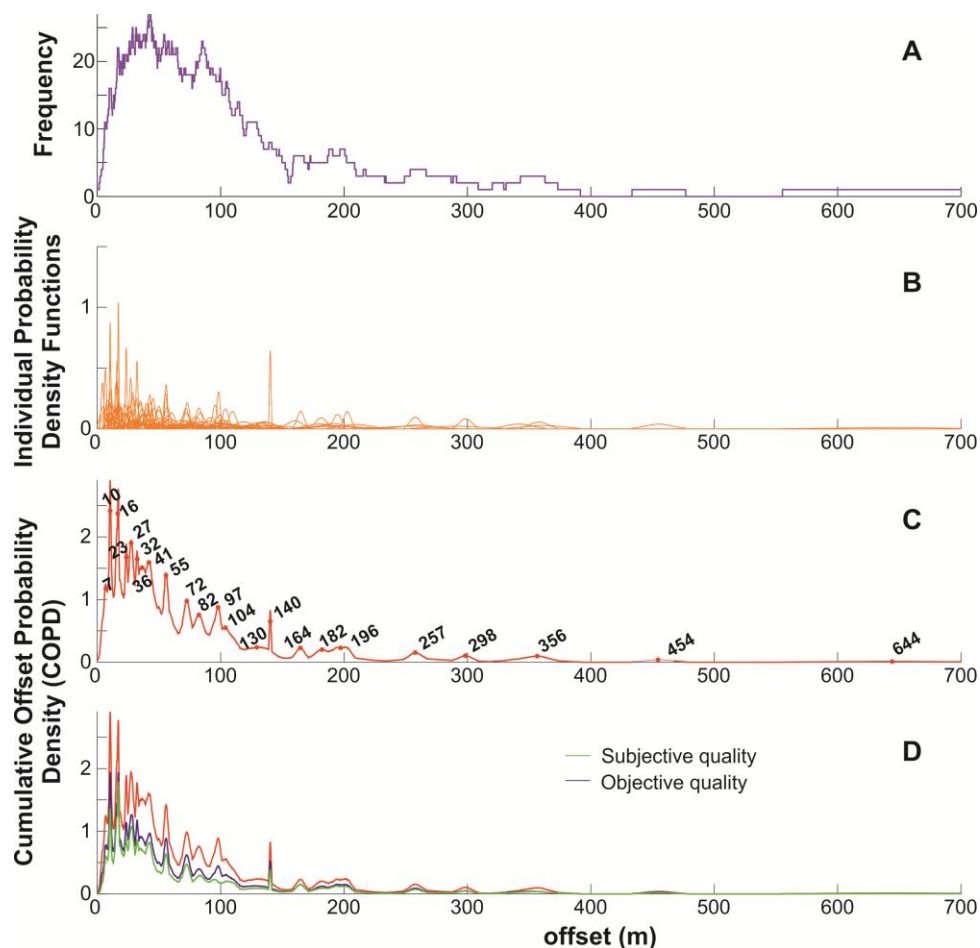


Figure 13. (A) Histogram of the offsets and uncertainties. (B) Individual Probability Density Functions (PDF) of all features along the fault. (C) Cumulative Offset Distribution Probability (COPD) with no weighting and peak values highlighted. (D) COPD weighted previously with subjective (**green**) and objective (**blue**) quality score. Notice the difference in the vertical axis in the probability values (B–D). In general, the subjectively weighed COPD (**green line**) is lower than the objective COPD (**blue line**).

The COPDs enable the identification of groups of offset features along the entire fault and by segments. We assume that the stacking of individual PDFs reinforces signals of common offset along analyzed fault reaches. Although fault segments usually are classically defined by geological, geomorphological and geophysical observations and inference [30,31], the analysis of the COPDs may

provide additional information on common amounts of offset further refining the location of segment boundaries and possibly highlighting slip rate variability between segments. To explore if all segments of the fault have the same slip-rate, we assume that all the features with the same offset were entrenched or formed at the same time, and thus, due to fault activity, they display the same amount of offset.

The COPDs of fault segments and traces are clustered. The best example is fault trace 2.2, where 15 offset features cluster in four peaks. Clustering is also evident along fault Segment 1.1 (three offsets in two peaks), in fault traces 1.11 and 3.2 (6 offsets in 4 peaks) and in fault trace 2.3 (28 offsets in 10 peaks).

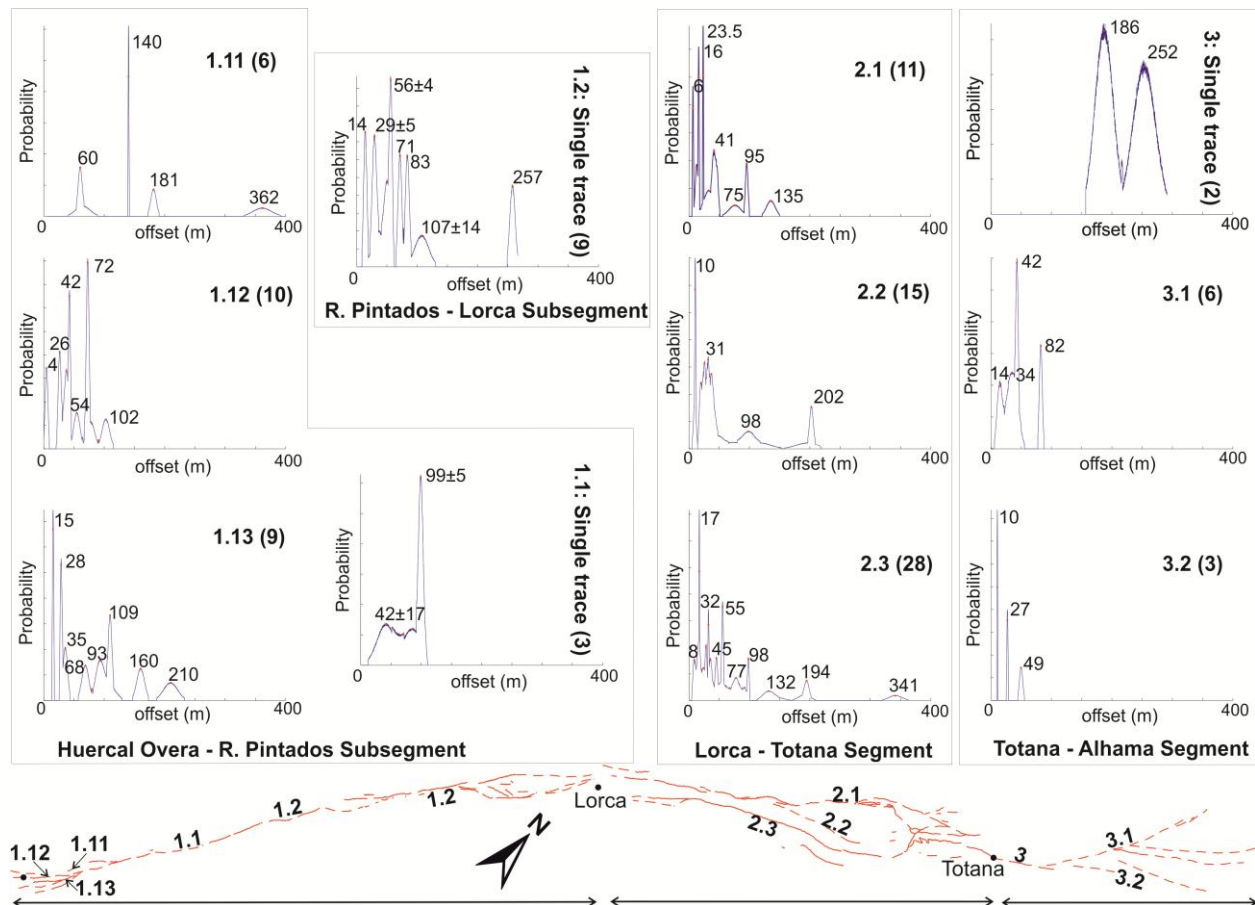


Figure 14. Individual non-weighted COPDs for the considered fault segments and fault traces (see text). The fault trace that corresponds to every COPD is indicated by number. Alhama de Murcia fault segmentation according to [29] (see Figure 1 for location and explanation). In brackets, the number of measurements involved in every COPD.

The first comparison between COPDs is made between Segments 1.1 and 1.2 (Huercal Overa-Lorca sub-segments). Two peaks coincide in these segments: (a) 42 ± 17 (Segment 1.1) and 56 ± 4 (1.2); and (b) 99 ± 5 (Segment 1.1) and 107 ± 14 (1.2). Despite the identification of only three offsets along Segment 1.1 (Huercal Overa-Rambla de los Pintados), the two common modes between Segments 1.1 and 1.2 support an inference that both sub-segments have the same slip-rate. Thus, there may be no need to divide the segment Huercal Overa-Lorca in two, as other geological data suggest [29,36].

The second comparison is done between Segments 1 (Huercal Overa-Lorca) and 3 (Totana-Alhama de Murcia). The low geomorphic evidence of Segment 3 (only two offsets where the fault is expressed

as a singular trace) limits the comparison. Thus, the coincidence between the peak in 252/257 m is not a sufficient condition to suggest that both segments have the same slip rate, because there are no other geological evidences.

The last general comparison is between sub-parallel fault traces within the same segment. The first case is the southwestern end of Segment 1 (Huercal Overa-Lorca) characterized by a horse-tail termination [30,31,34], where the COPDs along the fault traces show no common modes. Similarly, mismatched peaks exist for the traces (traces 3.1 and 3.2) in Segment 3 (Totana-Alhama de Murcia). We infer that variations in orientation of the individual fault traces within these zones result in accommodation of different amounts and styles of deformation, possibly resulting in slip rate variability.

Segment 2 (Lorca-Totana) has three fault traces (2.1, 2.2 and 2.3) along most of its length. The orientation of the segment (N 45 E) differs from the orientation of the other segments (N 65 E). This change in strike results in a higher vertical component of slip which may promote stream entrenchment [41]. As the slip here is divided in three fault traces, we cannot compare this segment with the others. Along strike of Segment 2, the four peaks of the COPD of fault trace 2.2 (10, 31, 98 and 202 m) coincide approx. with the amount of offset of the peaks 8, 32, 98 and 194 m in trace 2.3. According to our assumption (segments with similar COPDs have the same slip rate), fault traces 2.2 and 2.3 would thus slip at a similar rate. However, a geological criterion suggests that fault trace 2.3 has a higher slip rate, as its geomorphic expression is sharper (recent paleoseismic excavations, [25,32]). Thus, even if the entrenchment occurs at the same time along each of the traces, fault activity influences the number of preserved accumulative offsets.

In summary, the COPD analysis supports the previously defined fault segments, but the analysis should be done for fault segments with sufficient offset features identified along them. Fault segments that differ in orientation cannot be compared with the COPD, as deformation is absorbed in a different way (for example in segment Lorca-Totana). The analysis of the COPD allows relative comparison of the slip rates along the segments. It is not possible to calculate the slip rate by itself (this point is discussed in section 8). Moreover, even with good correlation, the coincidence of clusters between fault segments is not a sufficient condition to confirm that two fault traces have the same slip-rate as other geological criteria have to be taken into account (*i.e.*, geomorphic expression and paleoseismological results).

8. Entrenchment Correlation with Climate Variation

The main control in the relationship between erosion and accumulation in a fluvial system is the amount of protective vegetation cover in the area, and this varies with climate (strongly argued by [20]). Bull [20] do not specify which type of climate changes cause the loss of plant cover. Some authors relate alluvial fan aggradation with interglacial stages [6,14]. Alternatively, based on soil dating in SE Iberian Peninsula, [42] concluded that sedimentation occurs during glacial stages due to landscape instability. Their results indicate that climate during glacial stages in the southeastern Iberian Peninsula is apparently cold and dry, suggesting that climatic characteristics may vary regionally within individual marine isotope stages.

In this section, we explore the correlation between COPD with climatic curves to explore preferential climate channel entrenchment in the region. This information may be used in the future as a proxy to indicate the age of sedimentary units in which channels have entrenched, especially in a site where numerical dating is challenging. To do that, we assume that climatic variations triggered channel entrenchment synchronously across the region. If this assumption is correct, the channels (along the same fault segment) that were entrenched at the same time should display the same amount of offset. The peaks in the COPD for that segment represent these amounts of offset. As climatic events are well represented in the climatic curves, we compare the COPD with them [6]. This comparison has to be done with age control. In this test, we also consider other causes for channel entrenchment such as pulses of uplift.

Several authors have related known ages of depositional units (related to offset features) with climatic events [6,8,11,14]. In general, few offset features with age control are available to relate climatic events with entrenchment. Van der Woerd *et al.* [6] have well constrained ages of the (<20 ka) terraces into which the offsets are etched along Kunlun Fault (Tibet), and thus they compare the COPD with a climatic regional curve. They align the two equivalent portions of the curve and then extrapolate the ages to the largest offsets assuming a constant slip-rate of 11.5 mm/year. Moreover, they assume that the deposition of the dated fluvial terraces and the entrenchment happens always in interglacial periods because during glacial times that area is covered by ice. Chevalier *et al.* [11] analyze terraces as well, following the same methodology that [6] used, but their geological units are much older (up to 200 ka). They are able to correlate periods of fluvial deposition with interglacial periods along the Karakoram fault (>5 mm/year slip rate). Ferry *et al.* [8] analyze the offsets close to a lake. They correlate the age of the channels with known decreases of the lake level. Finally, [14] do not have dated units but assume that the analyzed features were entrenched in interglacial periods in order to obtain the slip-rate for Idrija fault (1.5 mm/year).

The COPD and climatic curve (e.g., $\delta^{18}\text{O}$ or paleotemperature) can be also compared according to the position of their peaks or troughs if we assume that the channels entrench synchronously with extreme of the climate proxy and a constant slip-rate. One problem we face when comparing the curves by their shapes alone is the attenuation of the geomorphic record (Figure 13A; [3]). The data for Alhama de Murcia fault presents the same decay relationship (Figure 13), and thus we did not further pursue this approach (along with the tenuous underlying assumptions).

Age control along the AMF is limited; however, at least one age is necessary to align the climatic and the COPD curves (assuming a constant slip rate). We have just one numerical age [25,35] and a few relative ages [30]. Moreover, the soil and landform chronosequence for the southeastern Iberian Peninsula is not well constrained [43] and there are no more chronosequences for similar climates in the Mediterranean region. The preliminary results in 3D trenches (Figure 1) show a buried approx. 15 ka channel (age determined by correlation with trenches in [25]) that displays 15 m of offset [35].

As there is just one absolute age, we use the relative ages as well. For offset features with the same relative maximum age (the maximum age of a channel is the age of the alluvial unit it is entrenched in), the feature with the largest amount of offset provides the maximum estimate of slip-rate (Figure S3). As discussed in the previous section, not all segments have the same slip-rate. Thus, the comparison both COPD and climatic curves have to be done for the individual segments. Just one of the maximum

slip-rates plotted in Figure S3 belongs to a feature set in a zone where the fault displays a single trace (Segment 1.2, Offset REF095: 258 m in 200 ka).

The comparison between climatic and COPD curves is done in Segment 1 (Huerca Overa-Lorca) and in Segment 2.3 (Lorca-Totana) (Figure 15). We employ the global sea level based on a benthic $\delta^{18}\text{O}$ curve constructed from 57 globally distributed records [44] and regional curves (based on drilling cores in the Alboran Sea) of [45] (benthic $\delta^{18}\text{O}$ curve) and [46]. This last curve was constructed from planktonic $\delta^{18}\text{O}$ curve and it represents the mean sea surface temperature. This last curve is a good reference for regional temperatures.

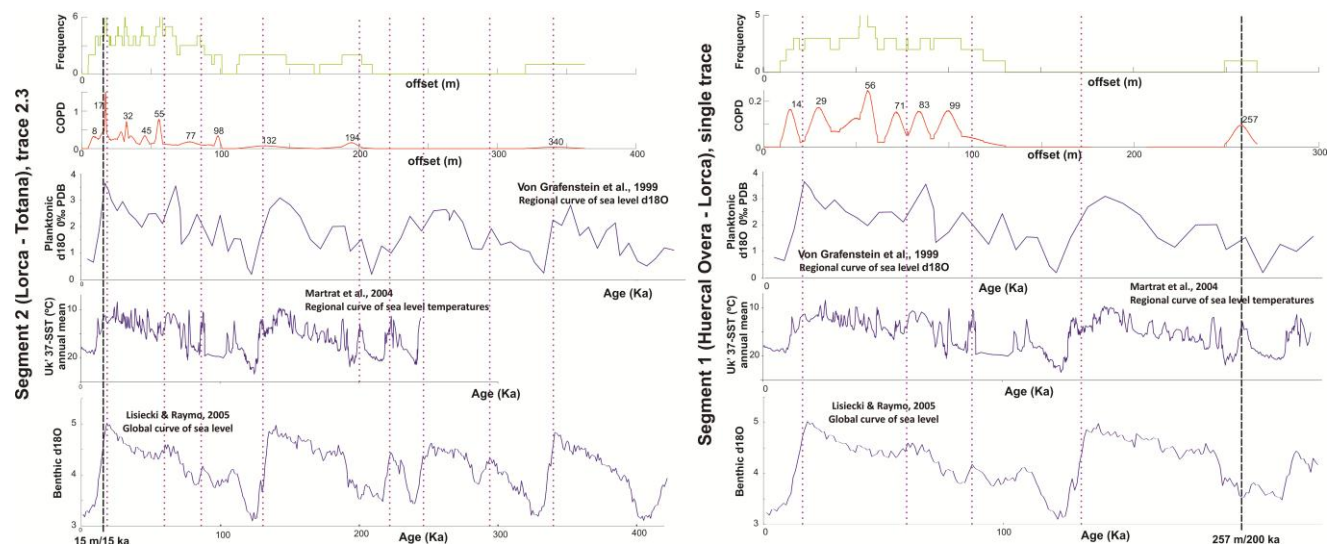


Figure 15. Correlation between the COPD (without weighting) of Segment 1 and trace 2.3 and climatic curves. Climatic curves are (1) the regional planktonic $\delta^{18}\text{O}$ curve in the Alboran Sea [45]; (2) the regional mean sea surface temperature of the Alboran Sea [46] and the benthic $\delta^{18}\text{O}$ global stack [44]. For the Segment 1 (right side), the slip-rate of 258 m in 200 ka [30] is used, whereas for trace 2.3, the approximate age obtained in the trenches (15 ka) for a 15 m buried offset channel [35] is applied. Dashed lines represent slip rate constraints for each segment. Dotted lines indicate maximum glacial stages.

Along Segment 2.3 (Figure 15), offsets appear to coincide with glacial to interglacial transitions. The younger age (15 ka) is from an erosive unit in the paleoseismic 3D-trenches [35]. In this case, we are not correlating sedimentary units, but moments of erosion. Thus, we would infer that erosion is triggered by transitions from glacial to interglacial. We also infer that peaks that do not coincide with climatic events may be the result of entrenchment due to the small vertical component of deformation along Segment 2 [25] or because of other stochastic processes.

Results from the comparison between Segment 1 COPD's and climatic curve are less conclusive (Figure 15). In this case, we align the curves using the relative age of a sedimentary unit. The estimated slip-rate is based on the offset of channel REF095 (offset 257 m) that is entrenched in an alluvial fan surface with a relative age of approx. 200 ka. The comparison suggests that maximum glacial stages coincide with periods of minimal sedimentation (Figure 15), however this relationship is not clear. This apparent lack of correlation derives basically from the uncertainty associated with the relative age used to do the superposition of the curves. However, the aforementioned correlation of

lack of sedimentation during glacial stages, agrees with suggested by other authors [6,11] for other parts of the world, but disagrees with [42] study in the SE Iberian Peninsula.

9. Conclusions

In this study, we propose a new methodology to score lateral offsets and we test it with a new offset dataset along the Alhama de Murcia slow-moving sinistral strike slip fault. We measured (amount of offset \pm uncertainty, expressed as 1σ) every offset feature and we rated it in terms of subjective and objective quality (every quality can take values between 0 and 1). Six parameters represent objective quality, although just three of them can be characterized in terms of metrics (lithological changes, associated morphotectonics and shape). All the variables (amount of offset, uncertainty, subjective quality, objective quality, lithological changes, associated morphotectonics and shape) are apparently independent, except objective quality and shape whose correlation value is close to 1. This methodology is useful to characterize the offset feature catalog.

Cumulative Offset Probability Density (COPD) is calculated from the individual PDF (previously weighted by subjective and objective qualities). COPDs are a useful tool to compare fault segments. The coincidence of the COPD peaks' position between fault segments is a necessary but not sufficient condition to ensure that the analyzed segments have the same slip-rate. COPD peaks of individual AMF traces show few coincidences between fault segments indicating that slip-rate may be different from one segment to the other, or that lack of data limits our results. Assuming that offset clusters observed in the COPD are entrenched at the same time, we test the possibility that entrenchment is triggered by climatic events. We compare the COPD with climatic curves to infer preferential climatic conditions for entrenchment. Along Segment 2.3 (Lorca-Totana), where we have some age control, channel incision may coincide with climatic transitions from glacial to interglacial stages. This approach may be used as a proxy for alluvial fan age, in order to calculate slip-rates for every fault segment.

Future work should be done testing this methodology for other faults. Another experiment is for the tectonic geomorphology along a fault to be analyzed by more than one geologist (see also discussion in [17]). That way, we can compare the scores, and assess which variables depend most on the operator criteria. Moreover, efforts will focus on obtaining more numerical ages to decrease the uncertainties in the comparison between COPDs and climatic curves.

Acknowledgments

This research was funded by SHAKE CGL2011-30005-C02-02 and partially by US NSF award EAR-1225810 (OpenTopography). The authors thank Anna Echeverria, Manuel J. Royán and J. Barrett Salisbury for helpful discussions and useful comments; Leticia Flores for teaching statistics; and Isabel Cacho for providing the climatic data. Olaf Zielke provided important coding guidance for the implementation of the COPD calculation. We also thank the four anonymous reviewers for their comments; they helped improve the original manuscript.

Author Contributions

Most of the work was done during a research stay of Miss Ferrater in the Arizona State University (supervised by Arrowsmith). Initial guidance was done by Masana. She also provided expertise in the geological characteristics of the Alhama de Murcia fault.

Conflicts of Interest

The authors declare no conflict of interest.

References

1. Wallace, R.E. Notes on stream channels offset by the San andreas Fault southern coast ranges, california. In *Geologic Problems of the San Andreas Fault System*; Dickson, W.R., Grantz, A., Eds.; Stanford Univ. Publ.: Stanford, USA, 1968; pp. 6–21.
2. Sieh, K. Slip along the San Andreas fault associated with the great 1857 earthquake. *Bull. Seismol. Soc. Am.* **1978**, *68*, 1421–1448.
3. Klinger, Y.; Etchebes, M.; Tapponnier, P.; Narteau, C. Characteristic slip for five great earthquakes along the Fuyun fault in China. *Nat. Geosci.* **2011**, *4*, 389–392.
4. Salisbury, J.B.; Rockwell, T.K.; Middleton, T.J.; Hudnut, K.W. LiDAR and field observations of slip distribution for the most recent surface ruptures along the Central San Jacinto Fault. *Bull. Seismol. Soc. Am.* **2012**, *102*, 598–619, doi:10.1785/0120110068
5. Zielke, O.; Arrowsmith, J.R.; Grant Ludwig, L.; Akciz, S.O. High-resolution topography-derived offsets along the 1857 Fort Tejon Earthquake Rupture Trace, San Andreas Fault. *Bull. Seismol. Soc. Am.* **2012**, *102*, doi:10.1785/0120110230.
6. Van der Woerd, J.; Tapponnier, P.; Ryerson, F.J.; Meriaux, A.; Meyer, B.; Gaudemer, Y.; Zhiqin, X. Uniform postglacial slip-rate along the central 600 km of the Kunlun Fault (Tibet), from 26Al, 10Be, and 14C dating of riser offsets, and climatic origin of the regional morphology. *Geophys. J. Int.* **2002**, *148*, 356–388.
7. Fu, B.; Awata, Y.; Du, J.; He, W. Late Quaternary systematic stream offsets caused by repeated large seismic events along the Kunlun fault, northern Tibet. *Geomorphology* **2005**, *71*, 278–292.
8. Ferry, M.; Meghraoui, M.; Karaki, N.A.; Al-Taj, M.; Amoush, H.; Al-Dhaisat, S.; Barjous, M. A 48-kyear-long slip rate history for the Jordan Valley segment of the Dead Sea Fault. *Earth Planet. Sci. Lett.* **2007**, *260*, 394–406.
9. Frankel, K.L.; Brantley, K.S.; Dolan, J.F.; Finkel, R.C.; Klinger, R.E.; Knott, J.R.; Wernicke, B.P. Cosmogenic ¹⁰Be and ³⁶Cl geochronology of offset alluvial fans along the northern Death Valley fault zone: Implications for transient strain in the eastern California shear zone. *J. Geophys. Res.* **2007**, *112*, doi:10.1029/2006JB004350.
10. Gold, R.D.; Cowgill, E.; Arrowsmith, J.R.; Chen, X.; Sharp, W.D.; Cooper, K.M.; Wang, X.F. Faulted terrace risers place new constraints on the late Quaternary slip rate for the central Altyn Tagh fault, northwest Tibet. *Geol. Soc. Am. Bull.* **2011**, *123*, 958–978.

11. Chevalier, M.L.; Tapponnier, P.; van der Woerd, J.; Ryerson, F.J.; Finkel, R.C.; Li, H. Spatially constant slip rate along the southern segment of the Karakorum fault since 200 ka. *Tectonophysics* **2012**, *530–531*, 152–179.
12. Walker, F.; Allen, M.B. Offset rivers, drainage spacing and the record of strike-slip faulting: The Kuh Banan Fault, Iran. *Tectonophysics* **2012**, *530–531*, 251–263.
13. Campbell, G.E.; Walker, R.T.; Abdrakhmatov, K.; Schwenninger, J.; Jackson, J.; Elliott, J.R.; Copley, A. The Dzhungarian fault: Late Quaternary tectonics and slip rate of a major right-lateral strike-slip fault in the northern Tien Shan region. *J. Geophys. Res. Solid Earth* **2013**, *118*, 5681–5698, doi:10.1002/jgrb.50367.
14. Moulin, A.; Benedetti, L.; Gosar, A.; Rupnik, P.J.; Rizza, M.; Bourlès, D.; Ritz, J.F. Determining the present-day kinematics of the Idrija fault (Slovenia) from airborne LiDAR topography. *Tectonophysics* **2014**, *628*, 188–205.
15. Cowgill, E. Impact of riser reconstructions on estimation of secular variation in rates of strike-slip faulting: Revisiting the Cherchen River site along the Altyn Tagh Fault, NW China. *Earth and Planet. Sci. Lett.* **2007**, *254*, 239–255.
16. Scharer, K.M.; Salisbury, J.B.; Arrowsmith, J.R.; Rockwell, T.K. Southern San Andreas fault evaluation field activity: Approaches to measuring small geomorphic offsets-challenges and recommendations for active fault studies. *Seismol. Res. Lett.* **2014**, *85*, 68–76.
17. Salisbury, J.B.; Haddad, D.E.; Rockwell, T.K.; Arrowsmith, J.R.; Madugo, C.; Zielke, O.; Scharer, K. Validation of meter-scale surface faulting offset measurements from high-resolution topographic data. *Geosphere* **2015**, doi:10.1130/GES01197.1.
18. McGill, S.F.; Sieh, K. Surficial offsets on the Central and Eastern Garlock Fault associated with prehistoric earthquakes. *J. Geophys. Res.* **1991**, *96*, 21597–21621.
19. Zielke, O.; Klinger, Y.; Arrowsmith, J.R. Tectonophysics Fault slip and earthquake recurrence along strike-slip faults—Contributions of high-resolution geomorphic data. *Tectonophysics* **2015**, *638*, 43–62.
20. Bull, W. *Tectonic Geomorphology of Mountains: A New Approach to Paleoseismology*; Blackwell Publishing Ltd.: Oxford, UK, 2007.
21. Haeussler, P.J.; Schwartz, D.P.; Dawson, T.E.; Stenner, H.D.; Lienkaemper, J.J.; Sherrod, B.; Personius, S.F. Surface rupture and slip distribution of the Denali and Totschunda Faults in the 3 November 2002 M 7.9 earthquake, Alaska. *Bull. Seismol. Soc. Am.* **2004**, *94*, S23–S52.
22. Yano, T.E.; Shao, G.; Liu, Q.; Ji, C.; Archuleta, R. Coseismic and potential early afterslip distribution of the 2009 Mw 6.3 L'Aquila, Italy Earthquake. *Geophys. J. Int.* **2014**, *199*, 23–40.
23. Bousquet, J.C. Quaternary strike-slip faults in south-eastern Spain. *Tectonophysics* **1979**, *52*, 277–286.
24. De Larouzière, F.D.; Bolze, J.; Bordet, P.; Hernández, J.; Montenat, C.; Ottd'Estevou, P. The Betic segment of the lithospheric Trans-Alboran shear zone during the Late Miocene. *Tectonophysics* **1988**, *152*, 41–52.
25. Masana, E.; Martínez-Díaz, J.J.; Hernández-enrile, J.L.; Santanach, P. The Alhama de Murcia fault (SE Spain), a seismogenic fault in a diffuse plate boundary: Seismotectonic implications for the Ibero-Magrebien region. *J. Geophys. Res.* **2004**, *109*, doi:10.1029/2002JB002359.

26. Masana, E.; Pallàs, R.; Perea, H.; Ortuño, M.; Martínez-Díaz, J.J.; García-Meléndez, E.; Santanach, P. Large Holocene morphogenic earthquakes along the Albox fault, Betic Cordillera, Spain. *J. Geodyn.* **2005**, *40*, 119–133.
27. IGN (Instituto Geográfico Nacional). Catálogo de Terremotos. Madrid, Spain. Available online: <http://www.ign.es/ign/layoutIn/sismoFormularioCatalogo.do> (accessed on 12 January 2012).
28. López-Comino, J.Á.; Mancilla, F.D.L.; Morales, J.; Stich, D. Rupture directivity of the 2011, Mw 5.2 Lorca earthquake (Spain). *Geophys. Res. Lett.* **2012**, *39*, 1–5.
29. Silva, P.G.; Goy, J.L.; Zazo, C. Características estructurales y geométricas de la falla de desgarre de Lorca-Alhama. *Geogaceta* **1992**, *12*, 7–10.
30. Silva, P.G. Evolución geodinámica de la Depresión del Guadalentín desde el Mioceno Superior hasta la actualidad: Neotectónica y Geomorfología. Ph.D. Thesis, Universidad Complutense de Madrid, Madrid, Spain, 1994.
31. Martínez-Díaz, J.J. *Neotectónica y Tectónica Activa del Sector Centro-Occidental de la Región de Murcia*. Ph.D. Thesis, Universidad Complutense de Madrid, Madrid, Spain, 1998.
32. Martínez-Díaz, J.J.; Masana, E.; Hernández-Enrile, J.L.; Santanach, P. Effects of repeated paleoearthquakes on the Alhama de Murcia Fault (Betic Cordillera, Spain) on the Quaternary evolution of an alluvial fan system. *Ann. Geophys.* **2003**, *46*, 775–791.
33. Echeverría, A.; Khazaradze, G.; Asensio, E.; Gárate, J.; Martín Dávila, J.; Suriñach, E. Crustal deformation in eastern Betics from CuaTeNeo GPS network. *Tectonophysics* **2013**, *608*, 600–612.
34. Ortuño, M.; Masana, E.; García-Meléndez, E.; Martínez-Díaz, J.J.; Stepanciková, P.; Cunha, P.P.; Murray, A. An exceptionally long paleoseismic record of a slow-moving fault: The Alhama de. *Geol. Soc. Am. Bull.* **2012**, *124*, 1474–1494.
35. Ferrater, M.; Ortuño, M.; Masana, E.; Perea, H.; Baize, S.; Pallàs, R.; Rockwell, T.K. First lateral slip-rates along the left-lateral strike-slip Alhama de Murcia fault obtained with eD trenching (SE Iberian Peninsula). In Proceedings of the 6th International INQUA Meeting on Paleoseismology, Active Tectonics and Archeoseismology, Fucino, Italy, 19–24 April 2015.
36. Martínez-Díaz, J.J.; Masana, E.; Ortuño, M. Active tectonics of the Alhama de Murcia fault, Betic Cordillera, Spain. *J. Iber. Geol.* **2012**, *38*, 253–270.
37. Langridge, R.M.; Ries, W.F.; Farrier, T.; Barth, N.C.; Khajavi, N.; de Pascale, G.P. Developing sub 5-m LiDAR DEMs for forested sections of the Alpine and Hope faults, South Island, New Zealand: Implications for structural interpretations. *J. Struct. Geol.* **2013**, doi:10.1016/j.jsg.2013.11.007.
38. Bond, C.E.; Gibbs, A.D.; Shipton, Z.K.; Jones, S. What do you think this is? “Conceptual uncertainty” in geoscience interpretation. *GSA Today* **2007**, *17*, 4–10.
39. Bond, C.E.; Philo, C.; Shipton, Z. When there isn’t a right answer: Interpretation and reasoning, key skills for twenty-first century geoscience. *Int. J. Sci. Educ.* **2011**, *33*, 37–41.
40. Martínez-Díaz, J.J.; Alonso Henar, J.; Álvarez-Gómez, J.A. Más de 100 m de roca de falla muestreados. Available online: <https://proyectointergeo.wordpress.com/2015/06/21/mas-de-100-m-de-roca-de-falla-muestreados/> (accessed on 20 July 2015).

41. Ferrater, M.; Booth-Rea, G.; Pérez-Peña, J.V.; Azañón, J.M.; Masana, E. From extension to transpression: Quaternary reorganization of an extensional-related drainage network by the Alhama de Murcia strike-slip fault (eastern Betics). *Tectonophysics* **2015**, doi:10.1016/j.tecto.2015.06.011.
42. Candy, I.; Black, S. The timing of Quaternary calcrete development in semi-arid southeast Spain: Investigating the role of climate on calcrete genesis. *Sediment. Geol.* **2009**, *218*, 6–15.
43. Schulte, L.; Julià, R. A Quaternary soil chronosequence of Southeastern Spain. *Z. Geomorph. NF* **2001**, *45*, 145–158.
44. Lisiecki, L.E.; Raymo, M.E. A Pliocene-Pleistocene stack of 57 globally distributed benthic $\delta^{18}\text{O}$ records. *Paleoceanography* **2005**, *20*, doi:10.1029/2004PA001071.
45. Von Grafenstein, R.; Zahn, R.; Tiedeman, R.; Murat, A. Planktonic $\delta^{18}\text{O}$ record at sites 976 and 977, Alboran Sea: Stratigraphy, forcing, and paleoceanographic implications. *Proc. Ocean Drill. Program Sci. Results* **1999**, *161*, 469–479.
46. Martrat, B.; Grimalt, J.O.; Lopez-Martinez, C.; Cacho, I.; Sierro, F.J.; Flores, J.A.; Hodell, D.A. Abrupt temperature changes in the Western Mediterranean over the past 250,000 years. *Science* **2004**, *306*, 1762–1765.

© 2015 by the authors; licensee MDPI, Basel, Switzerland. This article is an open access article distributed under the terms and conditions of the Creative Commons Attribution license (<http://creativecommons.org/licenses/by/4.0/>).



Case study

A 3D measurement of the offset in paleoseismological studies



Marta Ferrater^{a,*}, Anna Echeverria^a, Eulàlia Masana^a, José J. Martínez-Díaz^b,
Warren D. Sharp^c

^a RISKINAT Group. GEOMODELS. Departament de Geodinàmica i Geofísica, Facultat de Geologia, Universitat de Barcelona, c/ Martí i Franquès, s/n, 08028 Barcelona, Spain

^b Departamento de Geodinamica, Universidad Complutense, Instituto de Geociencias IGEO (UCM, CSIC), 28040 Madrid, Spain

^c Berkeley Geochronology Center, Berkeley, CA 94709, USA

ARTICLE INFO

Article history:

Received 23 December 2015

Received in revised form

15 February 2016

Accepted 29 February 2016

Available online 2 March 2016

Keywords:

3D offset

Paleoseismological trenches

Adjust 3D line

Strike-slip

Buried channel

ABSTRACT

The slip rate of a seismogenic fault is a crucial parameter for establishing the contribution of the fault to the seismic hazard. It is calculated from measurements of the offset of linear landforms, such channels, produced by the fault combined with their age. The three-dimensional measurement of offset in buried paleochannels is subject to uncertainties that need to be quantitatively assessed and propagated into the slip rate. Here, we present a set of adapted scripts to calculate the net, lateral and vertical tectonic offset components caused by faults, together with their associated uncertainties. This technique is applied here to a buried channel identified in the stratigraphic record during a paleoseismological study at the El Saltador site (Alhama de Murcia fault, Iberian Peninsula). After defining and measuring the coordinates of the key points of a buried channel in the walls of eight trenches excavated parallel to the fault, we (a) adjusted a 3D straight line to these points and then extrapolated the tendency of this line onto a simplified fault plane; (b) repeated these two steps for the segment of the channel in the other side of the fault; and (c) measured the distance between the two resulting intersection points with the fault plane. In doing so, we avoided the near fault modification of the channel trace and obtained a three-dimensional measurement of offset and its uncertainty. This methodology is a substantial modification of previous procedures that require excavating progressively towards the fault, leading to possible underestimation of offset due to diffuse deformation near the fault. Combining the offset with numerical dating of the buried channel via U-series on soil carbonate, we calculated a maximum estimate of the net slip rate and its vertical and lateral components for the Alhama de Murcia fault.

© 2016 Elsevier Ltd. All rights reserved.

1. Introduction

One of the fundamental parameters used to characterize the seismic potential of a fault is its net slip rate, as fast moving faults produce earthquakes more frequently than slow faults (e.g. Masana et al., 2001; Liu-Zeng et al., 2006; Rockwell et al., 2009). In strike-slip faults, the slip rate may be obtained from the offset of a linear feature (not necessarily straight linear) that crosses the fault (such as a channel, a limit of an alluvial fan, fluvial terrace risers, etc.) whose age is constrained (e.g. Gold et al., 2011; Salisbury et al., 2012; Frankel et al., 2007; Van der Woerd et al., 2002; Hall et al., 1999; Wesnousky et al., 1991). Channels are commonly used because they are widespread in the landscape. Moreover, in a simplified way, their intersection with the fault is a point, yielding a unique three-dimensional (3D) restitution (and thus a unique 3D

offset) between the two correlated segments of the channel (one in each block of the fault; in the methodological part of this paper, we use “fault block” to refer to either the hanging or the foot wall of a fault). Paleoseismological studies use two different approaches to measure the channel offsets: (1) surface analysis (using tectonic geomorphology) and (2) subsurface analysis of buried stratigraphic sequences in which the offset of a buried channel is estimated (using 3D trenching). These two approaches tend to underestimate the net offset because they often measure only the lateral component of the offset (e.g. Rittase et al., 2014; Liu-Zeng et al., 2006; Chevalier et al., 2016; Cowgill, 2007; Gold et al., 2011).

In the geomorphological approach, the offset measurement takes into account the far-field tendency of a channel and projects it into the fault (Wallace, 1968; Sieh, 1978; Salisbury et al., 2012; Zielke et al., 2012; Haddon et al., 2016). In this case, the precise morphology of the channel near the fault is not important. Different methods are used to define the general trending of the channel (or the terrace risers associated with it) and project this

* Corresponding author.

E-mail address: marta.ferrater@ub.edu (M. Ferrater).

tendency onto the fault plane (Van der Woerd et al., 2002; Cowgill, 2007; Gold et al., 2011; Ferrater et al., 2015a). Zielke and Arrow-smith, (2012) created a Graphical User Interface (GUI) for Matlab (Lateral Displacement Calculator, LaDiCaoz) updated recently (La-DiCaoz_v2; Zielke et al., 2015; Haddon et al., 2016) which measures the offset based on the perpendicular profile and the general trending of the channel.

In contrast, the offset of buried paleochannels identified in trenches is measured directly next to the fault by excavation of progressive exposures (examples of 3D trenches in McCalpin et al. (1996)). A long trench is usually dug parallel to the fault in each side to define the target channel and is progressively expanded towards the fault along the channel feature to expose the piercing points on the fault plane. This technique allows measurement of the lateral offset of one (e.g. Wesnousky et al., 1991) or more channels (e.g. Hall et al., 1999; Liu et al., 2004; Liu-Zeng et al., 2006; Marco et al., 2005). Zooming too much into the fault area, as is the case in trenching studies, may underestimate the offset owing to: (1) the possible distributed deformation next to the fault (i.e. not a unique fault line but different secondary faults which may be separated several metres or more from the fault), or (2) the smoothing of the erosive path of the channel within time since materials across the fault are easily eroded (Ouchi, 2004).

In this study, we adapted the geomorphological approach to project the three-dimensional far-field trend of a buried paleochannel onto the fault. Our aim was to avoid underestimation of the net offset produced by disregarding (1) the vertical component of the fault, and (2) near-fault modifications of the channel course (Huang, 1993). In the first part of the paper, we provide a group of modified scripts (Supplementary material, OffsetMeasurement3D) based on Matlab language to automate the calculation of the net, lateral and vertical offsets of buried channels. The proposed methodology includes: (a) the acquisition of the coordinates of the points belonging to a buried channel feature; (b) the adjustment of 3D straight lines to the selected points; (c) the calculation of the intersection points between these lines and the fault; and d) the measurement of the net, lateral and vertical offsets and their uncertainties. The main advantage of these scripts is that they allow assessing the general three-dimensional trending of a likely irregular feature whose exact direction is unknown. In the second part, we apply this method to a 3D paleoseismic trenching study in the seismogenic Alhama de Murcia fault (Southeastern Spain; Martínez-Díaz et al., 2003; Masana et al., 2004; Ortuño et al., 2012), where we identified a buried channel on both sides of the fault. Slip rate calculation of this fault represents a paleoseismological challenge, as (1) the ratio between its lateral and vertical components is unknown and, (2) previous estimations of the slip rate contain large uncertainties.

2. Methodology

The proposed method of offset determination consists of five steps: (1) trench design and excavation, (2) data acquisition, (3) computation of the piercing points and (4) estimation of the uncertainties, and, (5) calculation of the offset value. This approach is trustworthy for channels with low sinuosity or for channels whose sinuosity wavelengths are small, i.e. those cases where a straight line may be adjusted to the channel shape.

2.1. Trenching survey

At least one trench dug perpendicular to the fault is needed to locate the fault. After defining the fault position and its characteristics (orientation, dip and fault zone width), two trenches parallel to the fault, one in each side of the fault, are needed to identify the target channel in the stratigraphic sequence. A

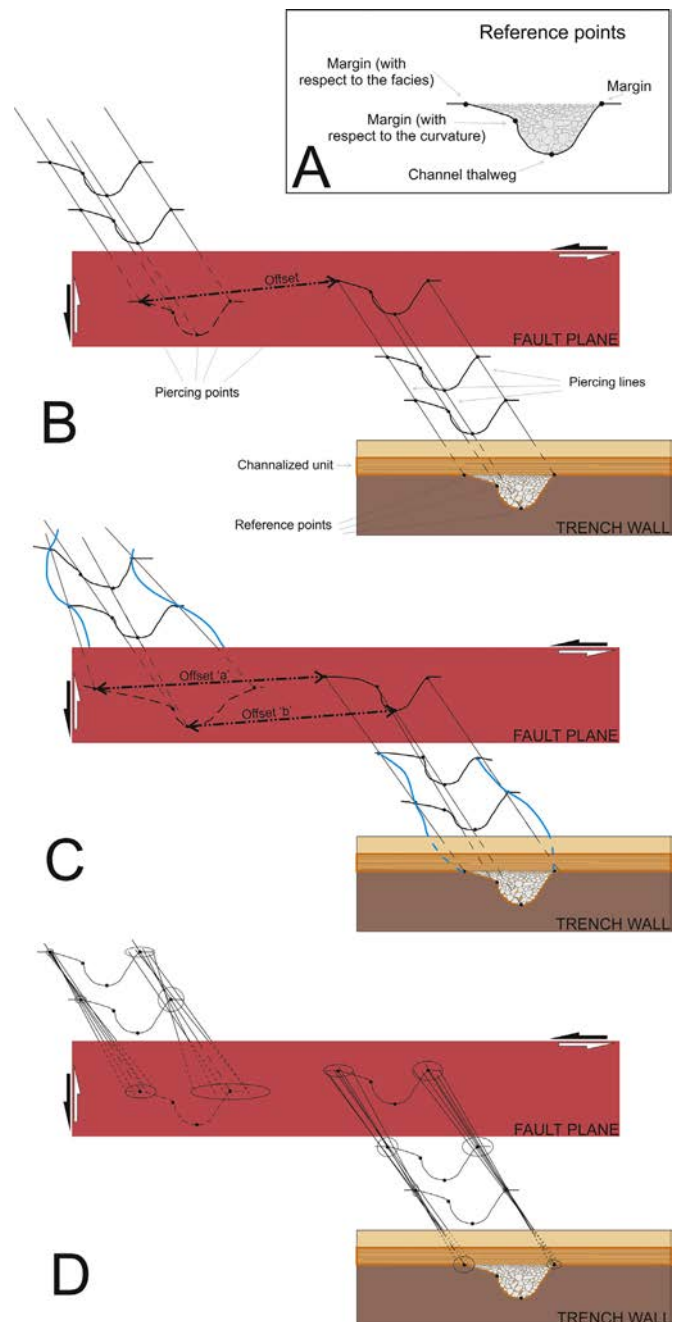


Fig. 1. Theoretical assumptions applied in the methodological workflow. (A) Nomenclature of channel features (reference points in section); (B) nomenclature of all the elements intervening in space (reference points, piercing lines and piercing points), and their situation in the ideal case study; (C) sketch of the resulting piercing lines and channel cross-sections when the channel is slightly sinuous, in this case the offset of the piercing point pairs differs from each other; and (D) schema of how the uncertainties are calculated by projecting them onto the fault: hundreds of random possible piercing lines within the area of the individual reference point uncertainties are projected against the fault.

minimum of one additional parallel trench is required on each side to yield enough points for the analysis along each piercing line. In this way, the channel should be identified in the sedimentary record in two trenches per fault block, i.e. total of eight trench walls.

2.2. Data acquisition

A channel can be simplified into a line (not indispensable to be straight) on a small scale but is more complex at a detailed scale.

The channel bed is curved and may be decomposed into an infinite number of lines, including the channel margins, the channel thalweg, and the lateral margins of distinctive depositional units that fill the channel (Fig. 1A). Henceforth, straight lines are specified in the text, otherwise lines may present some sinuosity. In paleoseismology, a piercing element (a line) is a feature that used to be continuous but has been offset by fault activity (Fig. 1B). Every linear channel feature constitutes a piercing line. The intersection between a piercing line and the fault plane defines a piercing point, whereas the intersection of every linear (not necessarily straight) channel feature with the trench wall is a reference point. Thus, every trench wall exposes a reference point belonging to each piercing line (Fig. 1B). For at least two trenches on both sides of the fault, we identify one reference point for each channel feature (Fig. 1B). In the field, we survey the coordinates (x , y and z in UTM coordinates) of every reference point together with their epistemic uncertainty. The epistemic uncertainty refers to the incertitude when locating the exact position of the reference points, as channel bed may be smooth and the curvature of the thalweg or the margins very lax. We assume that the uncertainty values in x and y are the same. Thus, we decompose the horizontal uncertainty into two identical values. We group all reference points belonging to the same channel feature on each fault block (margins or thalweg) in a.txt file (Supplementary material, OffsetMeasurement3D). This file has six columns (x , y , z , uncertainty in x , uncertainty in y and uncertainty in z) and as many rows as reference points for every channel feature that is identified. The fault plane file is a.txt file with four columns, one for each parameter of the general equation for a three-dimensional plane ($Ax + By + Cz + D = 0$).

2.3. Piercing point calculation

Channel exposures are not identical in all trench walls, which differ in sectional shape due to channel sinuosity (Fig. 1C). This results in reference points that are not perfectly aligned. The 3D straight line that best adjusts to the all identified reference points in each side of the fault is the line that represents the average orientation of each channel section. Accordingly, this straight line (representing the trending of the channel feature) is projected onto the fault. We obtain the xyz location of every piercing point by calculating the intersection between the fault (simplified as a plane) and the averaged piercing line (Supplementary material, OffsetMeasurement3D).

2.4. Determination of the uncertainties

To calculate the uncertainty of each piercing point location, we assume the uncertainty of the fault plane simplification to be negligible in comparison to the reference points coordinates. Thus, we focus on the epistemic errors associated with the acquisition of the points. We apply the statistical Monte-Carlo method to calculate the piercing points for a combination of hundreds of random possible straight lines that can be adjusted within the limits of the uncertainty ellipse of the reference point (Fig. 1D). We use a normal distribution of the random points within the uncertainty ellipse to calculate the possible random piercing straight lines (Supplementary material, OffsetMeasurement3D). The uncertainty of the piercing point is the standard deviation of all resulting random piercing points.

2.5. Offset measurements on the fault plane. Distance between piercing points

The final step is to measure the distance between piercing point pairs (that refer to the same channel feature but from each

fault block). These distances are the offsets for each channel piercing straight line (margins or thalweg). The net, lateral and vertical offsets are calculated, together with their associated uncertainties (Supplementary material, OffsetMeasurement3D). As piercing lines from the same channel may differ in orientation, the offsets calculated from them are likely also dissimilar (Fig. 1C). To obtain the channel offset we apply the displacement density functions proposed by Zechar and Frankel, (2009) to resolve the final estimates of slip. These functions yield the mean, the median and the statistical bounds of the three offset elements in which the channel was simplified (margins and thalweg).

3. Case study: a buried channel offset by the Alhama de Murcia fault

The new methodology of offset determination was used at the Alhama de Murcia fault to estimate the net, lateral and vertical slip components affecting a faulted buried channel. U-series dating of soil carbonate developed in gravels of the buried channel provided an estimate of the channel's age that was used to calculate slip rates.

3.1. Geological setting

The Alhama de Murcia Fault (AMF) is a left-lateral strike-slip fault with an apparently minor reverse component (Bousquet, 1979; Martínez-Díaz, 1998), situated in the SE of the Iberian Peninsula (Fig. 2). It is part of the Eastern Betics Shear Zone (EBSZ), which plays a major role in the Iberian plate by absorbing part of the convergence between the African and Euroasiatic plates (De Larouzière et al., 1988; Masana et al., 2004). The AMF is 87 km long and has been subdivided into four segments according to its seismic signature, geomorphological evidence, and geological history (Silva, 1994; Martínez-Díaz et al., 2012). The four segments, from south to north, are: (a) Góñar–Lorca, with a horse tail termination to the south; (b) Lorca–Totana, where the fault, N060E in trend, splits into several sub-parallel fault traces and shows the maximum concentration of seismicity; (c) Totana–Alhama de Murcia, where the fault recovers its NE–SW trend but still shows several strands; and (d) Alhama de Murcia–Alcantarilla, where the geomorphic manifestation of the fault is diffuse.

A number of studies have focused on calculating the seismic parameters of the AMF (Silva et al., 1997; Martínez-Díaz, 1998; Martínez-Díaz et al., 2003; Masana et al., 2004; Ortuño et al., 2012; Echeverría et al., 2013; Ferrater et al., 2015b). Several attempts to estimate the slip rate of the AMF have been done. Ortuño et al. (2012) suggested 0.16–0.22 mm/yr of vertical slip rate and 0.95–1.37 mm/yr of lateral slip rate on the southern termination of the fault (in the southernmost fault segment) acknowledging huge uncertainties in their assumptions and using markers of different ages. In the Lorca–Totana segment, Masana et al. (2004) examined two trenches, and proposed a first estimation of the lateral slip rate (0.06–0.53 mm/yr for the past 30 ka) based on (i) the estimation of the vertical offset (measured as the vertical step of the alluvial fan surface) and (ii) on the orientation of slickensides. These results contained large uncertainties mostly linked to the assumption that the topographical step observed in the fan surface was mostly produced by the dip slip movement of the fault, minimizing the lateral offset of a non-horizontal (i.e. the conic shape of a fan) surface; Martínez-Díaz et al. (2003) calculated 0.21 mm/yr of lateral slip rate for the Upper-Pleistocene by measuring offset channels on a fan surface assuming the channels to be formed close to the middle-Upper Pleistocene boundary. By means of an archeoseismic study, Ferrater et al. (2015b) suggested a lateral slip rate of 0.024–0.039 mm/yr for one strand of the

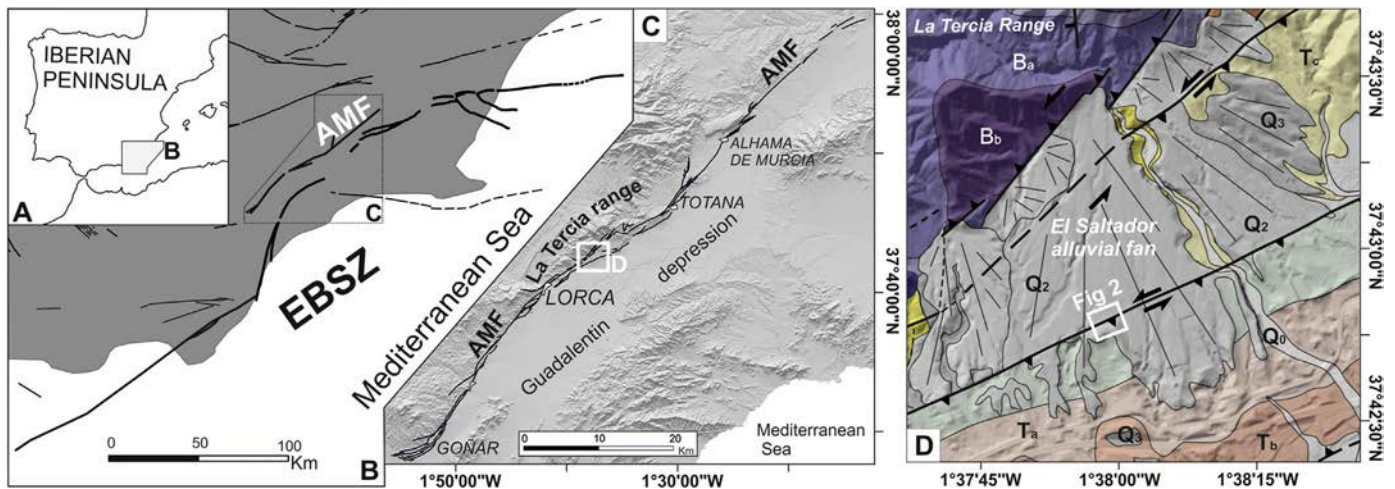


Fig. 2. (A) Alhama de Murcia fault (AMF) in the Iberian Peninsula; (B) the AMF is a part of the Eastern Betic Shear Zone (EBSZ faults in bold line); (C) structural map of the AMF; (D) geological map of the El Saltador alluvial fan: Ba–b, Palaeozoic basement rocks; Ta–c, Upper-Messinian rocks; Q0–4, Quaternary alluvial phases from older (3) to younger (0). The white square indicates the El Saltador trenching site.

Totana–Alhama de Murcia segment based on an offset wall of the Argaric culture (approx. 4000 years old). The different approaches used by the aforementioned authors, together with the suppositions made, result in a wide range of lateral slip rates for the AMF (from 0.02 to 1.37 mm/yr) that needs to be better constrained.

The El Saltador site, the focus of our study, is located in the southernmost strand of the Lorca–Totana segment that shows geomorphic evidence of lateral slip (SAMF; Martínez-Díaz, 1998; Ferrater et al., 2015a). This strand strongly dips to the south ($> 80^\circ$), and has a reverse component that uplifts the hanging wall. As a result, a smooth elongated NE–SW range is created. This small relief partially dams the drainage coming from the La Tercia Range running down to the Guadalentín depression, making the site an optimum location for a paleoseismological study. Geologically, the site is at the place where the El Saltador alluvial fan crosses the fault (Fig. 2D).

The 3D trenching survey consisted of the excavation of a total of ten trenches, four of them perpendicular to the fault, and six parallel to the fault. The former (TR 6, 7, 11 and 15) were intended to locate the fault and to identify paleoseismic events, whereas the latter (TR 5, 8, 10, 12, 13 and 14) were designed to identify buried offset channels in the stratigraphic sequence. The AMF has a diffuse deformation zone more than 5 m wide, outcropping in the perpendicular trenches. This precluded the use of widespread 3D trenching techniques that progressively excavate trenches towards the fault zone, as the offset measured in the main fault would underestimate the total offset. To solve this problem, and to use a similar geomorphic criterion to that used by Ferrater et al. (2015a) to measure geomorphologic offsets in the same fault, we projected the three-dimensional tendency of the channel considering a mid-distance (between 5 and 30 m) from the fault onto the fault plane, avoiding the near fault deformation.

3.2. U-series dating of pedogenic carbonate

Pedogenic carbonate generally forms in regions with annual precipitation of less than about 750–1000 mm, is common over a wide range of climates on more than half of the earth's land surface, and generally accumulates most markedly within soil profiles at depths of 0.3–2.0 m (Birkeland, 1984). If less than about 0.5 Myr old, dense and relatively pure pedogenic carbonate is amenable to U-series dating. Carbonate-rich clast-coatings that begin to form on the bottoms of clasts in the earliest stages of carbonate accumulation in gravelly soils can consist of dense, pure, laminated

carbonate that is highly suitable for U-series dating (e.g., Ludwig and Paces, 2002; Sharp et al., 2003). Samples of carbonate coatings developed on gravels of the offset buried channel (unit D) were collected on both sides of the fault and dated at the Berkeley Geochronology Center using methods similar to those of Sharp et al. (2016).

3.3. Results

The trenches exposed an alluvial fan sequence that alternates heterometric gravels and sands with defined levels of fine orange sands and silts. Within the gravels we identified two buried alluvial paleochannels, one in unit D and the other, much smoothed, in unit B (Fig. 3). To measure the offset of the channel in unit D we followed the proposed methodology. Given the particularities of channel B, we deal with its analysis as a special case.

Unit D comprises heterometric subangular clast-supported gravels (Fig. 3). The lower part of the unit is entrenched and filled with coarse and chaotic facies, whereas the upper part presents tractive structures, such as laminar bedding, and local cross-bedding and clast imbrication. The correlation of the identified channel on either side of the fault is accomplished using stratigraphic criteria, such as sedimentary position, shape and facies. Numerical dating provided by U-series supported the interpretation; the U-series ages of the pedogenic carbonate yielded reproducible ages of 12.39 ± 0.83 kyr in the hanging wall and 10.2 ± 2.9 kyr in the foot wall (Fig. 3), confirming the correlation of the channel on both sides of the fault. The channel was identified in four wall trenches in the foot wall (TR 5 and 10) and in four walls in the hanging wall (TR 13 and 14). The channel was approx. 5 m wide and 1.75 m deep, and its top was at a depth of 2 m in the foot wall and at 1 m in the hanging wall (SE).

Three channel features were used for reference in the channel of unit D: the two margins (where the channel facies changes from chaotic to laminated facies) and the channel thalweg. In the southeastern block (hanging wall), all channel features were surveyed in all four trench walls. However, in the northwestern block (foot wall), the margins were surveyed in four trench walls, but the thalweg in just two of them (Fig. 4). In the field, the coordinates of each reference point were surveyed using a differential GPS (Leica Zeno 5) together with the epistemic uncertainty of its 3D location (ranging from 5 cm to 2 m horizontally and 1 to 40 cm vertically). GPS error was considered negligible, as it was just 2 cm on the vertical axis and less than 2 cm on the horizontal axis. In the case

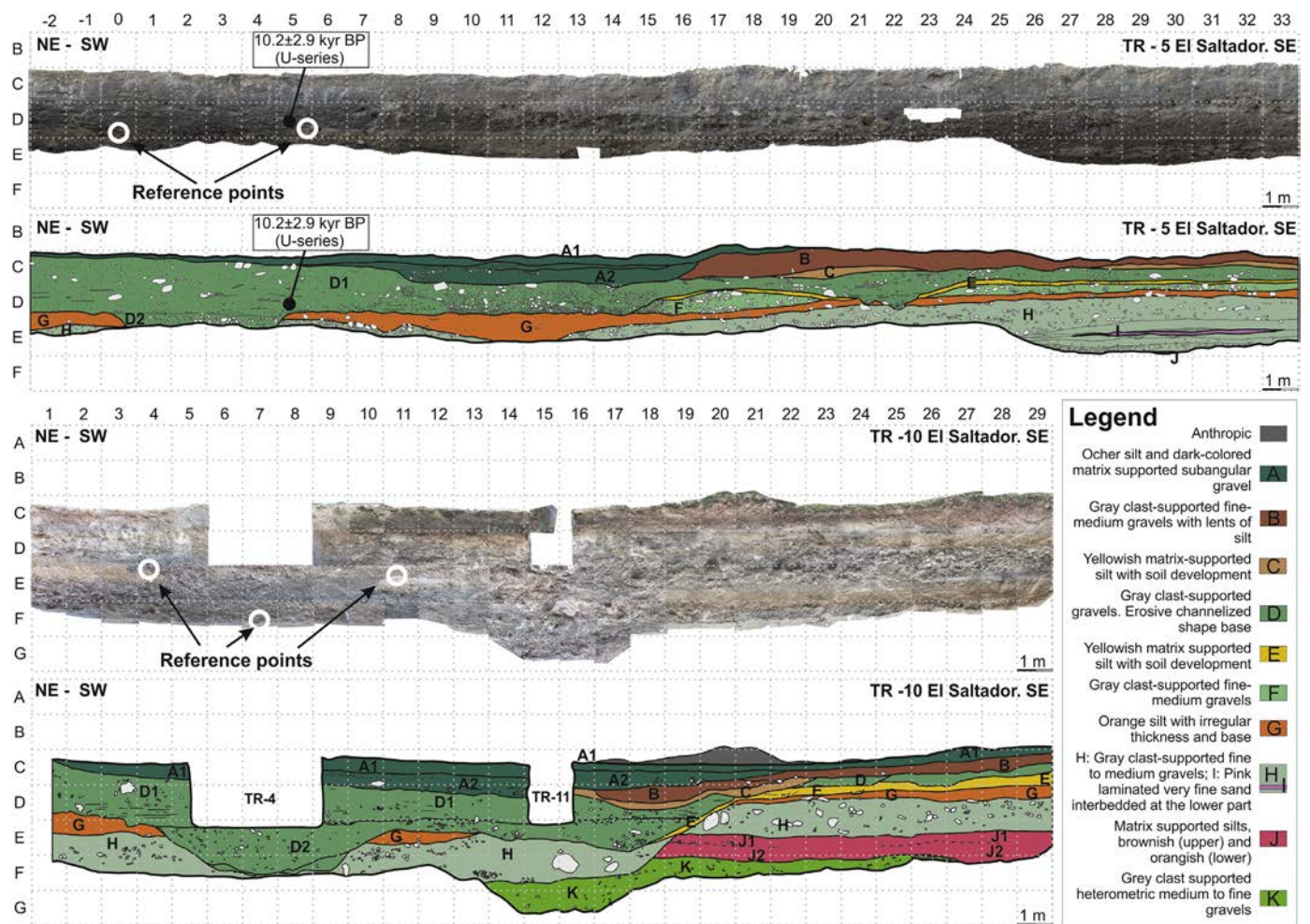


Fig. 3. Example of the used reference points for channel D identified in trenches 5 (SE wall) and 10 (SE wall). Due to the depth of trench 5, the thalweg of the channel was not identified. (For interpretation of the references to colour in this figure legend, the reader is referred to the web version of this article.)

of the SAMF, we projected the channels onto a vertical fault plane due to the high (near 90°) variable dipping angle of the fault observed in the field in TR11 (Fig. 4C). By verticalizing the fault plane, the net and the dip-slip offsets are slightly underrated, but their vertical and horizontal (lateral) components remain the same.

A 3D visualization of the elements in space was constructed using a 3D commercial programme (GoCAD) to ensure that the 3D adjusted straight lines were coherent with the trench positions. Different views of the site and the trench walls are shown in Fig. 4. Fig. 4F shows how the reference points for each feature were not perfectly aligned. This was due to the channel irregularities (Fig. 1C) and it means that the 3D adjusted straight lines did not coincide spatially with the reference points.

The values obtained for the net, lateral and vertical offsets of the three straight piercing lines are listed in Table 1 and shown in Fig. 5 (which includes only some trenches for clarity). The resulting mean minimum net offset value for unit D (2σ) was $16.0^{+2.5}_{-0.8}$ m. Moreover, the mean lateral offset was $15.9^{+2.5}_{-0.8}$ m and the mean vertical displacement was $1.4^{+0.2}_{-0.1}$ m. These values confirm that the main component of displacement along the fault is left lateral strike-slip.

Ages of pedogenic carbonate provide a minimum estimate for the depositional age of the buried channel since accumulation of pedogenic carbonate necessarily ensues after deposition of its host. Groups of pedogenic carbonate clast-coatings from unit D were collected from each side of the fault, with each group consisting of three or four sub-samples. U-series ages for the two

groups yielded similar weighted mean ages of 12.39 ± 0.83 ka (SE fault block) and 10.2 ± 2.9 ka (NW fault block; Fig. 5B; errors are 95% confidence interval), consistent with the proposed correlation of the buried channel across the fault. The mean of all the dates on unit D, 12.22 ± 0.80 ka, is our preferred age for the buried channel.

The combination of all values (the net, lateral and vertical offsets and the age of unit D) using the functions of Zecher and Frankel, (2009) yielded maximum net, lateral and vertical slip rates (2σ) of $1.3^{+0.2}_{-0.1}$ mm/yr, $1.3^{+0.2}_{-0.1}$ mm/yr, and $0.1^{+0.0}_{-0.0}$ mm/yr, respectively. As expected after the offset calculation, the lateral component of the fault was much higher than the vertical one. The obtained net slip rate was much larger than proposed to date using different approaches (Martínez-Díaz, 1998; Martínez-Díaz et al., 2003; Masana et al., 2004; Ortuño et al., 2012; Echeverría et al., 2013; Ferrater et al., 2015b).

3.4. A special case: the paleochannel in unit B

The paleochannel in unit B is only preserved in the foot wall of the fault and, thus, its direct correlation with the opposite side of the fault (as the workflow describes) is not possible. However, it can be correlated with the current channel to obtain a minimum offset value. The current channel in the foot wall is actively eroding the hill on its right bank as a consequence of the left lateral movement of the fault that incrementally places the hill in front of the water inflow and therefore the position of the current channel is the maximum position for channel B in the hanging wall. On the other

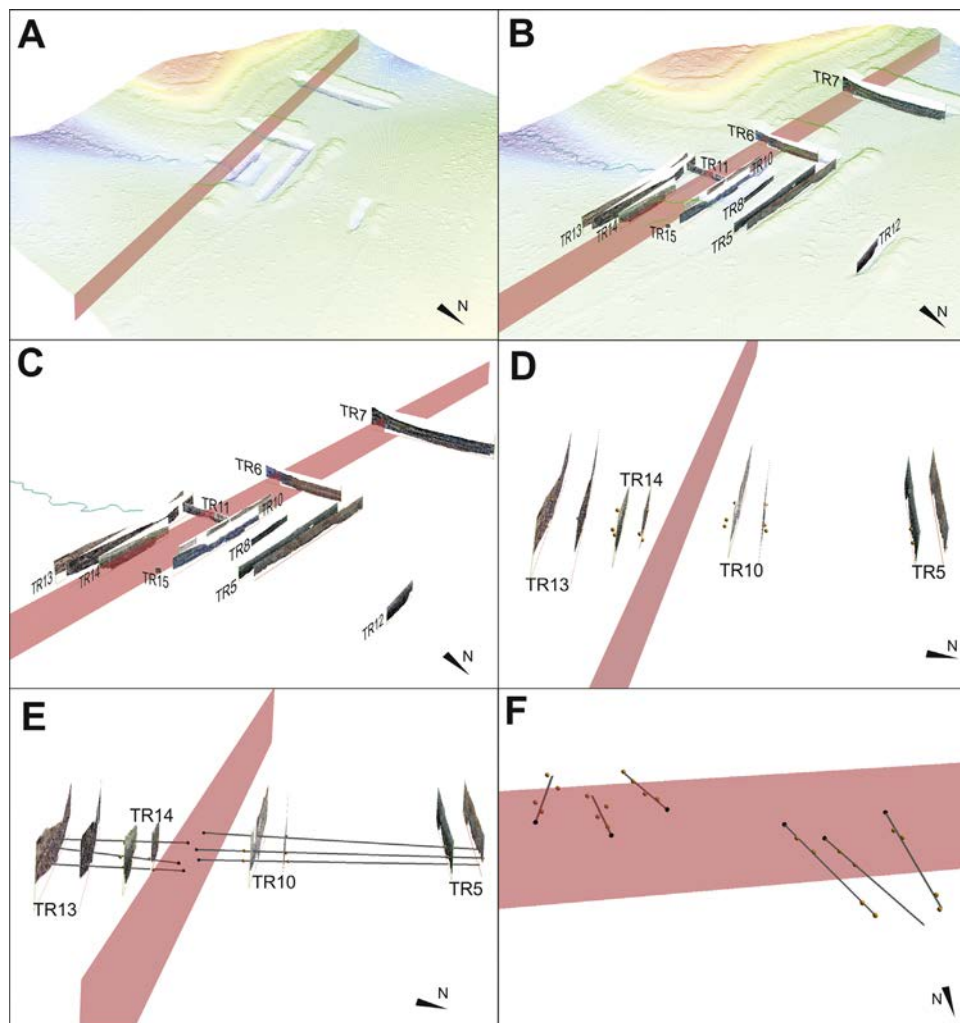


Fig. 4. Visualization of the 3D trenching. (A) Point cloud acquired from airborne lidar data in 2013 including the simplified vertical fault plane; (B) photomosaics and orthophotography of the exposed trenches in the point cloud; (C) photomosaics and orthophotography of the exposed trenches; (D) parallel view of the trenches in which the channel was identified (reference points in orange); (E) position of the adjusted 3D straight piercing lines (grey lines) with respect to the trench walls; (F) simplified fault, reference points (in orange), straight piercing lines (in grey) and piercing points (in black). Notice that the straight piercing lines do not contain the reference points. (For interpretation of the references to colour in this figure legend, the reader is referred to the web version of this article.)

Table 1

Summary of the calculated offsets (net, lateral and vertical) and their uncertainties for every channel feature: eastern margin, thalweg and western margin. Negative values indicate that the hanging wall is uplifted.

	Min. net offset	Net uncertainty	Lateral offset	Lateral uncertainty	Vertical offset	Vertical uncertainty
D eastern margin	17.25	0.60	17.19	0.60	−1.42	0.02
D thalweg	15.06	0.15	15.00	0.15	−1.34	0.02
D western margin	15.61	0.05	15.56	0.01	−1.30	0.05

hand, the position of channel B could have been located more to the NE, so we only obtained a minimum offset value.

In the foot wall, the channel crops out in TR 5, 8 and 10. We used the margins (where the entrenchment starts) to measure the offset of the channel. Just two reference points were acquired for each channel feature (one in TR 8 and one in TR 10), because the exposure of the channel in TR 5 is very diffuse (Fig. 3). In the hanging wall, the only piercing line that could be used was the channel thalweg, since the channel morphology is very vague and the two margins are not clear. To calculate the active channel tendency, we adjusted a straight line to a channel segment running from 10 (to avoid deflection in the diffuse deformation of the fault) to 30 m from the fault. We decided to use a 20-m segment because (a) sinuosity would be a greater influence in a smaller

segment, and b) a longer segment would not be consistent with the distances used to calculate the channel D tendency in the foot wall.

We correlated two channel features in the NW with only one feature in the SE (the thalweg): the distance between the western margin of the buried channel and the current thalweg is the maximum offset, whereas the distance between the eastern margin of channel B and the thalweg is the minimum offset (Fig. 5). As a result, we fitted a trapezoidal displacement density function (Zechar and Frankel, 2009) to reflect this reality and to calculate the final offset of channel B. The obtained minimum mean net offset for channel B was $4.8^{+1.1}_{-1.1}$ m (2σ). Minimum lateral and vertical offsets were $4.7^{+1.1}_{-1.1}$ m and $-0.7^{+0.2}_{-0.2}$ m, respectively.

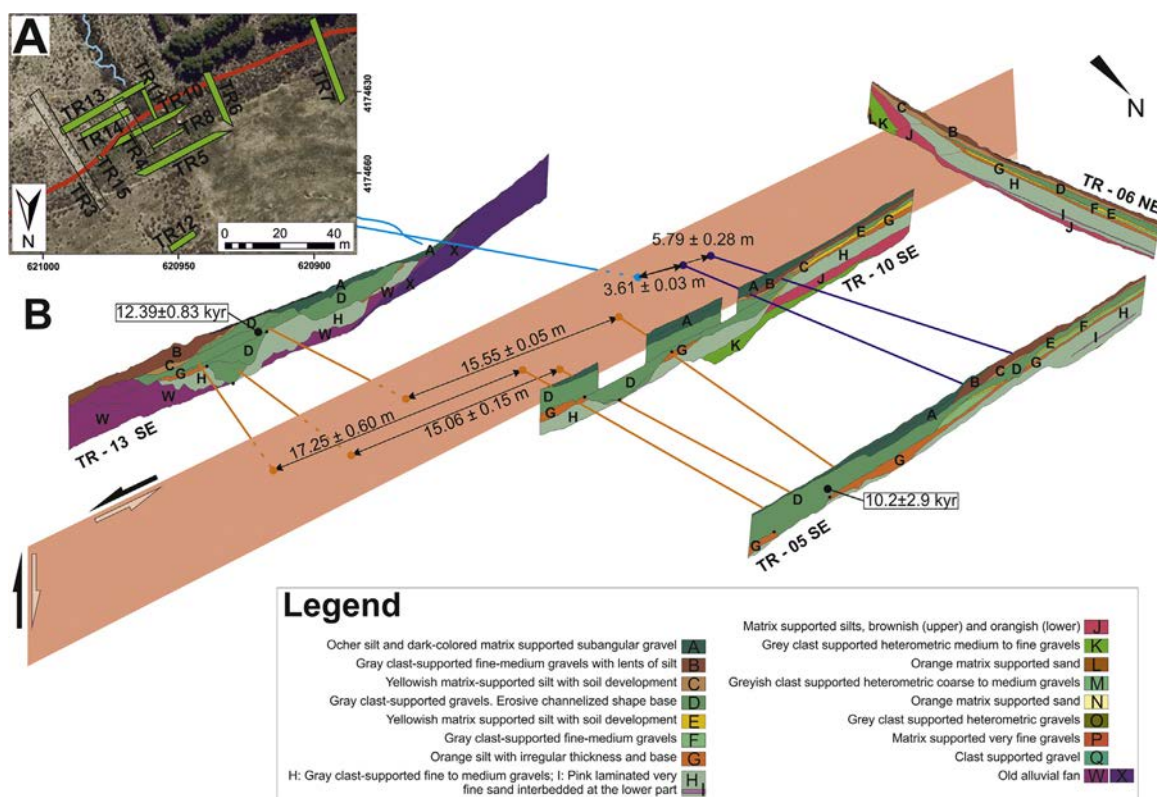


Fig. 5. Paleoseismic interpretation. (A) Plan view of the trenches; (B) interpretation of the exposed units (only one wall of TR 5, 6, 10 and 13 are shown as an example for clarity). Orange lines are the calculated piercing straight lines for channel D (see Fig. 4) and purple lines are the calculated piercing straight lines for channel B. Blue line is the active channel, and its straight projection onto the fault. (For interpretation of the references to colour in this figure legend, the reader is referred to the web version of this article.)

4. Discussion and conclusions

Geomorphological analyses show that the use of the straight full projection of linear features (such as channels or terrace risers) onto the fault provides a very good approximation of their offset. To do so, these analyses require considering the sinuosity of such features as being almost negligible. The proposed workflow to project the buried channels identified in 3D paleoseismological trenches was inspired by the criterion used in geomorphological studies. This procedure is limited to measure the offsets of channels with (a) low sinuosity or (b) small wavelengths of sinuosity. Otherwise, more trenches would be needed in order to adjust a circular arc or a polynomial curve to the reference points. We believe this method is valid based on the previous evaluation of the present-day analogue channels (i.e. their current sinuosity or the length of segments of the streams with constant trends). Our approach avoids the measurement of offsets in the near fault zone that may be subjected to channel deflection or diffuse deformation. Measurement in such near fault areas may result in many cases in an underestimation of the offset. In the El Salvador site, where we tested this technique, the channels show very low sinuosity on the alluvial fan surfaces (Ferrater et al., 2015a) and, as a consequence, we assume that this is the shape of the buried channels identified in the stratigraphic sequence.

The final outputs of the scripts we used are the offset measurements and their uncertainties for the two components of a fault movement. The set of scripts also provides a direct way to compare the two components of slip, improving previous results of 3D trenching studies. Moreover, these scripts imply methodological advantages. As this technique needs just three (at least) reference points, we were able to minimize the laborious and expensive field work associated with the traditional three-

dimensional paleoseismic surveys. In the example, we reduced the total amount of trenches parallel to the fault needed to calculate the offset of the buried channel to four.

The application of this approach to the Alhama de Murcia fault proves that the lateral component of the fault is much higher than the vertical one, implying that all previous trenching studies that excavated only perpendicular to the fault and calculated the lateral component of the fault based on slickensides underestimated its seismic potential.

Acknowledgements

This research was funded by SHAKE CGL2011-30005-C02-02. The authors are grateful to all the members of the trenching team, to César Ferrater for his comments on the first versions of the manuscript and mathematical advice and to Manuel Jesús Royán for its programming advice. We also thank Olaf Zielke and an anonymous reviewer for their comments improving the original manuscript. The Ministerio de Educación, Cultura y Deporte from Spain provided funding for the predoctoral FPU fellowship of M. Ferrater (FPU12/00921).

Appendix A. Supplementary material

Supplementary data associated with this article can be found in the online version at <http://dx.doi.org/10.1016/j.cageo.2016.02.024>.

References

Birkeland, P.W., 1984. Soils and Geomorphology. Oxford University Press, New York.

- Bousquet, J.C., 1979. Quaternary strike-slip faults in south-eastern Spain. *Tectonophysics* 52, 277–286.
- Chevalier, M.L., Van Der Woerd, J., Tapponnier, P., Li, H., Ryerson, F.J., Finkel, R.C., 2016. Late quaternary slip-rate along the central Bangong-Chaxikang segment of the Karakorum fault, western Tibet. *Bull. Geol. Soc. Am.* 128 (1–2), 284–314. <http://dx.doi.org/10.1130/B31269>.
- Cowgill, E., 2007. Impact of riser reconstructions on estimation of secular variation in rates of strike-slip faulting: revisiting the Charchen River site along the Altyn Tagh fault, NW China. *Earth Planetary Sci. Lett.* 254 (3–4), 239–255. <http://dx.doi.org/10.1016/j.epsl.2006.09.015>.
- De Larouzière, F.D., Bolze, J., Bordet, P.J., Hernández, J., Montecat, C., Ott d'Estevou, P., 1988. The Betic segment of the lithospheric Trans-Alboran shear zone during the Late Miocene. *Tectonophysics* 152, 41–52.
- Echeverría, A., Khazaradze, G., Asensio, E., Gárate, J., Martín Dávila, J., Suriñach, E., 2013. Crustal deformation in eastern Betics from CuaTeNeo GPS network. *Tectonophysics* 608, 600–612.
- Ferrater, M., Arrowsmith, R., Masana, E., 2015a. Lateral offset quality rating along low slip rate faults: application to the Alhama de Murcia fault (SE Iberian Peninsula). *Remote Sens.* 7 (11), 14827–14852. <http://dx.doi.org/10.3390/rs71114827>.
- Ferrater, M., Silva, P.G., Ortuño, M., Rodríguez-Pascua, M.Á., Masana, E., 2015b. Archaeoseismological analysis of a Late Bronze Age site on the Alhama de Murcia fault, SE Spain. *Geoarchaeology* 30, 151–164. <http://dx.doi.org/10.1002/gea.21505>.
- Frankel, K.L., Brantley, K.S., Dolan, J.F., Finkel, R.C., Klinger, R.E., Knott, J.R., Machette, M.N., Owen, L. A., Phillips, F.M., Slate, J.L., Wernicke, B.P., 2007. Cosmogenic ¹⁰Be and ³⁶Cl geochronology of offset alluvial fans along the northern Death Valley fault zone: Implications for transient strain in the eastern California shear zone. *J. Geophys. Res.* 112 (B6), B06407. <http://dx.doi.org/10.1029/2006JB004350>.
- Gold, R.D., Cowgill, E., Arrowsmith, J.R., Chen, X., Sharp, W.D., Cooper, K.M., Wang, X.-F., 2011. Faulted terrace risers place new constraints on the late Quaternary slip rate for the central Altyn Tagh fault, northwest Tibet. *Geol. Soc. Am. Bull.* 123 (5–6), 958–978. <http://dx.doi.org/10.1130/B30207.1>.
- Haddon, E.K., Amos, C.B., Zielke, O., Jayko, A.S., Bürgmann, R., 2016. Surface slip during large Owens Valley earthquakes. *Geochim. Geophys. Geosyst.* . <http://dx.doi.org/10.1002/2015GC006033>.
- Hall, N.T., Wright, H., Clahan, K.B., 1999. Paleoseismic studies of the San Francisco Peninsula segment of the San Andreas Fault zone near Woodside, California. *J. Geophys. Res.* 104, pp. 23215–23236.
- Huang, W., 1993. Morphologic patterns of stream channels on the active Yishi Fault, southern Shandong Province, Eastern China: implications for repeated great earthquakes in the Holocene. *Tectonophysics* 219, 283–304.
- Liu, J., Klinger, Y., Sieh, K., Rubin, C., 2004. Six similar sequential ruptures of the San Andreas fault, Carrizo Plain, California. *Geology* 32 (8), 649–652. <http://dx.doi.org/10.1130/G20478.1>.
- Liu-Zeng, J., Klinger, Y., Sieh, K., Rubin, C., Seitz, G., 2006. Serial ruptures of the San Andreas fault, Carrizo Plain, California, revealed by three-dimensional excavations. *J. Geophys. Res.* 111, B02306. <http://dx.doi.org/10.1029/2004JB003601>.
- Ludwig, K.R., Paces, J.B., 2002. Uranium-series dating of pedogenic silica and carbonate, Crater Flat, Nevada. *Geochim. Cosmochim. Acta* 66 (3), 487–506.
- Marco, S., Rockwell, T.K., Heimann, A., Frieslander, U., Agnon, A., 2005. Late Holocene activity of the Dead Sea Transform revealed in 3D palaeoseismic trenches on the Jordan Gorge segment. *Earth Planetary Sci. Lett.* 234 (1–2), 189–205. <http://dx.doi.org/10.1016/j.epsl.2005.01.017>.
- Martínez-Díaz, J.J., 1998. Neotectónica y Tectónica Activa del Sector Centro-Occidental de la Región de Murcia y Sur de Almería (Cordillera Bética – España). Universidad Complutense de Madrid, Madrid.
- Martínez-Díaz, J.J., Masana, E., Hernández-Enrile, J.L., Santanach, P., 2003. Effects of repeated paleoearthquakes on the Alhama de Murcia Fault (Betic Cordillera, Spain) on the Quaternary evolution of an alluvial fan system. *Ann. Geophys.* 46 (5), 775–791.
- Martínez-Díaz, J.J., Masana, E., Ortuño, M., 2012. Active tectonics of the Alhama de Murcia fault, Betic Cordillera, Spain. *J. Iber. Geol.* 38 (1), 253–270.
- Masana, E., Villamarín, J.A., Santanach, P., 2001. Paleoseismic results from multiple trenching analysis along a silent fault: The El Camp fault (Tarragona, north-eastern Iberian Peninsula). *Acta Geol. Hisp.* 36 (3–4), 329–354.
- Masana, E., Martínez-Díaz, J.J., Hernández-Enrile, J.L., Santanach, P., 2004. The Alhama de Murcia fault (SE Spain), a seismogenic fault in a diffuse plate boundary: seismotectonic implications for the Ibero-Magrebien region. *J. Geophys. Res.* 109, B01301. <http://dx.doi.org/10.1029/2002JB002359>.
- McCalpin, J.P., Rockwell, T.K., Weldon, R.J., 1996. Paleoseismology of strike-slip tectonic environments. In: McCalpin, J.P. (Ed.), *Paleoseismology, International Geophysics*. Academic Press, USA, p. 613.
- Ortuño, M., Masana, E., García-Meléndez, E., Martínez-Díaz, J., Stepánikova, P., Cunha, P.P., Sohbati, R., Canora, C., Buylaert, J.-P., Murray, A.S., 2012. An exceptionally long paleoseismic record of a slow-moving fault: The Alhama de Murcia fault (Eastern Betic shear zone, Spain). *Geol. Soc. Am. Bull.* 124 (9–10), 1474–1494. <http://dx.doi.org/10.1130/B30558.1>.
- Ouchi, S., 2004. Flume experiments on the horizontal stream offset by strike-slip faults. *Earth Surf. Process. Landf.* 29 (2), 161–173. <http://dx.doi.org/10.1002/esp.1017>.
- Rittase, W.M., Kirby, E., McDonald, E., Walker, J.D., Gosse, J., Spencer, J.Q.G., Herrs, A. J., 2014. Temporal variations in Holocene slip rate along the central Garlock fault, Pilot Knob Valley, California. *Lithosphere* 6 (1), 48–58. <http://dx.doi.org/10.1130/L286.1>.
- Rockwell, T., Ragona, D., Seitz, G., Langridge, R., Aksoy, M.E., Ucar, G., Ferry, M., Meltzner, A.J., Klinger, Y., Meghraoui, M., Satir, D., Barka, A., Akbalik, B., 2009. Paleoseismology of the North Anatolian Fault near the Marmara Sea: implications for fault segmentation and seismic hazard. *Geol. Soc. Lond. Special Publ.* 316, 31–54. <http://dx.doi.org/10.1144/SP316.3>.
- Salisbury, J.B., Rockwell, T.K., Middleton, T.J., Hudnut, K.W., 2012. LiDAR and field observations of slip distribution for the most recent surface ruptures along the Central San Jacinto Fault. *Bull. Seismol. Soc. Am.* 102, 598–619. <http://dx.doi.org/10.1785/0120110068>.
- Sharp, W.D., Ludwig, K.R., Chadwick, O.A., Amundson, R., Glaser, L.L., 2003. Dating fluvial terraces by ²³⁰Th/U on pedogenic carbonate, Wind River Basin, Wyoming. *Quat. Res.* 59, 139–150. [http://dx.doi.org/10.1016/S0033-5894\(03\)00003-6](http://dx.doi.org/10.1016/S0033-5894(03)00003-6).
- Sharp, W.D., Mertz-Kraus, R., Vallverdú, J., Vaquero, M., Burjachs, F., Carbonell, E., Bischoff, J.L., 2016. Archeological deposits at Abric Romaní extend to 110ka: U-series dating of a newly cored, 30meter-thick section. *J. Archaeol. Sci.* 5, 400–406. <http://dx.doi.org/10.1016/j.jasrep.2015.12.015>.
- Sieh, K., 1978. Slip along the San Andreas fault associated with the great 1857 earthquake. *Bull. Seismol. Soc. Am.* 68, 1421–1448.
- Silva, P.G., 1994. Evolución Geodinámica de la Depresión del Guadalentín desde el Mioceno superior hasta la Actualidad: Neotectónica y Geomorfología. Universidad Complutense de Madrid, Madrid.
- Silva, P.G., Goy, J.L., Zazo, C., Lario, J., Bargajá, T., 1997. Paleoseismic indications along “aseismic” fault segments in the Guadalentín depression (SE Spain). *J. Geodyn.* 24 (1–4), 105–115.
- Van der Woerd, J., Tapponnier, P., Ryerson, F.J., Meriaux, A., Meyer, B., Gaudemer, Y., Finkel, R.C., Caffee, M.W., Guoguang, Z., Zhiqin, X., 2002. Uniform postglacial slip-rate along the central 600 km of the Kunlun Fault (Tibet), from ²⁶Al, ¹⁰Be, and ¹⁴C dating of riser offsets, and climatic origin of the regional morphology. *Geophys. J. Int.* 148, 356–388.
- Wallace, R.E., 1968. Notes on stream channels offset by the San andreas Fault southern coast ranges, California. In: *Proceedings of Conference on Geologic Problems of San Andreas Fault System*, pp. 6–21.
- Wesnousky, S.G., Prentice, C.S., Sieh, K.E., 1991. An offset Holocene stream channel and the slip rate along the northern reach of the San Jacinto fault zone, San Bernardino Valley, California. *Geol. Soc. Am. Bull.* 103, 700–709.
- Zechar, J.D., Frankel, K.L., 2009. Incorporating and reporting uncertainties in fault slip rates. *J. Geophys. Res.* 114, B12407. <http://dx.doi.org/10.1029/2009JB006325>.
- Zielke, O., Arrowsmith, J.R., 2012. LaDiCaoz and LiDARimager—MATLAB GUIs for LiDAR data handling and lateral displacement measurement. *Geosphere* 8 (1), 206–221. <http://dx.doi.org/10.1130/GES00686.1>.
- Zielke, O., Arrowsmith, J.R., Grant Ludwig, L., Koc, S.O., 2012. High-resolution topography-derived offsets along the 1857 Fort Tejon earthquake rupture trace, San Andreas fault. *Bull. Seismol. Soc. Am.* 102, 1135–1154. <http://dx.doi.org/10.1785/0120110230>.
- Zielke, O., Klinger, Y., Arrowsmith, J.R., 2015. Tectonophysics fault slip and earthquake recurrence along strike-slip faults — contributions of high-resolution geomorphic data. *Tectonophysics* 638, 43–62.



Refining seismic parameters in low seismicity areas by 3D trenching: The Alhama de Murcia fault, SE Iberia

Marta Ferrater^{a,*}, Maria Ortuño^a, Eulàlia Masana^a, Raimon Pallàs^a, Hector Perea^b, Stephane Baize^c, Eduardo García-Meléndez^d, José J. Martínez-Díaz^e, Anna Echeverria^a, Thomas K. Rockwell^f, Warren D. Sharp^g, Alicia Medialdea^h, Edward J. Rhodes^h

^a RISK-NAT Group, GEOMODELS, Departament de Geodinàmica i Geofísica, Facultat de Geologia, Universitat de Barcelona, c/Martí i Franquès, s/n, 08028 Barcelona, Spain

^b Barcelona Center for Subsurface Imaging (B-CSI), Departament de Geociències Marines - Institut de Ciències del Mar - CSIC, 08003 Barcelona, Spain

^c Institut de Radioprotection et Sécurité Nucléaire - Seismic Hazard Division (BERSSIN), BP 17, 92262 Fontenay-aux-Roses, France

^d Área de Geodinámica Externa, Facultad de CC. Ambientales, Universidad de León, Campus de Vegazana s/n, 24071, León, Spain

^e Departamento de Geodinámica, Universidad Complutense, Instituto de Geociencias IGEO (UCM, CSIC), 28040 Madrid, Spain

^f Department of Geological Sciences, San Diego State University, San Diego, CA 92182, USA

^g Berkeley Geochronology Center, Berkeley, CA 94709, USA

^h Landscape Dynamics, Department of Geography, University of Sheffield, Sheffield S10 2TN, UK

ARTICLE INFO

Article history:

Received 18 November 2015

Received in revised form 29 April 2016

Accepted 10 May 2016

Available online 14 May 2016

Keywords:

Paleoseismology

Strike-slip fault

Recurrence

Slip rate

Slip per event

SE Iberian Peninsula

ABSTRACT

Three-dimensional paleoseismology in strike-slip faults with slip rates less than 1 mm per year involves a great methodological challenge. We adapted 3D trenching to track buried channels offset by the Alhama de Murcia seismogenic left-lateral strike-slip fault (SE Iberia). A fault net slip of 0.9 ± 0.1 mm/yr was determined using statistical analysis of piercing lines for one buried channel, whose age is constrained between 15.2 ± 1.1 ka and 21.9 – 22.3 cal BP. This value is larger and more accurate than the previously published slip rates for this fault. The minimum number of five paleo-earthquakes identified since the deposition of dated layers suggests a maximum average recurrence interval of approximately 5 ka. The combination of both seismic parameters yields a maximum slip per event between 5.3 and 6.3 m. We show that accurately planned trenching strategies and data processing may be key to obtaining robust paleoseismic parameters in low seismicity areas.

© 2016 Elsevier B.V. All rights reserved.

1. Introduction

Many regions undergoing rates of deformation below 5 mm per year are commonly perceived as seismically quiet even if a large historical earthquake has occurred. Hence, these regions are generally considered to be safe and to require low seismic protection standards. However, in such regions, elastic deformation may accumulate over long recurrence periods and be suddenly released in earthquakes that may be highly destructive, especially where the societal perception of hazard is limited (e.g. 2008 Mw 7.9 Sichuan earthquake in China, Liu et al., 2016; 2003 Mw 6.6 Bam earthquake in Iran, Wang et al., 2004). Paleoseismic studies were originally developed, and are most intensively applied, in active areas with high levels of seismicity. Few paleoseismic studies have focused on the characterization of the seismic potential of faults with slip rates under 5 mm/yr (Wesnowsky et al., 1991; Lindvall and Rockwell, 1995; Marco et al., 2005). Applying paleoseismological methodologies to these tectonic settings, where erosion and sedimentation

processes severely mask the effects of surface deformation, requires widening the time window and adapting widespread techniques originally developed in areas with high levels of seismicity (Ferrater et al., 2016).

The Alhama de Murcia fault (AMF; Fig. 1) belongs to the Eastern Betic Shear Zone (EBSZ), an active composite shear structure that absorbs part of the shortening between the Eurasian and African plates (4–6 mm/yr; Nocquet, 2012) in the SE Iberian Peninsula (De Larouzière et al., 1988). The AMF is a 87 km long left-lateral fault and has been subdivided into four sections (Silva, 1994; Martínez-Díaz, 1998; Martínez-Díaz et al., 2012a), the southernmost two showing the clearest evidence for late Quaternary activity (Goñar-Lorca and Lorca-Totana sections; Fig. 1C). The last significant earthquake caused by this seismogenic fault occurred in 2011 (Mw 5.2: López-Comino et al., 2012; Martínez-Díaz et al., 2012b), but paleoseismological information for the fault is scarce, incomplete, and involves large uncertainties (Silva et al., 1997; Martínez-Díaz et al., 2003; Masana et al., 2004; Ortuño et al., 2012).

Our study focuses on the 23 km long Lorca–Totana section of the AMF (Fig. 1C) where the 2011 earthquake occurred. The analysed

* Corresponding author.

E-mail address: marta.ferrater@ub.edu (M. Ferrater).

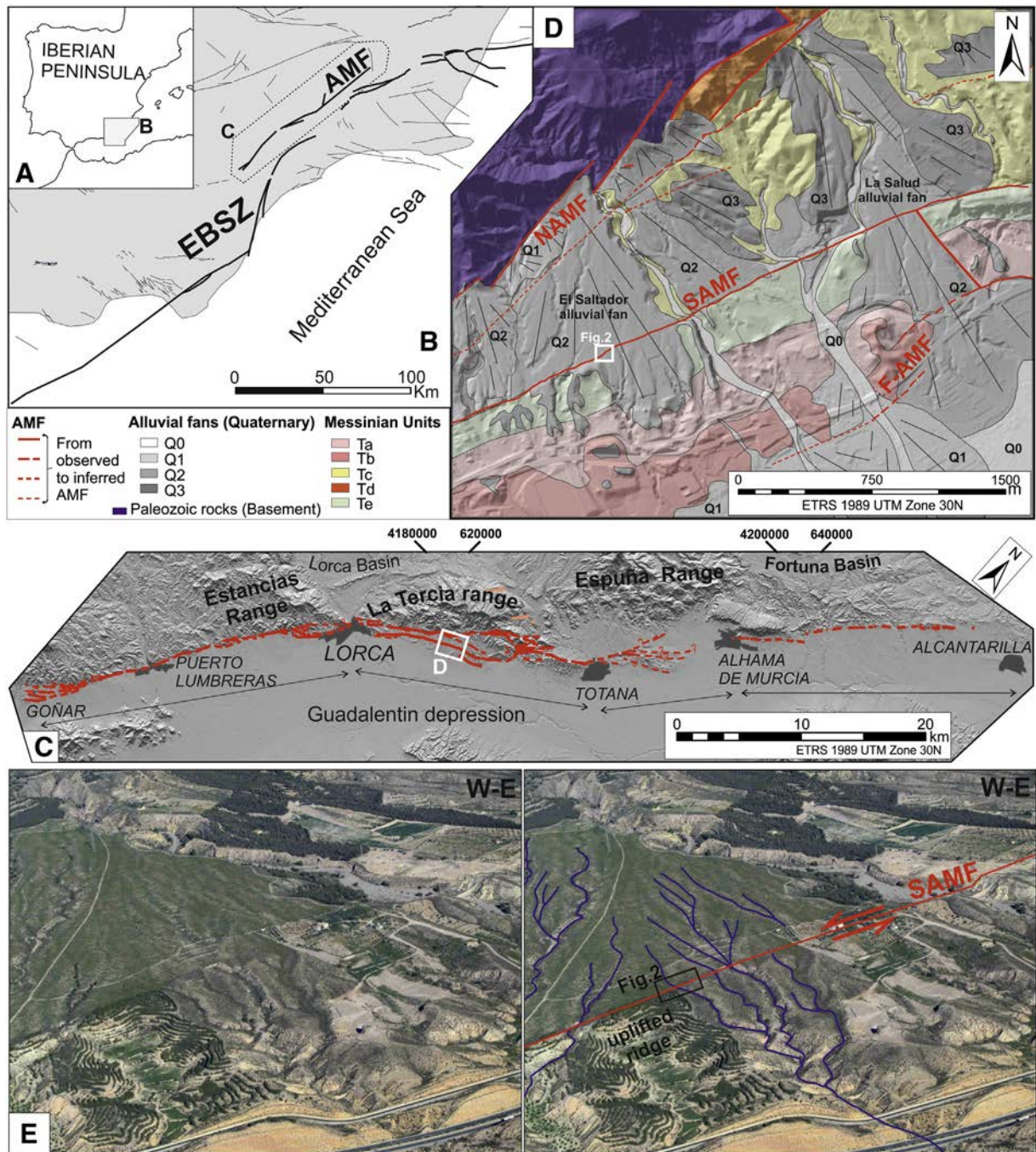


Fig. 1. A and B) Location of the study area in the Eastern Betic Shear Zone (EBSZ faults in bold line); C) structural map of the AMF, where fault sections are highlighted; D) geological map of El Saltador alluvial fan where the white square indicates the El Saltador trenching site (legend: Ta-e, Upper-Messinian rocks; Q₀₋₃, Quaternary alluvial phases from older (3) to younger (0)); E) oblique aerial view of the El Saltador alluvial fan surface towards the north; the streams maintain their orientation while crossing the fault.

section, with a N060E strike, in addition to a predominant strike-slip component, shows a vertical component of slip that leads to the uplift of La Tercia range (Martínez-Díaz, 1998; Ferrater et al., 2015), the source of extensive alluvial fans that drain towards the Neogene and Quaternary Guadalentín depression. Along this section, the fault splits into three major parallel strands: the north-dipping northern AMF (NAMF), the southern AMF (SAMF), that affects Pleistocene alluvial fans (Martínez-Díaz et al., 2003), and the frontal fault of the range (F-AMF); and minor sub-parallel traces (Fig. 1D). The NAMF is not amenable for a paleoseismic analysis because of the lack of late Quaternary sedimentation across the fault. Instead, paleoseismic studies along the SAMF demonstrate its seismogenic behavior and suggest the occurrence of a minimum of three paleoearthquakes in the past 27 kyr (Martínez-Díaz

et al., 2003; Masana et al., 2004). In these studies, however, the slip rate for the SAMF in the Late Pleistocene has only been broadly constrained, and estimated to be between 0.07 and 0.66 mm/yr (Masana et al., 2004).

We carried out a three-dimensional paleoseismological analysis along the south strand (SAMF) of the AMF to demonstrate that this type of trenching program, together with numerical dating, and advanced statistical analyses, can be used to better determine directly and indirectly the seismic parameters of a seismogenic fault, even in slow tectonic settings. The aims of this paper are: a) to identify a long sequence of paleoearthquakes and calculate its recurrence period; b) to quantify the net dislocation of buried channels and obtain accurate mean slip rates; and c) to estimate a slip per event value and the

maximum earthquake magnitude that is likely along the AMF. Our results improve the characterization of the seismic potential of the AMF and enhance the perception of its seismic hazard.

2. Paleoseismological site

At the El Salvador paleoseismological site, on the SAMF (Fig. 1D), the fault is vertical in deep creek outcrops and offsets the alluvial fans emanating from the La Tercia range. It uplifts the southeastern wall creating a smooth secondary NE–SW elongated ridge that blocks the southeastward-flowing drainages, an optimum context for paleoseismological studies (Fig. 1E). In the site area, the current creeks draining the fan surface do not show deflection at the fault crossing (Fig. 1E).

Ten new trenches were excavated at the El Salvador site (Fig. 2A): four were dug orthogonal to the fault trace to extend the paleoseismic catalogue, and six were excavated parallel to the fault to resolve the net slip rate of the SAMF. These parallel trenches were placed at a maximum distance of 40 m from the fault (TR12), and no closer than 2 m to it (TR14 and TR10) to avoid the zone of complex deformation within the

fault zone. From a stratigraphic point of view, the trenches expose several alluvial units (J–X) and a system of channels entrenched on top of it (A–H; Fig. 2).

3. Age control

To constrain the age of the units (A–X) exposed in the trenches, we used the radiocarbon technique on a snail and a charcoal sample, and Optically Stimulated Luminescence (OSL) dating of unit B, a fine-grained stratum (Table 1). The snail from unit G yielded a radiocarbon AMS age of 21,870–22,266 cal BP (2σ) and the charcoal sample from unit H (Fig. 2) an age of 25,883–25,279 cal BP (2σ ; Table 1). The sample from unit B, analysed with OSL, yielded an age of 15.2 ± 1.1 ka (1σ ; Table 1).

4. Evidence of paleoearthquakes

The trenches at the El Salvador site exposed a sequence of deformed gravel and sand strata, interpreted as deposited in an alluvial fan

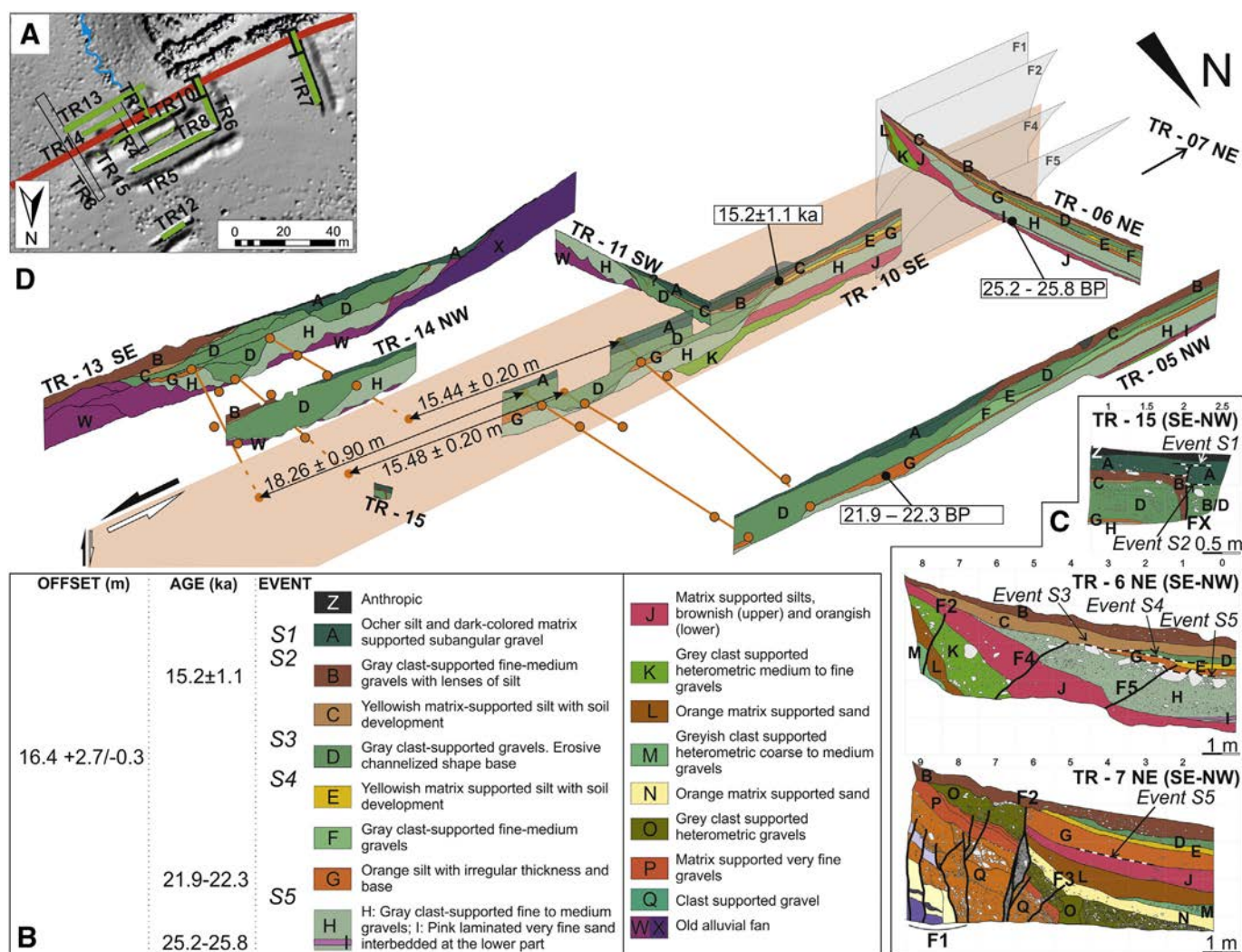


Fig. 2. Results at El Salvador site. A) Map with the trench locations of this study in green (the position of the trenches 3 and 4 in Masana et al., 2004 is highlighted), the fault zone in red, and the position of the active channel (blue). B) Legend summarizing units' description, offset measurements, numerical ages and identified events. C) Partial logs of the trenches dug across the fault showing deformed stratigraphic units (TR 6, 7 and 15, position indicated in 2A and D) with indication of the event horizons (dashed black and white lines, S1 to S5). Interpretation of events is based on: event S1: unit A is offset while unit Z shows no deformation (Trench 15); event S2: unit B is more strongly folded than unit A (Trench 15); event S3: angular discontinuity between units D and C (Trench 6); event S4: unit D is not affected by the deformation that folds unit G and E (Trench 6); events S5: the base of unit H dips more than the base of unit G (Trench 6); D) Perspective block diagram showing the location of some trench walls (TR 5 NW, 6 NE, 10 SE, 11 SW, 13 SE, 14 NW and 15; the others are not included for clarity), the reconstructed fault plane and the samples position. Orange dots on channels in the trench walls represent the position of all reference points. In orange, piercing lines and piercing points for channel D. The piercing lines have been adjusted using two to four reference points for each channel feature (rims or thalweg). Piercing lines are regression lines and thus do not necessarily contain the reference points due to channel irregularities.

Table 1

Dating results of units B, G and H in the El Salvador paleoseismological site. Used techniques are Optically Stimulated Luminescence (OSL) for unit B and Radiocarbon (units G and H).

	Sample	Unit	Depth (m)	Moisture (%)	Dose rate (Gy/ka)	Equivalent dose (Gy)	Age (ka)
OSL sample	SAL 27	B	0.87	5 ± 2	2.67 ± 0.11	40.6 ± 2.3	15.2 ± 1.1
	Sample	Unit	Nature	Modern fraction	D ¹⁴ C (‰)	¹⁴ C age (BP)	Calibrated age BP
Radiocarbon sample	SAL 20	G	Snail	0.1036 ± 0.0006	−896.4 ± 0.6	18,210 ± 45	21,870–22,266
	SAL 2	H	Charcoal			21,210 ± 140	25,228–25,832

environment, and a sequence of channelized units entrenched into the top of fan section. The alluvial sequence alternates with sand and silt layers with sparse matrix-supported clasts, interpreted as mudflow deposits (Fig. 2). The fault zone is composed mainly of a vertical fault and, north of it, a few faults displaying maximum dips of 45° to the south (Fig. 2; Masana et al., 2004), which together form a half flower structure. The secondary faults tend to increase their dip with depth (Masana et al., 2004) resulting in a fault zone that is locally more than five meters wide (Fig. 2, TR6). Faulting has locally generated fault-related folds, as that observed in trench 15, and has led to the formation of a progressive tectonic unconformity at the trench scale that is obvious in trenches 6 and 7 (Figs. 2C and 3).

The cumulated deformation is larger for the older exposed units, suggesting the occurrence of consecutive surface ruptures. The record of these ruptures is inferred using structural (tilting and fault displacement), stratigraphic (angular unconformities) and sedimentological (sudden changes in depositional environment caused by the obstruction of the drainage) criteria. Tracing the fault location was straightforward near the contact of different sedimentary units and particularly difficult through the silty layers. We will only describe here the five youngest ruptures recorded at this site (named events S1 to S5, from younger to older), which are the ones for which age-constraints are available. The event horizons are marked in Fig. 2C. Event S1 produced the displacement of the base of unit A and underlying units, and is only traceable in trench 15, where it produced 12.5 cm of apparent vertical offset. Event S2 occurred after the deposition of unit B and prior to A, producing the fold exposed in trench 15, with an apparent vertical slip of 60 cm. The summed effect of events S1 and S2 is recorded in trench 6 as a tilting of unit B, which dips ~12° towards the NW (against the natural slope of the fan, which drains towards the SE). Immediately below this tilted surface, we measured an 8 cm apparent dip displacement of the base of unit C along fault F4. Although it is not obvious, we cannot discard that this fault rupture propagates upwards through unit C. Because this unit is interpreted as a mudflow deposit (i.e. an instantaneous deposit), our preferred interpretation is to assume that F4 reaches the top of this layer. Placing the upward termination of the rupture at the base of C would imply that this rupture occurred

simultaneously with the previous event recorded (event S3). Prior to event S2, solid evidence for a previous surface rupture (event S3) occurred between the deposition of unit C and D, as evidenced in trench 6 by the difference in tilt of their bases, which has led to an angular unconformity at the base of C. This relationship is also observed between units B and D at trench 7, although there, it is less straightforward. The record of this surface rupture is reinforced by the sedimentological and stratigraphic features of unit C, interpreted as a ponded stratum in the sense referred to by Rockwell et al. (2014); unit C is a matrix supported silt with sparse floating clasts, which possibly records a mudflow. It mantles the surface and thickens down flow towards the fault trace. Uplift caused by the SAMF during event S3 probably produced either a sufficiently large tectonic barrier or a counter-slope tilting of the surface that caused the ponding of mudflows near the fault. These relatively extensive mudflows deposits are not observed other than in a narrow corridor along the fault trace. Event S4 is identified in trench 6 by the angular unconformity between the base of unit D and underlying units, which are folded along fault F5. The oldest event analysed here, event S5, can be situated at the contact between units G and H. The existence of this event is based on three observations: 1) the base of unit G has a lower counter-slope dip than the base of H, obvious at trench 6 between faults F4 and F5; 2) at trench 6, the apparent vertical displacement of unit G along F5 (16 cm) is smaller than that of unit H (37 cm); and 3) unit G is interpreted as a mudflow deposit that ponded near the fault trace, in the same sense as explained above for unit C.

Two of the events described above have been correlated with the two events identified in trenches 3 and 4 in previous studies done by Martínez-Díaz et al. (2003) and Masana et al. (2004) in this area: event S2 corresponds to Event T and event S5 here would correspond to Event N.

According to these observations, the mean maximum earthquake recurrence interval is roughly estimated to be 5.0–5.2 ka considering that 5 events (S1 to S5) occurred after the deposition of unit H (25.8–25.2 kyr cal BP). If instead of five events, we consider just the two most recent ones (S1 and S2, both of which occurred since deposition of unit B), this recurrence interval becomes ~7.5 ka.

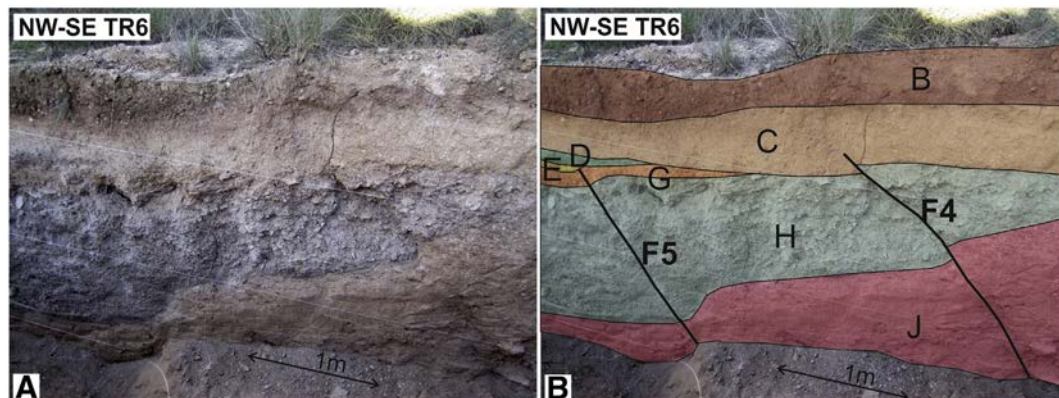


Fig. 3. Perspective view of the fault zone in trench 6 (NE wall) and interpretation of the exposed units and fault traces F4 and F5.

5. Slip rate

To estimate the net slip rate of the AMF, we followed the methodology proposed by Ferrater et al. (2016) valid for low sinuosity or short wavelength channels, i.e. those cases where a straight line may be adjusted to the channel shape. We used the present day channels on the surface of the El Saltador fan as an analogue for the shape of the past (buried) channels. The present-day channels (Fig. 1E) are not deflected by the fault and show very little sinuosity. Therefore, they can be simplified to a straight line.

Two possible channels may be recognized in unit D, although only the easternmost channel can be correlated univocally at both fault walls by its geometry and channel-fill facies with a low epistemic uncertainty (observed in trenches 14, 13, 10, and 5; Fig. 2D). To obtain the offset on this buried channel we identified reference points corresponding to the thalweg and to each of the channel margins in different trench walls and estimated the uncertainty on the position of each reference point. For the margins of the channel we used the top of unit D2 that is easy to differentiate from unit D1 in most of the trenches. Unit D1 presents tractive structures (laminar bedding and clast imbrication), whereas the lower part is erosive and has heterogenic and sub-angular blocks (Fig. 4 A and B). The uncertainties on the position of the reference points (taken with differential GPS) ranged between 2 m and 5 cm. In the southeastern wall, all channel features were surveyed in all trench walls (a total of four). However, in the northwestern wall, the margins were surveyed in four trench walls, and the thalweg in just two of them.

We estimated a piercing line for each channel margin and for the thalweg by mathematically fitting the best straight line along the reference points (Fig. 4C; note that the best line might not cut into all the points as the fit is mathematical and the real line of the channel thalweg or margin might not be completely straight). The intersections of the piercing lines on both sides of the fault with the fault plane defined the 3D location of the piercing points. The distance between each pair of piercing points yielded a net offset value. The uncertainties in the piercing point locations on the fault plane were determined through a Monte-Carlo approach: we calculated hundreds of piercing points by projecting random possible straight lines that can be adjusted within the limits of the uncertainty ellipse of the reference point (Fig. 4C). The uncertainty of the piercing point is the standard deviation of all resulting random piercing points. The mean offset values of the two margins and the thalweg and finally, the slip rate of the SAMF, were calculated using the Zechar and Frankel (2009) functions.

The dip of the fault plane can strongly influence the net offset results. Our model, following the field and trench observations, used a vertical fault plane (Fig. 2; Masana et al., 2004). In order to evaluate the influence of the dipping angle in the difference between the net and the vertical offset, we calculate the percentage difference for a few angles. For instance, for a fault dipping 80°, the net slip variation is 1%, and for a fault dipping 60°, the difference is 15%. We avoided the diffused deformation (among secondary faults) linked to the fault zone by taking reference points at a distance of a minimum of 2 m from the fault (trenches 10 and 14). The position of the modelled fault was set in the central part of the fault zone in order to calculate the contribution of the entire fault zone to the offset.

The result is a NNW–SSE oriented channel that cuts the fault at an oblique angle (Fig. 5). The mean net offset value for unit D (1σ) is $16.4^{+2.7}_{-0.3}$ m, with the strike slip component clearly predominant over the vertical one at a ratio of 12 to 1. The cumulated lateral displacement was caused by events S1, S2 and S3. The age of this channel is constrained between the ages of units B and G. Using the displacement probability distribution of the channel offsets and the age constraints (between 15.2 ± 1.1 ka and 21.9 – 22.3 cal BP), the best estimate for the net slip rate is 0.9 ± 0.1 mm/yr. Lateral and vertical slip rates are 0.9 ± 0.1 mm/yr and 0.1 ± 0.0 mm/yr, respectively.

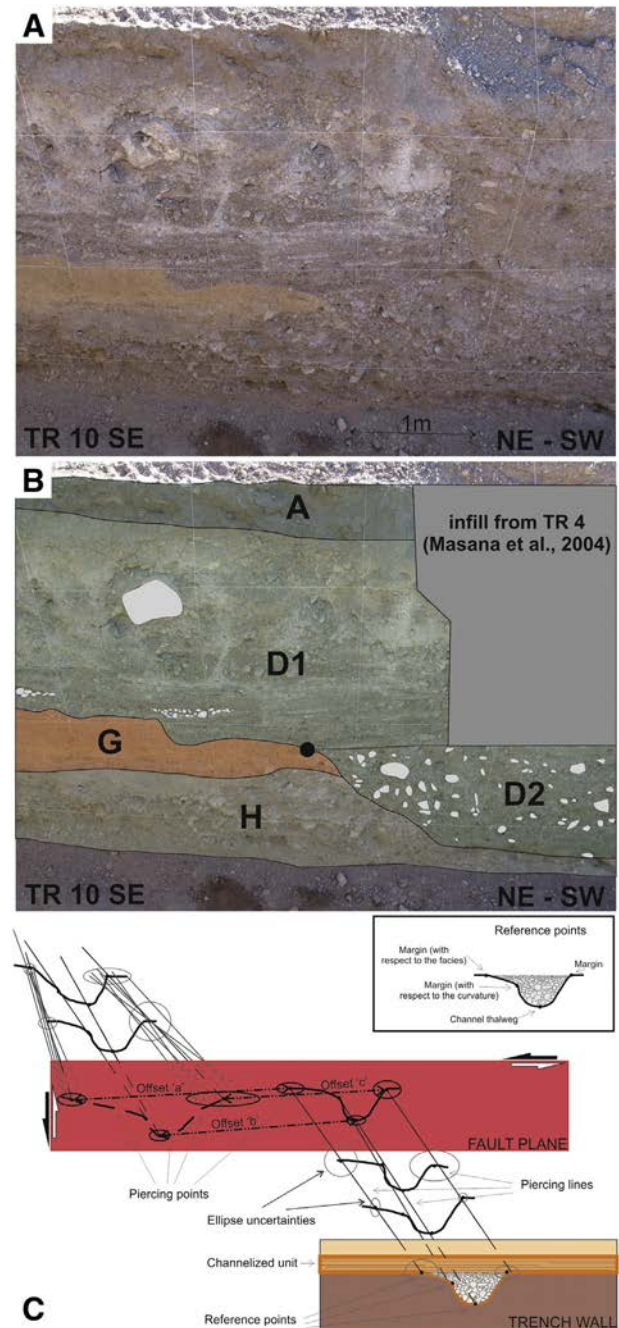


Fig. 4. A and B) Field view of unit D, an example of a reference point used to construct the piercing lines (trench 10, SE wall): the infilling of channel D can be divided in two subunits indicating a change in the depositional process: D2 composed of coarse gravels lacking internal organization and D1 composed with finer grained gravels showing better classification and laminar bedding. Unit D2 infills a channelized scar while unit D1 spreads over a wider area. We used the uppermost limit of unit D2 as an equivalent to the channel bank just before the deposition of unit D1. This same observation was obtained in the rest of the trenches and was used to obtain the piercing lines. An uncertainty on the exact position of each of these reference points was estimated directly in the field. C) Sketch of the channel features used for the analysis, their spatial relationships and the methodological approach to calculate the piercing points. Every channel profile is identified in one trench wall. For two channel features (in the downlifted wall) it is shown how we calculated the piercing point uncertainties on the fault plane based on a Monte-Carlo approach. The uncertainty ellipse around the piercing point was calculated with the intersection of hundreds of random possible piercing lines with the fault plane. The possible random lines are within the uncertainty areas of the reference points. The projection of piercing lines on the fault plane was used to define each piercing point and its associated uncertainty.

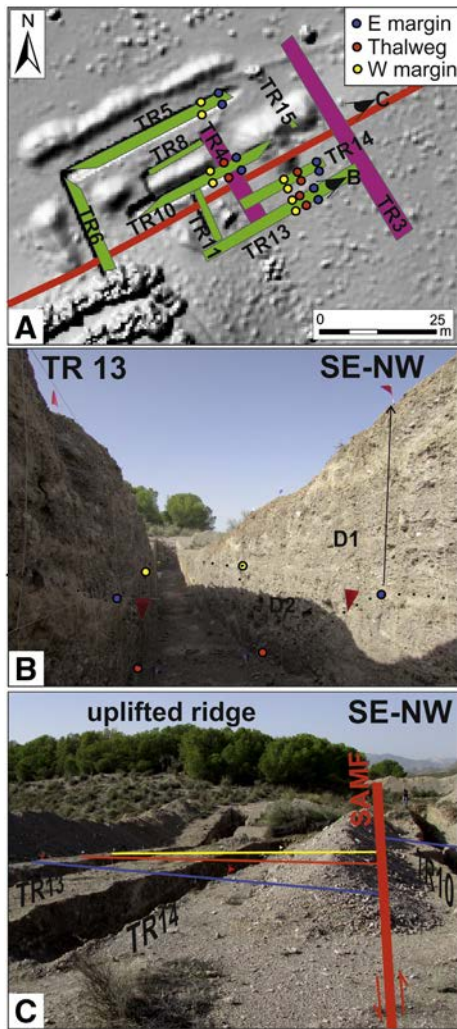


Fig. 5. Reference points identified in the trenches. A) Map of the trenches with respect to the surface projection of the reference points identified in the trench walls, the solid red line is the fault zone (the eye symbols indicate the perspectives of the pictures B and D); B) example of the identified reference points of unit D in the trench 13, and their projections on surface; C) field photograph of the trenches and the projection of the reference points indicated with flags (the approximation of the piercing lines is shown).

6. Discussion and conclusions

3d trenching at El Saltador site provided, on one hand, the longest record of paleoearthquakes (5 seismic events) reported to date for the AMF, with a mean recurrence interval of ~5.1 ka for the past 25 ka. On the other hand, accurate analyses on channel offsets combined with numerical dating allowed the direct determination of the net slip rate of the SAMF, with a best estimate of 0.9 ± 0.1 mm/yr.

The newly calculated slip rate, restricted to the SAMF strand of the Lorca–Totana section of the AMF, is clearly larger than those considered to date for this fault section (Martínez-Díaz et al., 2003; Masana et al., 2004). The total net slip rate of the AMF must be even higher, considering that the contribution of the morphologically expressive NAMF and F-AMF (Fig. 1) is not accounted for. The SAMF fault strand shows a clear dominant lateral sense of slip (the obtained ratio between the lateral and the vertical component is 12:1). However, the orientation of the fault section with respect to the direction of convergence between the tectonic plates suggests that there should be a larger vertical component for the fault system. The probable vertical component of the NAMF is also suggested by 1) the uplift of the La Tercia range associated with the AMF activity (Ferrater et al., 2015; Fig. 1C), and 2) the oblique focal mechanism of the Mw 5.2 earthquake that occurred in the vicinity

of Lorca in 2011 (Fig. 1C; López-Comino et al., 2012). This suggests that the NAMF and the F-AMF fault strands might absorb most of the vertical component of the deformation along this fault section.

We estimated the minimum slip per event by averaging the net offset by the total number of identified earthquakes. The calculated average of single event displacement since deposition of unit D is 5.3–6.3 m, considering an accumulated offset of 16.1–19.1 m produced by 3 events (a to c). As some seismic events may remain unrecognized in the paleoseismological record, the slip per event must generally be considered as a maximum value, which would also imply a considerably shorter recurrence interval if events are missing. Taking into account the very little sedimentation recorded for the past 15 ka (only unit A deposited during this period), it is plausible to consider the recurrence value, and thus the slip per event, as maximum values.

The maximum expected moment magnitude can be estimated from the empirical relationship determined by Anderson et al. (1996; $M_w = 5.12 + 1.16 \log L - 0.2 \log S$; where L is rupture length and S is net slip rate). The newly obtained slip rate (0.9 ± 0.1 mm/yr) and the length of the AMF Lorca–Totana section (23 km) applied to this equation yield a moment magnitude of 6.7 ± 0.3 . However, 5–6 m of lateral slip is large for this inferred magnitude and suggests that the AMF fault may rupture with adjacent fault sections in infrequent large earthquakes.

This study demonstrates that, even in slow tectonic settings, carefully selected paleoseismological sites may reveal long paleoearthquake records and allow estimation of key seismic parameters. A well-planned multi-trenching strategy may provide a sufficiently precise 3D reconstruction of depositional and deformational structures to support the application of rigorous statistical methods. This approach is crucial to achieve more robust results, especially in areas with neotectonic rates below 2 mm/a.

Acknowledgments

This research was funded by SHAKE CGL2011-30005-C02-02 and RISKINAT-2014SGR/1243. H. Perea was a fellow researcher under the “Juan de la Cierva” program. We thank José A. Álvarez Gómez and an anonymous reviewer for their comments improving the original manuscript.

References

- Anderson, J.G., Wesnousky, S.G., Stirling, M.W., 1996. Earthquake size as a function of fault slip rate. *Bull. Seismol. Soc. Am.* 86 (3), 683–690.
- De Larouzière, F.D., Bolze, J., Bordet, P., Hernández, J., Montecat, C., Ott d’Estevou, P., 1988. The Betic segment of the lithospheric Trans-Alboran shear zone during the Late Miocene. *Tectonophysics* 152, 41–52.
- Ferrater, M., Booth-Rea, G., Pérez-Peña, J.V., Azañón, J.M., Masana, E., 2015. From extension to transpression: Quaternary reorganization of an extensional-related drainage network by the Alhama de Murcia strike-slip fault (eastern Betics). *Tectonophysics* 663, 33–47. <http://dx.doi.org/10.1016/j.tecto.2015.06.011>.
- Ferrater, M., Echeverría, A., Masana, E., Martínez-Díaz, J.J., Sharp, W.D., 2016. A 3D measurement of the offset in paleoseismological studies. *Comput. Geosci.* 90, 156–163.
- Lindvall, S.C., Rockwell, T.K., 1995. Holocene activity of the Rose Canyon fault zone in San Diego, California. *J. Geophys. Res.* 100, 24121–24132.
- Liu, C., Zhu, B., Yang, X., Shi, Y., 2016. Geodynamic background of the 2008 Wenchuan earthquake based on 3D visco-elastic numerical modelling. *Phys. Earth Planet. Inter.* 252, 23–36.
- López-Comino, J.A., Mancilla, F.D.L., Morales, J., Stich, D., 2012. Rupture directivity of the 2011, Mw 5.2 Lorca earthquake (Spain). *Geophys. Res. Lett.* 39 (3), 1–5. <http://dx.doi.org/10.1029/2011GL050498>.
- Marco, S., Rockwell, T.K., Heimann, A., Frieslander, U., Agnon, A., 2005. Late Holocene activity of the Dead Sea Transform revealed in 3D palaeoseismic trenches on the Jordan Gorge segment. *Earth Planet. Sci. Lett.* 234, 189–205. <http://dx.doi.org/10.1016/j.epsl.2005.01.017>.
- Martínez-Díaz, J.J., 1998. *Neotectónica y Tectónica Activa del Sector Centro-Occidental de la Región de Murcia y Sur de Almería (Cordillera Bética – España)* (Ph.D. thesis) Universidad Complutense de Madrid, Madrid (466 pp.).
- Martínez-Díaz, J.J., Masana, E., Hernández-Enríle, J.L., Santanach, P., 2003. Effects of repeated paleoearthquakes on the Alhama de Murcia Fault (Betic Cordillera, Spain) on the Quaternary evolution of an alluvial fan system. *Ann. Geophys.* 46 (5), 775–791.
- Martínez-Díaz, J.J., Masana, E., Ortuño, M., 2012a. Active tectonics of the Alhama de Murcia fault, Betic Cordillera, Spain. *J. Iber. Geol.* 38 (1), 253–270.

- Martínez-Díaz, J.J., Bejar-Pizarro, M., Álvarez-Gómez, J.A., Mancilla, F.D.L., Stich, D., Herrera, G., Morales, J., 2012b. Tectonic and seismic implications of an intersegment rupture The damaging May 11th 2011 Mw 5.2 Lorca, Spain, earthquake. *Tectonophysics* 546–547, 28–37. <http://dx.doi.org/10.1016/j.tecto.2012.04.010>.
- Masana, E., Martínez-Díaz, J.J., Hernández-enrile, J.L., Santanach, P., 2004. The Alhama de Murcia fault (SE Spain), a seismogenic fault in a diffuse plate boundary: Seismotectonic implications for the Ibero-Magrebien region. *J. Geophys. Res.* 109, 1–17. <http://dx.doi.org/10.1029/2002JB002359>.
- Nocquet, J.M., 2012. Present-day kinematics of the Mediterranean: a comprehensive overview of GPS results. *Tectonophysics* 579, 220–242. <http://dx.doi.org/10.1016/j.tecto.2012.03.037>.
- Ortuño, M., Masana, E., García-Melendez, E., Martínez-Díaz, J., Stepancikova, P., Cunha, P.P., Sohbati, R., Canora, C., Buylaert, J.-P., Murray, A.S., 2012. An exceptionally long paleoseismic record of a slow-moving fault: the Alhama de Murcia fault (Eastern Betic shear zone, Spain). *Geol. Soc. Am. Bull.* 124 (9–10), 1474–1494. <http://dx.doi.org/10.1130/B30558.1>.
- Rockwell, T.K., Ragona, D.E., Meigs, A.J., Owen, L.A., Costa, C.H., Ahumada, E.A., 2014. Inferring a thrust-related earthquake history from secondary faulting: a long rupture record of La Laja fault, San Juan, Argentina. *Bull. Seismol. Soc. Am.* 104 (1), 269–284. <http://dx.doi.org/10.1785/0120110080>.
- Silva, P.G., 1994. Evolución Geodinámica de la Depresión del Guadalentín desde el Mioceno superior hasta la Actualidad: Neotectónica y Geomorfología (Ph.D. thesis) Universidad Complutense de Madrid, Madrid (642 pp.).
- Silva, P.G., Goy, J.L., Zazo, C., Lario, J., Bargají, T., 1997. Paleoseismic indications along “aseismic” fault segments in the Guadalentín depression (SE Spain). *J. Geodyn.* 24 (1–4), 105–115.
- Wang, R., Xia, Y., Grosser, H., Wetzel, H.-U., Kaufmann, H., Zschau, J., 2004. The 2003 Bam (SE Iran) earthquake: precise source parameters from satellite radar interferometry. *Geophys. J. Int.* 159, 917–922.
- Wesnousky, S.G., Prentice, C.S., Sieh, K.E., 1991. An offset Holocene stream channel and the slip rate along the northern reach of the San Jacinto fault zone, San Bernardino Valley, California. *Geol. Soc. Am. Bull.* 103, 700–709.
- Zechar, J.D., Frankel, K.L., 2009. Incorporating and reporting uncertainties in fault slip rates. *J. Geophys. Res.* 114 (B12), B12407. <http://dx.doi.org/10.1029/2009JB006325>.

Slip rate estimation of a slow-moving fault by combining paleoseismological 3D trenching and morphotectonic analysis: the strike-slip Alhama de Murcia fault (SE Iberian Peninsula)

Marta Ferrater¹, Maria Ortuño¹, Eulàlia Masana¹, José J. Martínez-Díaz², Raimon Pallàs¹, Alicia Medialdea³, Hector Perea⁴, Stephane Baize⁵, Eduardo García-Meléndez⁶, Anna Echeverria¹, Thomas Rockwell⁷, Warren D. Sharp⁸, , Edward J. Rhodes³, Ramon Arrowsmith⁹

(1) RISKNAT Group. GEOMODELS. Departament de Geodinàmica i Geofísica, Facultat de Geologia, Universitat de Barcelona, c/ Martí i Franquès, s/n, 08028 Barcelona, Spain. Email: marta.ferrater@ub.edu

(2) Departamento de Geodinamica, Universidad Complutense, Instituto de Geociencias IGEO (UCM, CSIC), 28040 Madrid, Spain

(3) Landscape Dynamics, Department of Geography, University of Sheffield, Sheffield S10 2TN, UK

(4) Barcelona Center for Subsurface Imaging (B-CSI), Departament de Geociències Marines - Institut de Ciències del Mar - CSIC, 08003 Barcelona, Spain

(5) Institut de Radioprotection et Sûreté Nucléaire - Seismic Hazard Division (BERSSIN), BP 17, 92262 Fontenay-aux-Roses, France

(6) Área de Geodinámica Externa, Facultad de CC. Ambientales, Universidad de León, Campus de Vegazana s/n 24071 León, Spain

(7) Department of Geological Sciences, San Diego State University, San Diego, CA 92182, USA

(8) Berkeley Geochronology Center, Berkeley, CA 94709, USA

(9) School of Earth and Space Exploration, Arizona State University, Tempe, AZ 85287-6004, USA

Quaternary International (Special Issue)

Keywords: tectonic geomorphology; strike-slip fault; Eastern Betics Shear Zone; offset channels

To define the seismic potential of the left-lateral strike-slip Alhama de Murcia fault (SE Iberian Peninsula, we calculated its slip rate by measuring offset linear features of known age using two methods: paleoseismology and morphotectonic analysis. The Lorca-Totana segment of the fault yielded a mean slip rate of 0.9 mm/a, based on three-dimensional trenching of a buried paleochannel, and age estimates based on OSL, radiocarbon and U-series dating. The minimum left-lateral slip rate of the Goñar-Lorca segment is 1.7-1.6 mm/a, based on eight offset surface channels, previously mapped alluvial fans dated by TL, and by new U-series dating of pedogenic carbonate.

According to the newly estimated slip rate values, the Alhama de Murcia fault is one of the most active faults in the Eastern Betics Shear Zone. We encourage the combination of paleoseismology and morphotectonic analysis to obtain reliable slip rates for faults with scarce evidence of late Holocene slip.

1. Introduction

Slip rate is an essential parameter to characterize the seismic potential of strike-slip faults. Estimation of lateral slip rate is based on reconstructing the offset of linear features of known age. Offsets can be determined through morphotectonic analysis of superficial features, such as offset channels (Rockwell et al., 1990; Van der Woerd et al., 2002; Fu et al., 2005; Ferry et al., 2007; Frankel et al., 2007; Chevalier et al., 2012; Salisbury et al., 2012; Campbell et al., 2013, among others), or can be measured from buried linear features, such as paleochannels, revealed by paleoseismological trenching (Wesnousky et al., 1991; Lindvall and Rockwell, 1995; Hall et al., 1999; Marco et al., 2005; Liu-Zeng et al., 2006; Rittase et al., 2014). Providing that accurate geochronological control is available, either morphotectonic analysis or paleoseismological trenching usually yield reliable slip rates in the case of fast-moving faults, allowing for a better estimation of seismic hazard.

In contrast, the determination of the seismic potential of slow- to moderate-moving strike-slip faults is more elusive. These faults, often found in highly populated areas where the perception of hazard is low because of the lack of historical seismicity, may produce infrequent but large and extremely destructive earthquakes (e.g. 2008 Mw7.9 Sichuan earthquake in China, and 2003 Mw6.6 Bam earthquake in Iran; USGS, 2015). The calculation of reliable slip rates in these cases is limited by the scarce evidence of slip, which results from subdued morphotectonic features and often from relatively high human surface disruption. To circumvent these difficulties, the few studies attempting the quantification of lateral slip rates in slowly deforming areas integrate all types of data and methodologies available. For instance, Vanneste et al. (2006) combined geomorphological, geophysical and trenching analyses; Moreno (2011) combined geodetic, paleoseismic and geomorphic information onshore and offshore; and Martínez-Díaz et al. (2003) analyzed offset surface channels and paleoseismological trenches. The large uncertainties in slip rate estimates along slow- to moderate-moving faults also result from an additional limiting factor: deformed landforms or units

requiring chronological control are rarely restricted to the last 50 ka, the timeframe covered by the radiocarbon dating method. Dating methods spanning older periods (luminescence, uranium series, and cosmogenic radionuclide dating) have to be used, inducing greater uncertainties and reduced precision in slip rate determination. Hence, the study of slow to moderate-moving faults is a great methodological challenge, requiring a complex combination of state of the art techniques in remote-sensing (e.g. LIDAR-based high resolution DEM), field work, 3D modelling, and geochronology.

The aim of this paper is to explore and assess the performance of innovative methodological combinations to estimate the slip rate of slow-moving faults using, as an example, the Alhama de Murcia fault (AMF; SE Iberian Peninsula; Fig. 1A). To obtain a reliable lateral slip rate for the AMF, we developed two different approaches: 1) we calculate the net, the lateral and the vertical slip rate along one segment of the AMF (the Lorca-Totana) by analyzing and reconstructing two offset buried paleochannels exposed in three-dimensional paleoseismic trenches at the El Saltador site; and 2) we calculate the lateral slip rate of two segments of the AMF (the Goñar-Lorca and the Lorca-Totana) by measuring offset channels on the surface of alluvial fans. The age constraints for the age of the channels are a) the luminescence-based chronological dataset of Ortuño et al. (2012), and b) new U-series dates on pedogenic carbonate, and new OSL and radiocarbon dates. Finally, we discuss the advantages and disadvantages of each approach, and the regional implications of the newly established slip rate for the AMF.

2. Geological setting

The AMF is located within the Eastern Betics, which is the northern branch of the Gibraltar arc and are divided into internal (Alpujarride, Malaguide and Nevadofilabride) and the external units. During middle to Late Miocene, upper-crustal extension occurred in the internal parts of the orogen (Martínez-Martínez and Azañón, 1997). The interplay between the Tortonian extension and a later phase of inversion (commencing in the latest Tortonian) resulted in a basin and range structure over the eastern Betics (Montenat et al., 1990; Meijninger and Vissers, 2006; Booth-Rea et al., 2004) giving rise to several Neogene to Quaternary basins. The Eastern Betics Shear Zone (EBSZ; Fig. 1; De Larouzière et al., 1988) is a large shear fault system that could be absorbing up to 31 % (Masana et al., 2004) of the 4–6 mm/yr of NW-SE convergence between the Eurasian and African plates (Serpelloni et al., 2007; Argus et al., 2011; Nocquet, 2012).

The faults forming the EBSZ from south to north are the Carboneras, Palomares, Alhama de Murcia, Carrascoy and Bajo Segura faults (Fig. 1).

The Alhama de Murcia fault is a N45E – N65E left-lateral strike-slip fault dipping to the northwest with a minor reverse component (Bousquet, 1979; Martínez-Díaz, 1998). It was formed during the tectonic inversion, probably reactivating a Tortonian extensional fault, initiating its strike-slip activity in the Pliocene or Quaternary (Bousquet, 1979; Meijninger and Vissers, 2006). The fault separates three mountain ranges (the Espuña, the La Tercia and the Las Estancias ranges) and two Neogene basins (the Fortuna and Lorca basins) from the Guadalentín and Huercal-Overa depressions (Fig. 1C). The fault zone cuts a) the Alpujárride and Maláguide complexes of the Betic basement in the Las Estancias and the La Tercia ranges, b) late Miocene formations and c) the continental Quaternary deposits that infill the Guadalentín and Huercal-Overa depressions (Bousquet, 1979).

Several damaging earthquakes have been produced by the AMF (IGN, 2012). The most significant historical earthquakes (\geq VII EMS) were recorded in 1743 and 1746 in Alcantarilla, in 1907 in Totana, and in 1579, 1674 and 1818 in Lorca (the 1674 event had an intensity of VIII; IGN, 2012; see Fig. 1 for location of the cities). The largest instrumental earthquake was recorded in Lorca on May 11th, 2011, with a moment magnitude (M_w) 5.2 and a maximum intensity VII (EMS), and was preceded by a M_w 4.5 foreshock. The focal mechanisms of the two events show oblique left lateral-reverse faulting (Lopez-Comino et al., 2012; Martínez-Díaz et al., 2012). No surface rupture in this seismic sequence has been identified.

Silva (1994) and Martínez-Díaz et al. (2012) proposed four segments along the AMF according to its orientation, geometry of the fault zone, geomorphic expression and seismicity. The segments from south to north are (Fig. 1): 1) Góñar–Lorca (NNE–SSW), characterized by a horse tail termination to the south that merges into a narrow fault zone to the north, the presence of the Las Estancias range in the hanging wall and moderate seismicity; 2) Lorca–Totana (NE–SW), where the fault turns into a N60E strike, splits into three main sub-parallel fault traces, related to the La Tercia range, and manifests the maximum concentration of seismicity along the entire fault; 3) Totana–Alhama de Murcia (NNE–SSW), where the fault still exhibits several strands, SE of the Espuña range; and 4) Alhama de Murcia–Alcantarilla (NNE–SSW), where the

geomorphic expression of the fault is diffuse, probably because deformation is transferred to the Carrascoy fault to the NE (Fig. 1).

Earlier paleoseismological (trench analysis) and morphotectonic studies have suggested uncertain slip rate values for the AMF. Martínez-Díaz et al. (2003) and Masana et al. (2004) suggested a vertical slip rate of 0.04 – 0.35 mm/yr at the El Salvador paleoseismic site in the Lorca-Totana segment and, based on the orientation of slickensides, estimated a 0.07 – 0.66 mm/yr net slip rate and 0.06 – 0.53 mm/yr lateral slip rate. These values should be considered with caution as they were based on an estimation of the vertical offset based on the morphology of the alluvial fan (microtopographic profiles) assuming no strong influence of its conic shape. Also by means of paleoseismic trenches, Ortuño et al. (2012) estimated a vertical and lateral slip rate of 0.16 – 0.22 mm/yr and 0.95 – 1.37 mm/yr, respectively, at the southern termination of the fault (at Goñar; Fig. 1), acknowledging huge uncertainties in their assumptions. The first lateral slip rate based on offset channels was done by and Martínez-Díaz (1998). He estimated a 0.6 m/kyr lateral long-term (1 Ma) slip rate for the Goñar-Lorca segment. Martínez-Díaz et al. (2003) obtained a 0.21 mm/yr lateral slip rate for Lorca – Totana fault segment without specifying the uncertainty associated with the measurement. Recently, Ferrater et al. (2015a) mapped 138 offset features along the fault but were not able to calculate a slip rate due to a lack of numerical age control. The first geodetic measurements based on GPS derived station velocities across the region, compared with the geological slip rates, have recently yielded a surprisingly high horizontal slip rate estimation of 1.5 ± 0.3 mm/yr that includes the AMF and the Palomares fault (Fig. 1B; Echeverria et al., 2013).

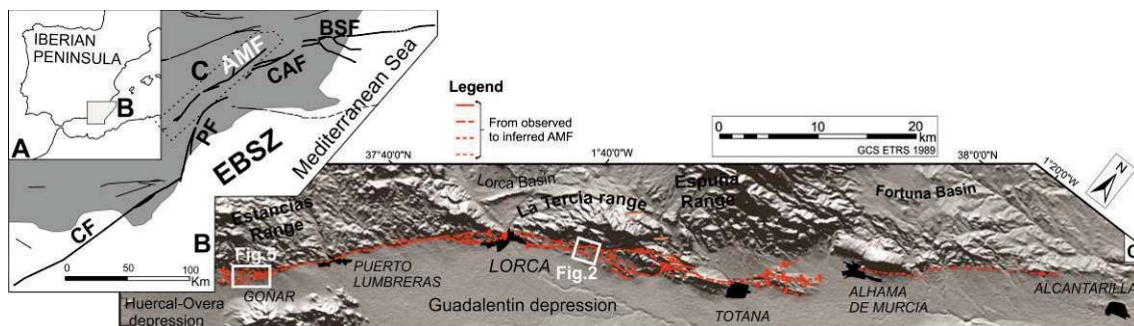


Figure 1. A) Alhama de Murcia fault (AMF) in the Iberian Peninsula; B) the AMF is part of the Eastern Betics Shear Zone (EBSZ faults in bold line: CF, Carboneras fault; PF, Palomares fault;

CAF, Carrascoy fault; BSF, Bajo Segura fault); C) structural map of the AMF, red lines are recently active faults..

The recent deposits along the AMF study area are mostly proximal facies of Plio-Quaternary alluvial fans draining the main ranges in the area towards the Guadalentin (central parts) and Huercal-Overa (southern parts) depressions (Fig. 1C). Several studies have focused on the cartography of the alluvial fans based on relative criteria, such as spatial relationships and entrenchment (Silva et al., 1992; Martínez-Díaz et al., 2003; Soler et al., 2003; Masana et al., 2004; Silva et al., 2008; Ortuño et al., 2012; Table 1). Moreover, Ortuño et al. (2012) classified the alluvial fans in the southernmost termination of the fault into seven alluvial fan generations (G0 to G6) based on 24 numerical ages obtained with thermoluminescence (TL) and post-IR IRSL (pIRIR) of 11 units exposed in paleoseismological trenches and natural outcrops.

Martínez-Díaz et al., 2001; Masana et al., 2004	Martínez-Díaz et al., 2003		Ortuño et al., 2012		Silva et al., 1992	Soler et al., 2003
Lorca-Totana	Lorca-Totana		Goñar		AMF	AMF
	F	Hol.-L. Pleist	G0	Hol	3r phase	G7
Young	E	Hol.-L. Pleist	G1-G2	Hol.-L. Pleist	2nd phase	G6
Intermediate	D-C	L.-M. Pleist	G3-G4	L.-M. Pleist	1st phase	G4
Old	C-B	M. Pleist-Plio	G5, G6	M. Pleist	1st phase	G3

Table 1. Correspondence between alluvial fan generations described by previous studies based on relative criteria, such as spatial relationships and entrenchment (Silva et al., 1992; Martínez-Díaz et al., 2001; Martínez-Díaz et al., 2003; Soler et al., 2003; Masana et al., 2004; Ortuño et al., 2012). Second row refers to the study area. Hol., Holocene; L., Late; M., Middle; Pleist., Pleistocene; Plio., Pliocene.

3. Numerical Dating of Quaternary sediments

The age of an offset feature is an essential parameter in a slip rate calculation, and often responsible for the high uncertainty values in the final result. The upper limit of the radiocarbon dating method (~50 ka) does not allow its application within most of the upper Pleistocene, a key interval for characterizing slow-moving faults. Moreover, in arid regions, organic materials suitable for radiocarbon dating may be thinly or discontinuously distributed and poorly preserved. For this reason, previous studies in this area have dated Quaternary units combining several dating techniques, such as radiocarbon (^{14}C ; Martínez-Díaz et al., 2003, Masana et al., 2004; Silva et al., 2008), thermoluminescence (TL; Martínez-Díaz et al., 2003, Masana et al., 2004; Ortuño et al.,

2012), U-series dating applied to calcrete (Masana et al., 2004) and cosmonuclide (^{10}Be and ^{26}Al ; Rodés et al., 2013) techniques. Here we provide new numerical ages by applying two additional dating methods: U-series to date pedogenic carbonate and Optically Stimulated Luminescence (OSL). The requirements and assumptions of these methods are distinct (Ku et al., 1979; Ludwig and Paces, 2002; Sharp et al., 2003; Thomsen et al., 2008; Buylaert et al., 2009; Rodés et al., 2011; Moreno et al., 2015; and references therein). Thus, using more than one extends the range of materials that may be dated and can enhance the reliability of the resulting ages.

3.1. *U-series of pedogenic carbonate*

Pedogenic carbonate accumulates in the soil profile in the Bw or K horizons in arid and semiarid regions (Gile et al., 1966; Machette, 1985; Birkland, 1999; Schaetzl and Anderson, 2005). In coarse alluvium, carbonate initially forms thin coatings at the bottom of the clasts (Arkley, 1963; Gile et al., 1966; Machette, 1985; Mayer et al., 1988). The CaCO_3 may come from dissolution of carbonate bearing rocks within the soil profile, from eolian dust accumulated on the surface, or by combining calcium from weathering of dust and soil parent material with carbon dioxide from atmospheric and soil sources. (e.g., Amundson et al. 1994; Cerling, 1999; Capo and Chadwick, 1999). Soil carbonate commonly contains a few ppm of uranium due to incorporation of uranium present in soil waters; however, thorium, which is relatively insoluble in typical soil waters, is extremely low in pure authigenic carbonate (e.g., Sharp et al. 2003).

U-series dating can be applied to clast-coatings younger than 0.5 Myr made of dense, pure and laminated carbonate (e.g., Ku et al., 1979; Ludwig and Paces, 2002; Sharp et al., 2003). U-series ages of pedogenic carbonate yield reliable dates for soil formation and minimum dates for the host alluvium because some time after deposition must elapse before dateable amounts of dense carbonate accumulate. The time lag between alluvial deposition and accumulation of dateable carbonate may vary from a few hundred to a few thousand years depending on the rate of carbonate accumulation in the soil and sampling techniques (e.g., Sharp et al., 2003; Blisniuk et al., 2012; this paper). Pedogenic carbonate dating has been successfully applied to alluvium as young as the mid-Holocene in the Anza Borrego Desert of southern California (Blisniuk et al., 2012).

Sample collection and preparation procedures in this study were similar to those described by Gold et al. (2015). To estimate the minimum age of the host alluvium, we calculated the weighted mean age of the three oldest U-series dates reproducible within analytical errors. This protocol is employed to help exclude biased ages—for example, those produced if the U-Th system fails to remain closed, or a clast-coating inherited from an older landform is dated—since such anomalous ages are unlikely to be reproducible. We reported the resulting U-series ages at the 1σ confidence level (Table 2 and Table S1 of the Supplementary material).

Sample Name	Preferred U-Th Age (ka, \pm ka)	Probability
SALT13A16	12.39 \pm 0.42	0.88
SALT13B19	20.9 \pm 2.5	0.62
SALT5CAN	11.0 \pm 1.7	0.97
CARR4	23.2 \pm 4.2	0.95
LiM4	11.7 \pm 2.6	0.84
LIMII5	46.6 \pm 5.7	0.75
PERA	23.8 \pm 3.2	0.76
LIM II7	105.1 \pm 4.2	0.12

Table 2. Weighted mean ages for pedogenic carbonate samples. The mean is calculated using the three oldest samples of Table S1 (Supplementary material). Probability indicates the probability that the observed scatter is due to analytical errors.

3.2. *Optically Stimulated Luminescence (OSL)*

OSL and IRSL (infra-red stimulated luminescence) are used to estimate the time since last exposure of mineral grains, quartz and feldspar in the case of this study, to sunlight. It has been applied to date the buried sedimentary units of the El Salvador alluvial fan. A total of 8 units have been sampled, 2 of which, SAL21 and SAL27, are used for this study (Table 3). OSL has been applied to quartz extracts of 180-250 μ m. 40-60 small multi-grain aliquots, containing \sim 30 grains each, have been measured using an automated Risø TL/OSL DA-20 luminescence reader (Bøtter-Jensen et al., 2010). The SAR (single aliquot regenerative) protocol (Murray and Wintle 2000) was used for quartz OSL. Possible feldspar contamination has been tested for by calculating the IR depletion ratio, i.e. the depletion of the blue OSL signal after using IR stimulation which would occur if feldspar was present in the aliquots. Equivalent doses have been estimated using the Central Age Model (CAM, Galbraith et al., 1999) which calculates a weighted average of the individual dose estimates. Less than 5% of the dose estimates have been identified as outliers (those out of 1.5 times the Inter Quartile Range, Tukey, 1977) and were excluded prior to the estimation of the equivalent dose.

Dose rates, i.e. the dose of ionizing radiation per unit time, are based on the concentration of ^{238}U , ^{232}Th and ^{40}K measured using high resolution and field gamma spectrometry.

Sample	Method	Depth (m)	Moisture (%)	Dose rate (Gy/ka)	Equivalent dose (Gy)	Age (ka)
SAL-21	OSL	1.92	5 \pm 2	2.49 \pm 0.10	42.6 \pm 2.5	17.1 \pm 1.2
SAL-27	OSL	0.87	5 \pm 2	2.67 \pm 0.11	40.6 \pm 2.3	15.2 \pm 1.1
SAL-21	IRSL	1.92	5 \pm 2	3.17 \pm 0.11	67.8 \pm 3.8	21.4 \pm 1.4
SAL-27	IRSL	0.87	5 \pm 2	3.36 \pm 0.12	51.2 \pm 4.7	15.2 \pm 1.5

Table 3. Summary of results from OSL (Optically Stimulated Luminescence) and IRSL (infra-red stimulated luminescence) dating which includes sample depth, water content and derived total quartz dose rates. An internal quartz dose rate of 0.06 \pm 0.03 Gy/ka has been assumed based on Mejdahl (1987). Estimated equivalent doses and derived ages are also summarized. Uncertainties represent one standard error.

3.3. Radiocarbon

Radiocarbon samples have been run in the Laboratoire de Mesure du Carbone 14 in Paris and at the KECK CAMS facility at the University of California, Irvine. Calibration was made with Calib7.0.2 using IntCal13 curve (Reimer et al., 2013).

4. Estimating the slip rate by 3D Paleoseismic analysis at El Salvador site

The El Salvador paleoseismological site is located in the Lorca-Totana segment. In this segment, the fault splits into three main strands: the north AMF (NAMF) and the south AMF (SAMF) described by Martínez-Díaz (1998); and a frontal fault (F-AMF) that separates the Guadalentin depression from the La Tercia frontal low relief areas (Fig. 2). The NAMF and the frontal fault coincide with a sudden change in the relief. The SAMF is the strand of the Lorca-Totana segment that shows recent geomorphic evidence of lateral slip (Martínez-Díaz, 1998; Ferrater et al., 2015a; Fig. 2). To the NW, the La Tercia range is the source of the Pleistocene alluvial fans deposited south of the NAMF. At the study zone, two alluvial fans (El Salvador and La Salud) were deposited over the SAMF (Fig. 2). The current sedimentation has migrated to the Guadalentin depression through the entrenchment of the main channels (Silva, 1994)

Ten new trenches were excavated (2013-2015) in the El Salvador alluvial fan (Fig. 2), four of them perpendicular and six parallel to the fault (Fig. 3). The aim was to better

constrain the lateral, the vertical and the net slip rate of the AMF by direct measurement of the offset of the exposed linear features (i.e. paleochannels). The trenches display two alluvial fan sequences and a system of infilled channels entrenched at top. The oldest alluvial fan units (W and X) have been interpreted as basement (Fig. 4). The youngest alluvial fan units exhibit a classical alluvial fan sequence, with poorly sorted gravels and sands interpreted as debris flow deposits (units H, I, K, M, O, Q), and also exhibit a number of well-defined levels of fine orange sands and silts (units G, J, L, N, P), interpreted as mud-flows (Ferrater et al., submitted). Although the fluvial entrenchment of the channel system began just before the deposition of unit H (units A-F; Fig. 4), the best-preserved channelized units are D and B. This channel system was interpreted to postdate the abandonment of the fan surface in which it is incised. Therefore, the superimposed channel system was only draining the abandoned surface of the fan, being disconnected from the ancient main source area.

4.1. Age estimates

The ages of the units exposed in the trenches were constrained by U-series, OSL, IRSL and radiocarbon dating (Table 4). The sequence revealed by the trenches is upper Pleistocene to Holocene in age (Table 4) suggesting that the alluvial fan sedimentation was active before long 25 ka (unit H), and the entrenchment of the main channel (unit D) occurred shortly before 15 ka. Two direct dates are available for channel in unit B (15.5 ± 1.0 ka and 16.6 ± 1.8 ka; Table 4), whereas the age of unit D is constrained between the age of units B and G. To calculate the slip rates, the age of unit B is considered to be the intersection of the two values from Table 4 (15.65 ± 0.85 ka); and the age of the radiocarbon sample is the age of unit G (20839 – 23014 cal BP).

Sample	Age (ka)	Method	Unit in El Salvador site	Trench
SAL-27	15.2 ± 1.1	OSL	B	TR 10 (Figs. 3 and 4)
SAL-27	15.2 ± 1.5	IRSL	B	TR 10 (Figs. 3 and 4)
SALT5CAN	11.0 ± 1.7	U-series	D (northwestern wall)	TR 5 (Figs. 3 and 4)
SALT13A16	12.39 ± 0.42	U-series	D (southeastern wall)	TR 13 (Figs. 3 and 4)
SAL-21	17.1 ± 1.2	OSL	G	TR 5 (Figs. 3 and 4)
SAL-21	21.4 ± 1.4	IRSL	G	TR 5 (Figs. 3 and 4)
SAL-20	20839 – 23014 cal BP	radiocarbon	G	TR 5 (Figs. 3 and 4)
SALT13B19	20.9 ± 2.5	U-series	H	TR 13 (Figs. 3 and 4)
SAL-2	25228 – 25832 cal BP	radiocarbon	H	TR 6 (Fig. 3)

MS-4	28.2±2.0	OSL	La Salud trenches (Fig. 2)
------	----------	-----	----------------------------

Table 4. Summary of new numerical ages in the El Saltador trenches. Errors for radiocarbon dates are given at the 2σ confidence level, whereas U-series, OSL and IRSL samples have 1σ errors.

4.2. *Offset measurement*

To measure the offsets of the identified channels, we used the technique described by Ferrater et al. (2016). We fit a 3D straight line to every group of the exposed key points of a segment of a buried channel (each group belongs to a channel feature, such as a margin or the thalweg and every trench wall exposes a key point). Then, we projected the three-dimensional trend of these lines onto the fault plane (simplified as a vertical unique fault plane) to obtain the corresponding piercing point. We repeated this operation for the segment of the channel in the opposite side of the fault. Finally, we measured the distance between each pair of resulting piercing points, i.e. the intersection points between the projected lines and the fault plane. As a result, we obtained three measures for the channel offset, two corresponding to the channel margins and the other to the thalweg. The positions of the reference points, together with their uncertainty, were recorded in the field with a differential GPS. Finally, the mean value for the offset was obtained using the probability density functions created by Zechar and Frankel (2009).

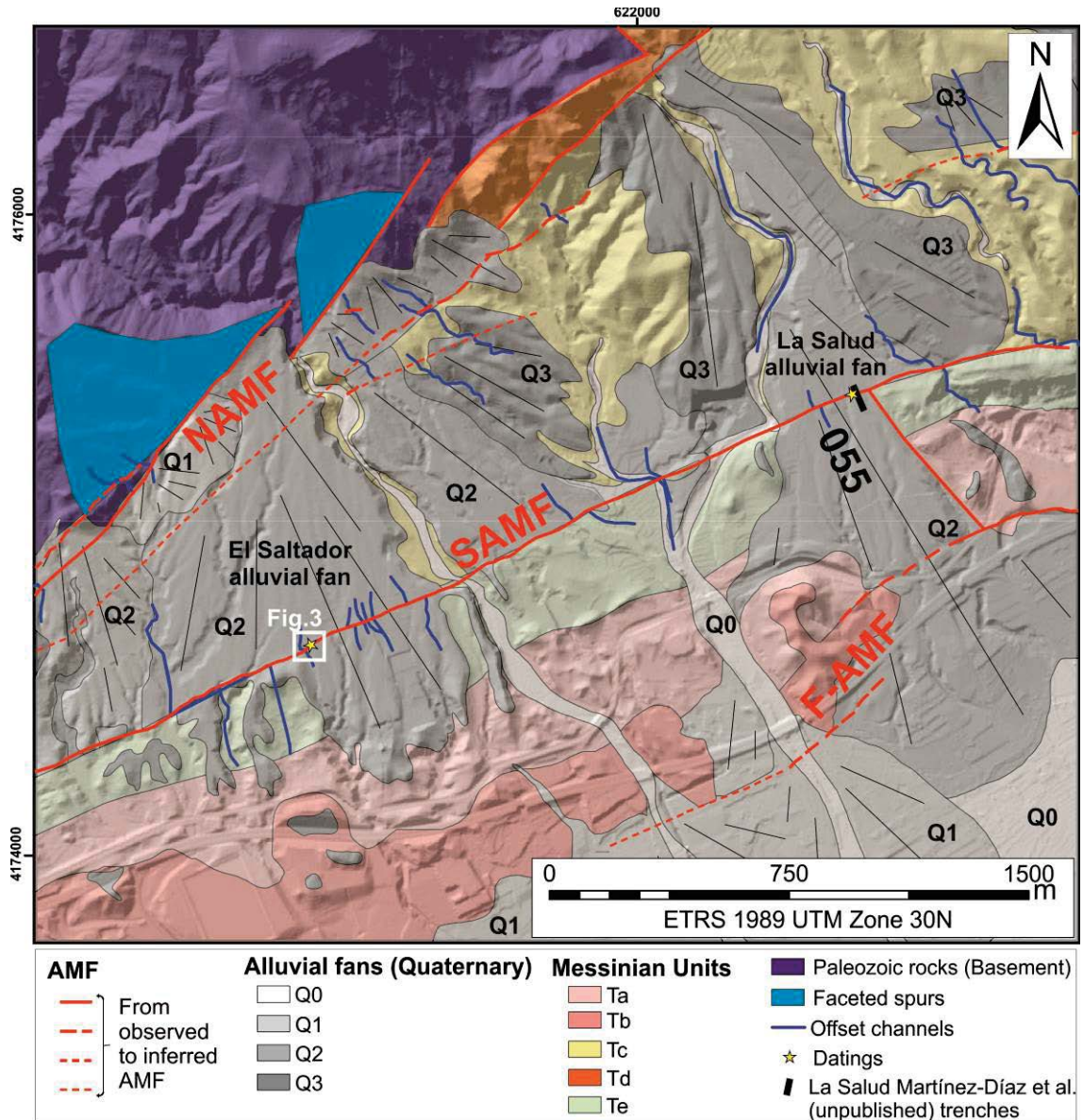


Figure 2. Geologic map of a zone from the Lorca-Totana segment. El Salvador trenching site is highlighted with a white square (Figure 3). Number 055 refers to an offset channel in surface. Modified from Ferrater et al., 2016.

4.3. Slip rate of the SAMF based on channel D

Unit D, made of anisometric subangular clast-supported gravels, displays two sequences. The lower part (D2; Fig. 4) is entrenched and filled with coarse and chaotic facies and fills a distinguishable channel, whereas the upper part (D1) presents tractive structures, such as laminar bedding, and local cross-bedding and clast imbrication. A correlation of the identified channel on either side of the fault was accomplished by stratigraphic criteria (sedimentary position, shape and facies). Dating results provided

by U-series of the channel at each wall of the fault supported the correlation (12.39 ± 0.42 ka and 11.0 ± 1.7 ka; Table 4). The mean of all the dates on unit D, 12.22 ± 0.80 ka, is our preferred minimum age for this unit. The channel was identified in four trench walls in the northwestern wall of the fault (trenches 5 and 10) and in four walls in the southeastern wall (trenches 13 and 14). The channel is approximately 5 m wide and 1.75 m deep, and its top was at a depth of 2 m in the northwestern wall and at 1 m in the uplifted southeastern wall. To measure the offset, the margins of the channel were surveyed in the eight walls and the thalweg, in six (trenches 10, 13 and 14).

The resulting mean net offset value for unit D (1σ) was $16.4^{+2.7}_{-0.3}$ m, with a mean lateral offset of $16.3^{+2.7}_{-0.3}$ m and a mean vertical displacement of 1.3 ± 0.1 m. As the U-series only provide the minimum age of unit D and the time lapse between the unit deposition and the pedogenic carbonate is unknown, its age was constrained by the available OSL and radiocarbon dates from unit B and unit G (Fig. 3). We calculated the slip rate, and its lateral and vertical components, assuming that the age of unit D is comprised between 15.2 ± 1.1 ka (SAL-27, unit B; Table 4) and 20839 – 23014 cal BP (SAL-20, unit G; Table 3). The application of the Zechar and Frankel (2009) functions considering a trapezoidal form for the age function yield a net slip rate (1σ) of 0.9 ± 0.1 mm/yr, and a lateral and vertical slip rates (1σ) of 0.9 ± 0.1 mm/yr, and 0.1 ± 0.0 mm/yr, respectively for the last ~20 ka.

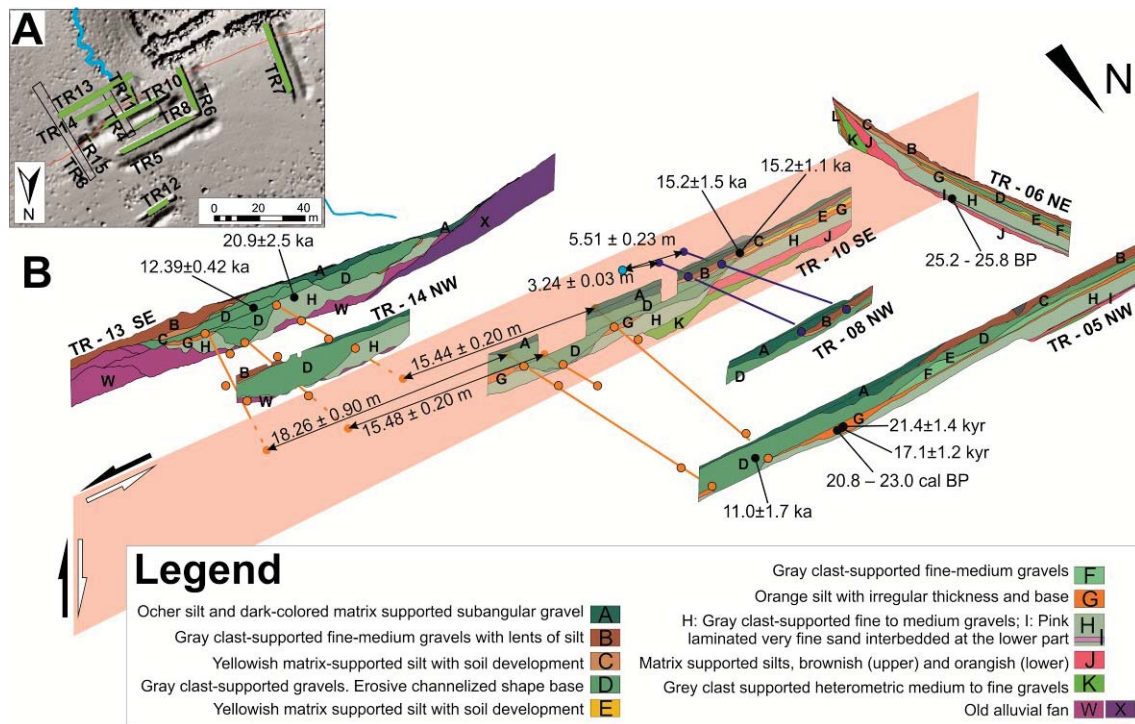


Figure 3. Slip measurements at the El Salvador site. A) Map with the trench locations, a simplified trace of the SAMF (orange), and the position of the active channel (blue); B) block diagram showing the location of the most relevant trenches (TR 5, 10 and 13, while TR 8 and 14 are not included for clarity), the reconstructed fault plane and the samples position. Small orange dots on channel D in the trench walls represent the position of the reference points used. The straight 3D line that best fits every group of reference points is the piercing line. In orange, piercing lines and piercing points for channel D; in purple, piercing lines and piercing points for channel B. Trench logs of all the trenches parallel to the fault are shown in Fig. 4.

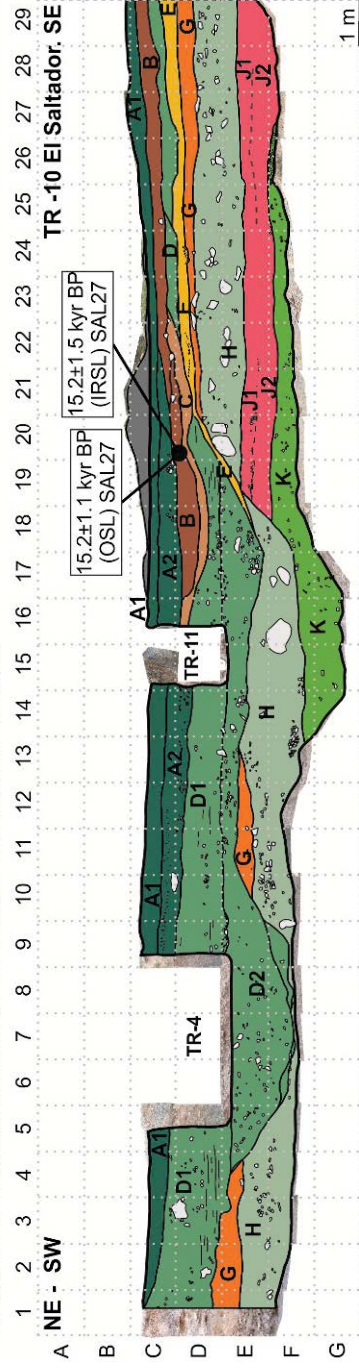
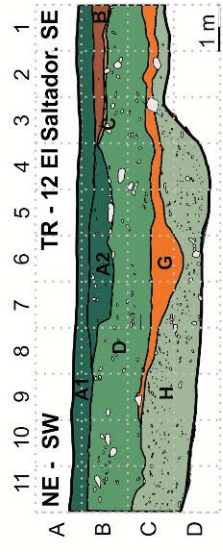
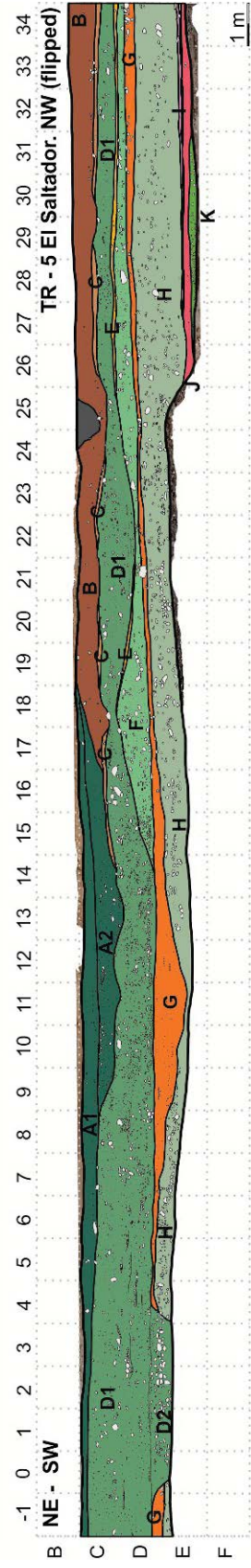
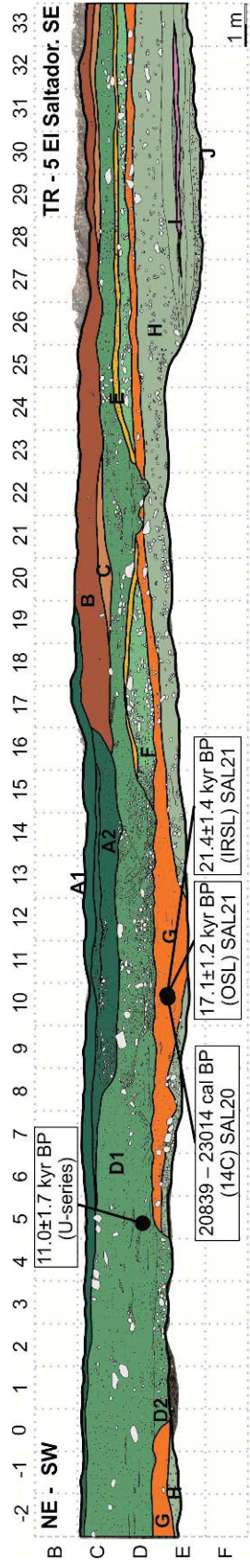
4.4. *Slip rate of the SAMF based on channel B*

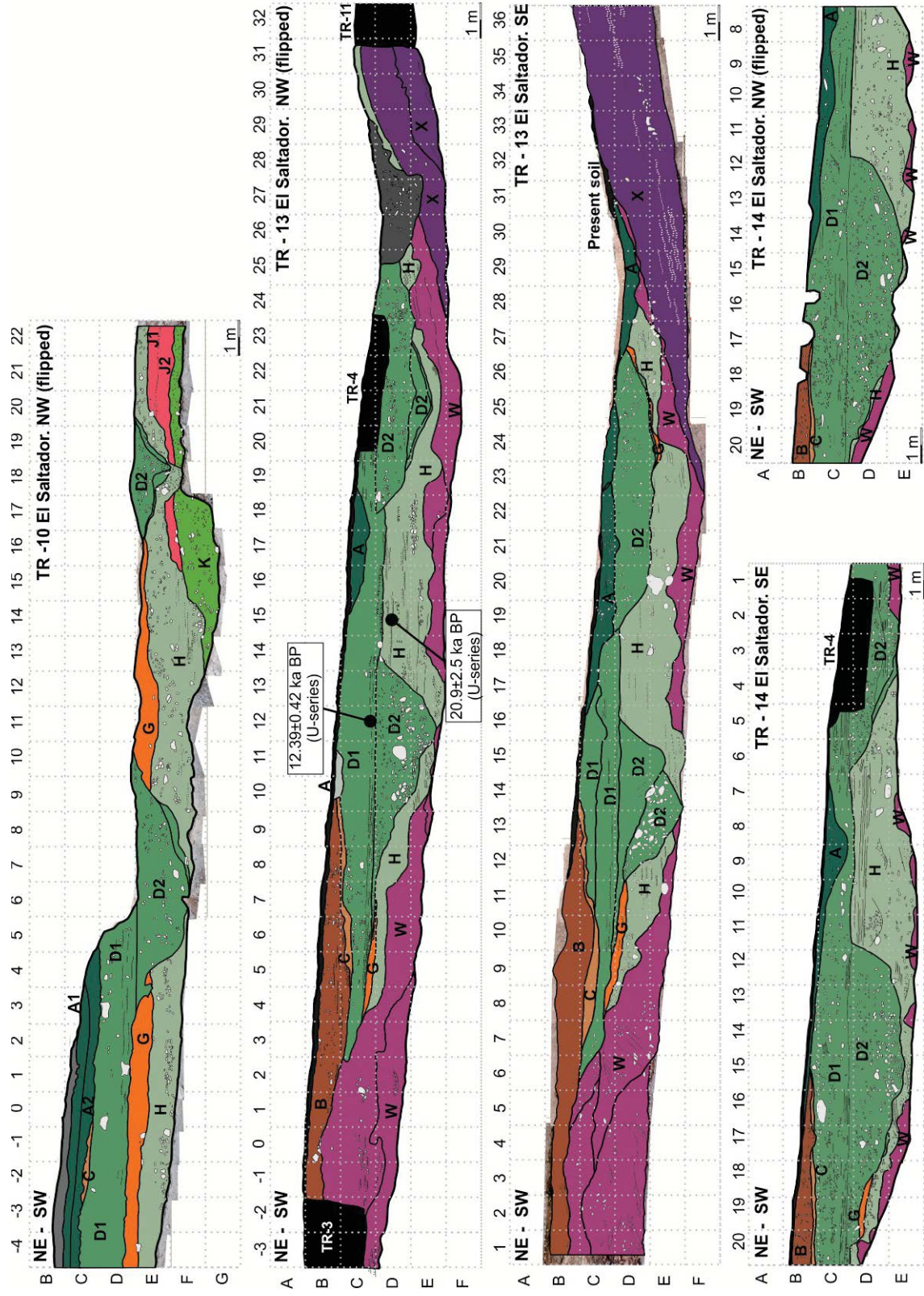
In the case of the channel filled by unit B (Figures 3 and 4), deposits were only preserved at the NW wall (downthrown by the fault movement) and thus direct correlation with the opposite side of the fault was not possible. However, a minimum offset value for this channel was estimated by correlating the buried channel deposits with the currently active morphological channel, which also shows a left lateral offset. The current channel in the uplifted wall is actively eroding the hill on its right bank as a consequence of the left lateral movement along the fault incrementally displacing the hill in front of the water inflow and therefore the position of the current channel is the maximum position for channel B in the hangingwall. To project the active channel, we fit a straight line to a channel segment running from 10 m (to avoid deflection in the diffuse deformation of the fault) to 30 m from the fault. We used this 20 m long channel segment because a) sinuosity has a smaller influence than if we used a shorter segment, and b) this distance is consistent with the distances used to calculate the projections in the northwestern wall (Fig. 3).

We correlated the two channel margins in the NW with only the thalweg in the SE: the distance between the western margin of the buried channel and the current thalweg is the upper-bound offset, whereas the distance between the eastern margin of channel B and the thalweg is the lower-bound offset (Fig. 3). To calculate the final offset of channel B, we used a trapezoidal displacement density function (Zecher and Frankel, 2009) to reflect our consideration of the offset. The obtained minimum mean net offset for channel B was $4.4^{+1.2}_{-1.1}$ m (1σ), the minimum lateral offset was 4.3 ± 1.1 m and the vertical offset was $-0.7^{+0.2}_{-0.1}$ m, respectively. As the age of unit B is 15.2 ± 1.1 ka

(SAL-27; Table 4), the net, lateral and vertical minimum (based on a minimum offset) slip rates (1σ) are 0.3 ± 0.1 mm/yr, 0.3 ± 0.1 mm/yr, and 0.0 ± 0.0 mm/yr, respectively. Because these slip rates are minima, they are consistent with the slip rates obtained using the offset of channel D for the past 20 ka.

Figure 4. Geological and stratigraphic interpretation of trenches 5, 8, 10, 12, 13 and 14. Dating results are shown. Explanation is the same as in in Fig. 3. Trenches exposed an alluvial fan sequence alternating heterometric gravels and sands with fine sands and silts (units from K to H). Units D and B correspond to a fluvial entrenched sequence. Photologs of the trenches in Fig. S3 (Supplementary material).





5. Estimating the fault slip rate by morphotectonic analysis

To obtain the minimum slip rate of the AMF, we measured the offset of surface channels along the fault and we estimated indirectly the maximum age of these channels. The age of the channels was assumed to be younger than the surface where they are entrenched, corresponding to the time of alluvial fan abandonment. Finally, we calculated the minimum lateral slip rate using Zechar and Frankel (2009) functions.

The 138 offset measurements that Ferrater et al. (2015a) obtained analyzing a 0.5×0.5 m pixel size Digital Elevation Model (DEM) and orthophotographs created from 1956 aerial photographs (1:33,000 scale) were reviewed in this paper. To measure the offset, the estimation of the pre-deformation morphology is required. In order to project the channel tendency into a fault and, thus, obtain the pair of piercing points of a channel, more than one piercing line can be defined. For instance, Gold et al. (2011) consider the near and full channel projections of either the margins or the thalweg. Ferrater et al. (2015a) followed this criterion, and computed the mean and mean standard deviation for all the combinations between the near and full projections of the identified channels offset by the AMF. In addition, these authors assigned a subjective and objective rating between 0 and 1 to each measurement (being 0 the lowest score and 1 the highest score). These values are used here when considering the reliability of the offset channel when obtaining the slip rate. The slip rate estimation was done in two segments: Goñar-Lorca and Lorca-Totana segments, using those offset channels with a) moderate to high quality score and b) available age control.

5.1. *Goñar-Lorca segment*

This segment includes the southern horse-tail termination of the fault (Fig. 5), which is made up of 1) two boundary faults, the northern and the southern Alhama de Murcia fault, and 2) several internal structures, known as the Goñar faults (Ortuño et al., 2012). Here, we modified slightly the nomenclature of the Goñar faults in order to simplify their references in the text when calculating their slip rates (Fig. 5).

We selected eight offset channels at the southernmost termination of the segment: 114-115, 122-125, 129 and 136 (Fig. 5 and Figs. S4-S11). Channels 114-115 are affected by fault strand F1 and are entrenched into slope debris deposits above a G2 alluvial fan. Channel 114 (Fig. S4) is still active; its sinuosity is low and the orientation of the two

channel segments very similar, providing a very good objective quality. Channel 115 has been modified by human action (Fig. S5), but the incision displayed in the old ortophotographs is similar for the two segments of the channel, yielding good quality ratings. Channels 122-124 are affected by fault strand F2. They are entrenched into alluvial fans of different generation: channel 122 is on a G3 alluvial fan, channel 123 is on a G5 alluvial fan; and 124 is entrenched into a G4 alluvial fan. Channel 125 is on a G4 alluvial fan and is the only one identified for the southernmost fault strand. The incision of channel 129 (Fig. S10) into the Quaternary sediments is smooth. These sediments onlap a G4 alluvial fan, and thus, we considered the maximum age of the channel to be the age of the alluvial fan generation G4. Finally, channel 136 is on the fault F2b. This fault is associated with significant relief and, thus, with an uncertain large vertical component, suggesting that erosion may play a significant role in entrenchment. Alternatively, it may also have influenced an initial diverted entrenchment due to the differences in resistance to erosion. The upper part of the channel is entrenched into a G5 alluvial fan.

5.1.1. Age control

To constrain the age of the alluvial fans where the offset channels are entrenched we used 1) the age estimates and the alluvial fan generations (G0-G6) from Ortuño et al. (2012), and 2) the new dates obtained from U-series of pedogenic carbonate (Table 5). Most of the ages from trenching sites provided by Ortuño et al. (2012) are from buried and/or local units and do not give the age of alluvial fan abandonment, but the age of an alluvial unit within the alluvial fan. Consequently, their use led to maximum ages (minimum slip rates). On the other hand, U-series dates indicate the minimum age of alluvial fan surface abandonment. The new numerical ages (CARR4, LIM4, LIMII5, LIMII7 and PERA; Fig. S2) belong to different alluvial fan generations described by Ortuño et al. (2012): CARR4 and LIM4 correspond to the G2 generation, LIMII5 to G3, and PERA and LIMII7 to the G4 alluvial fan generation (Fig. S2). Sample LIMII7 belongs to a buried paleosol developed on top of a G4 generation alluvial fan. In general, the new U-series ages in the Goñar-Lorca segment corroborates the age of the generations proposed by Ortuño et al. (2012) (Table 5). For generation G2, there is an agreement between the values of samples Gaba-3 and CARR4 (both samples from unit D1 in the trenches studied by Ortuño et al., 2012). On the other hand, although sample LIM4 is much younger than the others, its age does not affect the G2 age, as it is a

minimum value for the host unit. Samples for generation G3 are consistent, including LIMII5, slightly younger but in the same range. Samples PERA and LIMII7 are younger (PERA is much younger) than the other samples belonging to this generation. Sample LIMII7 indicates the minimum age for the alluvial fan, but differences between sample PERA and the preferred age for generation G4 may be due to the fact that the soil sample was rejuvenated, or that it corresponded to a small younger terrace or unit.

Where age control is available, we used the age of the alluvial fan unit where the channel is located to estimate the age of the channel. Otherwise, we utilized the preferred age of the alluvial fan generation considered in Table 5 or the spatially closest numerical dates. The maximum ages of the fan surface where offsets 122 and 123 are measured were obtained based on age estimates from trenches due to the proximity of the identified channels and the trenches. The maximum age of the alluvial fan of offset 136 was estimated using the age of sample Carrascos-3 which is the best constrained age of generation G5 top surface. For the remainder of the selected offsets, we used the preferred age of the alluvial generation (by correlation) to calculate the minimum slip rate. This results in large uncertainties (> 0.5 mm/yr) in the final slip rate (Table 6).

Sample	Age (ka)	Method	Alluvial fan generation	Depositional phase (Ortuño et al., 2012)	Preferred age for the alluvial fan generation (ka)
Gaba-3	23±2	pIRIR	Q2	G2	21-25
CARR4	23.2±4.2	U-series	Q2	G2	
LIM4	11.7±2.6	U-series	Q2	G2	
Carr-1-2	52.4 +7.9/-6.4	TL	Q3	G3	41-61
Carra-2-1	49±2	pIRIR	Q3	G3	
Berm-1	46.3 +6.1/-5.1	TL	Q3	G3	
LIMII5	46.6±5.7	U-series	Q3	G3	
Era-4	58±3	pIRIR	Q3	G3	
Sard-2	61.9+15/-11.2	TL	Q3	G3	
Sard-4	61±2	pIRIR	Q3	G3	
Carr-1	126 +0/-23	TL	Q3	G3-G4	90-147
Gaba-2	108±8	pIRIR	Q3	G3-G4	
Gaba-1	111 +36/-21	TL	Q3	G3-G4	
Era-3	107±5	pIRIR	Q3	G3-G4	
Sard-1	120+39/-21	TL	Q3	G3-G4	
Era-	110+33/-19	TL	Q3	G3-G4	

PERA	23.8±3.2	U-series	Q3	G4	125-149
LIMI17	105.1±4.2	U-series	Q3	G4	
Era-2	142±7	pIRIR	Q3	G4	
Era-0	131±6	pIRIR	Q3	G4	
Carrascos-3	191±17	pIRIR	Q4	G5	145-208
Era-1	152±7	pIRIR	Q4	G5	

Table 5. Summary of new numerical ages in AMF and available ages from Ortuño et al. (2012). New datings in gray. Errors for radiocarbon dates are given at the 2σ confidence level, whereas U-series, TL and OSL samples have 1σ errors. Legend: pIRIR, post-IR IRSL. New ages in grey.

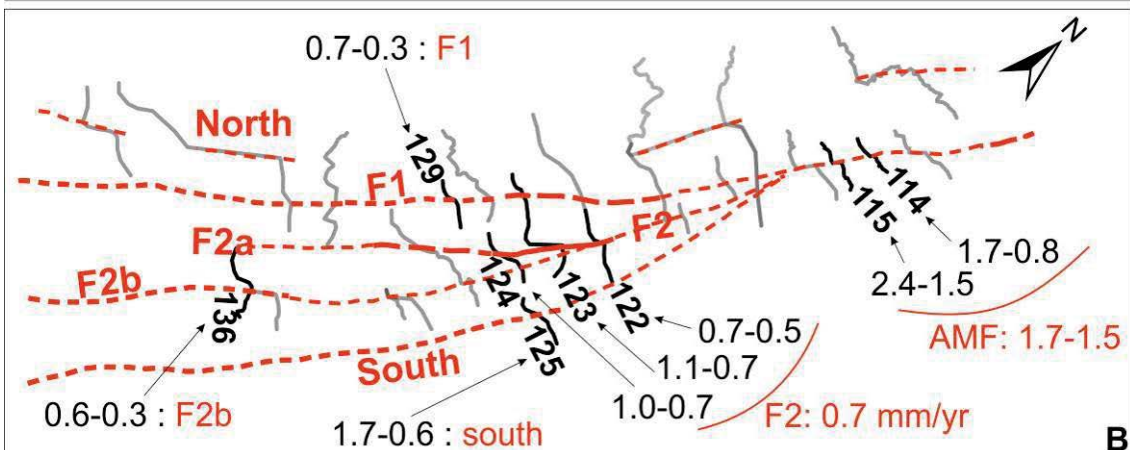
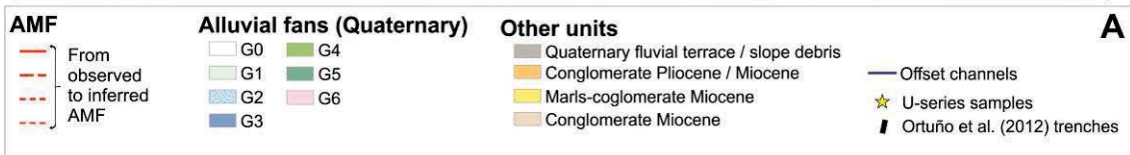
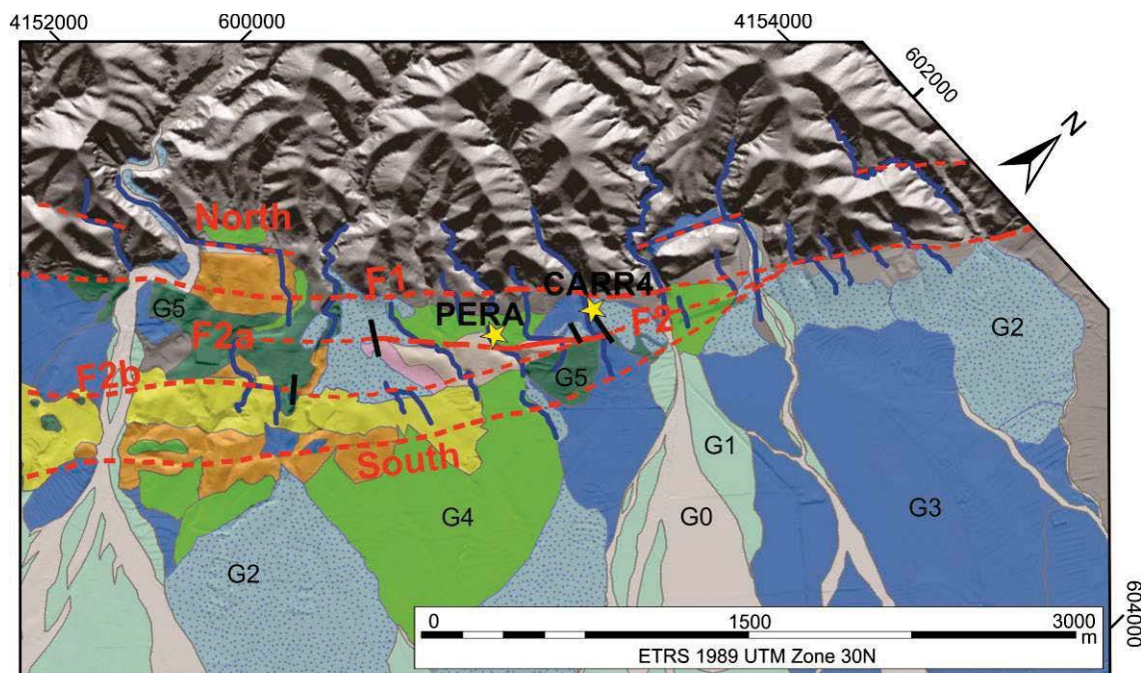


Figure 5. Geologic map (position in Figure 1) of the southern termination of the Goñar-Lorca segment with the different generations of alluvial fans interpreted in the area and with the location of the selected best quality offsets used to calculate the slip rates. Modified from Ortuño et al. (2012); B) summary of the slip rates obtained using the identified offsets. The offset measurements (indicated in the maps with three digit numbers next to a channel) are listed in Table 4.

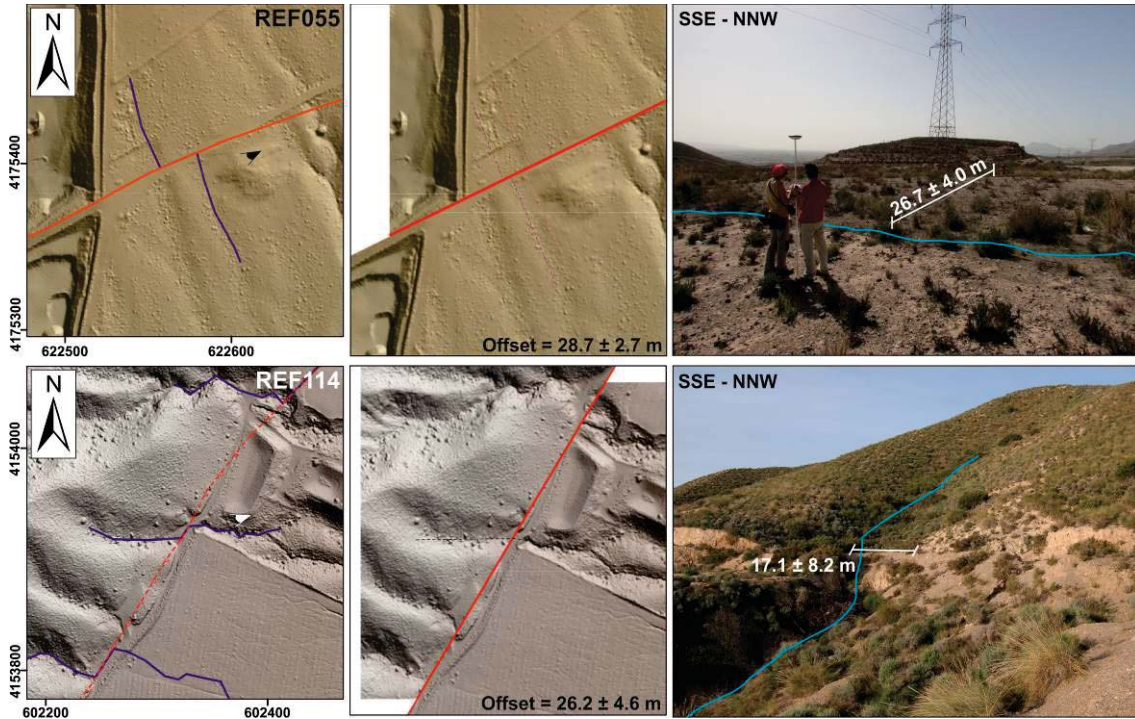


Figure 6. Examples of offsets measured remotely and in the field. In general, uncertainties measured in the field are larger. Location of the offsets in Fig. 2 (055) and in Fig. 5 (114). The eye symbol indicates the perspective of the pictures shown on the right. The interpretation of all the offsets used to calculate the slip rate is in the Supplementary material (Figs. S4-S11).

5.1.2. Slip rate calculation

The application of the Zechar and Frankel (2009) approach yields nine slip rates for the different strands of the Goñar-Lorca segment of the AMF (Table 6). We first analyzed the lateral slip rates obtained for each fault strand separately. The first group of offsets (114-115) is entrenched in slope debris above a G2 alluvial fan (Fig. 5). Using the age of G2 alluvial fan as the maximum age for the channel, the slip rates obtained differ slightly (2.4-1.5 to 1.7-0.8 mm/yr; Table 6). This difference might be explained because:

a) the entrenchment of all channels did not occur synchronously; or/and b) the largest offset corresponds to a channel entrenched with an initial non tectonic deviation coincident with the fault. The two slip rates intersect at 1.5-1.7 mm/yr, and, thus, we consider this range as the preferred value for this fault strand (Figure 5B and Table 5).

For the second group of offsets measured along the same fault strand (122-124, fault-F2; Fig. 5), the calculated minimum lateral slip rates coincide at 0.7 mm/yr (Table 5). Southwestwards, this fault strand splits in two (F2a and F2b). Along F2b we have identified an offset (136) with associated age information (this channel is entrenched in G5 alluvial fan deposits). The calculated minimum lateral slip rate is 0.6-0.3 mm/yr, smaller than the calculated slip rate for the fault-F2. Nevertheless, these results are consistent because the slip rate on F2 is split between F2a and F2b. Notice that with increasing age of the units (G3 to G5), the larger the calculated slip rate (Table 6). This reduction of the tectonic activity in the area from the middle Pleistocene and early Late Pleistocene has also been suggested by Silva et al. (1992) and Silva (1994). In the Huércal-Overa Basin, García-Meléndez (2000) and García-Meléndez et al. (2003) also detected this general decrease in the tectonic activity through the fact that late Pleistocene and Holocene landforms are less affected by tectonic deformations.

The slip rate along one single strand should be approximately equal to the sum of rates along the different faults in which it diverts, when no ductile deformation or distributed deformation is present. To verify this assertion at the AMF, we compared the 1.7-1.5 mm/yr lateral minimum slip rate obtained from offsets 114 and 115 with the individual contribution the sub-parallel strands of the horse tail termination. We summed the slip rates for the sub-parallel fault strands: 1) fault-F1 (129), 0.7-0.3 mm/yr; 2) fault-F2 (122-124), 0.7 mm/yr; and 3) southernmost strand (125), 1.7-0.6 mm/yr (Fig. 5B and Table 6), and we obtained 3.1-1.6 mm/yr. The slip rates obtained are compatible, as they intersect with the values for offsets 114 and 115 in the interval 1.7-1.6 mm/yr for the last 200 ka. Therefore, we considered this value the minimum lateral slip rate for the Goñar-Lorca segment of the AMF.

Offset		Age		Slip rate				
Offset (name)	Offset \pm std.dev. (m)	Sample name or depos. phase	Age (ka)	Mean (mm/a)	Mode (mm/a)	Median (mm/a)	95.45% Interval	Range (mm/a)

114	26.24±4.58	G2	23±2	1.2	1.1	1.1	+0.5/-0.4	1.7-0.8
114	17.10±8.20	G2	23±2	0.8	0.7	0.7	+0.8/-0.7	1.6-0.1
115	42.75±2.97	G2	23±2	1.9	1.8	1.8	+0.5/-0.4	2.4-1.5
122	28.70±3.11	Carra-2-1	49±2	0.6	0.6	0.6	+0.1/-0.1	0.7-0.5
123	160.21±12.80	Carrascos-3	191±17	0.9	0.8	0.8	+0.2/-0.2	1.1-0.7
124	109.72±5.88	G4	125-149	0.8	0.8	0.8	+0.2/-0.1	1.0-0.7
125	104.03±5.09	G3-G4	90-147	0.9	0.8	0.9	+0.8/-0.3	1.7-0.6
129	38.24±6.65	G3-G4	90-147	0.4	0.3	0.3	+0.3/-0.1	0.7-0.3
136	68.83±11.68	Carrascos-3	191±17	0.4	0.4	0.4	+0.2/-0.1	0.6-0.3

Table 6. Lateral slip rates resulting from the combination of morphotectonic analysis and numerical dating in Goñar-Lorca segment of Alhama de Murcia fault. Channel 114 is measured remotely and in the field: second row of results (Fig. 6). The interpretation of each offset can be found in the supplementary material from S4-S12. Legend: depos. depositional. The calculations were done applying Zechar and Frankel (2009) functions.

5.2. *Lorca-Totana segment*

The alluvial fan surfaces of this segment show few offset channels with high quality preservation (Fig. 2; Ferrater et al., 2015a). Channel 055 (Fig. 6), affected by the SAMF fault activity (Fig. 2), is well preserved and was evaluated as a robust reconstructed offset due to the lack of headwaters of the southeastern wall. We measured the offset of this channel remotely and in the field (Fig. 6). The two values are similar but the one calculated remotely has lower uncertainties (28.7 ± 2.7 m).

This channel is affected by the fault on the surface of the La Salud alluvial fan (SAMF; Fig. 2). Dating results on the alluvial fan suggest that it might have been active until shortly after 28.2 ± 2.0 ka BP (MS-4, Fig. 2 and Table 4). This age is consistent with the age of El Saltador alluvial fan, where units displaying alluvial characteristics are ~ 25 ka BP (unit H; Table 4) and the channel entrenchment is approximately 15 kyr BP (Table 4). As in the Goñar-Lorca segment, the maximum age considered for the channel analyzed is the age of the alluvial fan where it is entrenched. Considering the best constrained offset (28.7 ± 2.7 m) and its age, we calculated a minimum lateral slip rate of 1.0 ± 0.2 mm/yr for the SAMF for the past 30 ka.

6. Discussion

6.1. *Slip rate estimations: trenching versus geomorphology*

The most reliable way to compare the lateral slip rates obtained using trenches and those obtained using a geomorphological analysis is to carry out the two analyses in the same site, i.e. the same alluvial fan. This is especially true when considering that surface slip observed after an earthquake varies along strike (Zielke et al., 2012). Here, we compare the offset of channelized unit D measured in the El Saltador alluvial fan, with the surface channel measured in La Salud alluvial fan. Although these two alluvial fans are 1 km apart from each other (Figure 2), the ages of these alluvial fans are similar (Martínez-Díaz et al., 2003) and the comparison may be done.

The channel in unit D at El Saltador is a buried channel sequence infilling a scar dug on top of the fan surface (the channelized units truncate the alluvial fan sequence; examples are units G-B in trenches 13 or 10, Fig. 4). This stratigraphic relation suggests that the erosion related to unit D postdates the fan abandonment and occurred between ~15 and ~21 kyr (Table 4). On the other hand, the age of the channel on the La Salud alluvial fan surface is less constrained, being younger than the available age for the alluvial fan sequence (~28 kyr). The channel offsets in El Saltador and in La Salud alluvial fans are $16.3^{+2.7}_{-0.3}$ m and 28.7 ± 2.7 m, respectively, being the surface channel offset obtained at La Salud is slightly larger than the offset of the paleochannel at El Saltador. This might seem surprising considering that the cumulative offset measured on the surface is normally expected to be smaller than the offset of a buried paleochannel within the alluvial fan sedimentary sequence when no previous non-tectonic deviation is observed. We suggest that this inconsistency is due to the fact that the incision of the channel system of El Saltador alluvial fan is higher than the channel of La Salud, and the system is infilled and included in the stratigraphic sequence, but it occurred after the incision of the La Salud channel (055; Figure 2)

Our stratigraphic and sedimentological analysis allowed us to compare the slip rates obtained using different methods: a) a best estimate lateral slip rate of 0.9 ± 0.1 mm/yr obtained in the trenches, and b) a 1.0 ± 0.2 mm/yr minimum lateral slip rate using the geomorphological analysis. The values are consistent within the interval 0.8 – 1.0 mm/yr. For this reason, we considered this value to be the best constrained lateral slip rate of the SAMF of the Lorca-Totana segment for the past 30 kyr.

Here, we encourage the combination of 3D trenching and surface analyses as they complement each other and may help to discard or strengthen the values obtained.

However, we highlight the advantages and disadvantages of both techniques separately in Table 7. Paleoseismic trenching permits a precise analysis (small uncertainties, good correlation) but it is a time and money-consuming process. On the other hand, morphological analyses, as long as channels are preserved in anthropogenically modified sites, are much faster to assess and we recommend using them especially where the fault under analysis splits into more than one strand. The principal disadvantages of the morphological analysis are the high uncertainties related to the age constraints of the channel. While it is normally assumed that channels postdate the abandonment of the alluvial fan sedimentation, some of them may have been intermittently active during the last alluvial events invalidating the dating assumptions. Trenching devoted to constrain the age of offset surface channels could enhance the results. The main limiting factors are common for both methodologies: a) the presence of young material affected by the fault activity, and b) the possibility to date this material, difficult if the affected units are proximal facies of alluvial fans, which may not be suitable for most geochronologic approaches.

	Paleoseismic trenches	Morphotectonic analyses
Advantages	<p>Increased reliability in correlating offset features (based on age, morphology and facies)</p> <p>Increased measurement precision, smaller uncertainties</p> <p>Increased accuracy in channel age determination</p>	<p>Suited where deformation affects several sub-parallel fault strands</p> <p>Fast and less expensive</p> <p>Larger offsets can be measured</p>
Disadvantages	<p>Unsuited where more than one strand is present.</p> <p>Time and money consuming</p>	<p>Reduced accuracy in channel age determination.</p> <p>Potential for greater ambiguity (e.g. Salsibury, et al., 2015)</p> <p>Low precision in offset measurement</p> <p>Limited by human landform disruption</p>

Table 7. Summary of the advantages and disadvantages of paleoseismic trenches and morphotectonic analyses in slip rate determination.

6.2. *AMF segmentation*

The lateral slip rates obtained for the two segments analyzed (1.7-1.6 mm/yr for the Goñar-Lorca segment and 0.8 – 1.0 mm/yr for the SAMF in the Lorca-Totana segment) are larger and have smaller associated uncertainties than the lateral and net slip rates calculated by previous authors (Martínez-Díaz et al., 2003; Masana et al., 2004; Ortuño et al., 2012). The slip rates from this study support the interpretation of Echeverría et al. (2013) that suggest that most of their calculated horizontal deformation associated with the AMF and PF (1.5 ± 0.3 mm/yr) may be absorbed by AMF.

We obtained a net slip rate for one of the three traces of the fault at the Lorca-Totana segment (0.9 ± 0.1 mm/yr) and, therefore, the total net slip rate of the fault is probably larger than this value, because the contribution of the NAMF and the frontal fault of this segment remain unknown. Considering the orientation of this segment (NE-SW) and those of geodetic velocities from GNSS data (Echeverría et al., 2015), the Lorca-Totana segment may absorb a significant vertical component of deformation, probably along the NAMF and the frontal fault, taking into account that the vertical slip rate of the SAMF is small (0.1 ± 0.0 mm/yr). This is supported by 1) the dip-slip features (i.e. knick points in the creeks and faceted spurs) observed along these two faults (Fig. 2; Ferrater et al., 2015b) and 2) the dip-slip component of the Mw 5.2 Lorca earthquake whose hypocenter was in the northern fault branch of the segment (NAMF; López-Comino et al., 2012; Martínez-Díaz et al. 2012). Accordingly with these observations, we suggest the existence of partitioning between the fault strands of Lorca-Totana segment; the SAMF may be absorbing almost all the strike-slip deformation and a negligible dip-slip, whereas the other two fault strands would be accommodating the vertical component.

In the Goñar-Lorca segment, the summed vertical slip rates of all fault strands is 0.16-0.22 mm/yr since 47-63 ka (Ortuño et al., 2012), whereas we obtained a much larger value of lateral slip rate (1.7-1.6 mm/yr for the past 200 ka). These values confirm the main lateral component of the AMF in the Goñar-Lorca segment.

In spite of the differences revealed in slip rates along the fault, additional data are required to confirm a clearly differentiated behavior between the two analyzed segments, as a) the measured offsets are not evenly distributed along the fault, b) the slip rates are incomplete for both segments (Goñar-Lorca segment lacks information of the vertical slip rate, and no information is available for the northern and the frontal fault strands of the Lorca-Totana segment), and c) the results concern different periods of time (a decrease on the fault activity cannot yet be, thus, ruled out). Moreover, more information is required about in the northern half of Goñar-Lorca segment to confirm the segmentation in terms of slip rate.

6.3. *Regional block motions*

Our results indicate much higher slip rates for the AMF than previous estimates, revealing it as one of the most active in the Eastern Betic Shear Zone (EBSZ). The faults of this system have been the focus study of several authors aiming to obtain their seismic parameters (Fig. 7). Weijermars (1987) estimated a horizontal long-term slip rate of 2 mm/yr for the past 7 Ma for the Palomares fault based on his estimation of the age of the basin and range structure (Fig. 7). This value might be now under discussion according to the geodetic results, as GPS results in the AMF region suggest that the Alhama de Murcia and the Palomares faults together have 1.3 ± 0.2 mm/yr strike slip component (Echeverria et al., 2013). When this is compared with our estimation of the lateral slip rate, little deformation is left for the Palomares fault. Weijermars (1987) results could couple GPS and geological results only if a strong decrease in slip rate has taken place in time along the Palomares fault. Martín-Banda et al. (2015), through a paleoseismic analysis, obtained a net slip rate 0.37 ± 0.08 mm/yr (since 210 ka) for the SW segment of the Carrascoy fault (CF), which shows mainly a vertical sense of slip. South of the CF, Insua-Arévalo et al. (2015) described Los Tollos fault (LTF) and estimated, by means of a paleoseismological approach, a net slip rate of 0.12-0.17 mm/yr, considering most of it to be strike-slip. The obtained slip rates could confirm the deformation transference from the AMF to the Los Tollos and Carrascoy faults to the north (Fig. 7). The proposed vertical slip rate of Bajo Segura blind thrust fault (BSF) is 0.1-0.3 mm/yr for the Quaternary period (Alfaro et al., 2012). Finally, to the south, at the Carboneras fault, Moreno et al. (2015) obtained a minimum lateral slip rate of 1.31 mm/yr for the last 113 kyr, a value that is close to that of the GPS results (Echeverria et

al., 2015) and that is also consistent with those at the AMF. These values confirm that long-term slip rates tend to be larger than the short-term slip rates.

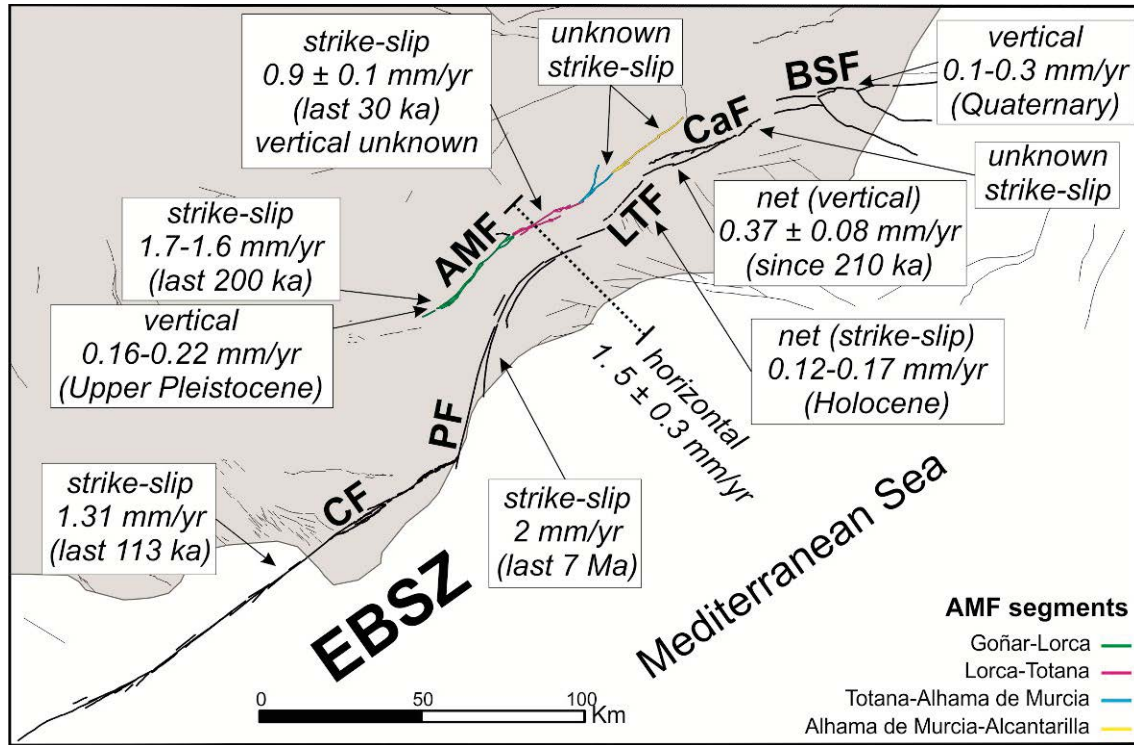


Figure 7. Summary of available slip rates for the Eastern Betics Shear Zone (EBSZ) faults (Weijermars, 1987; Alfaro et al., 2012; Ortuño et al., 2012; Echeverria et al., 2013; Moreno et al., 2015; Martín-Banda et al., 2015; this study). Legend: CF, Carboneras fault; PF, Palomares fault; LTF, Los Tollos fault; CAF, Carrascoy fault; BSF, Bajo Segura fault. Quaternary Active Faults Database of Iberia from IGME (2015). The dot line is the profile where Echeverria et al. (2013) projected the geodetic velocities. See text for details.

According to these values, the Alhama de Murcia and Carboneras faults are the faults with the greater strike slip component of the Eastern Betics Shear Zone for the last ~ 100 ka. This deduction does not take into account the undetermined 1) strike slip component along the NE segment of the Carrascoy fault, and b) the strike slip value of the recent period of time of the Palomares fault. Future studies concerning slip rates should focus on the Alhama de Murcia-Alcantarilla segment of the AMF, and the short term slip rate of the Palomares fault based on geological data.

6.4. Time lag between alluvial deposition and accumulation of dateable pedogenic carbonate

In order for datable amounts of pedogenic carbonate to accumulate, time is required after deposition of the host alluvium. This interval is termed the time lag (Sharp et al., 2003). Therefore, the age of the fan accumulation is not directly obtained by U series dating the carbonates but needs to be estimated by knowing or estimating the time lag. The availability of OSL and radiocarbon dates in the stratigraphic sequence (Table 4) provides an opportunity to estimate the time lag in the study area, which will be of use for future U-series datings. We calculated the time lag using as a reference the age of unit D (obtained with U-series) and the ages of units B and G (OSL technique). The age of unit D is constrained by OSL ages of 20839 – 23014 cal BP ka (unit G) and 15.65 ± 0.85 ka (unit B), whereas the age of pedogenic carbonate formation is 12.39 ± 0.42 ka. The resulting estimate of the time lag suggests it is ~3 to 8 ka. Unit H was also taken as reference to calculate the time lag. This unit is 25228 – 25832 a cal BP (Table 4), and pedogenic carbonate age is 20.9 ± 2.5 ka (Table 2). The estimated time lag in this case is about ~4.5 ka.

These estimates of the time lag may only be valid in the SE Iberian Peninsula for the transition from the last glacial maximum to the Holocene, since soil carbonate development is controlled by climate (e.g., soil moisture, biological activity, landscape stability and carbonate supply; Candy and Black, 2009). However, the values found herein are similar to the estimate of 5 ± 5 kyr determined for glacio-fluvial terraces in the Rocky Mountains, USA (Sharp et al., 2003). For comparison, much shorter time lags for formation of datable soil carbonate are implied by the concordance of U-series ages of soil carbonates and ^{10}Be surface exposure ages in the low desert of southern California (e.g., Blisniuk et al., 2012; Gold et al., 2015).

Conclusions

We obtained the lateral slip rate of the strike-slip Alhama de Murcia fault applying two different methodologies: 3D paleoseismic trenching and morphotectonic analysis. In the first case, a ~15.5-22.0 ka BP buried channel is laterally offset $16.3^{+2.7}_{-0.3}$ m, yielding 0.9 ± 0.1 mm/yr lateral slip rate for the last 20 ka for the SAMF of the Lorca-Totana segment. By means of a morphotectonic analysis, we obtained minimum lateral slip rates of 1.7-1.6 mm/yr (since middle Pleistocene) and 1.0 ± 0.2 mm/yr (for the last 30 ka) for the Goñar-Lorca and Lorca-Totana segments, respectively. These values agree with the recent geodetic estimations of 1.5 ± 0.3 mm/yr of horizontal slip

accommodated by the AMF and the Palomares fault. The slip rates obtained for the SAMF of the Lorca-Totana segment together with geomorphologic observations related with the tectonic behavior of the two other subparallel faults of the segment, suggest the partitioning of the deformation. Our results suggest, together with previous studies in the Eastern Betics Shear Zone, that Carboneras and Alhama de Murcia faults are the main strike-slip faults of the system, as Bajo Segura and Carrascoy fault have a larger dip slip component and the short-term slip rate of the Palomares fault is unknown.

We conclude that the techniques of 3D paleoseismic trenching and morphotectonic analysis are complementary and that each methodology has advantages and disadvantages. For instance, trenching provides the most precise measurement of slip rate, whereas morphotectonic analysis can be used to evaluate slip rates at more sites and at a lower cost. In slow moving faults, the use of the two techniques is desirable, since measurable offsets may be rare, but caution is needed when measuring channel offsets both buried and in surface in the same site.

The combination of different dating techniques provided the needed age control to estimate a 3 to 8 ka time lapse between a unit deposition and the precipitation of datable amounts of pedogenic carbonate by means of U-series dating. This value will be of interest for future U-series dating on pedogenic carbonates comprising the Holocene and the Late Pleistocene where no additional dates are available.

Acknowledgements

This research was funded by SHAKE CGL2011-30005-C02-02, RISK NAT-2014SGR/1243 and PREVENT (CGL2015-66263-R). H. Perea was a fellow researcher under the “Juan de la Cierva” program. The Ministerio de Educación, Cultura y Deporte from Spain provided funding for the predoctoral FPU fellowship of M. Ferrater.

REFERENCES:

- Alfaro, P., Bartolomé, R., Borque, M.J., Estévez, A., García-Mayordomo, J., García-Tortosa, F.J., Gil, A.J., Gràcia, E., Lo Iacono, C., Perea, H., 2012. The Bajo Segura Fault Zone: Active blind thrusting in the Eastern Betic Cordillera (SE Spain). *Journal of Iberian Geology* 38, 271-284.
- Amundson, R., Wang, Y.R., Chadwick, O.A., Trumbore, S.E., McFadden, L., McDonald, E., Wells, S., and DeNiro, M., 1994. Factors and processes governing the ^{14}C content of carbonate in desert soil. *Earth and Planetary Science Letters* 125, 385-405.
- Argus, D.F., Gordon, R.G., Demets, C., 2011. Geologically current motion of 56 plates relative to the no-net-rotation reference frame. *Geochemistry, Geophysics, Geosystems* 12 (11), doi.org/10.1029/2011GC003751.

- Arkley, R.J., 1963. Calculation of carbonate and water movement in soil from climatic data. *Soil Science* 96, 239-248.
- Birkland, P. W. (1999), *Soils and Geomorphology*, 3rd ed., Oxford University Press, New York.
- Blisniuk, K., Oskin, M., Fletcher, K., Rockwell, T., and Sharp, W., 2012. Assessing the reliability of U-series and ^{10}Be dating techniques on alluvial fans in the Anza Borrego Desert, California. *Quaternary Geochronology* 13, 26–41, doi: 10.1016/j.quageo.2012.08.004.
- Bøtter-Jensen, L., Thomsen, K.J., Jain, M., 2010. Review of optically stimulated luminescence (OSL) instrumental developments for retrospective dosimetry. *Radiation Measurements* 45 (3–6), 253–257.
- Bousquet, J., 1979. Quaternary strike-slip faults in south-eastern Spain. *Tectonophysics* 52, 277–286.
- Buylaert J.P., Murray A.S., Thomsen K.J. and Jain M., 2009. Testing the potential of an elevated temperature IRSL signal from K-feldspar. *Radiation Measurements* 44, 560–565.
- Campbell, G.E., Walker, R.T., Abdrakhmatov, K., Schwenninger, J., Jackson, J., Elliott, J.R., and Copley, a., 2013. The Dzhungarian fault: Late Quaternary tectonics and slip rate of a major right-lateral strike-slip fault in the northern Tien Shan region. *Journal of Geophysical Research: Solid Earth* 118 (10), 5681–5698, doi: 10.1002/jgrb.50367.
- Candy, I., and Black, S., 2009. The timing of Quaternary calcrete development in semi-arid southeast Spain: Investigating the role of climate on calcrete genesis. *Sedimentary Geology* 218 (1), 6–15.
- Capo, R.C. and Chadwick, O.A., 1999. Sources of strontium and calcium in desert soils and calcrete. *Earth and Planetary Science Letters* 170, 61–72.
- Cerling, T.E., 1999. Stable carbon isotopes in paleosol carbonates. *Special Publication of the International Association of Sedimentologists* 27, 43–60.
- Chevalier, M.L., Tapponnier, P., Van der Woerd, J., Ryerson, F.J., Finkel, R.C., and Li, H., 2012. Spatially constant slip rate along the southern segment of the Karakorum fault since 200ka. *Tectonophysics* 530–531, 152–179, doi: 10.1016/j.tecto.2011.12.014.
- Echeverría, A., Khazaradze, G., Asensio, E., Gárate, J., Martín Dávila, J., and Suriñach, E., 2013. Crustal deformation in eastern Betics from CuaTeNeo GPS network. *Tectonophysics* 608, 600–612.
- Echeverría, A., Khazaradze, G., Asensio, E., and Masana, E., 2015. Geodetic evidence for continuing tectonic activity of the Carboneras fault (SE Spain). *Tectonophysics* 663, 302–309, doi: 10.1016/j.tecto.2015.08.009.
- Ferrater, M., Arrowsmith, R., and Masana, E., 2015a. Lateral offset quality rating along low slip rate faults: application to the Alhama de Murcia fault (SE Iberian Peninsula). *Remote sensing* 7, 14827–14852.
- Ferrater, M., Booth-Rea G., Pérez-Peña, J. V., Azañón, J. M., Giaconia, F., and Masana, E. (2015b). From extension to transpression: Quaternary reorganization of an extensional-related drainage network by the Alhama de Murcia fault (eastern Betics). *Tectonophysics* 667, 33–47, doi: 10.1016/j.tecto.2015.06.011.
- Ferrater, M., Ortuño, M., Masana, E., Pallàs, R., Perea, H., Baize, S., García-Meléndez, E., Martínez-Díaz, J.J., Echeverría, A., Rockwell, T.K., and Sharp, W.D. (submitted to tectonophysics). Refining seismic parameters in low seismicity areas by 3D trenching: the not so slow Alhama de Murcia fault, SE Iberia.
- Ferrater, M., Echeverría, A., Masana, E., Martínez-Díaz, J.J., Sharp, W.D. (2016). A 3D measurement of the offset in paleoseismological studies. *Computers and Geosciences* 9, 156–163, doi.org/10.1016/j.cageo.2016.02.024
- Ferry, M., Meghraoui, M., Karaki, N.A., Al-Taj, M., Amoush, H., Al-Dhaisat, S., and Barjous, M., 2007. A 48-kyr-long slip rate history for the Jordan Valley segment of the Dead Sea Fault. *Earth and Planetary Science Letters* 260, 394–406, doi: 10.1016/j.epsl.2007.05.049.
- Frankel, K.L., Dolan, J.F., Finkel, R.C., Owen, L. a., and Hoeft, J.S., 2007. Spatial variations in slip rate along the Death Valley-Fish Lake Valley fault system determined from LiDAR topographic data and cosmogenic ^{10}Be geochronology. *Geophysical Research Letters* 34 (18), L18303, doi: 10.1029/2007GL030549.
- Fu, B., Awata, Y., Du, J., and He, W., 2005. Late Quaternary systematic stream offsets caused by repeated large seismic events along the Kunlun fault, northern Tibet. *Geomorphology* 71, 278–292, doi: 10.1016/j.geomorph.2005.03.001.
- Galbraith, R.F., Roberts, R.G., Laslett, G.M., Yoshida, H., Olley, J.M., 1999. Optical dating of single and multiple grains of quartz from Jinmium rock shelter, Northern Australia: Part 1, experimental design and statistical models. *Archaeometry* 41, 339–364.
- García-Meléndez, E., 2000. Geomorfología y Neotectónica del Cuaternario de la Cuenca de Huércal-Overa y Corredor del Almanzora. Análisis y Cartografía mediante Teledetección y SIG. Ph.D. thesis, Salamanca, Spain, Universidad de Salamanca, 528 p.

- García-Meléndez, E., Goy, J.L., and Zazo, C., 2003. Neotectonica and Plio-Quaternary landscape development within the eastern Huércal-Overa Basin (Betic Cordilleras, southeastern Spain). *Geomorphology* 50, 111–133, doi:10.1016/S0169-555X(02)00210-6.
- Gile, L.H., Peterson, F.F., and Grossman, R.B., 1966. *Soil science* 101, 347–360.
- Gold, R.D., Cowgill, E., Arrowsmith, J.R., Chen, X., Sharp, W.D., Cooper, K.M., and Wang, X.-F., 2011. Faulted terrace risers place new constraints on the late Quaternary slip rate for the central Altyn Tagh fault, northwest Tibet. *Geological Society of America Bulletin* 123 (5-6), 958–978, doi: 10.1130/B30207.1.
- Gold, P.O., Behr, W.M., Rood, D., Sharp, W.D., Rockwell, T.K., Kendrick, K., Salin, A., 2015. Holocene geologic slip rate for the Banning strand of the southern San Andreas Fault, southern California. *Journal of Geophysical Research-Solid Earth* 120, doi:10.1002/2015JB012004.
- Hall, N.T., Wright, H., and Clahan, K.B., 1999. Paleoseismic studies of the San Francisco Peninsula segment of the San Andreas Fault zone near Woodside, California. *Journal of Geophysical Research* 104, 23215–23236.
- IGME, 2015. QAFI v.3: Quaternary Active Faults Database of Iberia. Accessed on 15th of February 2016, <http://info.igme.es/QAFI>
- IGN (Instituto Geográfico Nacional), 2012. Catálogo de terremotos. Accessed on 12th of January 2012. <http://www.ign.es/ign/layoutIn/sismoFormularioCatalogo.do>.
- Ku, T.L., Bull, W.B., Freeman, S. Thomas, and Knauss, K.G., 1979. Th 230 -U 234 dating of pedogenic carbonates in gravelly desert soils of Vidal Valley, southeastern California. *Geological Society of America* 90, 1063–1073.
- De Larouzière, F.D., Bolze, J., Bordet, P., Hernández, J., Montenat, C., and Ott d'Estevou, P., 1988. The Betic segment of the lithospheric Trans-Alboran shear zone during the Late Miocene. *Tectonophysics* 152, 41–52.
- Lindvall, S.C., and Rockwell, T.K., 1995. Holocene activity of the Rose Canyon fault zone in San Diego, California. *Journal of Geophysical Research* 100, 24121–24132.
- Liu-Zeng, J., Klinger, Y., Sieh, K., Rubin, C., and Seitz, G., 2006. Serial ruptures of the San Andreas fault, Carrizo Plain, California, revealed by three-dimensional excavations. *Journal of Geophysical Research* 111, p. B02306, doi: 10.1029/2004JB003601.
- López-Comino, J.Á., Mancilla, F.D.L., Morales, J., and Stich, D., 2012. Rupture directivity of the 2011, Mw 5.2 Lorca earthquake (Spain). *Geophysical Research Letters* 39, 1–5, doi: 10.1029/2011GL050498.
- Ludwig, K.R., and Paces, J.B., 2002. Uranium-series dating of pedogenic silica and carbonate, Crater Flat, Nevada. *Geochimica et Cosmochimica Acta* 66 (3), 487–506.
- Machette, M.N., 1985. Calcic soils of the southwestern United States. *Geological Society of America* 203, 1–21.
- Marco, S., Rockwell, T.K., Heimann, A., Frieslander, U., and Agnon, A., 2005. Late Holocene activity of the Dead Sea Transform revealed in 3D palaeoseismic trenches on the Jordan Gorge segment. *Earth and Planetary Science Letters* 234, 189–205, doi: 10.1016/j.epsl.2005.01.017.
- Martín-Banda, R., García-Mayordomo, J., Insua-Arévalo, J.M., Salazar, Á.E., Rodríguez-Escudero, E., Álvarez-Gómez, J.A., Medialdea, A. and Herrero M.J. (2015). New insights on the seismogenic potential of the Eastern Betic Shear Zone (SE Iberia): Quaternary activity and paleoseismicity of the SW segment of the Carrascoy Fault Zone. *Tectonics*, 34, doi:10.1002/2015TC003997.
- Martínez-Díaz, J.J., 1998. Neotectónica y Tectónica Activa del Sector Centro-Occidental de la Región de Murcia y Sur de Almería (Cordillera Bética – España). Ph.D. thesis, Madrid, Spain, Universidad Complutense de Madrid.
- Martínez-Díaz, J.J., and Hernández-Enrile, J.L., 2001. Using travertine deformations to characterize paleoseismic activity along an active oblique-slip fault: the Alhama de Murcia fault (Betic Cordillera, Spain). *Acta Geologica Hispanica* 36, 297–313.
- Martínez-Díaz, J.J., Masana, E., Hernández-Enrile, J.L., and Santanach, P., 2003. Effects of repeated paleoearthquakes on the Alhama de Murcia Fault (Betic Cordillera, Spain) on the Quaternary evolution of an alluvial fan System. *Annals of geophysics* 46, 775–791.
- Martínez-Díaz, J.J., Masana, E., and Ortuño, M., 2012. Active tectonics of the Alhama de Murcia fault, Betic Cordillera, Spain. *Journal of Iberian Geology* 38, 253–270.
- Martínez-Martínez, J.M., and Azañón, J.M., 1997. Mode of extensional tectonics in the southeastern Betics (SE Spain): Implications for the tectonic evolution of the peri-Alborán orogenic system. *Tectonics* 16, 205–225.
- Masana, E., Martínez-Díaz, J.J., Hernández-Enrile, J.L., and Santanach, P., 2004. The Alhama de Murcia fault (SE Spain), a seismogenic fault in a diffuse plate boundary: Seismotectonic implications for

- the Ibero-Magrebien region. *Journal of Geophysical Research* 109, 1–17, doi: 10.1029/2002JB002359.
- Meijninger, B.M.L., and Vissers, R.L.M., 2006. Miocene extensional basin development in the Betic Cordillera, SE Spain revealed through analysis of the Alhama de Murcia and Crevillente Faults. *Basin Research* 18, 547–571, doi: 10.1111/j.1365-2117.2006.00308.x.
- Mejdahl, V., 1987. Internal radioactivity in quartz and feldspar grains. *Ancient TL* 5, 10-17
- Montenat, C., Ott d’Estevou, P. and Delort, T., 1990. Le Basin de Lorca. In: Montenat, C. (Ed.), *Les bassins Neogenes du Domaine Betique Oriental (Espagne)*, Documents et Travaux, 261–280.
- Moreno, X., Masana, E., Pallàs, R., Gràcia, E., Rodés, Á., and Bordonau, J., 2015. Quaternary tectonic activity of the Carboneras Fault in the La Serrata range (SE Iberia): Geomorphological and chronological constraints. *Tectonophysics*, doi: 10.1016/j.tecto.2015.08.016.
- Murray, A.S., Wintle, A.G., 2000. Luminescence dating of quartz using an improved single-aliquot regenerative-dose protocol. *Radiation Measurements* 32, 57-73.
- Nocquet, J.M., 2012. Present-day kinematics of the Mediterranean: A comprehensive overview of GPS results. *Tectonophysics* 579, 220–242, doi: 10.1016/j.tecto.2012.03.037.
- Ortuno, M., Masana, E., Garcia-Melendez, E., Martinez-Diaz, J., Stepancikova, P., Cunha, P.P., Sohbati, R., Canora, C., Buylaert, J.P., and Murray, A.S., 2012. An exceptionally long paleoseismic record of a slow-moving fault: The Alhama de Murcia fault (Eastern Betic shear zone, Spain). *Geological Society of America Bulletin* 124, 1474–1494, doi: 10.1130/B30558.1.
- Reimer, P.J., Bard, E., Bayliss, A., Beck, J.W., Blackwell, P.G., Bronk Ramsey, C., Buck, C.E., Cheng, H., Edwards, R.L., Friedrich, M., Grootes, P.M., Guilderson, T.P., Haflidason, H., Hajdas, I., Hatté, C., Heaton, T.J., Hogg, A.G., Hughen, K.A., Kaiser, K.F., Kromer, B., Manning, S.W., Niu, M., Reimer, R.W., Richards, D.A., Scott, E.M., Southon, J.R., Turney, C.S.M., van der Plicht, J. (2013). IntCal13 and MARINE13 radiocarbon age calibration curves 0-50000 years cal BP. *Radiocarbon* 55(4), doi: 10.2458/azu_js_rc.55.16947
- Rittase, W.M., Kirby, E., McDonald, E., Walker, J.D., Gosse, J., Spencer, J.Q.G., and Herra, A.J., 2014. Temporal variations in Holocene slip rate along the central Garlock fault, Pilot Knob Valley, California. *Lithosphere* 6, 48–58, doi: 10.1130/L286.1.
- Rodés, Á., Pallàs, R., Braucher, R., Moreno, X., Masana, E., Bourlés, D.L., 2011. Effect of density uncertainties in cosmogenic ^{10}Be depth-profiles: dating a cemented Pleistocene alluvial fan (Carboneras Fault, SE Iberia). *Quaternary Geochronology* 6, 186-194. doi:10.1016/j.quageo.2010.10.004
- Rockwell, T., Loughman, C., and Merifield, P., 1990. Late Quaternary rate of slip along the San Jacinto fault zone near Anza, Southern California. *Journal of Geophysical Research* 95, 8593-8605.
- Rodés, Á., Pallàs, R., Ortuño, M., García-Melendez, E., and Masana, E., 2013. Combining surface exposure dating and burial dating from paired cosmogenic depth profiles. Example of El Límite alluvial fan in Huércal-Overa basin (SE Iberia). *Quaternary Geochronology* 19, 127–134, doi: 10.1016/j.quageo.2013.10.002.
- Salisbury, J.B., Rockwell, T.K., Middleton, T.J., and Hudnut, K.W., 2012. LiDAR and Field Observations of Slip Distribution for the Most Recent Surface Ruptures along the Central San Jacinto Fault. *Bulletin of the Seismological Society of America* 102, 598–619, doi: 10.1785/0120110068.
- Schaetzl, R.J., Anderson, S., 2005. *Soil Genesis and geomorphology*. Cambridge University Press, Cambridge, UK. 817 pp.
- Serpelloni, E., Vannucci, G., Pondrelli, S., Argnani, A., Casula, G., Anzidei, M., Baldi, P., Gasperini, P., 2007. Kinematics of the western Africa–Eurasia plate boundary from focal mechanisms and GPS data. *Geophysical Journal International* 169 (3), 1180–1200. <http://dx.doi.org/10.1111/j.1365-246X.2007.03367.x>.
- Sharp, W.D., Ludwig, K.R., Chadwick, O.A., Amundson, R., and Glaser, L.L., 2003. Dating fluvial terraces by $^{230}\text{Th} / \text{U}$ on pedogenic carbonate, Wind River Basin, Wyoming. *Quaternary Research* 59, 139–150, doi: 10.1016/S0033-5894(03)00003-6.
- Silva, P.G., 1994. *Evolución Geodinámica de la Depresión del Guadalentín desde el Mioceno superior hasta la Actualidad: Neotectónica y Geomorfología*. Ph.D. thesis, Madrid, Spain, Universidad Complutense de Madrid, 642 p.
- Silva, P., Goy, J.L., and Zazo, C., 1992. Discordancias progresivas y expresión geomorfológica de los abanicos aluviales cuaternarios de la depresión tectónica del Guadalentín. *Geogaceta* 11, 67–70.
- Silva, P.G., Bardají, T., Calmel-Avila, M., Goy, J.L., and Zazo, C., 2008. Transition from alluvial to fluvial systems in the Guadalentín Depression (SE Spain) during the Holocene: Lorca Fan versus Guadalentín River. *Geomorphology* 100, 140–153, doi: 10.1016/j.geomorph.2007.10.023.
- Soler, R., Masana, E., and Santanach, P., 2003. Evidencias Geomorfológicas y estructurales del levantamiento tectónico reciente debido al movimiento inverso de la terminación sudoccidental

- de la Falla Alhama de Murcia (Cordillera Bética Oriental). *Revista Sociedad Geológica España* 16, 123–134.
- Thomsen, K.J., Murray, A.S., Jain, M., and Bøtter-Jensen, L., 2008. Laboratory fading rates of various luminescence signals from feldspar-rich sediment extracts. *Radiation Measurements* 43, 1474–1486, doi:10.1016/j.radmeas.2008.06.002.
- Tukey, J.W., 1977. *Exploratory Data Analysis*. Reading, Mass., Addison Wesley.
- USGS, 2014. Largest and Deadliest Earthquakes by Year: 1990-2014. Accessed on 29th of February 2016, <http://earthquake.usgs.gov/earthquakes/eqarchives/year/byyear.php>
- Van der Woerd, J., Tapponnier, P., Ryerson, F.J., Meriaux, A., Meyer, B., Gaudemer, Y., Finkel, R.C., Caffee, M.W., Guoguang, Z., and Zhiqin, X., 2002. Uniform postglacial slip-rate along the central 600 km of the Kunlun Fault (Tibet), from ²⁶Al, ¹⁰Be, and ¹⁴C dating of riser offsets, and climatic origin of the regional morphology. *Geophysical Journal International* 148, 356–388.
- Vanneste, K., Radulov, A., De Martini, P., Nikolov, G., Petermans, T., Verbeeck, K., Camelbeeck, T., Pantosti, D., Dimitrov, D., and Shanov, S., 2006. Paleoseismologic investigation of the fault rupture of the 14 April 1928 Chirpan earthquake (M 6.8), southern Bulgaria. *Journal of Geophysical Research* 111, B01303, doi:10.1029/2005JB003814
- Weijermars, R., 1987. The Palomares brittle-ductile Shear Zone of southern Spain. *Journal of Structural Geology* 9, 139–157.
- Wesnousky, S.G., Prentice, C.S., and Sieh, K.E., 1991. An offset Holocene stream channel and the slip rate along the northern reach of the San Jacinto fault zone, San Bernardino Valley, California. *Geological Society of America Bulletin* 103, 700–709.
- Zecher, J.D., and Frankel, K.L., 2009. Incorporating and reporting uncertainties in fault slip rates. *Journal of Geophysical Research* 114, B12407, doi: 10.1029/2009JB006325.
- Zielke, O., Arrowsmith, J.R., Grant Ludwig, L., and Akciz, S.O., 2012. High-Resolution Topography-Derived Offsets along the 1857 Fort Tejon Earthquake Rupture Trace, San Andreas Fault. *Bulletin of the Seismological Society of America* 102, 1135–1154, doi: 10.1785/0120110230.

Martínez-Díaz et al., 2001; Masana et al., 2004	Martínez-Díaz et al., 2003		Ortuño et al., 2012		Silva et al., 1992	Soler et al., 2003
Lorca-Totana	Lorca-Totana		Goñar		AMF	AMF
	F	Hol.-L. Pleist	G0	Hol	3r phase	G7
Young	E	Hol.-L. Pleist	G1-G2	Hol.-L. Pleist	2nd phase	G6
Intermediate	D-C	L.-M. Pleist	G3-G4	L.-M. Pleist	1st phase	G4
Old	C-B	M. Pleist-Plio	G5, G6	M. Pleist	1st phase	G3

Table 1. Correspondence between alluvial fan generations described by previous studies based on relative criteria, such as spatial relationships and entrenchment (Silva et al., 1992; Martínez-Díaz et al., 2001; Martínez-Díaz et al., 2003; Soler et al., 2003; Masana et al., 2004; Ortuño et al., 2012). Second row refers to the study area. Hol., Holocene; L., Late; M., Middle; Pleist., Pleistocene; Plio., Pliocene.

Sample Name	Preferred U-Th Age (ka, \pm ka)	Probability
SALT13A16	12.39 \pm 0.42	0.88
SALT13B19	20.9 \pm 2.5	0.62
SALT5CAN	11.0 \pm 1.7	0.97
CARR4	23.2 \pm 4.2	0.95
LiM4	11.7 \pm 2.6	0.84
LIMII5	46.6 \pm 5.7	0.75
PERA	23.8 \pm 3.2	0.76
LIM II7	105.1 \pm 4.2	0.12

Table 2. Weighted mean ages for pedogenic carbonate samples. The mean is calculated using the three oldest samples of Table S1 (Supplementary material). Probability indicates the probability that the observed scatter is due to analytical errors.

Sample	Method	Depth (m)	Moisture (%)	Dose rate (Gy/ka)	Equivalent dose (Gy)	Age (ka)
SAL-21	OSL	1.92	5 \pm 2	2.49 \pm 0.10	42.6 \pm 2.5	17.1 \pm 1.2
SAL-27	OSL	0.87	5 \pm 2	2.67 \pm 0.11	40.6 \pm 2.3	15.2 \pm 1.1
SAL-21	IRSL	1.92	5 \pm 2	3.17 \pm 0.11	67.8 \pm 3.8	21.4 \pm 1.4
SAL-27	IRSL	0.87	5 \pm 2	3.36 \pm 0.12	51.2 \pm 4.7	15.2 \pm 1.5

Table 3. Summary of results from OSL (Optically Stimulated Luminescence) and IRSL (infra-red stimulated luminescence) dating which includes sample depth, water content and derived total quartz dose rates. An internal quartz dose rate of 0.06 \pm 0.03 Gy/ka has been assumed based on Mejdahl (1987). Estimated equivalent doses and derived ages are also summarized. Uncertainties represent one standard error.

Sample	Age (ka)	Method	Unit in El Salvador site	Trench
SAL-27	15.2 \pm 1.1	OSL	B	TR 10 (Figs. 3 and 4)
SAL-27	15.2 \pm 1.5	IRSL	B	TR 10 (Figs. 3 and 4)
SALT5CAN	11.0 \pm 1.7	U-series	D (northwestern)	TR 5 (Figs. 3 and 4)

			wall)	
SALT13A16	12.39±0.42	U-series	D (southeastern wall)	TR 13 (Figs. 3 and 4)
SAL-21	17.1 ± 1.2	OSL	G	TR 5 (Figs. 3 and 4)
SAL-21	21.4 ± 1.4	IRSL	G	TR 5 (Figs. 3 and 4)
SAL-20	20839 – 23014 cal BP	radiocarbon	G	TR 5 (Figs. 3 and 4)
SALT13B19	20.9±2.5	U-series	H	TR 13 (Figs. 3 and 4)
SAL-2	25228 – 25832 cal BP	radiocarbon	H	TR 6 (Fig. 3)
MS-4	28.2±2.0	OSL	La Salud trenches (Fig. 2)	

Table 4. Summary of new numerical ages in the El Saltador trenches. Errors for radiocarbon dates are given at the 2σ confidence level, whereas U-series, OSL and IRSL samples have 1σ errors.

Sample	Age (ka)	Method	Alluvial fan generation	Depositional phase (Ortuño et al., 2012)	Preferred age for the alluvial fan generation (ka)
Gaba-3	23±2	pIRIR	Q2	G2	21-25
CARR4	23.2±4.2	U-series	Q2	G2	
LIM4	11.7±2.6	U-series	Q2	G2	
Carr-1-2	52.4 +7.9/-6.4	TL	Q3	G3	41-61
Carra-2-1	49±2	pIRIR	Q3	G3	
Berm-1	46.3 +6.1/-5.1	TL	Q3	G3	
LIMII5	46.6±5.7	U-series	Q3	G3	
Era-4	58±3	pIRIR	Q3	G3	
Sard-2	61.9+15/-11.2	TL	Q3	G3	
Sard-4	61±2	pIRIR	Q3	G3	
Carr-1	126 +0/-23	TL	Q3	G3-G4	
Gaba-2	108±8	pIRIR	Q3	G3-G4	
Gaba-1	111 +36/-21	TL	Q3	G3-G4	
Era-3	107±5	pIRIR	Q3	G3-G4	
Sard-1	120+39/-21	TL	Q3	G3-G4	
Era-	110+33/-19	TL	Q3	G3-G4	
PERA	23.8±3.2	U-series	Q3	G4	125-149
LIMII7	105.1±4.2	U-series	Q3	G4	
Era-2	142±7	pIRIR	Q3	G4	
Era-0	131±6	pIRIR	Q3	G4	
Carrascos-3	191±17	pIRIR	Q4	G5	145-208
Era-1	152±7	pIRIR	Q4	G5	

Table 5. Summary of new numerical ages in AMF and available ages from Ortuño et al. (2012). New datings in gray. Errors for radiocarbon dates are given at the 2σ confidence level, whereas U-series, TL and OSL samples have 1σ errors. Legend: pIRIR, post-IR IRSL. New ages in grey.

Offset		Age		Slip rate				
Offset (name)	Offset \pm std.dev. (m)	Sample name or depos. phase	Age (ka)	Mean (mm/a)	Mode (mm/a)	Media n (mm/a)	95.45% Interval	Range (mm/a)
114	26.24 \pm 4.58	G2	23 \pm 2	1.2	1.1	1.1	+0.5/-0.4	1.7-0.8
114	17.10 \pm 8.20	G2	23 \pm 2	0.8	0.7	0.7	+0.8/-0.7	1.6-0.1
115	42.75 \pm 2.97	G2	23 \pm 2	1.9	1.8	1.8	+0.5/-0.4	2.4-1.5
122	28.70 \pm 3.11	Carra-2-1	49 \pm 2	0.6	0.6	0.6	+0.1/-0.1	0.7-0.5
123	160.21 \pm 12.8 0	Carrascos-3	191 \pm 17	0.9	0.8	0.8	+0.2/-0.2	1.1-0.7
124	109.72 \pm 5.88	G4	125-149	0.8	0.8	0.8	+0.2/-0.1	1.0-0.7
125	104.03 \pm 5.09	G3-G4	90-147	0.9	0.8	0.9	+0.8/-0.3	1.7-0.6
129	38.24 \pm 6.65	G3-G4	90-147	0.4	0.3	0.3	+0.3/-0.1	0.7-0.3
136	68.83 \pm 11.68	Carrascos-3	191 \pm 17	0.4	0.4	0.4	+0.2/-0.1	0.6-0.3

Table 6. Lateral slip rates resulting from the combination of morphotectonic analysis and numerical dating in Goñar-Lorca segment of Alhama de Murcia fault. Channel 114 is measured remotely and in the field: second row of results (Fig. 6). The interpretation of each offset can be found in the supplementary material from S4-S12. Legend: depos. depositional. The calculations were done applying Zechar and Frankel (2009) functions.

	Paleoseismic trenches	Morphotectonic analyses
Advantage	Increased reliability in correlating offset features (based on age, morphology and facies)	Suited where deformation affects several sub-parallel fault strands
Disadvantage	Unsuited where more than one strand is present.	Reduced accuracy in channel age determination.

Table 7. Summary of the advantages and disadvantages of paleoseismic trenches and morphotectonic analyses in slip rate determination.

Sample Name	U (ppb)	^{232}Th (ppb)	$(^{230}\text{Th}/^{232}\text{Th})$	$(^{232}\text{Th}/^{238}\text{U})$	\pm (%)	$(^{230}\text{Th}/^{238}\text{U})$	\pm (%)	$(^{234}\text{U}/^{238}\text{U})$	\pm (%)	Uncorrected Age, (ka, \pm ka)	Corrected Age, Error (ka, \pm ka)	Preferred U-Th Age for Unit (ka, \pm ka)
SALT13A16a	4764	2794	1.052	0.19137	0.78	0.2014	$\pm 2.3\%$	0.789	$\pm 3.4\%$	32.6	8	WM (3) = 12.39
SALT13A16b	8891	869.3	4.353	0.03201	3.07	0.1393	$\pm 3.0\%$	1.043	$\pm 3.2\%$	15.6	12.8	± 0.42 ; prob. =
SALT13A16d	7142	208.1	12.40	0.00954	0.45	0.1182	$\pm 1.8\%$	1.0379	$\pm 0.51\%$	13.2	12.35	0.88
SALT13B19a2	2720	709.5	2.93	0.08505	5.68	0.249	$\pm 7.0\%$	0.990	$\pm 8.1\%$	31.7	23.6	WM (3 oldest) =
SALT13B19b1	2946	1088	1.99	0.12082	4.21	0.241	$\pm 6.4\%$	1.084	$\pm 4.4\%$	27.3	16.8	20.9 ± 2.5 ; prob. =
SALT13B19b2	3337	903.4	2.91	0.08846	2.57	0.2572	$\pm 3.0\%$	1.100	$\pm 3.1\%$	28.9	21.5	0.62
SALT13B19b3	2141	772.0	1.908	0.11802	1.96	0.2252	$\pm 2.9\%$	1.039	$\pm 2.9\%$	26.6	15.9	
SALT13B19c	1465	390.3	11.518	0.00869	0.37	0.1000	$\pm 0.82\%$	1.0590	$\pm 0.23\%$	10.8	10.07	
SALT13B19d	6474	608.3	4.31	0.03079	6.36	0.133	$\pm 13\%$	0.99	$\pm 16\%$	15.8	12.9	
SALT5CANa	4933	673.9	3.027	0.04471	0.68	0.1353	$\pm 1.3\%$	1.0543	$\pm 0.84\%$	15.0	11.1	WM (3 oldest) =
SALT5CANb	2049	1229	1.174	0.19526	6.46	0.229	$\pm 7.5\%$	1.00	$\pm 10\%$	28.4	9.2	11.0 ± 1.7 ; prob. =
SALT5CANc	2721	685.2	1.664	0.08229	5.35	0.1370	$\pm 3.4\%$	1.134	$\pm 7.2\%$	14.0	7.3	0.97
SALT5CAND	2121	2164	1.095	0.33394	0.98	0.3657	$\pm 1.6\%$	1.037	$\pm 1.8\%$	47.3	14	
CARR4 a1	1003	569.5	1.872	0.18651	0.56	0.3491	$\pm 2.8\%$	1.159	$\pm 6.6\%$	38.8	23.4	WM (3 oldest) =
CARR4 b1	1169	900.7	1.220	0.25167	4.22	0.307	$\pm 3.8\%$	1.22	$\pm 8.8\%$	31.3	11.2	23.2 ± 4.2 ; prob. =
CARR4 b2	1058	505.1	1.931	0.15617	0.97	0.302	$\pm 4.4\%$	1.077	$\pm 2.6\%$	35.7	21.8	0.95
CARR4 c	1030	676.7	1.713	0.21585	0.53	0.3697	$\pm 2.4\%$	1.095	$\pm 3.6\%$	44.6	25.4	
CARR4 d	1178	654.1	1.47	0.18228	6.29	0.268	$\pm 9.5\%$	1.46	$\pm 25\%$	21.9	10.2	
LiM4 a1	1803	477.3	1.811	0.08690	0.72	0.157	$\pm 9.2\%$	1.041	$\pm 2.0\%$	17.8	10.1	WM (3 oldest) =
LiM4 a2	1732	507.2	1.723	0.09578	0.22	0.1650	$\pm 2.5\%$	1.072	$\pm 1.5\%$	18.2	9.9	11.7 ± 2.6 ; prob.
LiM4 b	1183	458.4	1.667	0.12664	0.89	0.211	$\pm 6.1\%$	1.043	$\pm 5.9\%$	24.6	13.1	= 0.84
LiM4 c	1050	492.8	1.267	0.15406	0.45	0.195	$\pm 5.8\%$	1.068	$\pm 5.5\%$	22.0	8.2	
LiM4 d	1006	335.7	1.817	0.10921	1.77	0.198	$\pm 6.3\%$	1.035	$\pm 5.6\%$	23.2	13.2	± 4.8

LIMII5 b1	1679	649.7	3.382	0.12654	2.65	0.428	±2.4%	1.072	±4.1%	55.2	1.8	44.1	±5.9	WM (3 oldest) = 46.6 ±5.7; prob. = 0.75
LIMII5 b2	1849	786.2	3.242	0.13972	1.46	0.4529	±1.9%	1.022	±2.1%	63.7	0.97	50.7	±6.5	
LIMII5 c	1752	450.4	4.757	0.08409	1.20	0.4000	±2.3%	1.0244	±0.85%	53.9	1.1	46.2	±3.9	
LIMII5 d	1560	547.8	3.37	0.11479	6.12	0.386	±4.5%	0.989	±3.7%	54.0	1.3	43.0	±6.5	
PERA a	1719	957.1	1.498	0.18246	0.53	0.2733	±2.7%	0.965	±3.4%	36.4	0.78	17.8	±8.9	WM (3 oldest) = 23.8 ±3.2; prob. = 0.76
PERA b1	1407	478.4	2.441	0.11080	1.10	0.2704	±1.7%	0.987	±1.4%	35.0	1.21	24.3	±4.9	
PERA b2	1350	594.1	1.43	0.14354	3.23	0.205	±39%	1.042	±5.7%	23.8	12	11	±12	
PERA c	1138	368.4	2.595	0.10585	2.29	0.2747	±2.3%	0.995	±4.5%	35.2	1.2	25.2	±4.9	
PERA d	1387	381.4	2.259	0.08993	1.36	0.203	±5.5%	0.974	±2.7%	25.5	2.3	16.9	±4.2	
LIM II7a1	764	360.8	4.64	0.15450	0.20	0.717	±2.8%	1.0519	±0.18%	123.1	±6.3	109.3	±9.7	WM (3 oldest) = 105.1 ±4.2; prob. = 0.12
LIM II7a2	730	250.1	6.45	0.11210	0.16	0.723	±2.2%	1.0506	±0.20%	125.4	±5.2	115.5	±7.4	
LIM II7c	999	447.8	4.55	0.14634	0.17	0.666	±2.5%	1.0527	±0.26%	108.0	±4.6	94.9	±8.0	
LIM II7d	838	314.1	5.384	0.12260	0.17	0.6601	±1.3%	1.0470	±0.14%	107.4	±2.5	96.5	±6.0	
LIM II7e	803	382.1	4.24	0.15541	0.20	0.658	±2.7%	1.0806	±0.25%	100.8	±4.5	87.4	±7.9	

Table 2. U-Th isotopic data and ages for pedogenic carbonate. All isotope ratios are activity ratios. Uncertainties are given at 1 standard deviation. Uncorrected ages are calculated without correction for U and Th from detritus. Corrected ages are calculated assuming detritus with ($^{232}\text{Th}/^{238}\text{U}$) = 1.2 ±0.6, ($^{230}\text{Th}/^{238}\text{U}$) = 1.0 ±0.1, and ($^{234}\text{U}/^{238}\text{U}$) = 1.0 ±0.1. Decay constants are those of Jaffey (1971) for ^{238}U and Cheng et al. (2013) for ^{230}Th and ^{234}U . WM (N) = weighted mean, where N = no. of samples; prob. is the probability that the observed scatter is due to analytical errors. Sub-samples from different clast are indicated with letters (a to d) and sub-samples from the same clast, with numbers (1-3).

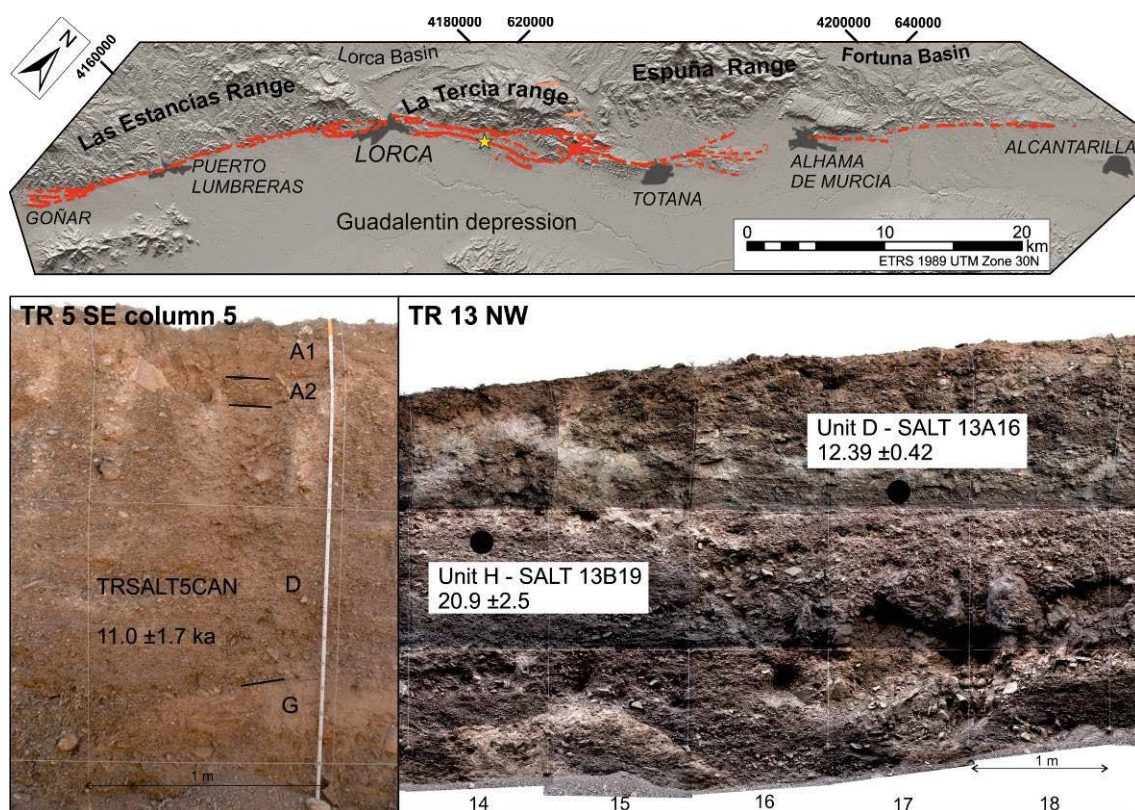


Figure S1. Stratigraphic and edafic position of the samples TRSALT5CAN, TRSALT13A16 and TRSALT13B19. The position of the star indicated the El Salvador trenching site.

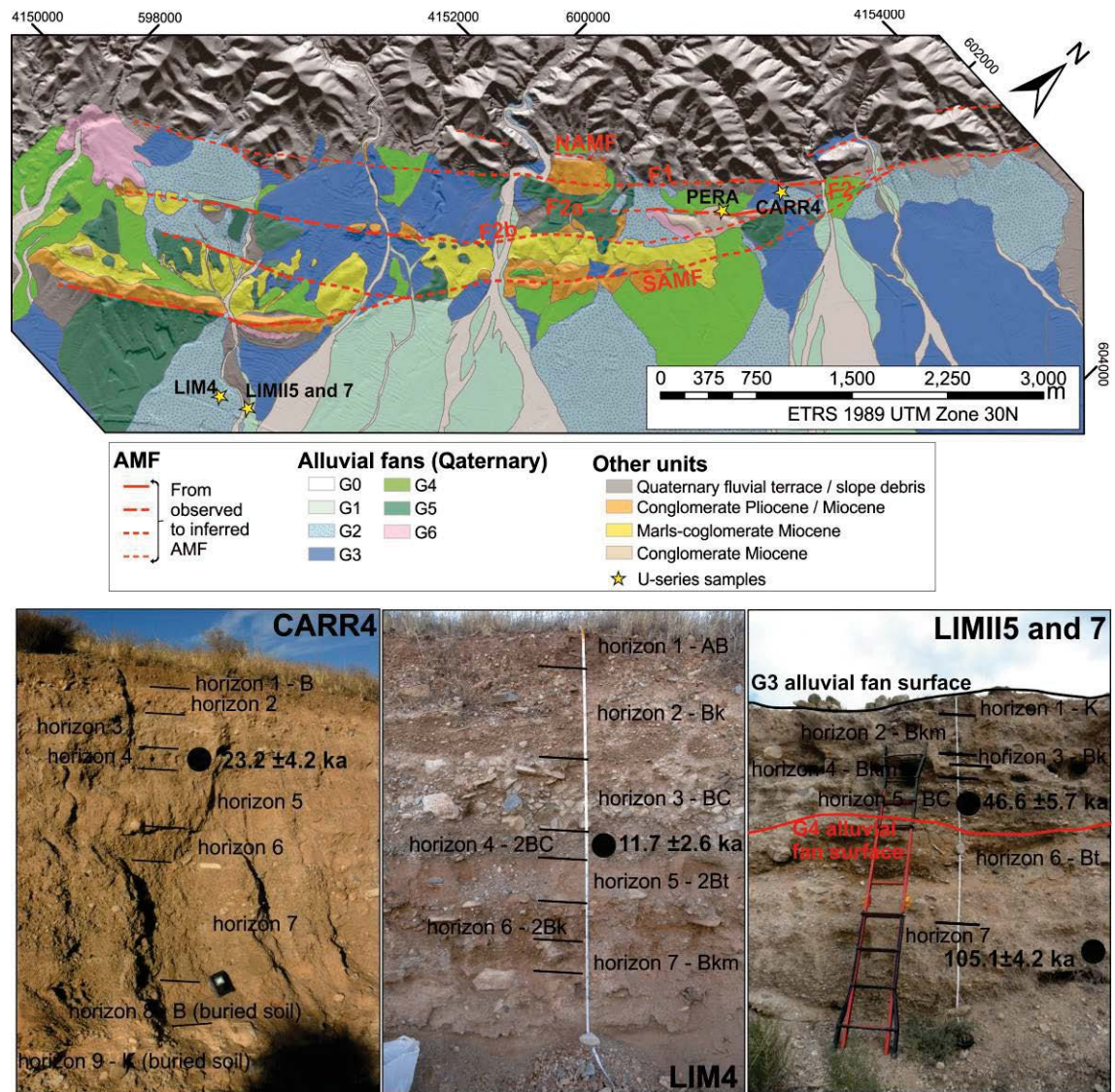


Figure S2. Stratigraphic and edafic position of the samples CARR4, LIM4, LIMII5 and LIMII7. We sampled the pedogenic carbonate of four soil profiles at the Goñar-Lorca segment, specifically in the southwestern termination of the segment.

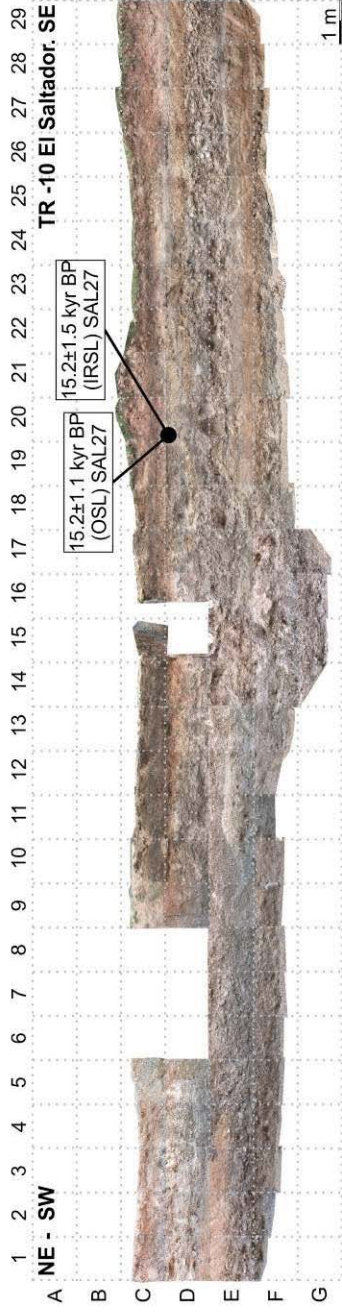
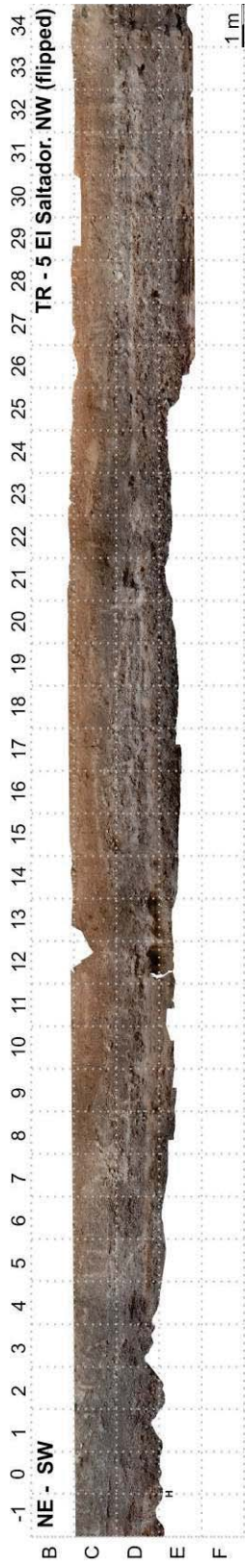




Figure S3. Fotologs of the trenches 5, 8, 10, 12 , 13 and 14 from the El Salvador paleoseismic site. The interpretation of the exposed units is shown in Fig. 5.

**Annex 2. Publicacions en revistes
indexades el contingut de les quals no
s'ha inclòs en la memòria**

Ferrater, M., Silva, P.G., Ortuño, M., Rodríguez-Pascua, M.A., Masana, E. (2015). **Archaeoseismologic analysis of a Late Bronze Age site on the Alhama de Murcia Fault: Tira del Lienzo (Murcia, SE Spain)**. *Geoarchaeoseismology*, 30, 151-164. Doi 10.1002/gea.215053

Ferrater M., Booth-Rea G., Pérez-Peña, J. V., Azañón, J. M., Giaconia, F., Masana, E. (2015). **From extension to transpression: Quaternary reorganization of an extensional-related drainage network by the Alhama de Murcia fault (eastern Betics)**. *Tectonophysics*, 667, 33-47. Doi: 10.1016/j.tecto.2015.06.011.

Archaeoseismological Analysis of a Late Bronze Age Site on the Alhama de Murcia Fault, SE Spain

Marta Ferrater,^{1,*} Pablo G. Silva,² Maria Ortuño,¹ Miguel Ángel Rodríguez-Pascua,³ and Eulàlia Masana¹

¹RISKINAT Group. GEOMODELS. Departament de Geodinàmica i Geofísica, Facultat de Geologia, Universitat de Barcelona, C/ Martí i Franquès, s/n, 08028 Barcelona, Spain

²Dpto. Geología, Universidad de Salamanca Escuela Politécnica Superior de Ávila, Avda. Hornos Caleros 50, 05003 Ávila, Spain

³Instituto Geológico y Minero de España (IGME), c/ Ríos Rosas 23, 28003 Madrid, Spain

Correspondence

*Corresponding author;

E-mail: marta.ferrater@ub.edu

Received

31 July 2014

Revised

9 December 2014

Accepted

11 December 2014

Scientific editing by Jamie Woodward

Published online in Wiley Online Library
(wileyonlinelibrary.com).

doi 10.1002/zea.21505

An archaeoseismological study of Tira del Lienzo (Totana, Spain) was undertaken. The site belongs to the Argar archaeological group (2200–1550 cal. B.C.; Bronze Age). It is located on the trace of the reverse left-lateral Alhama de Murcia fault (AMF) that was responsible for the 5.1 Mw 2011 Lorca earthquake. The constructive typology of the site consists of mortar-free irregular natural boulders (dry-set masonry) and differs from earlier archaeoseismological sites built on regular masonry constructions in the Betic Cordillera. Four Earthquake Archaeological Effects (EAEs) were identified as follows: (1) an apparent surface rupture (c. 18 cm left-lateral offset), (2) the differential coseismic uplift of several centimeters affecting the main building of the settlement, (3) the widespread development of fractures on the ground surface (ground cracks) in a NE-SW direction consistent with the kinematics of the AMF, and (4) fractures in boulders that constitute the remains of the dry stone walls at the site. Structural analysis of the two fracture types reveals two nearly orthogonal sets (NE-SW and NW-SE), matching the strike-slip kinematics of the AMF in the zone. Archaeoseismic evidence and related radiocarbon dates of the different building phases of the Bronze Age site indicate the probable occurrence of at least one strong seismic event (6.3–6.5 Mw; IX ESI-07) around 1550 cal. B.C., or soon after, triggering the destruction and probably the eventual abandonment of the site. We have identified an ancient lost earthquake from the Bronze Age and report the first archaeoseismological evidence of surface rupture in the Iberian Peninsula. This study also provides the first numerical data in the Totana-Alhama segment of the AMF based on the recorded archaeoseismic displacements. These data allowed us to characterize the related slip rates (0.05 mm/yr) to define the seismic potential of the analyzed fault segment of the AMF, which was poorly defined by previous seismic and geological data. © 2015 Wiley Periodicals, Inc.

INTRODUCTION

Although the oldest archaeoseismological evidence in the world is located in northern Iraq and dates from the middle Palaeolithic (c. 50,000 years old), archaeoseismological studies usually date from the Bronze Age (c. 1700 B.C.; Nur & Burgess, 2008). From an archaeoseismological perspective, the oldest archaeological sites in the Iberian Peninsula are *Baelo Claudia* in Cadiz (Silva et al., 2005, 2009) and *Ilunum* in Albacete (Tolmo de Minateda, Rodríguez-Pascua et al., 2010, 2013a). Both sites are

located in the Betic Cordillera and were affected by repeated earthquakes between the 1st and 4th centuries A.D. (Silva & Rodríguez-Pascua, 2014). These Roman sites show abundant archaeoseismic evidence of seismic ground shaking. Multiple Earthquake Archaeological Effects (EAEs) from the classification of Rodríguez-Pascua et al. (2011) have been identified, most of them associated with permanent deformations of the fabric of buildings and pavements and notable oriented damage.

The Tira del Lienzo site, from the Bronze Age, constitutes the oldest archaeoseismological record in Spain, as

preliminary evidence of fault offset in the archaeological remains suggest (Ferrater et al., 2013). In this study, we follow the guidelines of the classification of EAEs proposed by Rodríguez-Pascua et al. (2011) in order to characterize the site archaeoseismologically. However, the type of dry-set masonry (irregular boulders) construction style used at the site is not specifically considered in the EAE classification of these authors, and thereby new types of EAE are described in this paper for consideration in future updates of the classification. The described EAE come from the recognition of a suspect wall offset in a microtopographic map of the archaeological site and preliminary field research (Ferrater, 2013; Ferrater et al., 2013). The detailed map, published for the first time in this paper, was produced by the team from the Universitat Autònoma de Barcelona (UAB) in charge of archaeological research at the La Bastida de Totana site (La Bastida Project). This site is the largest fortified metropolis of the Late Bronze Age in the western Mediterranean, especially during its final occupation period (1900–1550 cal. B.C.; Lull et al., 2014). It is informally known in the archaeological community as the *Little Western Troy*.

Tira del Lienzo is a settlement at the top of a small hill forming part of the La Bastida metropolis (Lull et al., 2011a) and is located on the Alhama de Murcia fault (AMF) zone. In detail, the site is founded on a 35 m high elongated pressure ridge developed on the trace of the Totana-Alhama segment of the AMF, which has not been subjected to previous palaeoseismic analyses. Although the AMF is one of the more active faults in the Iberian Peninsula, and was responsible for the destructive 5.1 Mw 2011 Lorca earthquake (López-Comino et al., 2012), its historical earthquake record ($I_{\max} = \text{VIII EMS-98}$ European Macroseismic Scale) does not go beyond the 14th century. Owing to the poor preinstrumental record for this fault, several palaeoseismic studies have been carried out to assess late Pleistocene to late Holocene surface faulting events in the adjacent Lorca-Totana segment (Silva et al., 1997; Martínez-Díaz, 1998; Martínez-Díaz et al., 2001, 2003; Masana et al., 2004), and also in the southern horse tail termination of the fault (Ortuño et al., 2012). An archaeoseismological study, in a location known to be an on-fault location, would be able to detect ancient earthquakes, thereby allowing us to improve the preinstrumental record.

SEISMOTECTONIC FRAMEWORK OF THE ZONE: THE AMF ZONE

The site under study is located in the AMF zone that controls the recent development of the landscape and the

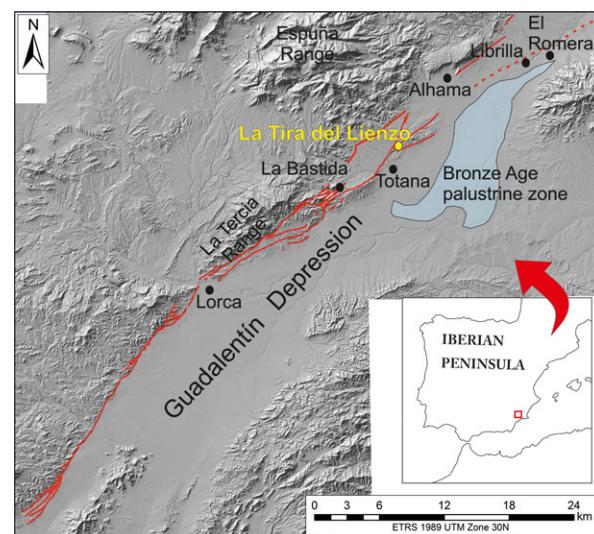


Figure 1 Tira del Lienzo site and Alhama de Murcia fault (AMF) zone. Dashed lines correspond to the El Romeral fault that is not visible in outcrop. The locations of other sites/localities cited in the text are also highlighted.

seismic activity in the area. The AMF is a $N45^{\circ}$ – 65° E left-lateral strike-slip fault with a reverse component, consistent with NW-SE convergence between the Eurasian and the African plates (Silva, 1994; Martínez-Díaz, 1998). This fault zone constitutes the key element of one of the main crustal-scale active tectonic structures of the Eastern Betic Cordillera, the Eastern Betic Shear Zone (EBSZ; Silva et al., 1993; Martínez-Díaz et al., 2001, 2012; Masana et al., 2004). The Totana-Alhama segment is the smallest central segment of the fault (11 km; Figure 1). Together with the adjacent Lorca-Totana segment, this segment displays fault branching, with a northern branch controlling the $N45^{\circ}$ E Espuña range composed of metamorphic Betic rocks, and a $N65^{\circ}$ E southern branch affecting Upper Neogene to Quaternary sediments (Silva et al., 2008). Fault branching promoted the generation of a set of triangular strike-slip basins between the main faulted mountain front and the southern fault branches. These basins are filled by a thick series of early to middle Pleistocene alluvial fan deposits (Silva et al., 2003). Crusted middle Pleistocene alluvial fan surfaces are distally offset and uplifted by the younger activity of the southern branch and incorporated into the pressure ridges developed in this area (Silva et al., 1992; Silva, 1994). Along this southern branch, a set of restraining strike-slip fault landforms such as pressure ridges, spur ridges, and sinistrally deflected stream channels are assembled on intervening $N65^{\circ}$ E linear tectonic landforms, separating the main mountain front from the Guadalestín Tectonic Depression (Figures 1 and 2A).

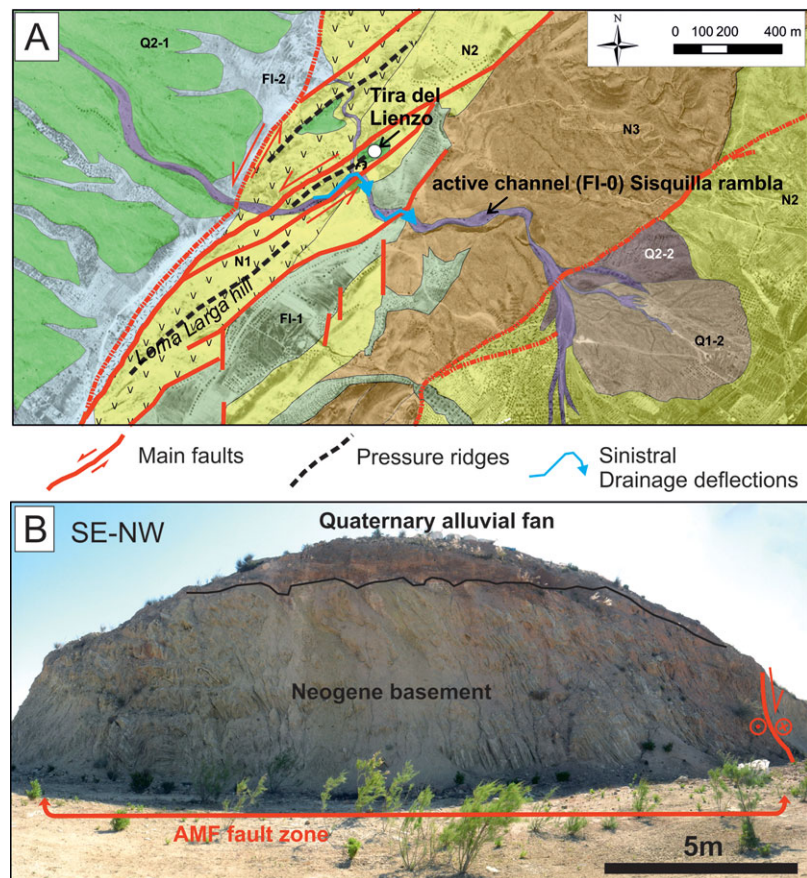


Figure 2 Tira del Lienzo. (A) The geological setting of Tira del Lienzo (legend: N1 [gypsum], N2 [shale], N3 [conglomerate and shale], Neogene basement); Q1-Q2-2, Quaternary alluvial fans younger to older; FI0-FI-2, Quaternary fluvial infill younger to older; Alhama de Murcia fault (AMF) fault traces in red, dashed (inferred traces); (B) Geological interpretation of the pressure ridge where La Tira del Lienzo is located.

Instrumental records of earthquakes indicate that 90% of the seismicity is shallow, that is less than 20 km in depth (Martínez-Díaz, 1998). The most significant historical earthquakes (VIII EMS) in the AMF are those that occurred in A.D. 1579, 1674, and 1818 at Lorca (Lorca-Totana fault segment). The only event reported in the Totana-Alhama segment, the subject of this study, is the A.D. 1907 event at Totana that reached an intensity of VII EMS (IGN, 2012). The strongest instrumentally recorded event along the fault zone occurred in Lorca on May 11 2011 (Mw 5.1) and had VII EMS intensity (López-Comino et al., 2012). None of these historical or instrumental seismic events triggered surface faulting along the AMF zone (Silva et al., 1997; Martínez-Díaz et al., 2012). However, the first palaeoseismic studies of the zone found robust evidence of late Pleistocene to Holocene surface faulting along the AMF zone (Silva, 1994; Silva et al., 1997; Martínez-Díaz, 1998). Other palaeoseismic studies based on fault-trenching analyses on this fault characterized a number of surface-faulting palaeoearthquakes, with maximum magnitude values in the range of Mw 6.1–7.0 (Martínez-Díaz et al., 2001; Masana et al. 2004; Ortuño

et al., 2012). These studies recorded a minimum of six palaeoseismic events during the last 274–174 kyr. Initial fault-trenching analyses (Martínez-Díaz et al., 2003) estimated average vertical slip rates of 0.21 mm/yr for the last 130 kyr. However, more systematic palaeoseismic analyses and recent regional reviews (Masana et al., 2004; Martínez-Díaz et al., 2012; Ortuño et al., 2012) report maximum vertical slip rates of 0.35 mm/yr, maximum lateral slip rates of 0.53 mm/yr, and maximum net slip rates of 0.66 mm/yr. Recent geodetic studies indicate that the ongoing horizontal slip rates for the last 15 years are 0.70 ± 0.2 mm/yr, in the range of the maximum rates obtained by palaeoseismic analyses (CuaTeNeo GPS network; Echeverría et al., 2013). DinSar and GPS analyses after the 2011 Lorca earthquake (Mw 5.1) revealed coseismic vertical deformation of about 3–4 cm along the trace of the AMF north of Lorca (Frontera et al., 2012).

These studies were, however, mainly focused on the Lorca-Totana segment, rather than on the smaller Totana-Alhama segment in which our site is located. This segment only records the aforementioned VII EMS

A.D. 1907 event and few V-IV EMS earthquakes occurred during the 19th and 20th centuries. The seismic potential of this fault segment is determined on the basis of theoretical approaches, suggesting a capacity to generate 5.9–6.5 Mw events (Martínez-Díaz et al., 2012).

TIRA DEL LIENZO: GEOLOGICAL AND ARCHAEOLOGICAL SETTING

Geology and Geomorphology

The archaeological site is located on strongly cemented, fairly deformed, and uplifted Quaternary alluvial fan deposits on the top of an elongated pressure ridge developed on the trace of the southern branch of the AMF (Figure 2A). In this zone, the fault has an overall ENE-WSW trend and mainly left-lateral to inverse kinematics, resulting in the development of well-preserved high-pressure ridges, several hundred meters long, and 7–12 m high (Figure 2A; Silva et al., 1993; Silva, 1994). The pressure ridge on which the site is located is currently affected by quarry works (Figure 2B) that display nearly the whole fault zone under the site (c. 100 m wide). The fault zone is constituted by faulted and strongly folded marls dipping SE and mylonitic gypsums of the Miocene (Figure 2B). At the top there are uplifted alluvial fan deposits.

Uplifted Quaternary alluvial fan deposits beneath the archaeological remains display thick (1–2 m) calcrete soil profiles, which on the basis of regional studies on alluvial fan sequences and calcrete development (Alonso-Zarza et al., 1998; Silva, 2014) date from c. 780 kyr (early–middle Pleistocene transition) to c. 380 kyr (Silva, 2014). Also of note, alluvial fan deposits record an accumulated uplift of c. 8–7 m and the adjacent Sisquilla rambla creek (60 m from the site) shows a significant left-lateral displacement of 23–20 m (Figure 2A) from the last c. 350 kyr (middle Pleistocene; Silva, 1994).

Archaeology and Geoarchaeology

Tira del Lienzo is a small early Bronze Age archaeological site, belonging to the so-called “Argaric Culture” located near Totana in Murcia, SE Spain. This ancient culture prospered between 2200 and 1550 cal. B.C. in the southeastern sector of the Iberian Peninsula, comprising the present provinces of Almería, Granada, and Murcia (Lull, 1983; Lull et al., 2011a, 2014). According to these authors, the site under study is related to one of the largest metropolises of early Bronze Age culture in SE Spain—La Bastida de Totana—which is located about 7 km SW from the site (Figure 1). The first human occupation recorded

at the La Bastida site dates from 2200 cal. B.C. and it was finally abandoned between 1600 and 1550 cal. B.C. (Lull et al., 2011a, 2014). However, Tira del Lienzo was occupied from 2050 to 1600/1550 cal. B.C. There are two main phases of occupation and building development at this site, the first in 2050–1900 cal. B.C. and the second in 1900–1550 cal. B.C., bracketed by the radiocarbon ages reported by the La Bastida archaeological project (e.g. Lull et al., 2011a; Delgado-Raack et al., 2014). Our study is focused on the second phase of occupation (1900–1550 cal. B.C.) from where the archaeoseismological evidence is preserved (Figure 3). Archaeological data indicate that this site constituted a small settlement used for administration and management of agricultural production, linked to La Bastida (Delgado-Raack et al., 2014).

During the second phase (1900–1550 cal. B.C.), the structure of the settlement consisted of a minimum of seven rectangular or trapezoidal houses/enclosures (each of c. 15–27 m²) around a larger rectangular central building (c. 90 m²) oriented NE-SW (Figure 3; Delgado-Raack et al., 2014). The dimensions of the remains are about 750 m² surrounded by a wall about 1–1.20 m wide. The main architectural features of the buildings consist of rectangular rooms with dry stone walls 50–60 cm wide made up of boulders of decimetric size (Figure 4; Lull et al., 2011b). The rocky ground of the site is constituted by indurated calcrete soils developed on top of the middle Pleistocene alluvial fan deposits. At present, the remains display the lower three to four rows (<1 m high) of the original dry-set masonry walls, in which the apparent archaeoseismic damage is recorded. Archaeological excavations started in the year 2010 when the settlement was completely buried by numerous stone blocks, a consequence of the collapse and downfall of the original dry stone walls (González Guerao, 2005).

ARCHAEOSEISMOLOGY OF THE SITE

The archaeoseismological analysis of the site is focused on: (1) the inventory of EAEs recorded at the site on the basis of the classification of Rodríguez-Pascua et al. (2011), and on (2) structural analysis of the observed fractures and the AMF zone.

EAEs

Four types of EAE were recorded at the site (Figure 5): (a) ground fractures (Figures 3 and 4A), (b) broken wall-boulders (Figure 4B), (c) offset/folded walls (Figures 3 and 5), and (d) seismic uplift/subsidence (Figure 3). The first two of these EAE (a and b) are not included in

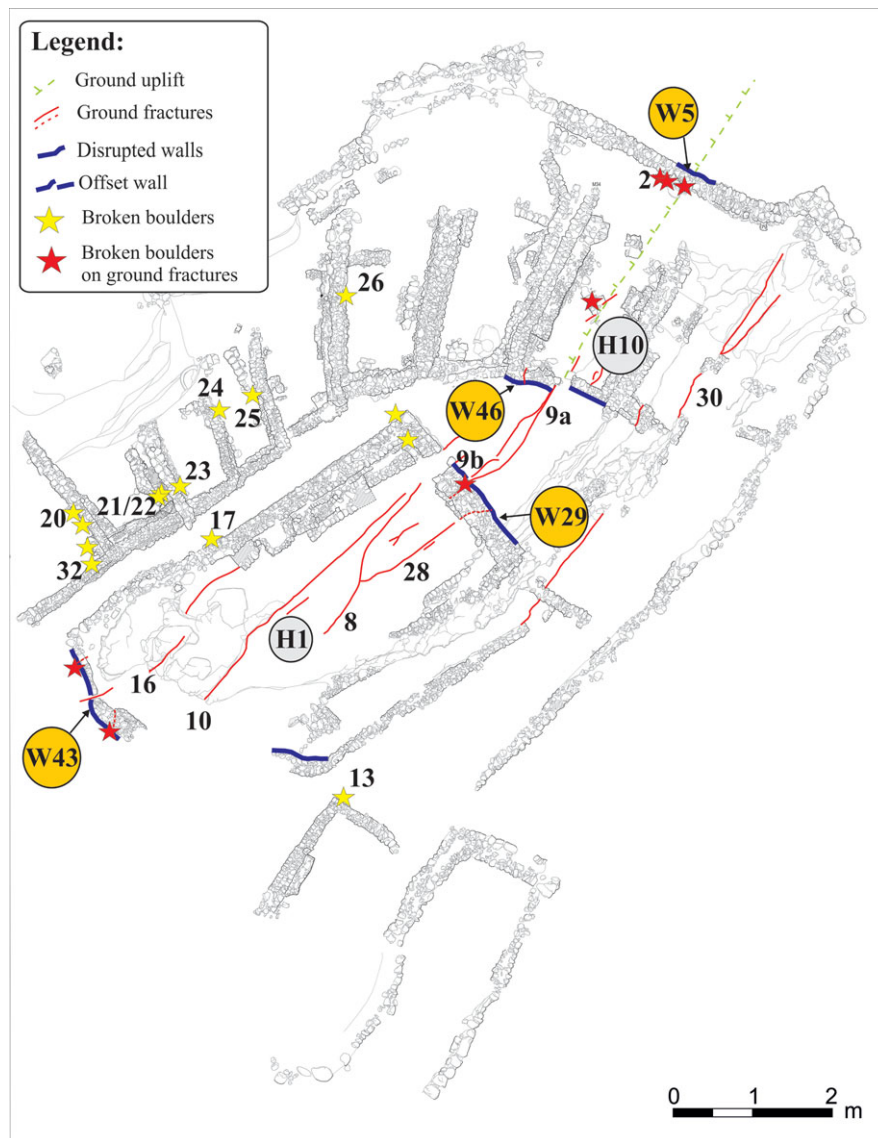


Figure 3 Planimetric map of the site provided by the archaeological group of the Universitat Autònoma de Barcelona (La Bastida Project). Location of all the Earthquake Archaeological Effects (EAEs). Numbers correspond to the fractures in Figure 4. Houses and walls where earthquake effects were identified are highlighted.

the classification of Rodríguez-Pascua et al. (2011) because the construction method (dry-set masonry) and building material (boulders) featured in the site were not considered by these authors. These two new EAE have been described by Ferrater (2013) and Ferrater et al. (2013). These authors acknowledge that these two EAE have their respective equivalents in the classification of Rodríguez-Pascua et al. (2011), albeit affecting other construction types and materials. Rocky ground fractures (a) in the natural floor (indurate calcrete surface) correspond to the “regular and irregular fractures and folds in pavements” (Figure 5) of Rodríguez-Pascua et al. (2011). On

the other hand, the broken boulders (b) recorded in the dry stone walls at this site are equivalent to the “penetrative fractures in masonry blocks” of the aforementioned authors (Figure 5).

Ground fractures

The rocky surface where the Tira del Lienzo archaeological remains are located can be considered as an almost rigid element owing to the surface (calcrete) cementation of the alluvial deposits (Figures 2B). This hardened surface would behave as any thick (c. 1 m)

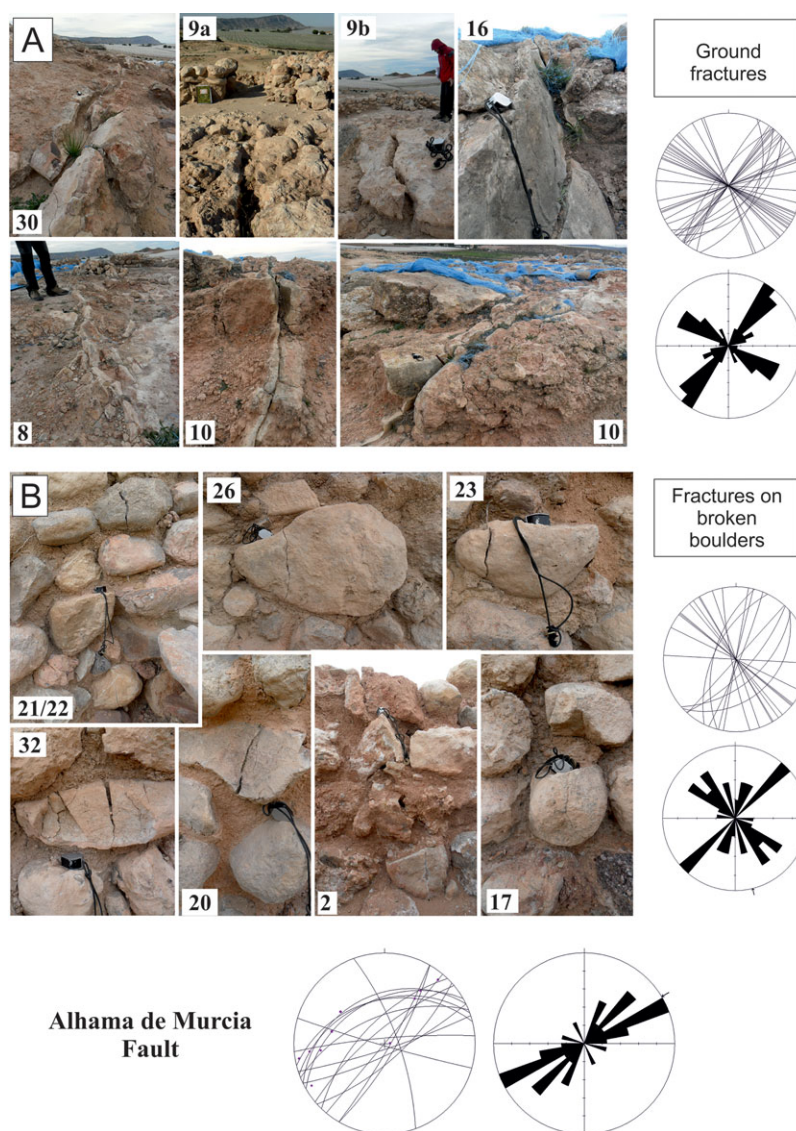


Figure 4 Photographs and structural analysis of ground fractures and fractures on broken wall-boulders (numbers correspond to the position of the fractures in the map in Figure 3). Structural analysis includes stereographic projections and rose diagrams. In the Alhama de Murcia fault (AMF), structural analysis fault planes and striae are shown. Some photographs were taken after repair work was done by the La Bastida project for conservation of the site.

anthropogenic cemented pavement. In the event of ground shaking, this surface undergoes similar deformations (mainly cracking) to those listed for human-made pavements in the EAE classification of Rodríguez-Pascua et al. (2011; Figure 5) and in the ESI-07 macroseismic scale (Michetti et al., 2007). The surface calcrete horizon overlays the 2–3 m thick weakly cemented alluvial materials outcropping at the top of the pressure ridge (see Figure 2B). These alluvial deposits, with soil-like geotechnical properties, constitute a relatively soft layer between the more competent underlying rocks of the fault zone and the overlying calcrete horizon. Ground cracks display NE–SW dominant orientations. Some of them exceed 4–5 m in length and have a millimetric width at indoor locations (Figure 4A). Cracks are arranged in a fracture

system that crosses the entire archaeological site parallel to the AMF zone (Figure 4). This fracture system mainly affects the central building (H1) and House 10 (H10; Figure 3), extending outdoors along the whole hilltop of the site (c. 40 m length). These ground cracks are decametric in length and some of them are a few centimeter to millimeter wide, a large number of them showing partial or complete thin calcrete coatings. This indicates that ground cracking was a recurrent process in this hilltop site before, and probably after, its occupation during the early Bronze Age. The largest ground cracks affecting the site appear as open cracks, in some cases 1–1.5 cm wide, and they are currently filled with soil. Figure 3 shows that the main indoor fracture system is closely associated with most of the other EAE recorded in this study.




COSEISMIC EFFECTS (DIRECT EFFECTS)				
GEOLOGICAL EFFECTS	Primary geological effects on the ground surface	<ul style="list-style-type: none"> ☆ Coseismic Uplift / subsidence ☆ Ground cracks and fractures in surface calcrete horizons 	EEEs ESI-07	NEW
	Strain structures generated by ground deformation	<ul style="list-style-type: none"> - Fractures, folds & pop-ups on regular pavements - Fractures, folds & pop-ups on irregular pavements ☆ Folded walls ☆ Displaced /offset walls 		
EFFECTS IN THE BUILDING FABRIC	Strain structures generated in the building fabric	<ul style="list-style-type: none"> - Penetrative fractures in masonry regular blocks ☆ Penetrative fractures in masonry irregular blocks (broken wall-boulders) 	EAEs EMS-98 (MSK, MCS)	NEW

Figure 5 Earthquake Archaeological Effects (EAEs) identified at Tira del Lienzo and their equivalence in the Rodríguez-Pascua et al. (2011) EAEs classification. New EAEs proposed in this work are highlighted.

Broken wall-boulders

Individual blocks of varying dimensions are vertically cracked (Figure 4B), preferentially in the NW-SE walls (88%). These walls are orthogonal to the ground fracture system and in some cases (30%) the broken boulders are spatially related to rocky ground cracks (Figure 3). As regards ground failure, vertical propagation of these ground fractures toward and in the walls is likely to have occurred. However, these fractures are not clearly recorded after the works that repaired most of the stone walls. The original mortar-free construction of the dry stone walls probably contributed to the vertical interblock propagation of the fractures, although intrablock cracking occurred in some cases. An intricate arrangement of inter- to intrablock fracture propagation within the dry stone wall is feasible. This was probably facilitated by the jagged assemblage of the rows of rough blocks in the walls, resulting in irregular and discontinuous vertical fracture propagation unlike the almost-linear propagation of penetrative fractures in regular masonry blocks described in Rodríguez-Pascua et al. (2011). In fact, dry stone walls appear to be more resistant to earthquakes than are walls constructed with mortar (which serves as a clamp), and thus they could undergo interblock sliding and then resettle without collapsing (Senthivel, Lourenco, & Vasconcelos, 2006). Analytical models suggest that interblock propagation of the fractures is the main deformation control in dry stone walls, although intrablock cracking or crushing can

occur in the lower third of the wall, especially in cases of ground failure (Senthivel, Lourenco, & Vasconcelos, 2006; Colas, Morel, & Garnier, 2013). According to these authors, the intrablock fracture system opens progressively upwards, causing extensive damage to the upper halves of the walls and leading to their collapse. Fracture generation has also been attributed to other causes such as thermal contrast caused by fire. In such cases, the fractures would-be parallel to the wall.

Offset and folded walls

This is the most striking archaeoseismological feature recorded at Tira del Lienzo. Folding and disruption of dry stone walls are always recorded in the NW-SE walls and are in direct relationship with the two EAE described above, especially with the ground fractures (Figure 3). As shown in Figure 3, wall folding was recorded in two walls (W43 and W29) of the main building (House 1), in the southern wall (W46) of House 10 and in the northern wall of the site (W5). The most significant relationship between a folded wall and a ground crack is well preserved in the ancient doorway of House 10 (W46; Figure 3). In this zone, one of the main ground fractures of millimetric width propagates NE-SW indoors and outdoors, affecting the entire building over at least c. 10 m and reaching the northern wall of the site. The ground rupture coincides with an apparent differential uplift of several centimeters (5–8 cm) between the eastern (up)

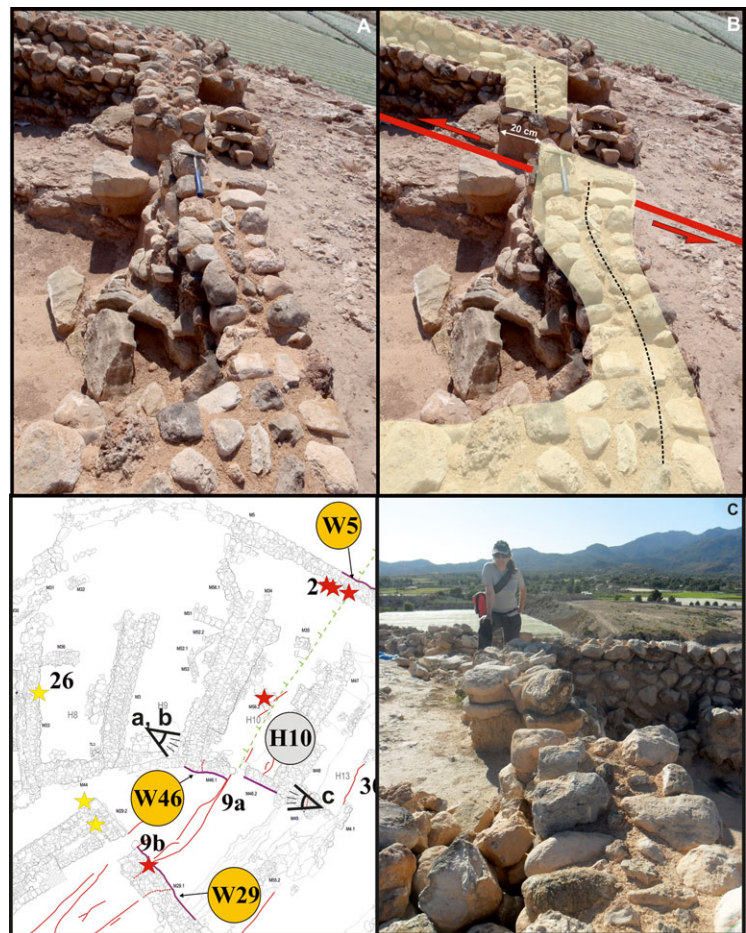


Figure 6 Detail of the offset wall (W46) in relation to the other EAEs (broken boulders, ground fractures, and ground deformation); same legend as in Figure 3. (A), (B), and (C) are images of the W46 wall from different angles.

and western (down) portions of the house. At the ancient doorway, these two portions of the building record a visible left-lateral offset of 18 cm (Figure 6) that is consistent with the kinematics of the AMF under the site. In fact, NW-SE-oriented walls (orthogonal to the overall NE-SW fault strike) constitute linear markers that record the strike slip. In detail, the NW segment of the disrupted wall W46 displays a left-lateral drag bend-like deformation (Figure 6A and B). The recorded wall offset can be considered a reliable feature for surface rupture related to the fracture system crossing the archaeological site. As shown in Figure 3, the mapping of ground fractures records similar left-lateral anomalies in the other folded walls. All these fractures are related to the main NE-SW fracture system affecting House 10 (W46), House 1 (W29) and the northern wall (W5). To the SE, the zone is not excavated, and it is not possible to follow the fractures. It is therefore reasonable to consider this NE-SW fracture system as evidence of the left-lateral surface deformation and of the centimetric differential uplift along the trace of the AMF. The coincidence of surface faulting with the

ancient doorway of House 10 allows measurement of the offset (18 cm) since in the other cases the walls are only folded.

Wall folding above the trace of the NE-SW fracture system was probably facilitated by the relatively interblock free sliding favored by the dry stone masonry style and the absence of wall foundations (Senthivel, Lourenco, & Vasconcelos, 2006). All cases of wall folding are linked to the occurrence of broken wall-boulders (Figure 3) that is interpreted as occasional intrablock cracking in the lower portions of the wall due to ground failure, as described in laboratory analogs (Colas, Morel, & Garnier, 2013; see *Broken wall-boulders* section). In this case, inter- and intrablock sliding linked to the process of wall bending will be the result of the upward propagation into the buildings of the centimetric left-lateral displacement along the NE-SW ground fracture system. As discussed in the *Broken wall-boulders* section, this mechanism of deformation will cause the destruction of the upper portions of the walls and buildings (Senthivel, Lourenco, & Vasconcelos, 2006; Colas, Morel, & Garnier, 2013).

Seismic uplift/subsidence

The site displays centimetric ground uplift related to the ground rupture in H10 (Figures 3 and 6). As stated above, this uplift coincides with the offset wall and with the broken boulders in some walls. The magnitude of the vertical offset ranges between 5 and 8 cm and uplifts the SE portion of the house (H10).

Structural Analysis of EAEs

The structural analysis was performed using data for rocky ground fractures ($n = 60$) and broken boulders ($n = 28$). The results indicate the occurrence of two consistent NE-SW and NW-SE orientations of fracturing in both data sets with a NE-SW dominant orientation (Figure 4). The dominant orientation coincides with the AMF orientation in the fault zone outcrop located beneath the site (see Figure 2B). Therefore, the consistent fault and fracture orientations (including the main surface rupture recording left-lateral offset in House 10; W46) strongly suggest that the generation of the analyzed fractures was controlled by fault activity. Damage to the buildings due to other causes would, by contrast, have produced randomly oriented wall displacements and fractures in dry stone wall-boulders, not necessarily consistent with the ground fractures affecting the site. Coseismic left-lateral displacement and differential uplift probably triggered on-fault ground failure. As a result, the upper halves of the walls were destroyed, whereas their lower halves underwent fracturing. This has been corroborated by analyses of dry-set masonry constructions (Senthivel, Lourenco, & Vasconcelos, 2006; Colas, Morel, & Garnier, 2013).

DISCUSSION: PALAEOSEISMIC ANALYSIS

On the basis of (1) the left-lateral displacement recorded by offset wall 46 in House 10 (18 cm) and on (2) the apparent surface uplift (5–8 cm) related to the NE-SW fracture system affecting the site (Figure 3), it is possible to obtain empirical approximations of the size of the suspected palaeoseismic event and slip rates of the AMF in this fault segment.

Application of the empirical magnitude–displacement relationship for strike-slip faults (Wells & Coppersmith, 1994) to the ground rupture data (which considers both the 18 cm of lateral displacement and 8 cm of maximum uplift) would imply the occurrence of a 6.4 ± 0.1 Mw earthquake. The magnitude of this event is consistent with the theoretical seismic potential of the Totana-Alhama fault segment (5.9–6.5 Mw; Martínez-Díaz et al., 2012). The above relationship is at the limit of its

magnitude range of application; however, it has been extensively used in all the previous palaeoseismic analyses developed in the AMF and is the most reliable tool for comparing calculated magnitudes along the whole fault zone (e.g., Martínez-Díaz et al., 2012). The application of other existing empirical earthquake scaling relationships (e.g., Stirling, Rhoades, & Berryman, 2002; Wesnousky, 2008; Stirling et al., 2013) to the site yield similar magnitude values between 5.7 and 6.5 Mw. Surface faulting is rare for magnitudes smaller than 6.5 Mw, and the population of earthquakes used in all the mentioned relationships (including Wells & Coppersmith, 1994) is sparse. This fact results in large uncertainties and accumulated errors that decrease for earthquakes above 6.5 Mw with metric-scale displacements. Another reason for using the Wells and Coppersmith (1994) relationships is that the other empirical earthquake scaling equations do not directly relate magnitude and displacement (Stirling, Rhoades, & Berryman, 2002; Wesnousky, 2008; Stirling et al., 2013).

Application of the ESI-07 intensity scale to the surface deformation data implies the occurrence of a palaeoseismic event of IX ESI-07 intensity. This scale takes into account the surface faulting for this minimum intensity value in nonvolcanic areas, which results in ground ruptures over a few kilometers with offsets of several centimeters and coseismic uplift of only few centimeters, such as those recorded in the studied site (Michetti et al., 2007). Regarding probable EMS-98 intensity, based on building damage, Karabacak et al. (2013) developed a comparative scheme for EMS-98 (Grünthal, 1998) and ESI-07 (Michetti et al., 2007) intensities recorded in different archaeological sites in the Mediterranean and Europe. In all cases this resulted in bracketed intensity values between VIII and X EMS-98. The work of Karabacak et al. (2013) provides a case of left-lateral surface faulting (c. 20 cm), affecting the walls and pavement of the Stadium of the ancient Roman city of Kirbyra in Turkey, reporting an intensity of VIII–IX EMS-98.

In the case of Tira del Lienzo, due to its construction style, ground shaking of intensity VIII would be sufficient to promote the destruction of the Bronze Age buildings (Rodríguez-Pascua et al., 2013b). Additionally, analytical models of deformation for this construction style (Senthivel, Lourenco, & Vasconcelos, 2006; Colas, Morel, & Garnier, 2013) indicate that, apart from ground shaking, ground failure in this context triggers the opening of large interblock fractures in the upper halves of the walls and their subsequent destruction. Furthermore, given the hilltop position of the site (narrow pressure ridge), a topographic amplification of seismic shaking is expected. According to the ESI-07 macroseismic scale (Michetti et al., 2007), the record of ground left-lateral

displacement of 18 cm at Tira del Lienzo strongly suggests a maximum intensity of IX (destructive event).

The palaeoseismic analysis of lateral-slip data (18 cm) results in a fault slip rate of 0.046 mm/yr for the last 3914 years. Moreover, the striae pitch orientations measured on the fault plane beneath the archaeological site (10° – 45° ; Figures 2B and 4) allow us to estimate net lateral slip rates between 0.024 and 0.039 mm/yr. These values are smaller than those reported by earlier palaeoseismic research in the adjacent segment of the AMF (Lorca-Totana; c. 23 km length, Martínez-Díaz et al., 2012), which attained maximum net slip-rate values of c. 0.66 mm/yr. Our values are, however, consistent with the theoretical seismic potential of the Totana-Alhama fault segment (c. 11 km length; Martínez-Díaz et al., 2012). Although we assume that ground displacements occurred during a single Bronze Age seismic event in a location known to be on-fault, calculated slip rates are significant for further seismic hazard analyses. In this sense, this study provides the first slip-rate data based on field analysis for this fault segment, following the preliminary estimations of Ferrater et al. (2013).

GEOARCHAEOLOGICAL APPROACH TO ARCHAEOSEISMIC DAMAGE

Given the (1) generic magnitude (c. 6.4 Mw) and maximum intensity (IX) value resulting from the palaeoseismic analysis and (2) the dry-set masonry construction style of the site, the occurrence of an event more than and equal to VIII EMS-98 would have triggered the near destruction of Tira del Lienzo (Senthivel, Lourenco, & Vasconcelos, 2006; Rodríguez-Pascua et al., 2013b).

Taking into account the two building phases of construction at the archaeological site (2050–1900 and 1900–1550 cal. B.C.), the event could have occurred after the construction of the buildings (1900 cal. B.C.), although most likely it was around or soon after 1550 cal. B.C. (c. 3550 years ago). The event could have triggered the eventual abandonment of the site since there is no reconstruction or occupation evidence after this date (Delgado-Raack et al., 2014). Neither, however, is there any evidence to suggest that the settlement was abandoned as a result of an earthquake. The hypothesized date coincides with the decline of Bronze Age populations in the area and the depopulation of the La Bastida metropolis (Lull et al., 2014). Apart from the earthquake, other causes, such as social unrest or depopulation in response to unsustainable agricultural practices, are considered by the La Bastida Project (Lull, Mico, Rihuete & Risch, personal communication, 2013) as potential explanations for the abandonment of Tira del Lienzo.

Thus, the final abandonment of the La Bastida and Tira del Lienzo sites almost coincide at 1600/1550 B.C. (c. 3600–3550 B.P.; Lull et al., 2014), and this is consistent with significant palaeoenvironmental changes in the zone, resulting in a notable depopulation around the Guadalentin Depression (Calmel-Avila, 2002). Geoarchaeological analyses strongly suggest that around 3500 B.P., tectonic activity of the El Romeral rock-bar fault (Librilla) led to generalized fluvial dissection within the Guadalentin Depression upstream of Librilla (Silva et al., 2008; Calmel-Avila et al., 2009). The headward fluvial incision between Librilla and Totana triggered the fragmentation and partial disappearance of the palustrine environments, and this brought about the late Bronze Age depopulation of the zone (Silva et al., 2008; Calmel-Avila et al., 2009). The El Romeral rock-bar fault is mainly a reverse blind $N65^{\circ}$ – 70° E fault considered by some authors (Silva, 1994; Martínez Díaz, 1998) to be the prolongation of the Totana-Alhama fault segment beneath the sedimentary filling of the Guadalentin Depression. This fault only crops out at El Romeral (Librilla; Figure 1) in the Guadalentin rambla valley, and provides palaeoseismic evidence (sediment perturbation) after 3885 ± 60 B.P. (Calmel-Avila, 2002).

Whatever the case, at least one earthquake occurred during or soon after the second phase of occupation at Tira del Lienzo (1900–1550 cal. B.C.; Figure 7). The preferred age is around or shortly after the eventual abandonment of the site in 1550 cal. B.C., since the presence of broken boulders in the walls is consistent with a structure that is unaffected by the passage of time (Senthivel, Lourenco, & Vasconcelos, 2006). The seismic event would have destroyed the upper halves of the walls (Senthivel, Lourenco, & Vasconcelos, 2006; Colas, Morel, & Garnier, 2013) and would have triggered the abandonment of the site if it had occurred during occupation. The archaeological remains would, otherwise, present another phase of reconstruction.

Figure 7 shows that an event within this time frame is consonant with (1) the event dated by fault trenching in the Lorca-Totana segment of the AMF dated at 1760–830 cal. B.C. (Masana et al., 2004), and with (2) the event that caused sediment perturbation in El Romeral (Calmel-Avila, 2002). We do not rule out the possibility that the archaeoseismic damage reported in this study was a consequence of the rupture of more than one segment of the AMF, as illustrated in Table I. An event affecting both the Lorca-Totana and Totana-Alhama segments can be considered because the magnitude obtained by Masana et al. (2004) is within the range of the hypothetical rupture of both segments ($M_w = 6.9 \pm 0.2$; Table I). However, the resulting magnitudes for the rupture of more than one segment of the AMF are higher

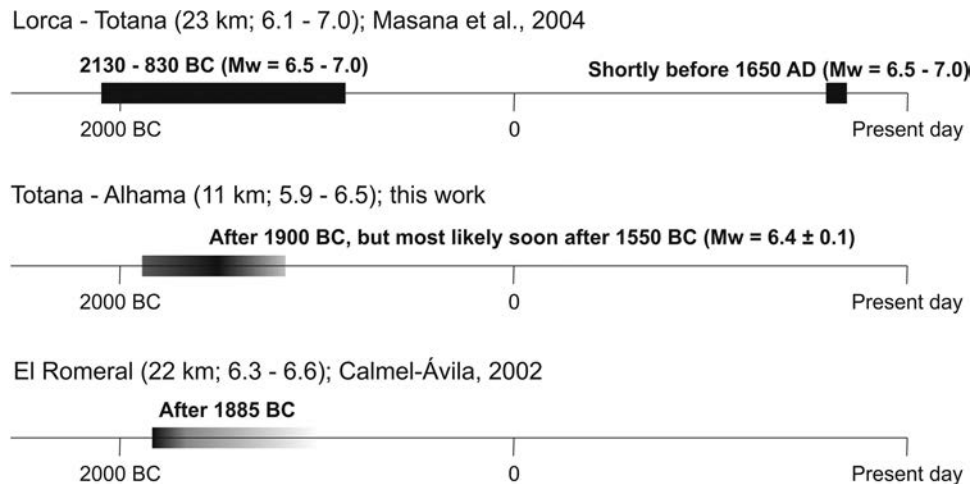


Figure 7 Proposed time span for palaeoseismic, ancient (this study), and historical seismic events in the central sector of the Alhama de Murcia fault (AMF). Information: fault segment (length km; Mw is theoretical as calculated in Martínez-Díaz et al., 2012) and references for the proposed events. El Romeral is not considered in Martínez-Díaz et al. (2012), but we have calculated its theoretical magnitude based on the methodology followed by these authors (magnitude vs. area with width of 12 km).

than the magnitude evaluated from the EAE at Tira del Lienzo, such that a Late Bronze Age seismic period in the central sector of the AMF fault can also be considered. In fact, although the decline of the Bronze Age population in the zone is still not well understood (Lull et al., 2014), some authors (Silva et al., 2008; Calmel-Avila et al., 2009) point to the occurrence of tectonically induced fragmentation of palustrine zones in the central sector of the Guadalentin Depression upstream of El Romeral rock-bar fault at Librilla. In this scenario, the occurrence of moderate to strong seismic events in the zone would enhance the decline of civilization in the area. In fact, following the Bronze Age decline in c. 1550 B.C., the next urban settlements in the area did not appear until Phoenician times, around the 6th century B.C. (c. 500 B.C.).

CONCLUSIONS

Tira del Lienzo, a Bronze Age site, is located in the Totana-Alhama segment of the AMF in an on-fault location. We identified four EAEs (Figure 5) that support the occurrence of a palaeoseismic event around 1550 B.C. (or soon after). Two of them are primary EAE (surface rupture and uplift) and the other two are secondary (ground fractures and broken wall-boulders). The latter are reported for the first time in this study, although they have equivalents in the EAE classification of Rodríguez-Pascua et al. (2011). The structural analysis of fracture orientations reveals two main fracture orientations (NE-SW and NW-SE) consistent with the left-lateral kinematics of the

Table I Theoretical moment magnitude for different fault segments and combinations of fault segments according to their length.

Segment	Length (e = 1 km)	Mw Theoretical (Magnitude vs. Length; Wells & Coppersmith, 1994)
Lorca-Totana + Totana-Alhama	34 km	6.9 ± 0.2
El Romeral (blind fault)	22 km	6.6 ± 0.2
Totana-Alhama + El Romeral	33 km	6.9 ± 0.2
Lorca-Romeral	56 km	7.1 ± 0.2

AMF zone in the area. The coinciding orientations lend support to the coseismic origin of the fractures. The main fracture produces a left lateral displacement (18 cm) of one of the walls and an apparent differential uplift of 5–8 cm.

Numerical analysis of the data indicates that the recorded deformation is consistent with a 6.4 ± 0.1 Mw palaeoseismic event of intensity IX ESI-07 in the fault zone. The estimated net lateral slip rates range between 0.024 and 0.039 mm/yr and are reported for the first time in this fault segment. It is therefore possible to relate the palaeoseismic event to the abandonment of the site in 1550 cal. B.C. (Delgado-Raack et al., 2014). This date matches (1) the tectonically induced environmental changes that triggered a large depopulation of the zone during the late Bronze Age (Calmel-Avila, 2002; Silva et al., 2008), and (2) the age of one earthquake (1760–830 cal. B.C.; Masana et al., 2004).

This work affords the first compelling evidence in the Iberian Peninsula of surface rupture recorded by means of archaeoseismological analysis, and provides numerical data on the seismic potential of the analyzed segment (Totana–Alhama) of the AMF, previously only characterized by theoretical approaches. An interdisciplinary analysis (archaeology, geology, and seismology) of an ancient “lost” earthquake from the Bronze Age has allowed us to make a significant contribution to the historical seismic catalogue.

This research was funded by SHAKE CGL2011-30005-C02-02 and QTECTBETICA CGL2012-37581-C02-01 projects and supported by CSD2006-0004 “Topo-Iberia” (Consolider-Ingenio 2010). The authors are indebted to the entire team of La Bastida Project (directors: Vicente Lull, Rafael Micó, Cristina Rihuete-Herrada, Roberto Risch) for all the information supplied. La Bastida is supported by the projects: HUM2006-04610, HAR2011-25280, TSI-070100-2008-133, and 2009SGR778. The authors thank Mari Hernández, Antonio Caño, Nil Domínguez, and Cèsar Ferrater, as well as Klaus Reicherter and a further anonymous reviewer for their comments that improved the original manuscript.

REFERENCES

- Alonso-Zarza, A.M., Silva, P.G., Goy, J.L., & Zazo, C. (1998). Fan-surface dynamics, plant-activity and calcrete development: Interactions during ultimate phases of fan evolution in the semiarid SE Spain (Murcia). *Geomorphology*, 24, 147–167.
- Carmel-Avila, M. (2002). The Librilla “rambla” an example of morphogenetic crisis in the Holocene (Murcia, SE Spain). *Quaternary International*, 93–94, 101–108.
- Carmel-Avila, M., Silva, P.G., Bardají, T., Goy, J.L., & Zazo, C. (2009). Drainage system inversion in the Guadalentín depression during the late Pleistocene–Holocene (Murcia, Spain). In: Romero, C., Belmonte, F., Alonso, F. & López-Bermudez, F. (Eds.), *Advances in studies of desertification*. Servicio de publicaciones Universidad de Murcia, Murcia, 461–464.
- Colas, A.S., Morel, J.C., & Garnier, D. (2013). Assessing the two-dimensional behaviour of drystone retaining walls by full-scale experiments and yield design simulation. *Géotechnique*, 63(2), 107–117.
- Delgado-Raack, S., Lull, V., Martin, K., Micó, R., Rihuete Herrada, C., & Risch, R. (2014). Die Silberschmiede von Tira del Lienzo, Totana, Prov. Murcia, im Kontext der El Argar Metallurgie. In Meller, H., Risch, R., & Pernicka, E. (Eds.), *Metalle der Macht—Frühes Gold und Silber*, 6. Mitteldeutscher Archäologentag vom 17. bis 19. Oktober 2013 in Halle (Saale), 577–591.
- Echeverría, A., Khazaradze, G., Asensio, E., Gárate, J., Dávila, J.M., & Suriñach, E. (2013). Crustal deformation in eastern Betics from CuaTeNeo GPS network. *Tectonophysics*, 608, 600–612. DOI: 10.1016/j.tecto.2013.08.020.
- Ferrater, M. (2013). *Arqueosismología en La Tira del Lienzo* (Totana, Murcia). VI Young Researchers in Archaeology Conference, Barcelona, Spain.
- Ferrater, M., Ortuño, M., Masana, M., Silva, P.G., Rodríguez-Pascua, M.A., Booth-Rea, G. & Azañón, J.M. (2013). Archaeoseismology in a Bronze aged settlement: La Tira del Lienzo (Totana, Spain). In Grützner, C., Rudersdorf, A., Pérez-López, R., & Reicherter, K. (Eds.), *Seismic hazard, critical facilities and slow active faults, Proceedings of the 4th International INQUA meeting on Paleoseismology, Active Tectonics and Archeoseismology* (pp. 63–66) Aachen: Grützner & Reicherter Geosolutions UG. ISBN: 978-3-00-042796-1.
- Frontera, T., Concha, A., Blanco, P., Echeverría, A., Goula, X., Arbiol, R., Khazaradze, G., Pérez, F., & Suriñach, E. (2012). DinSar coseismic deformation of the May 2011 Mw 5.1 Lorca earthquake, (Southern Spain). *Solid Earth*, 3, 111–119.
- González Guerao, J.A. (2005). Prospección arqueológica de urgencia en paraje Tira del Lienzo, Totana. XVI Jornadas de Patrimonio Histórico. Intervenciones en el Patrimonio arquitectónico, arqueológico y etnográfico de la Región de Murcia, Murcia, 390–391. ISBN 84-7564-318-3.
- Grünthal, G. (Ed.). (1998). *European macroseismic scale*, European Seismological Commission, Sub-commission on Engineering Seismology, Working Group Macroseismic scales, Luxembourg, 99 pp.
- Instituto Geográfico Nacional, IGN. (2012). Servicio de información sísmica, catálogo de terremotos. Instituto Geográfico Nacional. <http://www.01.ign.es/ign/layoutIn/sismoFormularioCatalogo>.
- Karabacak, V., Yönlü, Ö., Dökü, E., Kiyak, N. G., Altunel, E., Özüdoğru, Ş., Yalçiner, C. Ç., & Akyüz, H. S. (2013). Analyses of seismic deformation at the Kibyra Roman Stadium, Southwest Turkey. *Geoarchaeology*, 28, 531–543.
- López-Comino, J.A., Mancilla, F., Morales J., & Stich, D. (2012). Rupture directivity of the 2011, Mw 5.2 Lorca earthquake (Spain). *Geophysical Research Letters*, 39, L03301, 1–5. DOI: 10.1029/2011GL050498.
- Lull, V. (1983). *La cultura de El Argar. Un modelo para el estudio de las formaciones económico-sociales prehistóricas*. Akal, Madrid, 488pp.
- Lull, V., Micó, R., Rihuete Herrada C., & Risch, R. (2011a). El Argar and the Beginning of Class Society in the Western Mediterranean. In S. Hansen & J. Müller (Eds.) *Sozialarchäologische Perspektiven: Gesellschaftlicher Wandel 5000-1500 v. Chr. Zwischen Atlantik und Kaukasus* (pp. 381–414). Berlin: Deutsches Archäologisches Institut.
- Lull, V., Micó, R., Rihuete Herrada, C., & Risch, R. (2011b). Proyecto La Bastida: Economía, urbanismo y territorio de una capital argárica. *Verdolay*, 13, 57–70. ISSN: 1130-9776.
- Lull, V., Micó, R., Rihuete Herrada, C., & Risch, R. (2014). The La Bastida fortification: New light and new questions

- on early Bronze Age societies in the western Mediterranean. *Antiquity*, 88, 395–410.
- Martínez-Díaz, J.J. (1998). *Neotectónica y Tectónica Activa del Sector Centro-Occidental de la Región de Murcia y Sur de Almería (Cordillera Bética-España)*. Ph.D., UCM, Madrid, Spain, 466 pp.
- Martínez-Díaz, J.J., Masana, E., Hernández-Enrile, J.L., & Santanach, P. (2001). Evidence for coseismic events of recurrent prehistoric deformation along the Alhama de Murcia fault, southwestern Spain. *Acta Geologica Hispanica*, 36(3–4), 315–327.
- Martínez-Díaz, J.J., Masana, E., Hernández-Enrile, J.L., & Santanach, P. (2003). Effects of repeated paleoearthquakes on the Alhama de Murcia Fault (Betic Cordillera, Spain) on the Quaternary evolution of an alluvial fan system. *Annals of Geophysics*, 46(5), 775–791.
- Martínez-Díaz, J.J., Masana, E., & Ortuño, M. (2012). Active tectonics of the Alhama de Murcia fault, Betic Cordillera, Spain. *Journal of Iberian Geology*, 38(1), 170–181.
- Masana, E., Martínez-Díaz, J.J., Hernández-Enrile, J.L., & Santanach, P. (2004). The Alhama de Murcia Fault (SE Spain), a seismogenic fault in a diffuse plate boundary: Seismotectonic implications for the Ibero-Magrebien región. *Journal of Geophysical Research*, 109, B01301, 1–17. DOI: 10.1029/2002JB002359.
- Michetti, A.M., Esposito, E., Guerreri, L., Porfido, S., Serva, L., Tatevosian, R., Vittori, E., Audemard, F., Azuma, T., Clague, J., Comerci, V., Gürpınar, A., McCalpin, J., Mohammadioun, B., Mörrner, N.A., Ota, Y., & Roghazin, E. (2007). Intensity Scale ESI-2007. Mem. Descr. Carta Geologica d'Italia, 74. Servizio Geologico d'Italia—Dipartimento Difesa del Suolo. APAT, Roma, Italia, 41 pp.
- Nur, A., & Burgess, D. (2008). *Apocalypse: Earthquakes, archaeology and the wrath of God*. Princeton, NJ and Oxford: Princeton University Press, 309 pp.
- Ortuño, M., Masana, E., García-Meléndez, E., Martínez-Díaz, J.J., Stepanciková, P., Cunha, P.P., Sohbat, R., Canora, C., Buylaert, J.P., & Murray, A.S. (2012). An exceptionally long paleoseismic record of a slow-moving fault: The Alhama de Murcia fault (Eastern Betic Shear Zone, Spain). *The Geological Society of America Bulletin*, 124(9–10), 1474–1494. DOI: 10.1130/B30558.1.
- Rodríguez-Pascua, M.A., Silva, P.G., Garduño-Monroy, V.H., Pérez-López, R., Israde-Alcántara, I., Giner-Robles, J.L., Bischoff, J.L., & Calvo, J.P. (2010). Ancient earthquakes from archaeoseismic evidence during the Visigothic and Islamic periods in the archaeological site of “Tolmo de Minateda” (SE Spain). *Geological Society of America Special Papers*, 471, 171–184.
- Rodríguez-Pascua, M.A., Pérez-López, R., Giner-Robles, J.L., Silva, P.G., Garduño-Monroy, V. H., & Reicherter, K. (2011). A comprehensive classification of earthquake archaeological effects (EAE) in archaeoseismology: Application to ancient remains of roman and mesoamerican cultures. *Quaternary International*, 242, 20–30.
- Rodríguez-Pascua, M.A., Abad Casal, L., Pérez-López, R., Gamo Parra, B., Silva, P.G., Garduño-Monroy, V.H., Giner-Robles, J.L., Perucha-Atienza, M.A., Israde-Alcántara, I., Bischoff, J., & Calvo, J.P. (2013a). Roman, Visigothic and Islamic evidence of earthquakes recorded in the archaeological site of “El Tolmo de Minateda” (Prebetic Zone, southeast of Spain). *Cuaternario y Geomorfología*, 27(3–4), 65–72.
- Rodríguez-Pascua, M.A., Silva, P.G., Pérez-López, R., Giner-Robles, J.L., Martín-González, F., & Perucha-Atienza, M.A. (2013b). Preliminary intensity correlation between macroseismic scales (ESI-07 and EMS-98) and Earthquake Archaeological Effects (EAEs). In Grützner, C., Rudersdorf, A., Pérez-López, R., & Reicherter, K. (Eds.), *Seismic hazard, critical facilities and slow active faults*, Proceedings of the 4th International INQUA meeting on Paleoseismology, Active Tectonics and Archeoseismology (pp. 221–224). Aachen: Grützner & Reicherter Geosolutions UG. ISBN: 978-3-00-042796-1.
- Senthivel, R., Lourenco, P.G., & Vasconcelos, G. (2006). Analytical modeling of dry stone masonry wall under monotonic and reversed cyclic loading. In P.B. Lourenço, P. Roca, C. Modena, & S. Agrawal (Eds.), *Structural analysis of historical constructions* (pp. 1005–1012). Macmillan India Ltd, New Delhi.
- Silva, P.G. (1994). *Evolución Geodinámica de la Depresión del Guadalentín desde el Mioceno Superior hasta la actualidad: Neotectónica y Geomorfología*. Ph.D. UCM, Madrid, Spain. 642 pp.
- Silva, P.G. (2014). The Guadalentín tectonic depression (Betic Cordillera, Murcia). In F. Gutiérrez & M. Gutiérrez (Eds.), *Landscapes and landforms of Spain*. World geomorphological landscapes series (pp. 25–35). Dordrecht, Germany: Springer Science.
- Silva, P.G., Harvey, A.M., Zazo, C., & Goy, J.L. (1992). Geomorphology, depositional style and morphometric relationships of Quaternary alluvial fans in the Guadalentín Depression (Murcia, SE Spain). *Z F Geomorphologie*, 36, 661–673.
- Silva, P.G., & Rodríguez-Pascua, M.A. (Eds.). (2014). *Catálogo de los Efectos Geológicos de los Terremotos en España*. Serie Riesgos Geológicos/Geotécnia, 4. Instituto Geológico y Minero de España (IGME), Madrid, 358 pp.
- Silva, P.G., Goy, J.L., Somoza, L., Zazo, C., & Bardají, T. (1993). Landscape response to strike-slip faulting linked to collisional settings: Quaternary tectonics and basin formation in the Eastern Betics, Southeast Spain. *Tectonophysics*, 224, 289–303.
- Silva, P.G., Goy, J.L., Zazo, C., & Bardají, T. (1997). Paleoseismic indications along “aseismic” fault segments in the Guadalentín Depression (SE Spain). *Journal of Geodynamics*, 24(1–4), 105–115.

- Silva, P.G., Goy, J.L., Zazo, C., & Bardají, T. (2003). Fault-generated mountain fronts in southeast Spain: Geomorphologic assessment of tectonic and seismic activity. *Geomorphology*, 50, 203–225.
- Silva, P.G., Borja, F., Zazo, C., Goy, J.L., Bardají, T., De Luque, L., Lario, J., & Dabrio, C. (2005). Archaeoseismic record at the ancient Roman City of Baelo Claudia (Cádiz, South Spain). *Tectonophysics*, 408(1–4), 129–146.
- Silva, P.G., Calmel-Avila, M., Bardají, T., Goy, J.L., & Zazo, C. (2008). Transition from alluvial to fluvial systems in the Guadalentin Depression (SE Spain) during the Holocene: Lorca Fan versus Guadalentín River. *Geomorphology*, 100, 144–153.
- Silva, P.G., Reicherter, K., Grützner, C., Bardají, T., Lario, J., Goy, J.L., Zazo, C., & Becker-Heidmann, P. (2009). Surface and subsurface palaeoseismic records at the ancient Roman city of Baelo Claudia and the Bolonia Bay area, Cádiz (south Spain). *Geological Society, London, Special Publications*, 316, 93–121.
- Stirling, M., Goned, T., Berryman, K., & Litchfield, N. (2013). Selection of earthquake scaling relationships for seismic-hazard analysis. *Bulletin of the Seismological Society of America*, 103(6), 2993–3011.
- Stirling, M.W., Rhoades, D.A., & Berryman, K. (2002). Comparison of earthquake scaling relations derived from data of the instrumental and preinstrumental era. *Bulletin of the Seismological Society of America*, 92(2), 812–830.
- Wells, K., & Coppersmith, D.L. (1994). New empirical relationships among magnitude, rupture length, rupture width, rupture area, and surface displacement. *Bulletin of the Seismological Society of America*, 84, 974–1002.
- Wesnousky, S.G. (2008). Displacement and geometrical characteristics of earthquake Surface ruptures: Issues and implications for seismic-hazard analysis and the process of earthquake rupture. *Bulletin of the seismological Society of America*, 98(4), 1609–1632.



From extension to transpression: Quaternary reorganization of an extensional-related drainage network by the Alhama de Murcia strike-slip fault (eastern Betics)

Marta Ferrater^{a,*}, Guillermo Booth-Rea^{b,c}, José Vicente Pérez-Peña^{b,d}, José Miguel Azañón^{b,c}, Flavio Giaconia^b, Eulàlia Masana^a

^a RISKINAT Group, GEOMODELS, Departament de Geodinàmica i Geofísica, Facultat de Geologia, Universitat de Barcelona, c/ Martí i Franquès, s/n, 08028 Barcelona, Spain

^b Departamento de Geodinámica, Facultad de Ciencias, Universidad de Granada, Campus Fuentenueva s/n, 18071, Granada, Spain

^c Instituto Andaluz de Ciencias de la Tierra (CSIC-UGR), Avda. de las Palmeras 4, 18100 Armilla, Granada, Spain

^d Instituto Andaluz de Geofísica, Campus Universitario de Cartuja, Universidad de Granada, 18071 Granada, Spain

ARTICLE INFO

Article history:

Received 6 October 2014

Received in revised form 20 April 2015

Accepted 2 June 2015

Available online 19 June 2015

Keywords:

Drainage system

Landscape analysis

Eastern Betics

Tectonic inversion

Geomorphic indexes

ABSTRACT

The complex present-day drainage network of the Lorca–Totana area records the changing tectonic setting, from extension to transpression, in the eastern Betics. Through a detailed morphometric analysis we evaluate the topographic response to this major change in the tectonic setting and the influence in the drainage of Miocene extension and middle Pleistocene to present day transpression. The present-day drainage network preserves geomorphic features inherited from Late Miocene extension that are being overprinted by a new transverse fluvial system. This new system advanced towards the NW since the middle Pleistocene in response to a localized base-level drop related to the NE–SW oriented Alhama de Murcia sinistral-reverse fault. Geomorphic indexes calculated in this work suggest the present-day activity of the Alhama de Murcia fault and the Sierra de la Tercia anticline, the two major tectonic structures in the area. The landscape rejuvenation associated with this process results in: contrasting mountain front sinuosity values between old and new mountain fronts, high SLk index anomalies, convex-shaped and complex hypsometric curves, knickpoints in river profiles, contrasting slope-area plots and high steepness index values. This fluvial reorganization was driven progressively by successive fluvial captures preserved as wind-gaps in the present-day drainage network.

© 2015 Elsevier B.V. All rights reserved.

1. Introduction

Drainage network systems adapt to changes in the surface slope, having the potential to record the evolution of tectonic structures driving surface uplift in a region (Booth-Rea et al., 2004a; Cotton, 1942; Giaconia et al., 2013; Jackson et al., 1996; Kirby and Whipple, 2012; Ollier, 1981; Pérez-Peña et al., 2009a). The growth of new tectonic structures produces new mountain fronts, promoting the reorganization or replacement of previous drainage networks (e.g. Babault et al., 2012; Giaconia et al., 2013; Harvey and Wells, 1987). Furthermore, different types of tectonic structures develop distinctive morphotectonic features; extensional faults produce footwall ranges, associated alluvial fans, and tilting of hanging-walls, whereas strike-slip faults are normally linked to both uplifted and sunken landscape associated with releasing and restraining bends respectively (e.g. Aydin and Nur, 1985; Booth-Rea et al., 2004a; Densmore et al., 1998; Keller and Pinter, 2002; Osmundsen et al., 2010; Stein et al., 1988; Sylvester, 1988; Walker

and Jackson, 2002). Longitudinal valleys and benches are other common morphotectonic features that occur parallel to strike-slip fault segments (Keller and Pinter, 2002; Legg et al., 1989). In tectonic transcurrent settings, shortening and extensional structures can occur together with strike-slip faults producing complex landscapes (e.g. Booth-Rea et al., 2004a; Montecatini et al., 1990; Sylvester, 1988).

Landscape analysis and active tectonic evaluation through morphometric indexes are one of the most interesting approaches in tectonic-geomorphology studies. Tectonic derived topographic uplift generates anomalies in river gradients, catchment areas and topographic profiles that can be analyzed with Digital Elevation Models with appropriate resolution. In the last decade the recent evolution of GIS technology and the availability of high-resolution DEMs have produced an extensive use of geomorphic indexes in studies of recent tectonic activity (e.g. Gao et al., 2013; Giaconia et al., 2012a,b; Keller and Pinter, 2002; Kirby and Whipple, 2012; Matoš et al., 2014; Pérez-Peña et al., 2010; Scotti et al., 2014; Troiani and Della Seta, 2008).

Tectonic inversion from an extensional to a strike-slip tectonic setting occurred recently in the eastern Betics (SE Spain). Pliocene to Quaternary large strike-slip faults reactive previous Late Miocene normal faults associated with NW–SE and NE–SW extension (Booth-Rea

* Corresponding author at. Departament de Geodinàmica i Geofísica, Facultat de Geologia, Universitat de Barcelona, c/ Martí i Franquès, s/n, 08028 Barcelona, Spain.

E-mail address: marta.ferrater@ub.edu (M. Ferrater).

et al., 2004b; Meijninger and Vissers, 2006). This is the case of the Alhama de Murcia NE–SW sinistral fault (Bousquet, 1979) that formed in a zone with inherited features from Late Miocene extension. This extension produced tilted and uplifted blocks that were later modified by the sinistral-reverse kinematics of the Alhama de Murcia fault (Booth-Rea et al., 2004b; Lonergan and Schreiber, 1993; Meijninger and Vissers, 2006). This fault is divided in well-known segments according to their seismic signature, geomorphological features and structural orientation (Martínez-Díaz, 1998; Silva, 1994). This study is focused in the Lorca–Totana segment, which presents the highest inverse component.

The drainage system in that area inherits some features related to the tectonic inversion, thus providing valuable information about the complex landscape evolution in this region. Until the present, no detailed morphometric analyses have been carried out in this area, and some general and specific open questions remain unsolved; how Quaternary landscape evolved in this changing tectonic scenario? and what driven mechanisms were used by the drainage network to adapt to the new tectonic setting? Moreover, the interplay between active folding and strike-slip faulting and their effects on the topography is

still unknown. Whereas the Quaternary and present-day activities of the Alhama de Murcia are reasonably well assessed through paleoseismic and seismic studies (Martínez-Díaz et al., 2003, 2012a; Masana et al., 2004; Ortuño et al., 2012; Silva et al., 1992).

The aim of this paper is to study the effects that a changing tectonic scenario had in the topography, and at the same time evaluate the Quaternary activity and the influence of active simultaneous folding and strike-slip faulting in the drainage network evolution. We carry out a structural analysis of the Alhama de Murcia fault Lorca–Totana segment and a relief analysis identifying river capture sites and associated wind-gaps, together with a detailed morphostructural analysis by using geomorphic indices. We selected the geomorphic indices considered most effective to accomplish our study objectives; i) Smf index to quantitatively discern among inactive-to-active mountain fronts, ii) river topographic profiles and gradient-based indices (SLk and ksn) to detect possible differences in uplift rates and analyze knickpoints, iii) ridgeline profiles to record a feasible influence of extensional tectonics on river courses, and iv) hypsometry to evaluate the mass-balance of river basins lying on different tectonic settings.

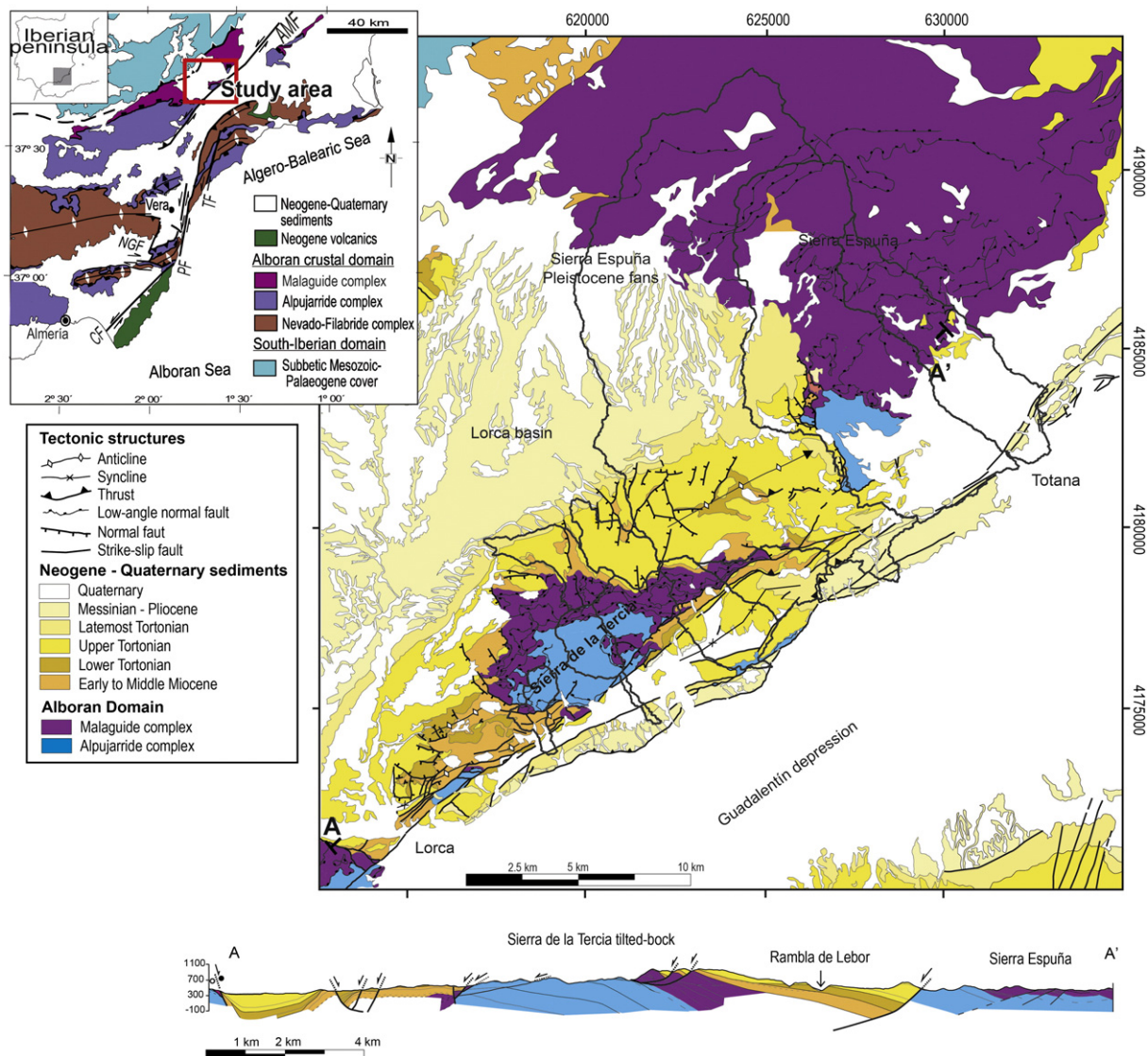


Fig. 1. Geological map of the study area. Geological profile A–A' runs perpendicular to the main Miocene extensional structures. The inset shows the location of the study area within the eastern Betic Cordillera; legend: AMF, Alhama de Murcia fault; CF, Carboneras fault; PF, Palomares fault; TF, Terreros fault. For basin reference see Fig. 2. Inset modified from Giaconia et al. (2012b).

2. Geologic setting

The eastern Betics (Fig. 1) are located in the northern branch of the Gibraltar arc that encloses the westernmost-Mediterranean Alboran and Algero-Balearic basins. The Gibraltar arc and the basins it encloses formed in the Early to Late Miocene during the westward slab roll-back and oblique collision of the Alboran domain over the South-Iberian and Maghrebien margins (Balanyá and García-Dueñas, 1987; Booth-Rea et al., 2007; Faccenna et al., 2004; Lonergan and White, 1997). Large-scale upper-crustal extension occurred during middle to Late Miocene in the internal parts of the orogen and exhumed HP–LT metamorphic rocks from the Alboran domain and the South Iberian subducted passive margin (e.g. Behr and Platt, 2012; Booth-Rea et al., 2004b, 2005; Martínez-Martínez and Azañón, 1997; Martínez-Martínez et al., 2002; Platt et al., 2006). Intramontane marine sedimentary basins like the Lorca, Fortuna, Mazarrón and Vera basins in the eastern Betics formed under this extensional context coeval to back-arc oceanic accretion in the Algero-Balearic basin (Booth-Rea et al., 2007, 2012; Mauffreit et al., 2004).

Two orthogonal sets of normal faults were active during the Tortonian (11.3–7.2 Ma) in the southeastern Betics, producing NW–SE and SW–NE directed extension (Alvarez et al., 1989; Booth-Rea et al., 2004b, 2012; Lonergan and Schreiber, 1993; Meijninger and Vissers, 2006). These normal faults were sealed by carbonates and fan-delta conglomerates deposited during the “Tortonian salinity crisis” dated between 7.8 and 7.6 Ma (Booth-Rea et al., 2004a; Krijgsman et al., 2000). As these extensional faults became inactive due to the westward migration of the extensional loci, a generalized tectonic inversion related to NW–SE convergence between Africa and Europe occurred. This tectonic inversion in the southeastern Betics is well registered in some intramontane basins as the Vera and Sorbas basins, and recorded by progressive unconformities in late-most Tortonian temperate carbonates and folds affecting Messinian sediments (Booth-Rea et al., 2004a; Giaconia et al., 2012b, 2013; Weijermars et al., 1985).

The Alhama de Murcia fault (AMF) is one of the main transpressive tectonic structures that formed during tectonic inversion. Some authors have proposed that the Alhama de Murcia fault initiated its activity in Late Miocene, thus producing an “intra-Tortonian unconformity” at the base of Tortonian carbonates of the Tercia formation (Montenat et al., 1990). However, the tilted sediments underlying this formation are cut by syngenetic extensional normal faults, thus relating this unconformity to Late Miocene extension. According to this interpretation, some authors have pointed that the Alhama de Murcia Fault should have started its activity after Tortonian (e.g. Booth-Rea et al., 2012; Lonergan and Schreiber, 1993; Meijninger and Vissers, 2006). The oldest alluvial fans related to the AMF deposited during the Pleistocene (Silva et al., 1992). Therefore, initial strike-slip activity and folding associated with the Alhama de Murcia fault probably initiated in the Pliocene or Quaternary (Bousquet, 1979; Meijninger and Vissers, 2006).

The Alhama de Murcia fault (Figs. 1, 2), together with other strike-slip faults in the SE Betics (like the Palomares or Carboneras fault zones farther south) and their related shortening structures, absorbs a great part of the shortening produced by the convergence between the Eurasian and African Plates at a rate of 4.5–5.6 mm/yr (Demets et al., 1994; McClusky et al., 2003). Echeverría et al. (2013) proposed an average reverse-sinistral geodetic lateral slip rate for the Alhama de Murcia fault of 1.5 mm/yr. This fault is seismogenic, having produced paleoseismic events up to Mw 7.0 (Masana et al., 2004), several I_{MSK} VII–VIII earthquakes in the last 500 years, and the 2011 Mw = 5.2 Lorca earthquake, the most recent damaging earthquake in Iberia (López-Comino et al., 2012; Martínez-Díaz et al., 2012b; Vissers and Meijninger, 2011).

3. Geomorphic setting

The relief in the eastern Betics is the result of the interplay between Neogene extensional tectonics and the later tectonic inversion, and it is

characterized by a basin and range structure, especially within the Internal Zones of the cordillera (e.g. Booth-Rea et al., 2004a,b; Giaconia et al., 2013; Meijninger and Vissers, 2006; Montenat et al., 1990). The main mountain ranges of the study area (Sierra Espuña and Sierra de la Tercia, Figs. 2, 3a) formed under the Late-Miocene extensional tectonic setting as proto-ranges of low-to-moderate elevation in the footwall of extensional faults (Fig. 1).

The Sierra de la Tercia is limited by the Lorca basin to the NW, and by the Guadalentín depression to the S and SE (Fig. 2). The contact between the Guadalentín depression and Sierra de la Tercia range is the Alhama de Murcia fault. The Sierra Espuña is bounded by the Lorca basin to the W and the Alhama–Fortuna basin to the S and SE.

The morphotectonic features related to Late Miocene extension are NW–SE and SW–NE oriented mountain fronts associated with normal faults in the Sierra Espuña (Booth-Rea et al., 2004b, Fig. 2; Lonergan and Schreiber, 1993) and thick Late-Miocene alluvial fans developed at the foot of extensional structures (Booth-Rea et al., 2004a). As the extensional mountain fronts became inactive and retreated north-eastwards, a second generation of alluvial fans overlapped the Miocene alluvial fans. These alluvial fans continued to be active until the middle Pleistocene (Silva, 1994; Fig. 3b).

Due to Alhama de Murcia fault reactivation as a reverse left-lateral fault, the Sierra de la Tercia footwall turned into one of the main ranges in the area (Figs. 2, 3a). Pleistocene to Holocene alluvial fans developed as a result of the main tectonic activity along the southern border of the Sierra de la Tercia. They include a first phase (middle Pleistocene) dominated by aggradation, and a second dissectional phase (Late Pleistocene to Holocene) with distal aggradation (Martínez-Díaz et al., 2003; Silva, 1994; Silva et al., 1992). Even though alluvial fan ages are not accurate enough to take into account climatic variations, fan growth and aggradation should occur during cold/dry periods because of the increase in sedimentation supply experienced during glacial stages, whereas in the warm stages calcretes developed (Candy and Black, 2009; Harvey and Wells, 1987; Harvey et al., 1995; Kelly et al., 2000).

Stream capture processes in the study area can be evidenced by wind gaps, abrupt changes in river courses and high fluvial incision. Wind gaps are abandoned valleys that are preserved preferably in river divides and evidence old drainage courses. We have identified several wind gaps within the Totana and Lébor basins (Figs. 2, 3d). These wind gaps preserve in most cases fluvial sediments (Fig. 3d) and produce distinctive landscape morphologies that can be identified in the used high-resolution 4 m Digital Elevation Model (Fig. 2). The identified wind gaps are also associated with steep changes in river courses and/or river segments with high fluvial incision (Fig. 2).

4. Structural analysis of the Alhama de Murcia fault in the study area

The Alhama de Murcia fault in the study area has a NE–SW orientation and shows two main segments: a first segment running from Lorca town to the Zarcico basin (southern segment), and a second one, from the Carboneros basin to NE of Totana town (northern segment, Fig. 2). The first segment can be divided, in turn, in two to four main fault traces that cause a wide area of deformation and uplift from the Guadalentín depression to the Sierra de la Tercia range (Fig. 2). These fault traces separate benches corresponding to the Sierra de la Tercia, an intermediate area with uplifted middle and Late Pleistocene alluvial fan generations, and the Guadalentín depression, where Holocene fans occur (Martínez-Díaz, 2002; Silva et al., 1997). The AMF has controlled the spatial distribution and deposition of the different Pleistocene alluvial fan generations (Martínez-Díaz, 2002; Martínez-Díaz et al., 2003; Masana et al., 2004). The deformation in the second segment is distributed in a narrower area where the above-mentioned fault traces merge. This fault zone is marked by a band of strongly deformed Tortonian sediments that runs from the Rambla de los Carboneros to Totana town. Middle Pleistocene alluvial fans also occur along this fault segment both on the northern and southern fault blocks.

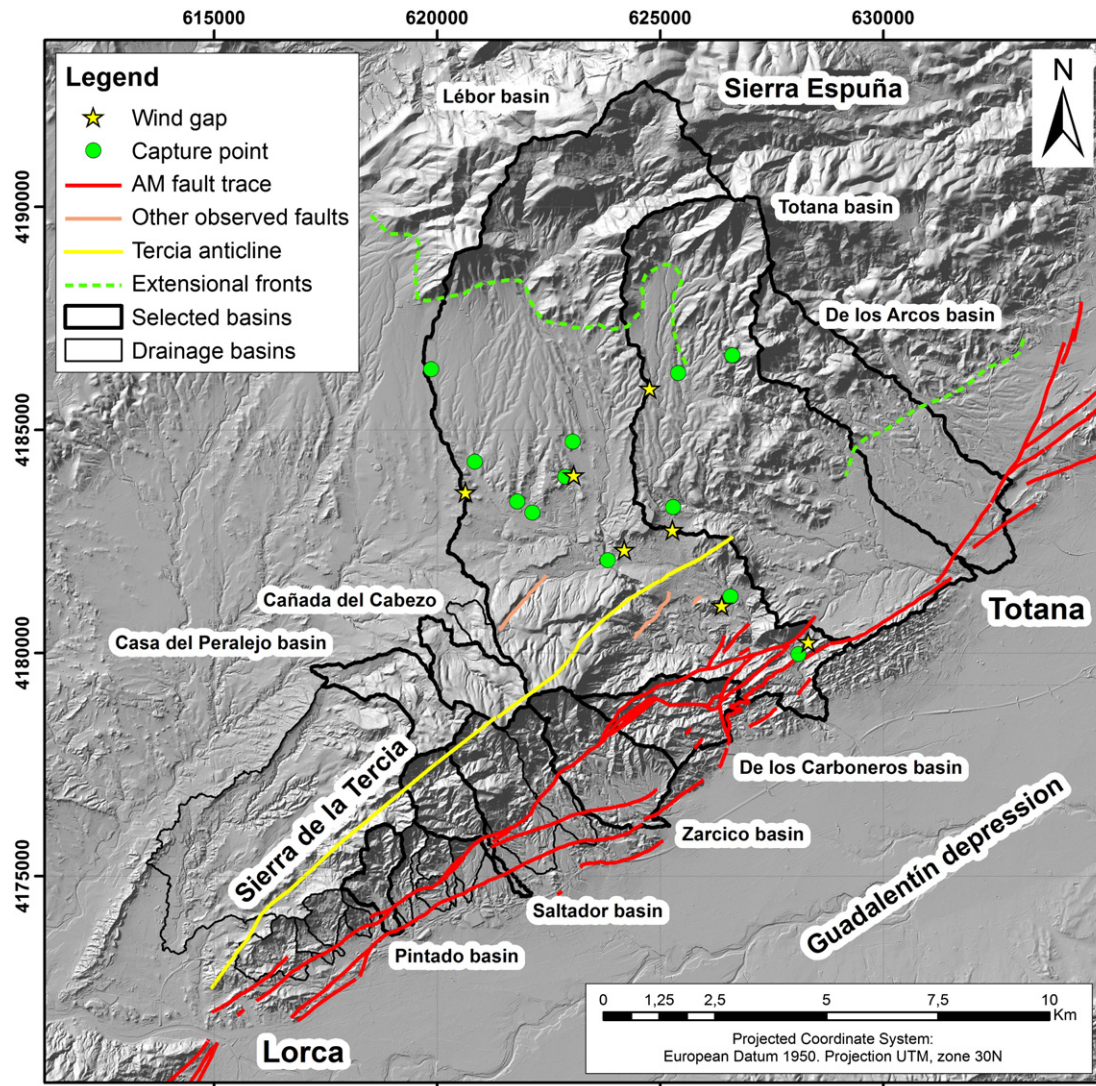


Fig. 2. Shaded relief (obtained from 4 m DEM) showing the topography of the study area and the location of the main structures; Alhama de Murcia Fault (AMF), Tercia anticline and the main Miocene extensional fronts. Capture points and wind-gaps are indicated in the figure.

5. Methodology

In order to analyze the topography of the study area, apart from the field work (Sections 3 and 4), we carried out a calculation of several geomorphic indexes for the main drainage basins. We have determined the following morphometric indexes: i) mountain front sinuosity, ii) SLk index, iii) river topographic profiles, iv) hypsometric curves, and v) slope–area analysis and normalized steepness index. For the geomorphic analysis we used a high-resolution 4 m DEM obtained from LIDAR data for the NatMur-08 project (<http://www.murcianatural.carm.es/natmur08/>).

5.1. Mountain front sinuosity

Mountain-front sinuosity was defined by Bull (1977) as:

$$Smf = Lmf / L_s$$

where Smf is the mountain front sinuosity, Lmf is the length of the mountain front along the foot of the mountain, i.e., the topographic break in the slope, and L_s is the length of the mountain front measured along a straight line. In active mountain fronts, uplift will prevail over erosional processes, yielding straight fronts with low values of Smf,

whereas in less active fronts, erosional processes will generate irregular or sinuous fronts with high values of Smf (e.g. Azañón et al., 2012; Bull and McFadden, 1977; Giaconia et al., 2012a; Pérez-Peña et al., 2010; Silva et al., 2003). Generally, values of the Smf index lower than 1.4 are indicative of tectonically active fronts, whereas values higher than 3.0 are characteristic of fronts that are not controlled by active faults (Azañón et al., 2012; Giaconia et al., 2012a; Rockwell et al., 1984; Silva et al., 2003). We have calculated the Smf index at a scale of 1:10,000 for several fronts located at the foot of the main mountain ranges; Sierra de la Tercia and Sierra Espuña.

5.2. SLk index

The SLk index is a normalization of the traditional stream length–gradient index (SL) (Hack, 1973). This normalization of the SL index is made by using the river graded gradient (named as K parameter) (Chen et al., 2003; Pérez-Peña et al., 2009a; Seeber and Gornitz, 1983). SLk index correlates to stream power, and it is especially useful to depict river gradient anomalies and knickpoints (Giaconia et al., 2012a; Pedrera et al., 2009; Pérez-Peña et al., 2009a, 2010; Troiani and Della Seta, 2008). Anomalies in this index are principally due to tectonic activity and/or lithologic changes of the riverbed. The SLk index allows comparing rivers with different lengths and the elaboration of SLk

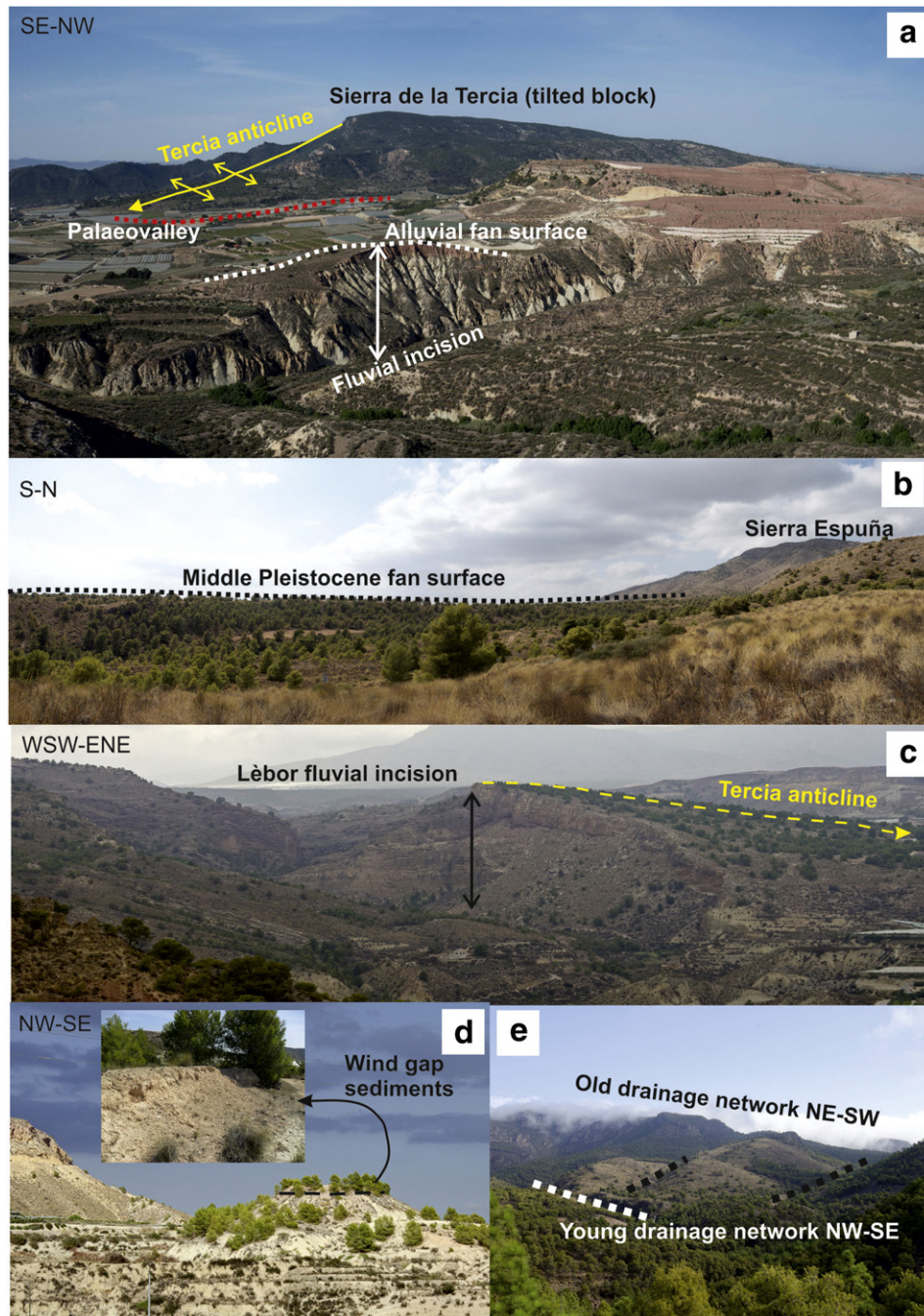


Fig. 3. Field photographs: a) Lorca basin from Sierra Espuña towards de SW, paleovalley and fluvial incision in previous alluvial fans; b) Lorca basin from Sierra Espuña towards the W, flat surface formed in the footwall of normal faults in Sierra Espuña; c) Rambla de Lébor fluvial incision; d) wind gap in Totana basin; and e) different orientations of the drainage system in Rambla de Totana.

anomaly maps (Pérez-Peña et al., 2009a). In order to analyze the SLk index, we followed the methodology proposed by Pérez-Peña et al. (2009a) using the semivariogram model approach for the construction of SLk anomaly maps.

5.3. Hypsometric curves

The hypsometric curve represents the distribution of relative areas versus relative altitudes of a particular basin (Strahler, 1952). The shape of the hypsometric curve correlates with the stage of geomorphic development of the basin; old basins give concave shapes, mature basins draw S-shaped curves, and young basins produce convex-shaped curves (Ohmori, 1993; Strahler, 1952).

The analysis of hypsometric curves is a valuable tool to infer the geomorphic evolution of a drainage basin, since processes as river captures can produce clear variations in hypsometric curves (Gao et al., 2013; Matoš et al., 2014; Ohmori, 1993; Pedrera et al., 2009; Pérez-Peña et al., 2009b, 2010; Scotti et al., 2014; Willgoose and Hancock, 1998). In order to analyze the hypsometric curves of the study area we used the CalHypso ArcGIS-extension developed by Pérez-Peña et al. (2009b).

5.4. River topographic profiles

The longitudinal topographic profile of a river provides a reference to its present-day erosion level (Antón et al., 2014; Bull, 1991; Perron

and Royden, 2013). This is particularly useful when longitudinal profiles are plotted together with ridge-line profiles (Menéndez et al., 2008; Pérez-Peña et al., 2010). A ridge-line profile is calculated by projecting the channel thalweg onto an imaginary surface interpolated by joining the altitudes of both sides of the main watershed. If no other data are available, this imaginary surface can be deemed as a proxy or reference surface to evaluate river erosion (Azañón et al., 2012; Brocklehurst and Whipple, 2002; Menéndez et al., 2008; Pérez-Peña et al., 2010). We have calculated the longitudinal and ridge-line profiles of nine streams in the study area.

5.5. Slope–area analysis and normalized steepness index

Graded rivers in detachment-limit systems (bedrock channels) show an exponential relationship between channel slope (S) and upstream area (A) (Hack, 1957). This well-known relation is described by the power-law:

$$S = ksA^{-\Theta}$$

where ks is the channel steepness-index and Θ the concavity index (Flint, 1974). This power relation is depicted by most rivers when they reach a critical threshold drainage area in the range of 0.1–5 km (Kirby and Whipple, 2001; Wobus et al., 2006). This power-law relation has been used in several tectonic studies, since rivers that are affected by active tectonics, changes in river bed lithology, and/or climate, present different area–slope relations and thus dissimilar ks and Θ (Kirby and Whipple, 2012; Wobus et al., 2006).

One way to determine ks and Θ for a river is to perform regressions in logarithmic slope–area plots (Fig. 4). Channels under the same factors will yield a linear relation in slope–area logarithmic plot. Moreover, changes within the same river profile will depict different linear relations. These plots constitute very useful tools when analyzing river knickpoints and can be used to differentiate migrating or vertical-step knickpoints from slope-break knickpoints that separate areas with differential uplift (Burbank and Anderson, 2013; Kirby and Whipple, 2012; Whipple et al., 2013; Wobus et al., 2006). A topographic knickpoint is generated when a stream reach is steepened with respect to adjacent reaches, thus increasing stream power and erosion in it (Gardner, 1983). In logarithmic slope–area plots a vertical-steep knickpoint will appear as an anomalous steepened reach separating reaches with similar trends, i.e. ks (Fig. 4a), whereas slope-breaks knickpoints will be represented by transitional zones separating reaches with different ks (Fig. 4b). Mobile vertical-step knickpoints in transient landscapes form in response to discrete drops in relative base level

caused by stream capture, sea-level fall, or a pulse of rock uplift (Crosby and Whipple, 2006; Reinhardt et al., 2007; Snyder et al., 2002; Whipple et al., 2013), whereas anchored vertical-step knickpoints can respond to local changes of riverbed lithology (Whipple et al., 2013; Whittaker et al., 2007). In contrast, slope-breaks knickpoints develop in response to permanent changes in boundary conditions such as an increase or decrease in the rate of relative base-level fall (driven by differences in rock uplift rate) or a change in climate conditions (Bishop et al., 2005; Kirby and Whipple, 2012; Snyder et al., 2003).

Some studies have proposed that concavity index (Θ) varies in most natural channels in a narrow range between 0.4 and 0.6, and it is relatively insensitive to differences in uplift rate, lithology and/or climate at steady-state (Kirby and Whipple, 2012; Whipple et al., 2013). By contrary, steepness index (ks) is highly sensitive to all the mentioned factors.

However, there is a problem when comparing ks values extracted from slope–area logarithmic plots. Small deviations in concavity index cause large deviations in ks , being very difficult to compare river reaches with different concavities. Wobus et al. (2006) proposed the use of a “normalized” steepness index (ks_n) that can be calculated for a river reach by using a fixed “reference” concavity. This method allows the comparison of profiles with different parameters and it has been widely used in tectonic geomorphology studies (Bellin et al., 2014; Kirby and Whipple, 2012; Matoš et al., 2014; Scotti et al., 2014; Whipple et al., 2013; Wobus et al., 2006).

6. Results

In order to apply the geomorphic indexes, nine representative basins have been selected; Pintado, Saltador, Zarcico, de los Carboneros, Lébor, Totana, de los Arcos, Casa del Peralejo and Cañada del Cabezo (Fig. 2). Drainage basins south of the Sierra de la Tercia range are short and roughly perpendicular (NW–SE) to the main fault direction (Fig. 2), except the Rambla de los Carboneros with a NE–SW orientation (parallel to the AMF). Some channels in these basins show left-lateral offsets (up to 27 m) at their intersections with the AMF that evidence its recent activity (Martínez-Díaz et al., 2003). Drainage basins on the northern side of the Sierra de la Tercia are shorter and do not cross the AMF but we have considered them for the analysis due to their relationship with the Tercia anticline. Drainage basins of the Rambla de Lébor and Totana are very different from the latter basins. These rivers have their sources in the Sierra Espuña range, and cross the anticline of the Sierra de la Tercia to discharge into alluvial fans at the Guadalentín depression. These two basins have a complex geometry (L-shaped), with NE–SW

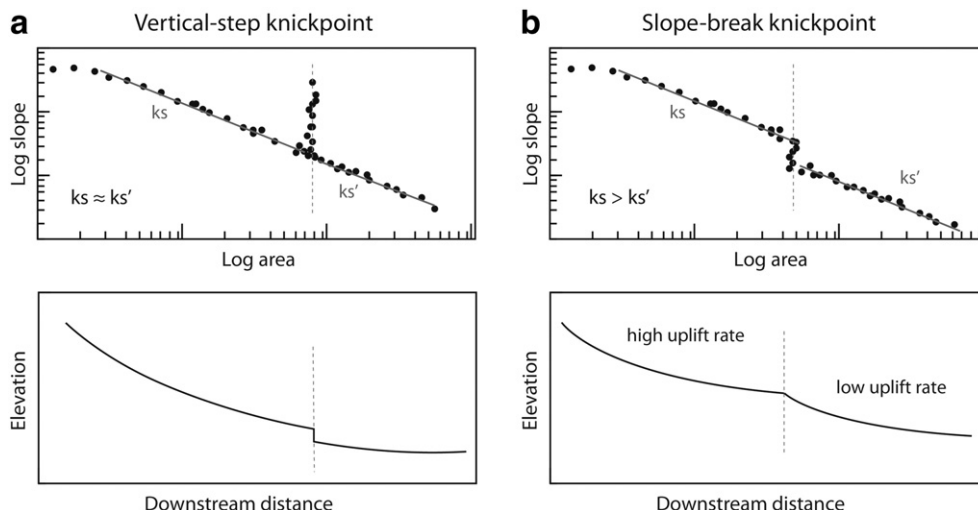


Fig. 4. Differences between vertical-steep and slope break knickpoints.

orientation at the source and NW–SE orientation as they get closer to the AMF (Fig. 2).

6.1. Mountain front sinuosity

Mountain front sinuosity was calculated at the boundaries of the Sierra de la Tercia and the Sierra Espuña (Fig. 5). We differentiated 12 different mountain fronts; fronts A to H correspond to Alhama de Murcia fault, I and J occur between the Guadalentín depression and the southeastern termination of Sierra de la Tercia, and fronts K and L correspond to the retreated extensional front at the western termination of Sierra Espuña.

Mountain fronts A, B, C, D, E and G show Smf values lower than 1.4 (Table 1), indicative of active fault segments. Mountain fronts F, I and J have values close to 1.4 (Table 1) and correspond to faults with moderate–low displacement rates (F) or to erosional unconformities related to folding (I and J). Finally, mountain fronts H, K and L yield sinuosity values up to 2 (Table 1) and can be associated with inactive structures. K and L segments represent relic, retreated mountain fronts inherited from extension that occur several km NE of the normal faults and associated Late Miocene alluvial fans. Segment H coincides with an

Table 1
Sinuosity values for analyzed mountain fronts.

Name	Lmf	Ls	Sinuosity (Smf)
A	5254.82	4401.38	1.19
B	5779.78	4789.33	1.21
C	6122.67	5956.80	1.03
D	2516.88	2034.52	1.24
E	4687.64	3702.57	1.27
F	7650.00	5286.38	1.45
G	3647.76	2920.85	1.25
H	3821.83	1869.72	2.04
I	4999.59	3206.07	1.56
J	2022.37	1378.68	1.47
K	11,511.16	3752.34	3.14
L	36,995.54	9876.42	3.75

unconformity between two generations of folded Pleistocene alluvial fans at the border of the Guadalentín depression, similar to mountain fronts I and J. Most of the mountain fronts with high Smf coincide with lithological resistance contrast, such as cases F, L and K where metamorphic rocks are in contact with Pliocene and Quaternary alluvial fans.

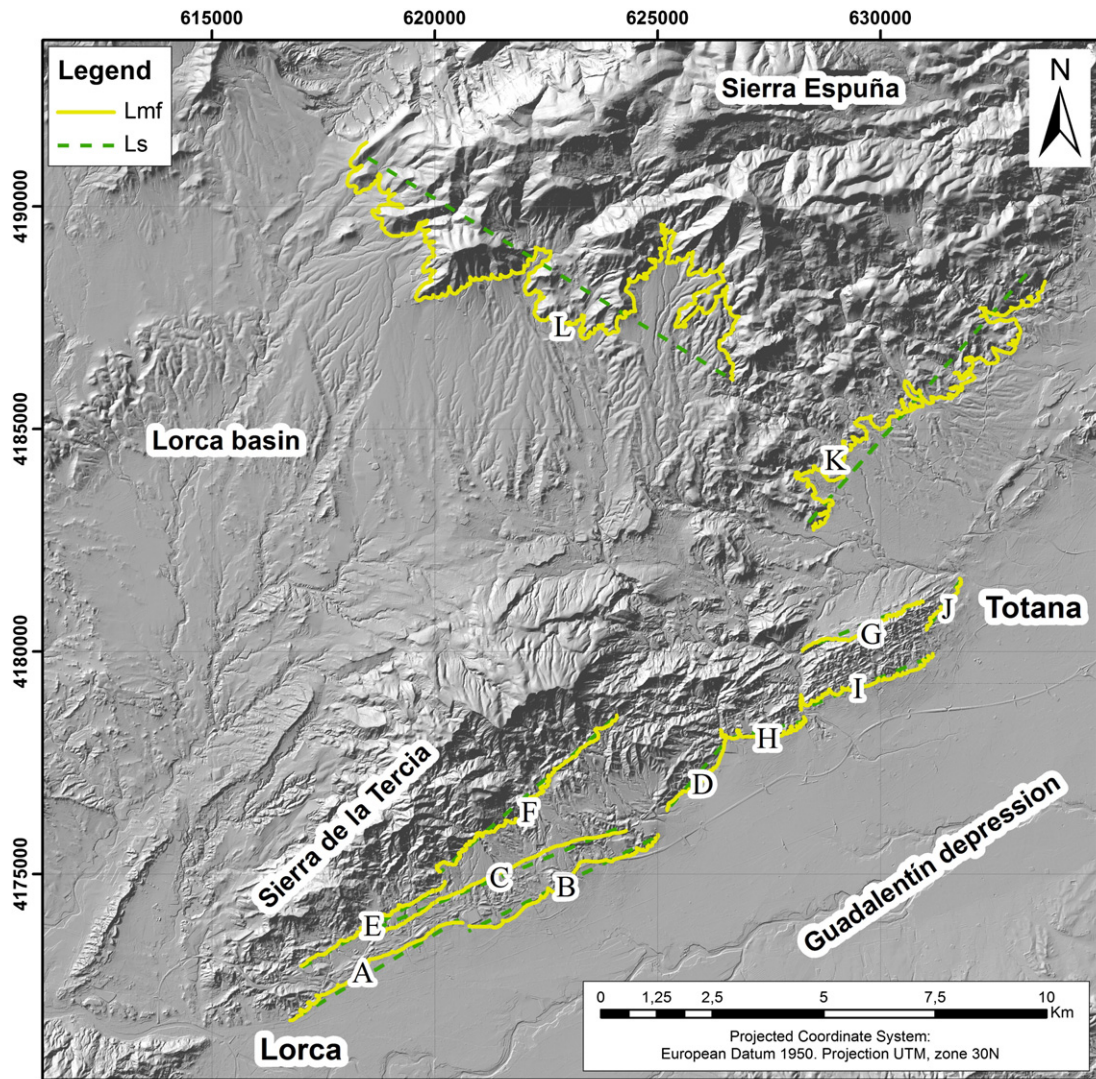


Fig. 5. Mountain fronts sinuosity (Smf). Lmf: length of the mountain front along the foot of the mountain, Ls: length of the mountain front measured along a straight line. See Table 1 for Smf values.

6.2. SLk anomalies

The SLk index was calculated for the main rivers in segments of 250 m. The SLk index value distribution shows a highly left-skewed distribution, causing that extreme high values mask lower-order anomalies. In order to take into account this variability, we classified the SLk map in 10 classes by using geometric intervals (Fig. 6). This method can be considered a hybrid between quantiles (that differentiate classes with the same number of elements), natural breaks (that consider the main breaks in the histogram) and equal intervals. It creates a balance between highlighting changes in the middle values and the extreme values, thereby producing a result that takes into account the high variability of SLk values in the area.

The SLk anomaly map of the study area shows several anomalies (areas with high gradients, Fig. 6). The main SLk anomalies are located within the Lébor and the Totana basins, and they correspond to the capture points of the old Miocene drainage network. SLk anomalies in the Totana basin are more restricted to capture points, whereas in the Lébor basin they cover a larger area (Fig. 6), with the highest values related to the eastern closure of the Sierra de la Tercia anticline. High values also occur in the Casa del Peralejo and Cañada del Cabezo basins, related to northwestern limb of the Sierra de la Tercia anticline.

Anomalies at the Saltador, Zarcico and de los Arcos basins coincide with transpressive segments of the AMF (Fig. 6).

6.3. Hypsometric curves

Most hypsometric curves are complex with several inflection points, i.e. points where the curve changes from convex to concave shape (Fig. 7). However, some of the shorter basins located on both limbs of the Sierra de la Tercia anticline show convex shapes. The three largest basins, Totana, Lébor and de los Arcos, have concave-shaped hypsometric profiles. These hypsometric curves are similar except in the middle-lower part, where the Lébor basin is clearly convex-shaped (Fig. 7). This convex-curvature coincides with Sierra de la Tercia anticline, where streams are highly entrenched and form deep gorges (Fig. 3c).

6.4. River topographic profiles

The longitudinal and ridge-line topographic profiles, together with the SLk values and the position of fault traces and major knickpoints, are presented in Fig. 8. In the case of the Lébor and Totana basins, we can recognize three different sectors, a first sector located in headwater where longitudinal and ridgeline-profiles show the largest differences,

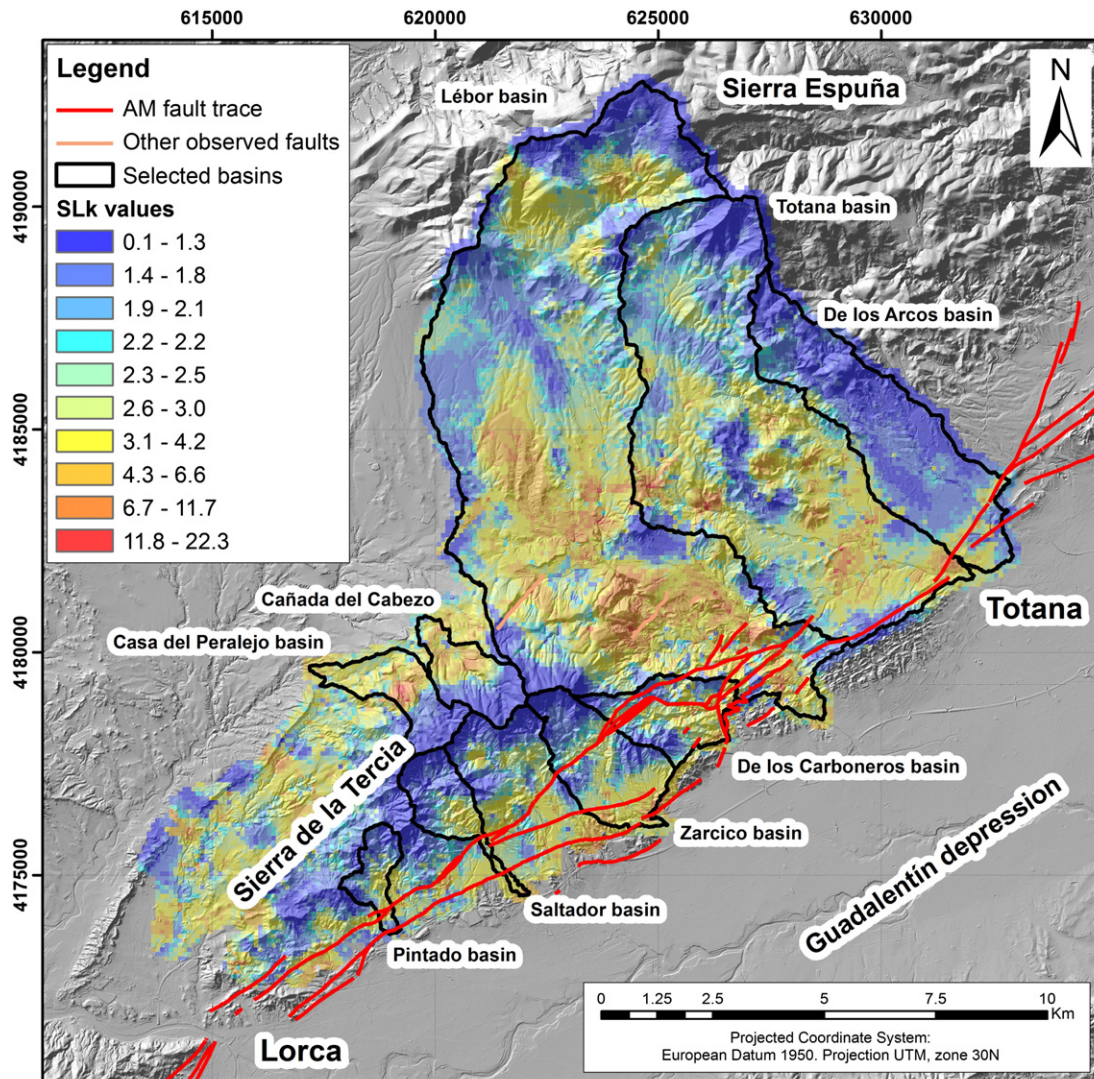


Fig. 6. SLk map of the study area calculated by ordinary kriging method. Interpolated values have been classified into 10 classes by using geometric intervals (see text for further explanation).

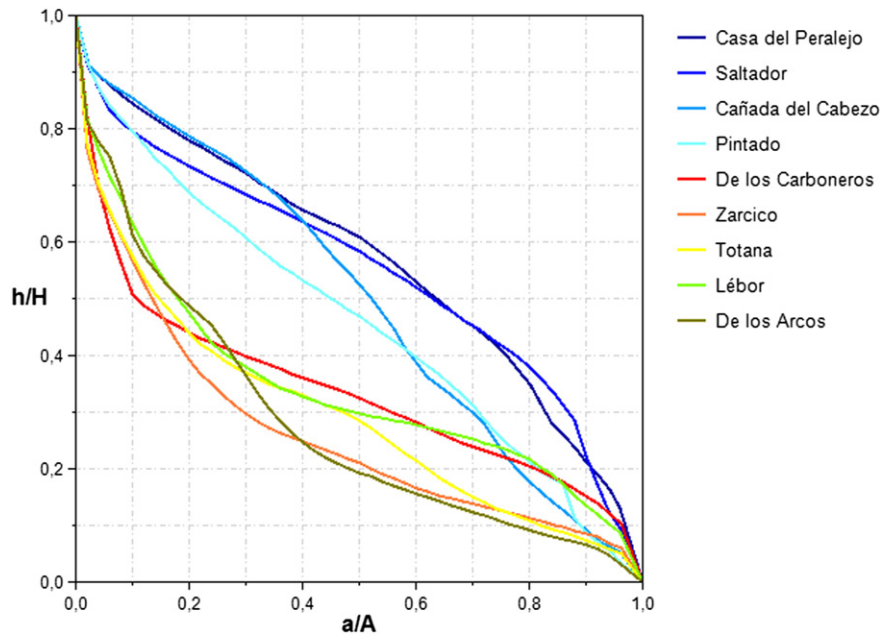


Fig. 7. Hypsometric curves of selected basins. h/H relative altitude, a/A relative area.

an intermediate sectors where both profiles merge, and a third sector in the middle–lower part where both profiles present again differences in elevation (Fig. 8). Moreover, the last sector in both basins shows several knickpoints in the longitudinal profiles and high values of SLk index coinciding with fault traces. Rambla de los Arcos is very similar to Lébor and Totana except for the last sector, where both profiles do not present significant altitude differences. The Rambla del Saltador and Rambla del Pintado basins present clear changes coinciding with AMF fault traces. In the Zarcico basin these differences are less pronounced, but still can be identified (Fig. 8). The Carboneros basin that is oriented parallel to the AMF presents the highest step in the ridgeline profile near to its source coinciding with the main fault trace. Finally, the Cañada del Cabezo and Casa del Peralejo basins that are located at the northern limb of the Sierra de la Tercia anticline show the maximum differences between both profiles in their middle and upper parts.

6.5. Slope area analysis and steepness index

Slope–area analysis for the northern basins was limited to the zone of detachment-limited control, i.e. the area upstream the Guadalentín River plain, whereas for the northern rivers, we restricted the analysis to the northern limb of Sierra de la Tercia anticline, where river have a well-defined bedrock character.

In order to obtain slope–area logarithmic plots we used the open-source codes available from <http://www.geomorphtools.org>. Longitudinal profile elevations were smoothed with a kernel of 150 m and profile slopes were extracted by resampling at equal vertical interval of 6 m. slope–area logarithmic plots were calculated for the Totana and Lébor basins whereas steepness index and concavity were estimated for the selected basins network. We selected a reference concavity of 0.5 for the analysis. This reference concavity is slightly larger than the 0.45 value proposed in bibliography (Kirby and Whipple, 2012; Wobus et al., 2006 and references herein), but it fits better with the mean concavity values obtained from the regression of the longitudinal profiles of the main rivers of the study area (Table 2).

The Totana and Lébor basins show two well-differentiated parts, separated by prominent knickpoints (Fig. 9). These profile segments also show slightly decreasing ksn values towards the river mouth.

We also computed the normalized steepness index in segments of 250 m obtained with a drainage threshold area of 50 km² and using a

reference concavity of 0.5. As well as with the SLk index, the steepness index shows a left-skewed histogram. Extreme high values of major knickpoints of the Totana and Lébor basins mask other lower-order peaks. For this reason, we classified the ksn values in the same way as the SLk index, by using the geometric intervals method. Two areas with high ksn values can be well differentiated; the middle-to-upper reaches of the Totana and Lébor basins and high values associated with the Alhama de Murcia fault (Fig. 10).

7. Discussion

7.1. Present-day tectonic activity based on geomorphic indexes

The geomorphic indexes obtained in this work are consistent with the AMF and the Sierra de la Tercia anticline recent activity. Mountain fronts controlled by the AMF yield Smf values lower than 1.4, characteristic of active faulting (Fig. 5 and Table 1). According to mountain front sinuosity values, the southern segment of the AMF (from Lorca to Zarcico basin; Figs. 2, 5) is more linear than the northern one. On the other hand, mountain fronts of Sierra Espuña, inherited from Late Miocene extension, have higher Smf values (up to 3.0) indicative of quiescence and no tectonic activity. Associated with the NE retreat of this front, Pleistocene alluvial fans retrograded over inactive Miocene fans related to extension (Fig. 11).

SLk index anomalies (i.e. areas with high river gradients, Pérez-Peña et al., 2009a) display an interesting distribution. The highest values are located within the Lébor basin, and related to the north-eastern closure of Sierra de la Tercia anticline (Fig. 6), where rivers present remarkable incision (Fig. 3c). These higher gradients in the Lébor basin are also visible in the ksn map and area–slope plots (Figs. 9, 10) and suggest a recent activity of the Sierra de la Tercia anticline. On the other hand, SLk index anomalies are also visible in the Totana basin, but contrary to those of the Lébor basin, these anomalies are only restricted to capture points.

High values of SLk are also related to the AMF fault trace between the Saltador and Zarcico basin as well as in the de los Arcos basin, thus indicating a recent activity of the AMF. However, anomalies of SLk index related to the AMF present important differences for the south basins. These differences could be associated with transpressive AMF fault segments with higher inverse component due to changes in fault

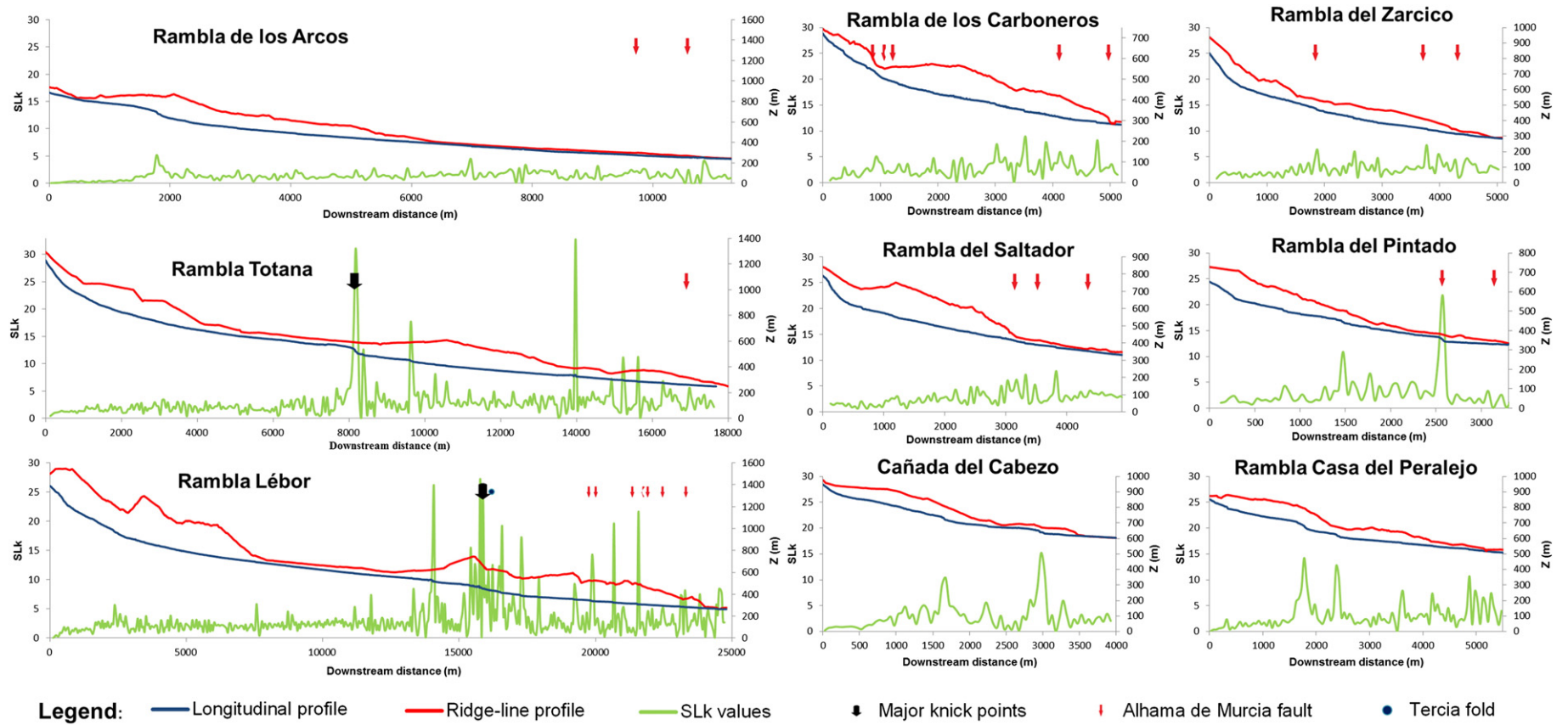


Fig. 8. Longitudinal and ridge-line profiles of selected rivers (units in meters). SLk values, fault traces and major knickpoints are indicated.

Table 2

Slope area analysis and steepness index values. In the case of different segments, only the first one is given.

River	Length (km)	Drainage area (km ²)	q*	ksn
De los Arcos	11.41	13.27	0.58	48.15
Totana	17.68	37.34	0.61	104
Lébor	24.79	63.25	0.40	138
De los Carboneros	5.18	4.14	0.44	63
Zarcico	5.08	5.68	0.59	89.7
Saltador	5.25	2.80	0.49	80.6
Pintado	3.40	1.70	0.50	65.7
Casa del Peralejo	5.54	3.38	0.42	43.2
Cañada del Cabezo	3.99	3.10	0.48	42.6

orientation, as the anomaly between Saltador and Zarcico basins, where AMF runs almost E–W. The high anomaly in the northern fault trace in the Pintado basin is influenced by lithology, as in this zone small travertine bodies crop out locally.

In the case of the anomalies located in the northern limb of Sierra de la Tercia (Cañada del Cabezo and Casa del Peralejo basins) they are related to the northern anticline limb and they point to the present-day growth of Sierra de la Tercia.

Hypsometric curves of basins draining the NW and SE limbs of the Tercia anticline have convex-shapes, thus indicating a young drainage system related to active folding (Casa del Peralejo, Saltador, Cañada del Cabezo and Pintado basins, Fig. 7). The Totana, Lébor and de los Arcos basins show roughly concave hypsometric curves with similar shapes, with high gradients in their upper parts indicative of a mature stage of geomorphic development. These curves have complex shapes as a result of the combination of geomorphic features from the old and the present-day drainage network. These concave shapes are associated with the different topographic features within these basins; i) an upper part that corresponds with the source area in the Sierra Espuña range with elevation up to 1600 m, ii) a large upper-middle part with low relief amplitude ranging from 500 to 600 m formed by middle Pleistocene alluvial fan surfaces at the foot of Sierra Espuña (Fig. 3b), and iii) a middle-lower part where the rivers cross the Sierra de la Tercia anticline ending at the Guadalentín depression (100 masl).

In spite of these particularities, we can observe a sound difference in the middle-lower part of the hypsometric curves. The Lébor hypsometric curve presents a higher convexity coinciding with the Tercia

anticline (Fig. 7). This convexity points to a younger landscape in this part that agrees with the high SLk and ksn values related to the recent river incision driven by the growth of the Sierra de la Tercia anticline. Finally, the Zarcico and Carboneros basins show concave profiles, slightly higher in the latter (Fig. 7). In spite of the tectonic activity of the AMF and the Tercia anticline suggested by the geomorphic indexes, the concavity in these basins can be explained by the larger distance between the two main branches of the AMF (Fig. 2). This fact leaves an intermediate area with low topographic gradients between both fault segments that produces generalized concavity in the hypsometric curve of the Zarcico basin. As this distance decreases towards the NE, the hypsometric curve convexity of the Carboneros basin increases (Figs. 2, 7).

The morphology of the longitudinal and ridge-line topographic profiles of the Lébor, Totana and de los Arcos basins shows different parts suggesting the superposition of two drainage networks (Miocene and present-day). Longitudinal and ridge-line topographic profiles of the Lébor and Totana basins depict three well-differentiated parts; i) an upper part with meaningful altitude differences between both profiles, ii) a middle-upper part where both profiles merge, and iii) a middle-lower part again with differences between longitudinal and ridge-line profiles. The upper and middle parts of the river longitudinal profiles are representative of an old drainage network that has been captured by a new drainage network represented this latter one in the middle and lower parts of the longitudinal profiles. Moreover, major knickpoints and SLk high values concentrate in the middle-lower part of the Totana and Lébor longitudinal profiles (Fig. 8). In de los Arcos basins just the two first segments are represented, because there is no influence of the Tercia anticline. The other analyzed profiles show roughly similar shapes in longitudinal and ridgeline profiles and present high SLk values coinciding with transpressive segments of the AMF, local lithological contrast (Pintado basin) and Tercia anticline northern limb.

Slope–area plots of the Lébor and Totana basins show prominent knickpoints that separate upper and lower segments with roughly similar steepness indexes (Fig. 9). These plots are characteristics of vertical-steep knickpoints (Burbank and Anderson, 2013; Kirby and Whipple, 2012; Wobus et al., 2006), and suggest no tectonic control. These morphologies can respond to finite drops in local base level in the case of mobile knickpoints (Crosby and Whipple, 2006; Reinhardt et al., 2007; Whipple et al., 2013), or to lithological changes for anchored ones (Whipple et al., 2013; Whittaker et al., 2007). There are not significant lithological changes coinciding with knickpoint location and they present similar topographic altitudes (500 and 540 m in Lébor and Totana respectively, Fig. 8). Moreover, in both basins knickpoints locate upstream from the contact with the AMF fault trace, just in the transition between middle and middle-lower sectors of longitudinal and ridgeline profiles (Fig. 8). Vertical steep knickpoints should be formed due to a local base level drop driven by the capture of both basins by Guadalentín river. They mark the present-day position of the erosion wave that separates relict Miocene drainage features (preserved in the upper and middle-upper parts of Lébor and Totana basins) from modern fluvial network (Fig. 10).

More interestingly, the Lébor basin yields higher values of ksn (130–140) than Totana basin (104–91), thus pointing to higher uplift rates than the latter (Fig. 9). This feature is also observed in the automatic ksn map, where the highest values occur in a wider area within the Lébor basin but are restricted to capture points at the Totana basin (Fig. 10). These higher rock uplift rates could be caused by the growth of Sierra de la Tercia anticline, which is affecting more intensively to the Lébor basin (Fig. 2).

The automatic calculation of normalized steepness index (ksn) for the whole study area also provides interesting conclusions. High values of ksn in the southern limb of the Tercia lay in the middle-upper parts of the rivers coinciding with the Sierra de la Tercia anticline (Fig. 10), whereas the SLk anomalies concentrate at the southeasternmost step

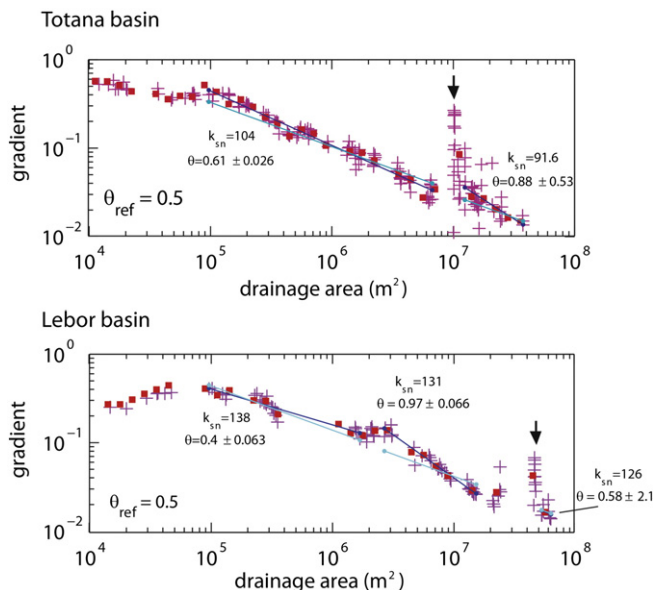


Fig. 9. Slope–area logarithmic plots for the Totana and Lébor basins. Normalized steepness index has been calculated with a reference concavity of 0.5.

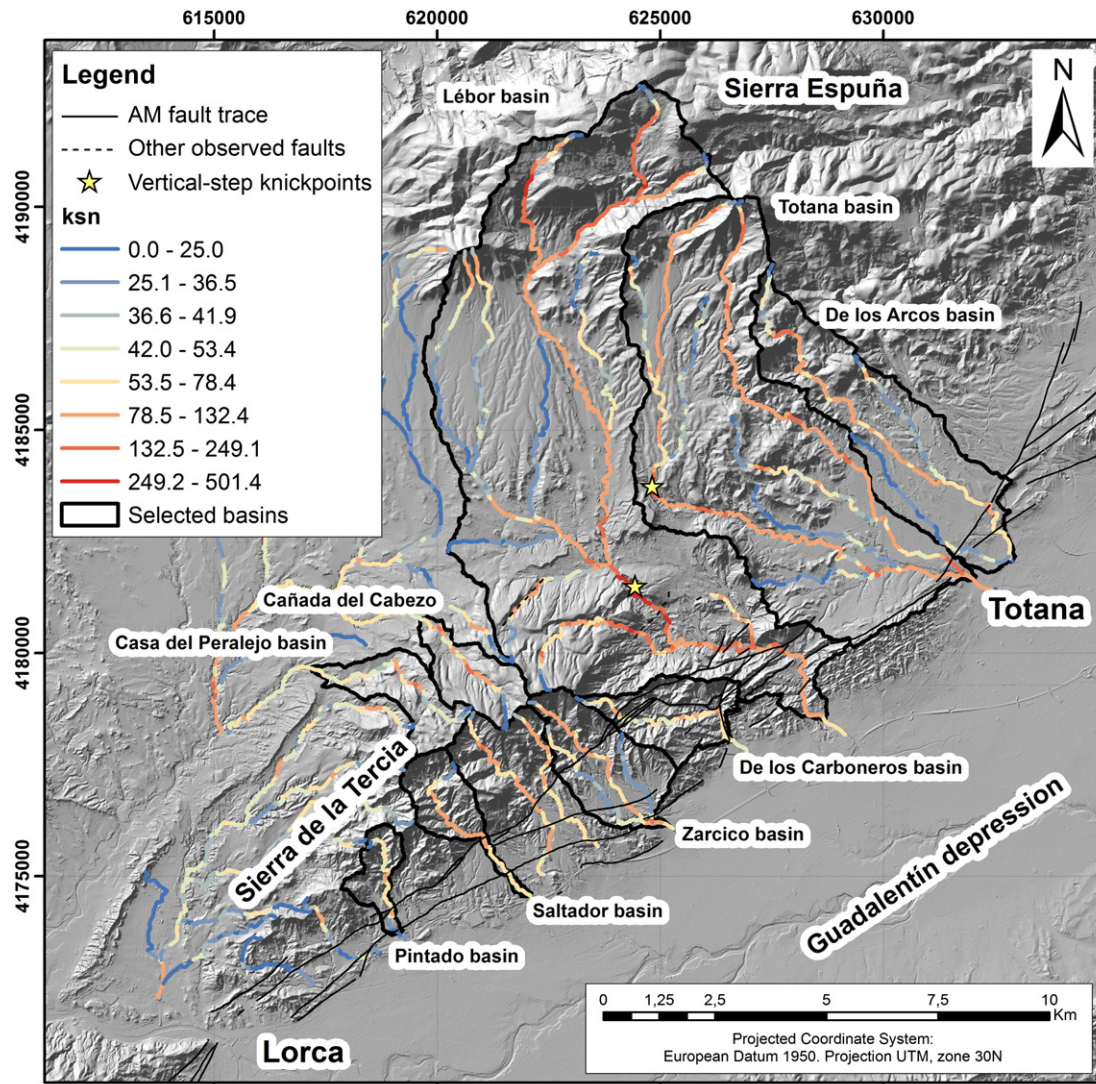


Fig. 10. Automatic calculation of the normalized steepness index (ksn) for river segments of 250 m, a drainage threshold area of 50 km² and a reference concavity of 0.5. Ksn values have been classified into 8 classes by using geometric intervals (see text for further explanation).

of the AMF (Fig. 6). As both structures are active, the two indexes give complementary information. The SLk index highlights localized knickpoints along river profiles (those related to the AMF), whereas ksn differentiates segments with different uplift rates (those related to the Tercia anticline, Fig. 3e).

7.2. Proposed geomorphic evolution

The distribution of wind gaps evidences an old drainage network with SW to NE orientation related to the Sierra de la Tercia tilted block and NE to SW orientation associated with the Sierra Espuña footwall range (Fig. 11). These old drainage networks were overprinted by the present-day N–S to NW–SE network that formed in response to the activity of the AMF and the growth of the Tercia anticline.

The capture of the old Miocene drainage network was probably due to a local base-level drop and driven by headward erosion, as can be deduced from slope–area plots (Fig. 9). This base-level drop promoted the capture of the drainage network at the foot of the Sierra Espuña by the Lébor and Totana basins (Fig. 11). These two basins still preserve some geomorphic features in their upper and middle parts inherited from the Miocene extension that are clear from longitudinal and ridge-line profiles (Fig. 8). Upper parts of Totana and Lébor basins correspond to the Miocene headwaters draining Sierra Espuña and present

mature hypsometric curves and meaningful differences between longitudinal and ridgeline profile. Middle parts of both rivers, where longitudinal and ridgeline profiles merge, run over alluvial fan surfaces deposited under extensional tectonics. Middle–lower parts of Lébor and Totana are separated from the latter by prominent vertical-step knickpoints and respond to the erosion-wave of the Pleistocene-to-present-day drainage network. De los Arcos basin was probably also formed in Miocene related to the Sierra Espuña tilted block (Fig. 11), but contrary to Lébor and Totana it drained towards the SE. This basin presents only two of the three sectors described in river profiles of Lébor and Totana (upper and middle upper sectors, Fig. 8), thus indicating that no capture process was active in this area. The lower incision of the de los Arcos basin (Fig. 8) can be attributed to the change in orientation of the AMF, which runs in this area N45E and does not show inverse component.

Geomorphic indexes have shown that the anticline of Sierra de la Tercia presents clear activity in Quaternary times. The development and growth of this anticline played a crucial role in the present-day drainage system configuration. It prevented part of the drainage system of the Lorca basin to be captured by the Lébor catchment and caused a generalized uplift in the latter (Fig. 11). It also caused uplift and high river incision in the basins draining their northern and southern limbs. The influence of the active uplift of Sierra de la Tercia is higher in the

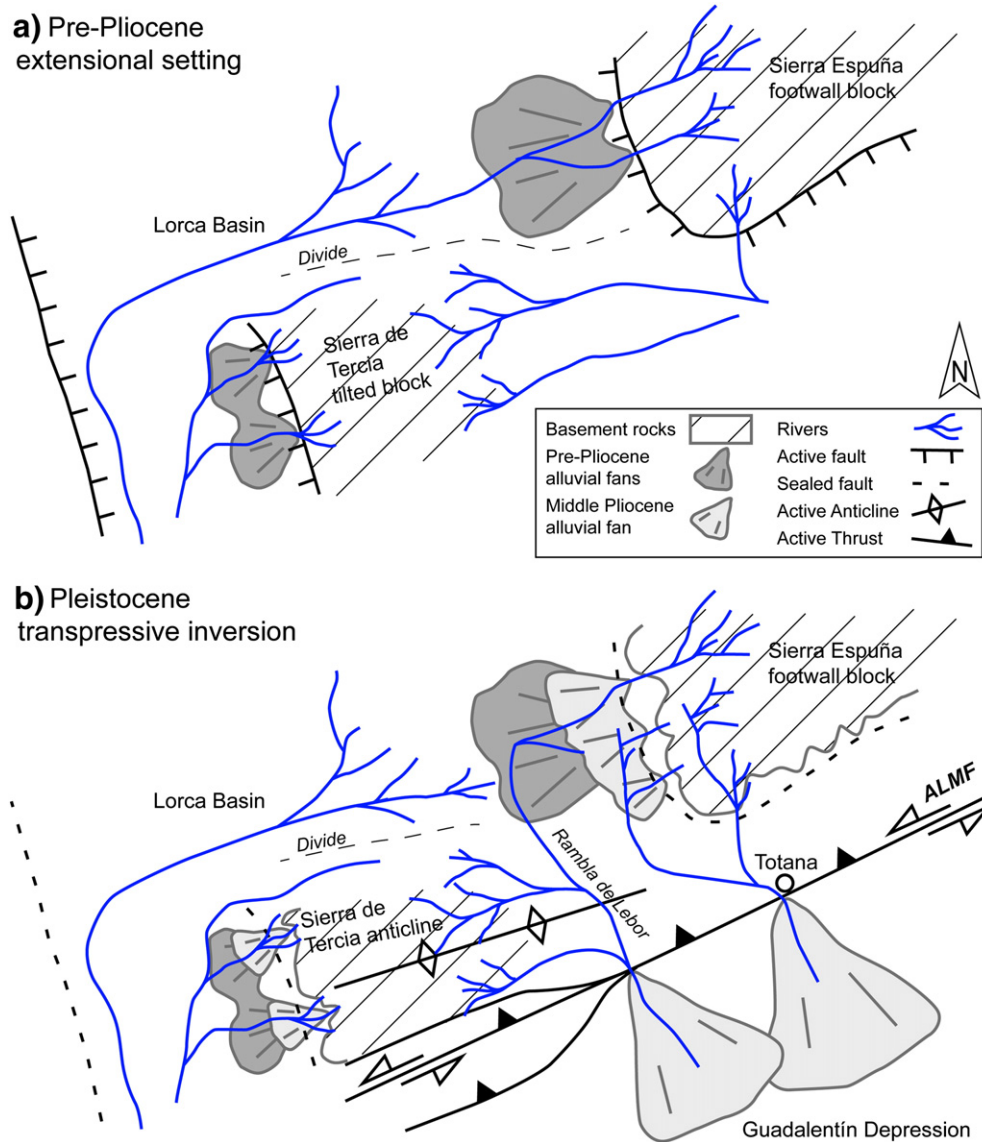


Fig. 11. Cartoon showing the landscape evolution in the study area. Main features associated with the extensional and transpressive setting are indicated. See text for detailed description.

Lébor basin, has a lower influence in Totana basin and it is absent in de los Arcos basin, where the AMF display a pure left-lateral strike-slip character.

8. Conclusions

The drainage network of the Lorca and Totana basins shows the effects of a changing tectonics setting, from extension to transpression. The development of new tectonic structures as the AMF and Tercia anticline promoted the replacement of the old Miocene drainage by the present-day drainage network. The activity of these two structures is clear from the analyzed geomorphic indexes. Smf values point to the activity of the AMF, whereas hypsometry, SLk index, and steepness index suggest a recent activity of the Tercia anticline. Tectonic activity of the AMF causes localized steps, whereas the Tercia anticline produces wider areas of tectonic uplift. Longitudinal and ridgeline profiles show in their middle–upper parts geomorphic features inherited from Miocene extension.

The capture of the old Miocene drainage network was probably due to a local base-level drop related with the AMF that propagated by headward erosion, as indicated by the knickpoints analysis in slope–

area profiles. The growth of the Sierra de la Tercia anticline prevented part of the Lorca basin to be captured by the Lébor catchment.

This work provides an excellent example of the evolution of a drainage network in a changing tectonic scenario. This reorganization is driven progressively by successive fluvial captures and headward erosion. In the intermediate stages of this process, drainage system can assimilate geomorphic features from the old fluvial network thus yielding complex geometries. Geomorphic indexes can record this evolution and they agree with the AMF and the Sierra de la Tercia anticline recent activity as well as with the relict geomorphic features inherited from the Miocene extension.

Acknowledgments

The authors were supported by research projects CGL2011-29920, CSD2006-00041 TOPOIBERIA CONSOLIDER-INGENIO2010, CTM2007-66179-C02-01/MAR, CGL2011-30005-C02-02 SHAKE, and the CTM2011-30400-C02-01 HADES projects from the Spanish Ministry of Science and Innovation. The Ministerio de Educación, Cultura y Deporte (FPU12/00921) from Spain provided funding for the predoctoral FPU fellowship of M. Ferrater.

References

- Alvarez, F., Aldaya, F., Navarro-Vilá, F., 1989. Miocene extensional deformation in the region of Aguilas-Mazarrón (eastern Betic Cordillera). *Estud. Geol.* 45, 369–374.
- Antón, L., De Vicente, G., Muñoz-Martín, A., Stokes, M., 2014. Using river long profiles and geomorphic indices to evaluate the geomorphological signature of continental scale drainage capture, Duero basin (NW Iberia). *Geomorphology* 206, 250–261. <http://dx.doi.org/10.1016/j.geomorph.2013.09.028>.
- Aydin, A., Nur, A., 1985. The types and role of stepovers in strike-slip tectonics. In: Biddle, K.T., Christie-Blick, N. (Eds.), *Strike-slip Deformation, Basin Formation, and Sedimentation*. Society of Economic Paleontologists and Mineralogist Special Publication, pp. 35–44.
- Azañón, J.M., Pérez-Peña, J.V., Giacomia, F., Booth-Rea, G., Martínez-Martínez, J.M., Rodríguez-Peces, M.J., 2012. Active tectonics in the central and eastern Betic Cordillera through morphotectonic analysis: the case of Sierra Nevada and Sierra Alhamilla. *J. Iber. Geol.* 38, 225–238. http://dx.doi.org/10.5209/rev_JIGE.2012.v38.n1.39214 (225).
- Babault, J., Van Den Driessche, J., Teixell, A., 2012. Longitudinal to transverse drainage network evolution in the High Atlas (Morocco): the role of tectonics. *Tectonics* 31, TC4020. <http://dx.doi.org/10.1029/2011tc003015>.
- Balaný, J.C., García-Dueñas, V., 1987. Les directions structurales dans le Domaine d'Alborán de part et d'autre du Déroit de Gibraltar. *Comptes Rendus de l'Académie des Sciences de Paris* 304 pp. 929–932.
- Behr, W.M., Platt, J.P., 2012. Kinematic and thermal evolution during two-stage exhumation of a Mediterranean subduction complex. *Tectonics* 31, TC003121. <http://dx.doi.org/10.1029/2012TC003121>.
- Bellin, N., Vanacker, V., Kubik, P.W., 2014. Denudation rates and tectonic geomorphology of the Spanish Betic Cordillera. *Earth Planet. Sci. Lett.* 390, 19–30. <http://dx.doi.org/10.1016/j.epsl.2013.12.045>.
- Bishop, P., Hoey, T.B., Jansen, J.D., Artza, I.L., 2005. Knickpoint recession rate and catchment area: the case of uplifted rivers in Eastern Scotland. *Earth Surf. Process. Landf.* 30 (6), 767–778.
- Booth-Rea, G., Azañón, J.M., Azor, A., García-Dueñas, V.C., 2004a. Influence of strike-slip fault segmentation on drainage evolution and topography. A case study: the Palomares Fault Zone (southeastern Betics, Spain). *J. Struct. Geol.* 26, 1615–1632. <http://dx.doi.org/10.1016/j.jsg.2004.01.007>.
- Booth-Rea, G., Azañón, J.M., García-Dueñas, V.C., 2004b. Extensional tectonics in the northeastern Betics (SE Spain): case study of extension in a multilayered upper crust with contrasting rheologies. *J. Struct. Geol.* 26, 2039–2058. <http://dx.doi.org/10.1016/j.jsg.2004.04.005>.
- Booth-Rea, G., Azañón, J.M., Martínez-Martínez, J.M., Vidal, O., García-Dueñas, V., 2005. Contrasting structural and P–T evolution of tectonic units in the southeastern Betics: key for understanding the exhumation of the Alboran Domain HP/LT crustal rocks (western Mediterranean). *Tectonics* 24, 1–23. <http://dx.doi.org/10.1029/2004TC001640>.
- Booth-Rea, G., Ranero, C.R., Martínez-Martínez, J.M., Grevemeyer, I., 2007. Crustal types and Tertiary tectonic evolution of the Alborán sea, western Mediterranean. *Geochim. Geophys. Geosyst.* 8, Q10004. <http://dx.doi.org/10.1029/2007GC001639>.
- Booth-Rea, G., Giacomia, F., Martínez-Martínez, J.M., 2012. The Almenara detachment (southeastern Betics). *Geotemas* 16, 1615–1618.
- Bousquet, J.C., 1979. Quaternary strike-slip faults in south-eastern Spain. *Tectonophysics* 52, 277–286.
- Brocklehurst, S.H., Whipple, K.X., 2002. Glacial erosion and relief production in the Eastern Sierra Nevada, California. *Geomorphology* 42, 1–24.
- Bull, W.B., 1977. Tectonic Geomorphology of the Mojave Desert. U.S. Geological Survey Contract Report 14-08-001-G-394, Office of Earthquakes and Engineering.
- Bull, W.B., McFadden, L.D., 1977. Tectonic geomorphology north and south of the Garlock fault, California. In: Doehering, D.O. (Ed.), *Geomorphology in Arid Regions*. Proceedings at the Eighth Annual Geomorphology Symposium. State University of New York, Binghamton, NY, pp. 115–138.
- Bull, W.B., 1991. *Geomorphic Responses to Climatic Change*. Oxford University Press, Oxford.
- Burbank, D.W., Anderson, R.S., 2013. *Tectonic Geomorphology*, 2nd ed. Blackwell Science, Oxford.
- Candy, I., Black, S., 2009. The timing of Quaternary calcrete development in semi-arid southeast Spain: investigating the role of climate on calcrete genesis. *Sediment. Geol.* 218 (1), 6–15. <http://dx.doi.org/10.1016/j.sedgeo.2009.03.005>.
- Chen, Y.C., Sung, Q., Cheng, K.Y., 2003. Along-strike variations of morphotectonic features in the Western Foothills of Taiwan: tectonic implications based on stream-gradient and hypsometric analysis. *Geomorphology* 56, 109–137. [http://dx.doi.org/10.1016/S0169-555X\(03\)00059-X](http://dx.doi.org/10.1016/S0169-555X(03)00059-X).
- Cotton, C.A., 1942. *Climatic Accidents in Landscape-making*. Whitcombe & Tombs, Christchurch.
- Crosby, B.T., Whipple, K.X., 2006. Knickpoint initiation and distribution within fluvial networks: 236 waterfalls in the Waipaoa River, North Island, New Zealand. *Geomorphology* 82, 16–38.
- Demets, C., Gordon, R.G., Argus, D.F., Stein, S., 1994. Effect of recent revisions to the geomagnetic reversal time scale on estimates of current plate motions. *Geophys. Res. Lett.* 21, 2191–2194.
- Densmore, A.L., Ellis, M.A., Anderson, R.S., 1998. Landsliding and the evolution of normal-fault-bounded mountains. *J. Geophys. Res.* B: Solid Earth 103, 15203–15219.
- Echeverría, A., Khazaradze, G., Asensio, E., Gárate, J., Dávila, J.M., Suriñach, E., 2013. Crustal deformation in eastern Betics from CuaTeNeO GPS network. *Tectonophysics* 608, 600–612. <http://dx.doi.org/10.1016/j.tecto.2013.08.020>.
- Faccenna, C., Piromallo, C., Crespo-Blanc, A., Jolivet, L., Rossetti, F., 2004. Lateral slab deformation and the origin of the western Mediterranean arcs. *Tectonics* 23, TC1012. <http://dx.doi.org/10.1029/2002TC001488>.
- Flint, J.J., 1974. Stream gradient as a function of order, magnitude, and discharge. *Water Resour. Res.* 10, 969–973.
- Gao, M., Zeilinger, G., Xu, X., Wang, Q., Hao, M., 2013. DEM and GIS analysis of geomorphic indices for evaluating recent uplift of the northeastern margin of the Tibetan Plateau, China. *Geomorphology* 190, 61–72. <http://dx.doi.org/10.1016/j.geomorph.2013.02.008>.
- Gardner, T.W., 1983. *Experimental study of knickpoint and longitudinal evolution in cohesive, homogeneous material*. *Geol. Soc. Am. Bull.* 94, 664–672.
- Giacomia, F., Booth-Rea, G., Martínez-Martínez, J.M., Azañón, J.M., Pérez-Peña, J.V., 2012a. Geomorphic analysis of the Sierra Cabrera, an active pop-up in the constrictional domain of conjugate strike-slip faults: the Palomares and Polopos fault zones (eastern Betics, SE Spain). *Tectonophysics* 580, 27–42. <http://dx.doi.org/10.1016/j.tecto.2012.08.028>.
- Giacomia, F., Booth-Rea, G., Martínez-Martínez, J.M., Azañón, J.M., Pérez-Peña, J.V., Pérez-Romero, J., Villegas, I., 2012b. Geomorphic evidence of active tectonics in the Sierra Alhamilla (eastern Betics, SE Spain). *Geomorphology* 145–146, 90–106. <http://dx.doi.org/10.1016/j.geomorph.2011.12.043>.
- Giacomia, F., Booth-Rea, G., Martínez-Martínez, J.M., Azañón, J.M., Pérez-Romero, J., Villegas, I., 2013. Mountain front migration and drainage captures related to fault segment linkage and growth: the Polopos transpressive fault zone (south-eastern Betics, SE Spain). *J. Struct. Geol.* 46, 76–91. <http://dx.doi.org/10.1016/j.jsg.2012.10.005>.
- Hack, J.T., 1957. Studies of longitudinal profiles in Virginia and Maryland. *U.S. Geol. Surv. Prof. Pap.* 294-B, 1.
- Hack, J.T., 1973. Stream profile analysis and stream-gradient index. *J. Res. U. S. Geol. Surv.* 1, 421–429.
- Harvey, A., Wells, S., 1987. Response of Quaternary fluvial systems to differential epeirogenic uplift: Aguas and Feos river systems, southeast Spain. *Geology* 15, 689–693.
- Harvey, A.M., Miller, S.Y., Wells, S.G., 1995. Quaternary soil and river terrace sequences in the Aguas/Feos River systems: Sorbas basin, southeast Spain. In: Lewin, J., Macklin, M.G., Woodward, J.C. (Eds.), *Mediterranean Quaternary River Environments*. Balkema, Rotterdam, pp. 263–281.
- Jackson, J., Norris, R., Youngson, J., 1996. The structural evolution of active fault and fold systems in central Otago, New Zealand: evidence revealed by drainage patterns. *J. Struct. Geol.* 18, 217–234.
- Keller, E.A., Pinter, N., 2002. *Active Tectonics. Earthquakes, Uplift, and Landscape*. Prentice Hall, New Jersey.
- Kelly, M., Black, S., Rowan, J.S., 2000. A calcrete-based U/Th chronology for landform evolution in the Sorbas basin, southeast Spain. *Quat. Sci. Rev.* 19, 995–1010. [http://dx.doi.org/10.1016/S0277-3791\(99\)00050-5](http://dx.doi.org/10.1016/S0277-3791(99)00050-5).
- Kirby, E., Whipple, K.X., 2001. Quantifying differential rock-uplift rates via stream profile analysis. *Geology* 29, 415. [http://dx.doi.org/10.1130/0091-7613\(2001\)029<0415:QDRURV>2.0.CO;2](http://dx.doi.org/10.1130/0091-7613(2001)029<0415:QDRURV>2.0.CO;2).
- Kirby, E., Whipple, K.X., 2012. Expression of active tectonics in erosional landscapes. *J. Struct. Geol.* 44, 54–75. <http://dx.doi.org/10.1016/j.jsg.2012.07.009>.
- Krijgsman, W., Garcés, M., Agustí, J., Raffi, I., Taberner, C., Zachariasse, W.J., 2000. The 'Tortonian salinity crisis' of the eastern Betics (Spain). *Earth and Planetary Science Letters* 181, 497–511. [http://dx.doi.org/10.1016/S0012-821X\(00\)00224-7](http://dx.doi.org/10.1016/S0012-821X(00)00224-7).
- Legg, M.R., Luyendyk, B.P., Mammertickx, J., De Moustier, C., Tyce, R.C., 1989. Sea Beam survey of an active strike-slip fault: the San Clemente fault in the California Continental Borderland. *J. Geophys. Res.* 94, 1727–1744.
- Loneragan, L., Schreiber, B.C., 1993. Proximal deposits at a fault-controlled basin margin, Upper Miocene, SE Spain. *J. Geol. Soc. Lond.* 150, 719–727.
- Loneragan, L., White, N., 1997. Origin of the Betic-Rif mountain belt. *Tectonics* 16, 504–522.
- López-Comino, J.A., Mancilla, FdL, Morales, J., Stich, D., 2012. Rupture directivity of the 2011, Mw 5.2 Lorca earthquake (Spain). *Geophys. Res. Lett.* 39, L03301. <http://dx.doi.org/10.1029/2011GL050498>.
- Martínez-Díaz, J.J., 1998. *Neotectónica y Tectónica Activa del Sector Centro-Occidental de la Región de Murcia y Sur de Almería (Cordillera Bética – España)* (Doctoral Thesis). Universidad Complutense de Madrid, Madrid.
- Martínez-Díaz, J.J., 2002. Stress field variation related to fault interaction in a reverse oblique-slip fault: the Alhama de Murcia fault, Betic Cordillera, Spain. *Tectonophysics* 356, 291–305. [http://dx.doi.org/10.1016/S0040-1951\(02\)00400-6](http://dx.doi.org/10.1016/S0040-1951(02)00400-6).
- Martínez-Díaz, J.J., Masana, E., Hernández-Enrile, J.L., Santanach, P., 2003. Effects of repeated paleoearthquakes on the Alhama de Murcia fault (Betic Cordillera, Spain) on the Quaternary evolution of an alluvial fan system. *Ann. Geophys.* 46, 775–792.
- Martínez-Díaz, J.J., Masana, E., Ortuño, M., 2012a. Active tectonics of the Alhama de Murcia fault, Betic Cordillera, Spain. *J. Iber. Geol.* 38 (1), 170–181.
- Martínez-Díaz, J.J., Bejar-Pizarro, M., Álvarez-Gómez, J.A., Mancilla, FdL, Stich, D., Herrera, G., Morales, J., 2012b. Tectonic and seismic implications of an intersegment rupture. *Tectonophysics* 546–547, 28–37. <http://dx.doi.org/10.1016/j.tecto.2012.04.010>.
- Martínez-Martínez, J.M., Azañón, J.M., 1997. Mode of extensional tectonics in the south-eastern Betics (SE Spain): implications for the tectonic evolution of the peri-Alborán orogenic system. *Tectonics* 16, 205–225.
- Martínez-Martínez, J.M., Soto, J.L., Balanyá, J.C., 2002. Orthogonal folding of extensional detachments: structure and origin of the Sierra Nevada elongated dome (Betics, SE Spain). *Tectonics* 21. <http://dx.doi.org/10.1029/2001TC001283>.
- Masana, E., Martínez-Díaz, J.J., Hernández-Enrile, J.L., Santanach, P., 2004. The Alhama de Murcia fault (SE Spain), a seismogenic fault in a diffuse plate boundary: seismotectonic implications for the Ibero-Magrebien region. *J. Geophys. Res. B: Solid Earth* 109, B01301. <http://dx.doi.org/10.1029/2002JB002359>.
- Matoš, B., Tomljenović, B., Trenc, N., 2014. Identification of tectonically active areas using DEM: a quantitative morphometric analysis of Mt. Medvednica, NW Croatia. *Geol. Q.* 58, 1–19. <http://dx.doi.org/10.7306/gq.1130>.
- Mauffret, A., Frizon de Lamotte, D., Lallemand, S., Gorini, C., Maillard, A., 2004. E–W opening of the Algerian Basin (Western Mediterranean). *Terra Nova* 16, 257–264. <http://dx.doi.org/10.1111/j.1365-3121.2004.00559.x>.

- McClusky, S., Reilinger, R., Mahmoud, S., Ben Sari, D., Tealeb, A., 2003. GPS constraints on Africa (Nubia) and Arabia plate motions. *Geophys. J. Int.* 155, 126–138. <http://dx.doi.org/10.1046/j.1365-246X.2003.02023.x>.
- Meijninger, B.M.L., Vissers, R.L.M., 2006. Miocene extensional basin development in the Betic Cordillera, SE Spain revealed through analysis of the Alhama de Murcia and Crevillente Faults. *Basin Res.* 18, 547–571. <http://dx.doi.org/10.1111/j.1365-2117.2006.00308.x>.
- Menéndez, I., Silva, P.G., Martín-Betancor, M., Pérez-Torrado, F.J., Guillou, H., Scaillet, S., 2008. Fluvial dissection, isostatic uplift, and geomorphological evolution of volcanic islands (Gran Canaria, Canary Islands, Spain). *Geomorphology* 102, 189–203. <http://dx.doi.org/10.1016/j.geomorph.2007.06.022>.
- Montenat, C., Ott d'Estevou, P., Delort, T., 1990. Le Bassin de Lorca. In: *Les bassins Neogènes du Domaine Betique Oriental (Espagne)*. In: Montenat (Ed.), Documents et Travaux. IGAL, Paris, pp. 261–280.
- Ohmori, H., 1993. Changes in the hypsometric curve through mountain building resulting from concurrent tectonics and denudation. *Geomorphology* 8, 263–277.
- Ollier, C.D., 1981. *Tectonics and Landforms*. Longman, Harlow (England).
- Ortuño, M., Masana, E., García-Meléndez, E., Martínez-Díaz, J.J., Stepánciková, P., Cunha, P.P., Sohbati, R., Canora, C., Buylaert, J.P., Murray, A.S., 2012. An exceptionally long paleoseismic record of a slow-moving fault: the Alhama de Murcia fault (Eastern Betic Shear Zone, Spain). *Geol. Soc. Am. Bull.* 124 (9–10), 1474–1494. <http://dx.doi.org/10.1130/B30558.1>.
- Osmdunsen, P.T., Redfield, T.F., Hendriks, B.H.W., Bergh, S., Hansen, J.A., Henderson, I.H.C., Dehls, J., Lauknes, T.R., Larsen, Y., Anda, E., Davidsen, B., 2010. Fault-controlled alpine topography in Norway. *J. Geol. Soc.* 167, 83–98. <http://dx.doi.org/10.1144/0016-76492009-019>.
- Pedraza, A., Pérez-Peña, J.V., Galindo-Zaldívar, J., Azañón, J.M., Azor, A., 2009. Testing the sensitivity of geomorphic indices in areas of low-rate active folding (eastern Betic Cordillera, Spain). *Geomorphology* 105, 218–231. <http://dx.doi.org/10.1016/j.geomorph.2008.09.026>.
- Pérez-Peña, J.V., Azañón, J.M., Azor, A., 2009a. CalHypso: an ArcGIS extension to calculate hypsometric curves and their statistical moments. Applications to drainage basin analysis in SE Spain. *Comput. Geosci.* 35, 1214–1223. <http://dx.doi.org/10.1016/j.cageo.2008.06.006>.
- Pérez-Peña, J.V., Azañón, J.M., Azor, A., Delgado, J., González-Lodeiro, F., 2009b. Spatial analysis of stream power using GIS: SLk anomaly maps. *Earth Surf. Process. Landf.* 34, 16–25. <http://dx.doi.org/10.1002/esp>.
- Pérez-Peña, J., Azor, A., Azañón, J., Keller, E., 2010. Active tectonics in the Sierra Nevada (Betic Cordillera, SE Spain): insights from geomorphic indexes and drainage pattern analysis. *Geomorphology* 119, 74–87. <http://dx.doi.org/10.1016/j.geomorph.2010.02.020>.
- Perron, J.T., Royden, L., 2013. An integral approach to bedrock river profile analysis. *Earth Surf. Process. Landf.* 38, 570–576. <http://dx.doi.org/10.1002/esp.3302>.
- Platt, J.P., Anczkiewicz, R., Soto, J.J., Kelley, S.P., Thirlwall, M., 2006. Early Miocene continental subduction and rapid exhumation in the western Mediterranean. *Geology* 34, 981. <http://dx.doi.org/10.1130/G22801A.1>.
- Reinhardt, L.J., Bishop, P., Hoey, T.B., Dempster, T.J., Sanderson, D.C.W., 2007. Quantification of the transient response to base-level fall in a small mountain catchment: Sierra Nevada, southern Spain. *J. Geophys. Res. Earth Surf.* 112, F03S05.
- Rockwell, T.K., Keller, E.A., Johnson, D.L., 1984. Tectonic geomorphology of alluvial fans and mountain fronts near Ventura, California. In: Morisawa, M., Hack, T.J. (Eds.), *Geomorphology*. State University of New York, Binghamton, pp. 183–207.
- Scotti, V.N., Molin, P., Faccenna, C., Soligo, M., Casas-Sainz, A., 2014. The influence of surface and tectonic processes on landscape evolution of the Iberian Chain (Spain): quantitative geomorphological analysis and geochronology. *Geomorphology* 206, 37–57. <http://dx.doi.org/10.1016/j.geomorph.2013.09.017>.
- Seeber, L., Gornitz, V., 1983. River profiles along the Himalayan arc as indicators of active tectonics. *Tectonophysics* 92, 335–367.
- Silva, P.G., 1994. *Evolución geodinámica de la Depresión del Guadalentín desde el Mioceno Superior hasta la actualidad: Neotectónica y Geomorfología* (Doctoral Thesis). Universidad Complutense de Madrid, Madrid.
- Silva, P.G., Harvey, A.M., Zazo, C., Goy, J.L., 1992. Geomorphology, depositional style and morphometric relationships of Quaternary alluvial fans in the Guadalentín Depression (Murcia, southeast Spain). *Z. Geomorphol.* 36, 325–341.
- Silva, P.G., Goy, J.L., Zazo, C., Lario, J., Bardají, T., 1997. Paleoseismic indications along 'aseismic' fault segments in the Guadalentín Depression (SE Spain). *J. Geodyn.* 24, 105–115.
- Silva, P.G., Goy, J.L., Zazo, C., Bardají, T., 2003. Fault-generated mountain fronts in southeast Spain: geomorphologic assessment of tectonic and seismic activity. *Geomorphology* 50, 203–225. [http://dx.doi.org/10.1016/S0169-555X\(02\)00215-5](http://dx.doi.org/10.1016/S0169-555X(02)00215-5).
- Snyder, N.P., Whipple, K.X., Tucker, G.E., Merritts, D.J., 2002. Interactions between onshore bedrock-channel incision and nearshore wave-base erosion forced by eustasy and tectonics. *Basin research* 14, 105–127.
- Snyder, N.P., Whipple, K.X., Tucker, G.E., Merritts, D.J., 2003. Channel response to tectonic forcing: field analysis of stream morphology and hydrology in the Mendocino triple junction region, northern California. *Geomorphology* 53, 97–127.
- Stein, R.S., King, G.C.P., Rundle, J.B., 1988. The growth of geological structures by repeated earthquakes: 2. field examples of continental dip-slip faults. *J. Geophys. Res.* 93, 13,319–13,331.
- Strahler, A.N., 1952. Hypsometric (area-altitude) analysis of erosional topography. *Geol. Soc. Am. Bull.* 63, 1117–1142.
- Sylvester, A.G., 1988. Strike-slip faults. *Geol. Soc. Am. Bull.* 100, 1666–1703. [http://dx.doi.org/10.1130/0016-7606\(1988\)100<1666:SSF>2.3.CO;2](http://dx.doi.org/10.1130/0016-7606(1988)100<1666:SSF>2.3.CO;2).
- Troiani, F., Della Seta, M., 2008. The use of the stream length–gradient index in morphotectonic analysis of small catchments: a case study from Central Italy. *Geomorphology* 102, 159–168. <http://dx.doi.org/10.1016/j.geomorph.2007.06.020>.
- Vissers, R.L.M., Meijninger, B.M.L., 2011. The 11 May 2011 earthquake at Lorca (SE Spain) viewed in a structural-tectonic context. *Solid Earth* 2, 199–204. <http://dx.doi.org/10.5194/se-2-199-2011>.
- Walker, R., Jackson, J., 2002. Offset and evolution of the Gowk fault, S.E. Iran: a major intra-continental strike-slip system. *J. Struct. Geol.* 24, 1677–1698. [http://dx.doi.org/10.1016/S0191-8141\(01\)00170-5](http://dx.doi.org/10.1016/S0191-8141(01)00170-5).
- Weijermars, R., Roep, T.B., Van den Eckhout, B., Postma, G., Kleverlaan, K., 1985. Uplift history of a Betic fold nappe inferred from Neogene–Quaternary sedimentation and tectonics (in the Sierra Alhamilla and Almería, Sorbas and Tabernas Basins of the Betic Cordilleras, SE Spain). *Geol. Mijnb.* 64, 397–411.
- Whipple, K.X., DiBiase, R.A., Crosby, B.T., 2013. Bedrock rivers. In: Shroder, J.F. (Ed.), *Treatise on Geomorphology*. Elsevier, Poland, pp. 550–573.
- Whittaker, A.C., Cowie, P.A., Attal, M., Tucker, G.E., Roberts, G., 2007. Bedrock channel adjustment to tectonic forcing: implications for predicting river incision rates. *Geology* 35, 103–106. <http://dx.doi.org/10.1130/G23106A.1>.
- Willgoose, G., Hancock, G., 1998. Revisiting the hypsometric curve as an indicator of form and process in transport-limited catchment. *Earth Surf. Process. Landf.* 23, 611–623.
- Wobus, C., Whipple, K.X., Kirby, E., Synder, N., Johnson, J., Spyropolou, K., Crosby, B., Sheehan, D., 2006. Tectonics from topography: procedures, promise, and pitfalls. In: Willett, S.D., Hovius, N., Brandon, M.T., Fisher, D.M. (Eds.), *Tectonics, Climate and Landscape Evolution*. Geology Society of America Special Papers, pp. 55–74.

Annex 3. Codi CHannel OFfset (CHOF)


```

clear all
close all

% ChannelOffsets
% This script measures 3D channel offsets by calculating the piercing
line based on the drainage network obtained automatically. After
finding the intersection between the fault and the piercing line
(piercing point), it calculates the distance.
%
% Marta Ferrater Gómez, 6th of march 2015

%% Import the digital elevation model
% The file has to be in a .txt. format

% Import the DEM
DEM=GRIDobj();

% Filling sinks in the DEM to avoid problems when creating the
drainage network
DEMf=fillsinks(DEM);
figure;
imagesc(DEMf);

% The user is asked the cell size of the DEM
fprintf(1, 'write the cell size of the model \n');
cellsize(1,1)=input('cell_size =');

% Creation of the hillshade
hs=hillshade(DEMf);
hs_simple=hs.Z;
figure;
imagesc(hs_simple);
title('Hillshade');
colormap(gray)
axis equal;

%% Fault definition and drawing

% The user is asked to define two points of the vertical fault
fprintf(1, 'click two points to define the strike of the fault\n');

% The cursor appears in the figure to allow the user to click twice on
it in order to obtain X and Y
[X,Y] = ginput(2);

falla(1,1)=X(1,1);
falla(1,2)=Y(1,1);
falla(1,3)=100;
falla(2,1)=X(2,1);
falla(2,2)=Y(2,1);
falla(2,3)=falla(1,3);

% With the defined values and a vertical vector, the fault plane is
calculated

vector=[0, 0, 1];
vector(2,1)=falla(2,1)-falla(1,1);
vector(2,2)=falla(2,2)-falla(1,2);
vector(2,3)=0;

```

```

AA=vector(2,2)*vector(1,3)-vector(1,2)*vector(2,3);
BB=-(vector(2,1)*vector(1,3)-vector(1,1)*vector(2,3));
CC=0;
DD=AA*falla(1,1)+BB*falla(1,2);

%% Creation of the drainage network
% Flow direction
FD=FLOWobj(DEMf);

% Flow accumulation
A=flowacc(FD);

% Get just the biggest streams
W=A>20000;

% Have the coordinates of all the biggest streams

[mZ,nZ] = size(A.Z);
k = 0;

for i = 1: nZ;
    for j = 1: mZ;

        if W.Z(j,i) == 1;

            k=k+1;

            S_xyz(k,1)=i*cellsize;
            S_xyz(k,2)=j*cellsize;
            S_xyz(k,3)=DEMf.Z(j,i);

            S_x(k,1)=i;
            S_y(k,1)=j;
            S_z(k,1)=DEMf.Z(j,i);

        end
    end
end

%% Choose the parts of the streams we are interested on, by selecting
the points we want to calculate the piercing line with.

% Draw the drainage network

figure;
imshow(hs_simple);
hold on;
load seamount
scatter3(S_x,S_y,S_z);
hold off;

% Draw the fault into the figure

falla_x=[falla(1,1),falla(2,1)];
falla_y=[falla(1,2),falla(2,2)];

figure;

```

```

imshow(hs_simple);
hold on;
load seamount
scatter3(S_x,S_y,S_z);
plot(falla_x,falla_y, 'r-');
hold off;

% Select the area of the stream that contains the points that are
needed to calculate each of the piercing lines in each bloc of the
fault

%Upstream
fprintf(1, 'click on lower left and upper right of the area that
contains the interesting points of the upper stream \n');

[Xup,Yup] = ginput(2);

xminup=min(Xup);
xmaxup=max(Xup);
yminup=min(Yup);
ymaxup=max(Yup);

tf_up = S_x <= xmaxup & S_x >= xminup & S_y <= ymaxup & S_y >= yminup;
up = find(tf_up);

%Upstream
fprintf(1, 'click on lower left and upper right of the area that
contains the interesting points of the downer stream \n');

[Xdown,Ydown] = ginput(2);

xmindown=min(Xdown);
xmaxdown=max(Xdown);
ymindown=min(Ydown);
ymaxdown=max(Ydown);

tf_down = S_x <= xmaxdown & S_x >= xmindown & S_y <= ymaxdown & S_y >=
ymindown;
down = find(tf_down);

% The figure shows the points used to calculate the piercing line
figure;
imshow(hs_simple);
hold on;
load seamount
scatter3(S_x(up),S_y(up),S_z(up),'b. ');
scatter3(S_x(down),S_y(down),S_z(down),'b. ');
plot(falla_x,falla_y, 'r-');
hold off;

%% Piercing line in the upper stream

[n,mx] = size(S_x(up)); [ny,my] = size(S_y(up)); [nz,mz] =
size(S_z(up));

upm = [mean(S_x(up)),mean(S_y(up)),mean(S_z(up))];
w = [S_x(up)-upm(1),S_y(up)-upm(2),S_z(up)-upm(3)]; % Use "mean" point
as base
a = (1/n)*w'*w; % 'a' is a positive definite matrix

```



```

[u,d,v] = svd(a); % 'eig' & 'svd' get same eigenvalues for this matrix
% el p és el vector per a la recta!
upp = u(:,1)'; % Get eigenvector for largest eigenvalue
s = d(2,2)+d(3,3); % Sum the other two eigenvalues

%% Intersection between the fault and the piercing line --> piercing
point
k1 = (DD-AA*upm(1,1)-BB*upm(1,2)-
CC*upm(1,3))/(AA*upp(1,1)+BB*upp(1,2)+CC*upp(1,3));

for ii=1:3

IP_up(1,ii) = upm(1,ii)+k1*upp(1,ii);

end

%% Piercing line in the downer stream

[n,mx] = size(S_x(down)); [ny,my] = size(S_y(down)); [nz,mz] =
size(S_z(down));

downm = [mean(S_x(down)),mean(S_y(down)),mean(S_z(down))];
w = [S_x(down)-downm(1),S_y(down)-downm(2),S_z(down)-downm(3)]; % Use
"mean" point as base
a = (1/n)*w'*w; % 'a' is a positive definite matrix
[u,d,v] = svd(a); % 'eig' & 'svd' get same eigenvalues for this matrix
downp = u(:,1)'; % Get eigenvector for largest eigenvalue
s = d(2,2)+d(3,3); % Sum the other two eigenvalues

%% Intersection between the fault and the piercing line --> piercing
point
k2 = (DD-AA*downm(1,1)-BB*downm(1,2)-
CC*downm(1,3))/(AA*downp(1,1)+BB*downp(1,2)+CC*downp(1,3));

for jj=1:3

IP_down(1,jj) = downm(1,jj)+k2*downp(1,jj);

end

%% Offset calculation

% 2D
Distancia_horitzontal = (sqrt ((IP_up(1,1)-
IP_down(1,1))^2+(IP_up(1,2)-IP_down(1,2))^2)).*cellsize;

% 3D
Distancia_3D = (sqrt ((IP_up(1,1)-IP_down(1,1))^2+(IP_up(1,2)-
IP_down(1,2))^2+(IP_up(1,3)-IP_down(1,3))^2)).* cellsize;

%Vertical
Distancia_vertical = (IP_up(1,3)-IP_down(1,3)).* cellsize;

```

```

% Final figure, with the piercing points, the streams and the fault

IP=[IP_up;IP_down];
m=[upm;downm];

figure;
imshow(hs_simple);
hold on;
load seamount
scatter3(S_x,S_y,S_z, 'b.');
plot(falla_x,falla_y, 'r-');
scatter(IP(:,1),IP(:,2), 'ko');
hold off;

% Write in the command line the final value
fprintf(1,'The horizontal offset is %.3f\n',Distancia_horitzontal);
fprintf(1,'The total offset is %.3f\n',Distancia_3D);
fprintf(1,'The vertical offset is %.3f\n',Distancia_vertical);

```

**Annex 4. Catàleg d'elements
geomorfològics dislocats per
l'activitat de la falla d'Alhama de
Murcia**

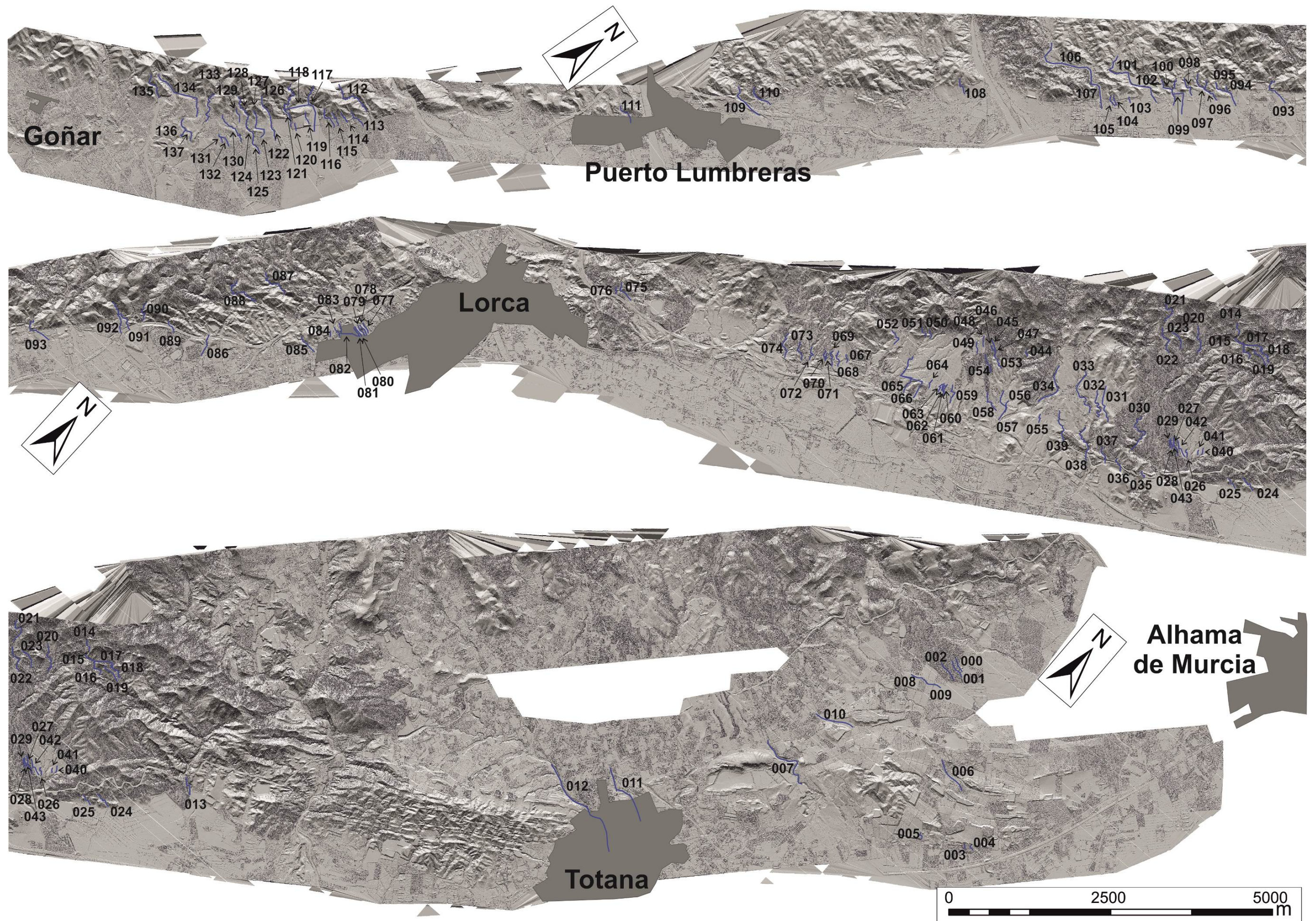
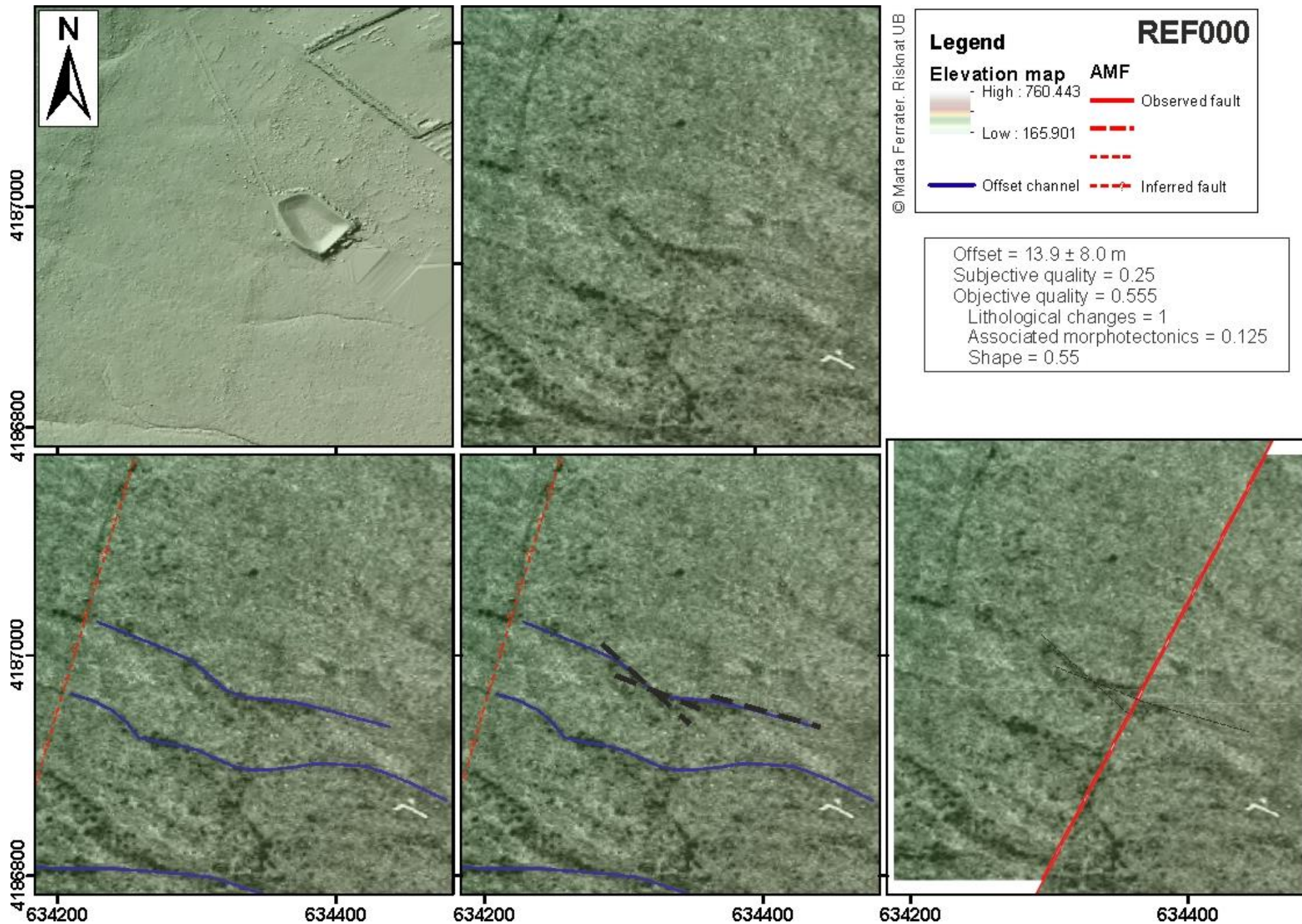
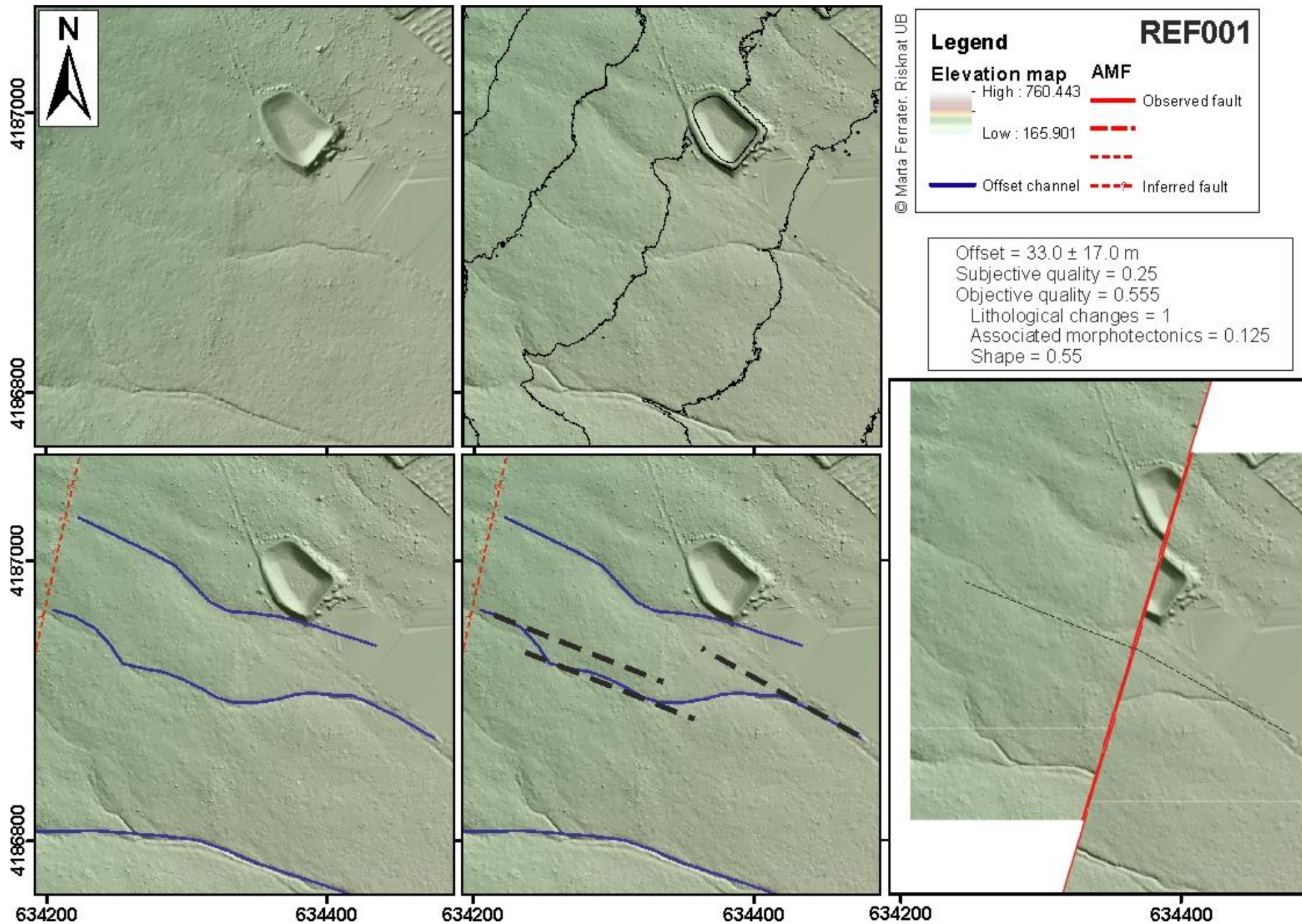
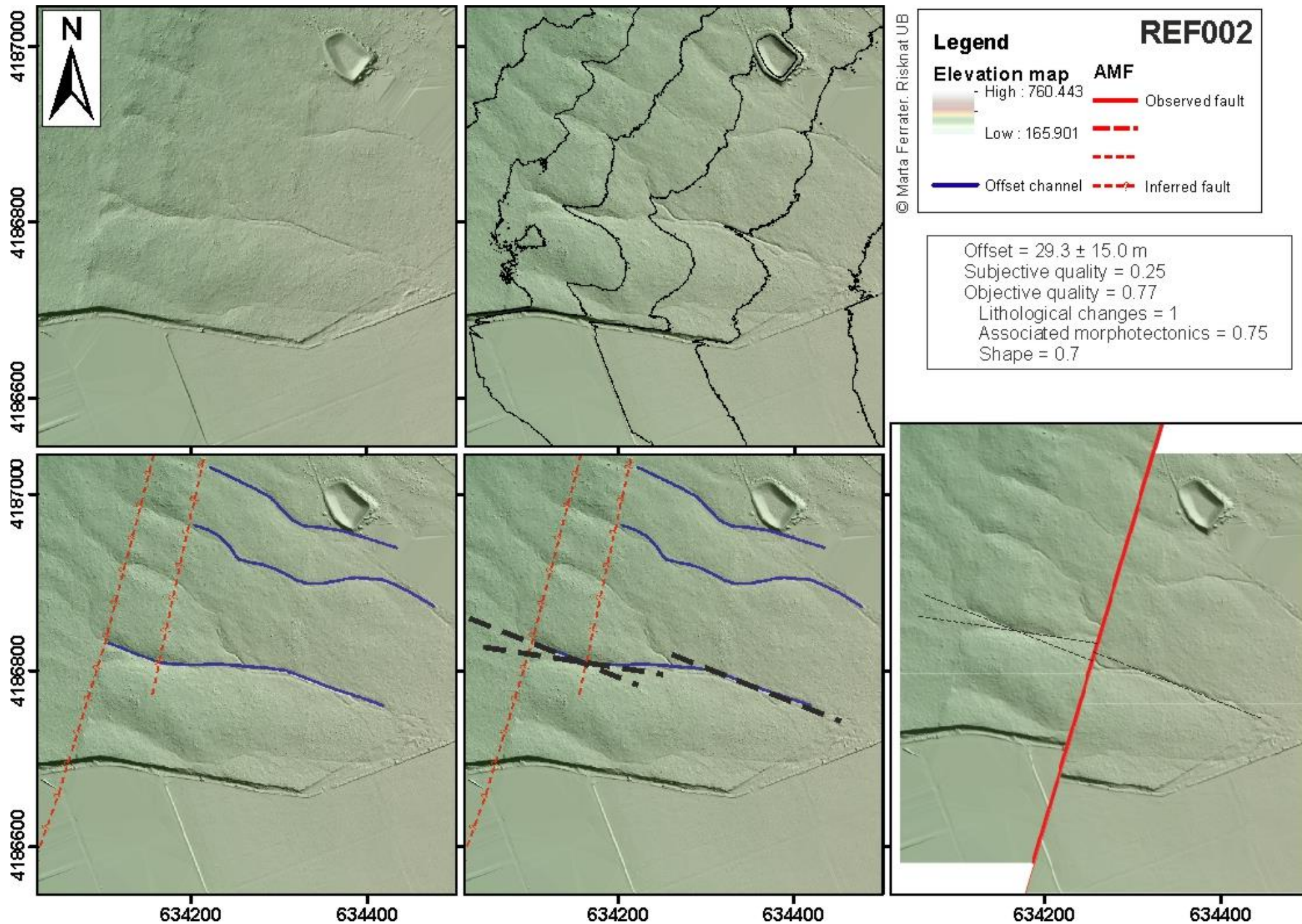
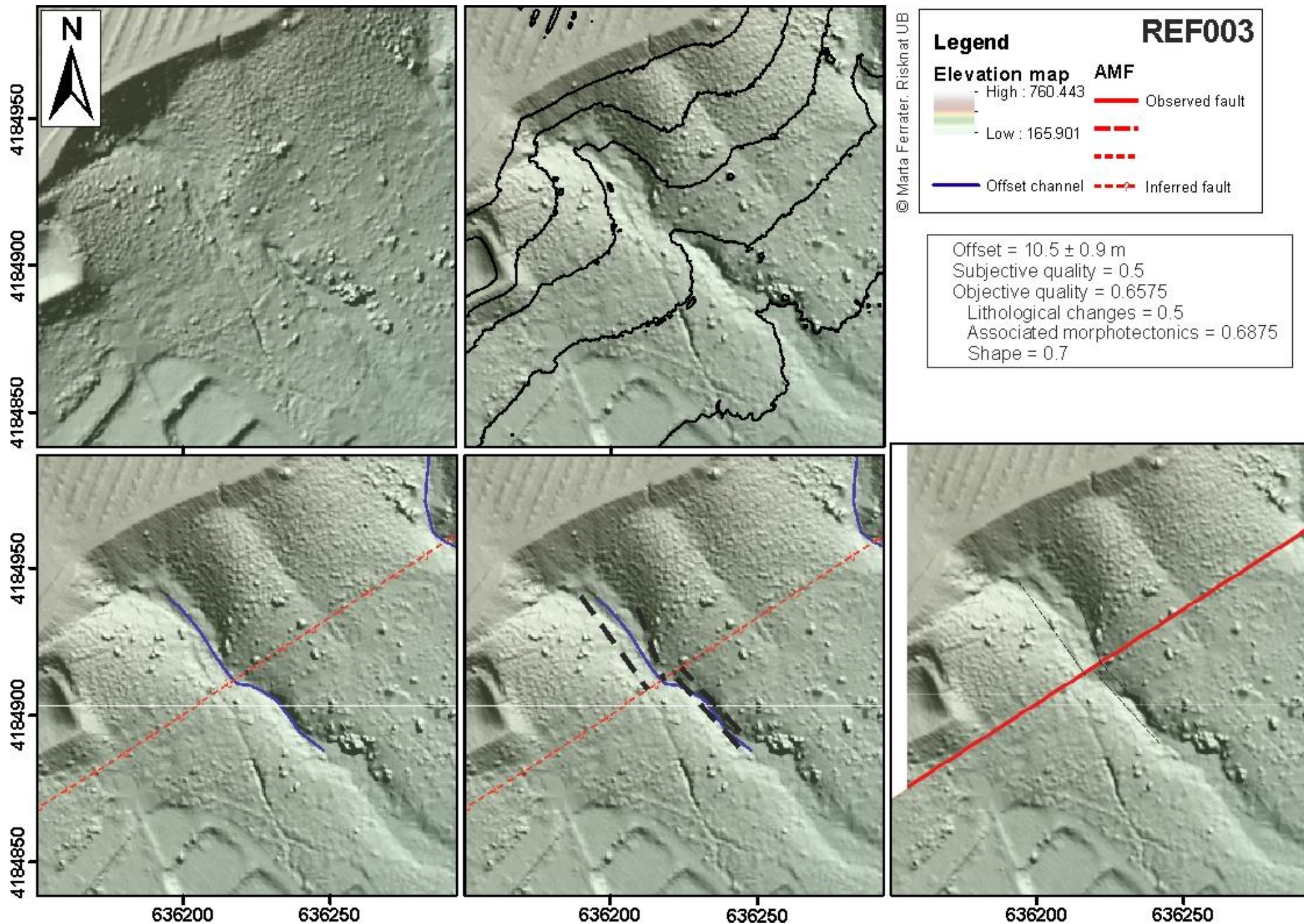


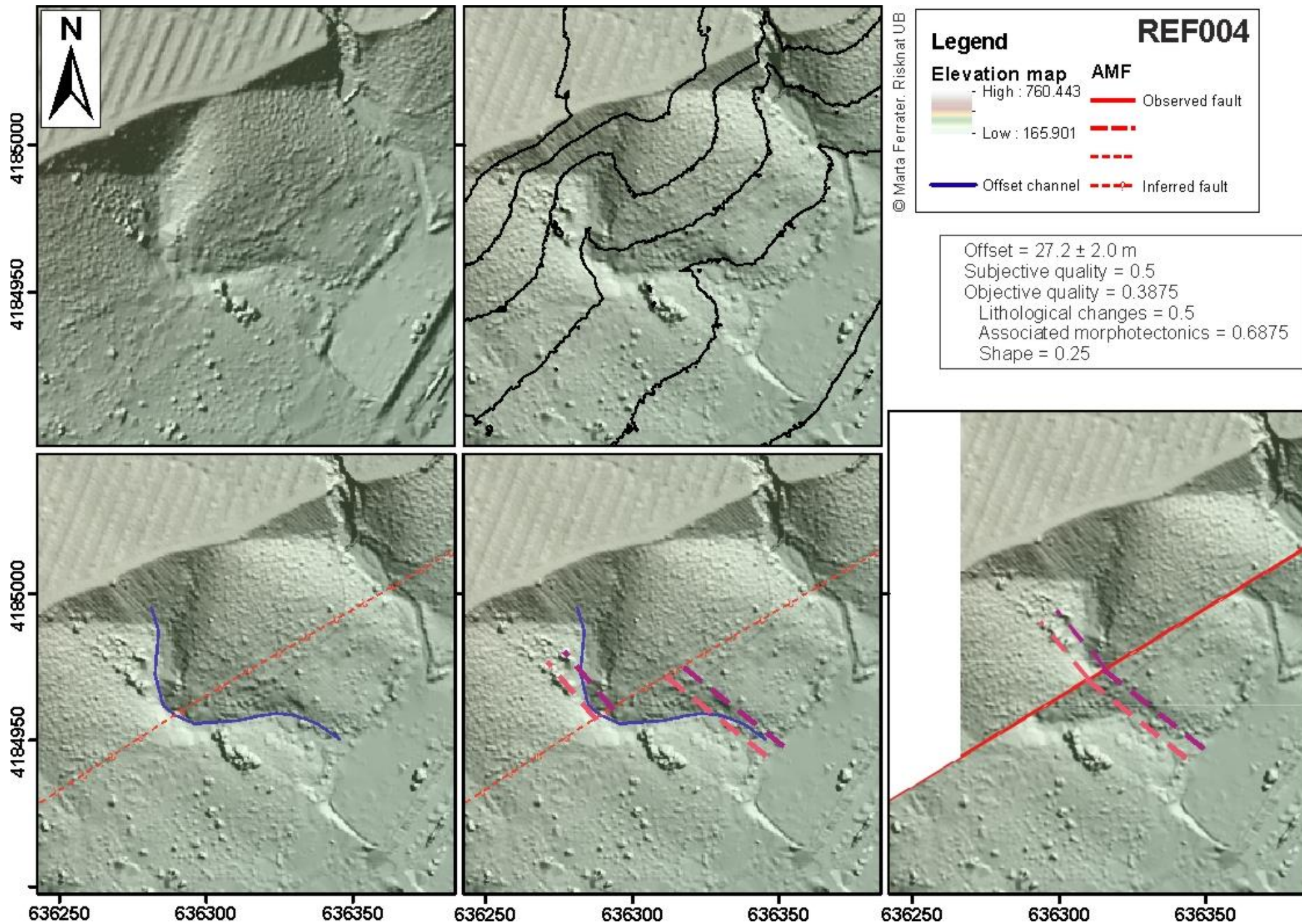
Figura i. Situació de tots els elements en superfície dislocats per l'activitat tectònica de la falla d'Alhama de Murcia

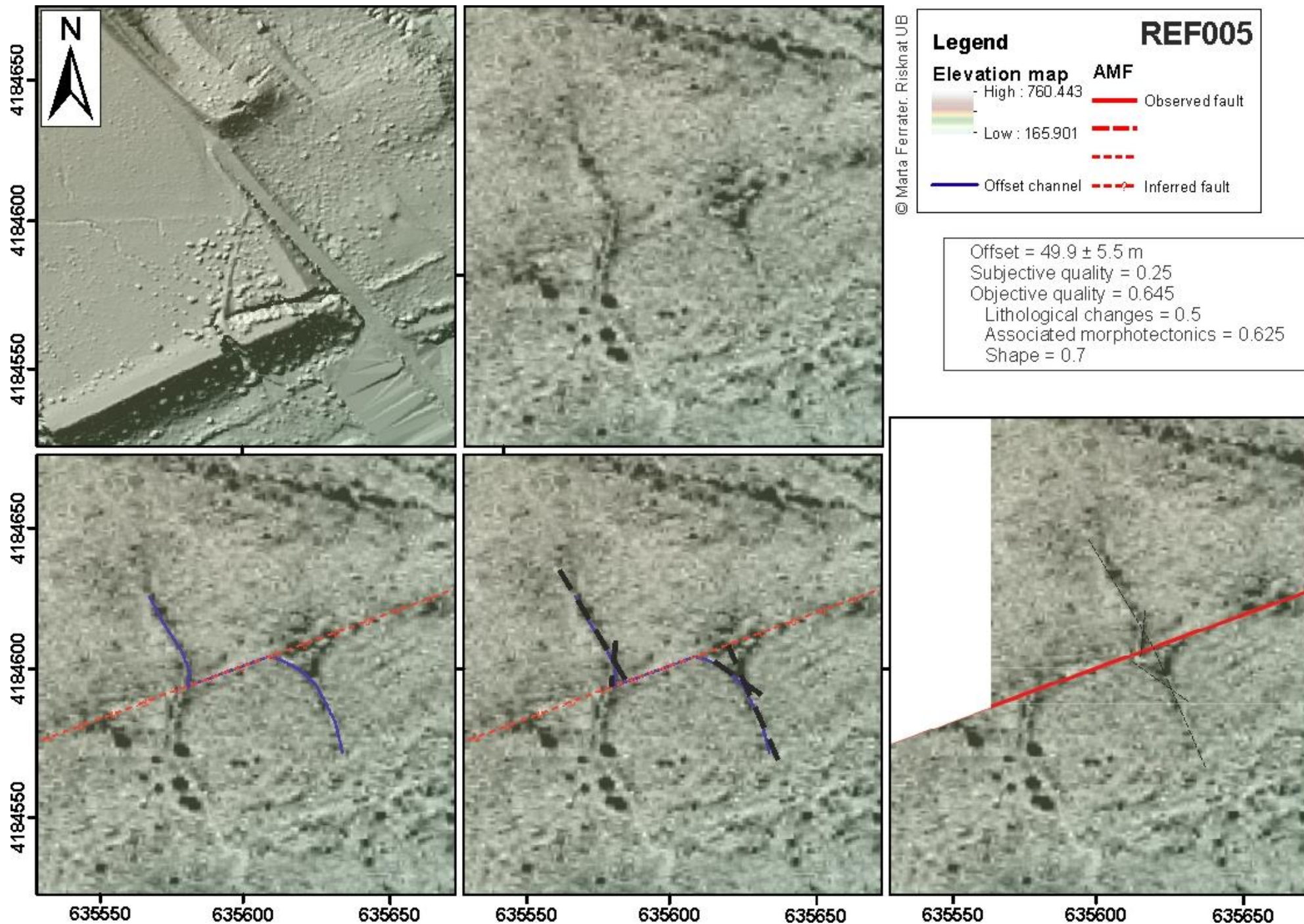


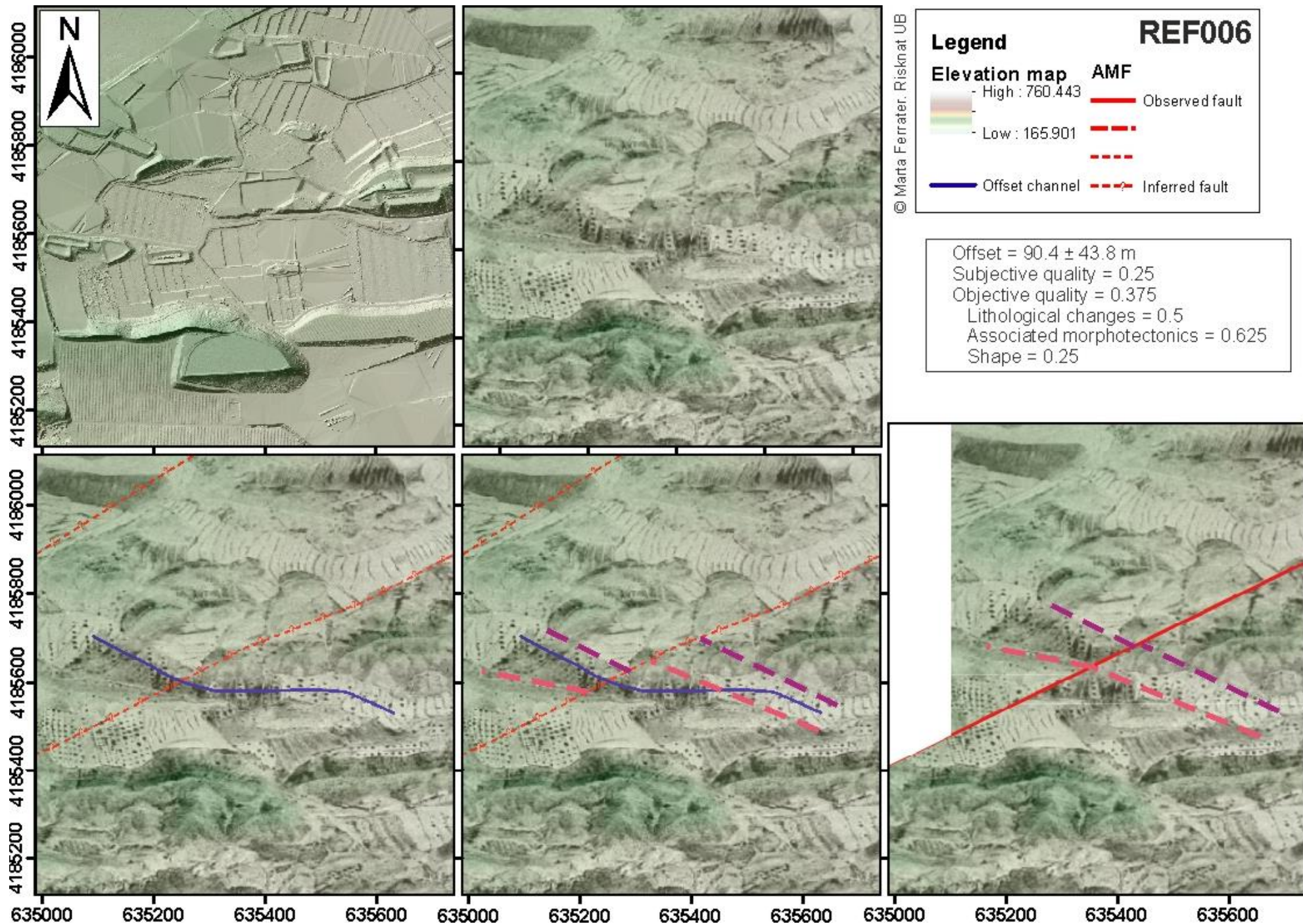


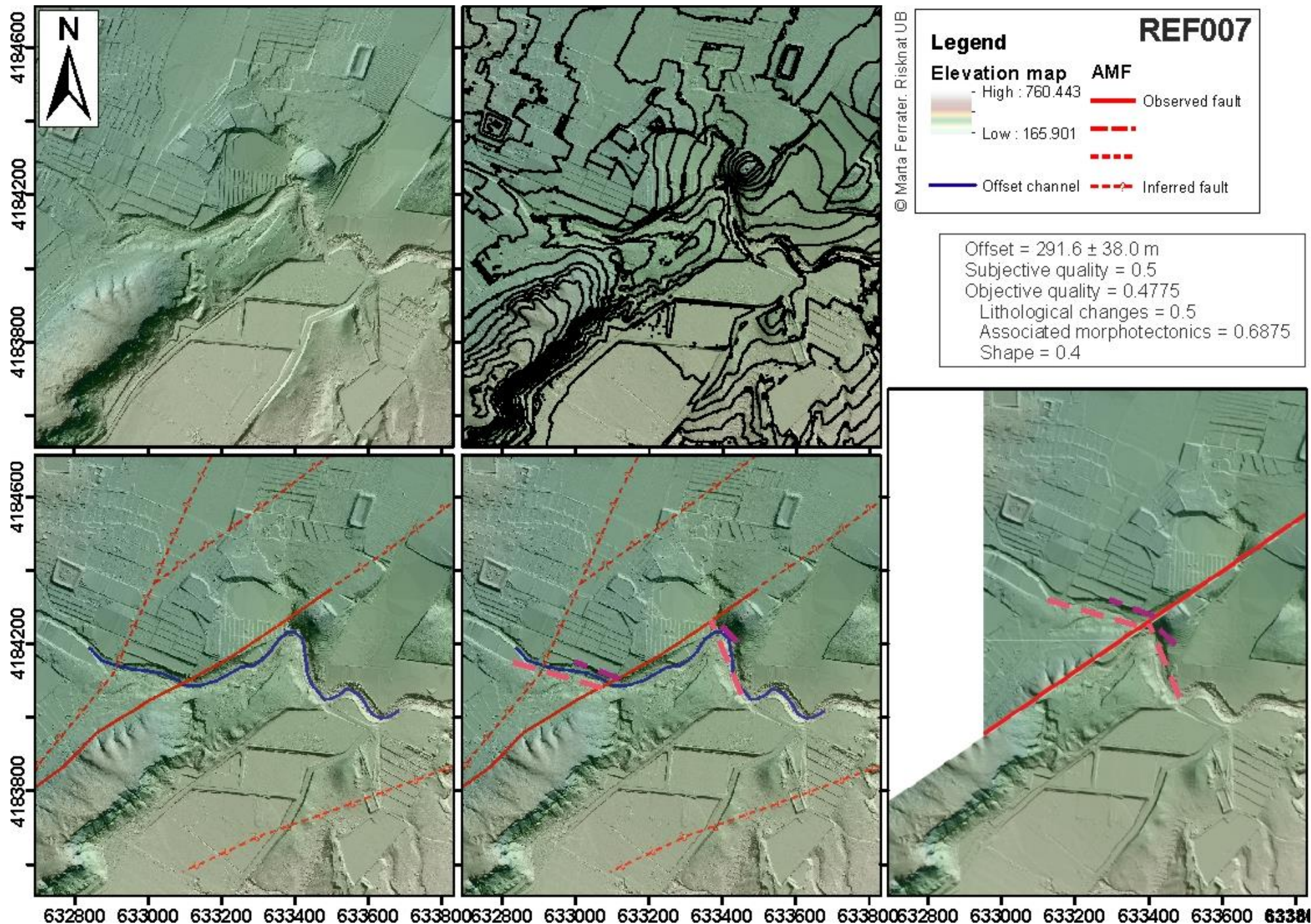


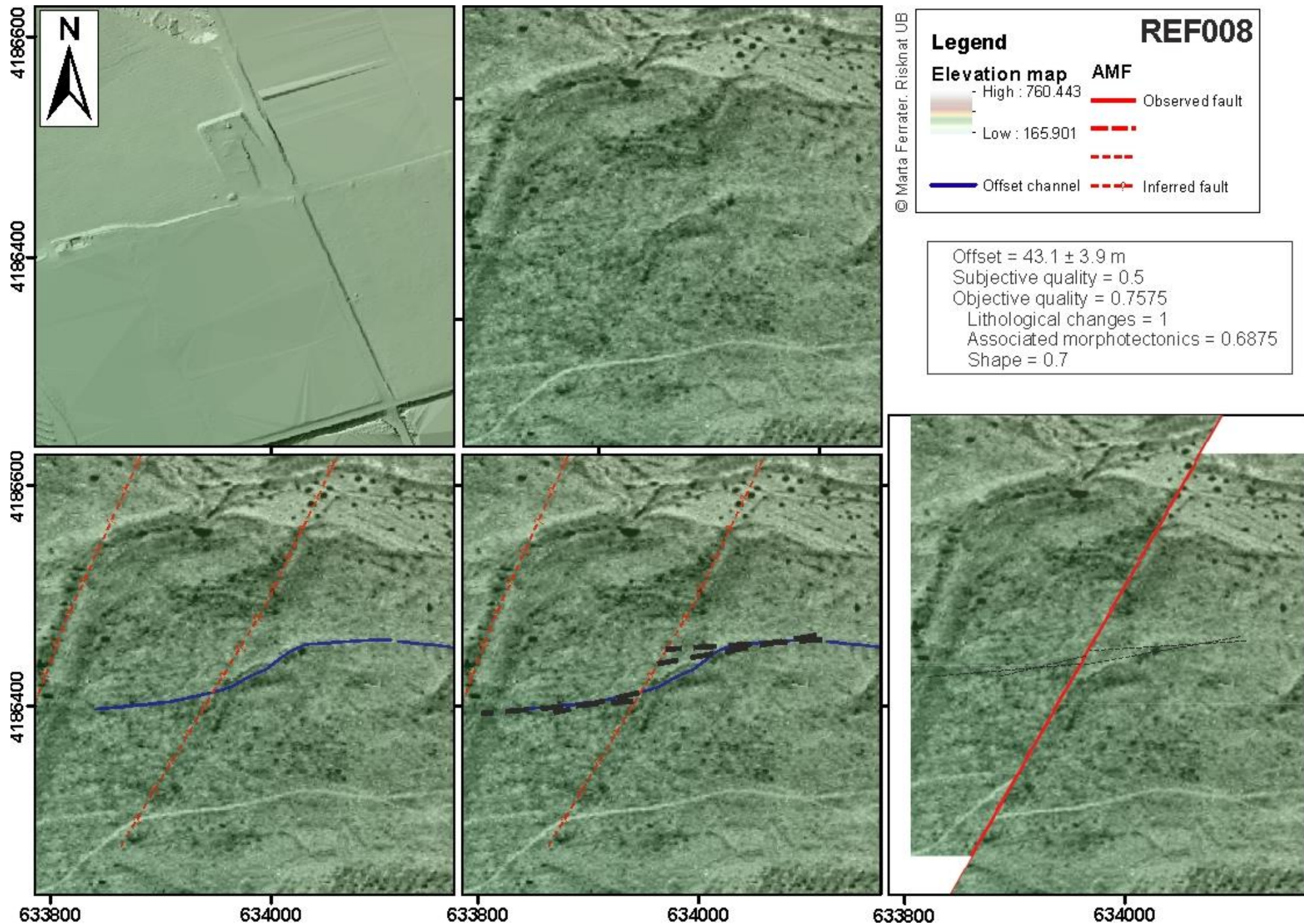


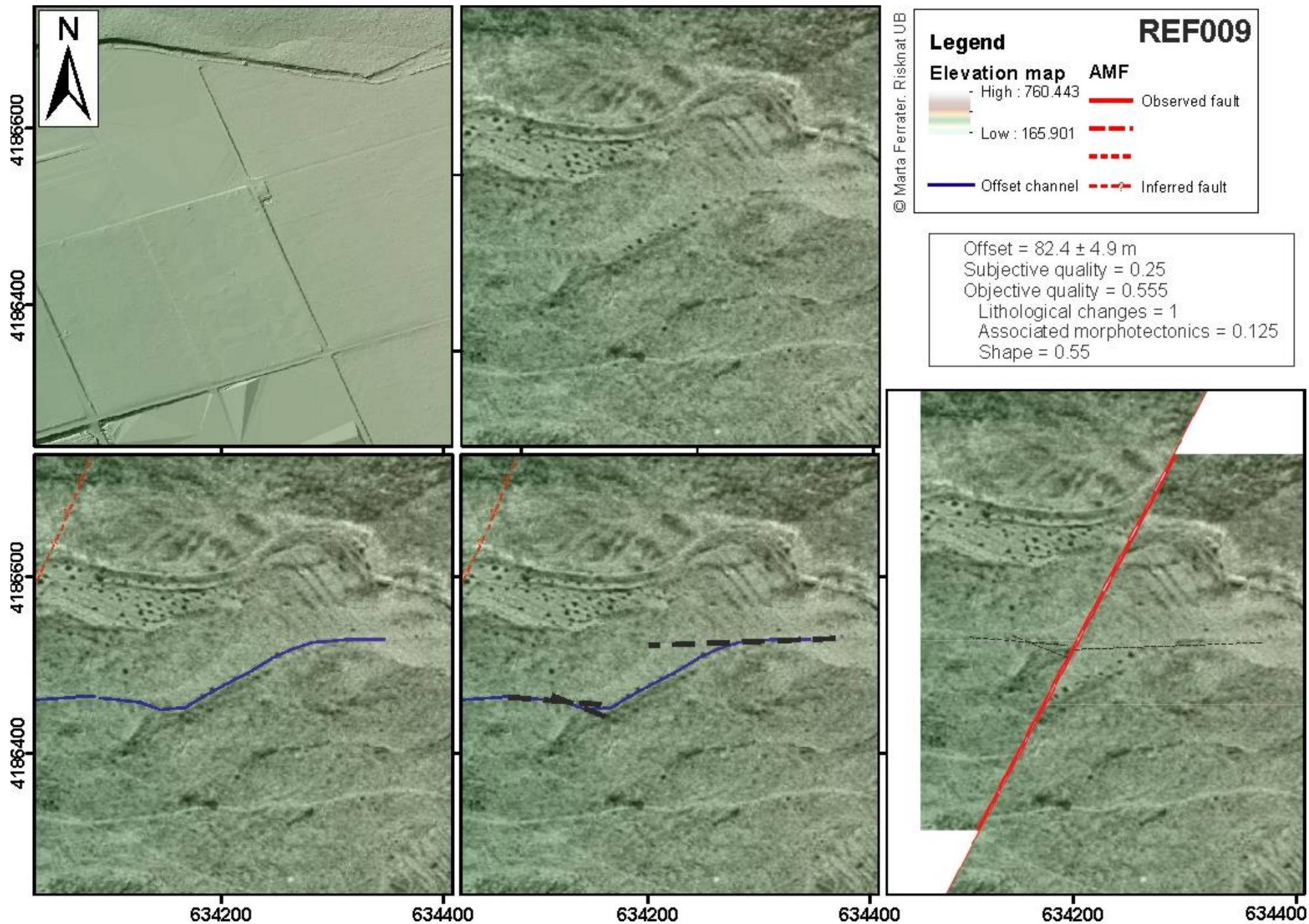


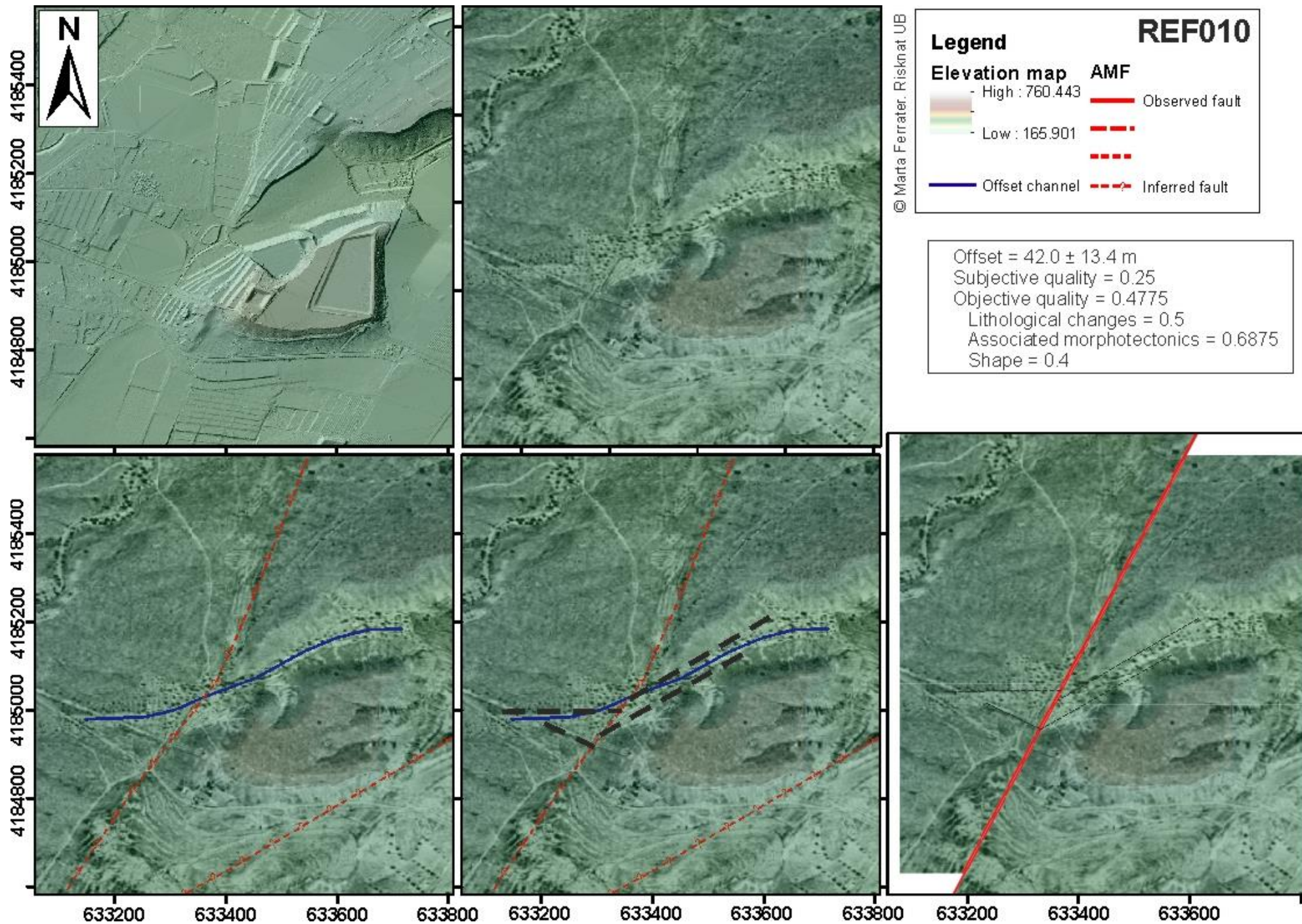


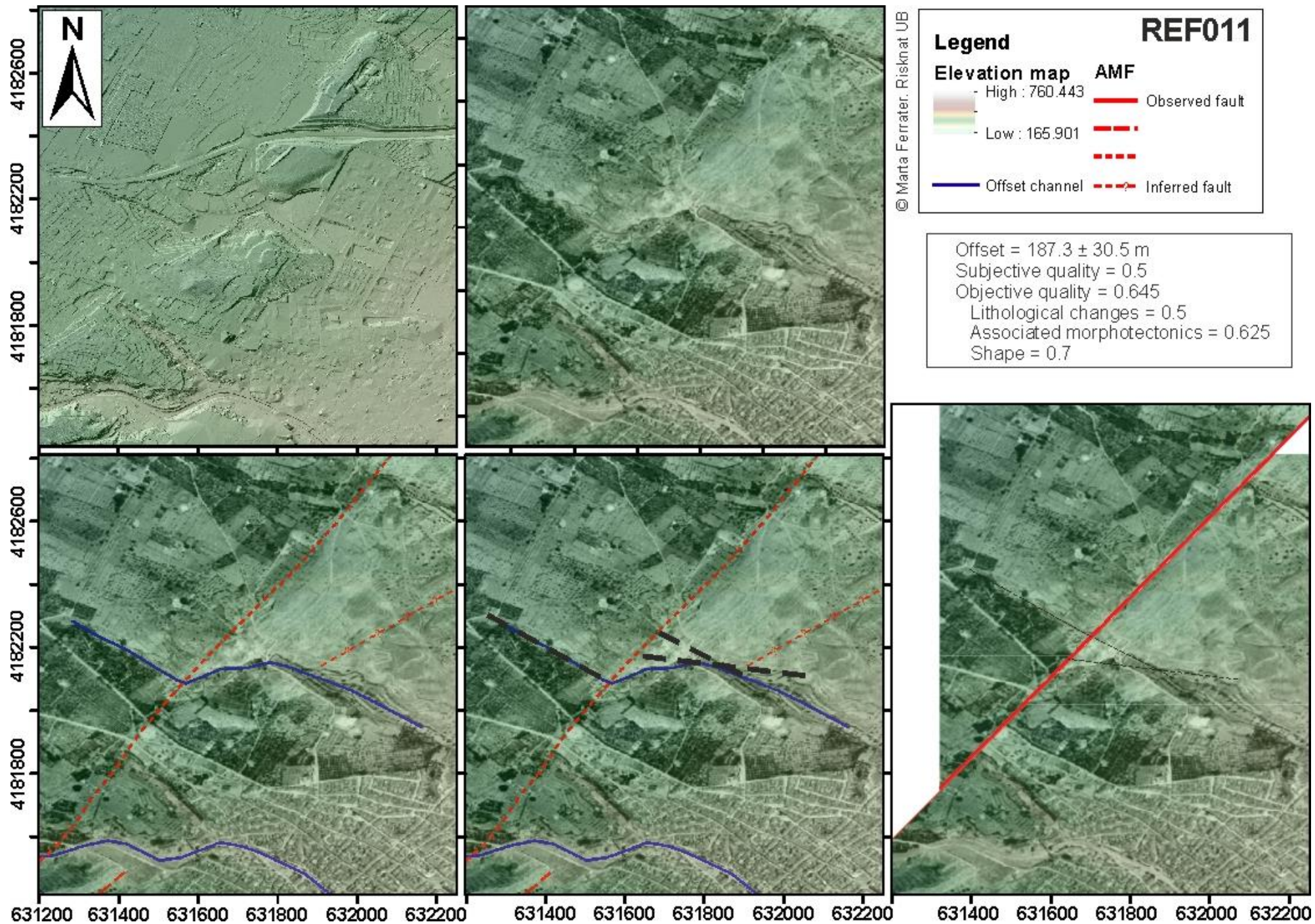


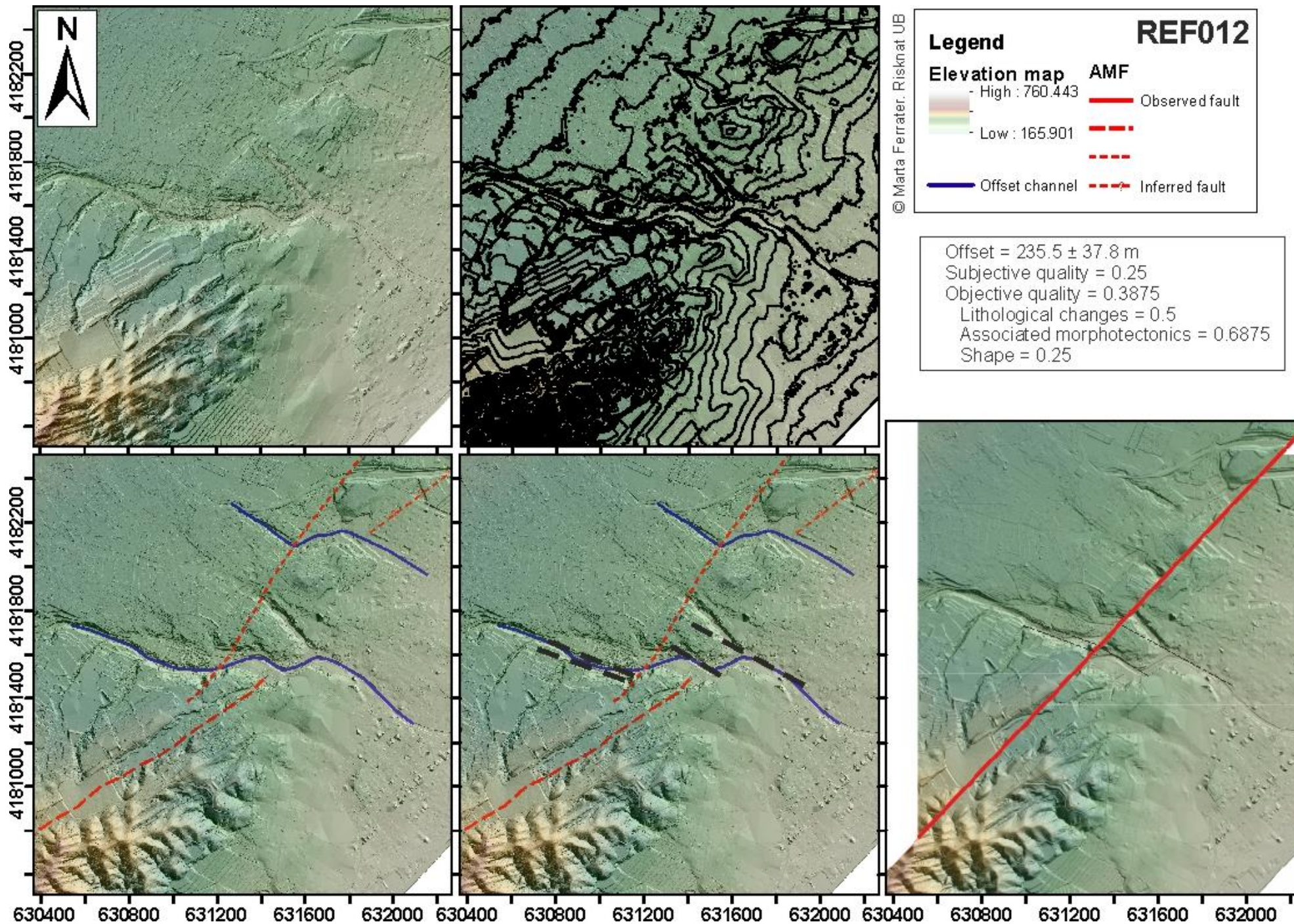


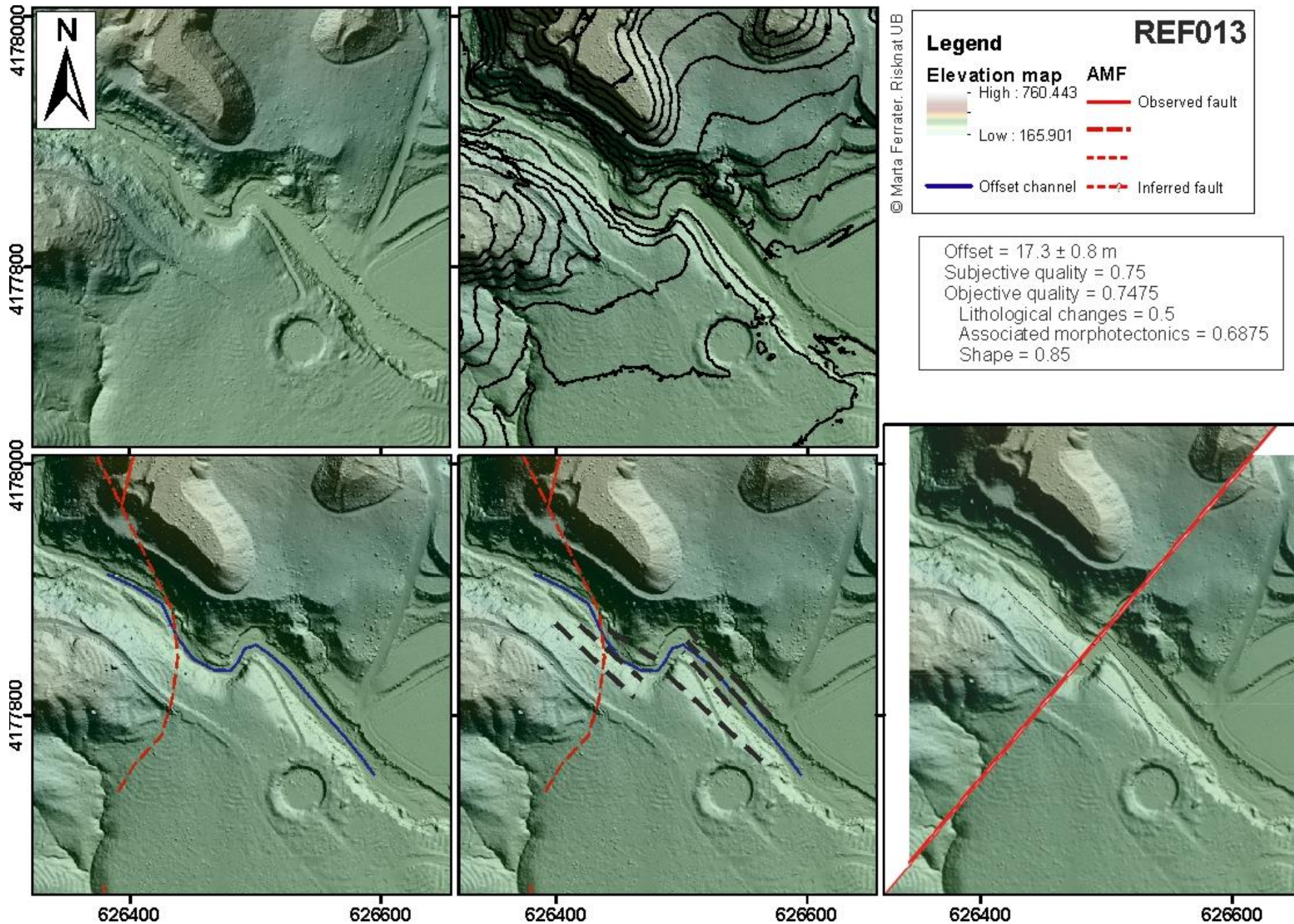


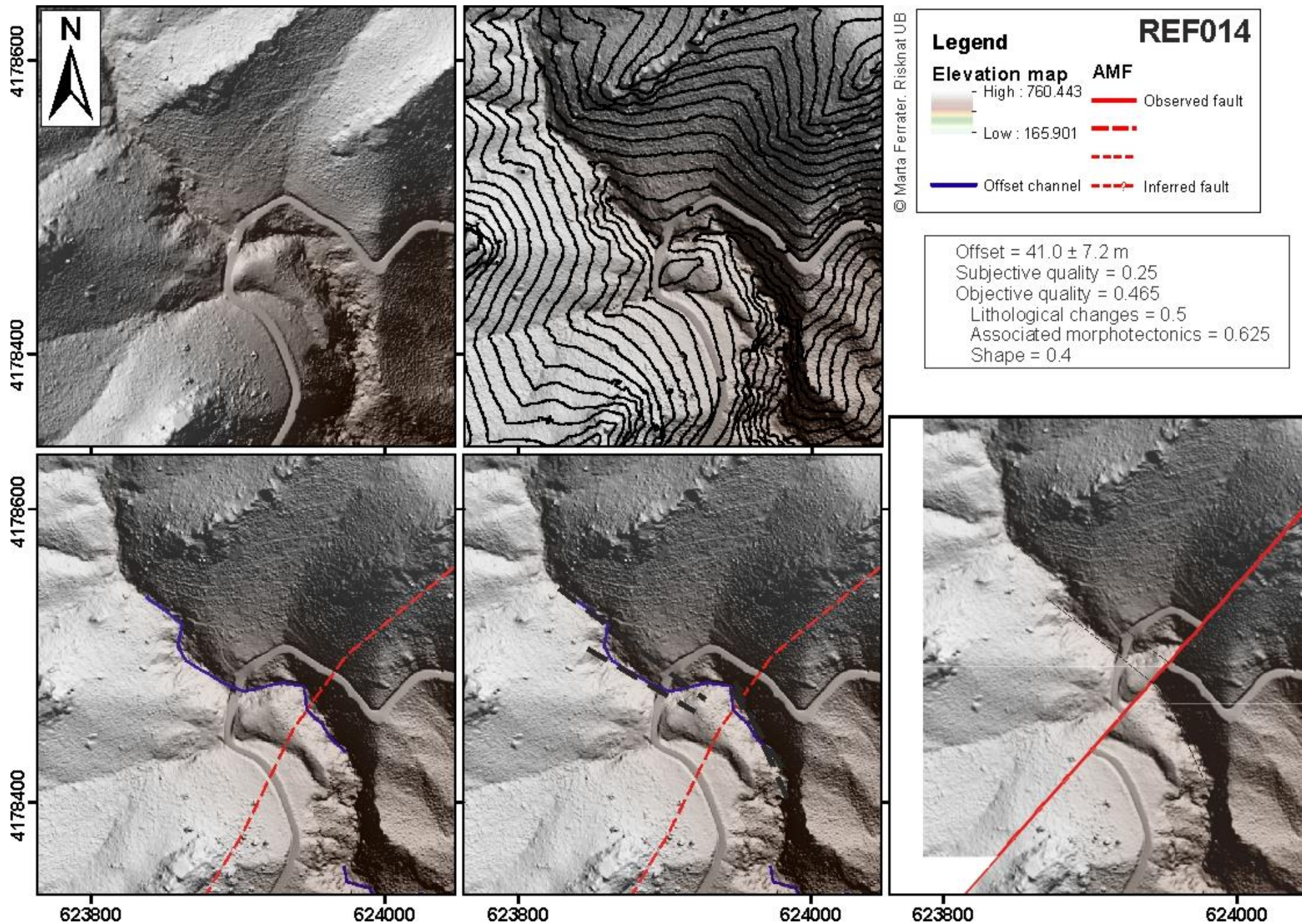


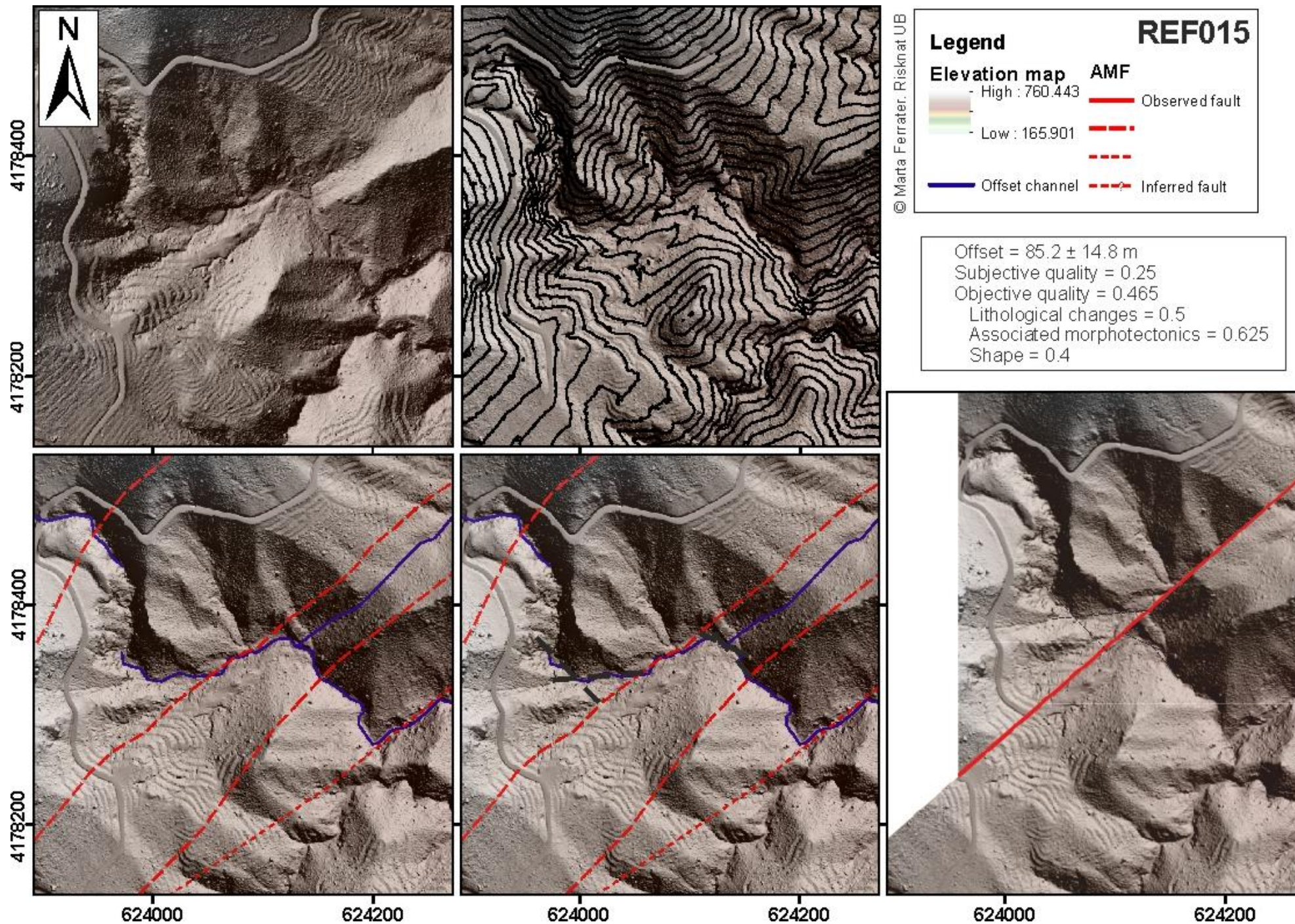


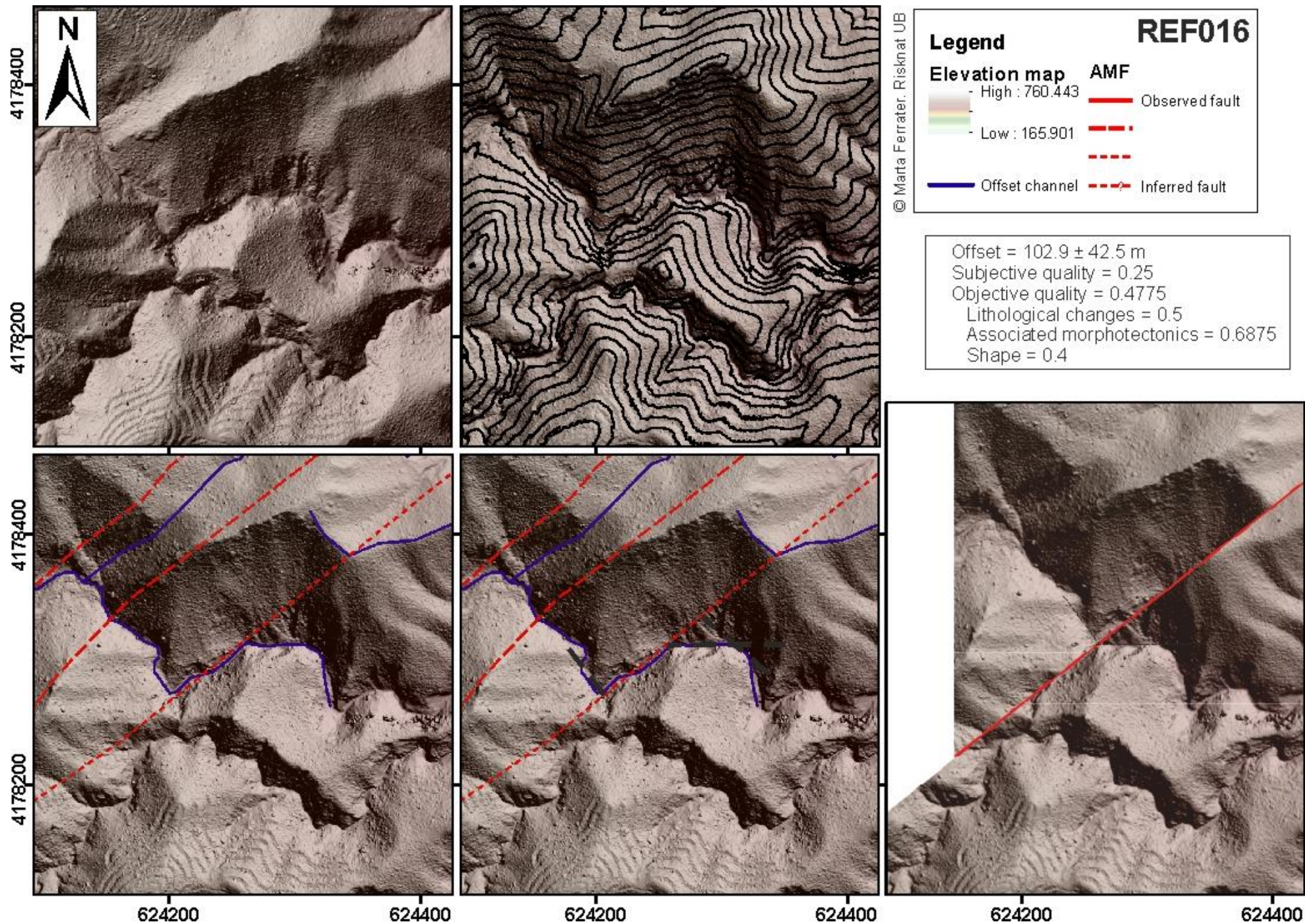


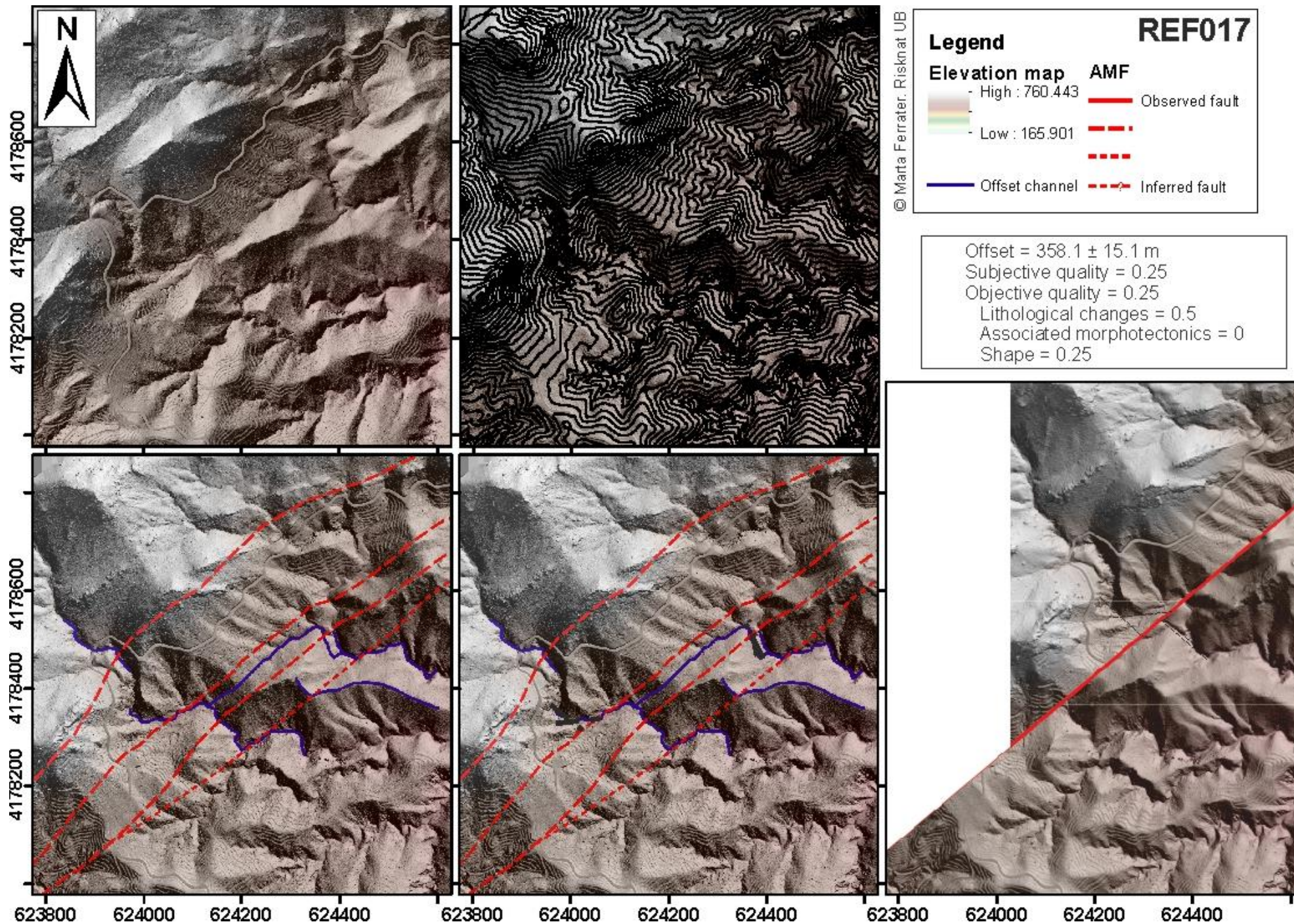


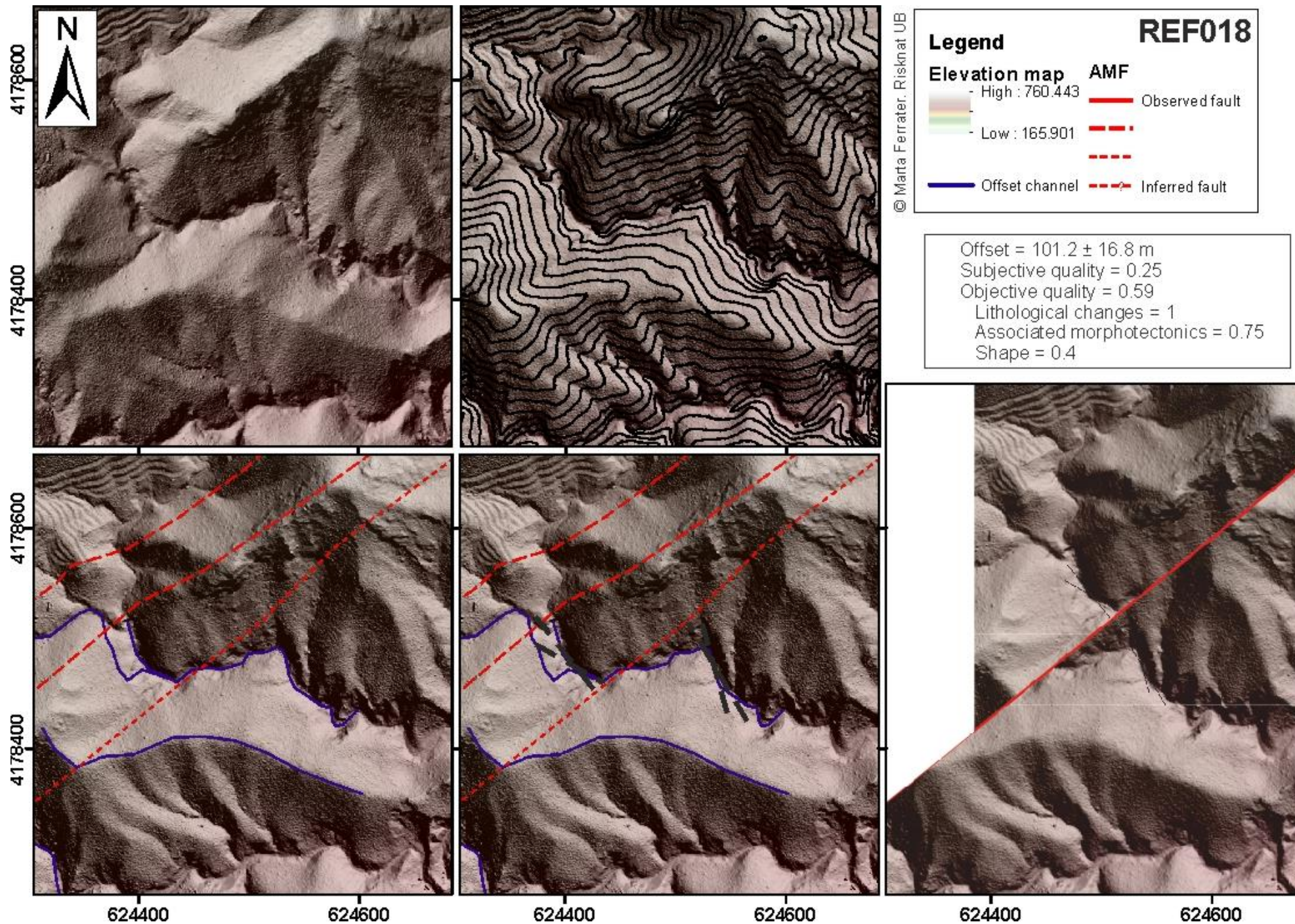


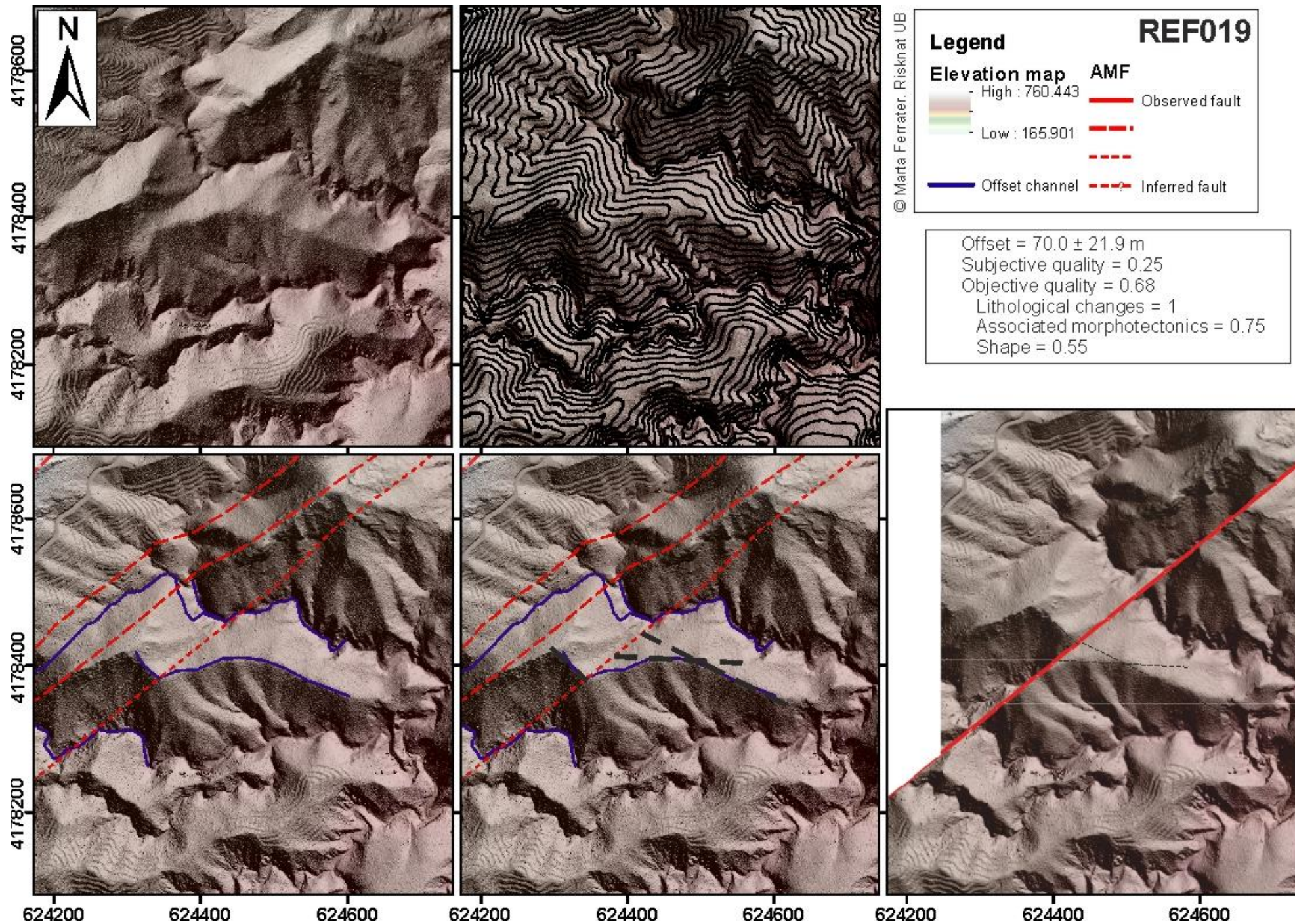


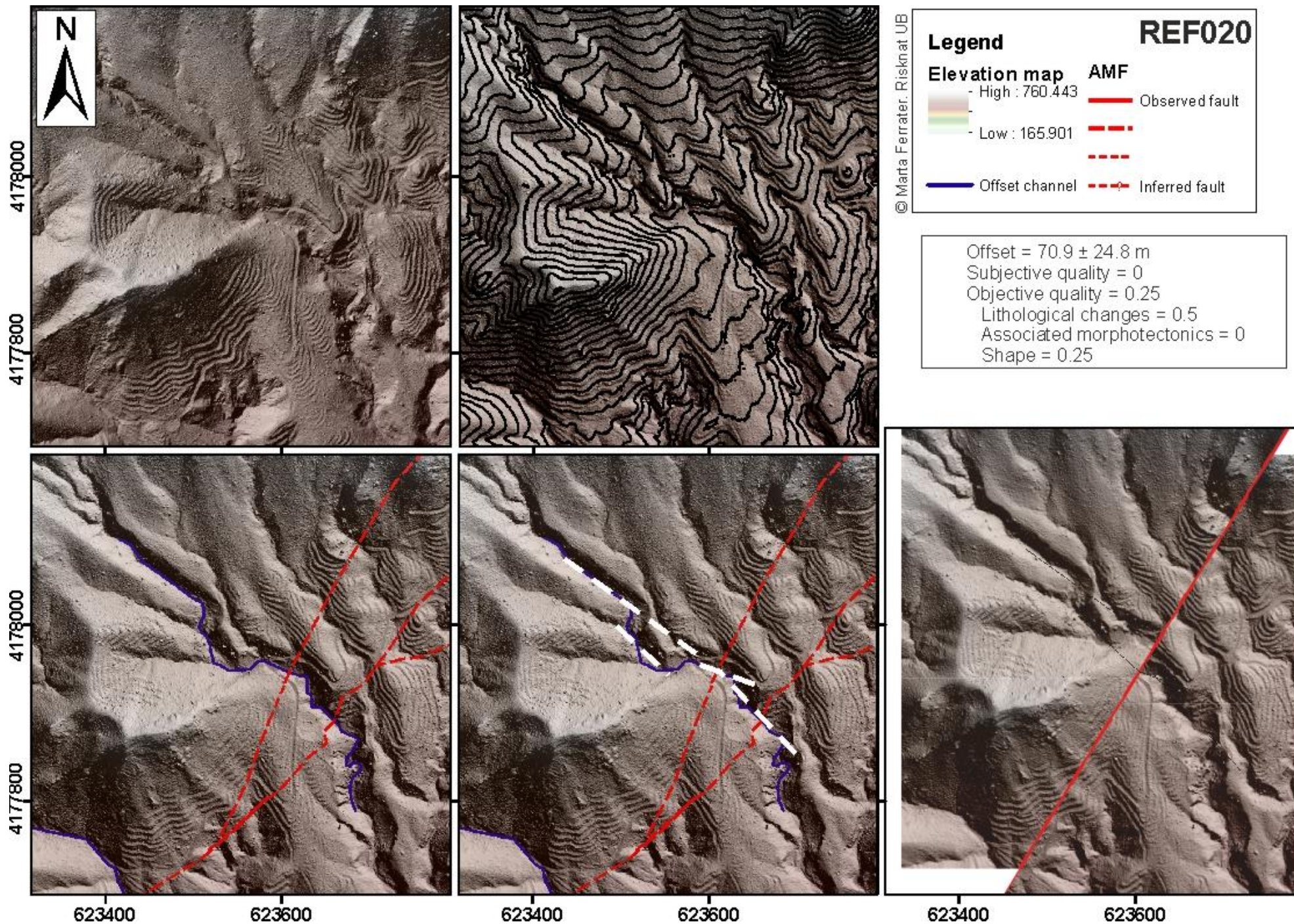


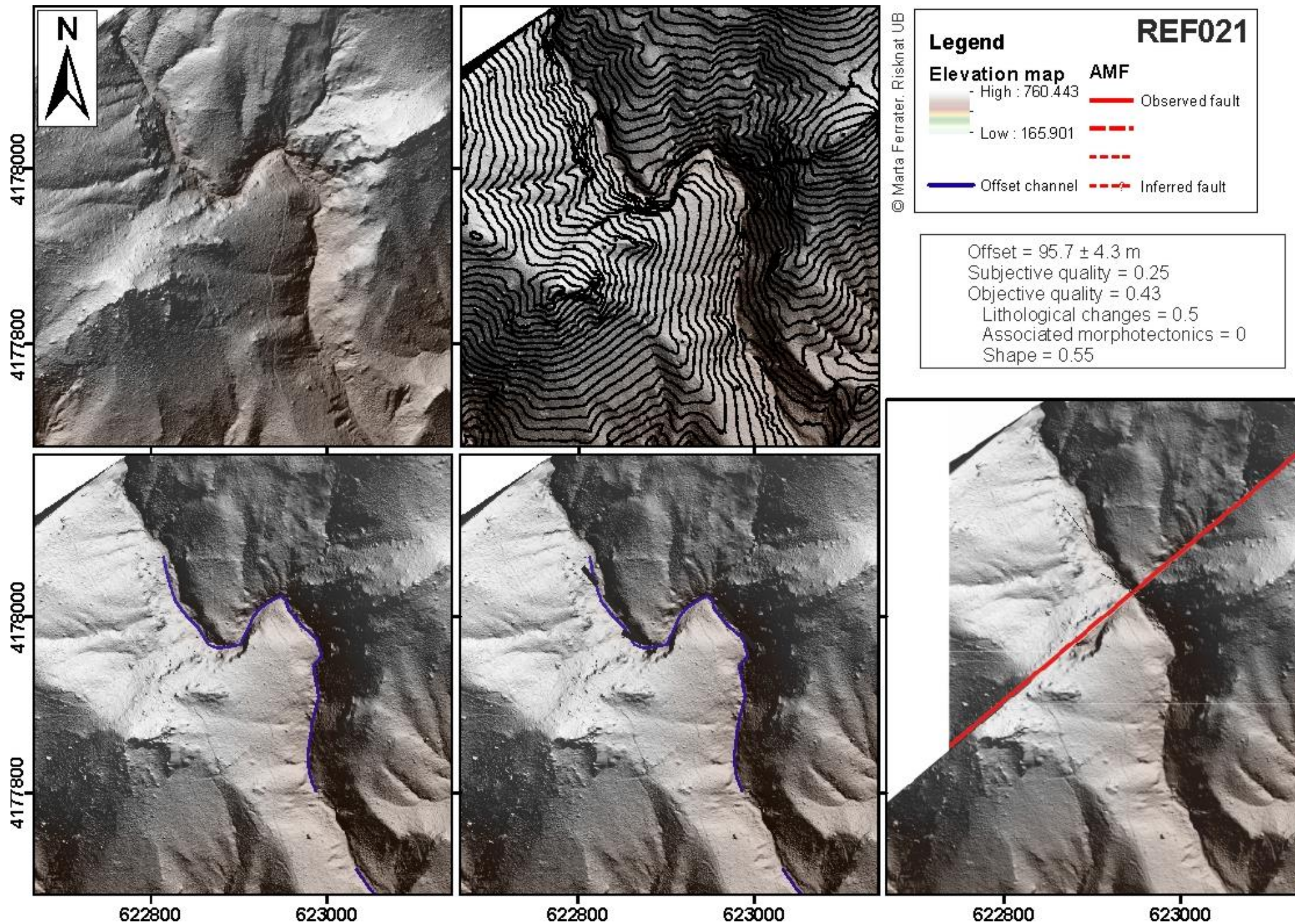


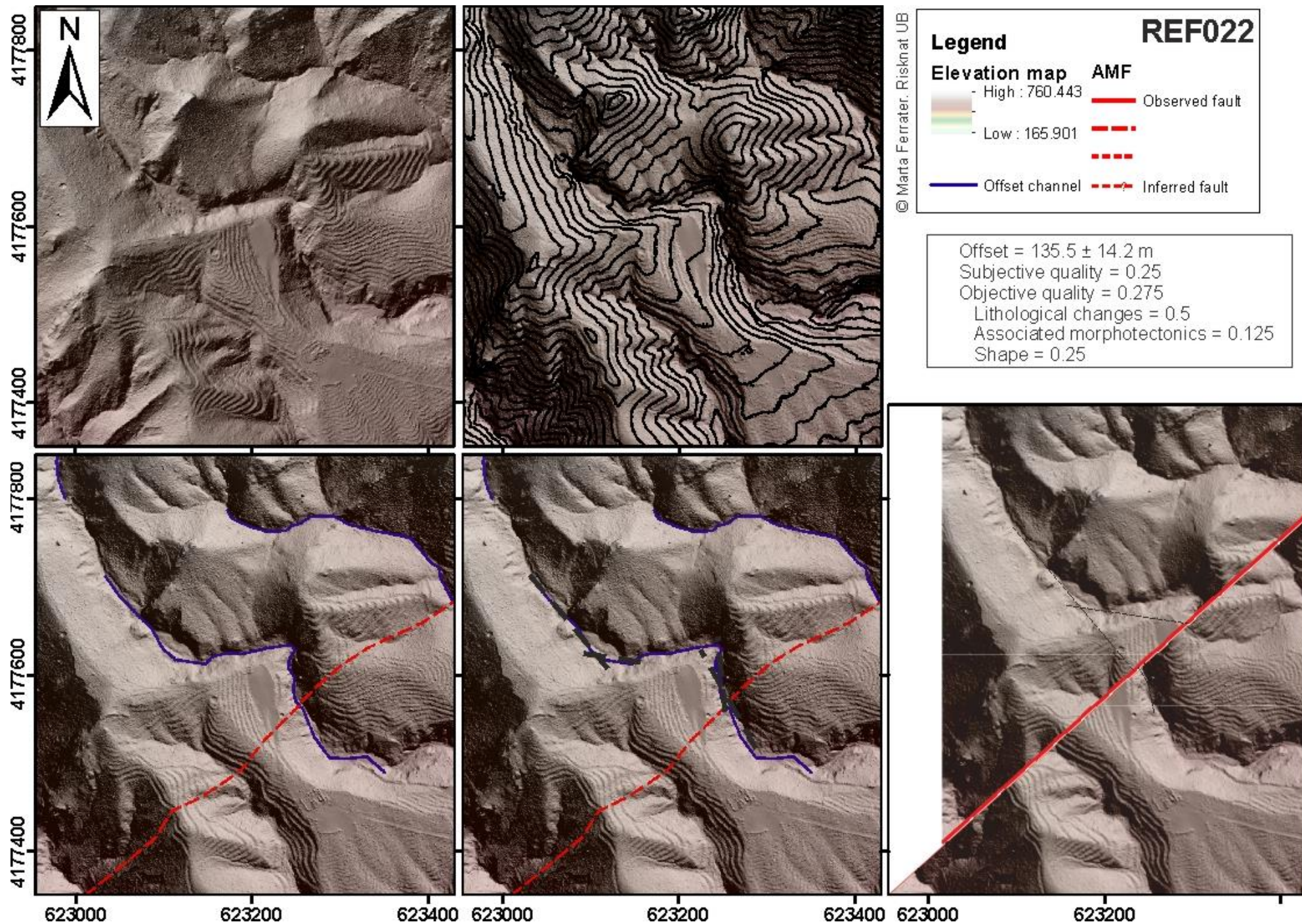


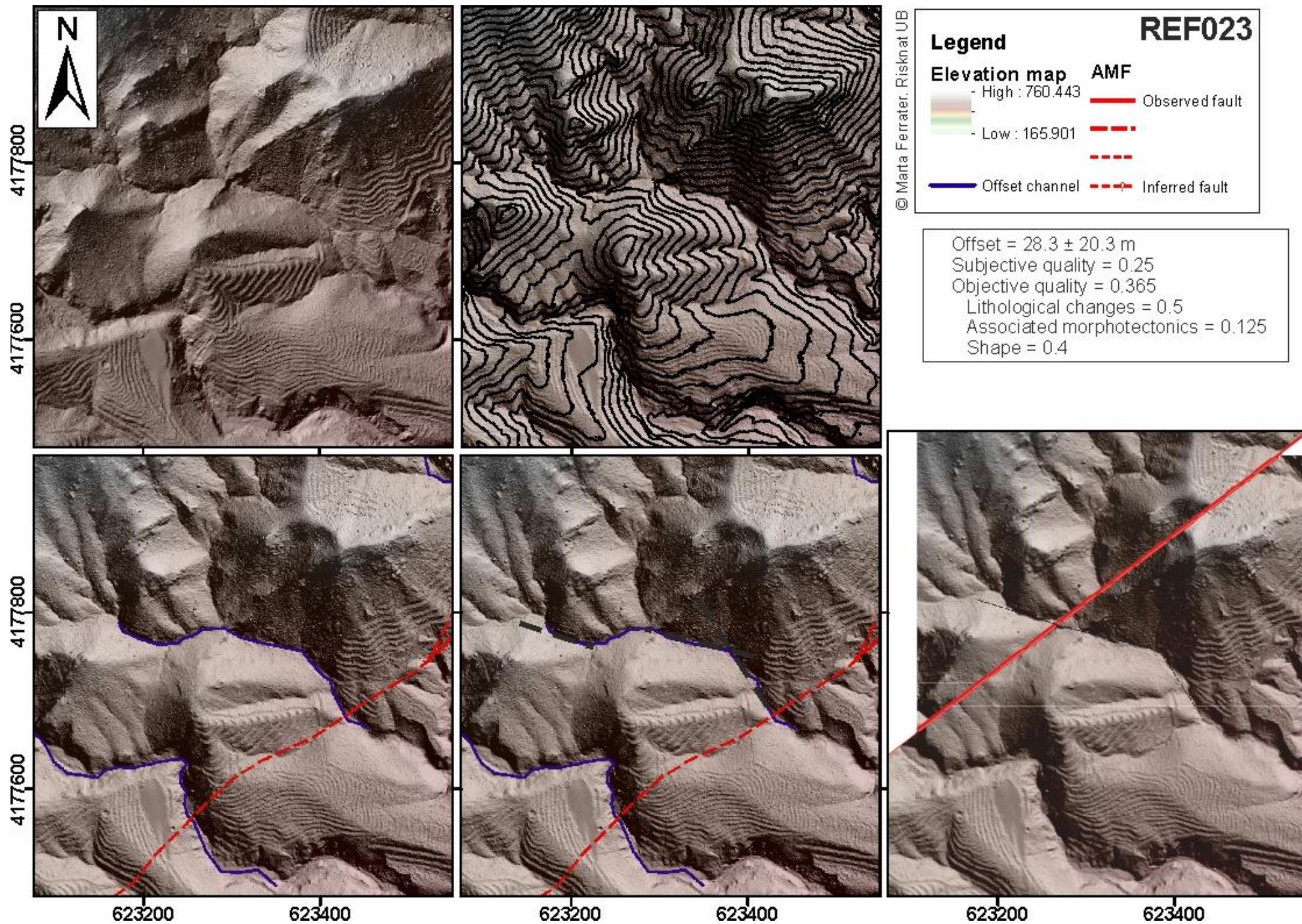


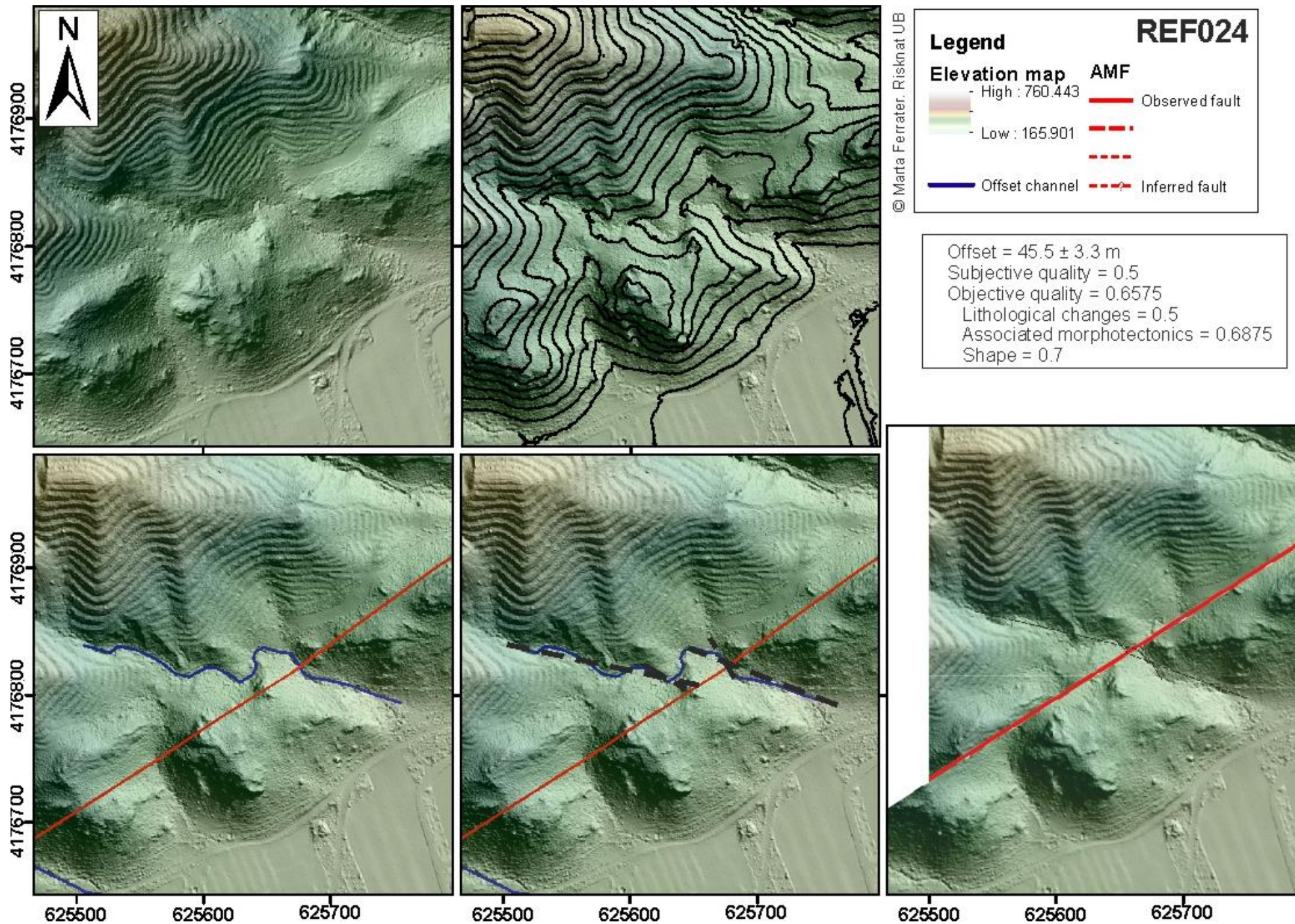


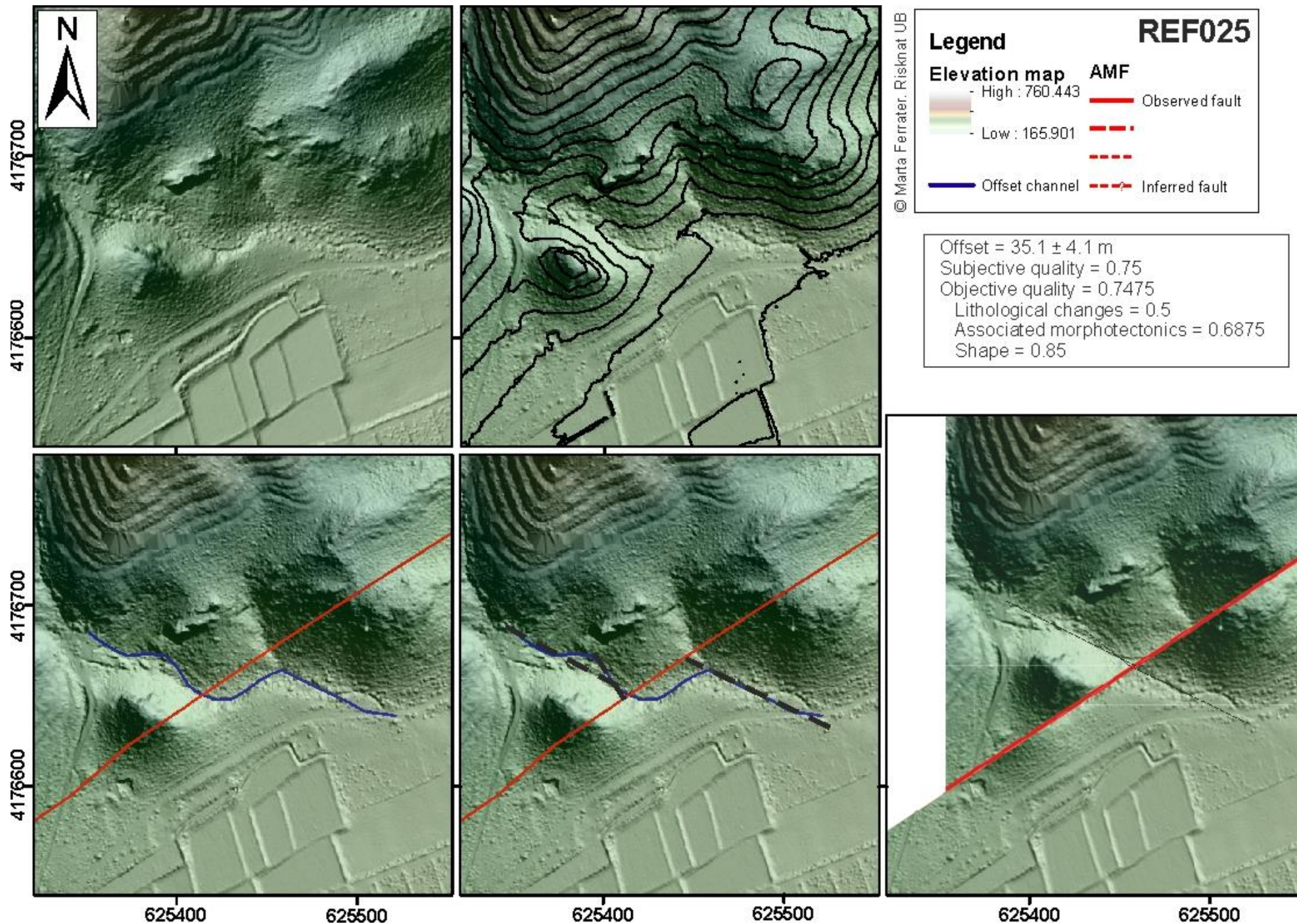


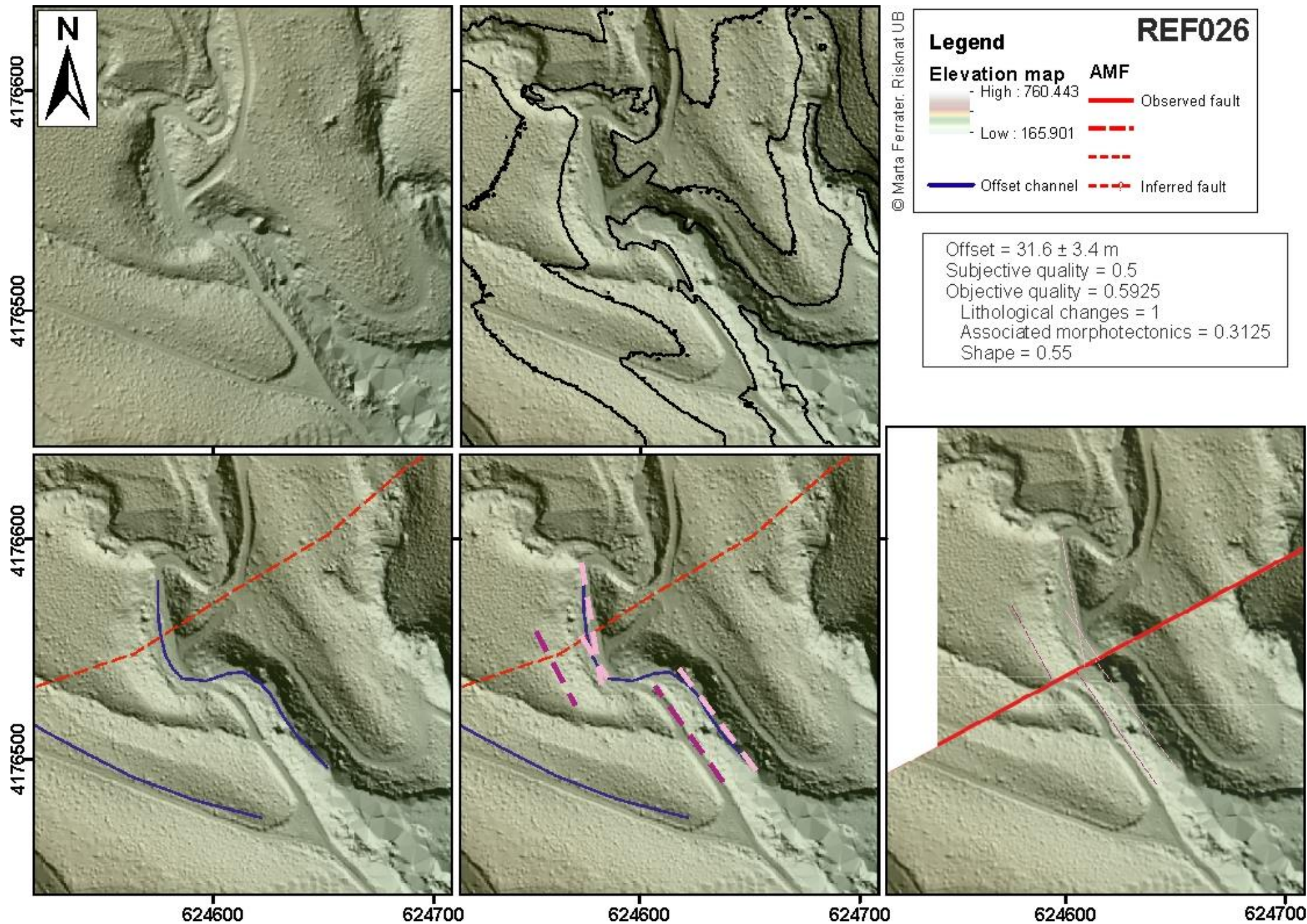


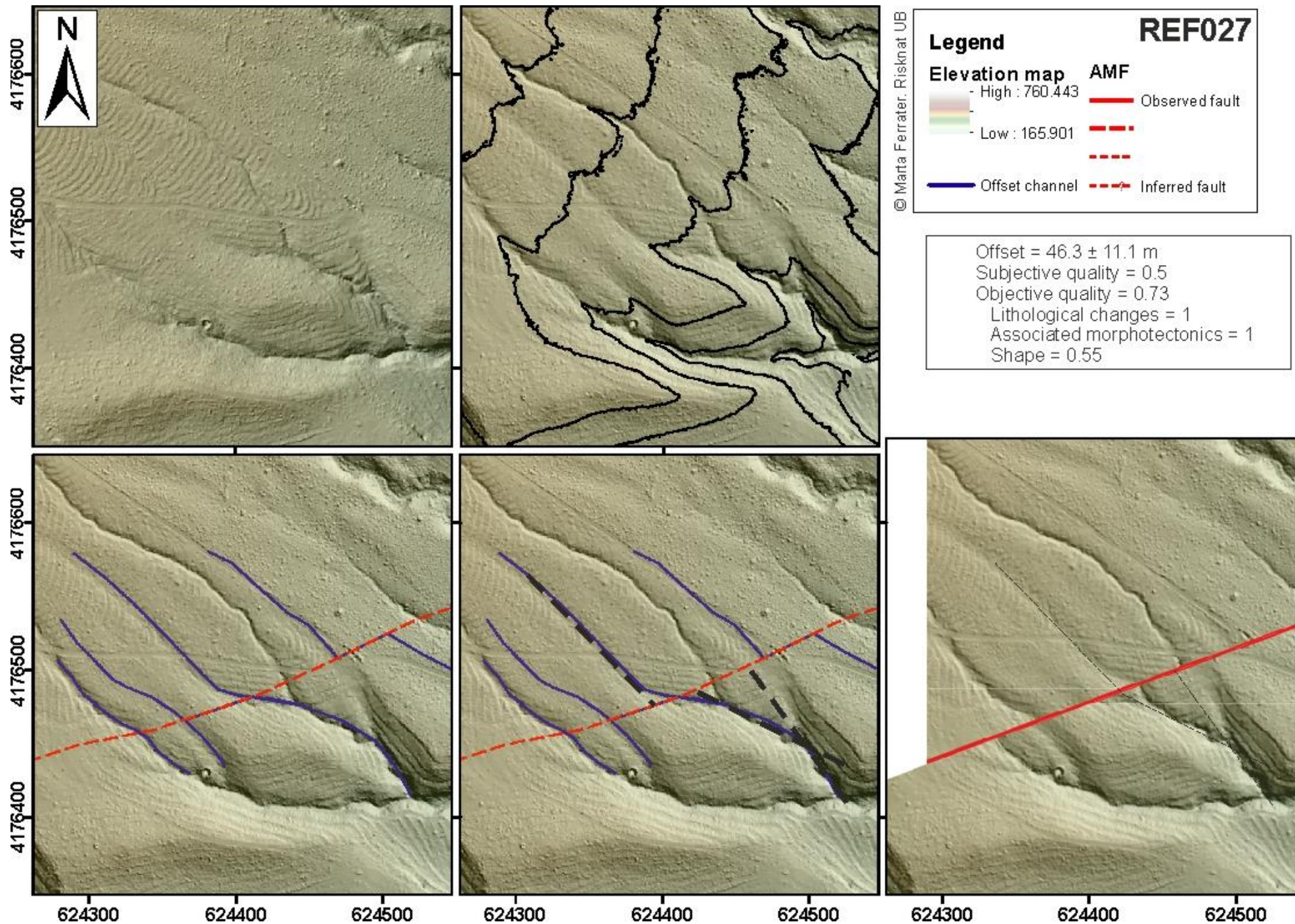


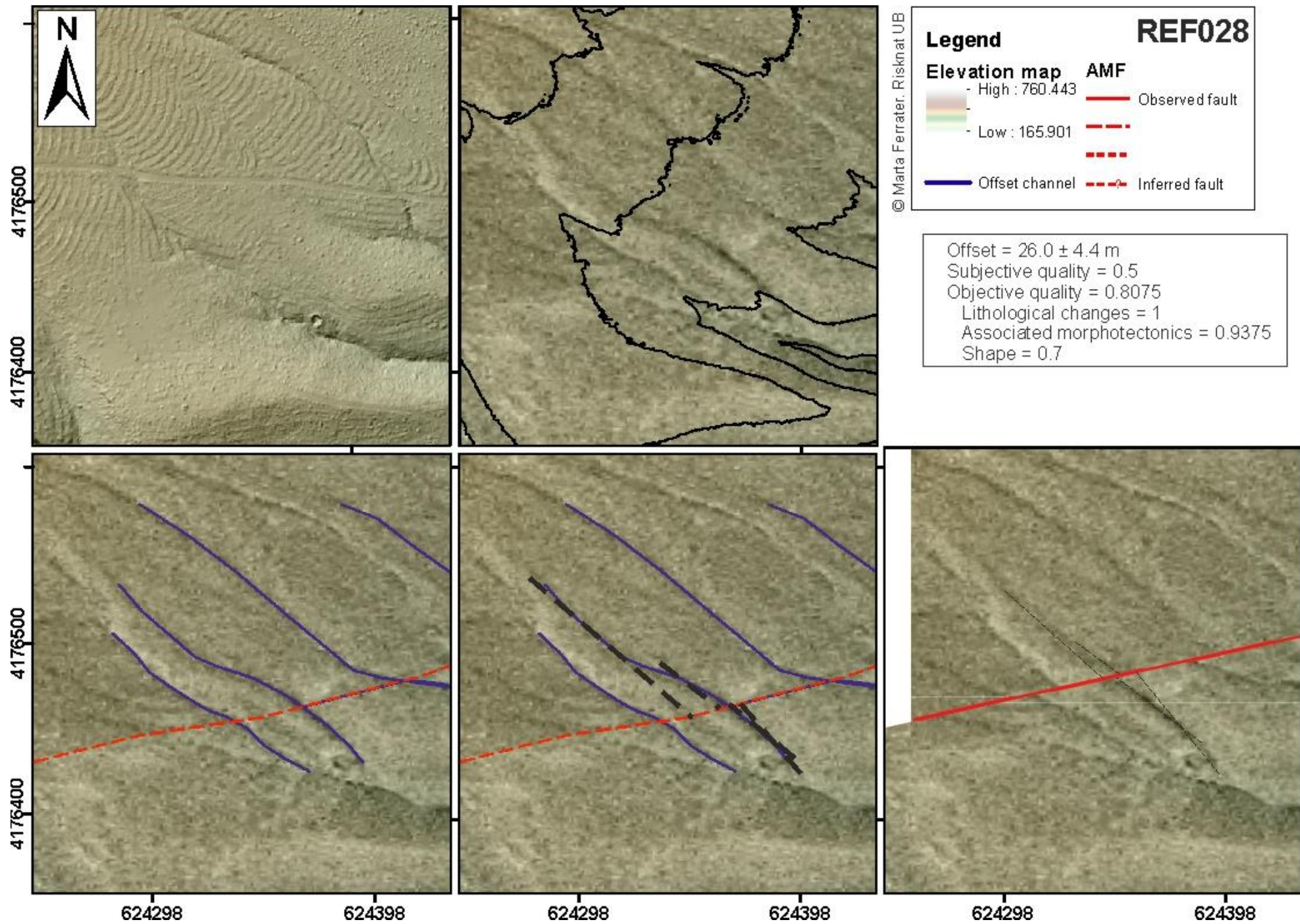


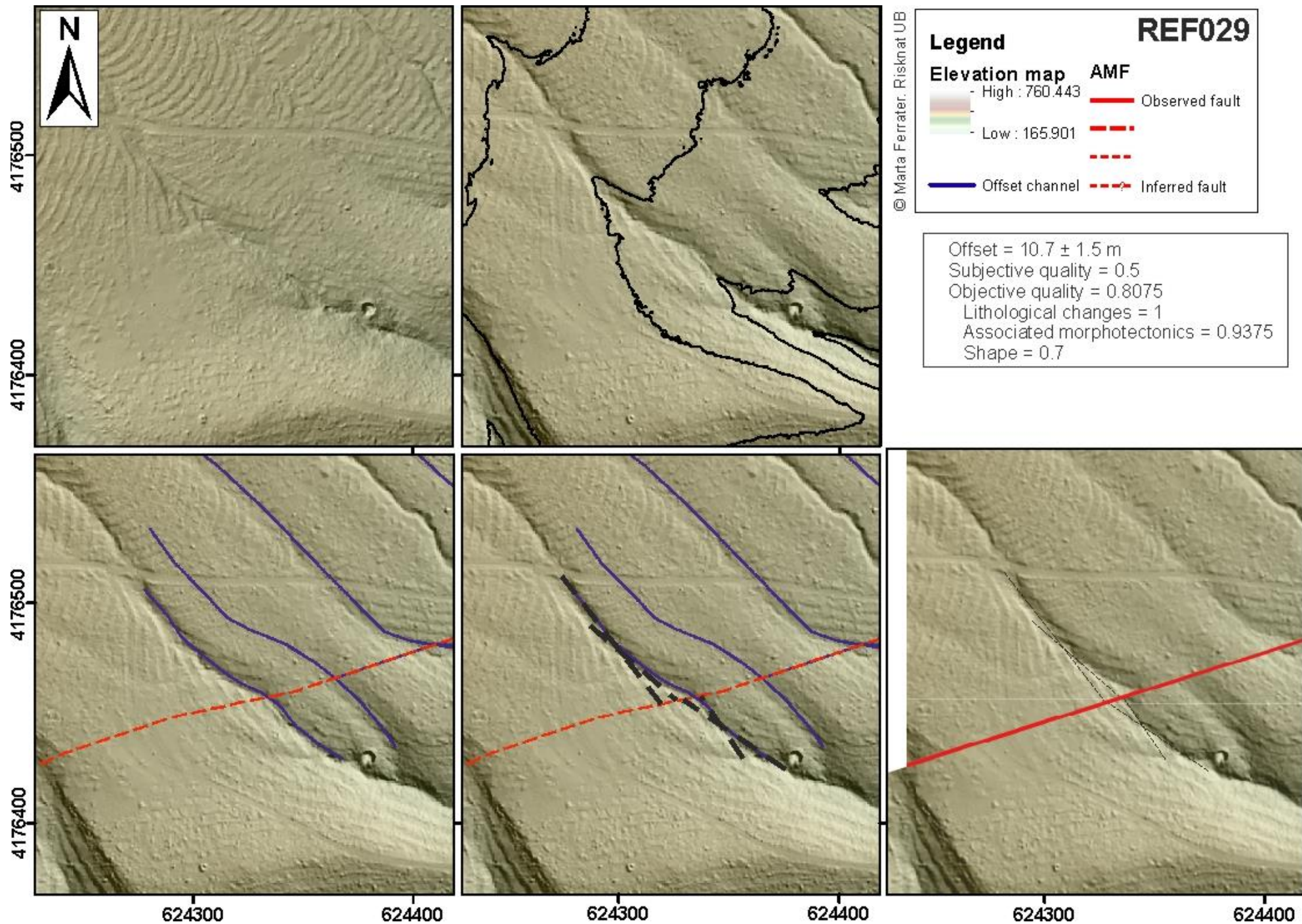


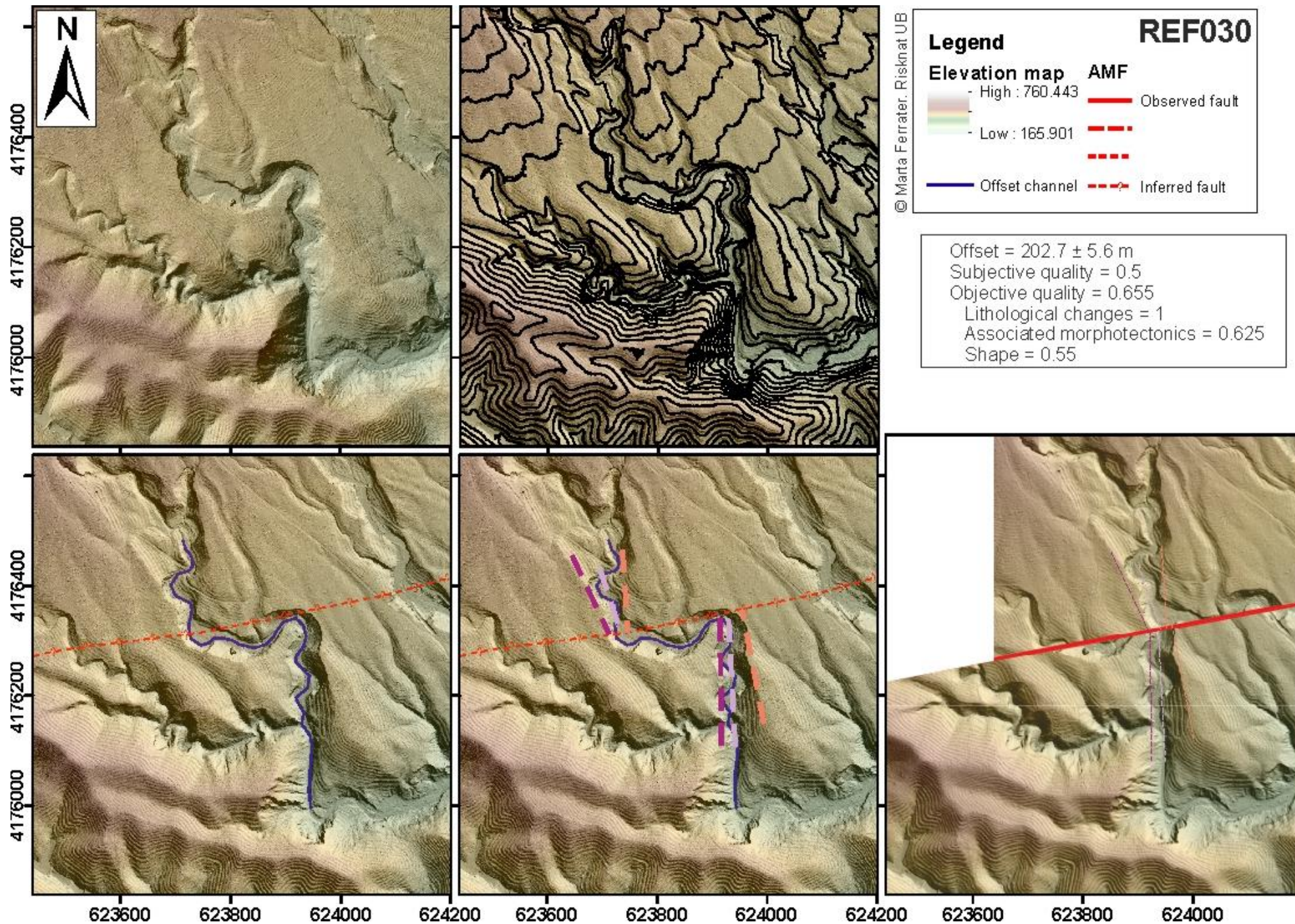


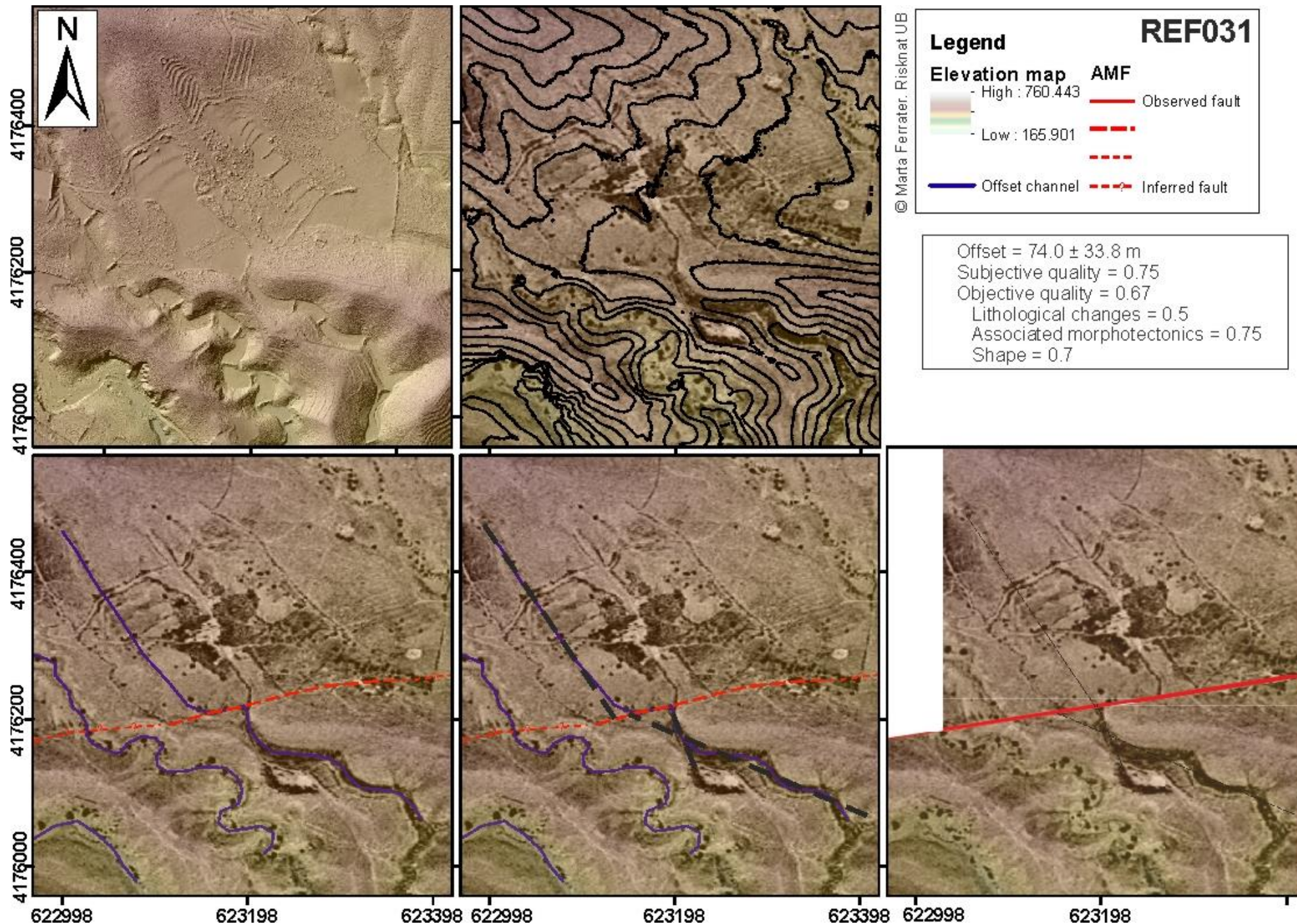


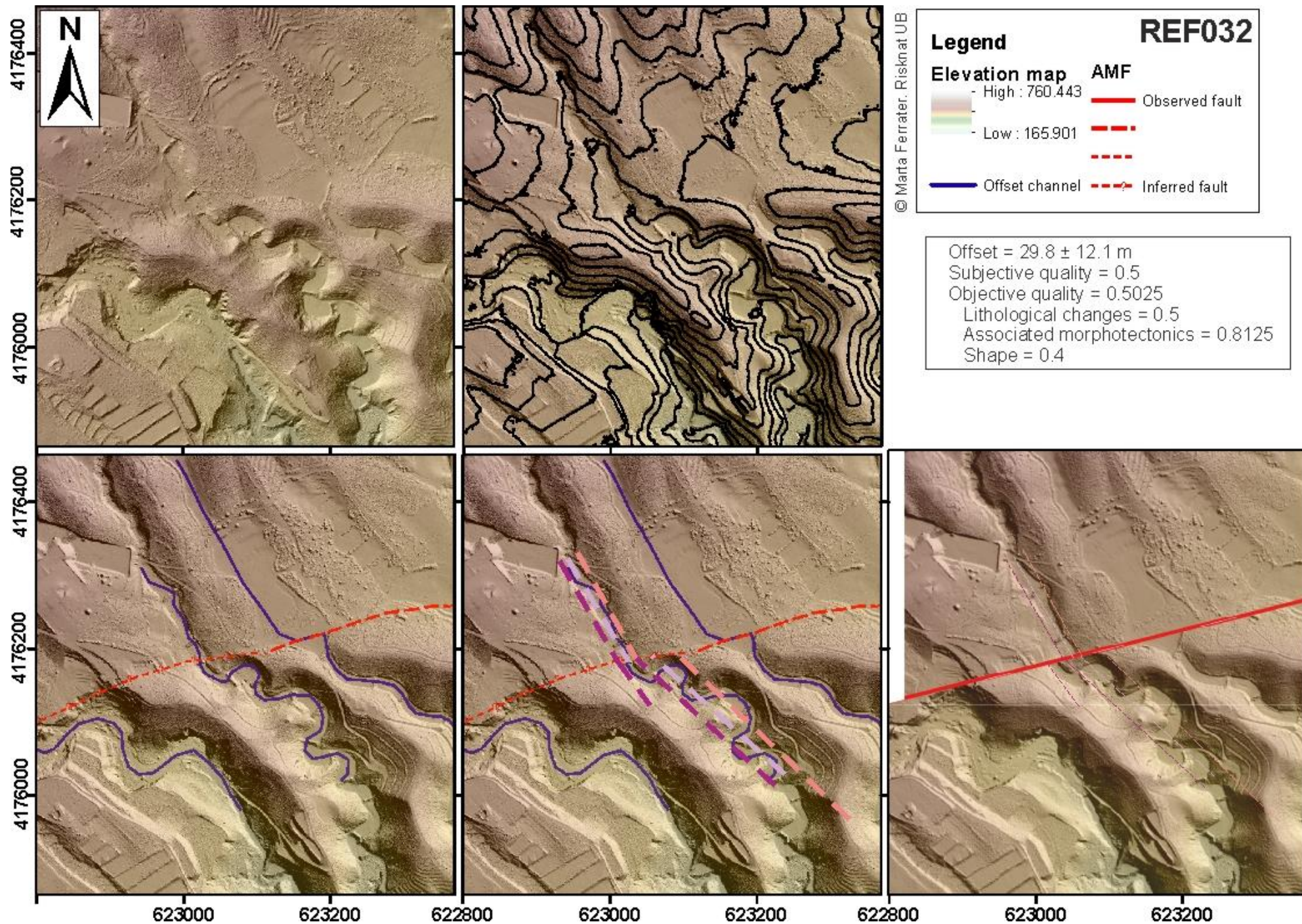


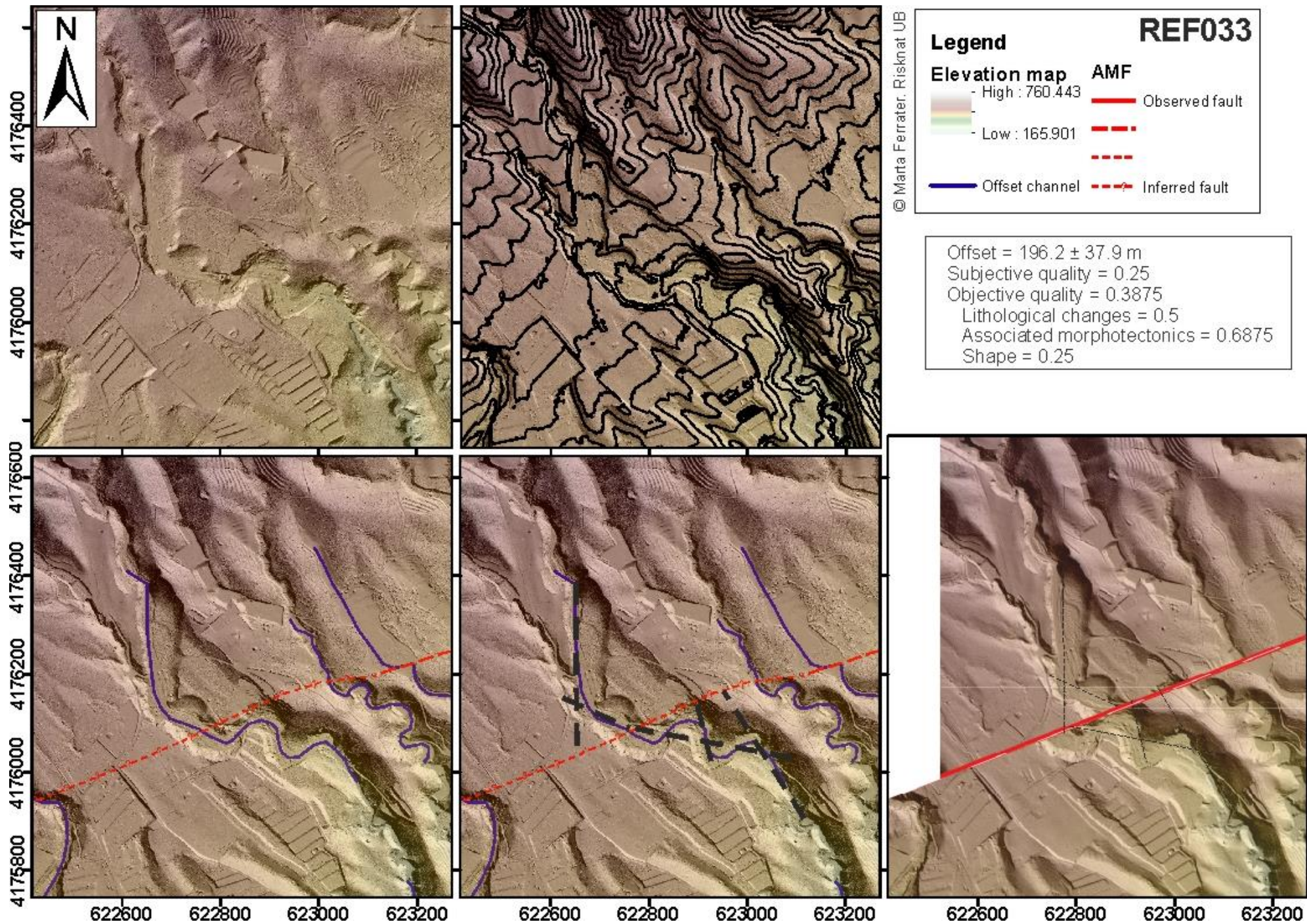


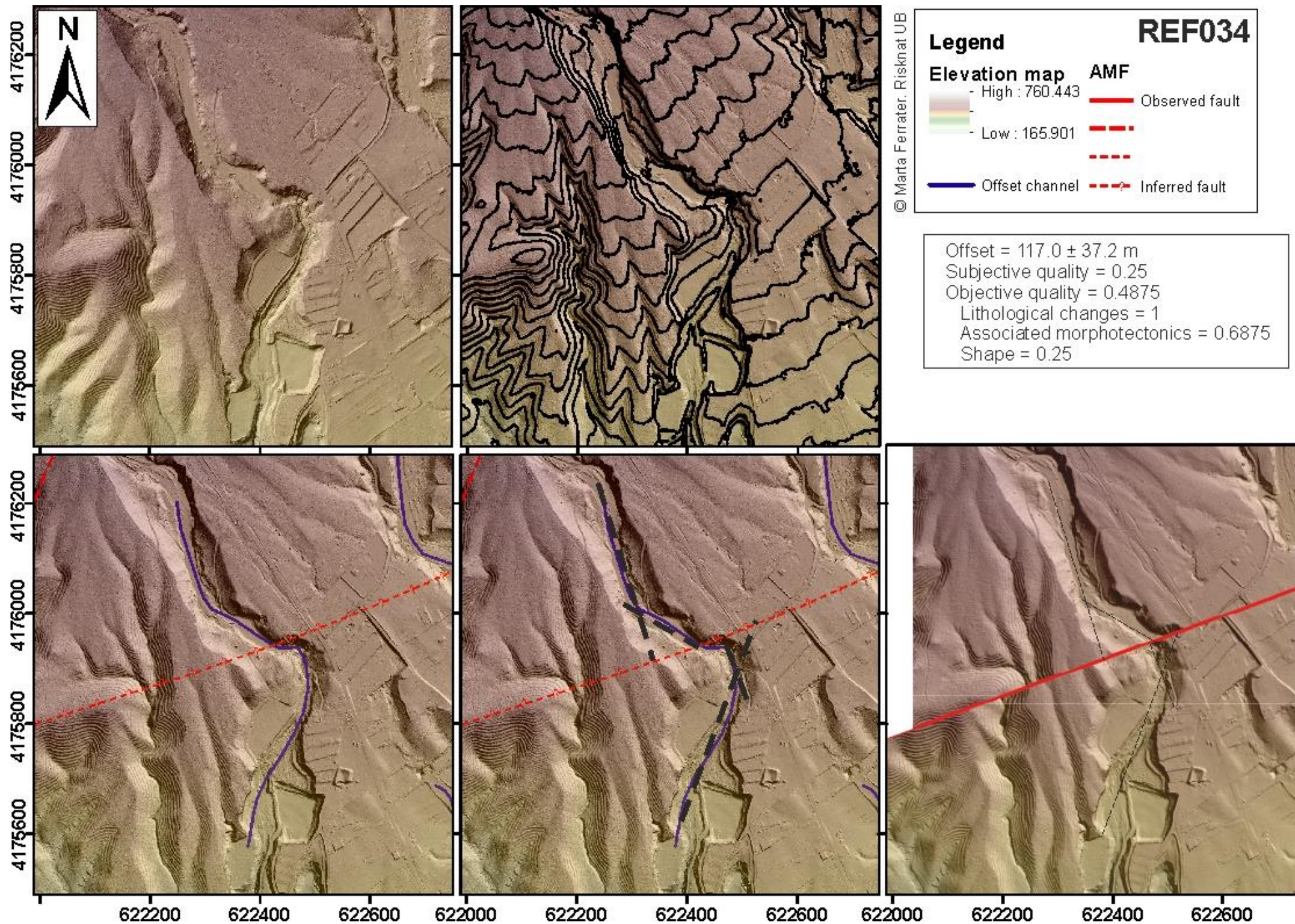


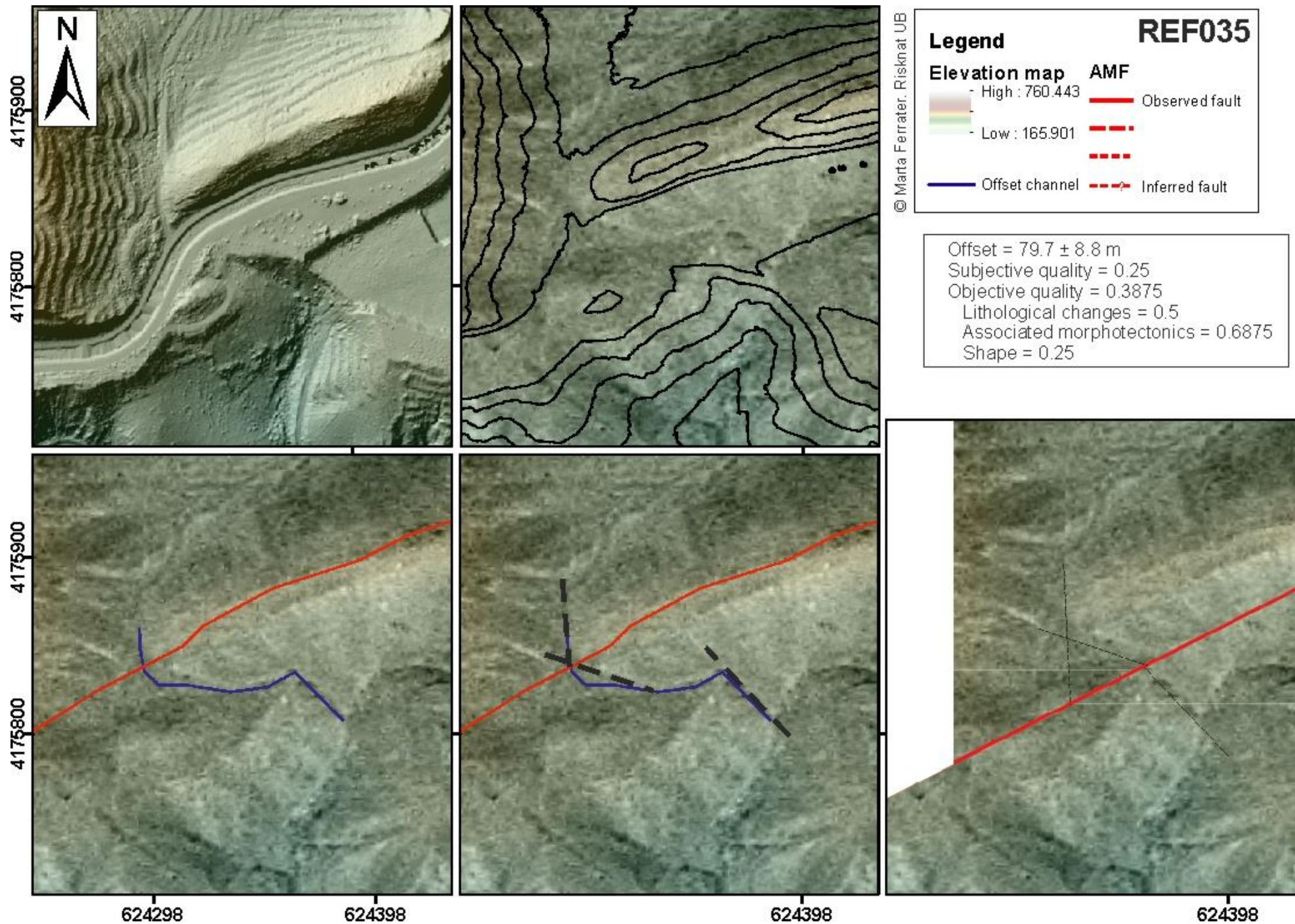


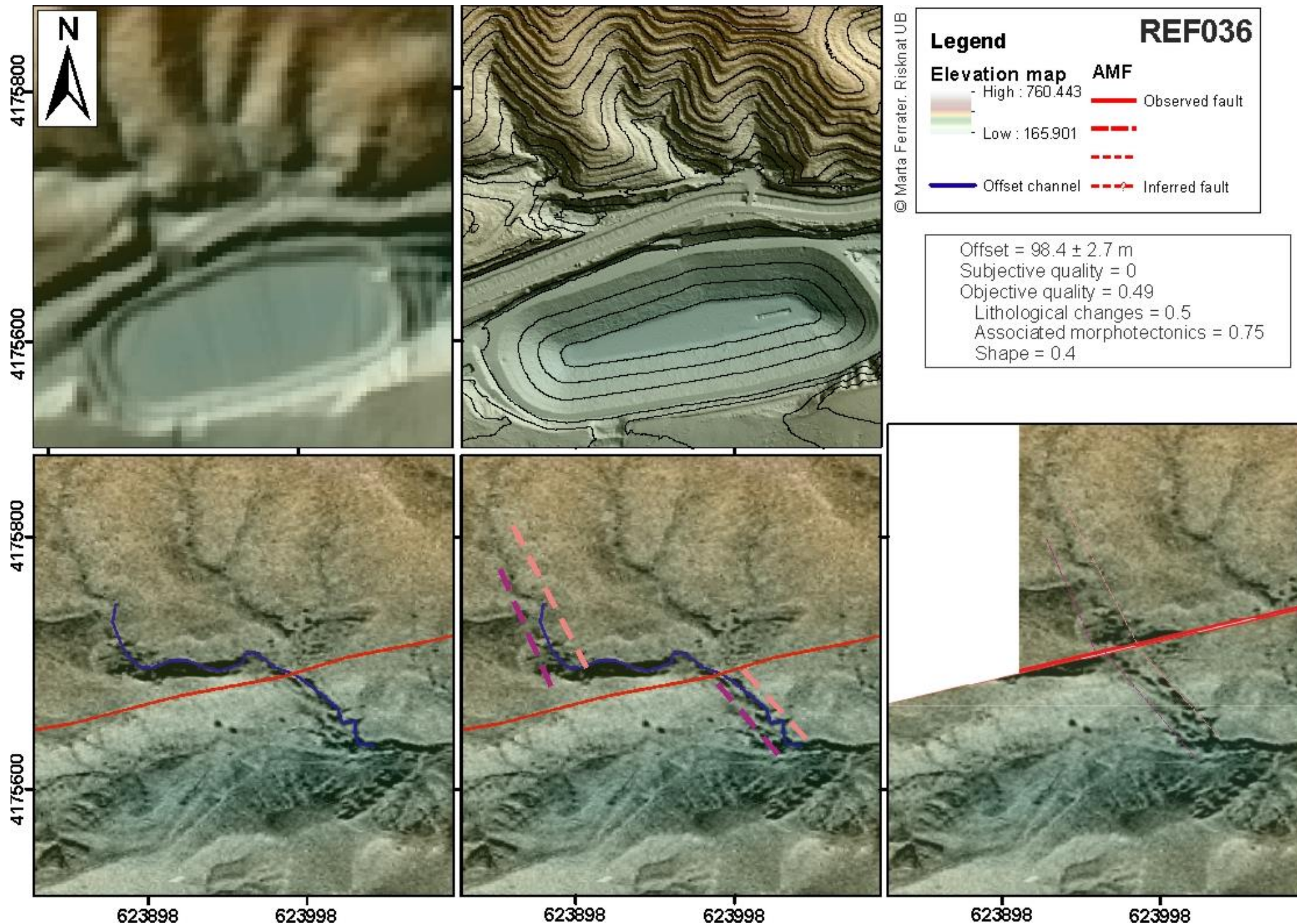


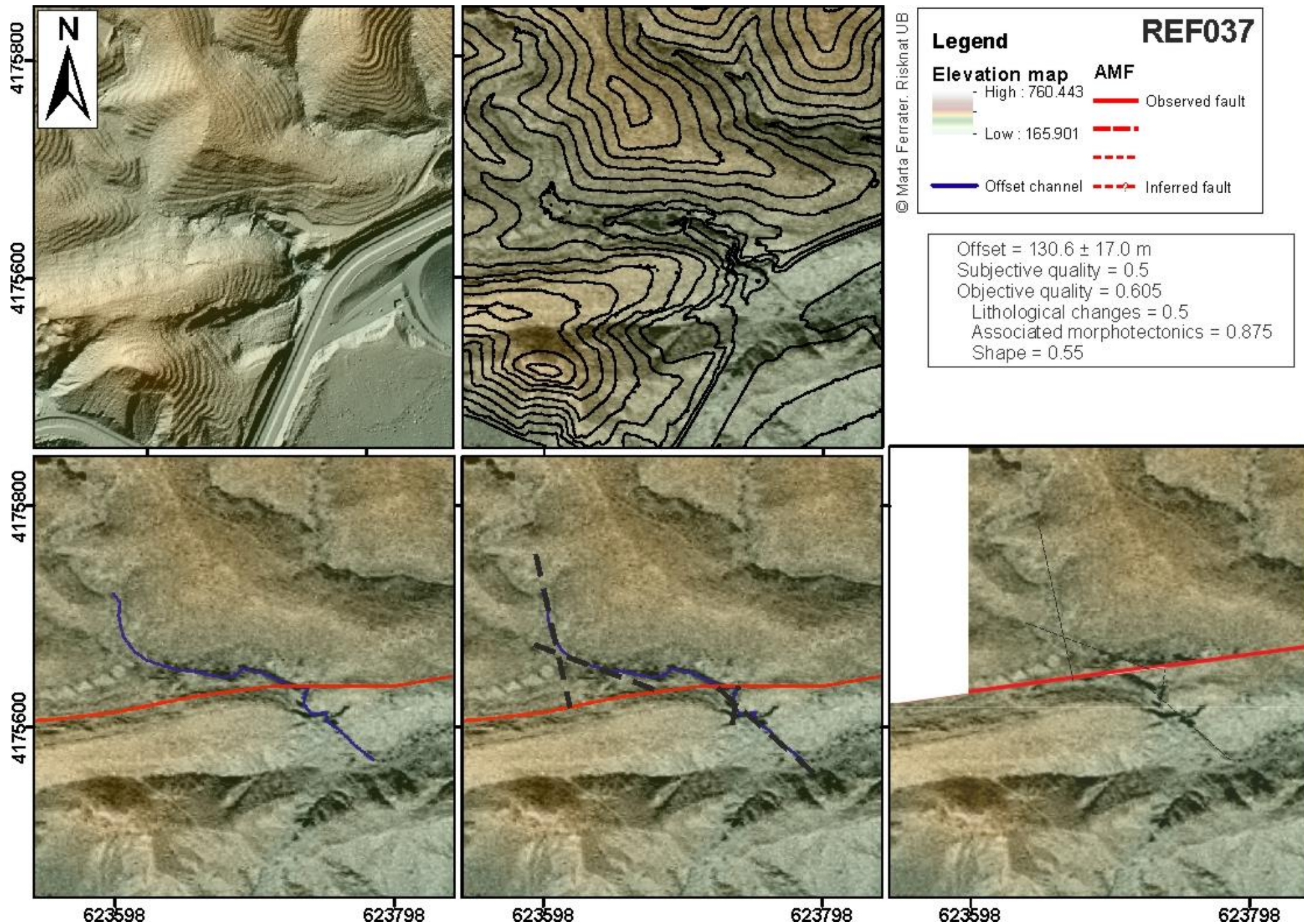


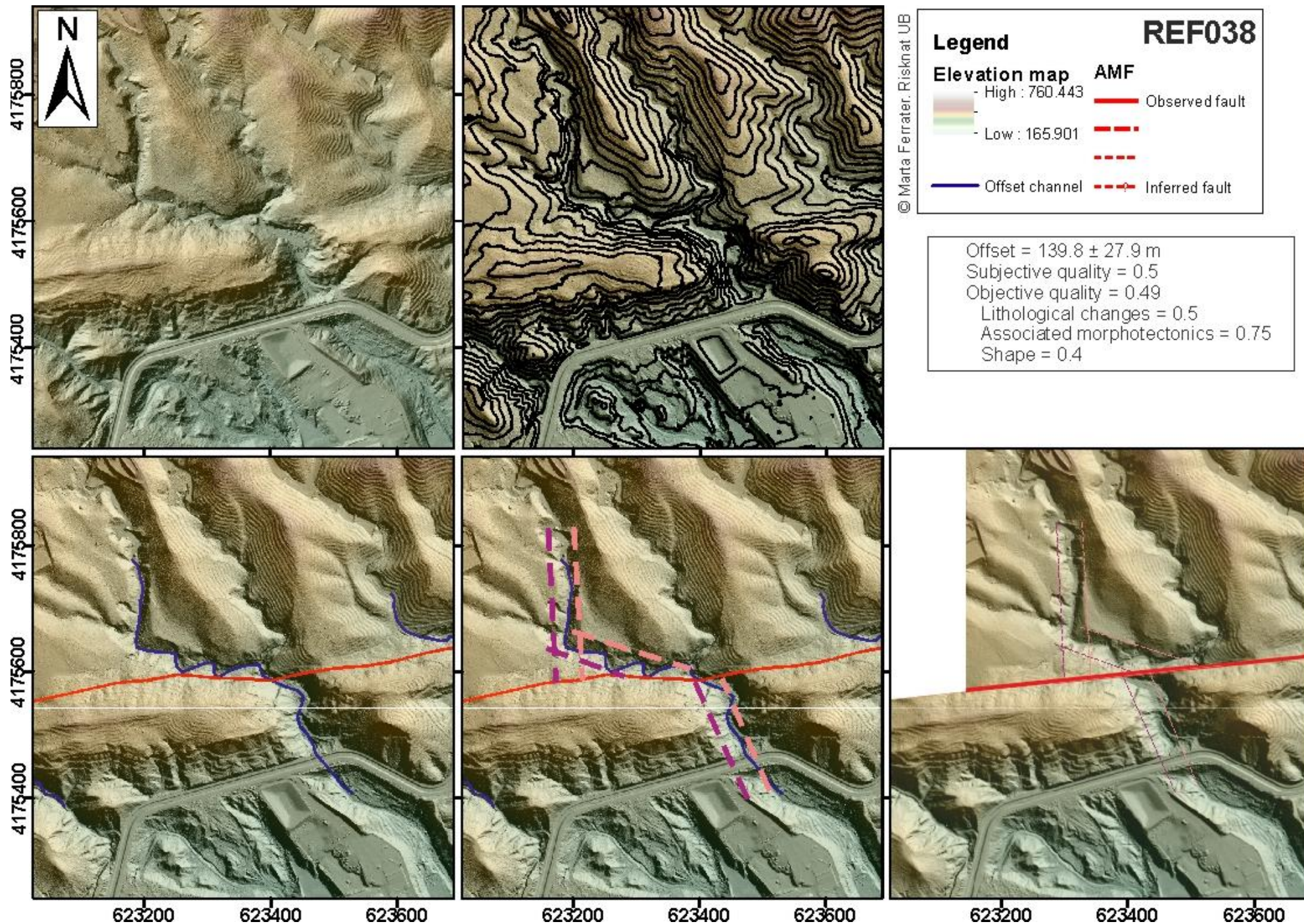


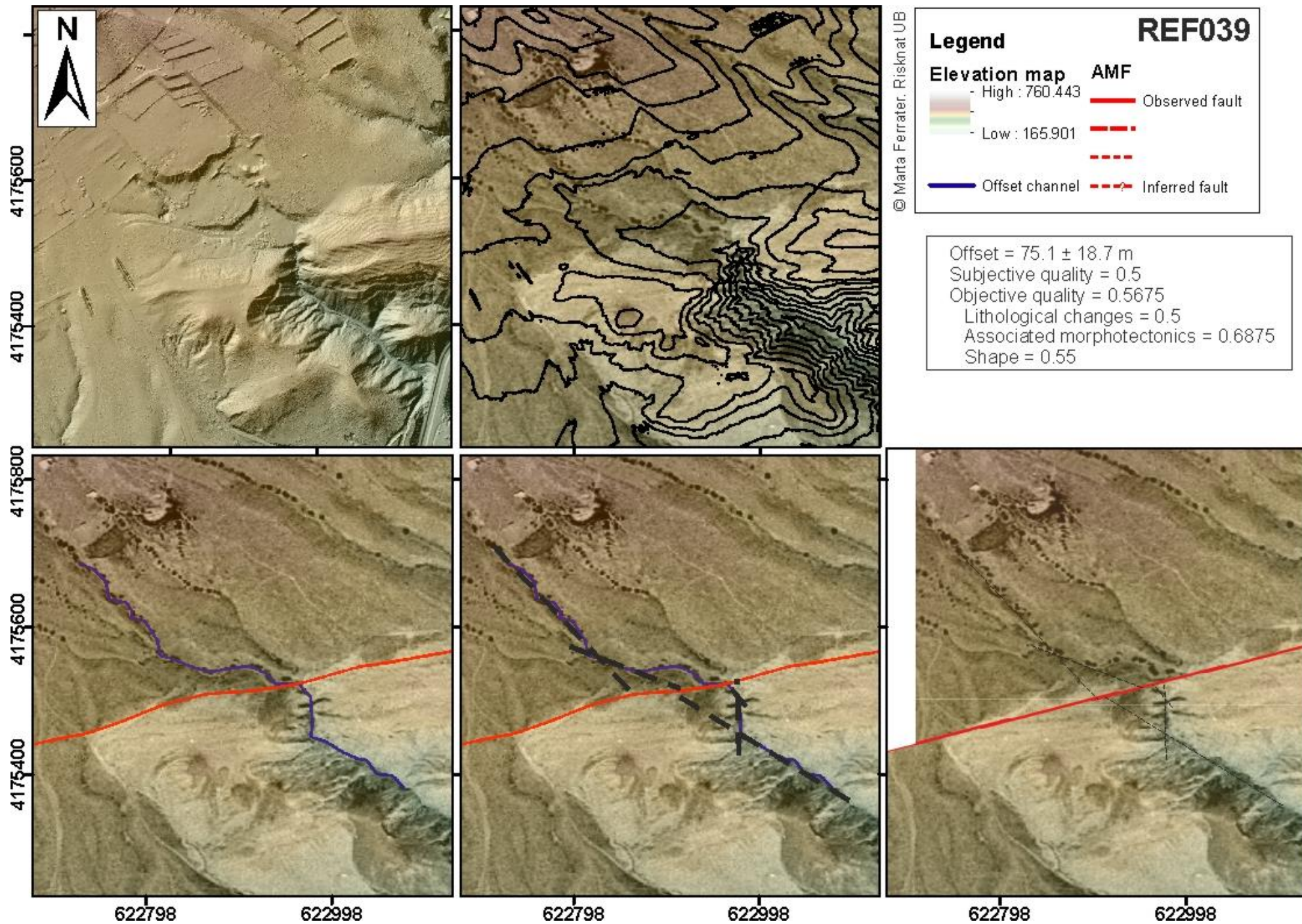


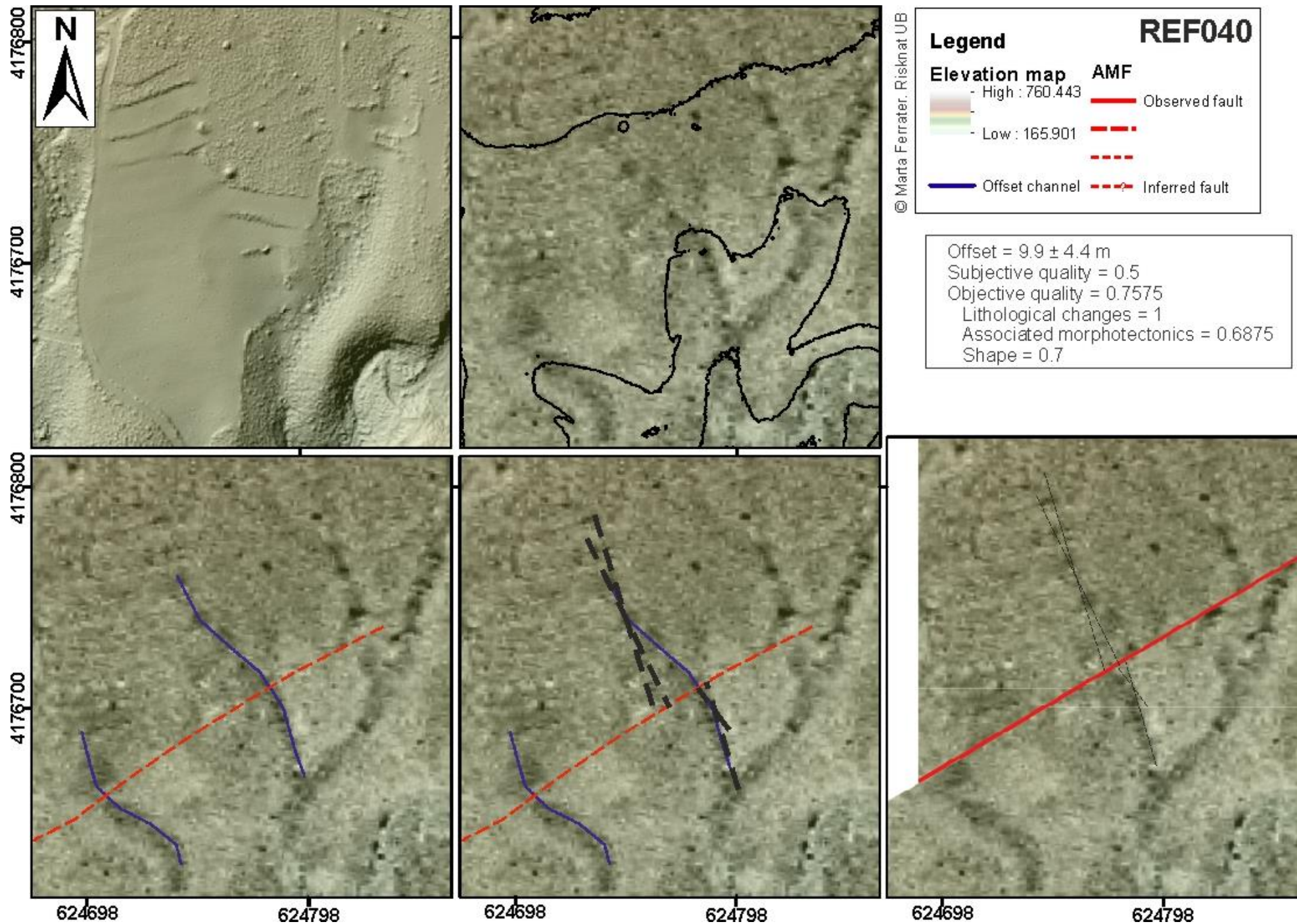


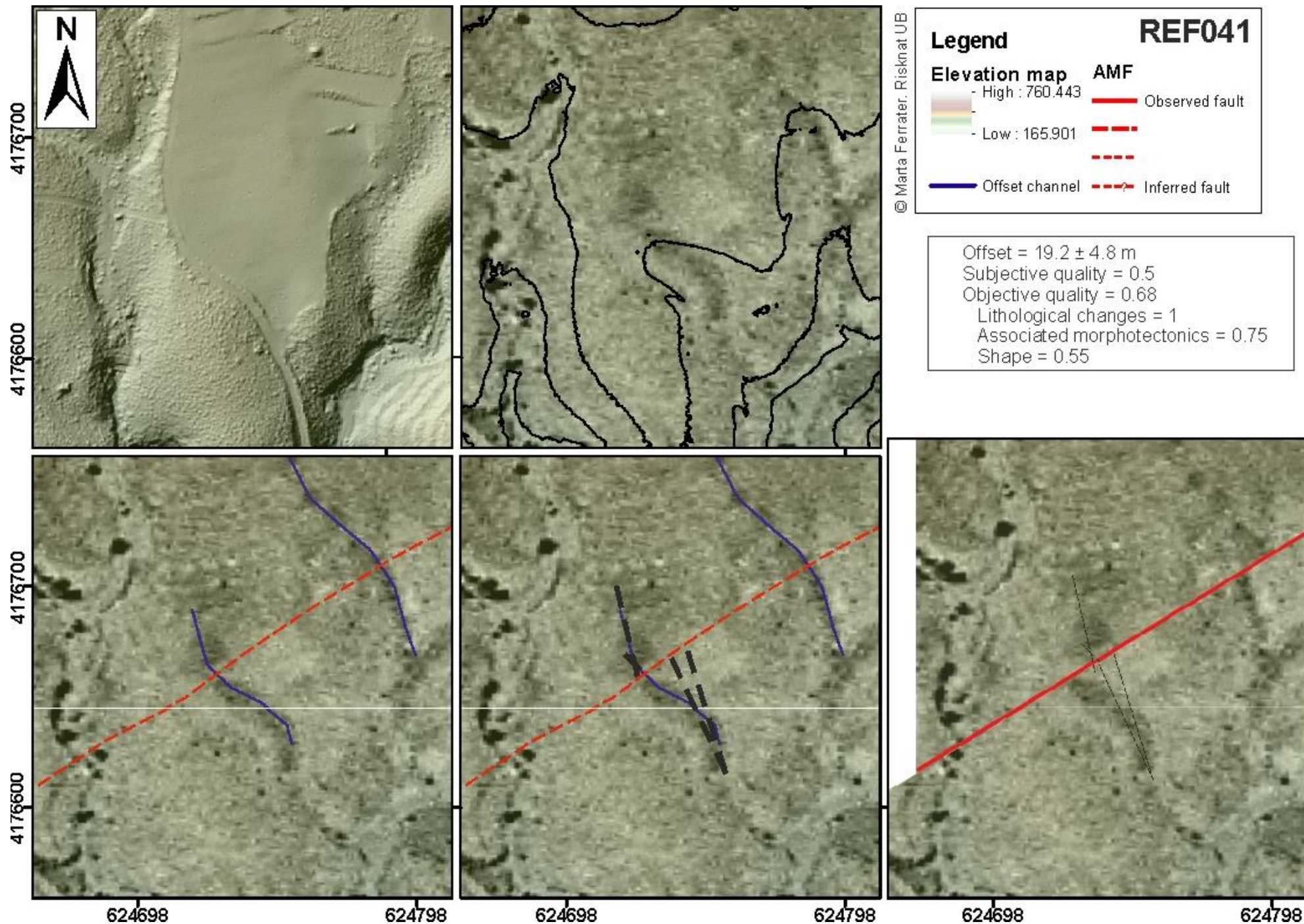


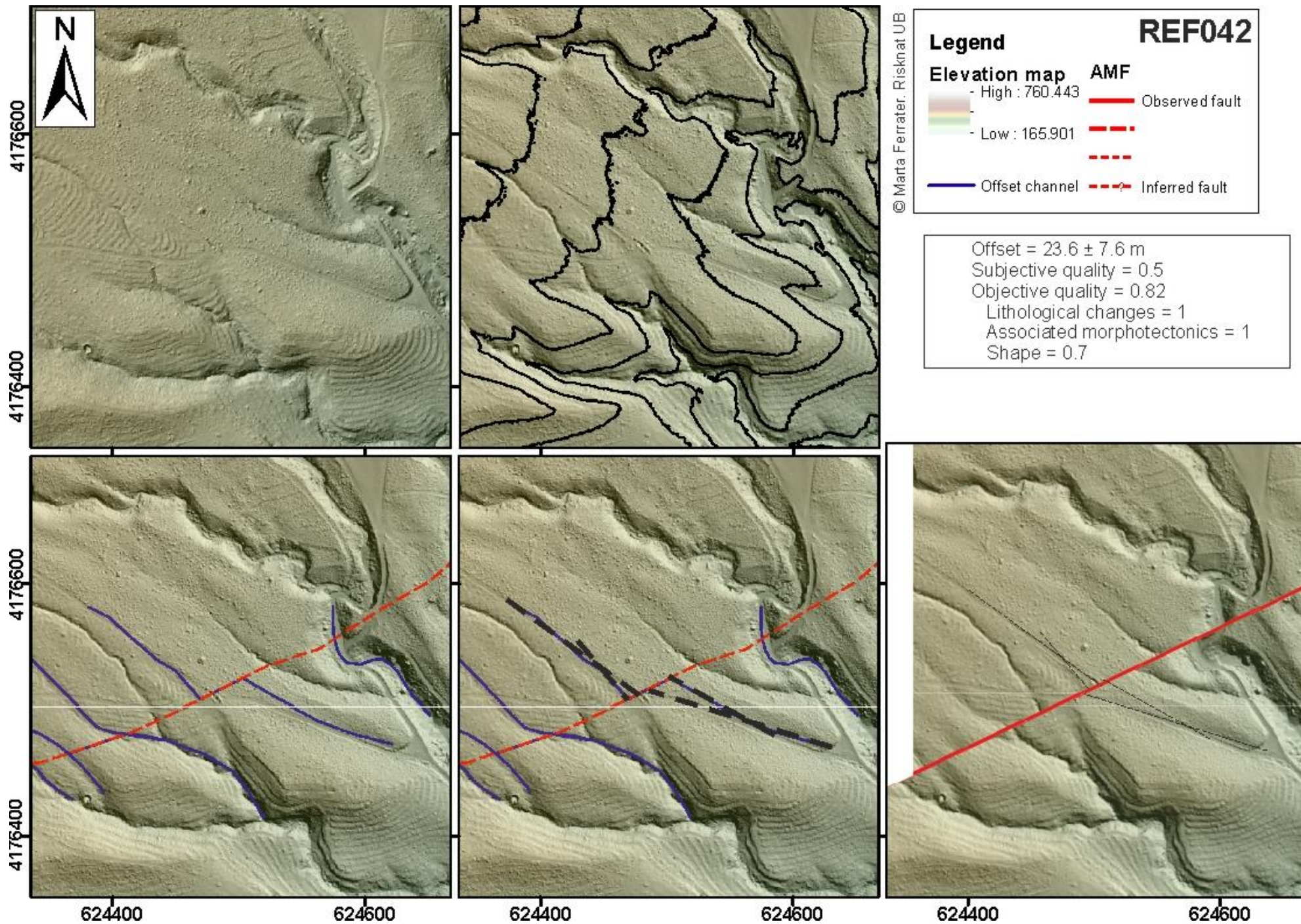


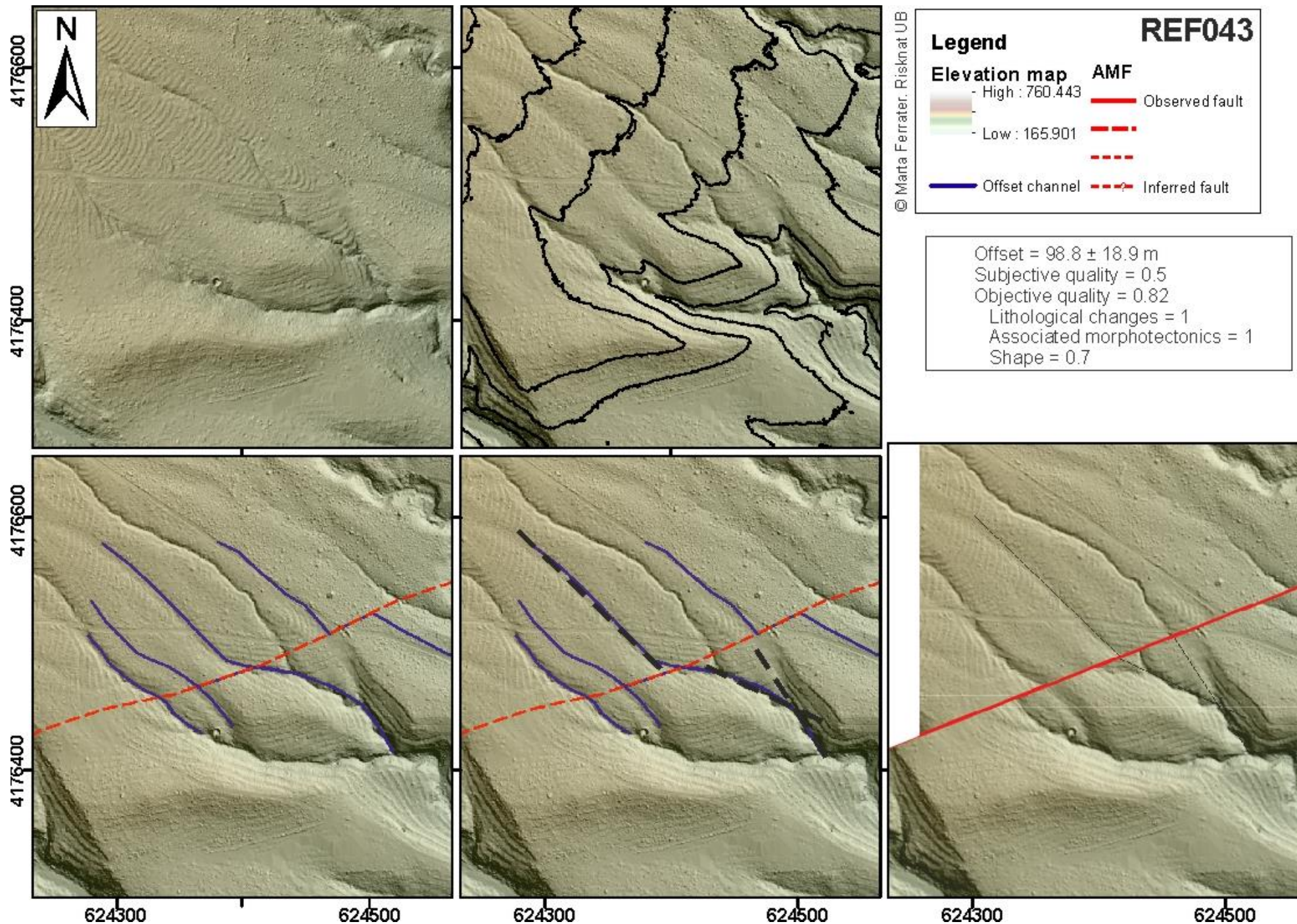


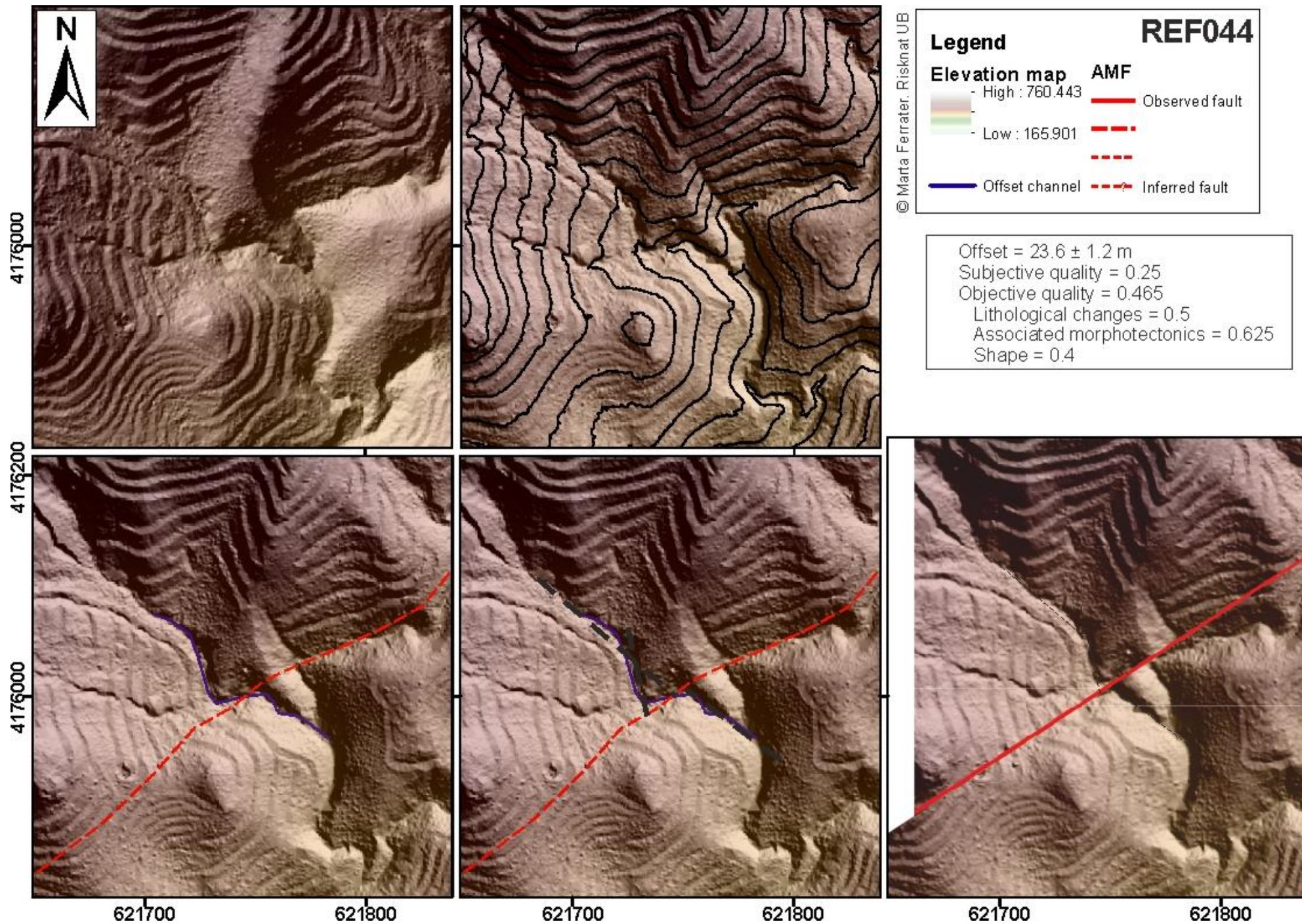


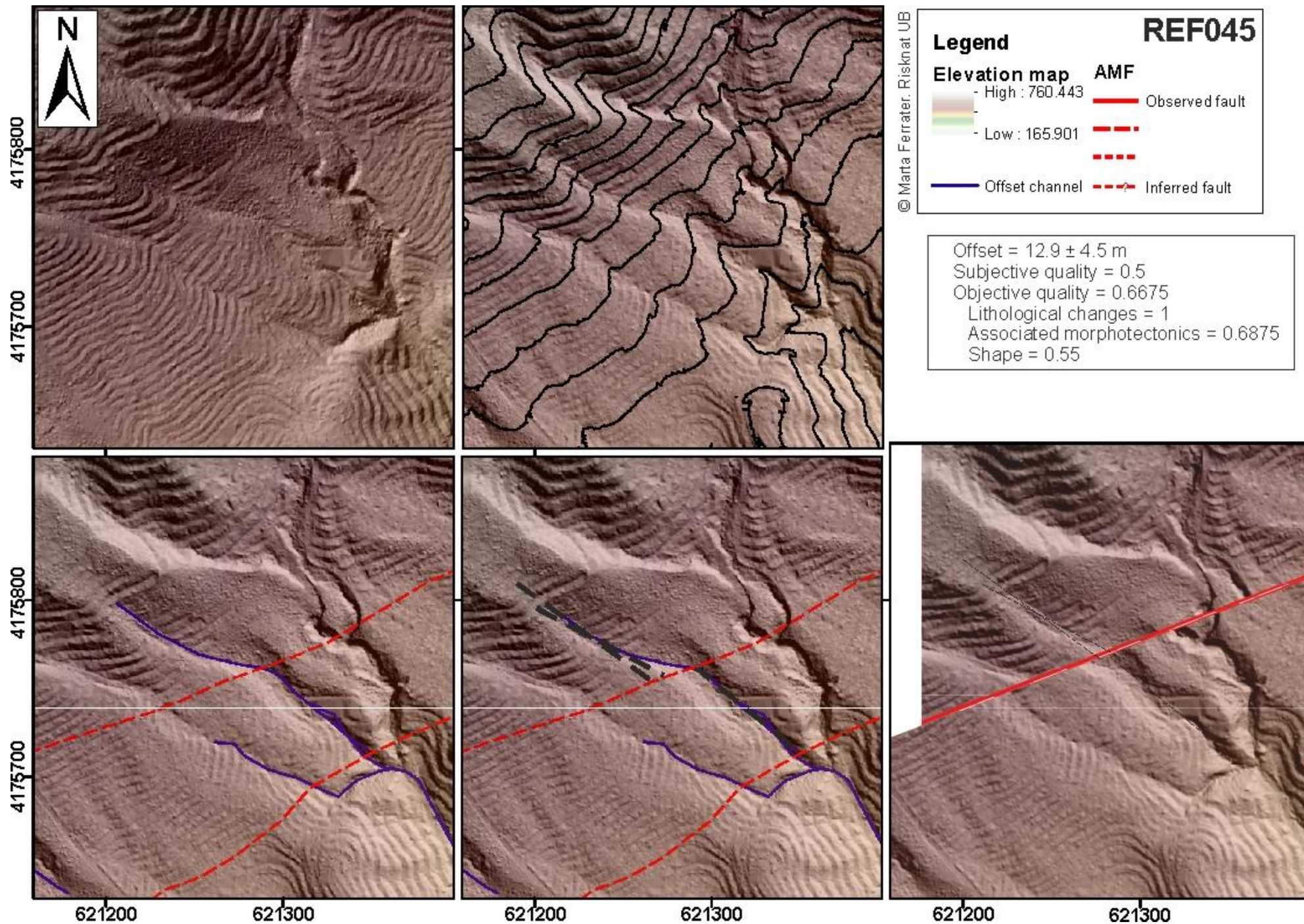


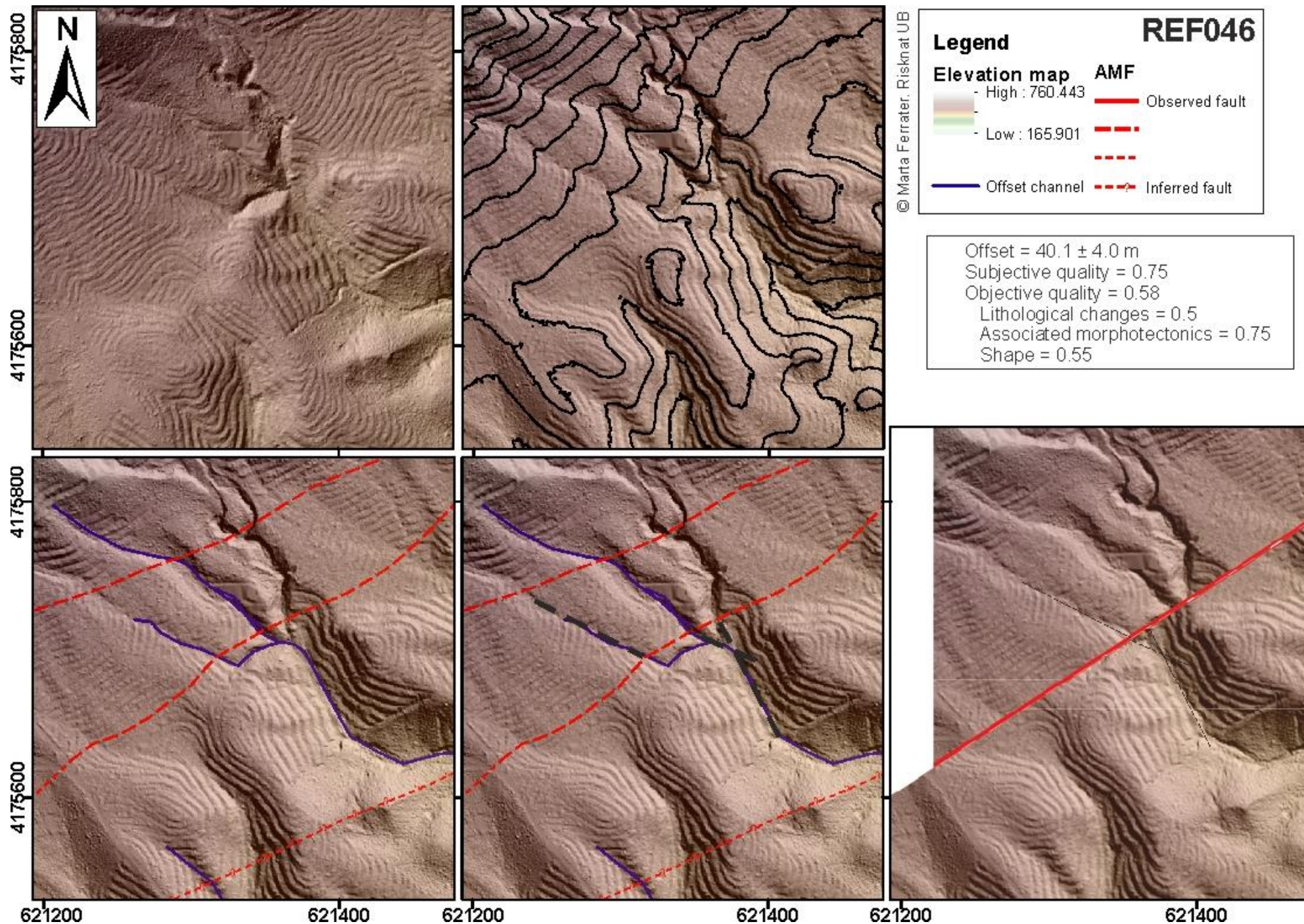


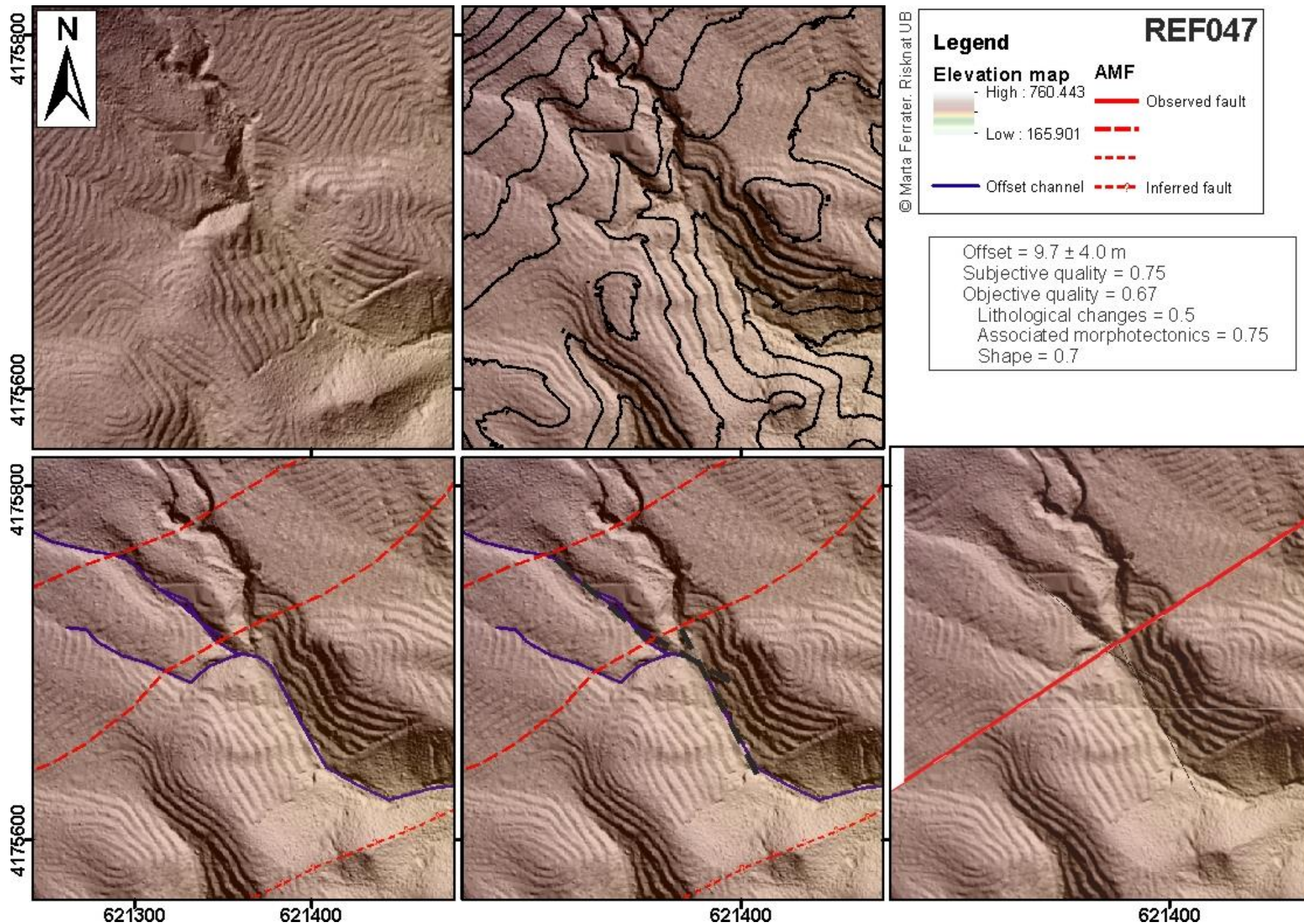


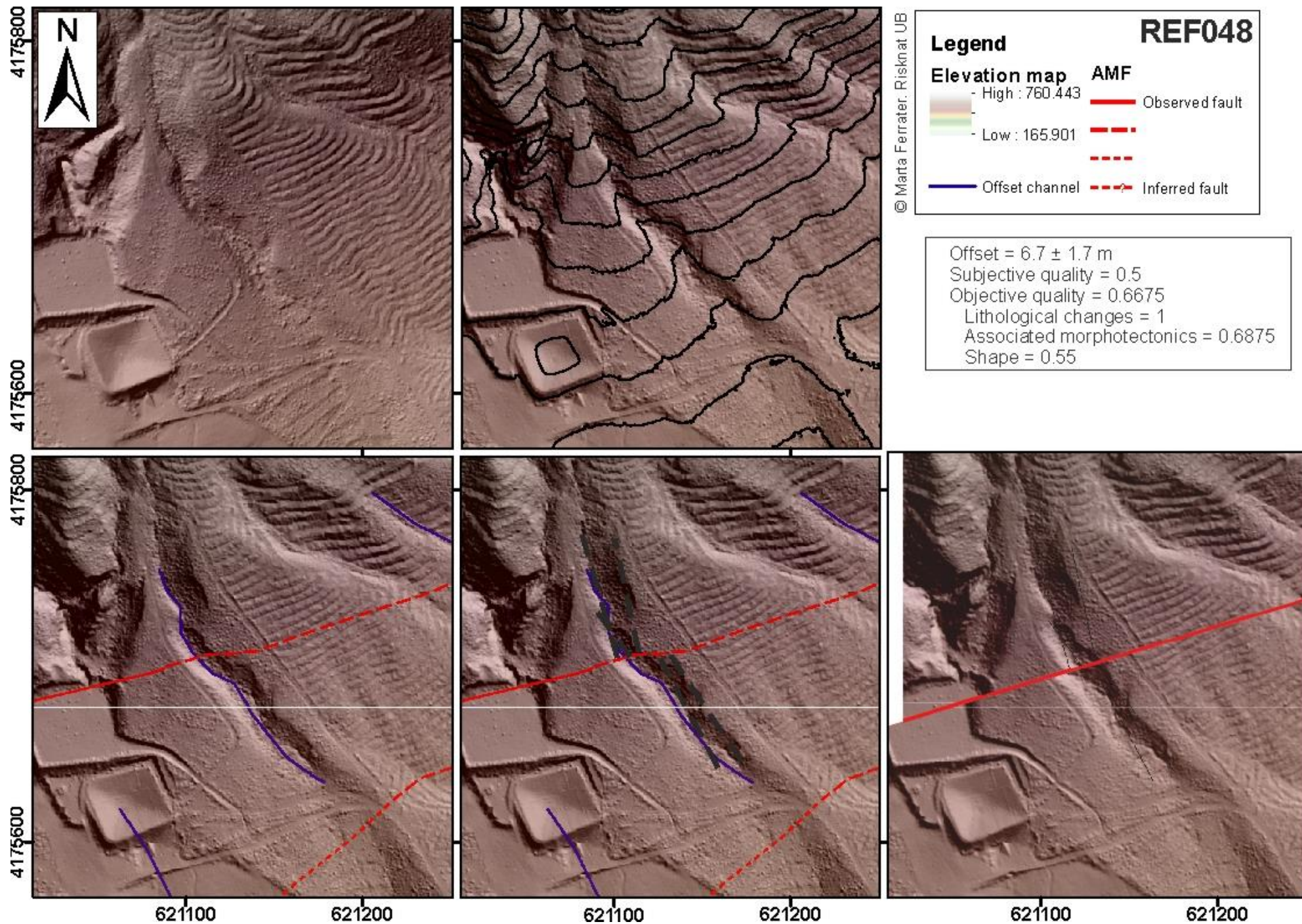


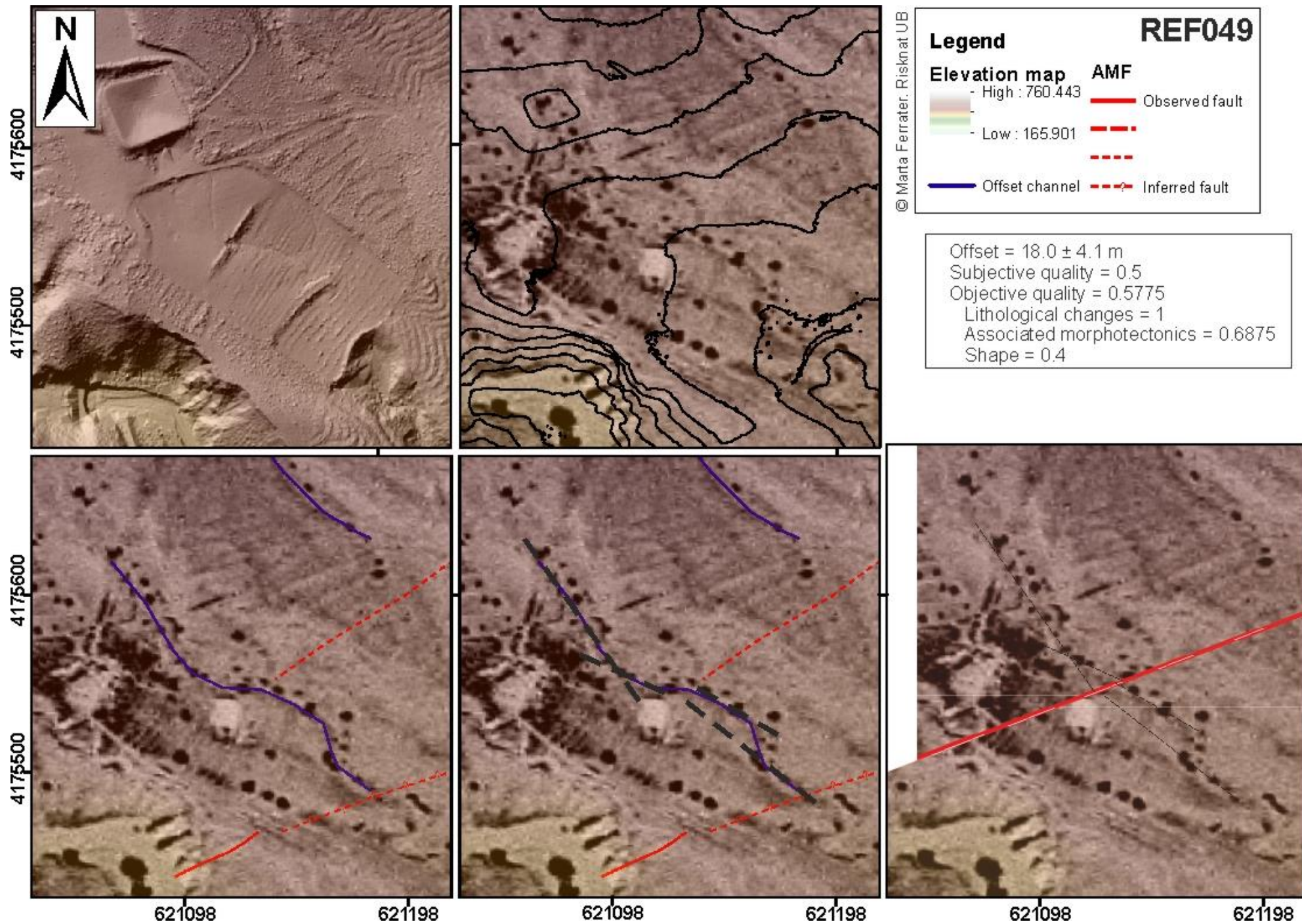


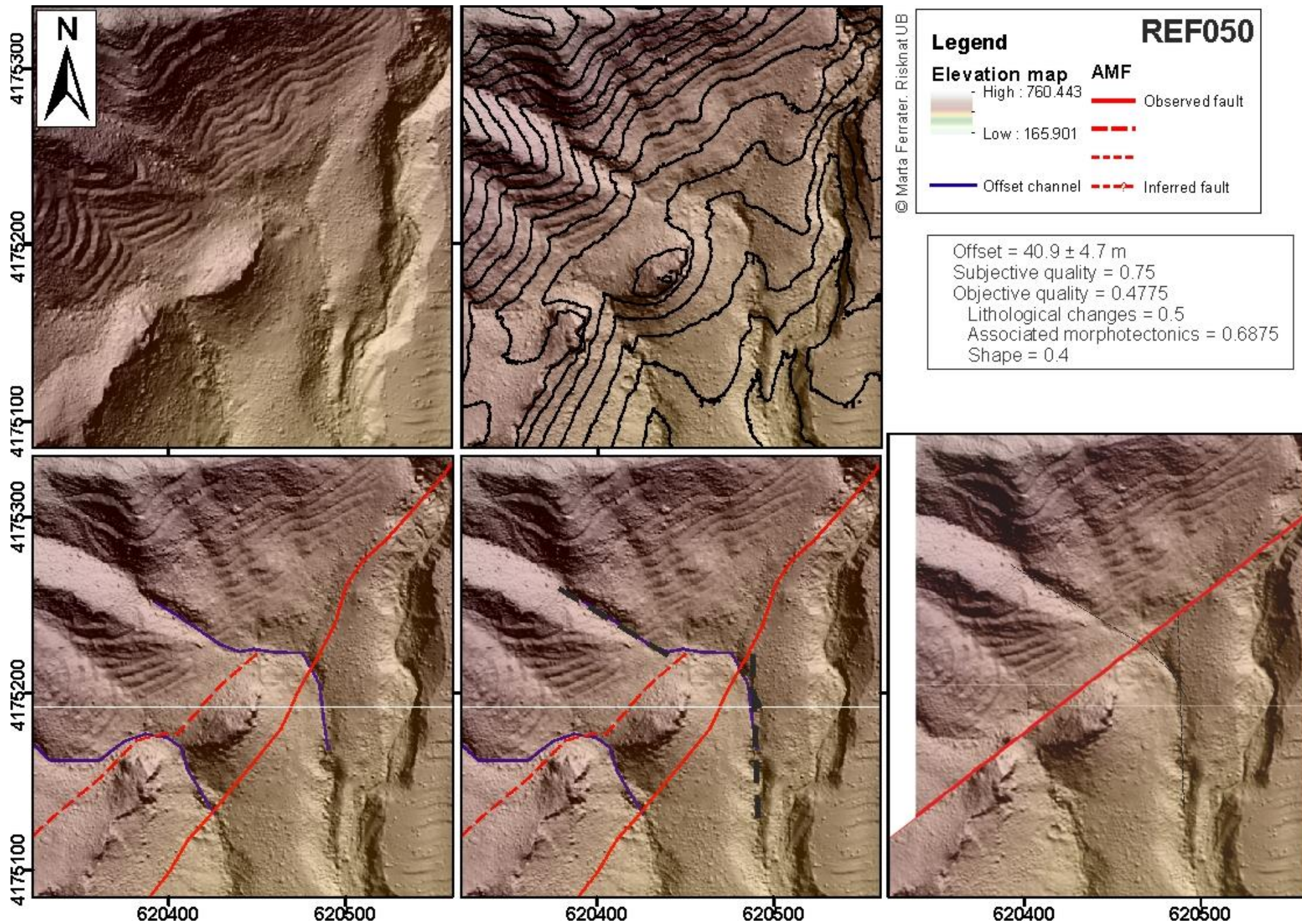


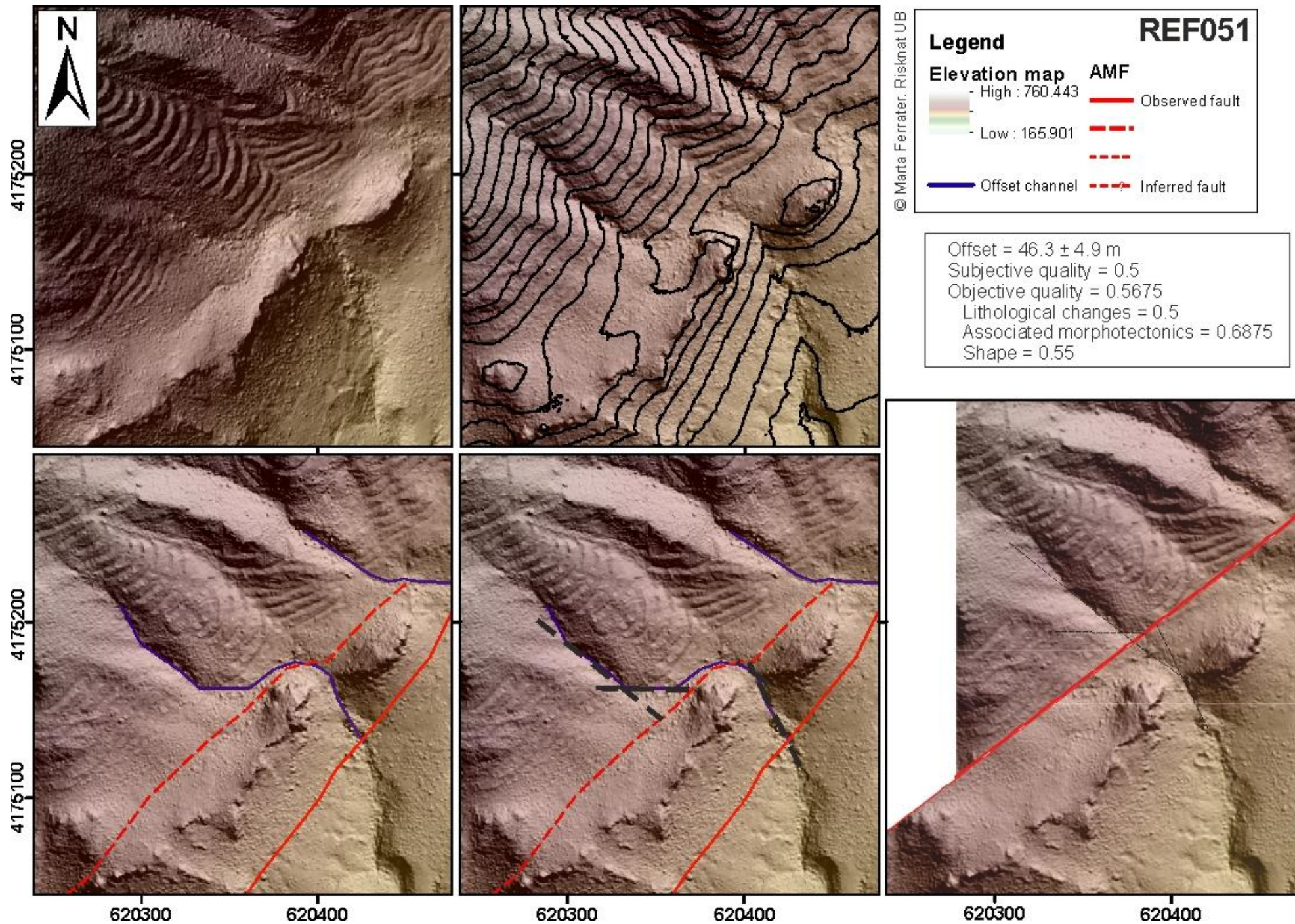


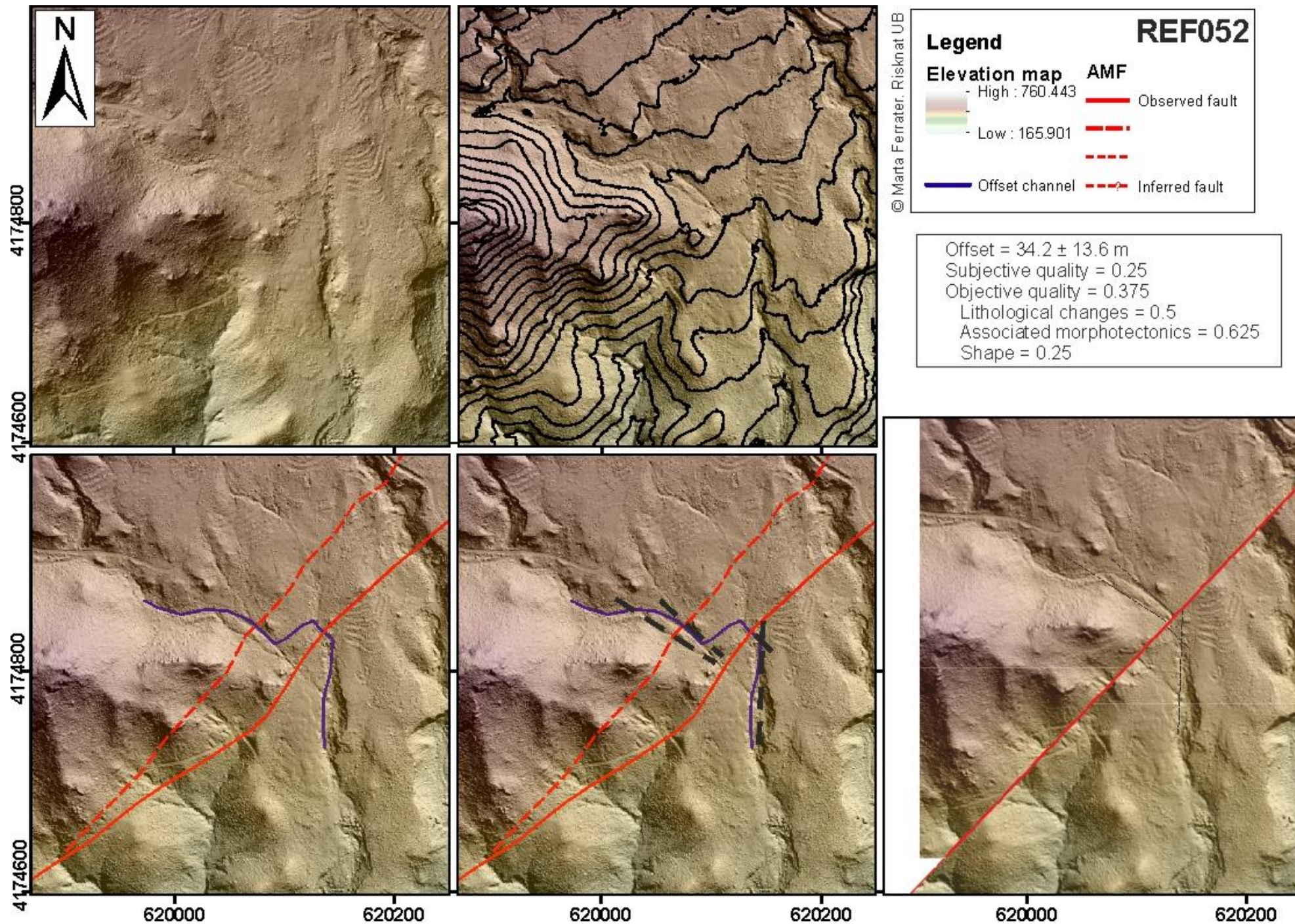


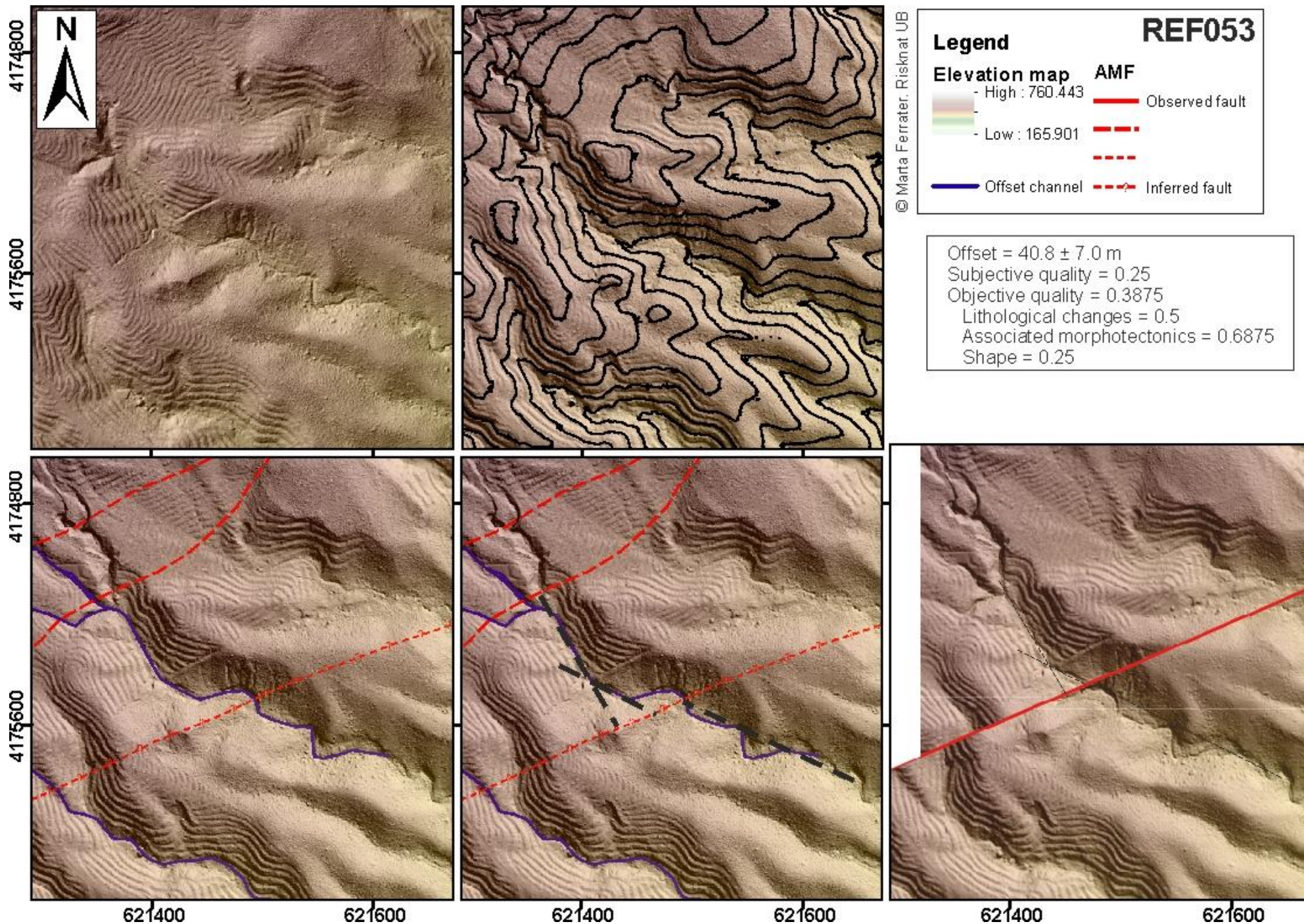


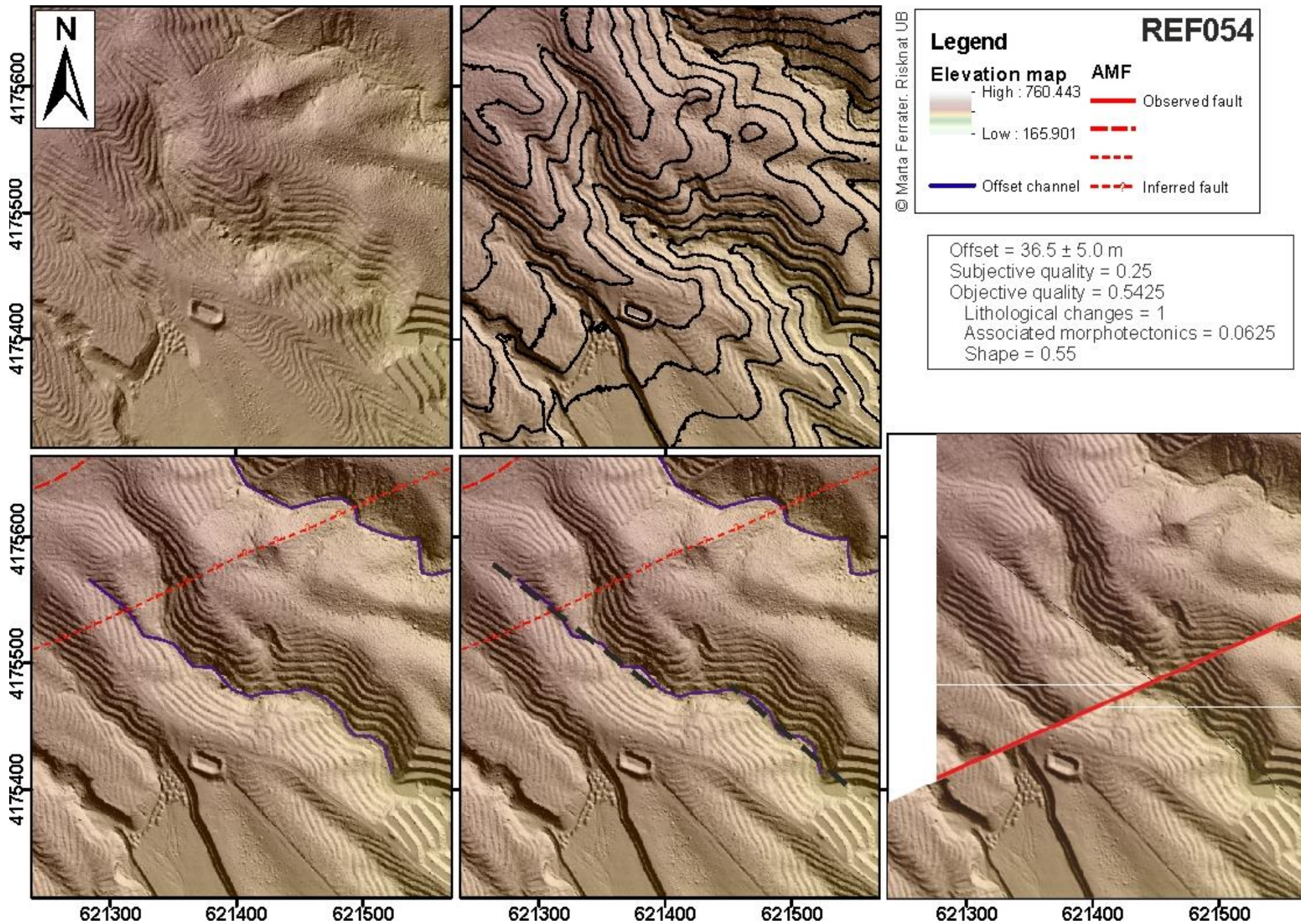


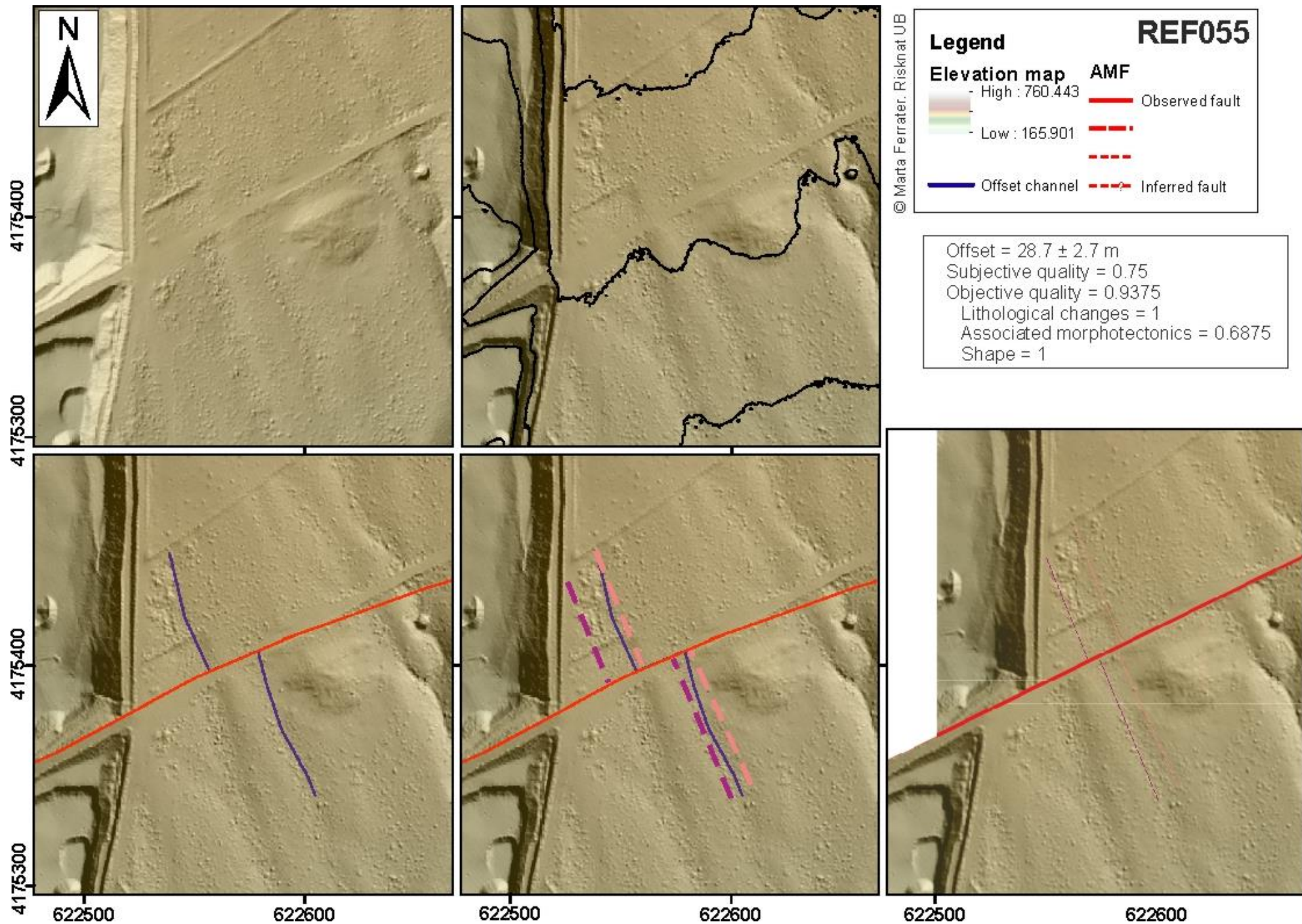


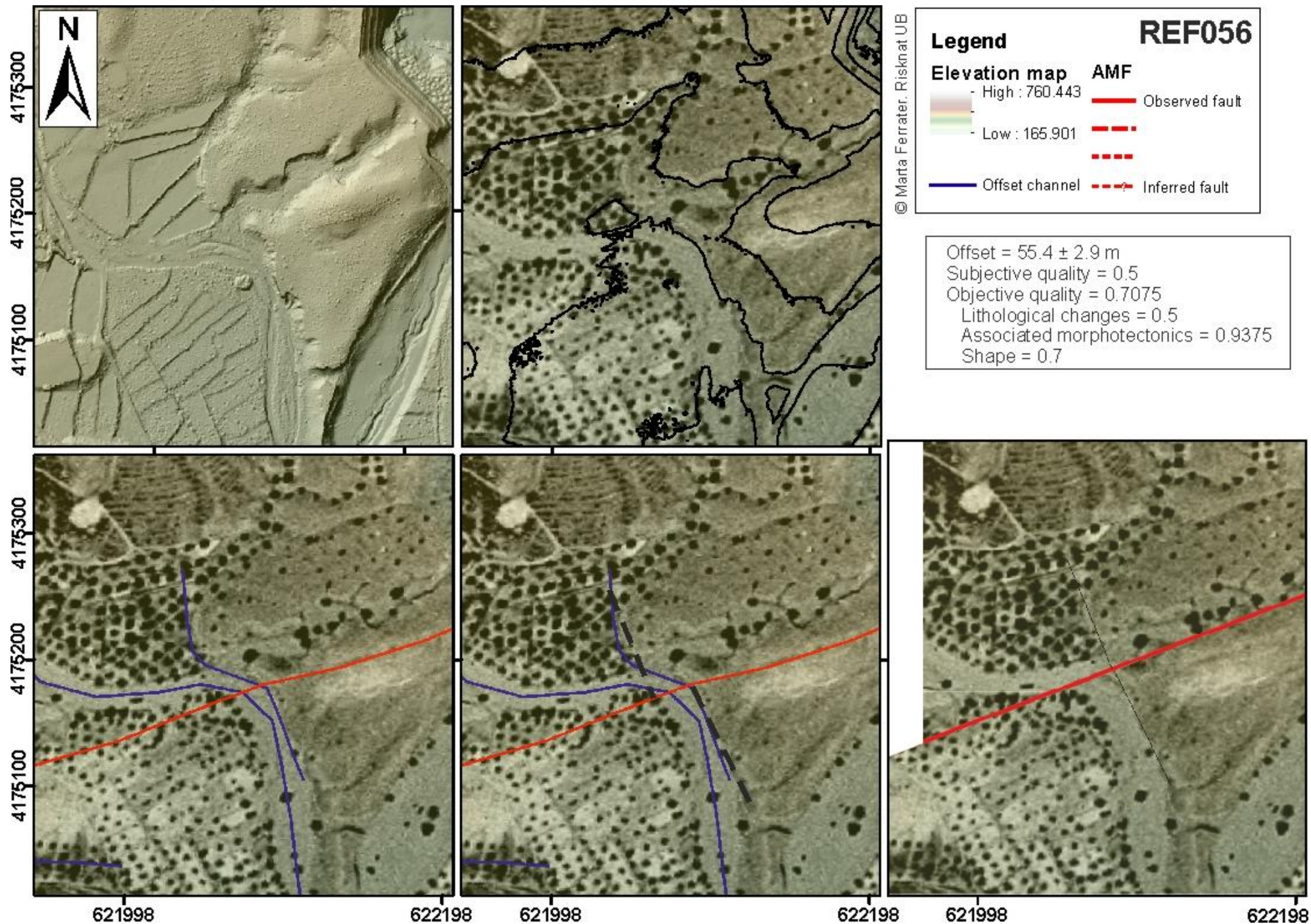


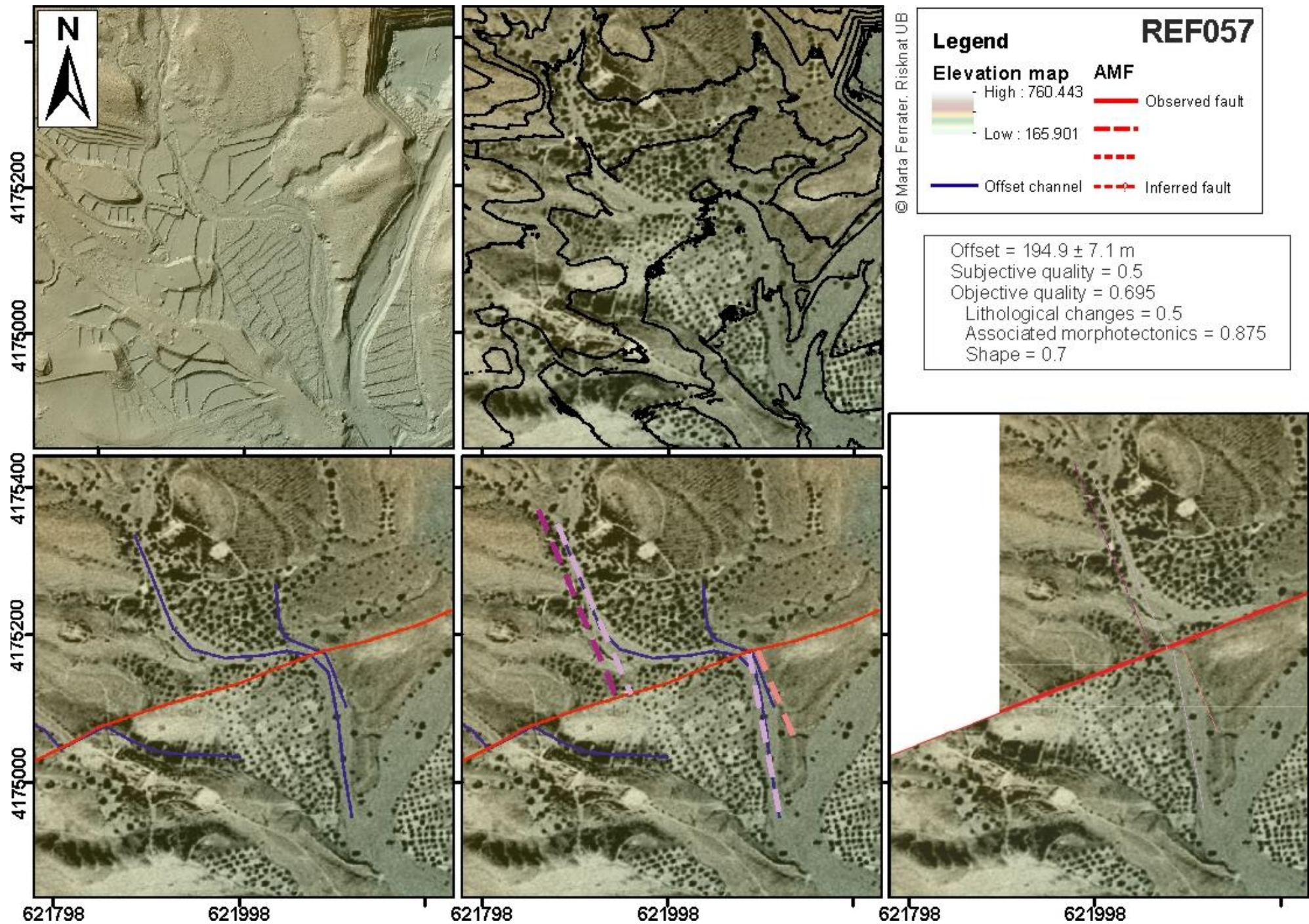


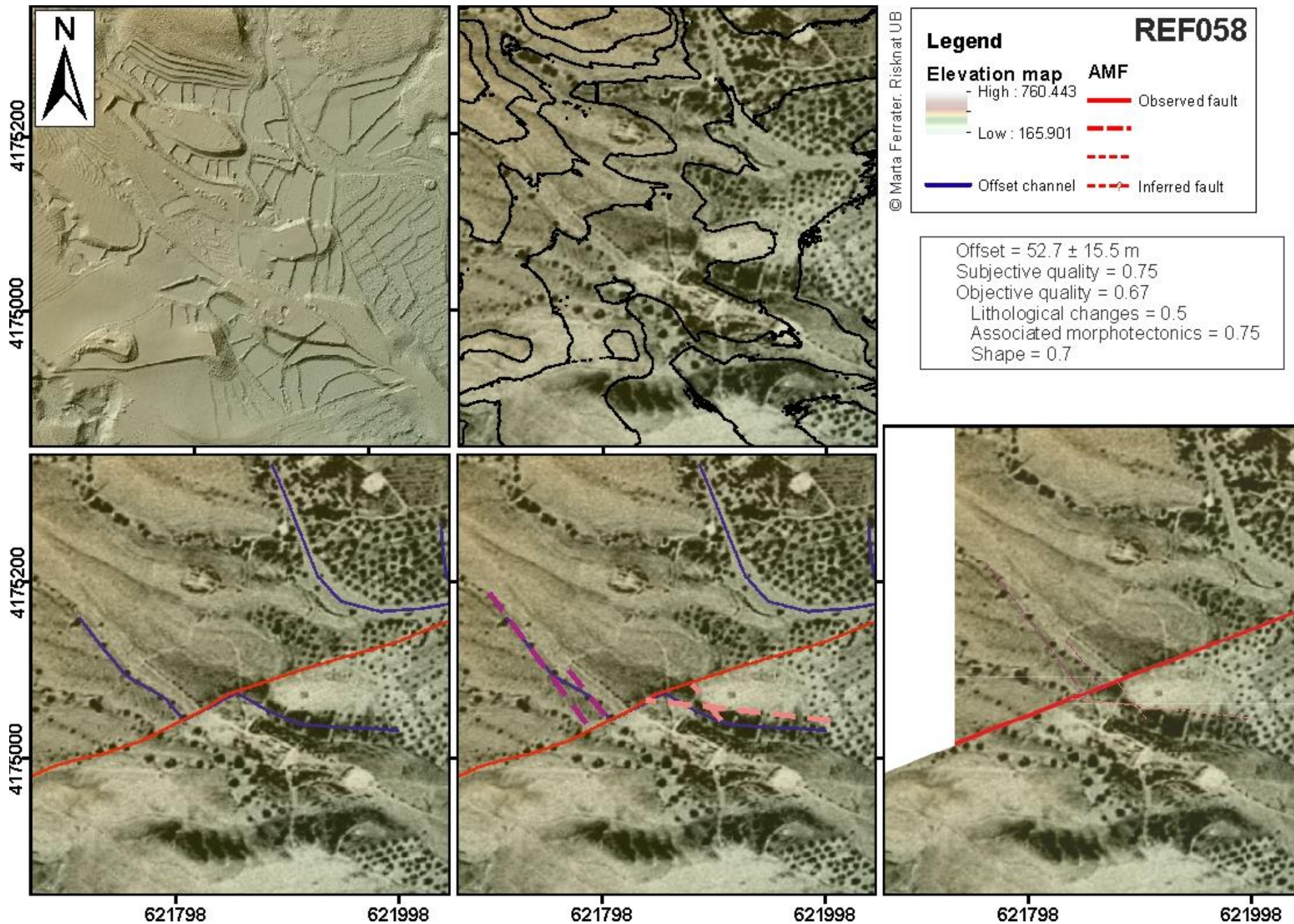


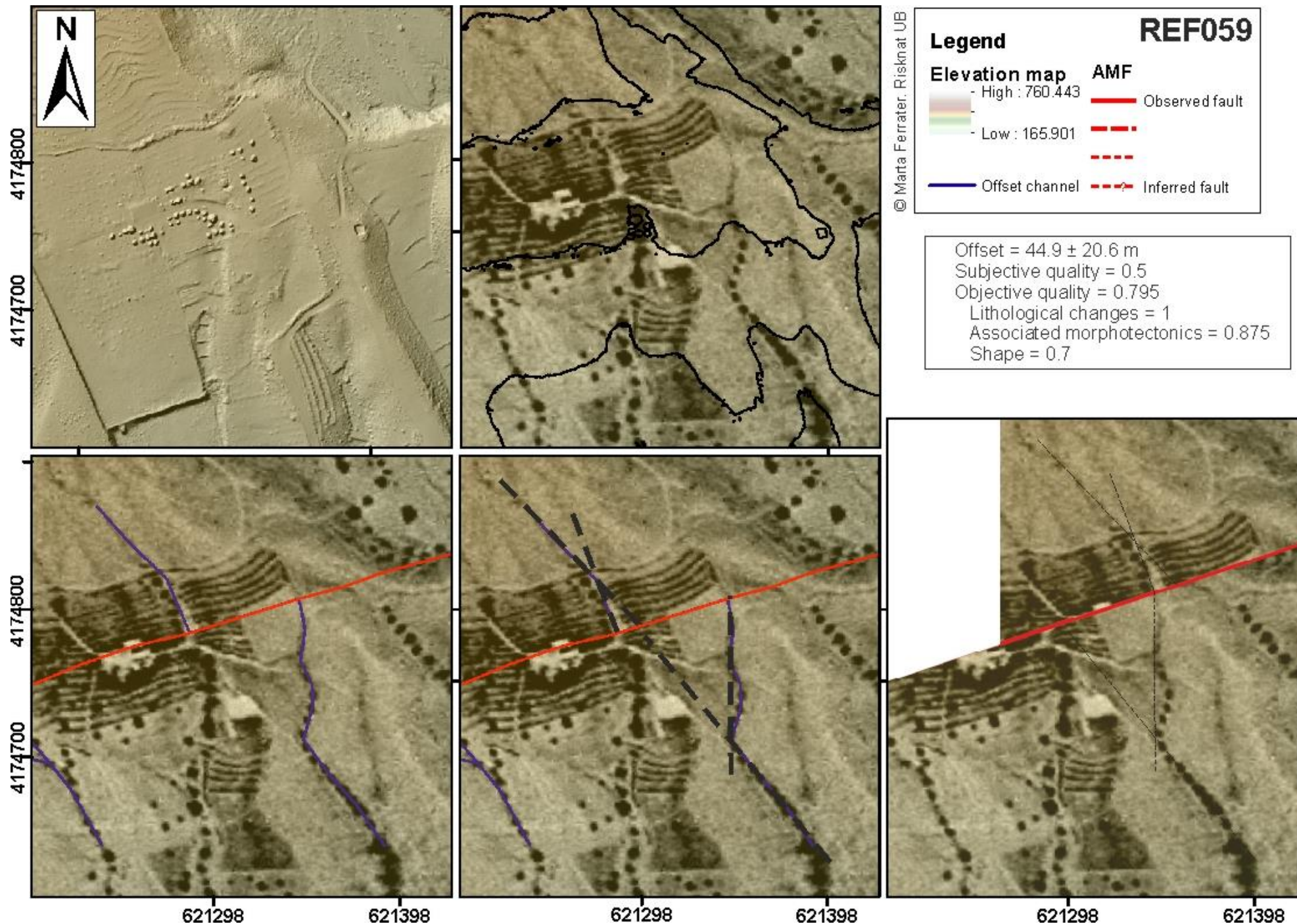


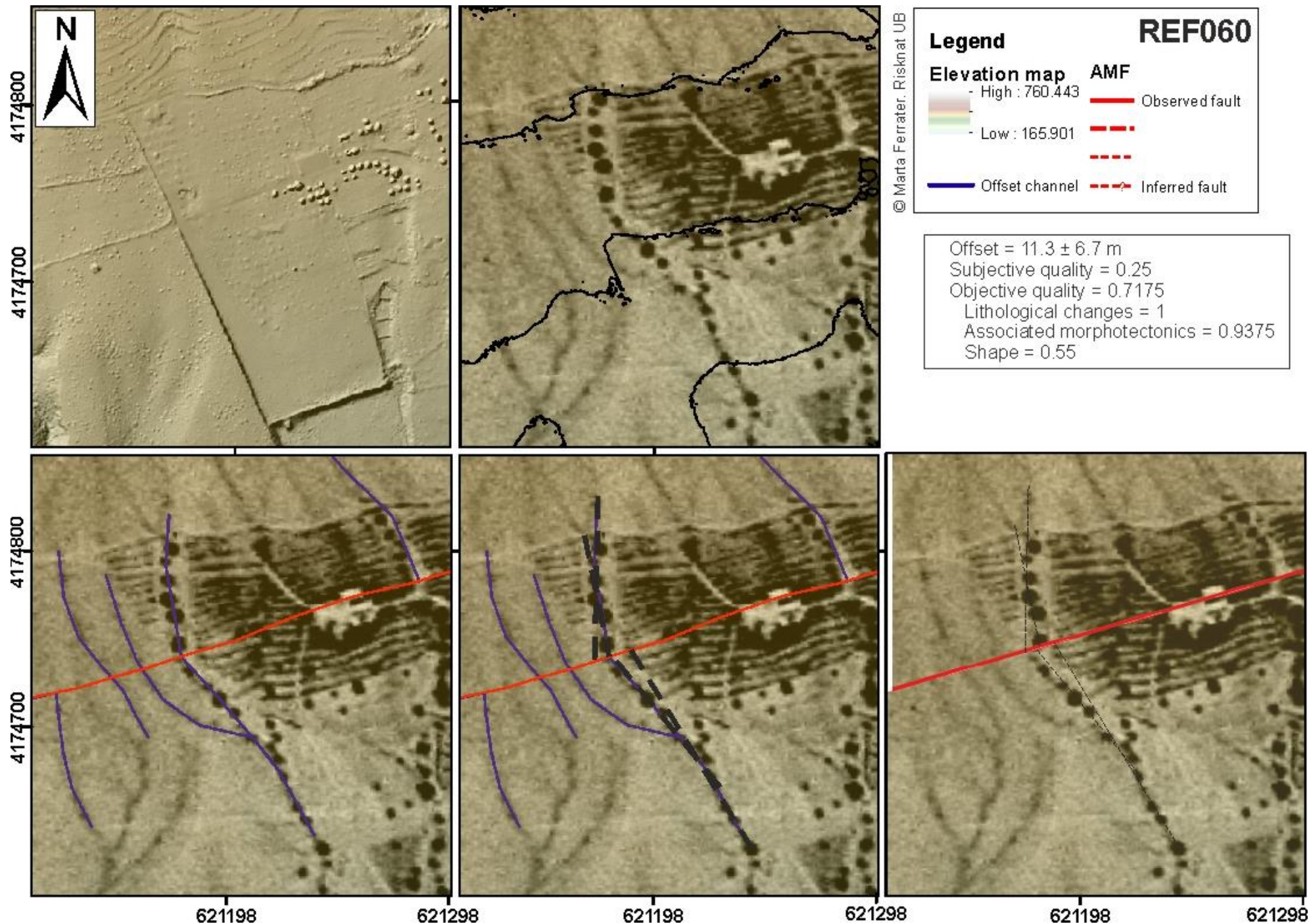


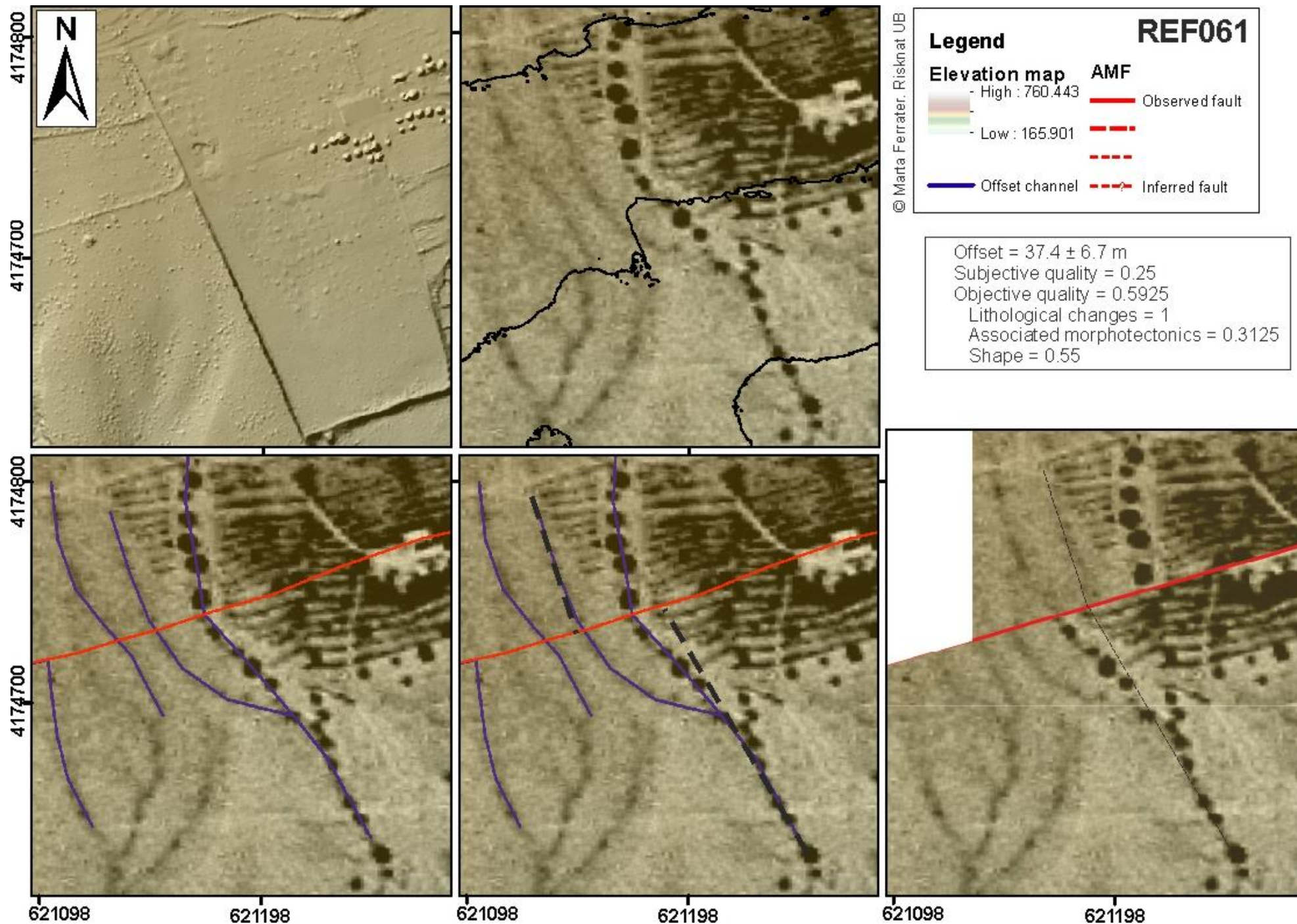


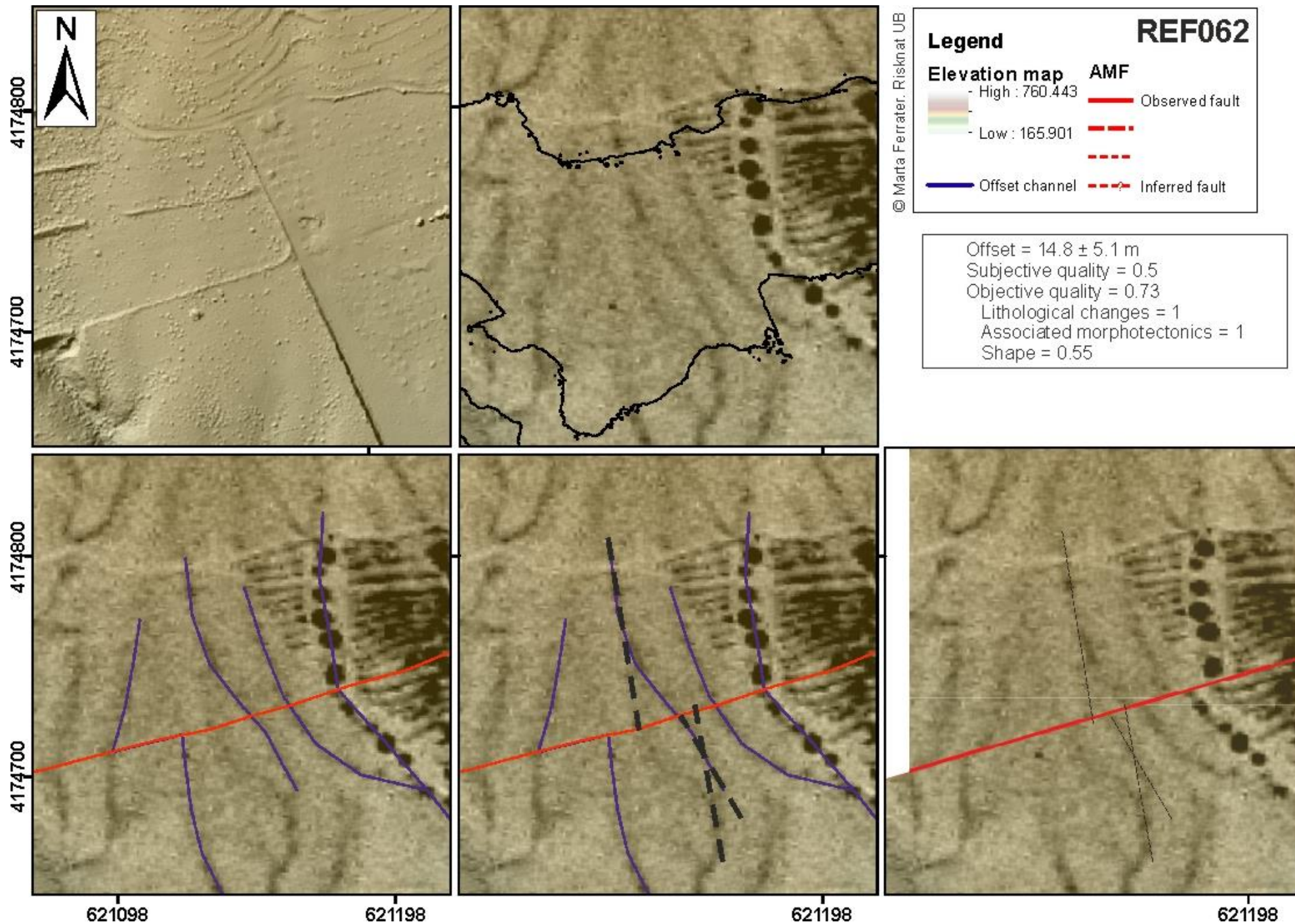


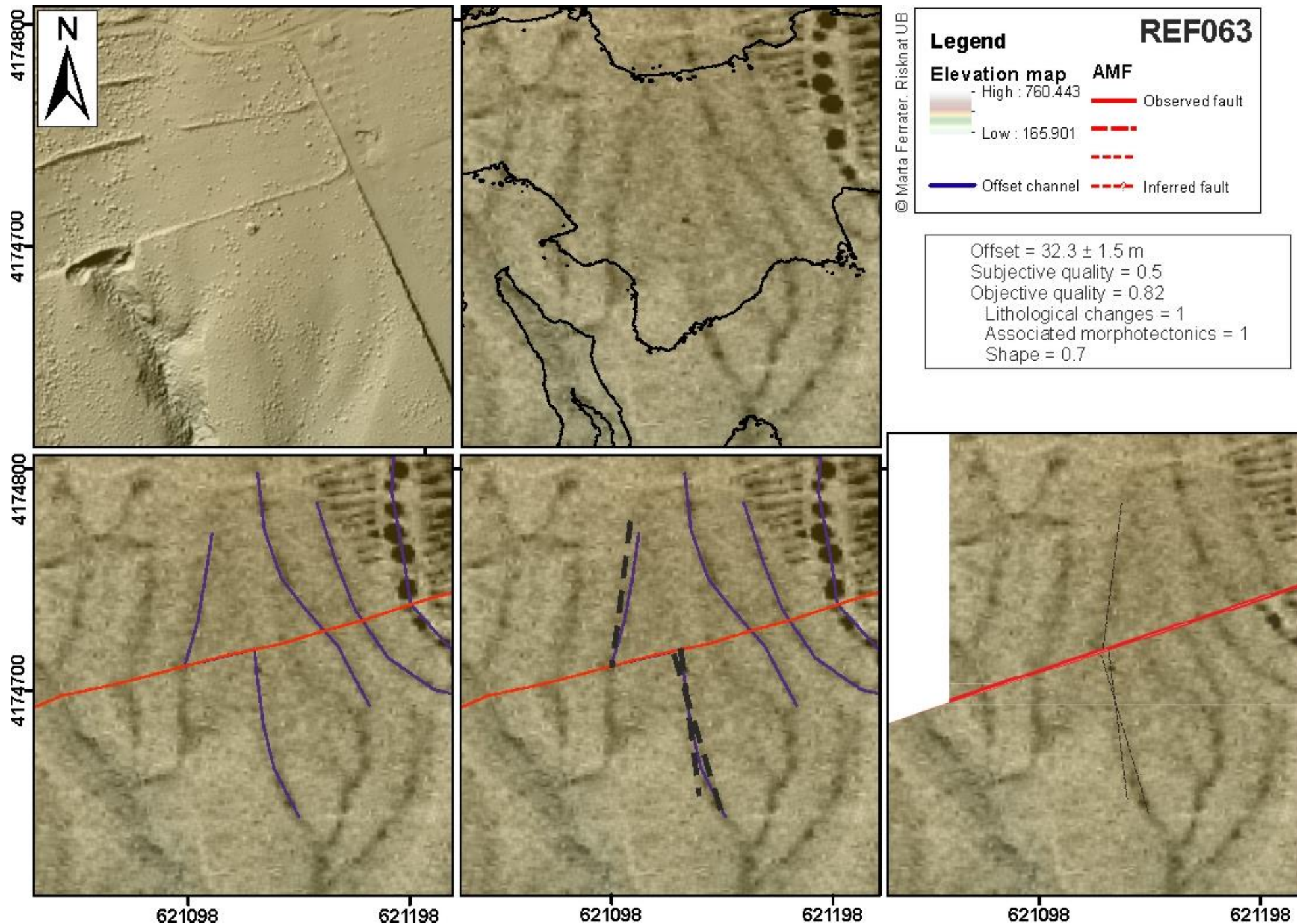


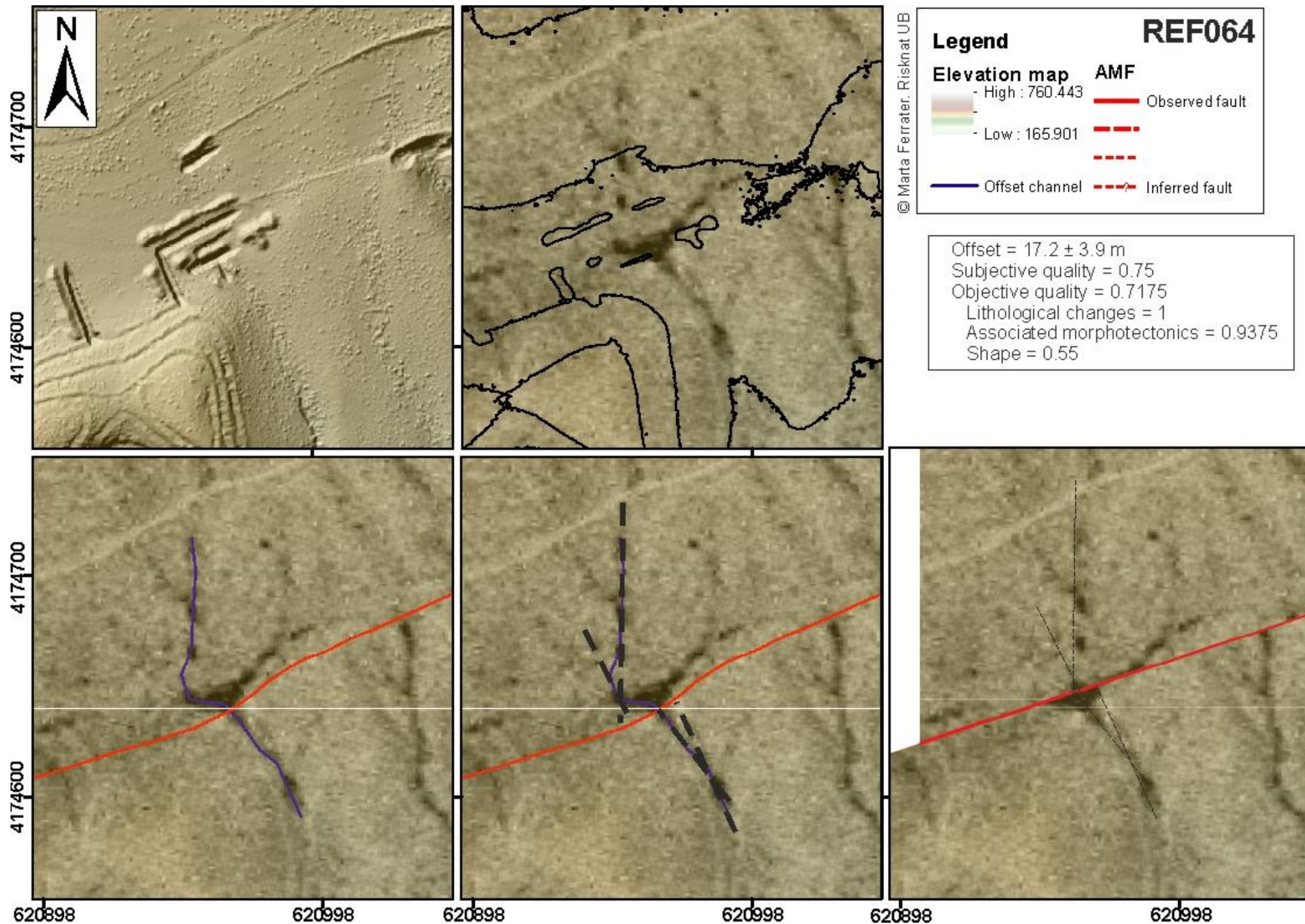


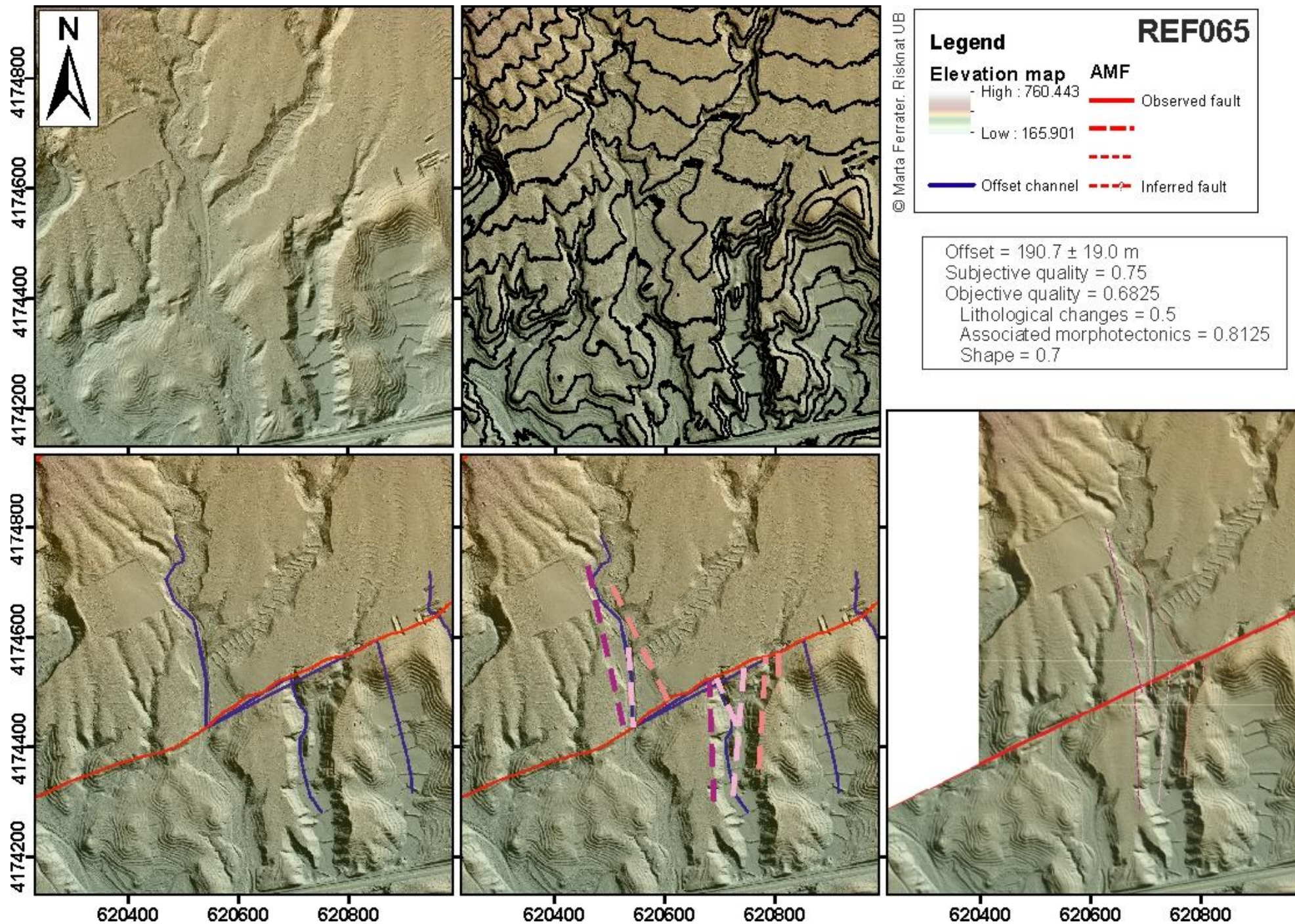


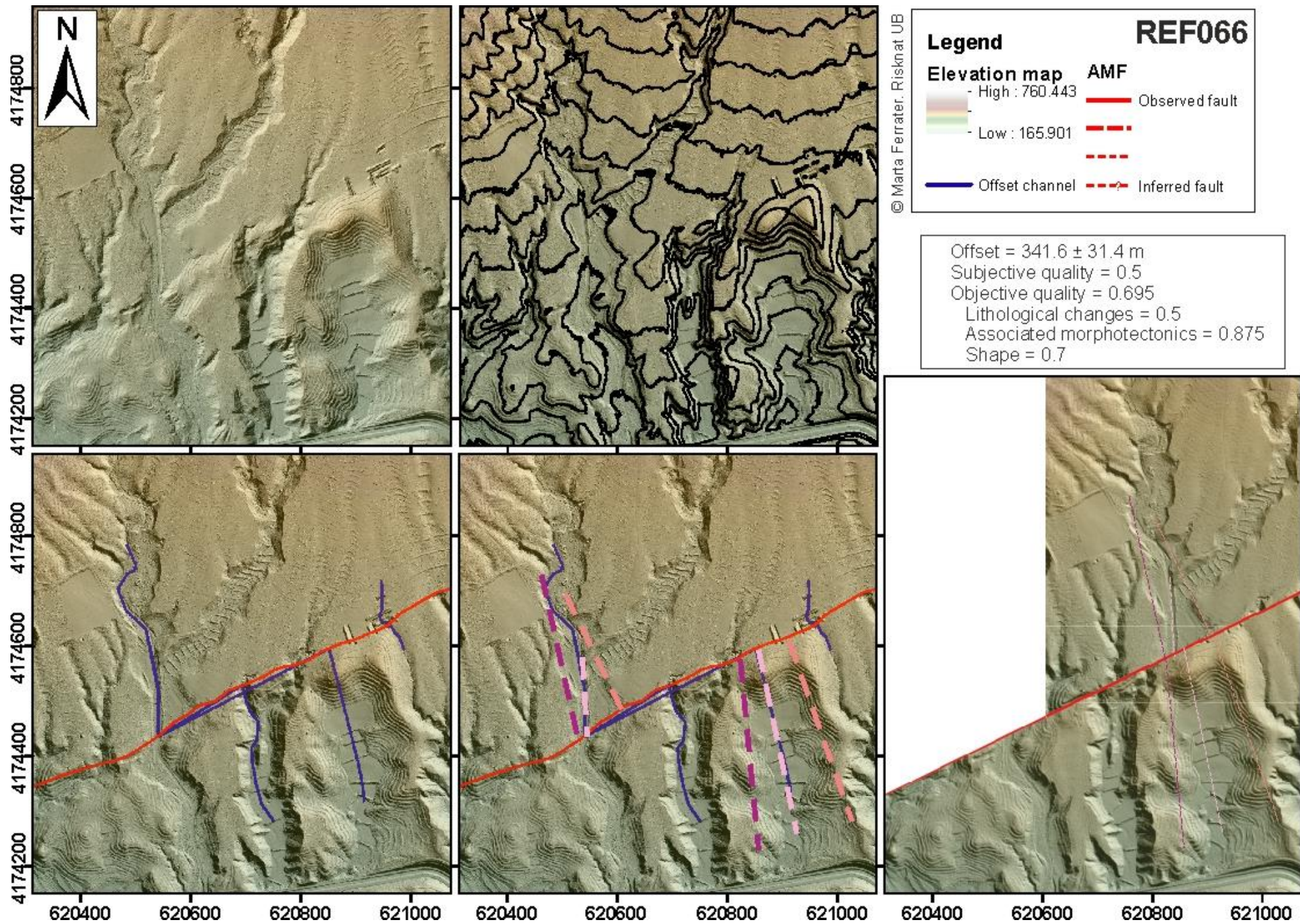


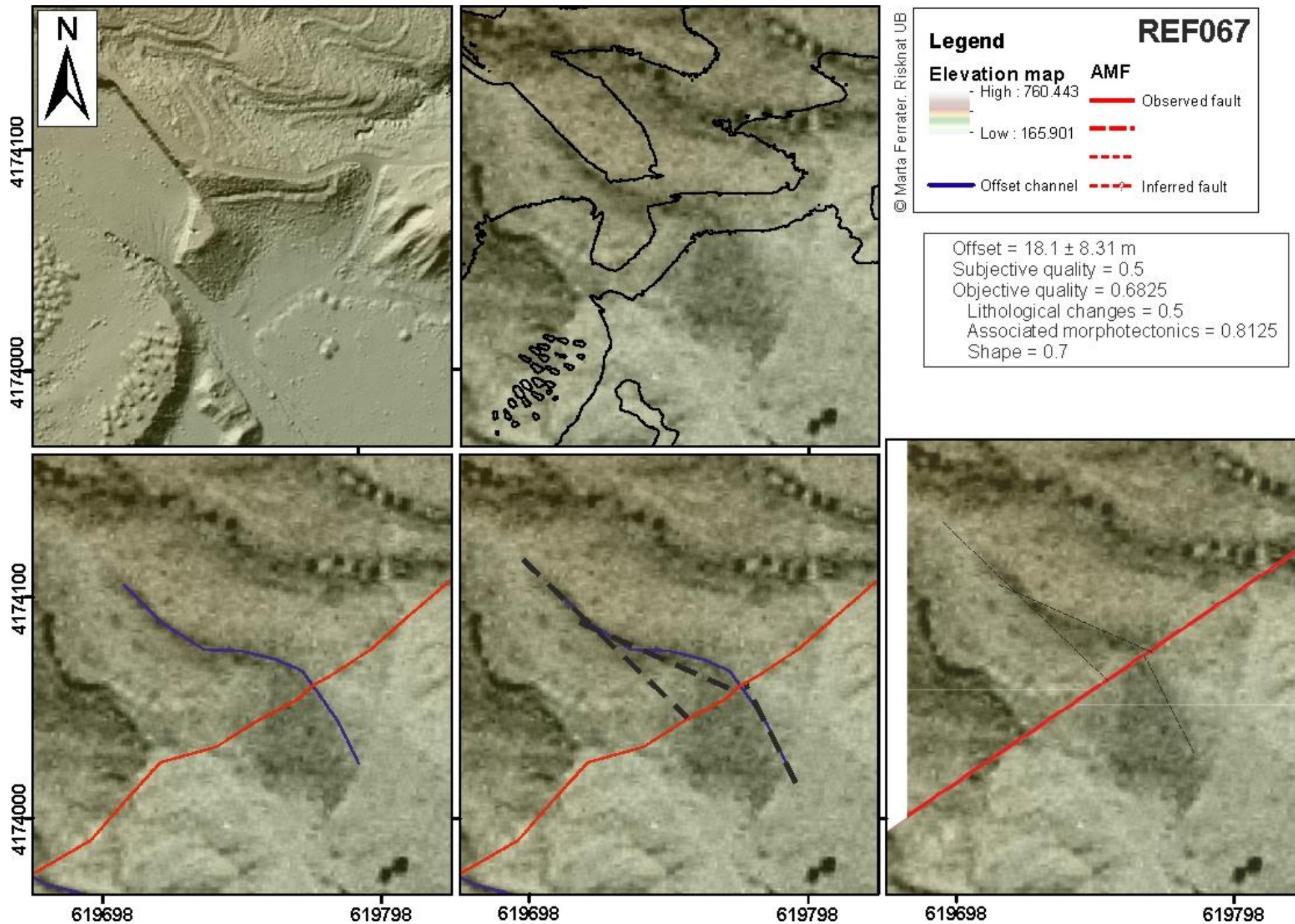


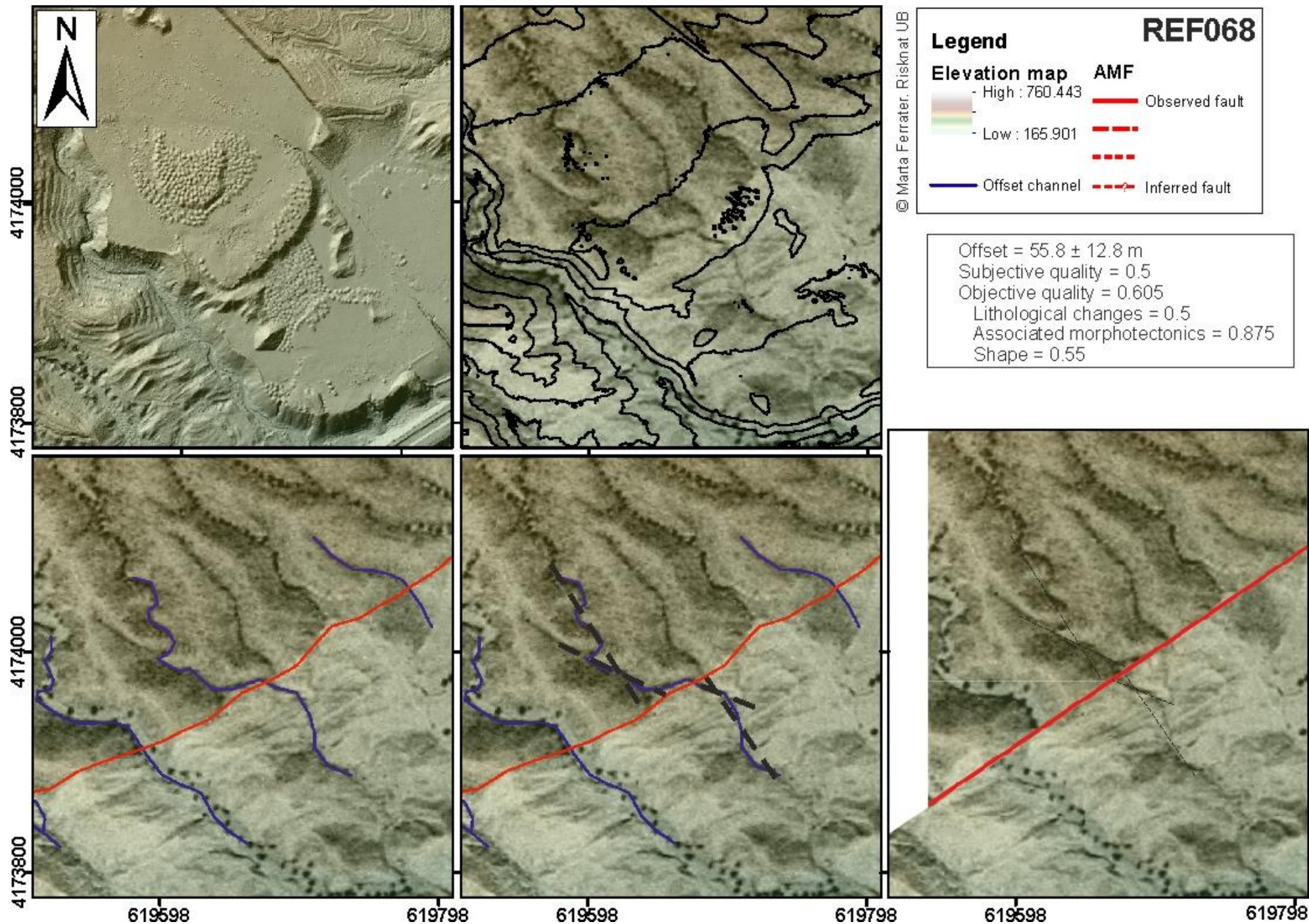


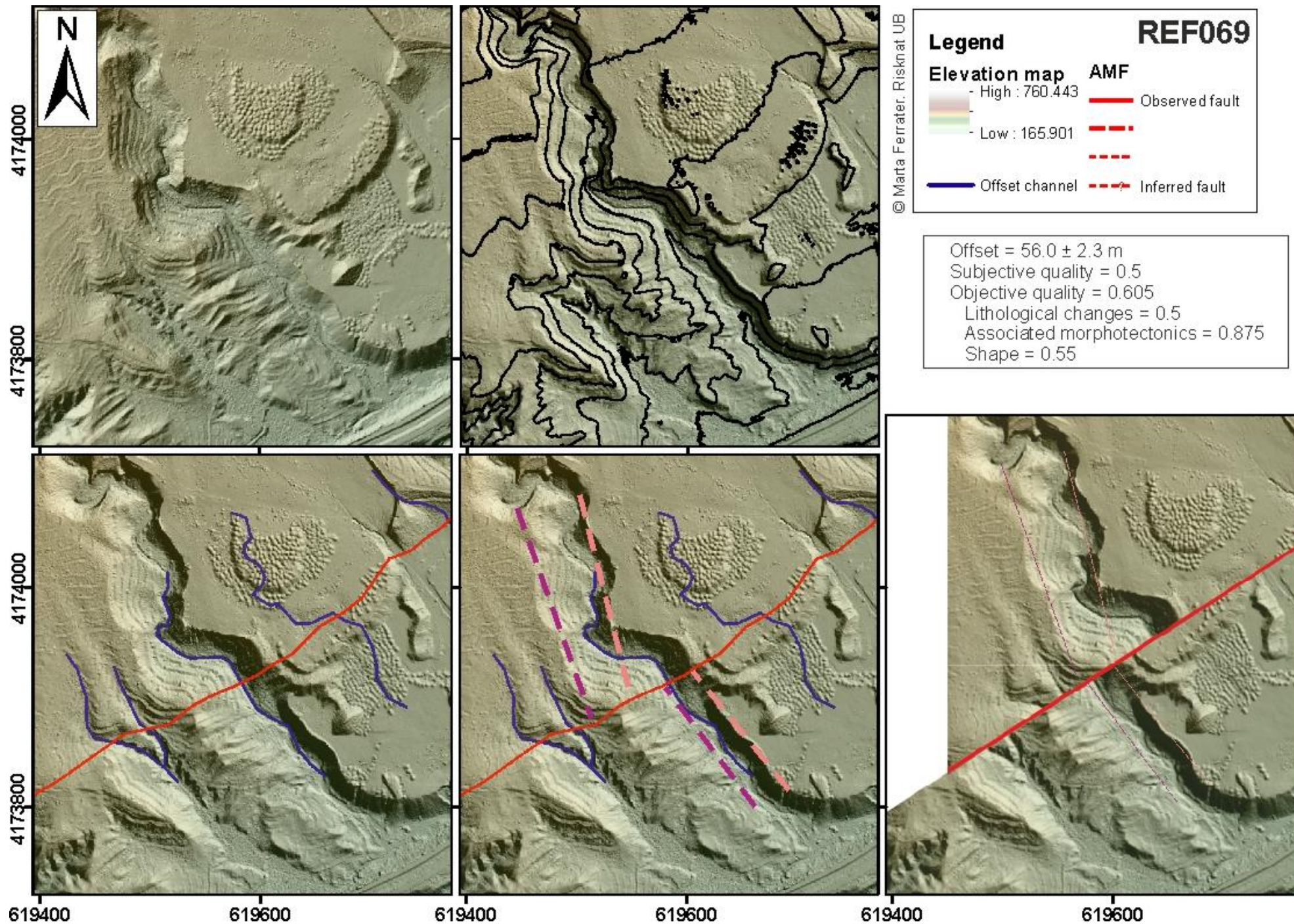


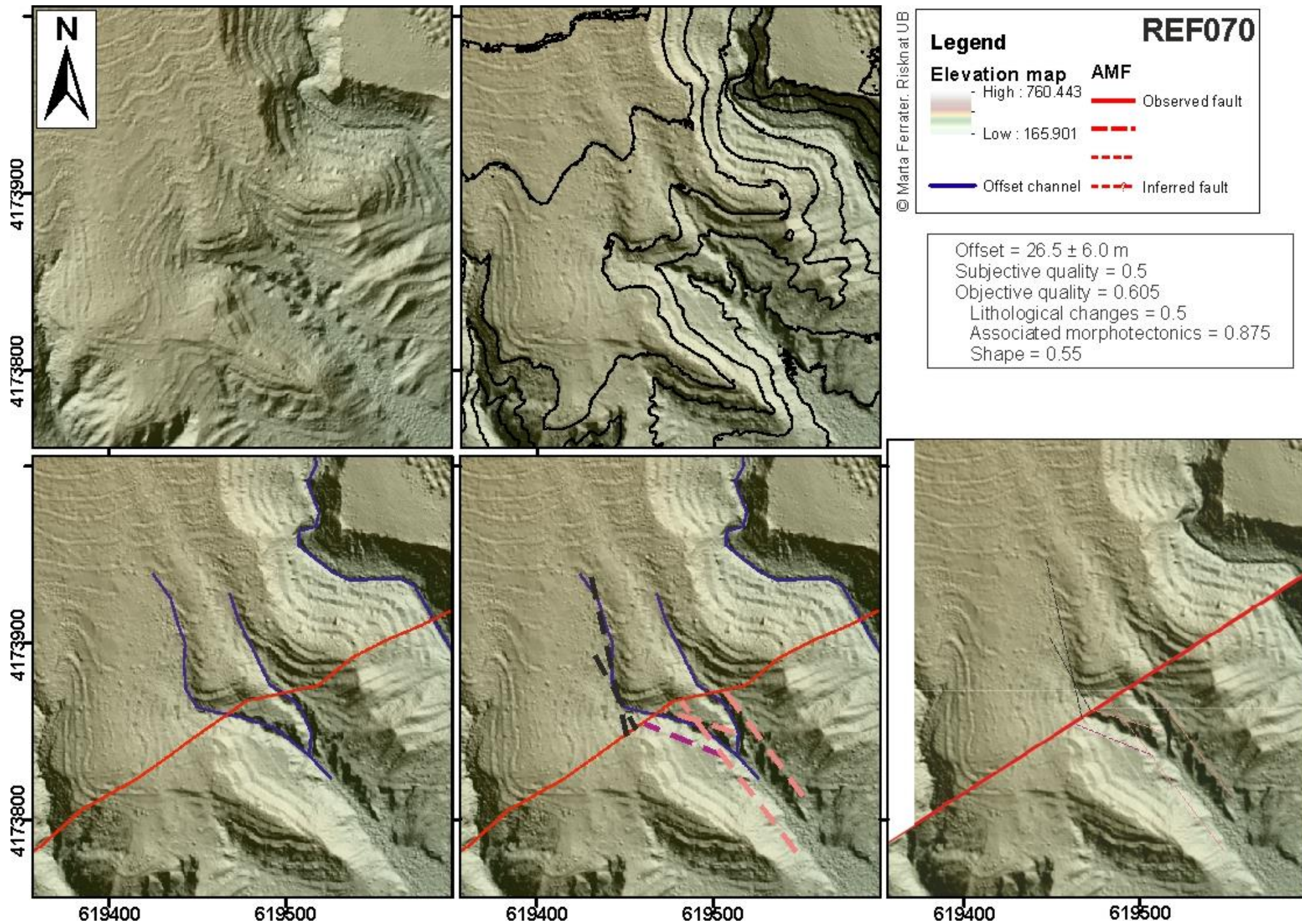


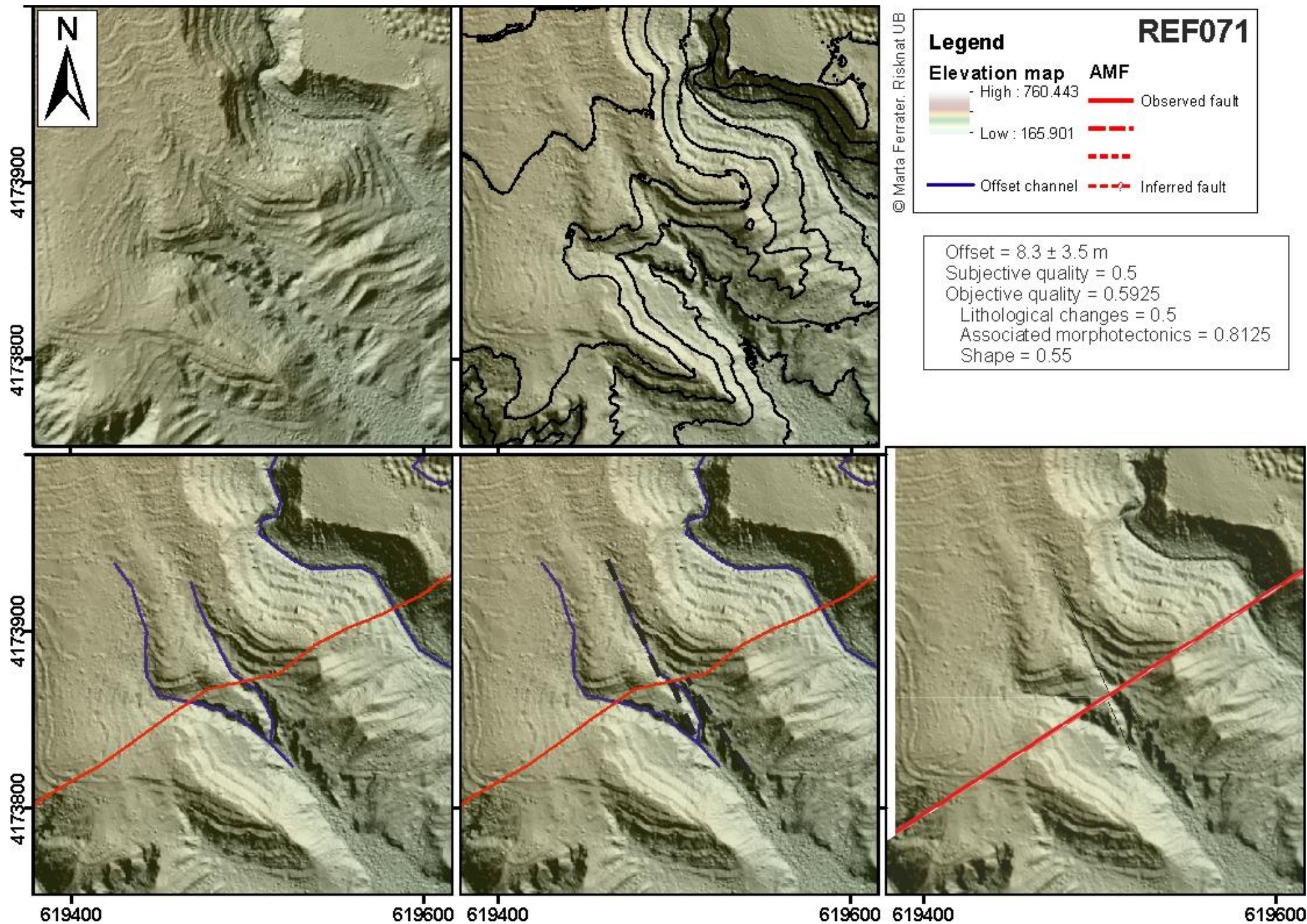


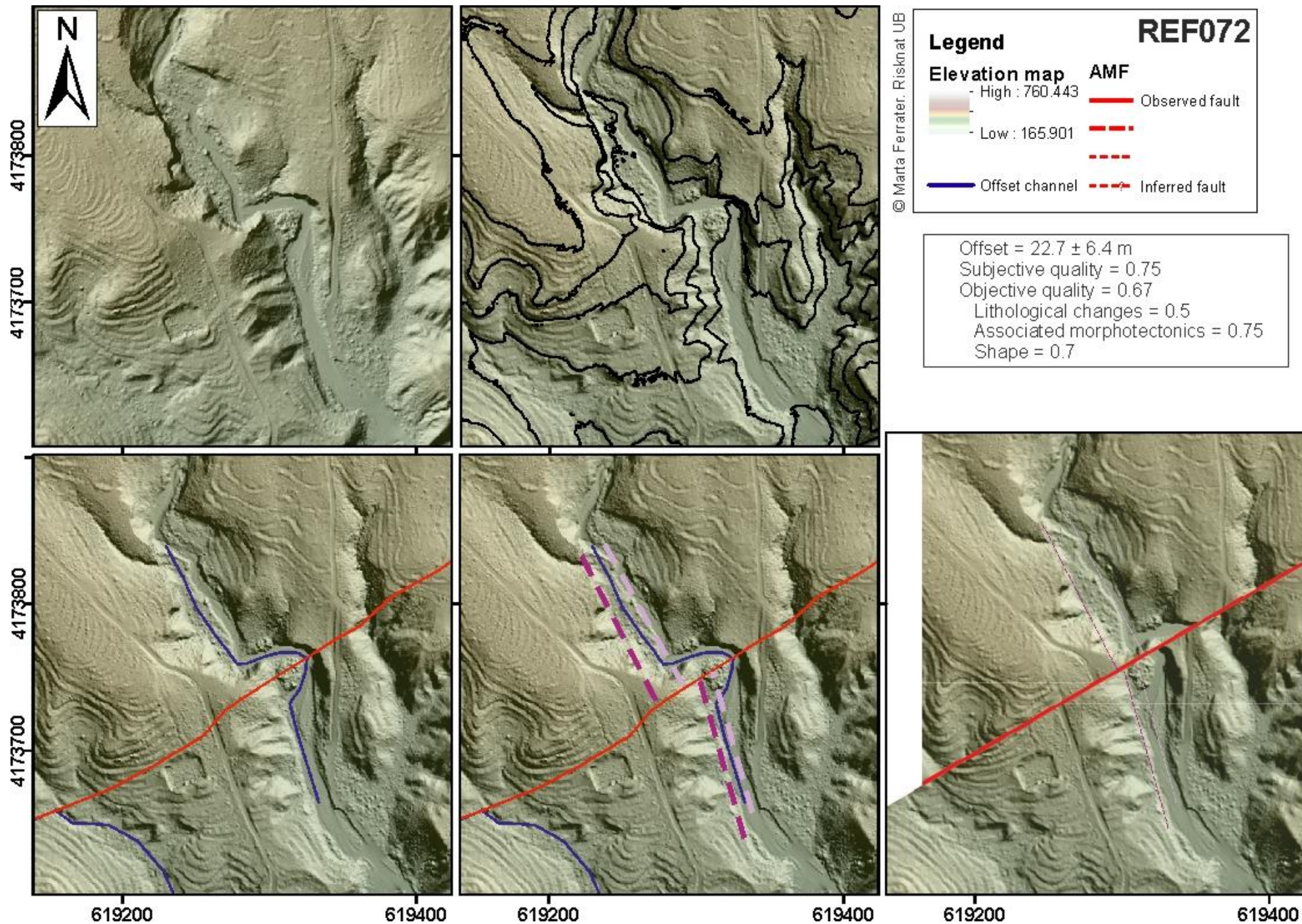


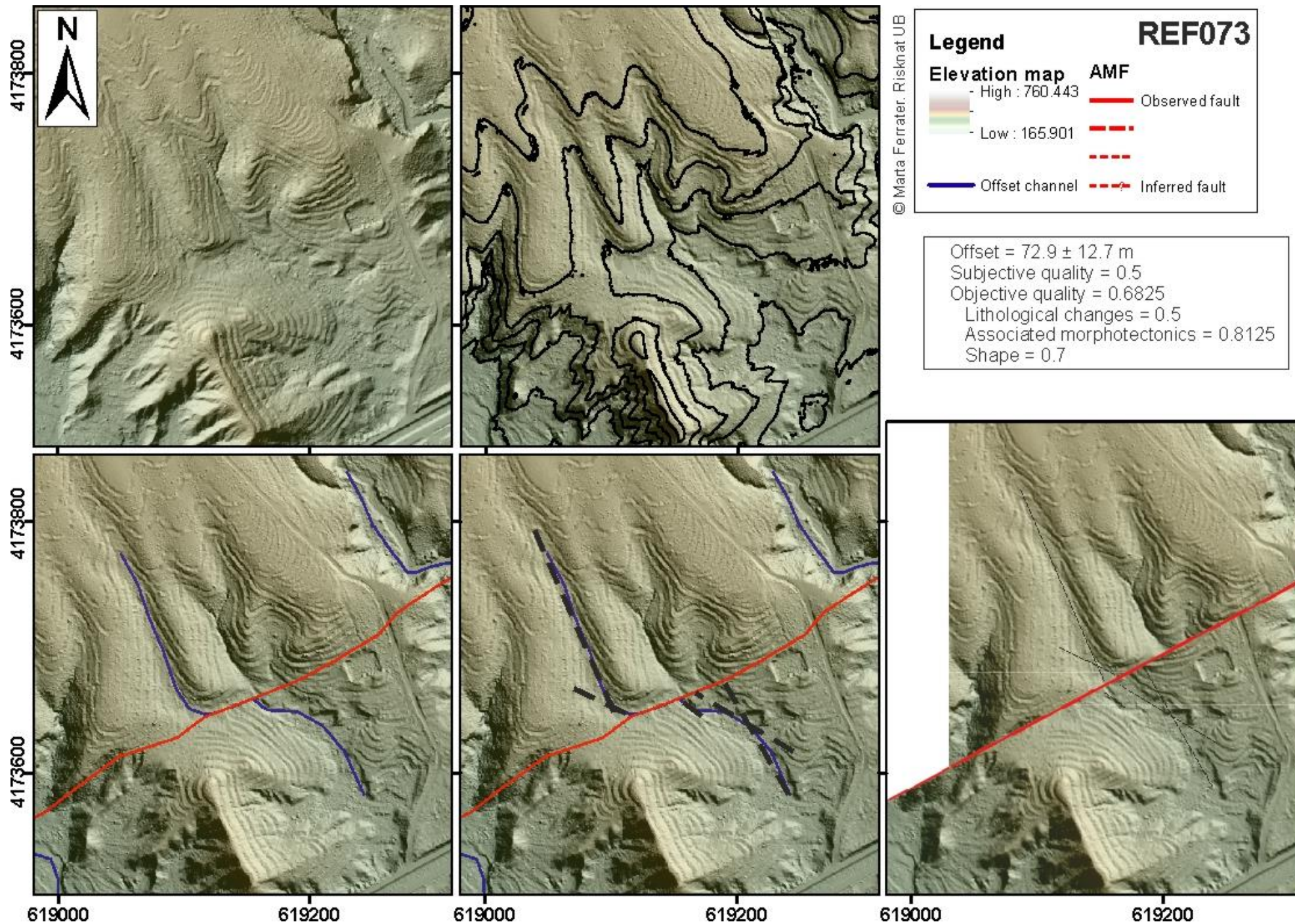


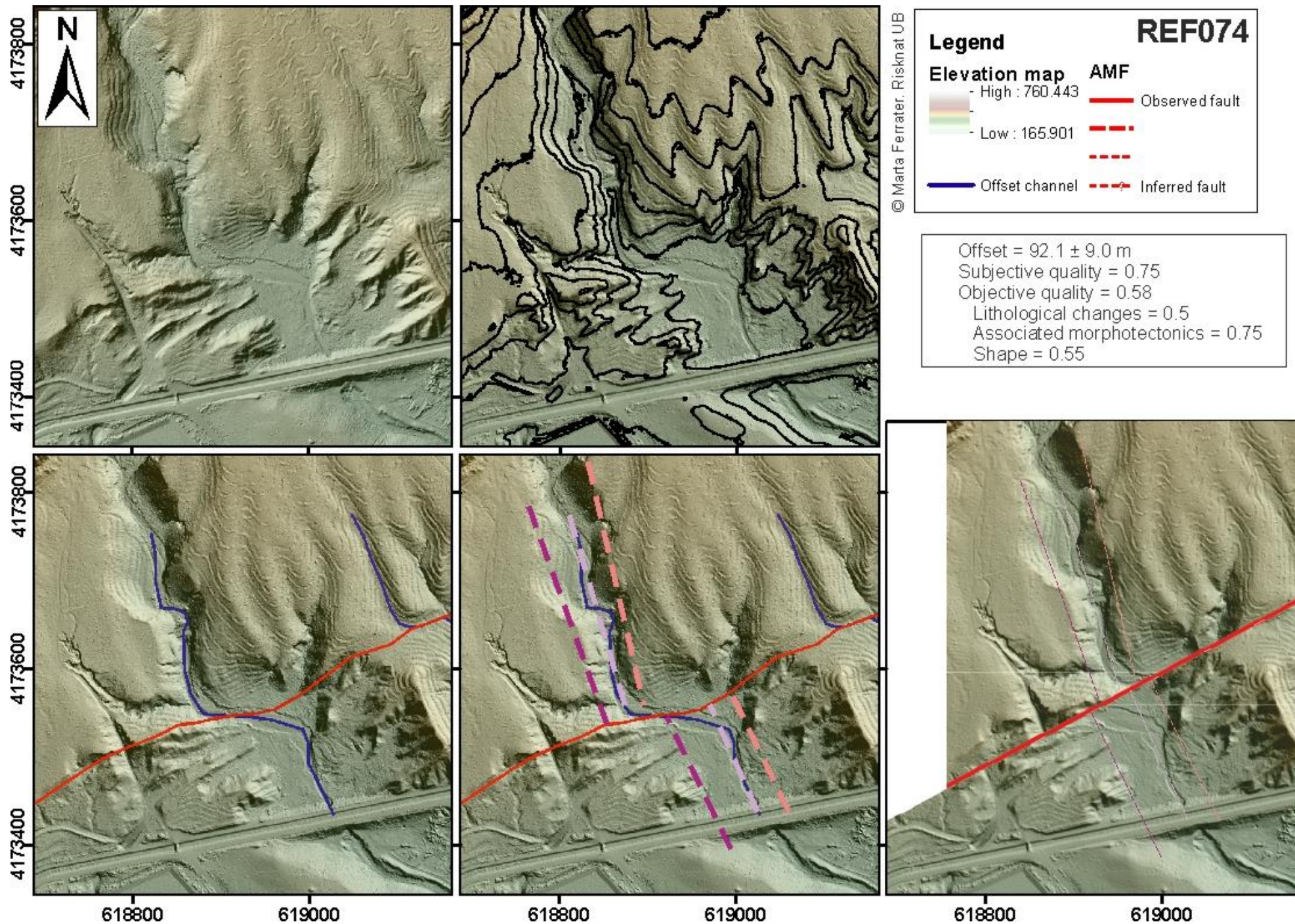


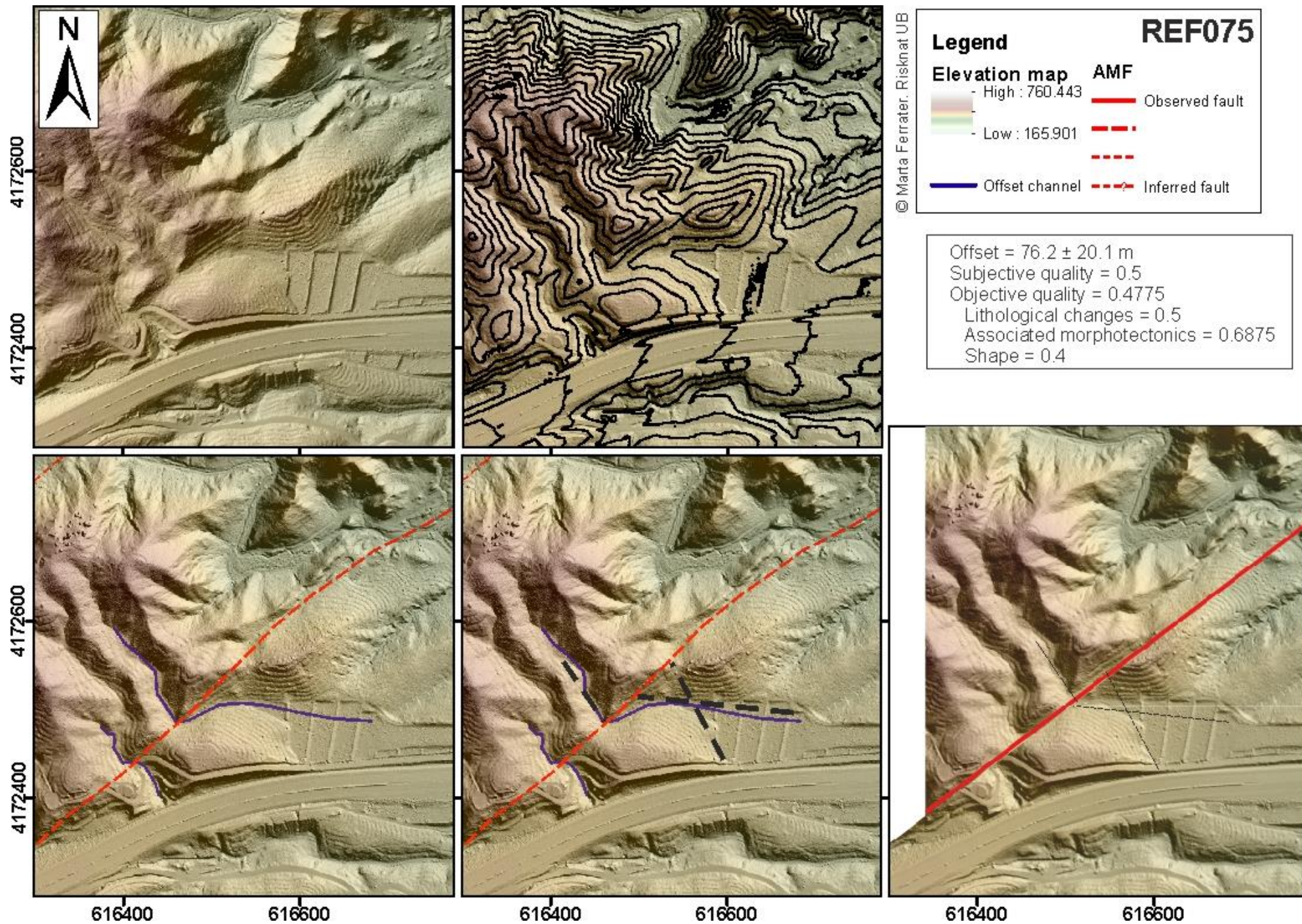


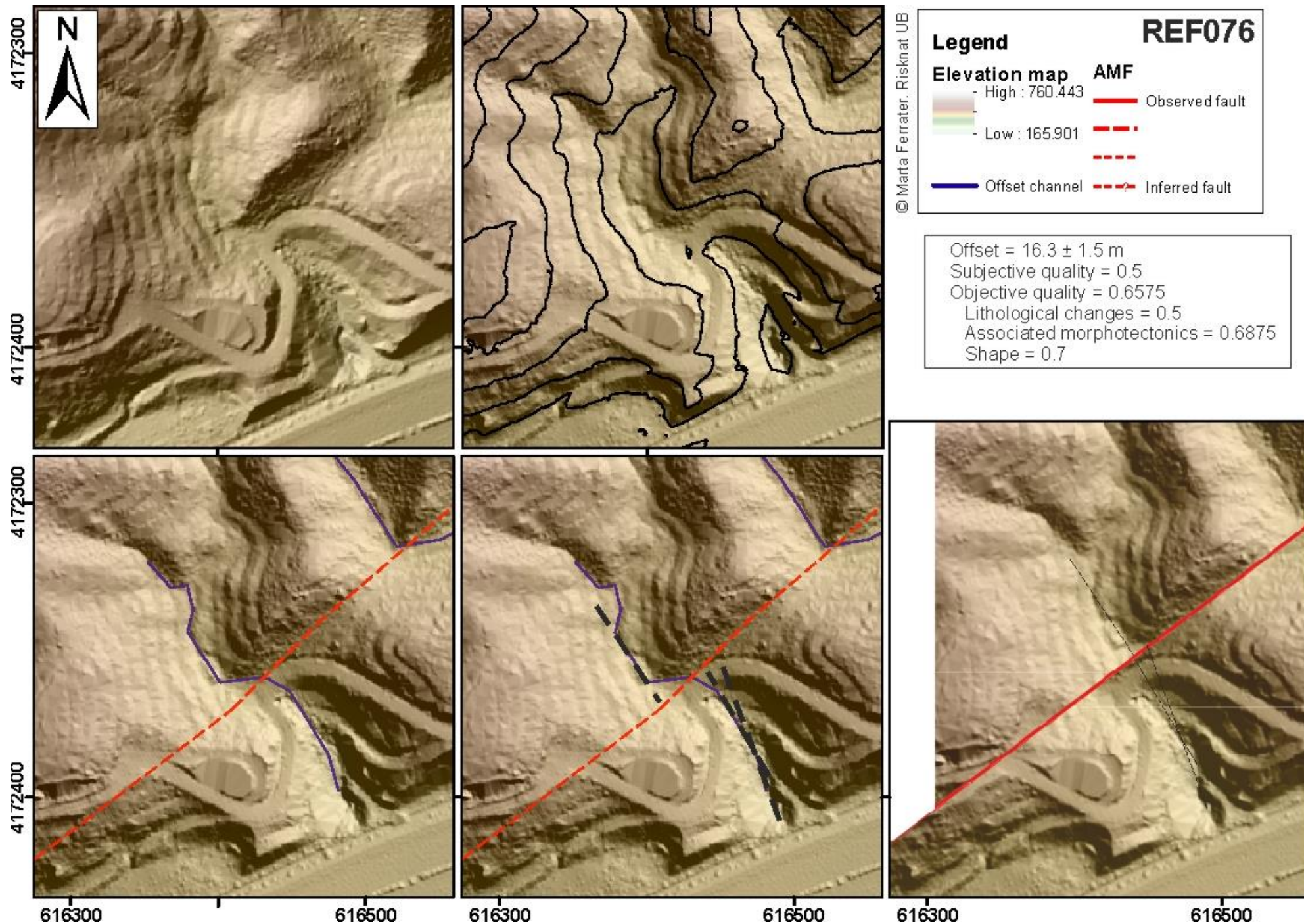


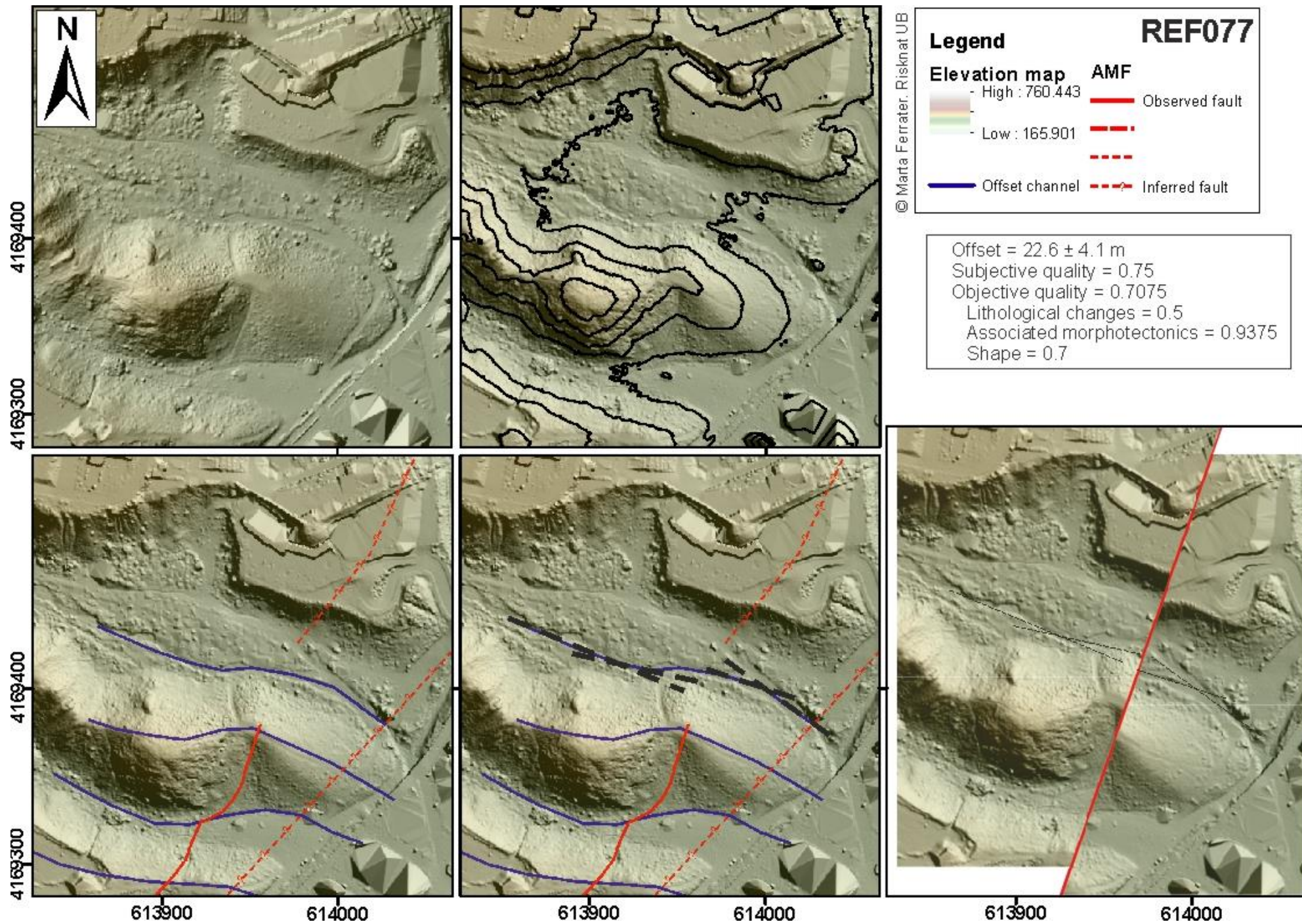


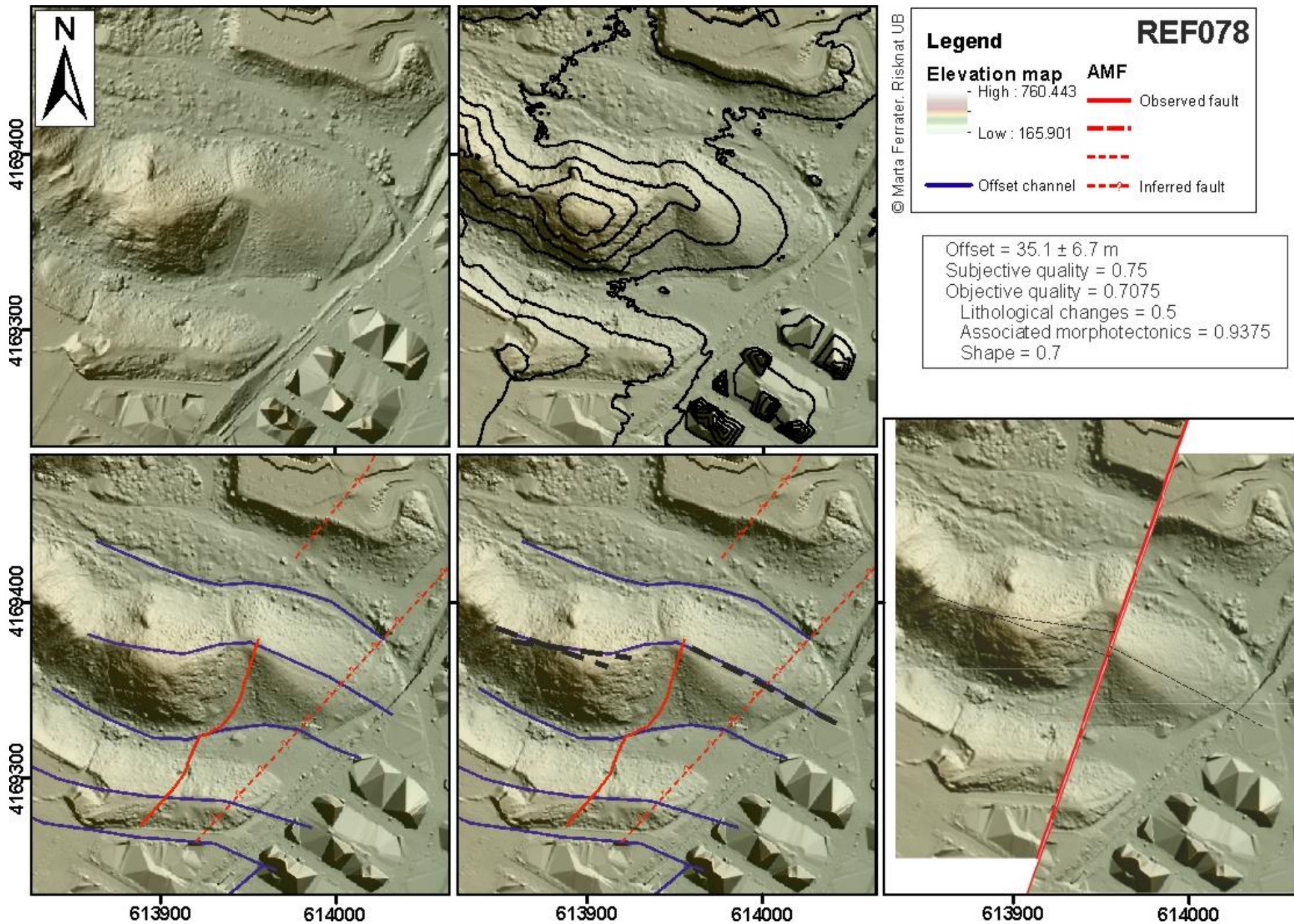


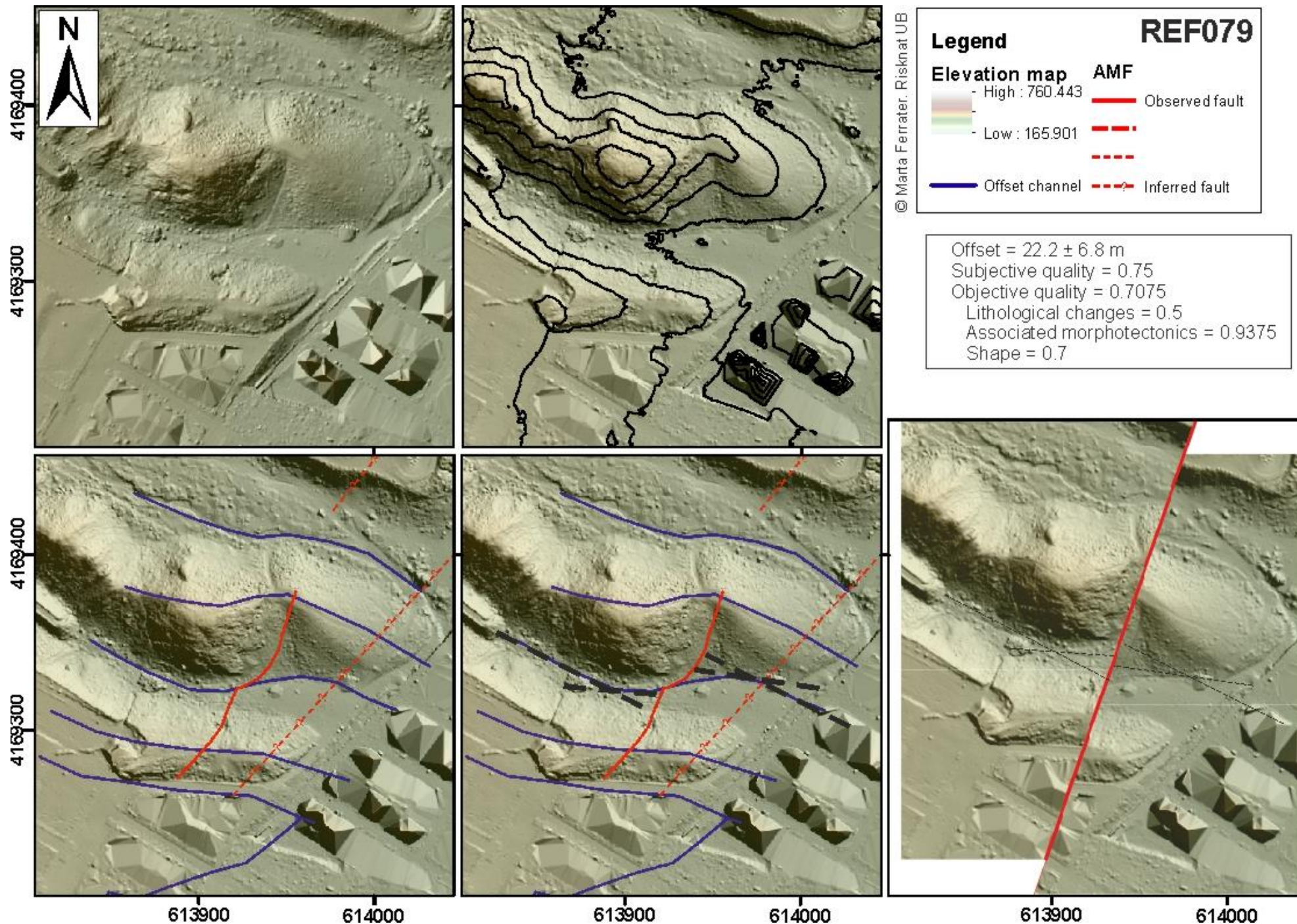


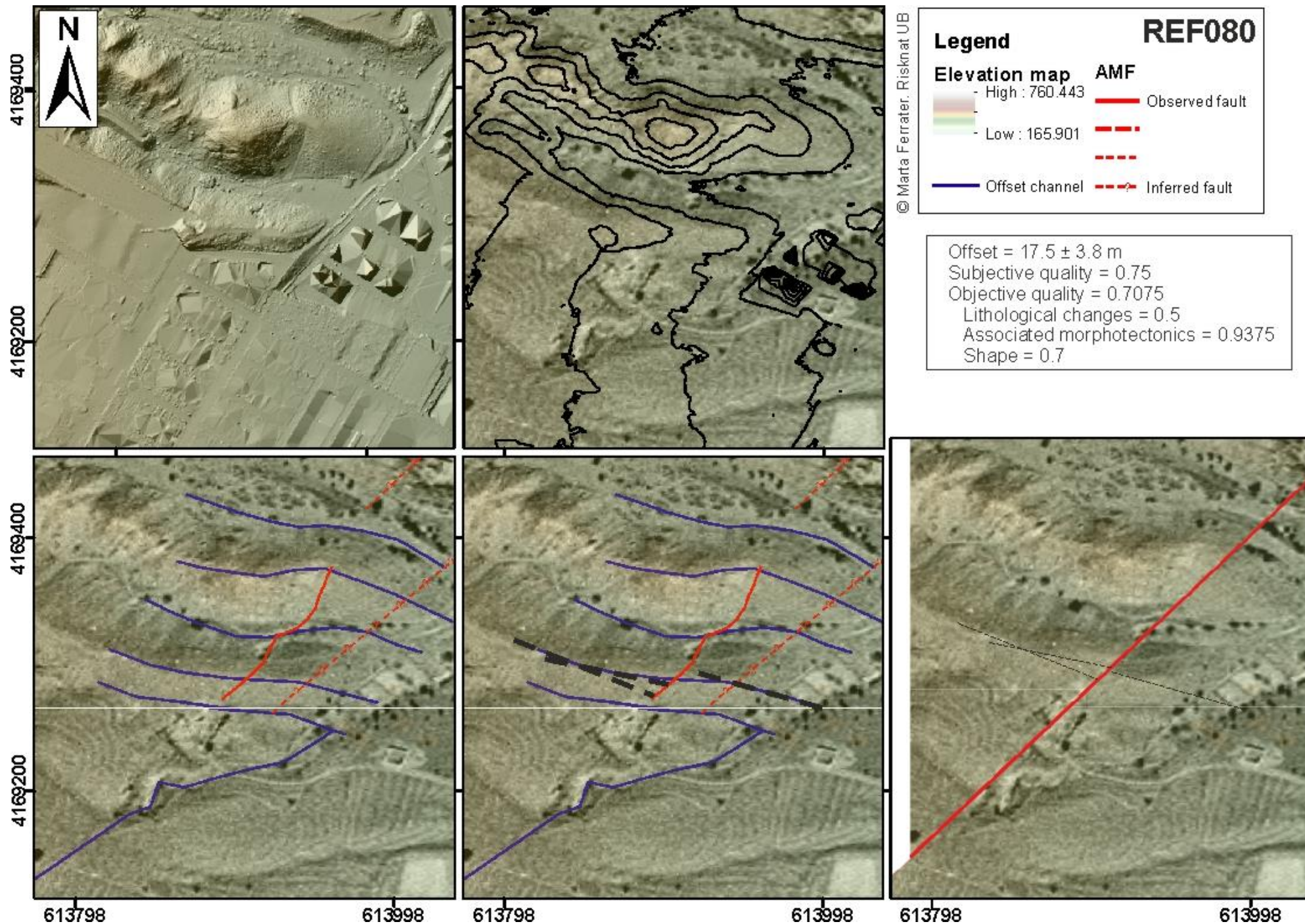


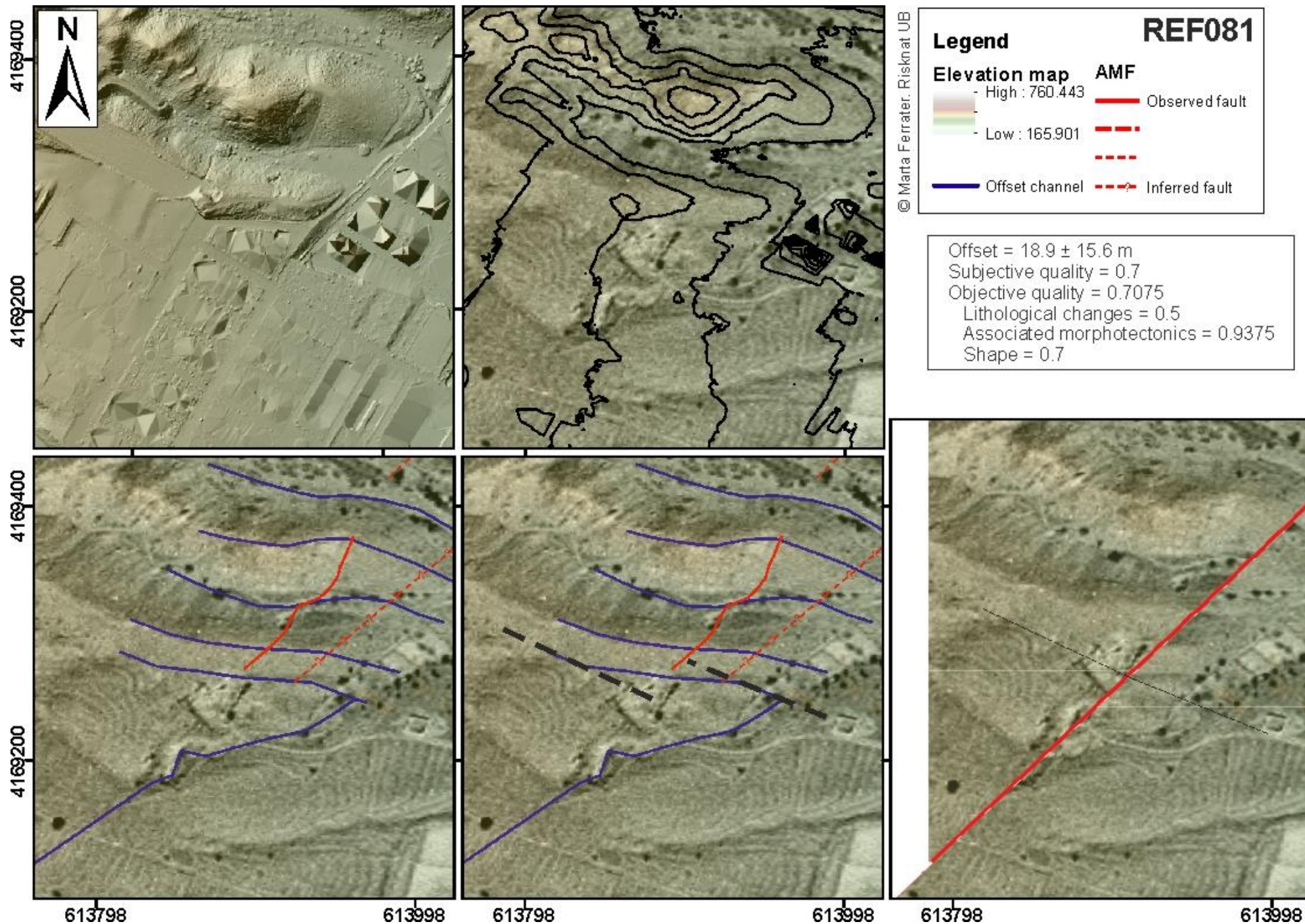


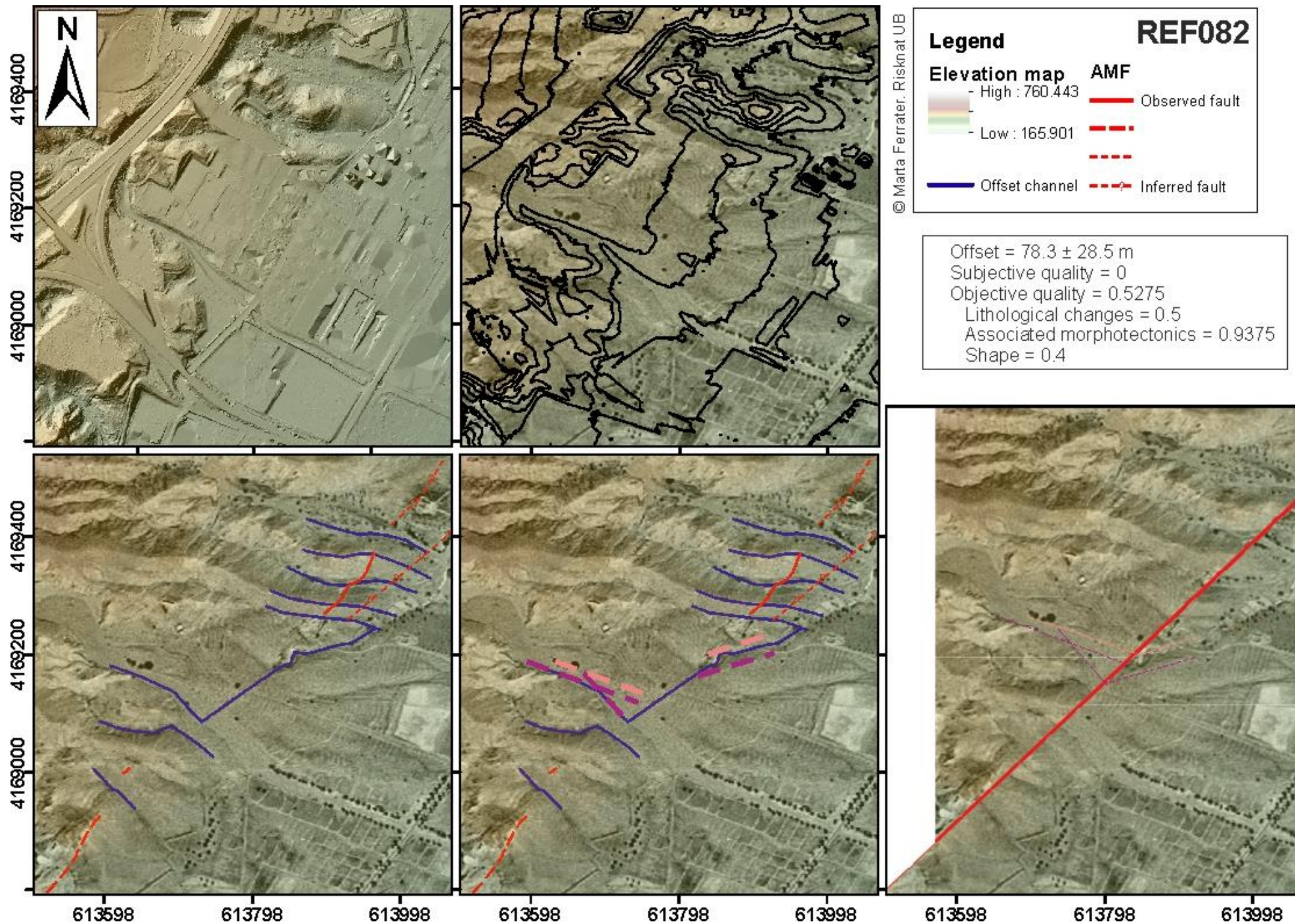


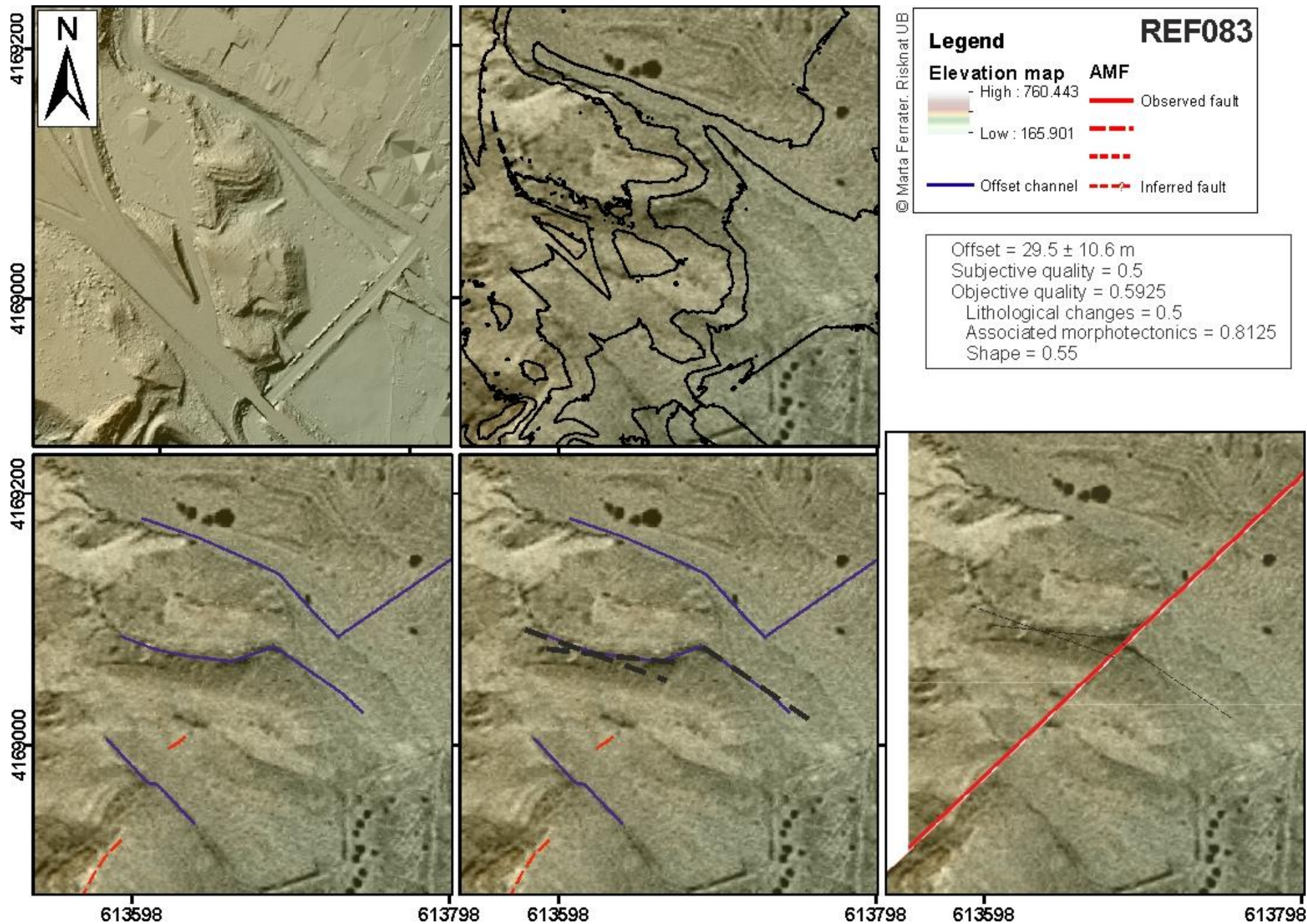


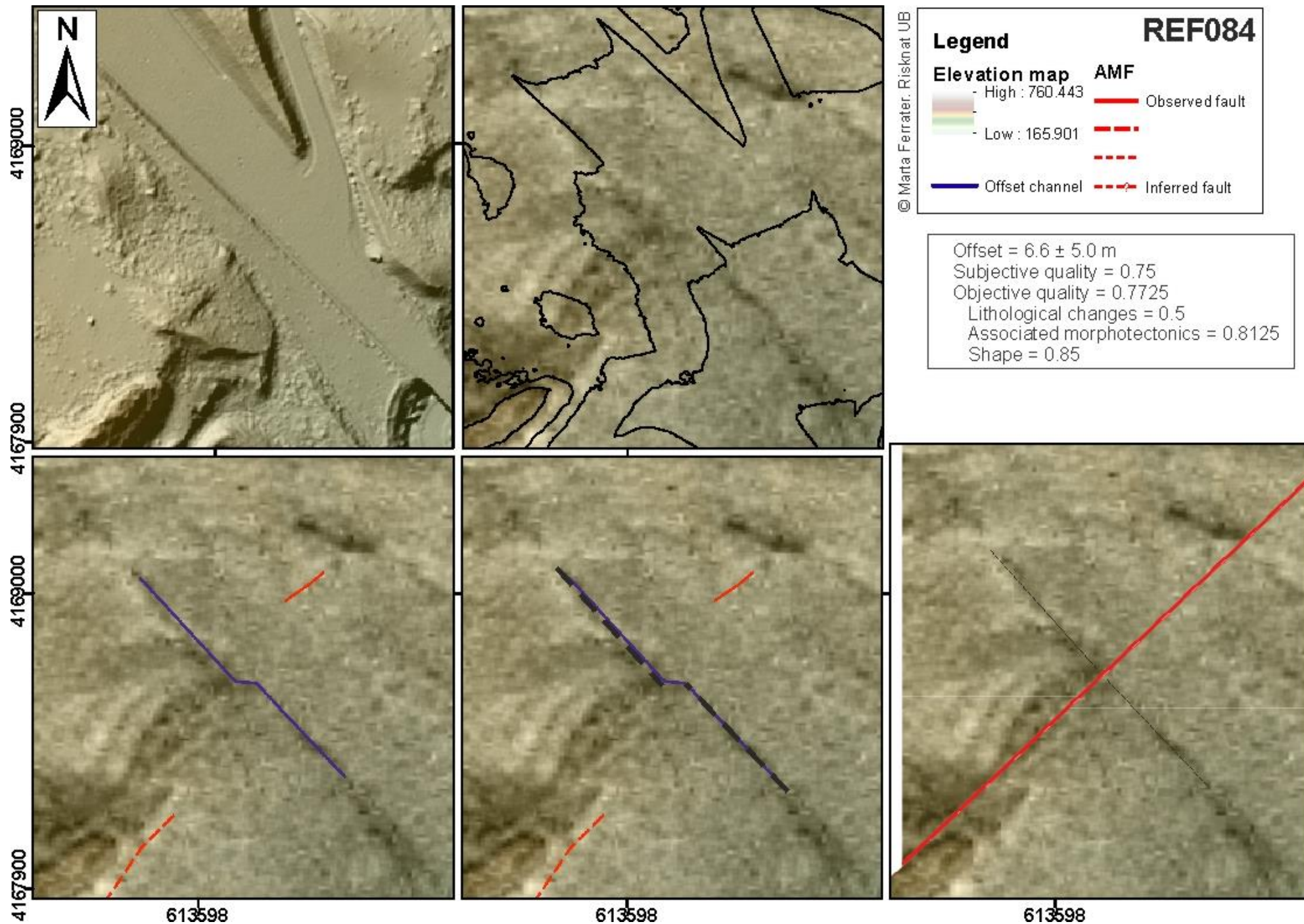


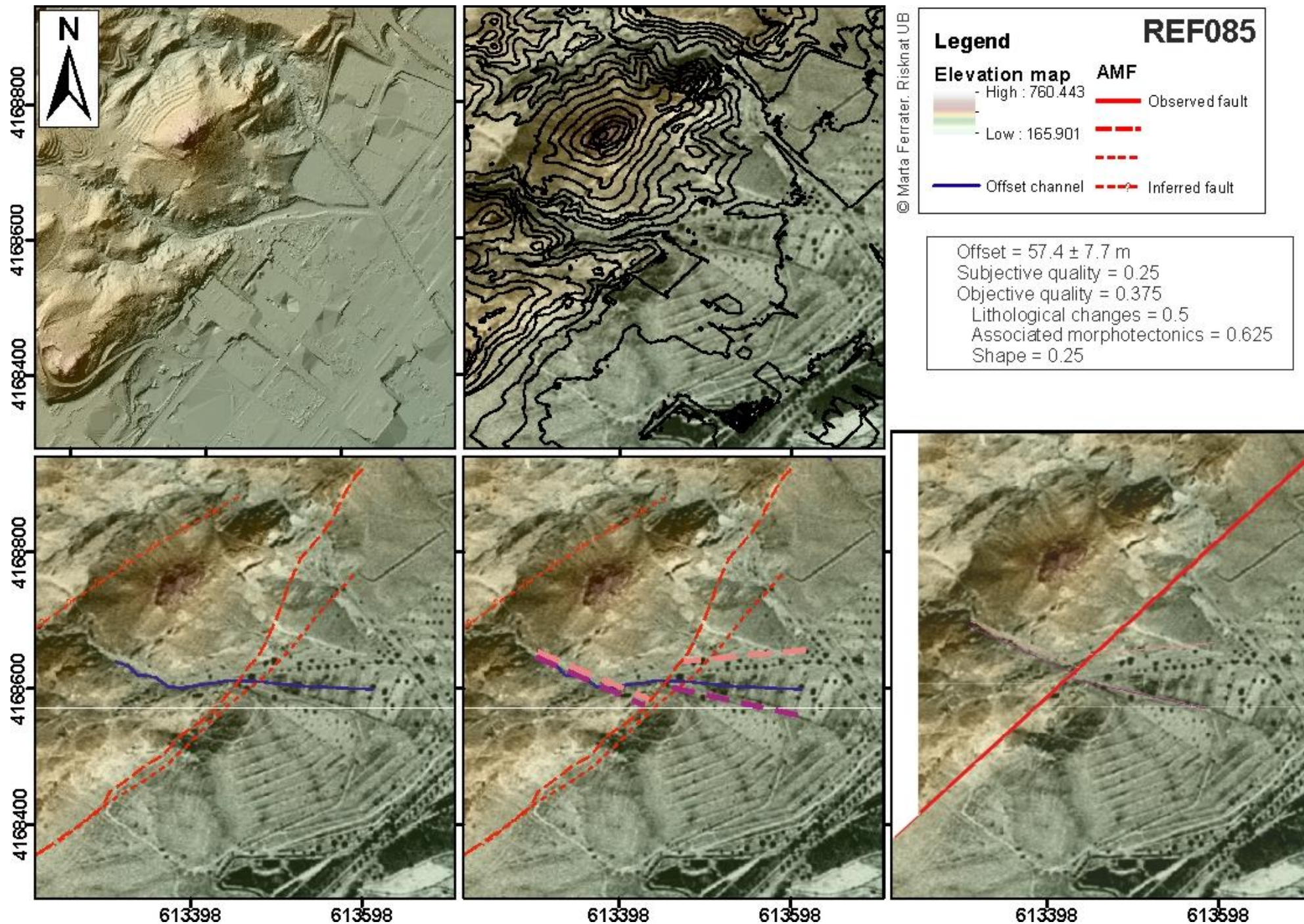


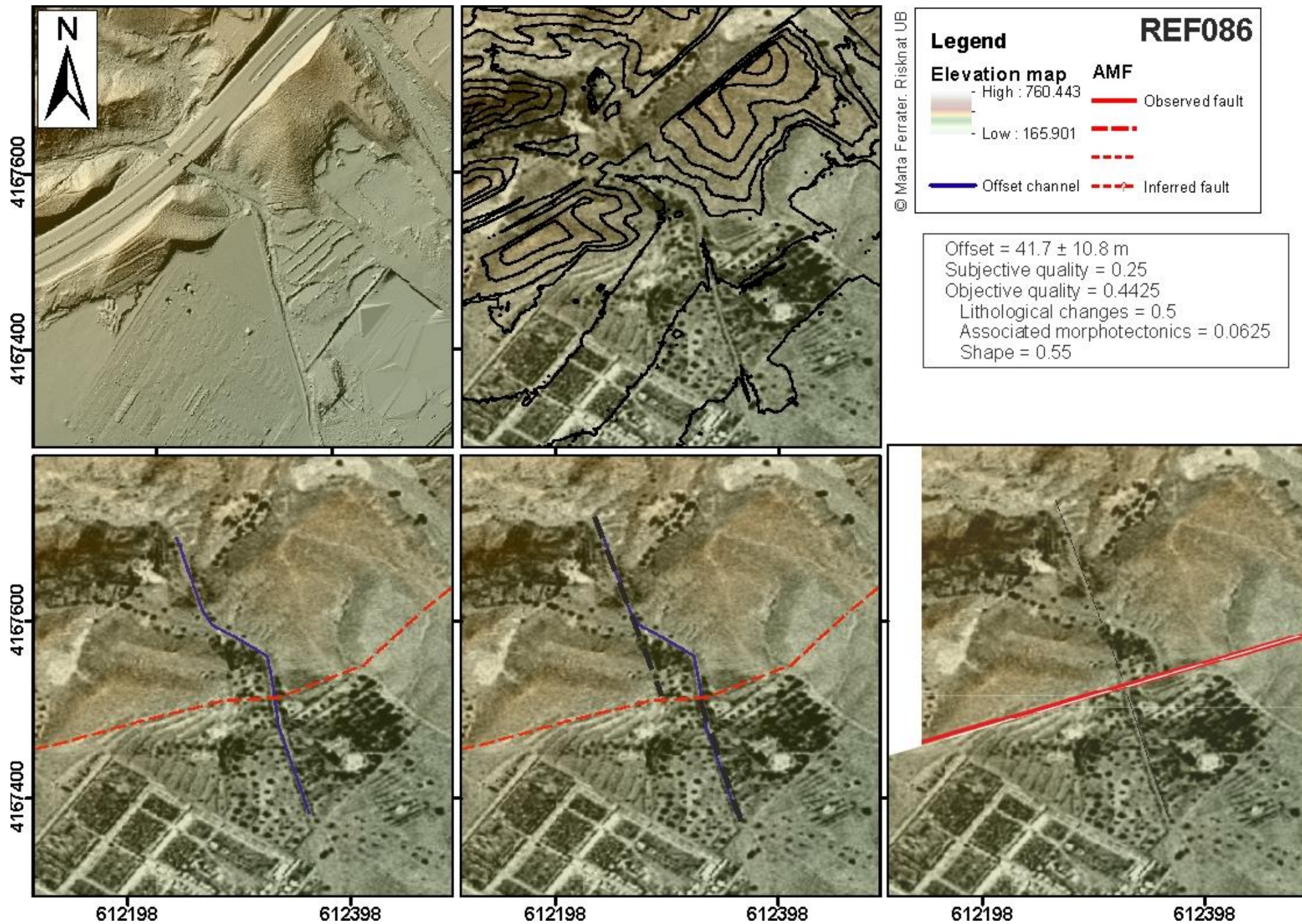


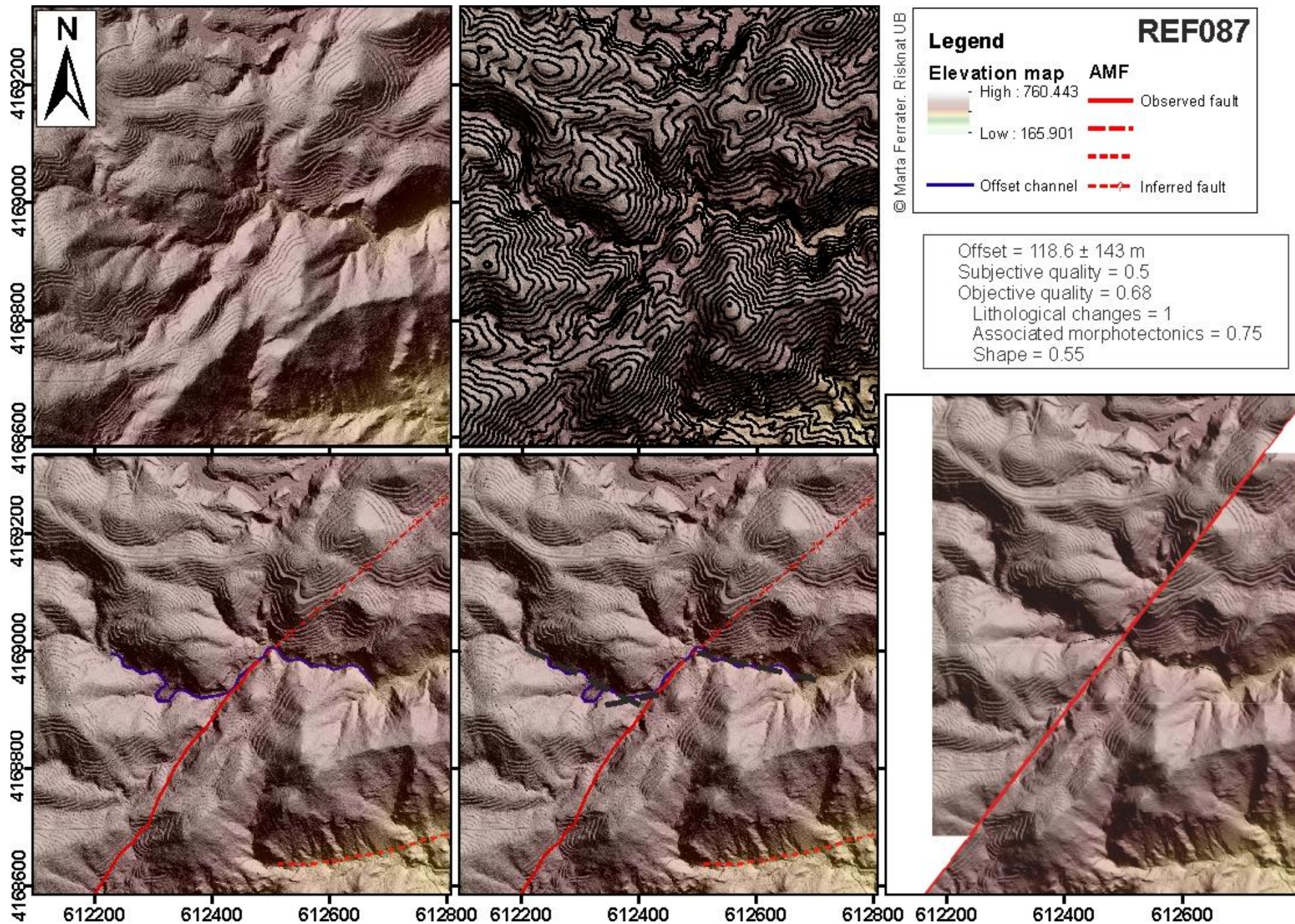


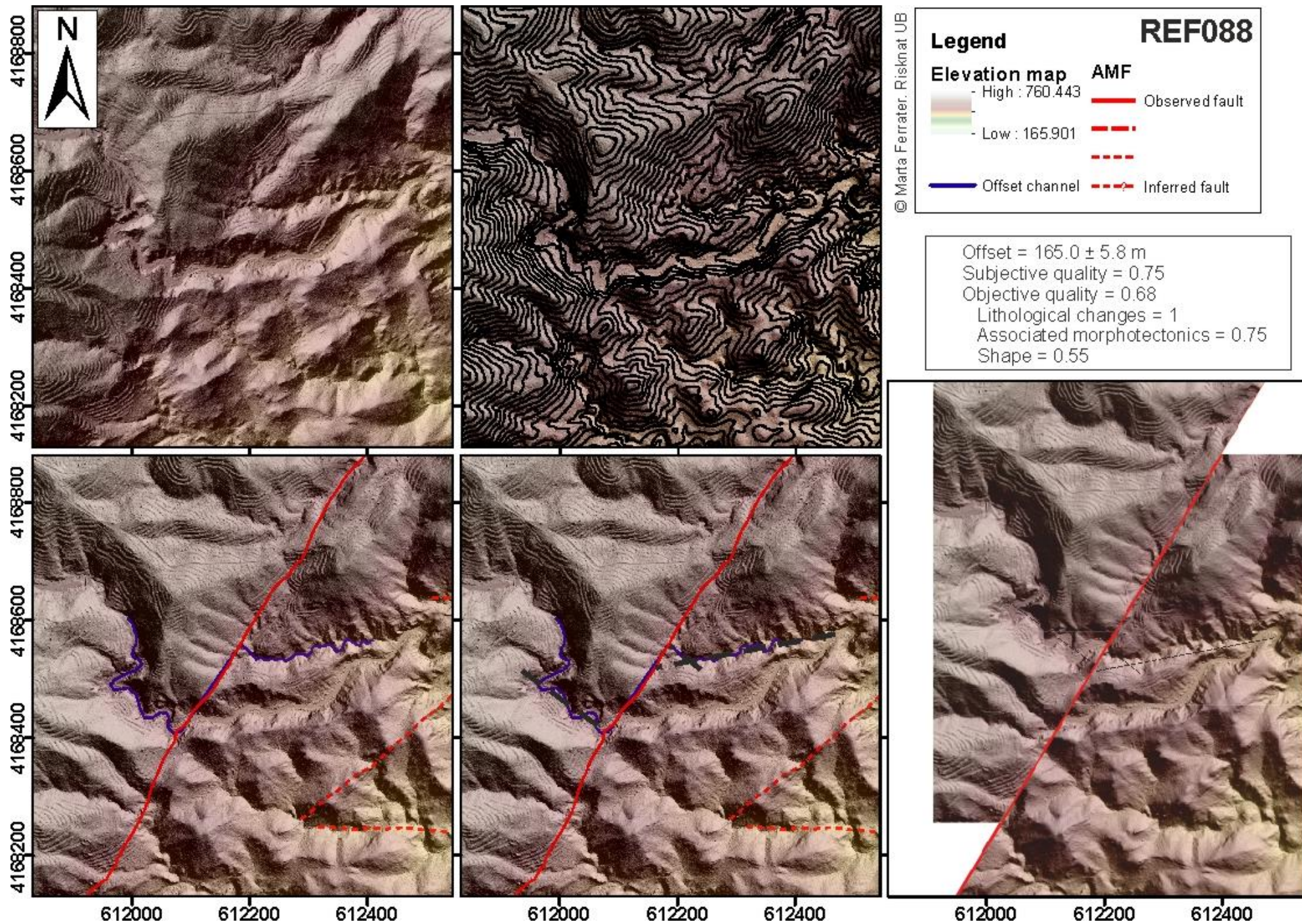


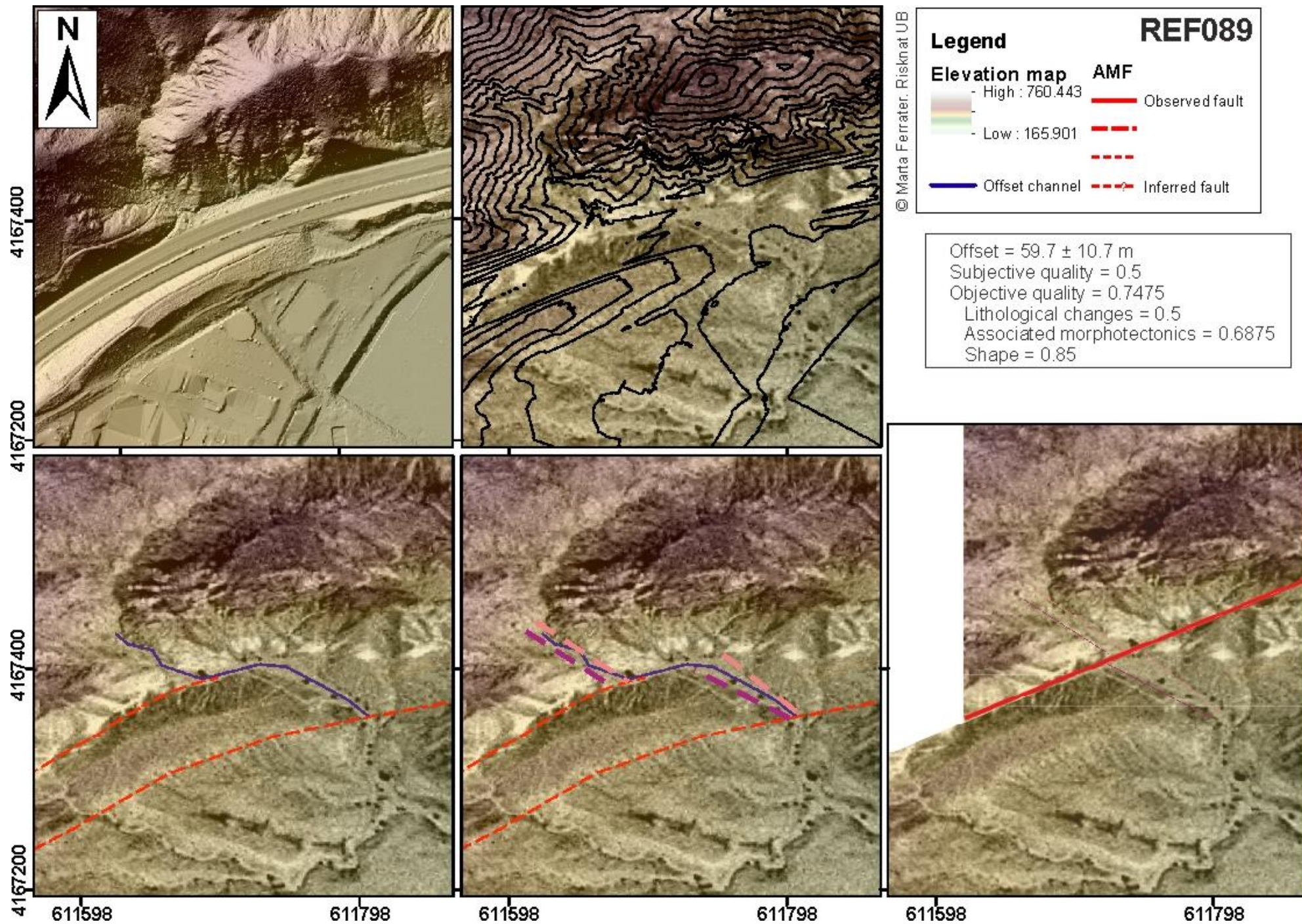


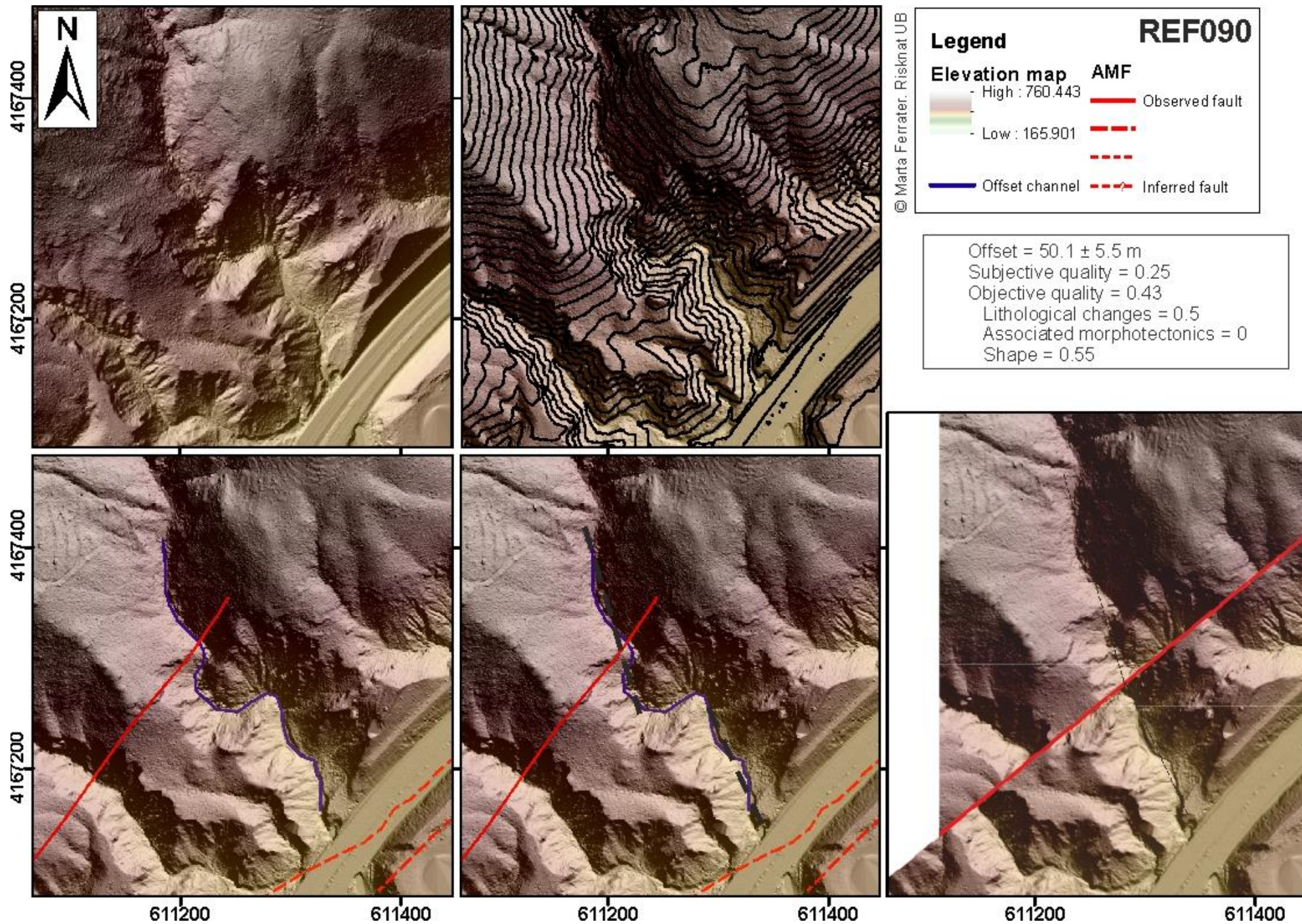


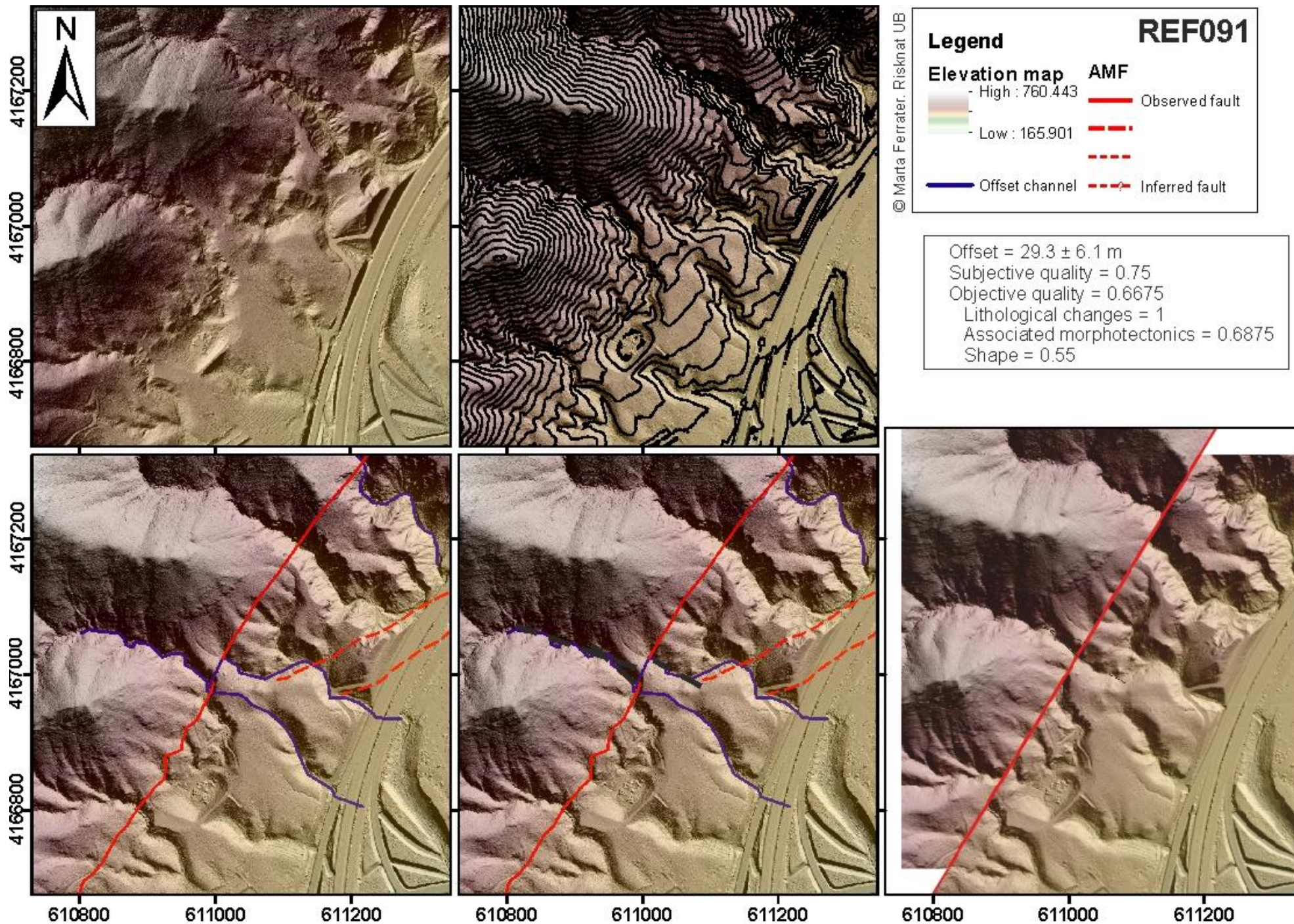


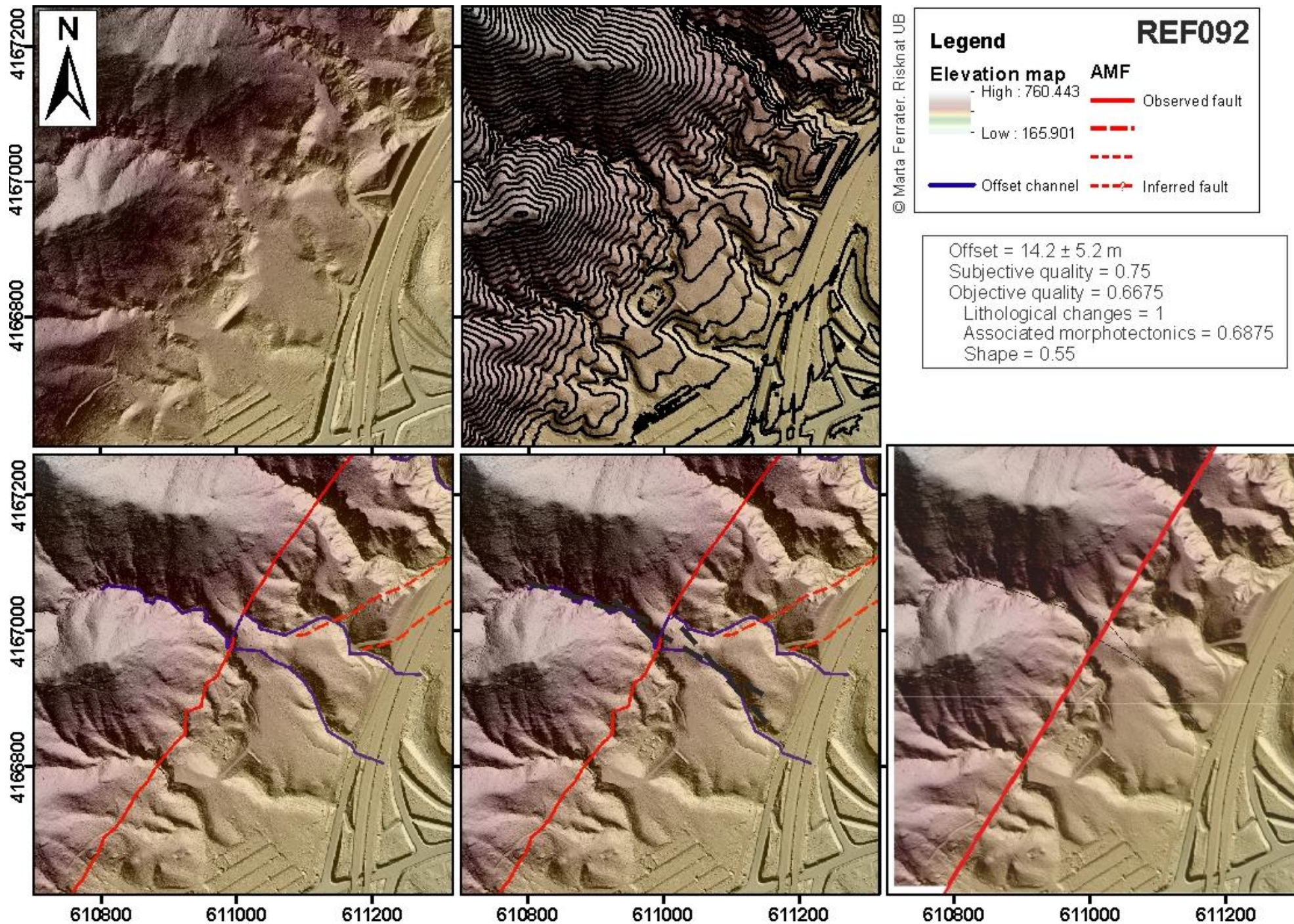


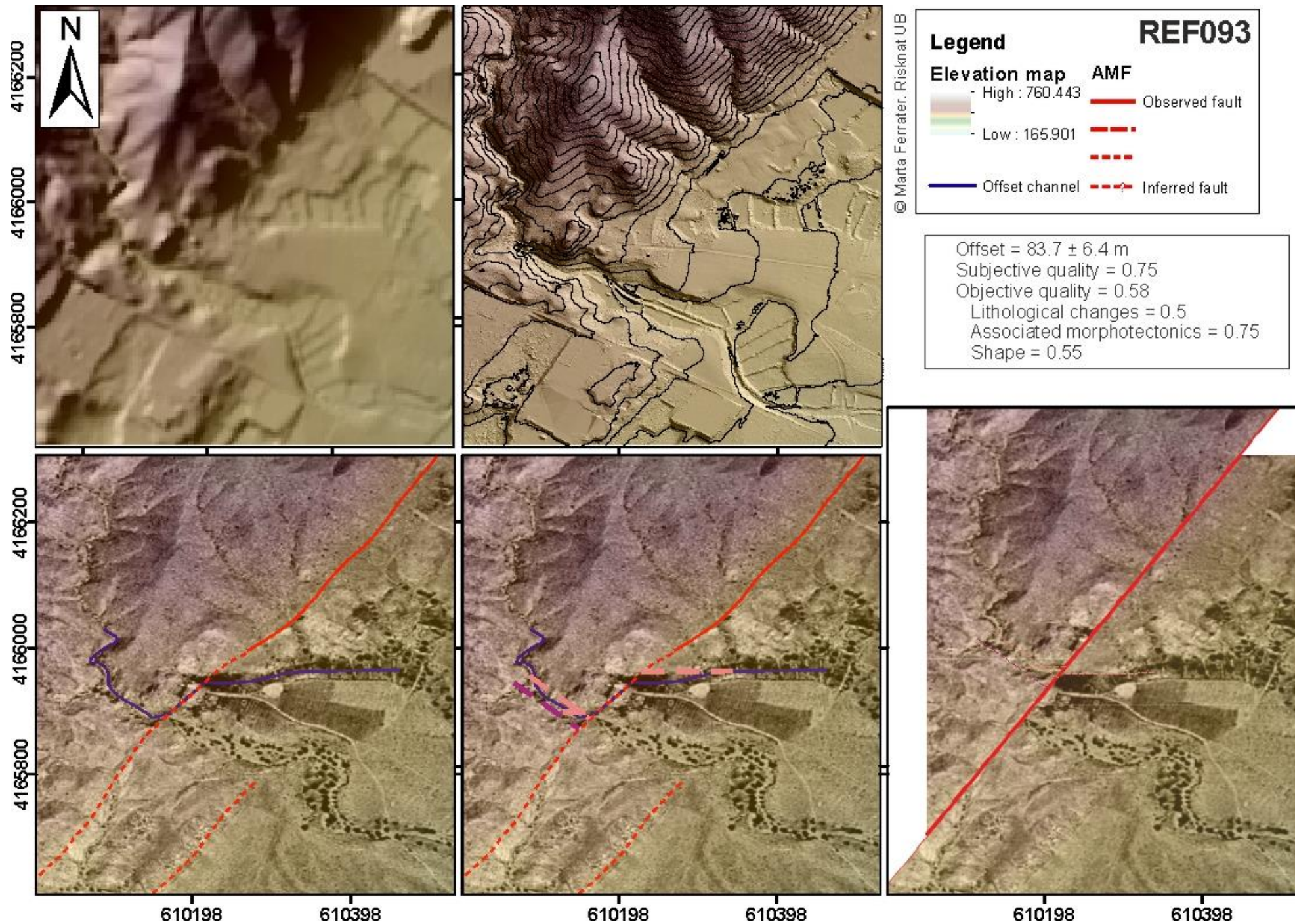


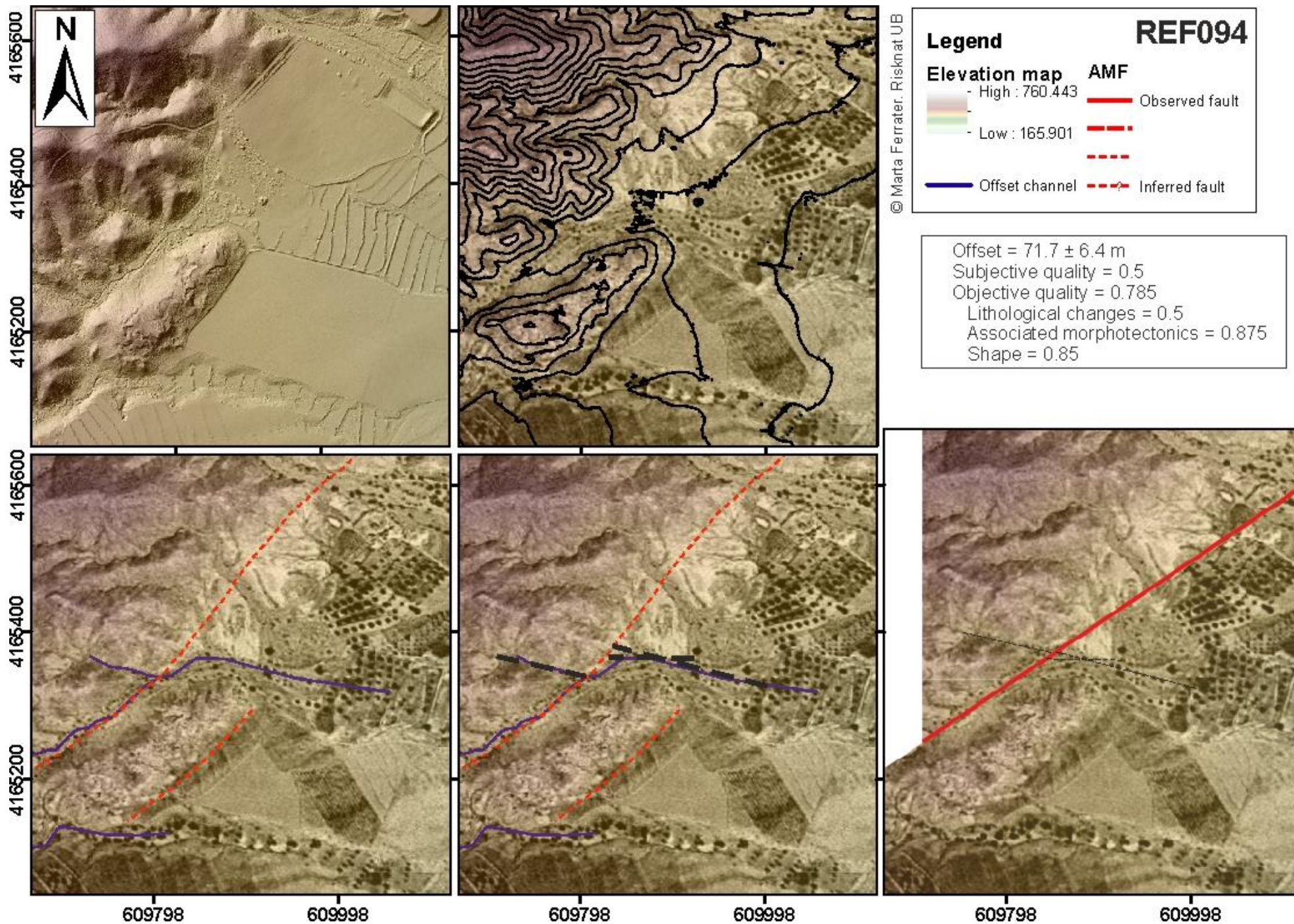


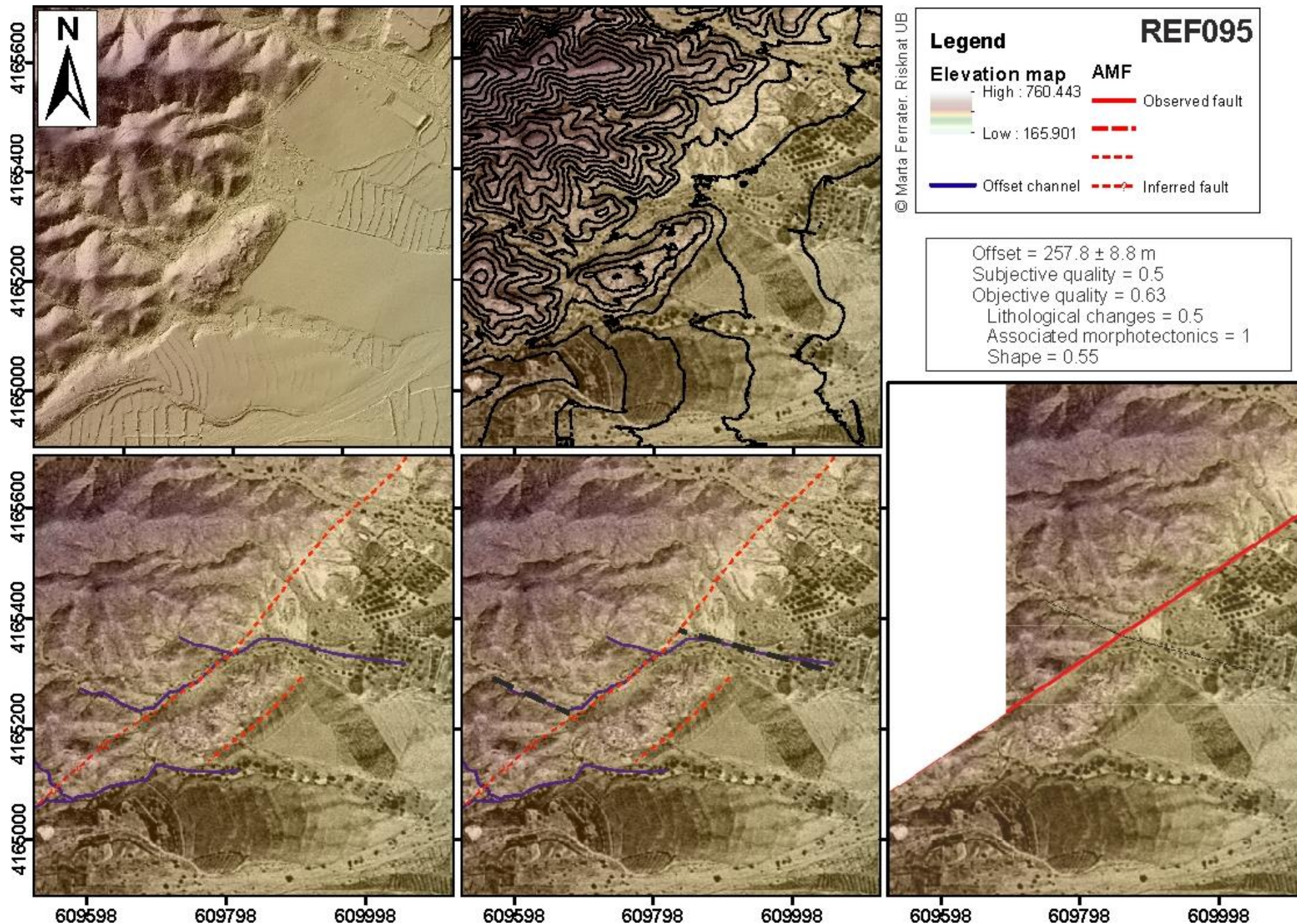


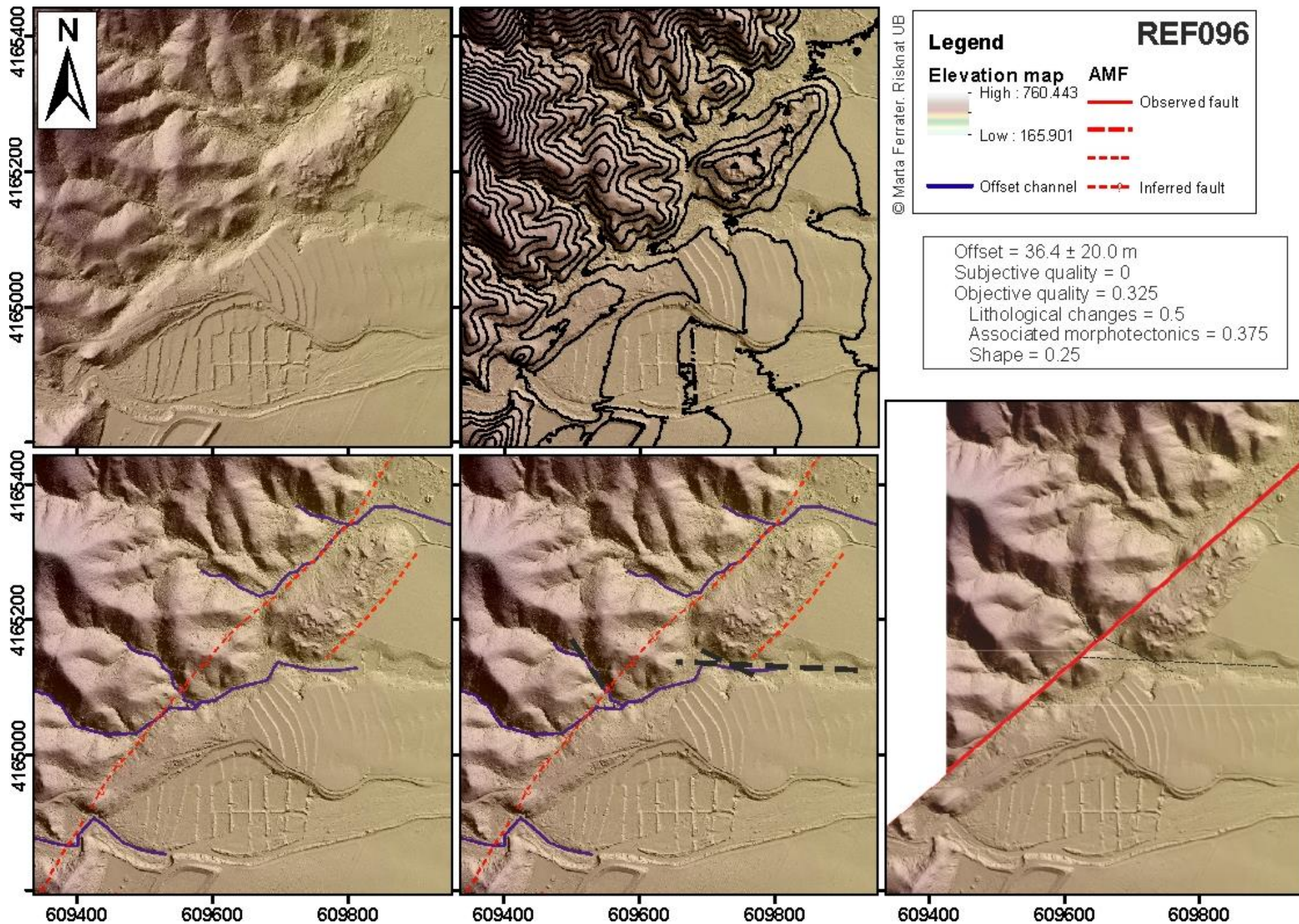


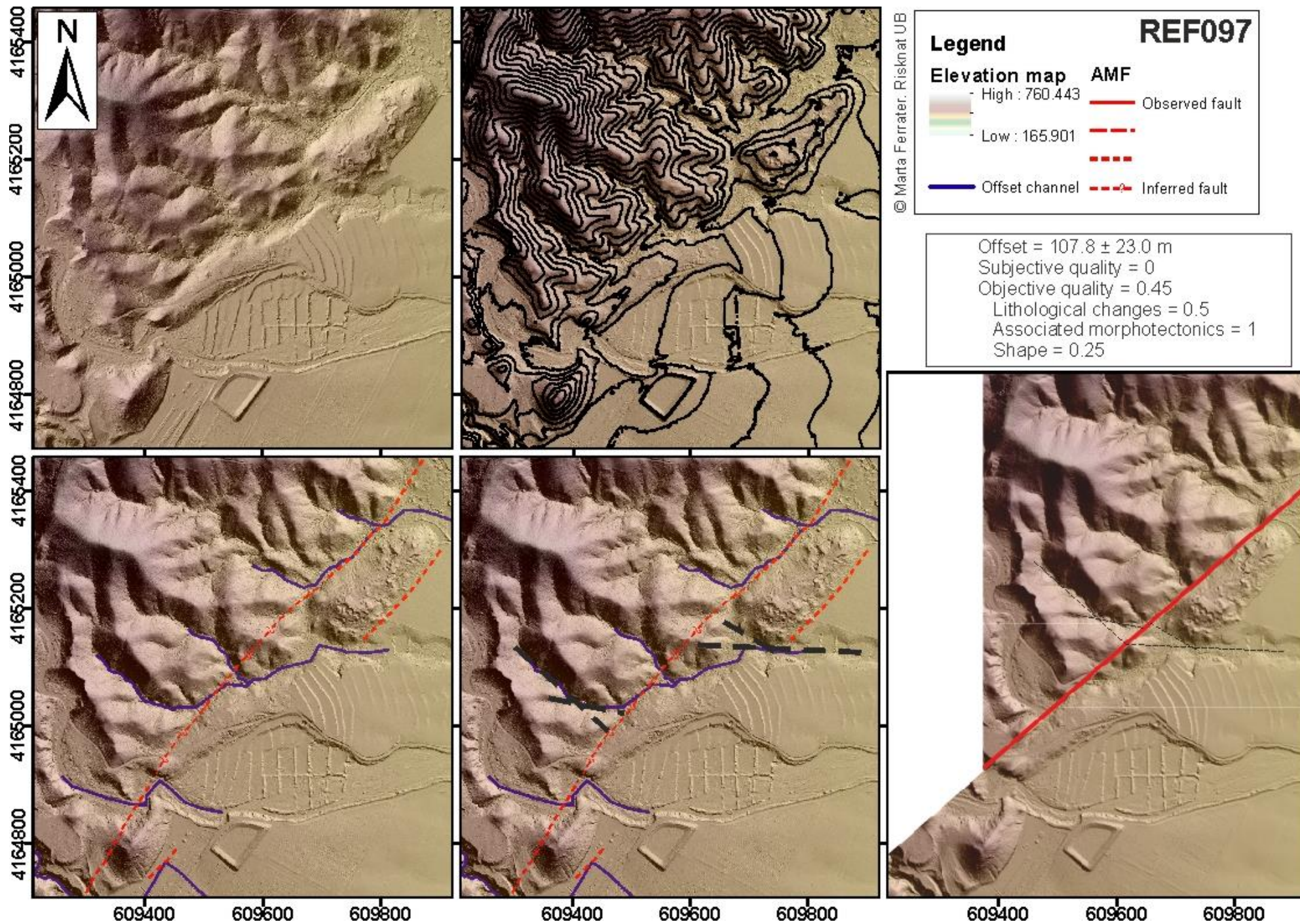


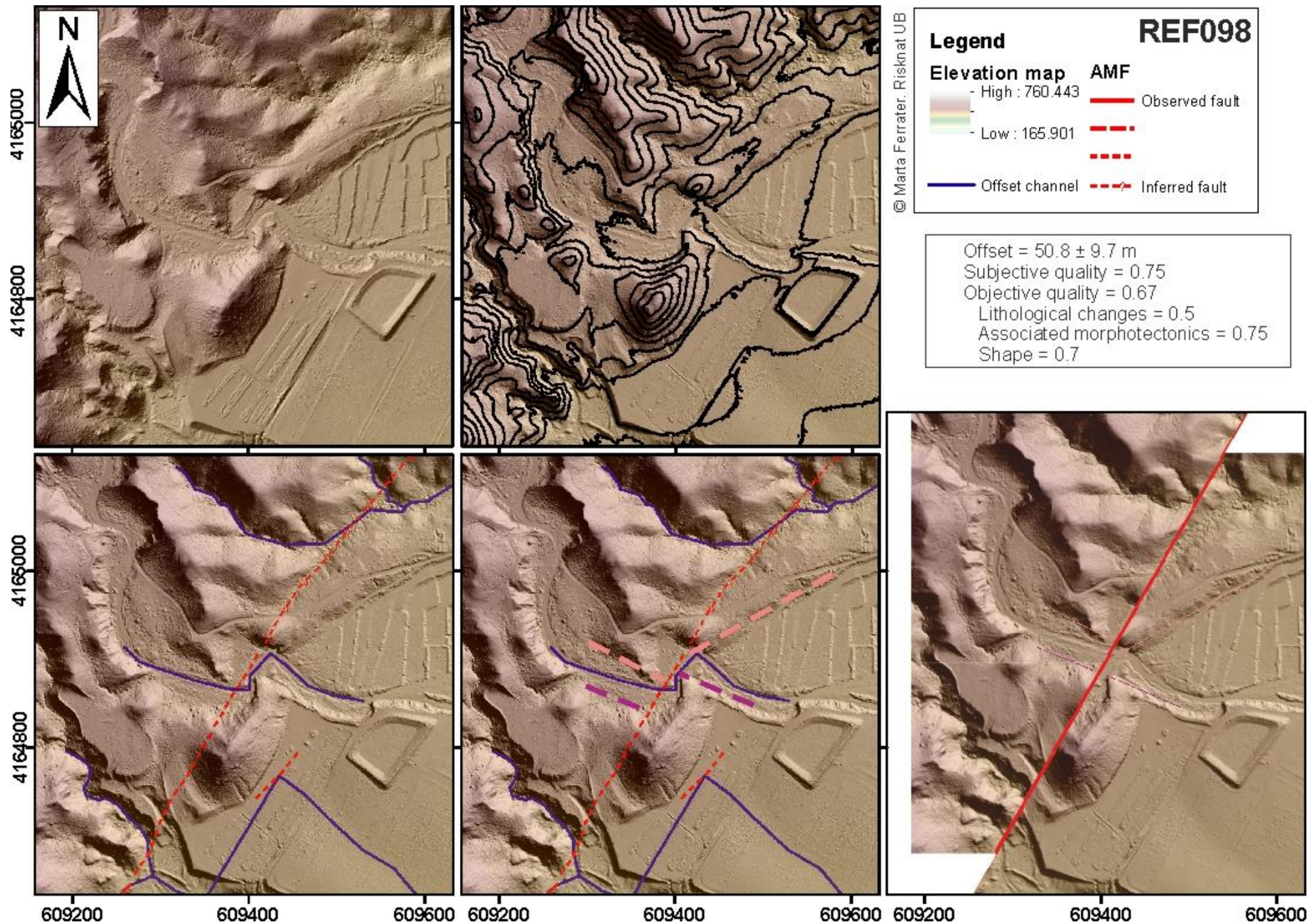


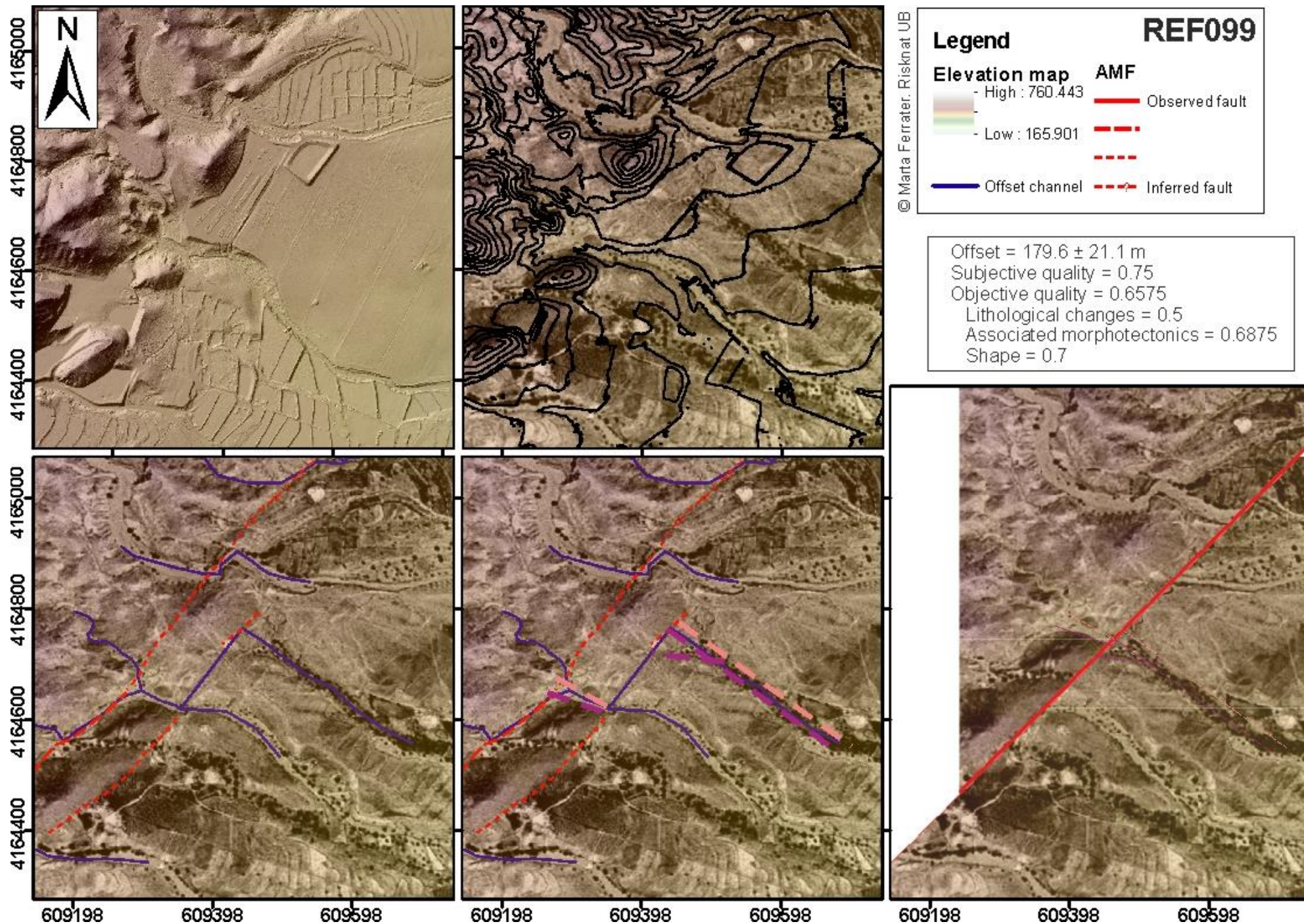


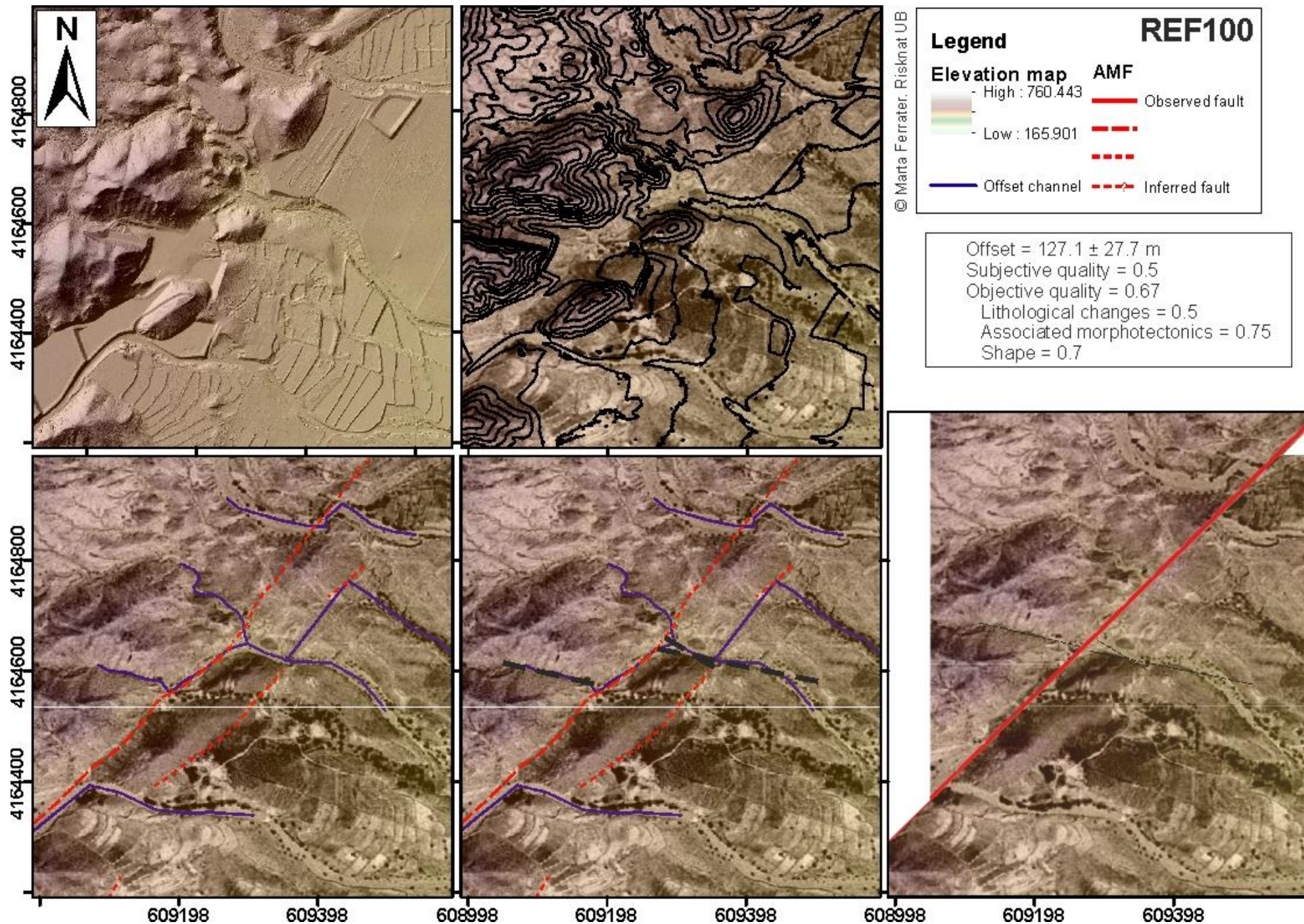


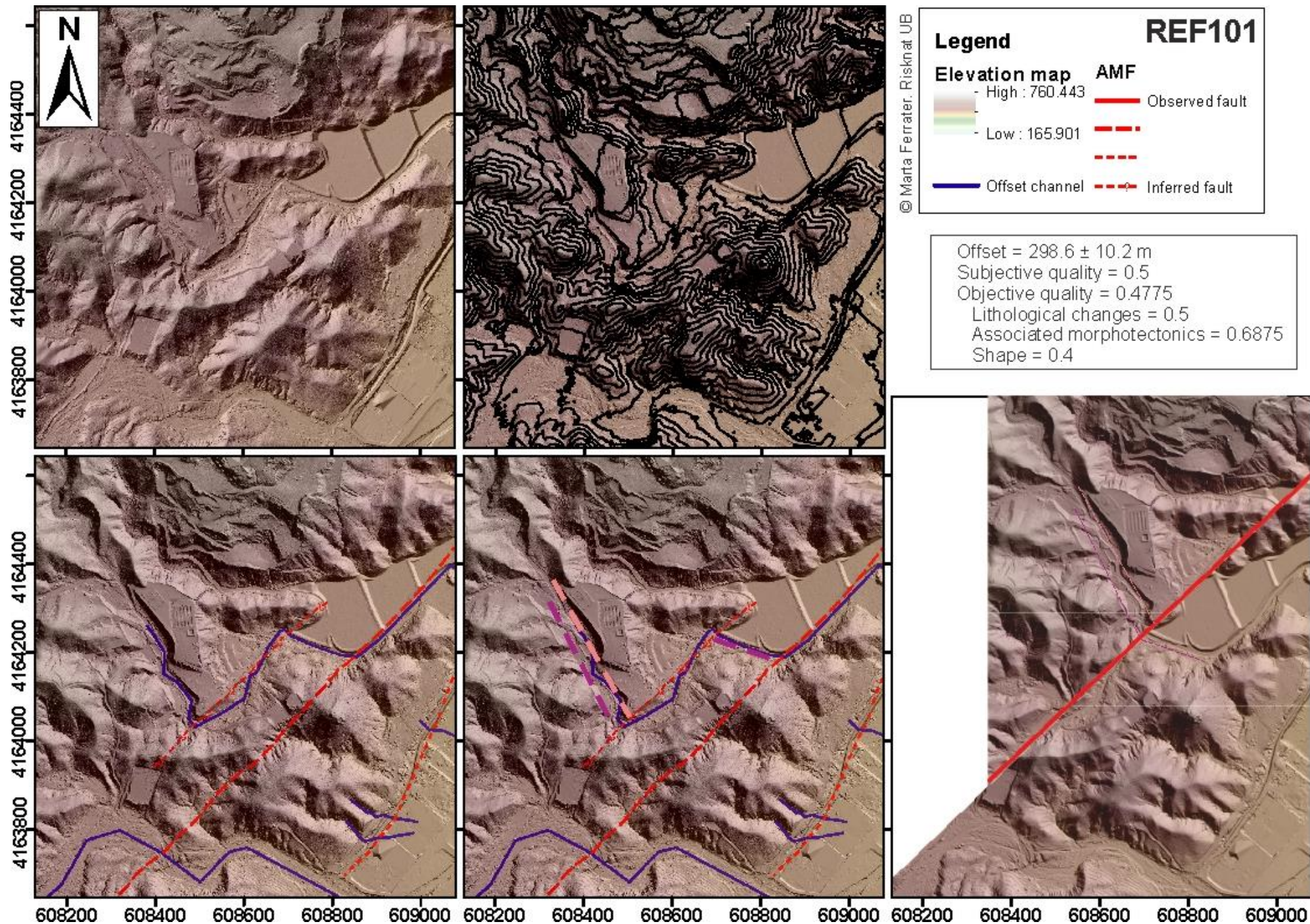


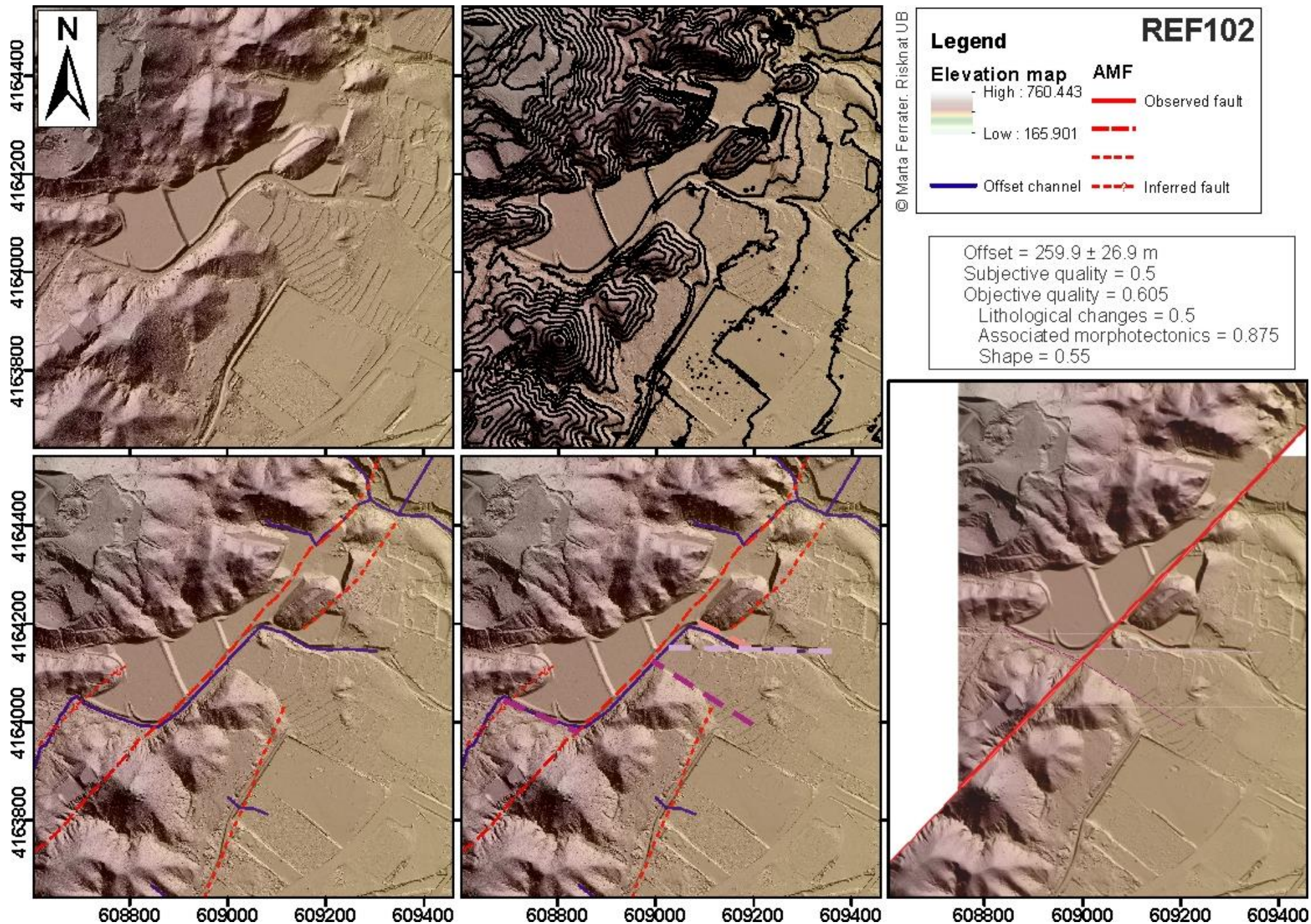


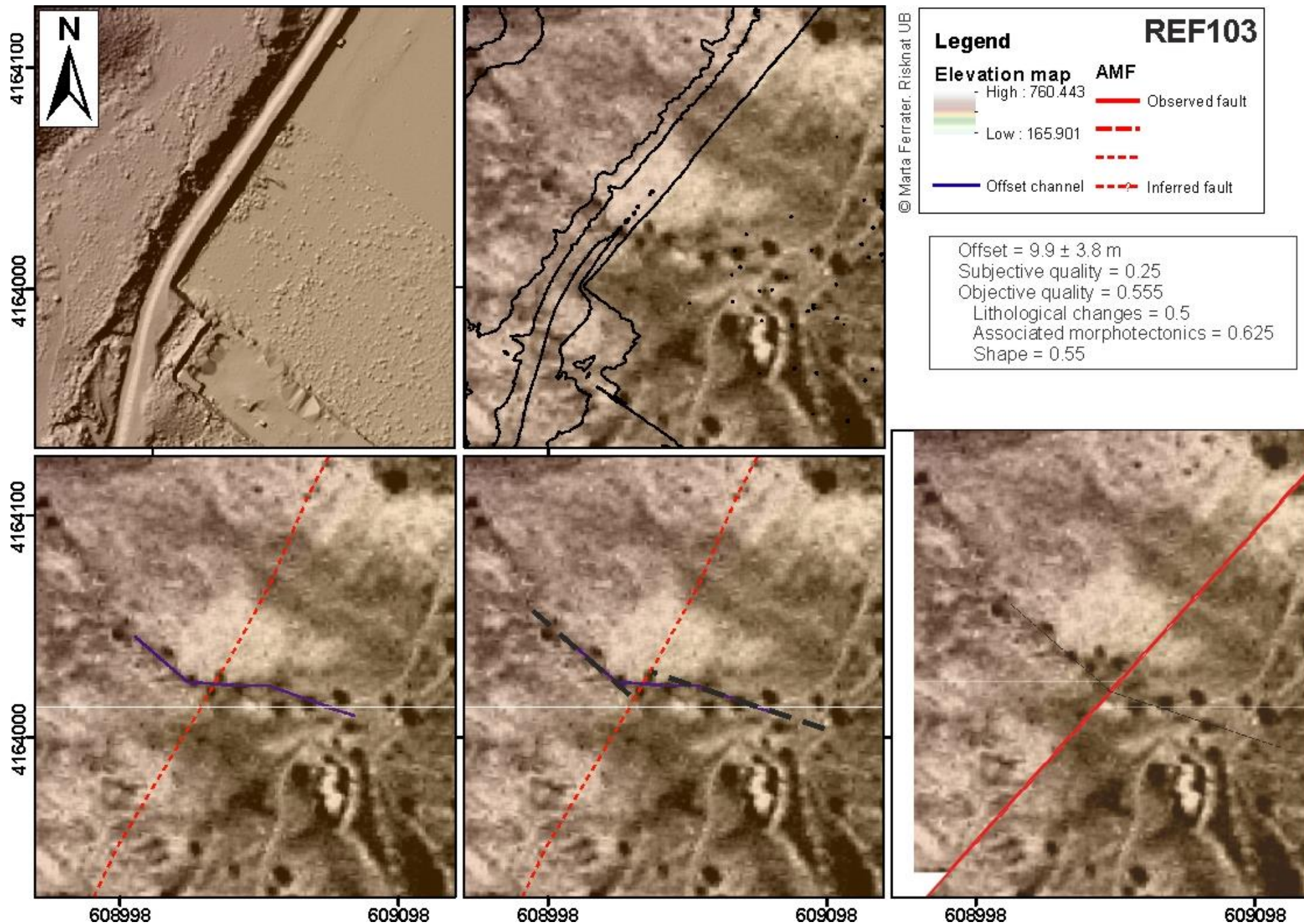


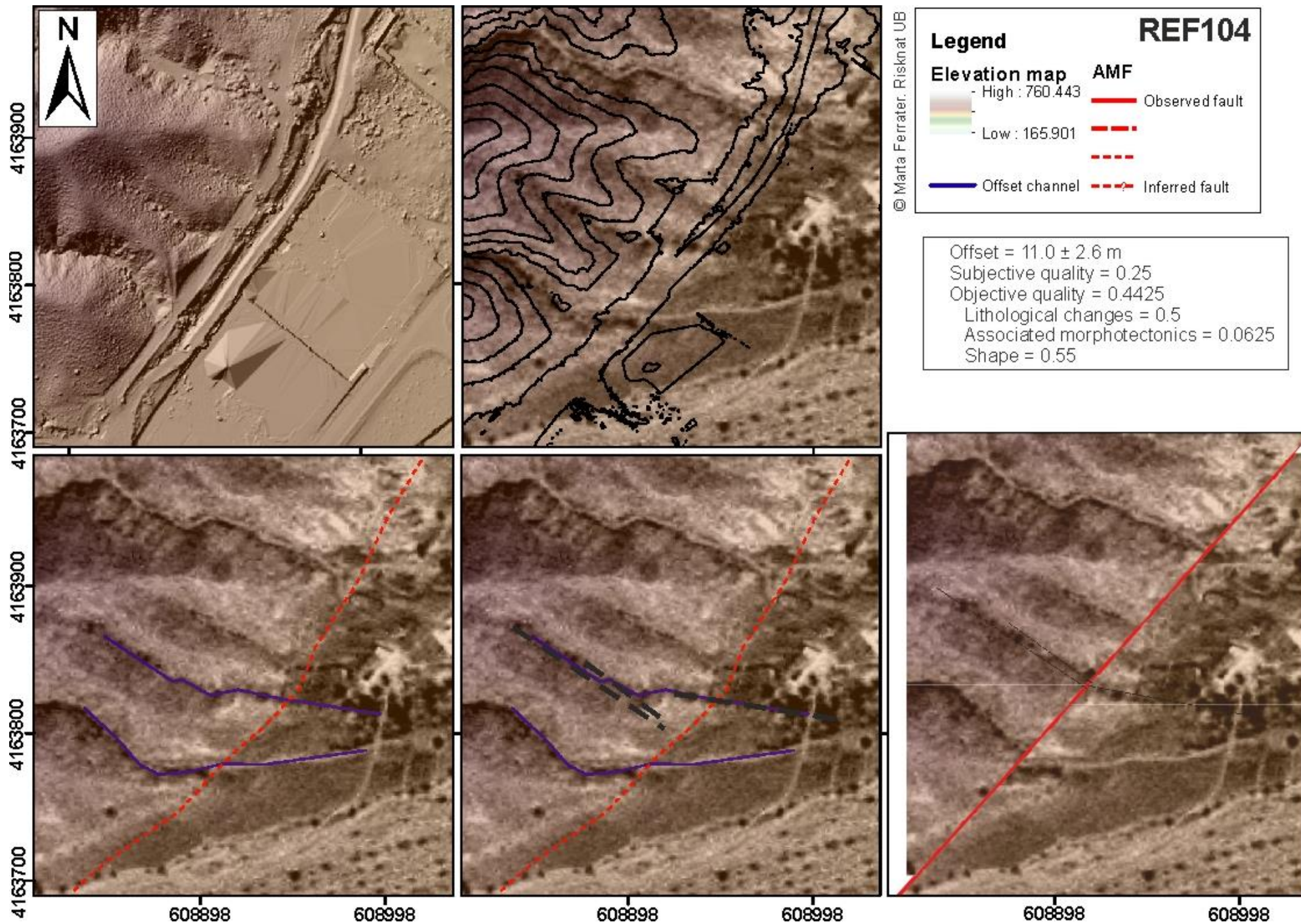


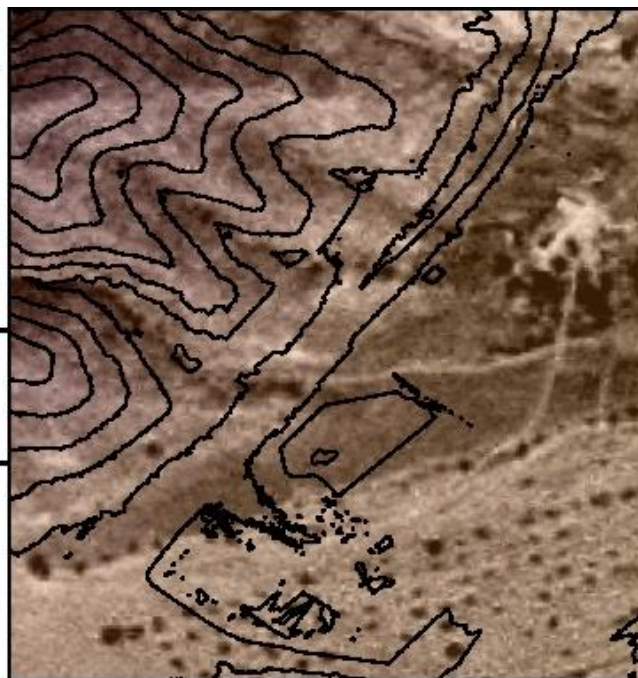
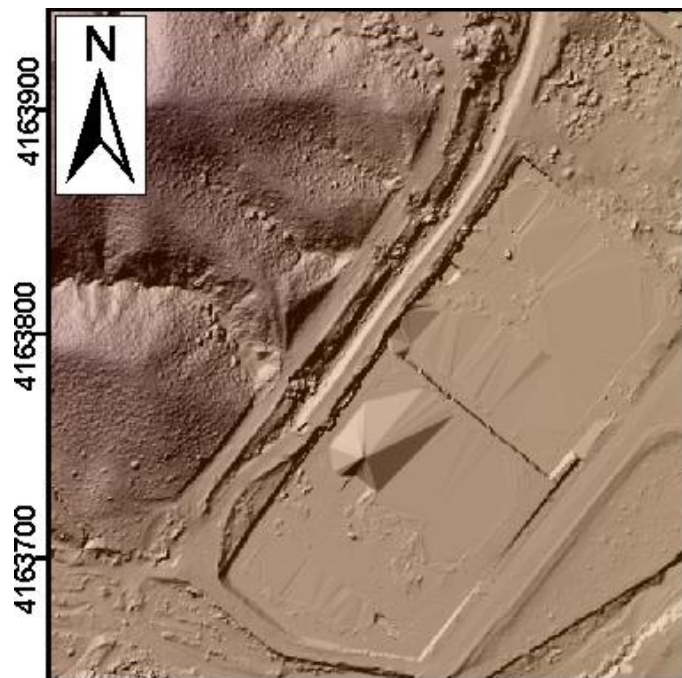












© Marta Ferrater, Risknat UB

Legend

REF105

Elevation map

- High : 760.443
- Low : 165.901

AMF

Observed fault

Inferred fault

Offset channel

Inferred fault

Offset = 4.5 ± 2.2 m

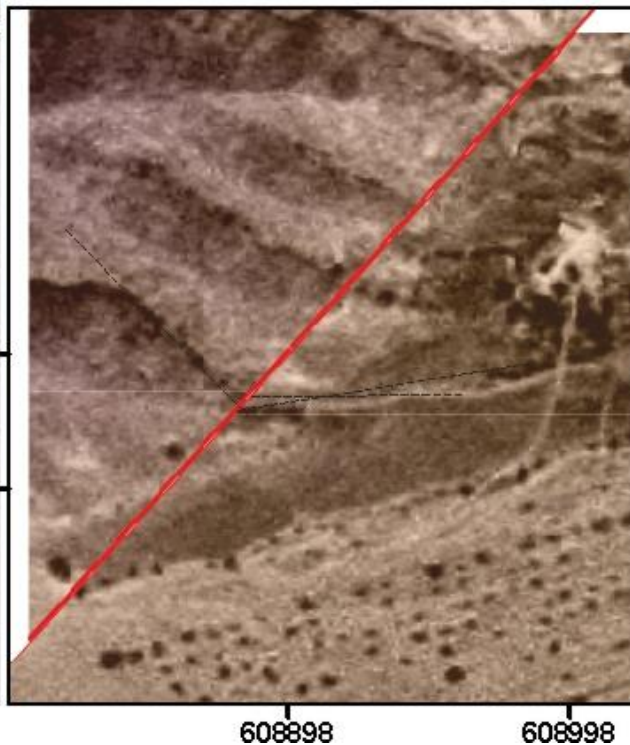
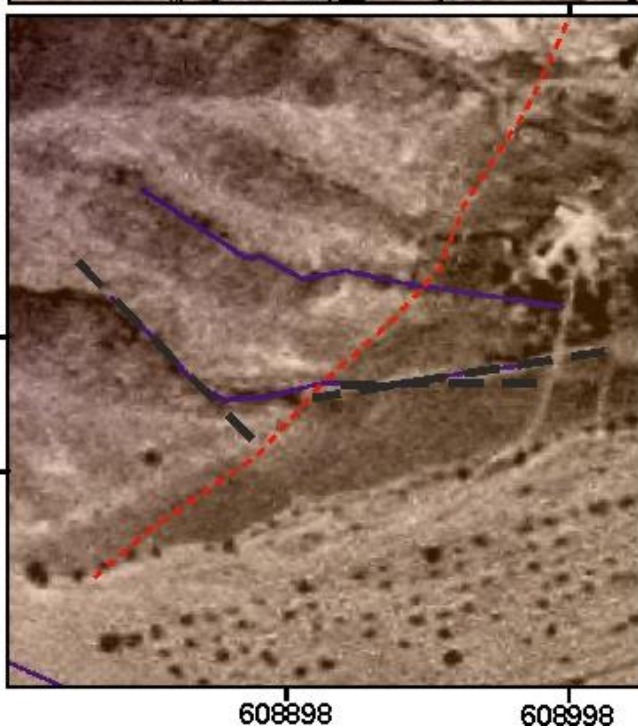
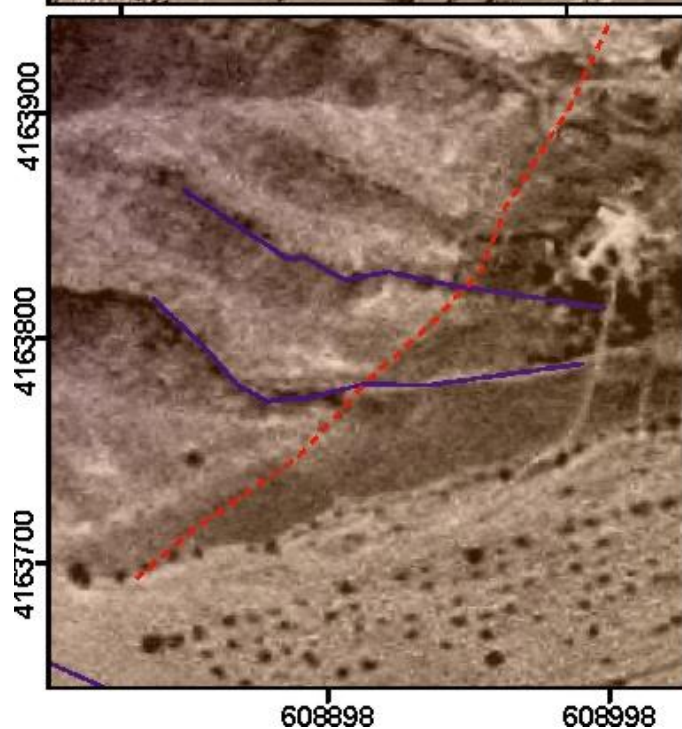
Subjective quality = 0.25

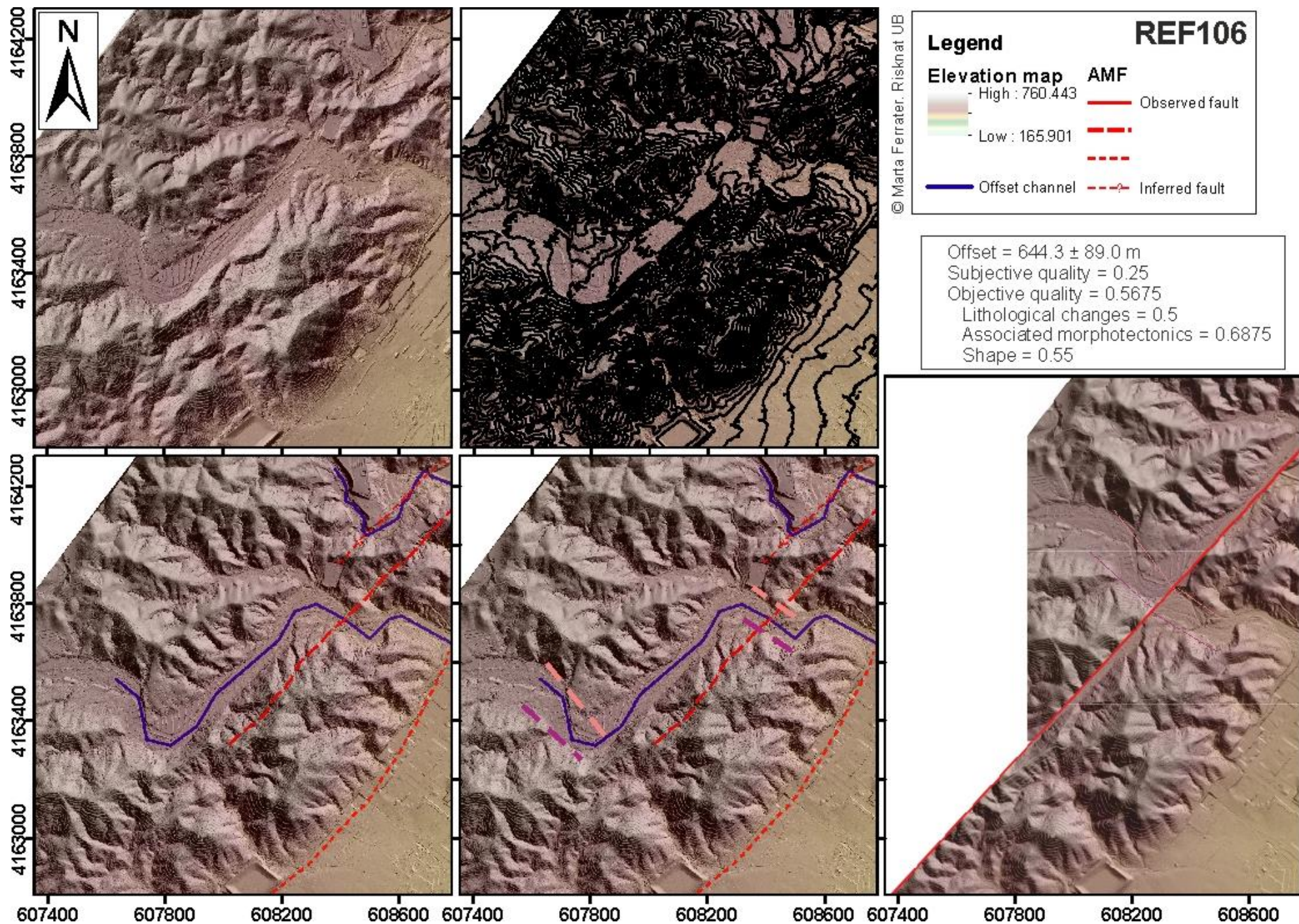
Objective quality = 0.5675

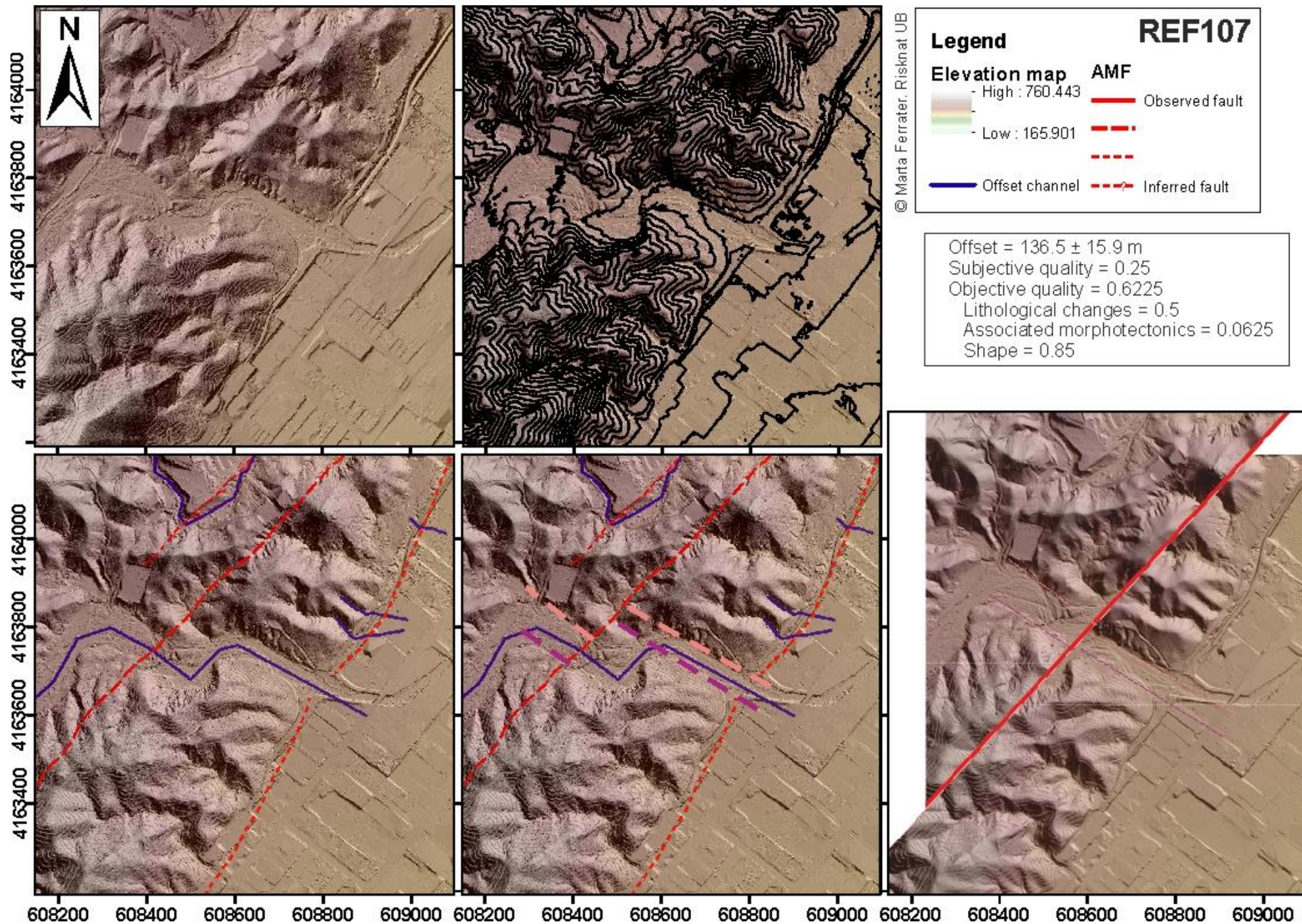
Lithological changes = 0.5

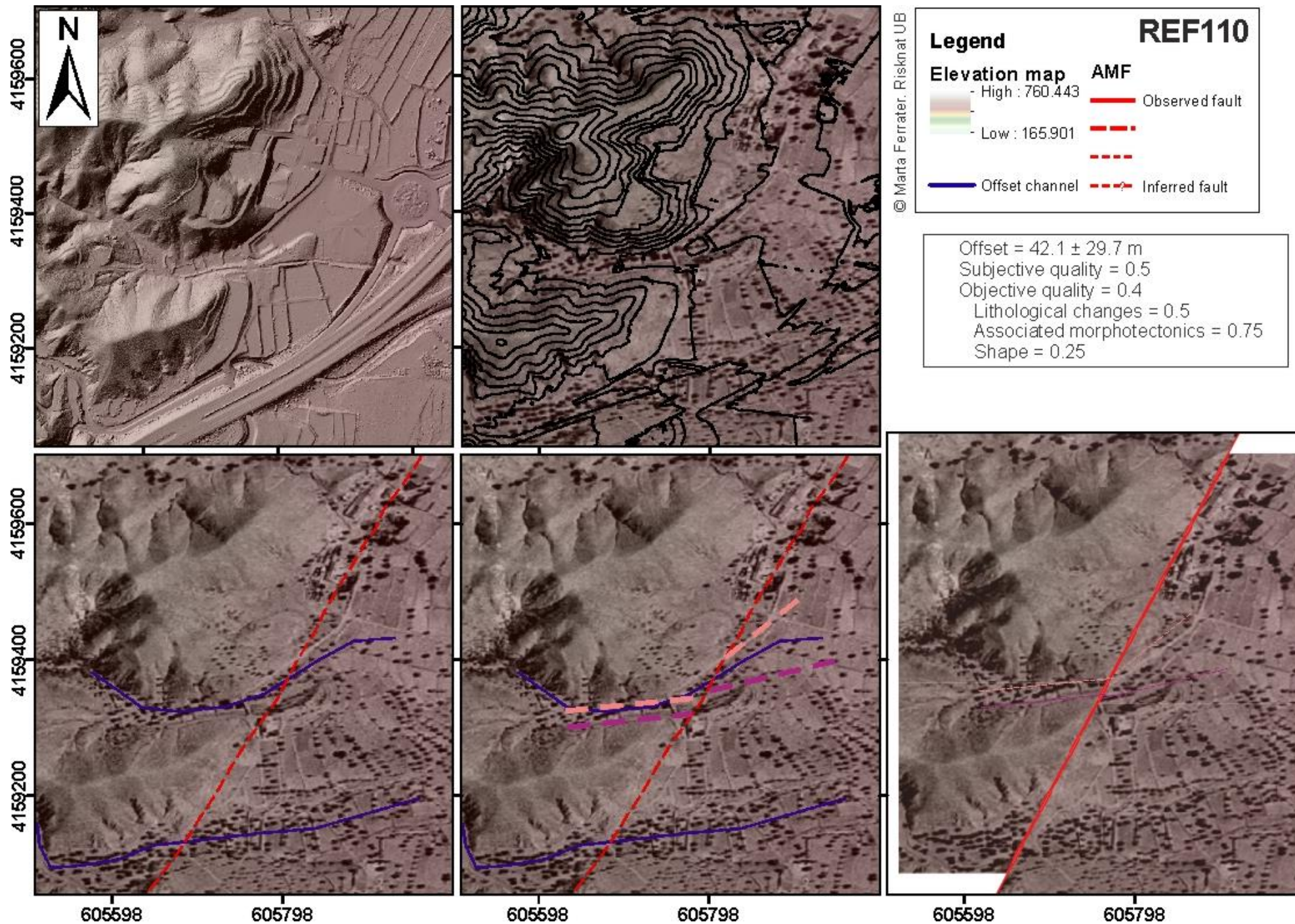
Associated morphotectonics = 0.6875

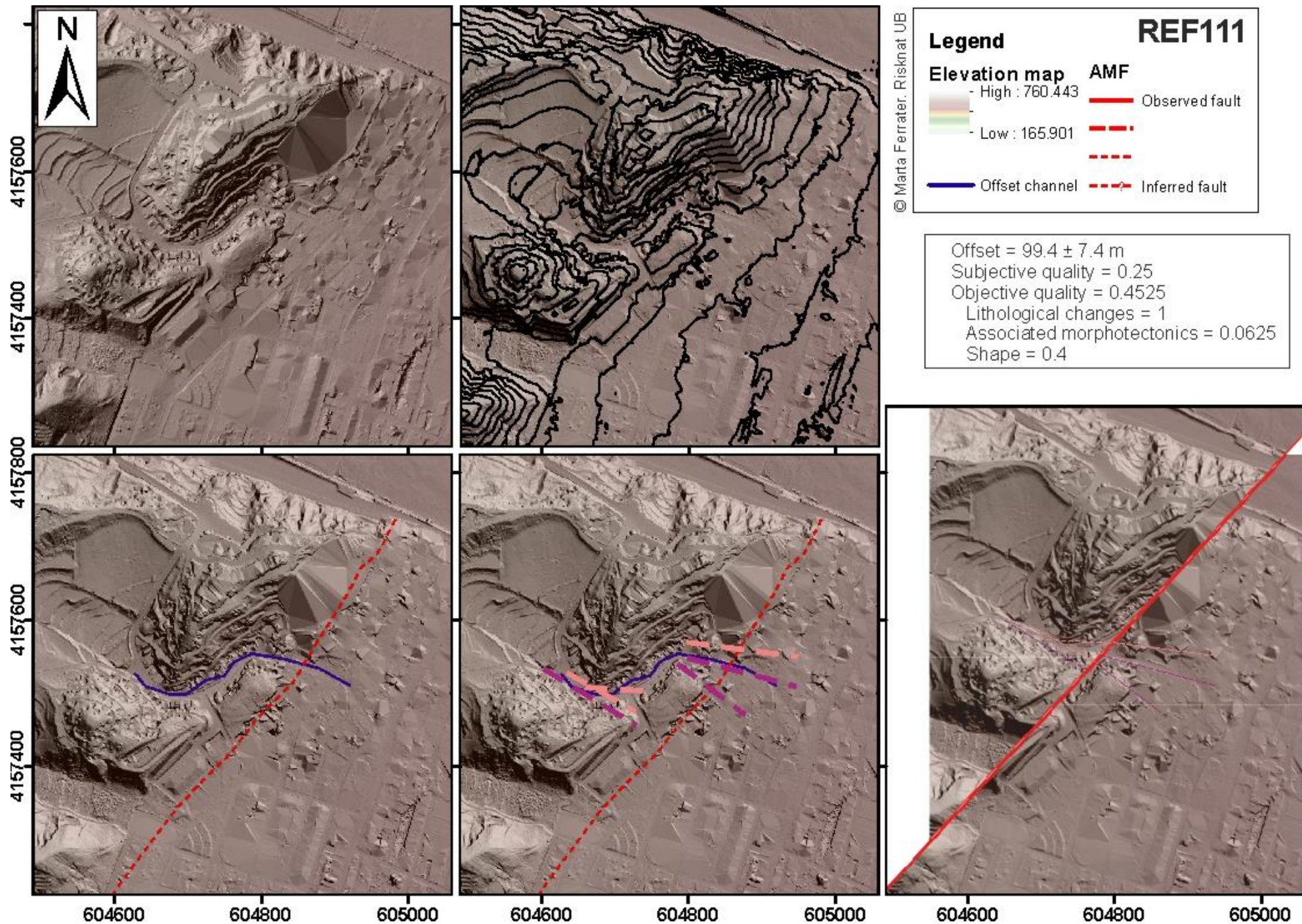
Shape = 0.55

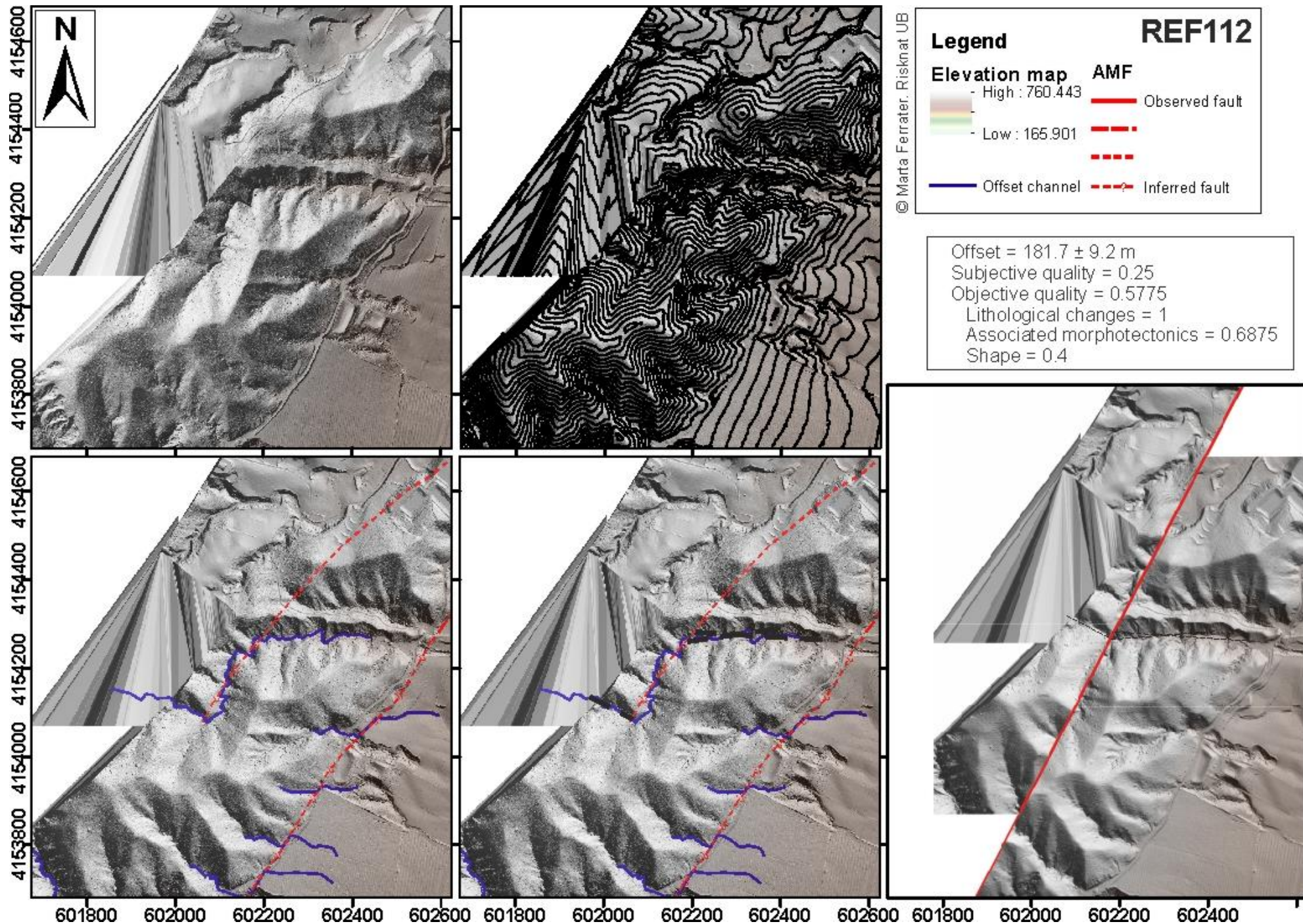


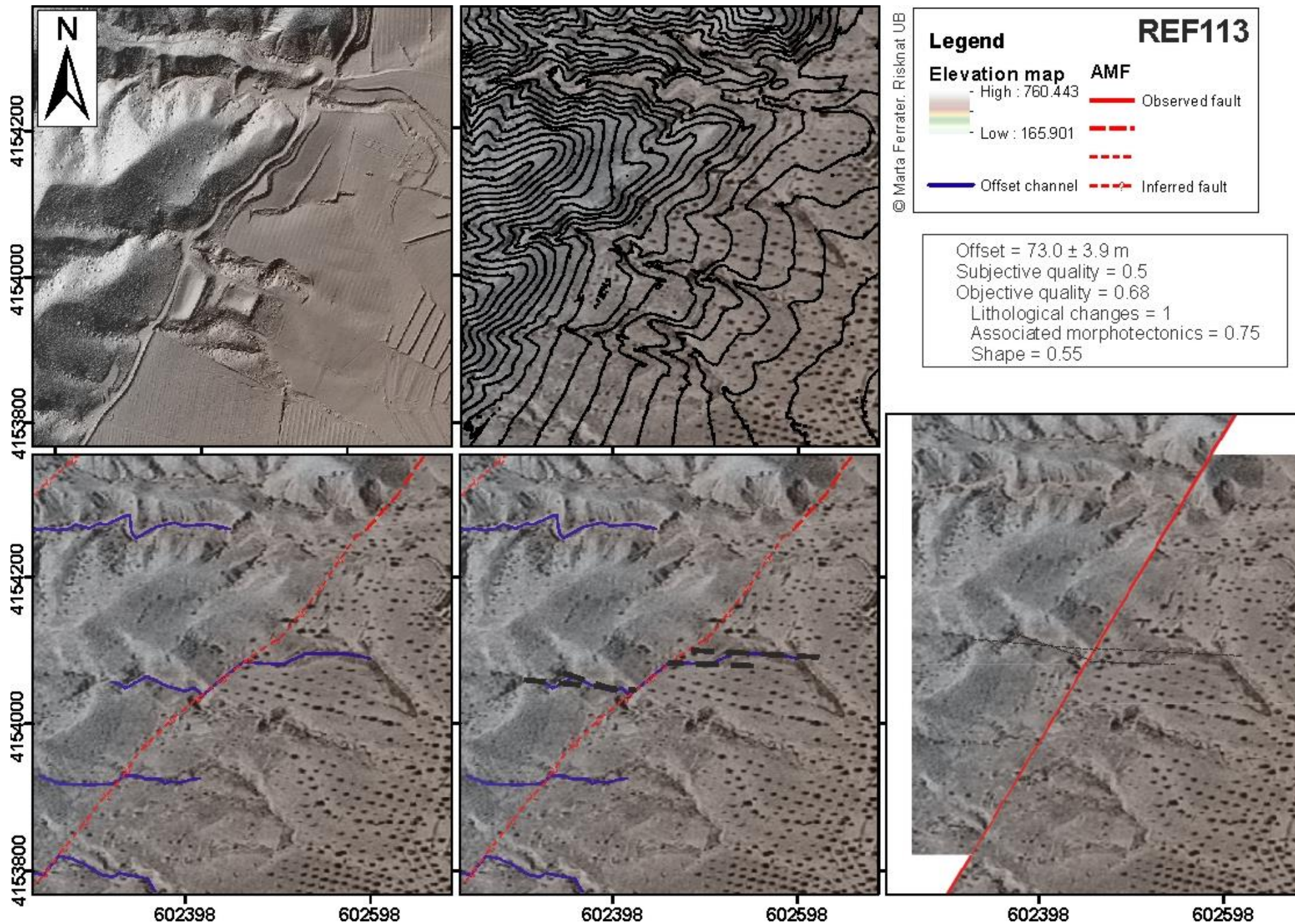


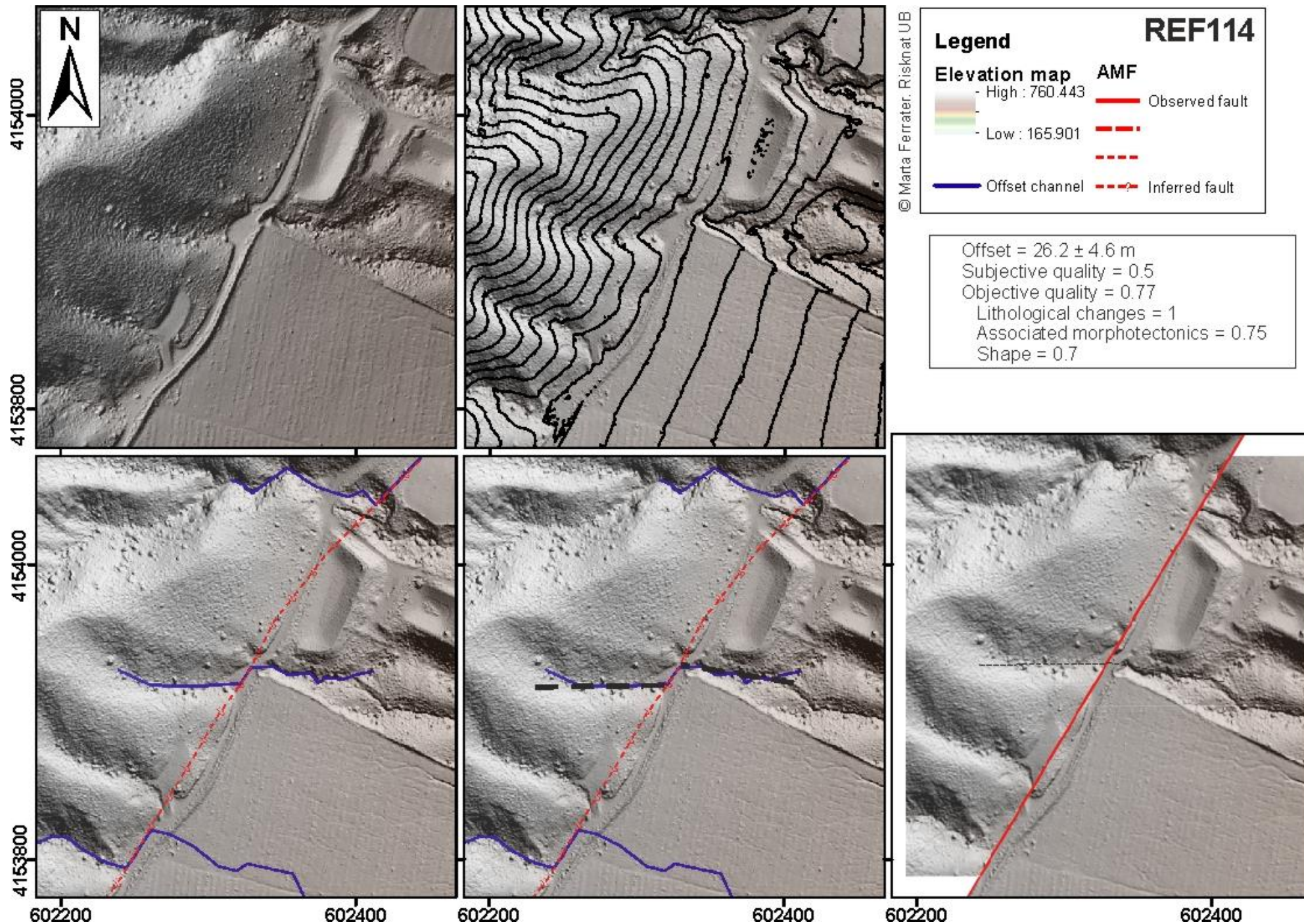


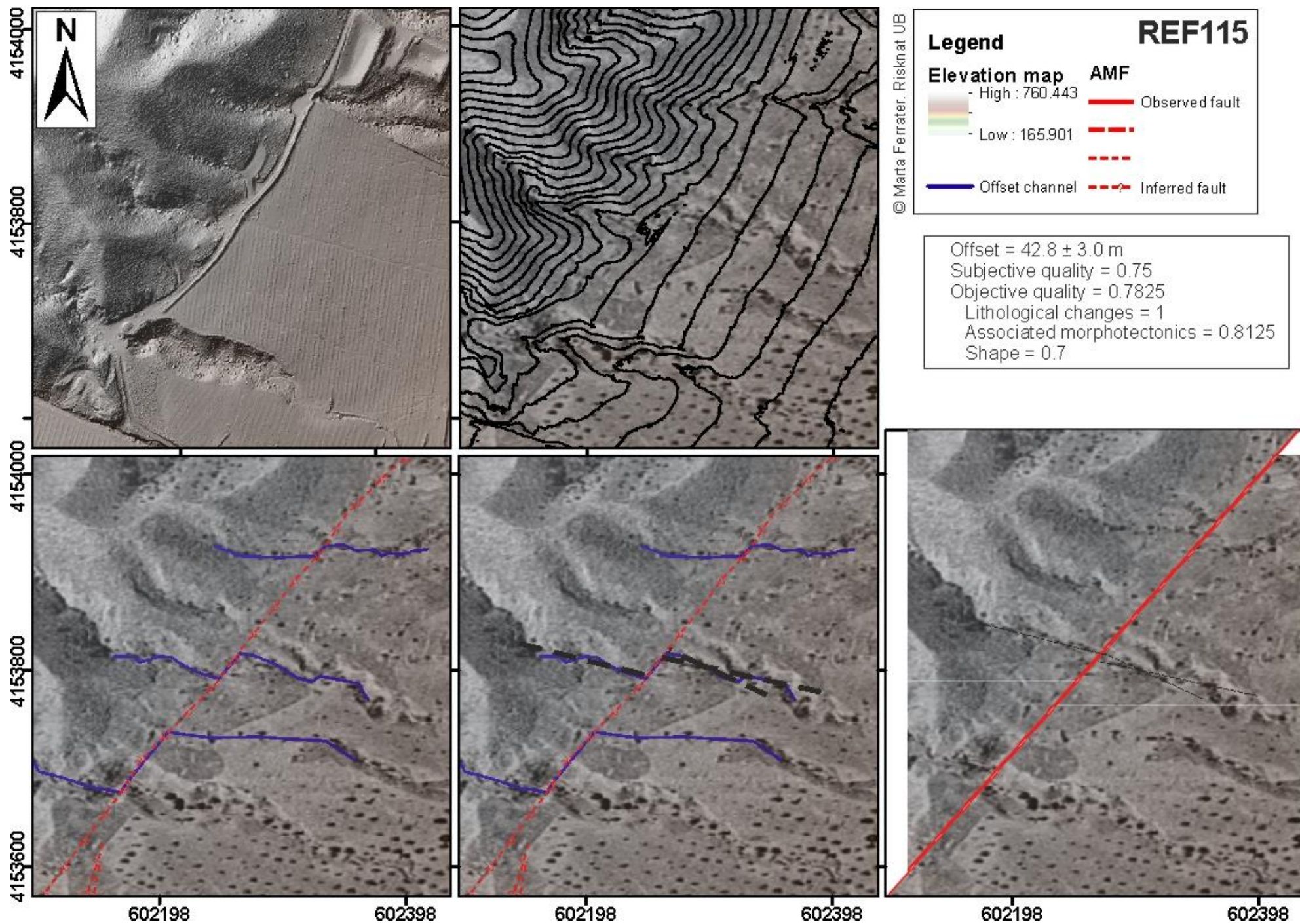


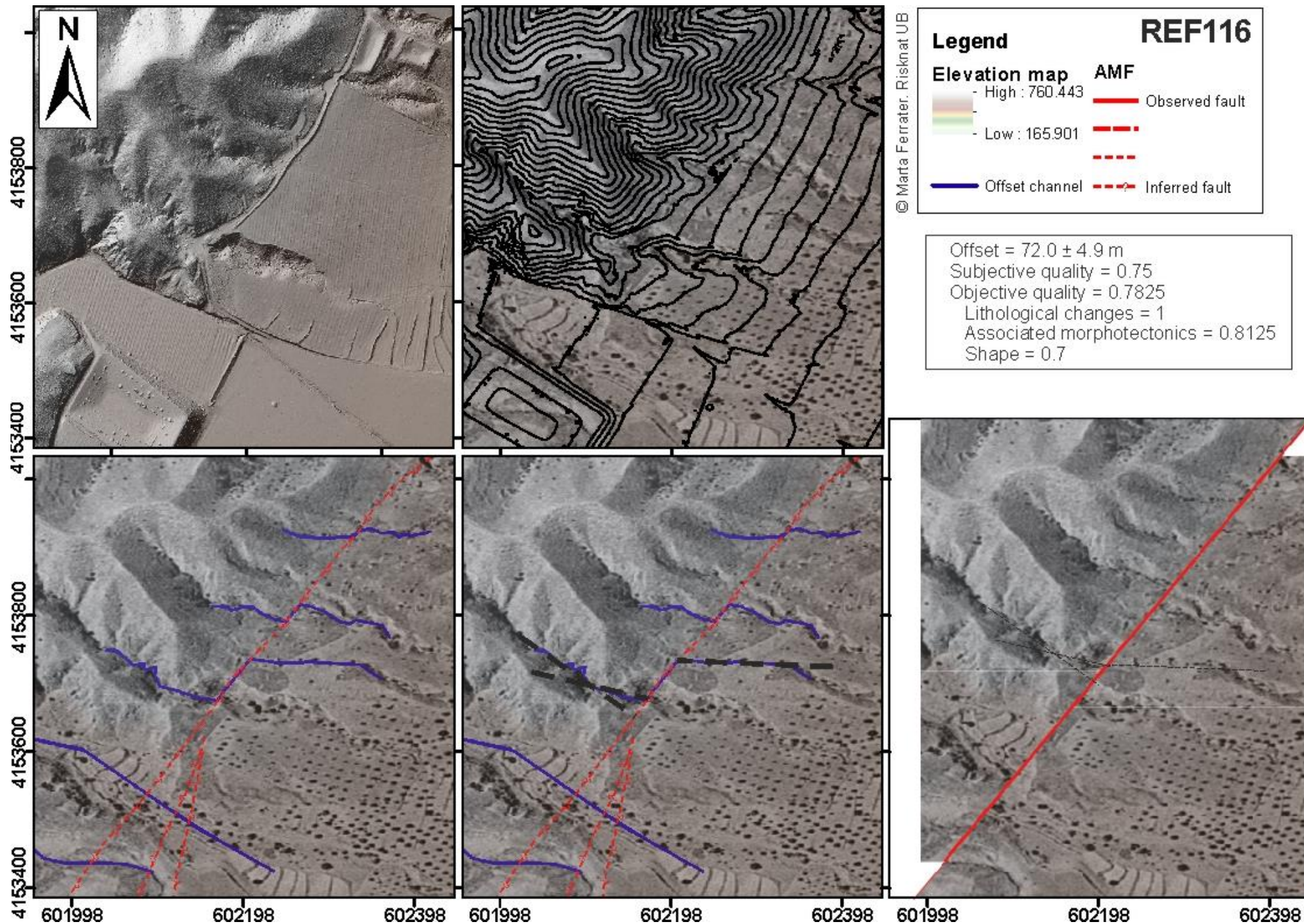


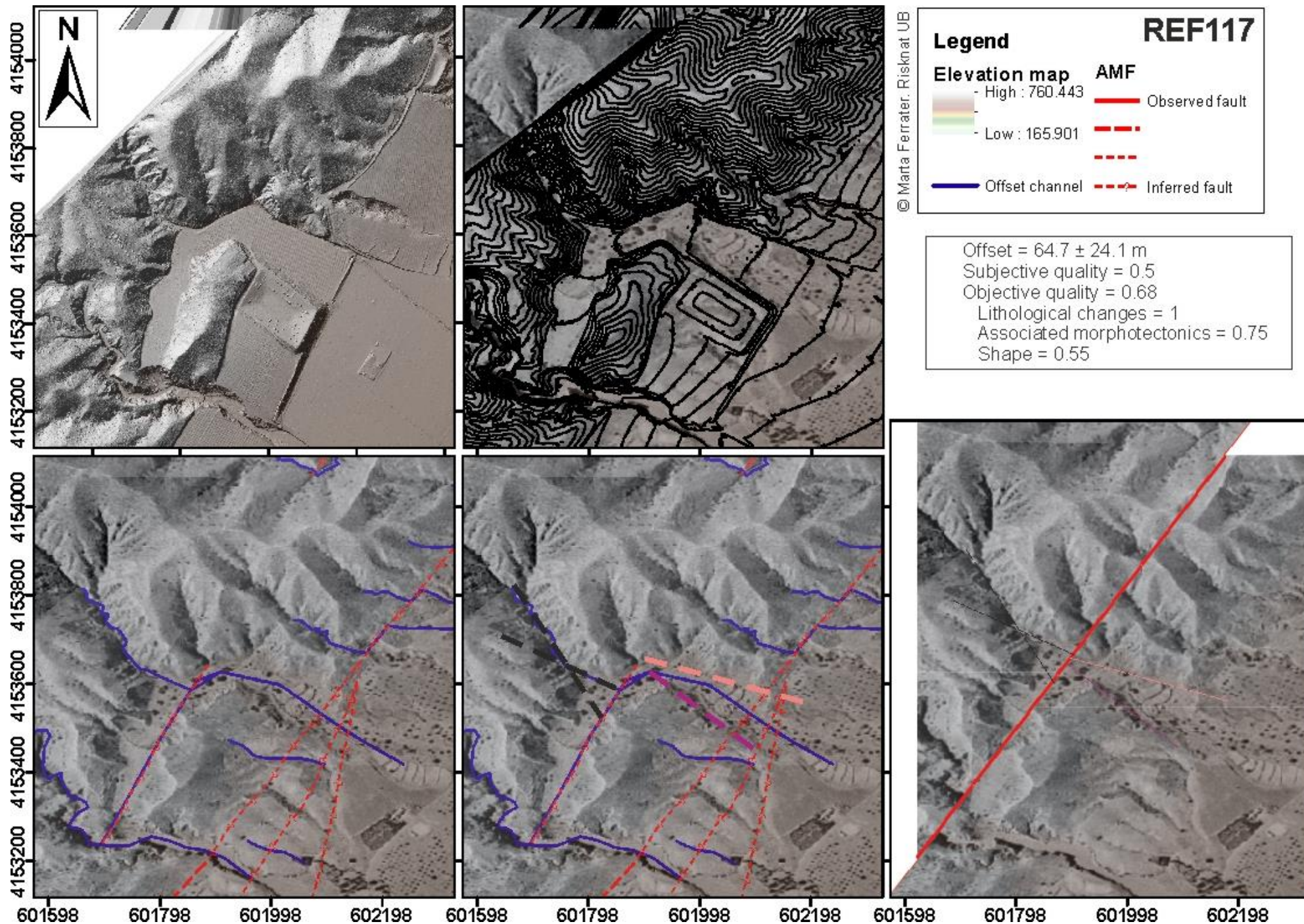


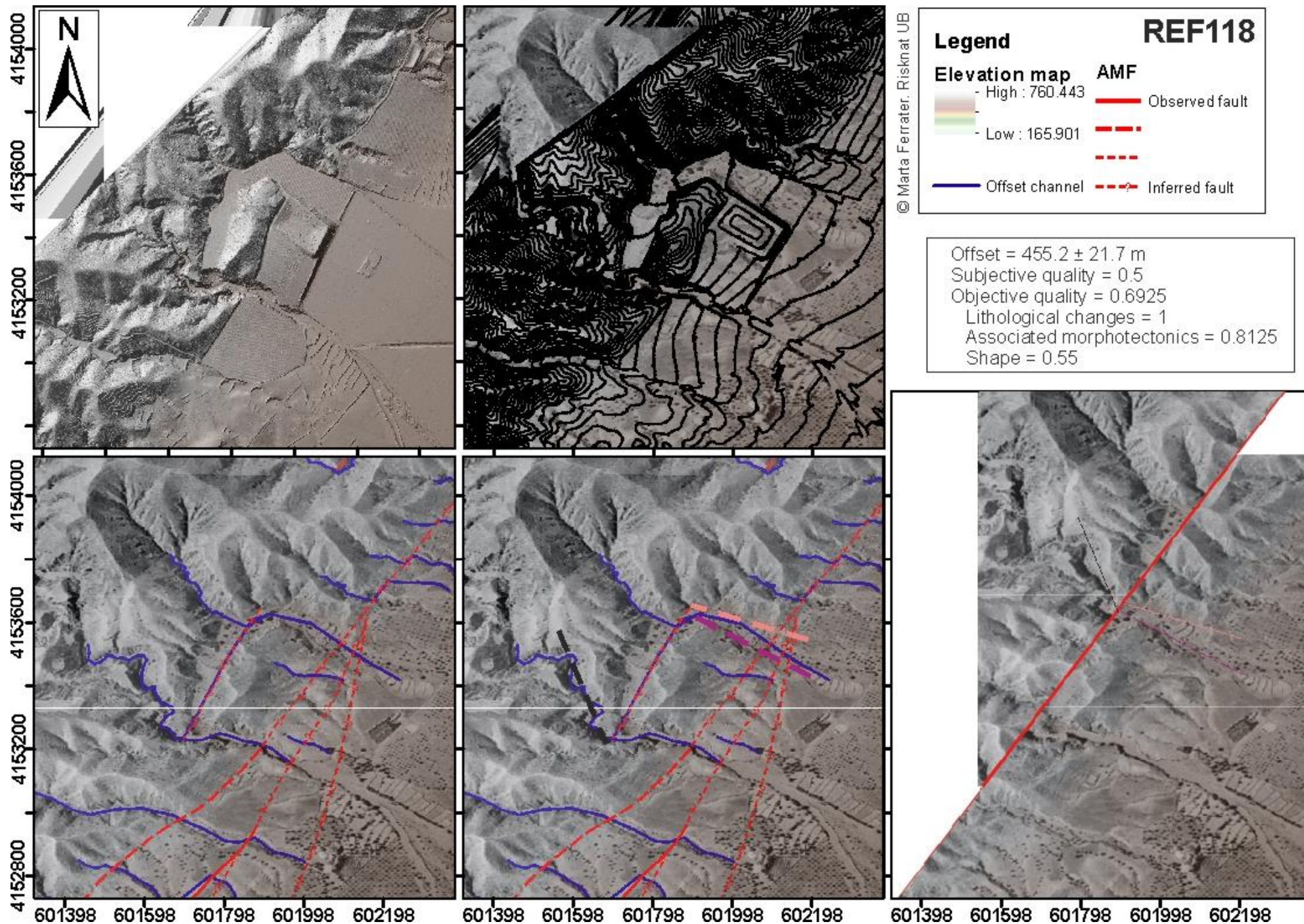


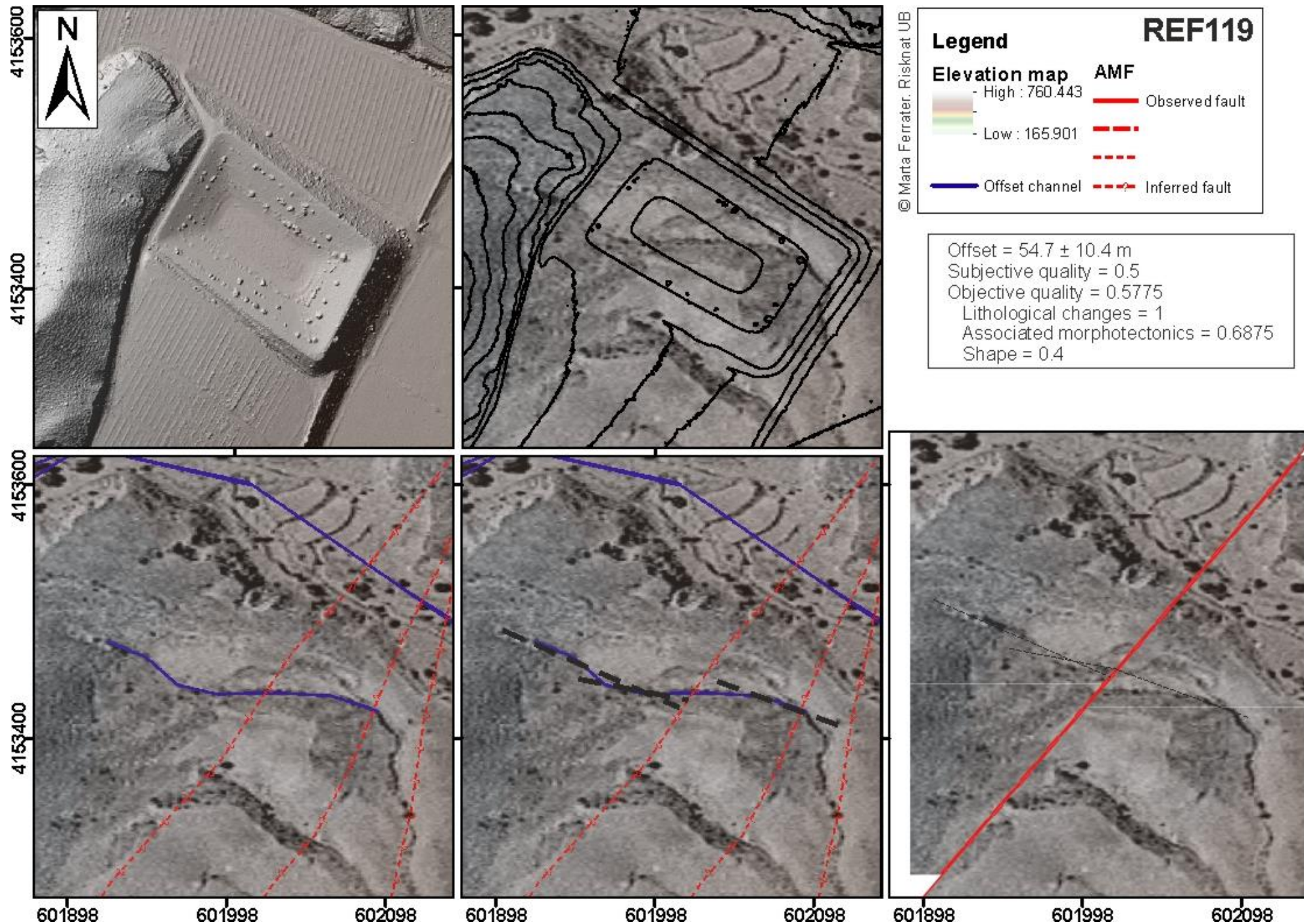


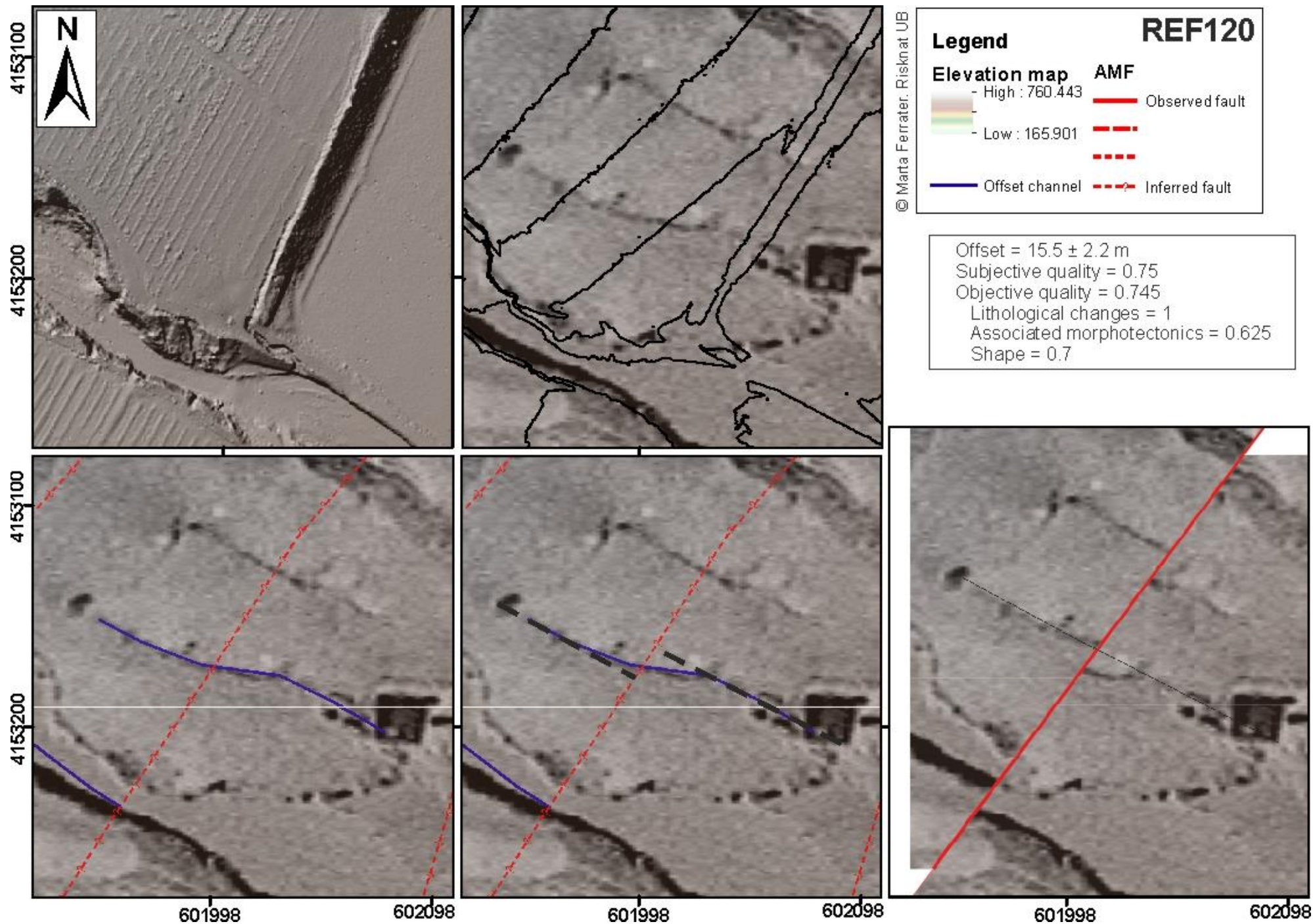


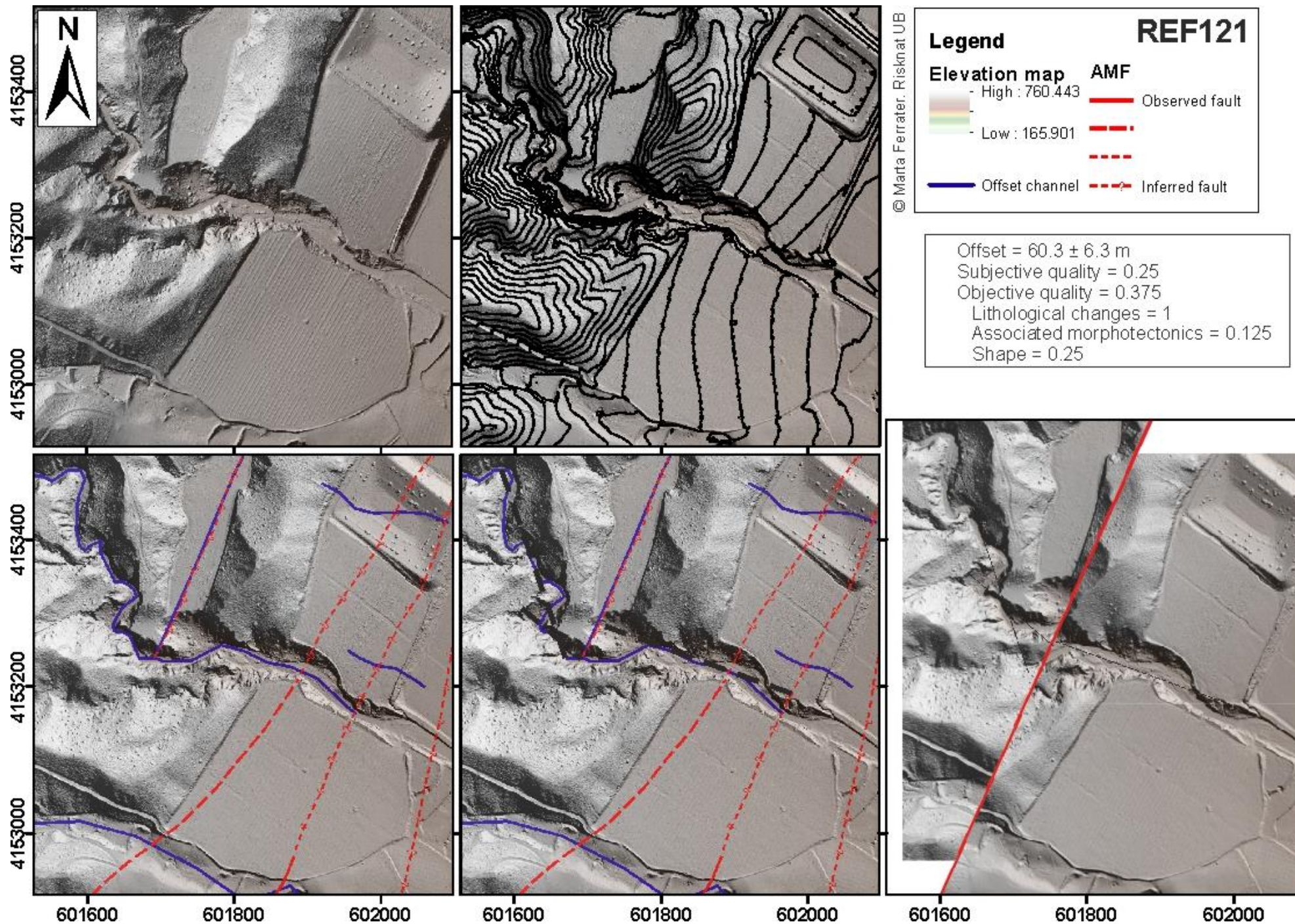


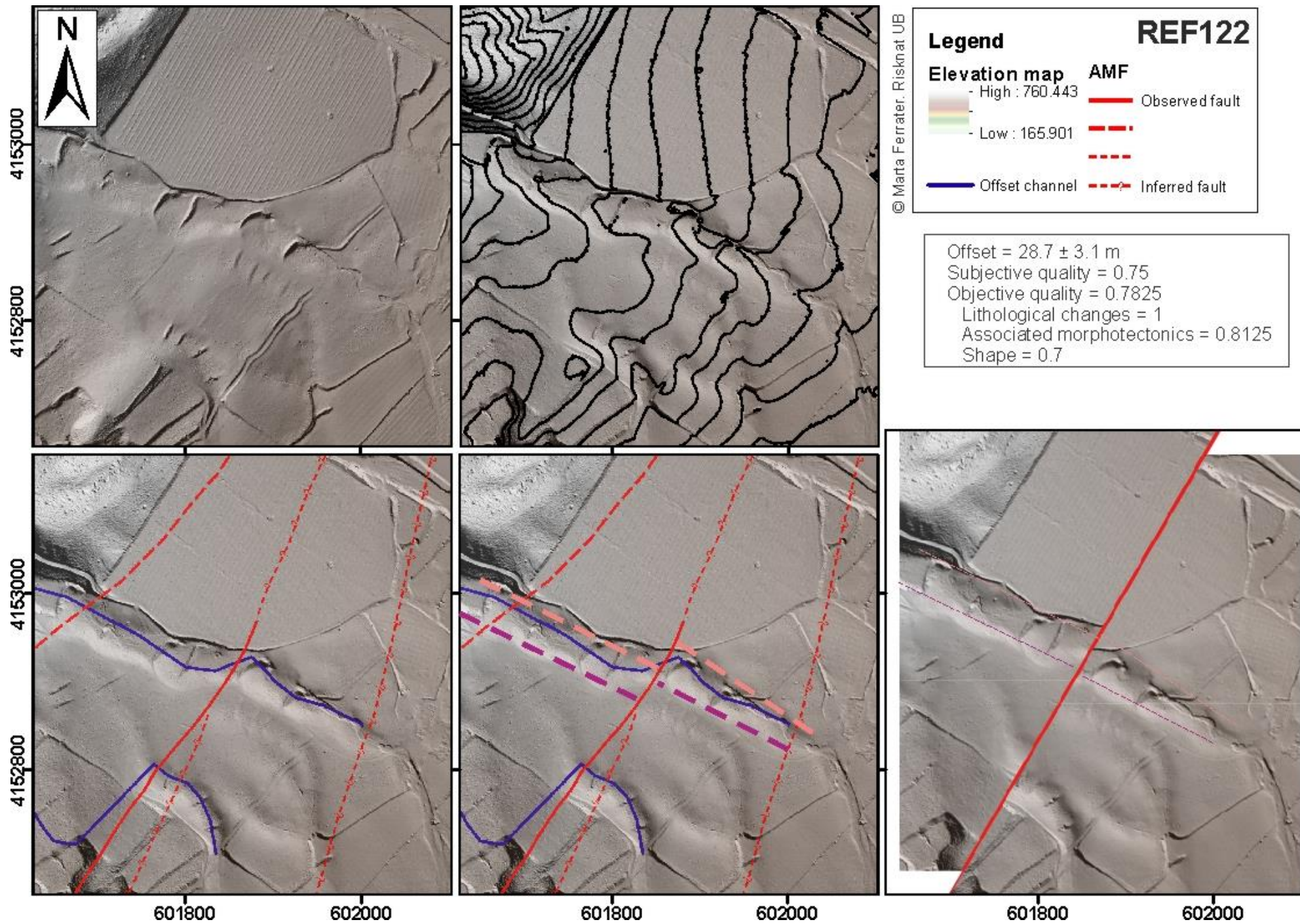


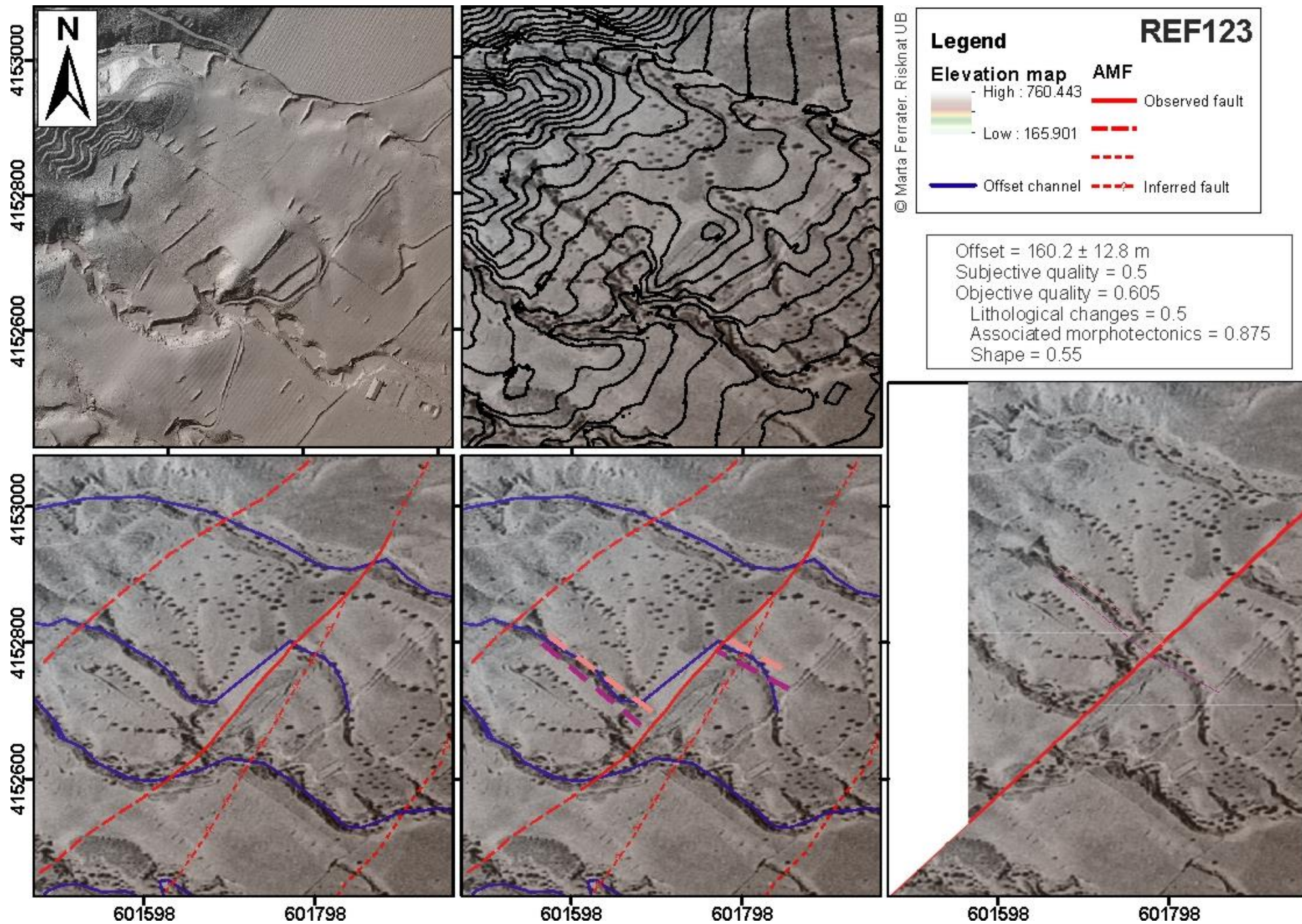


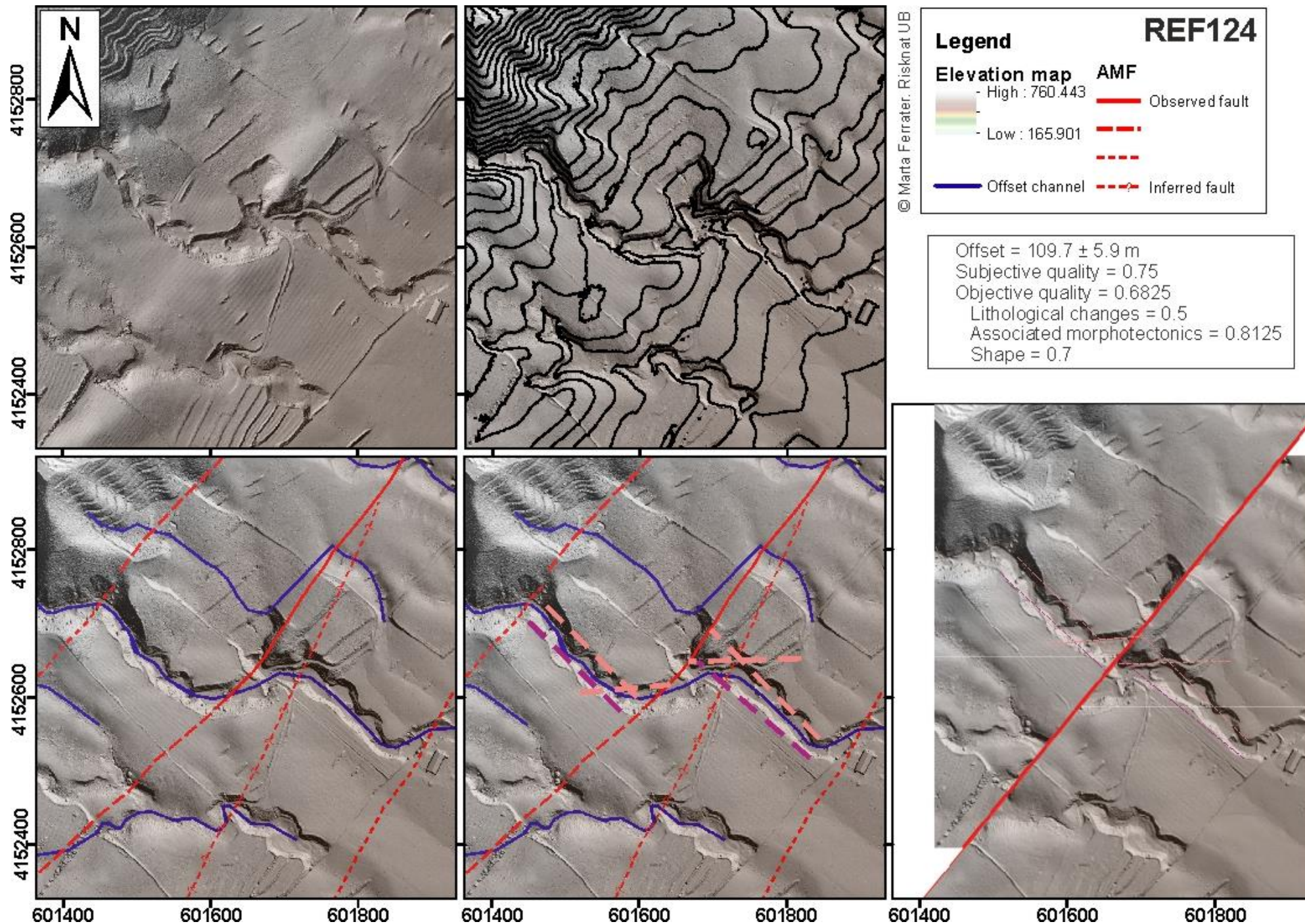


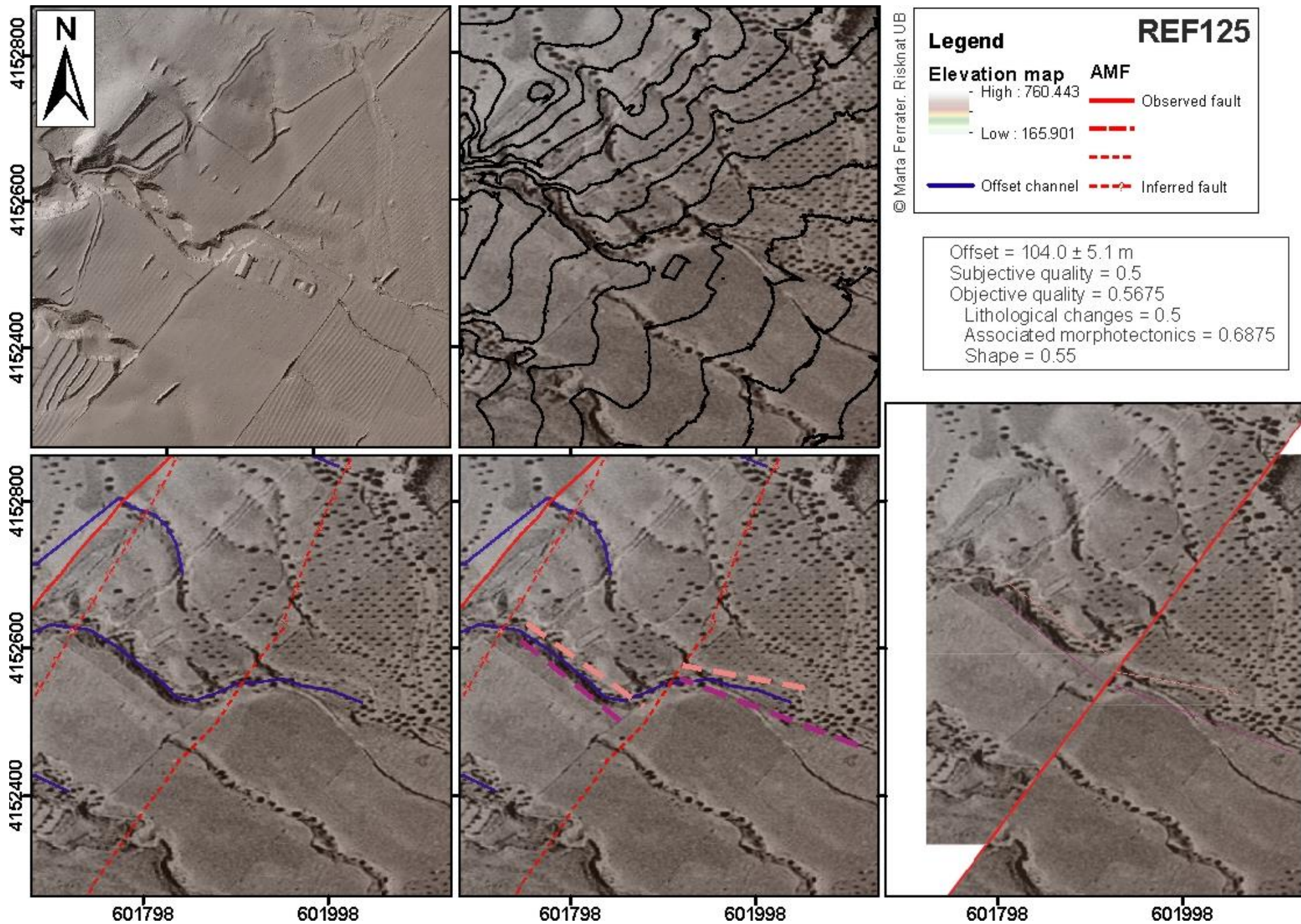


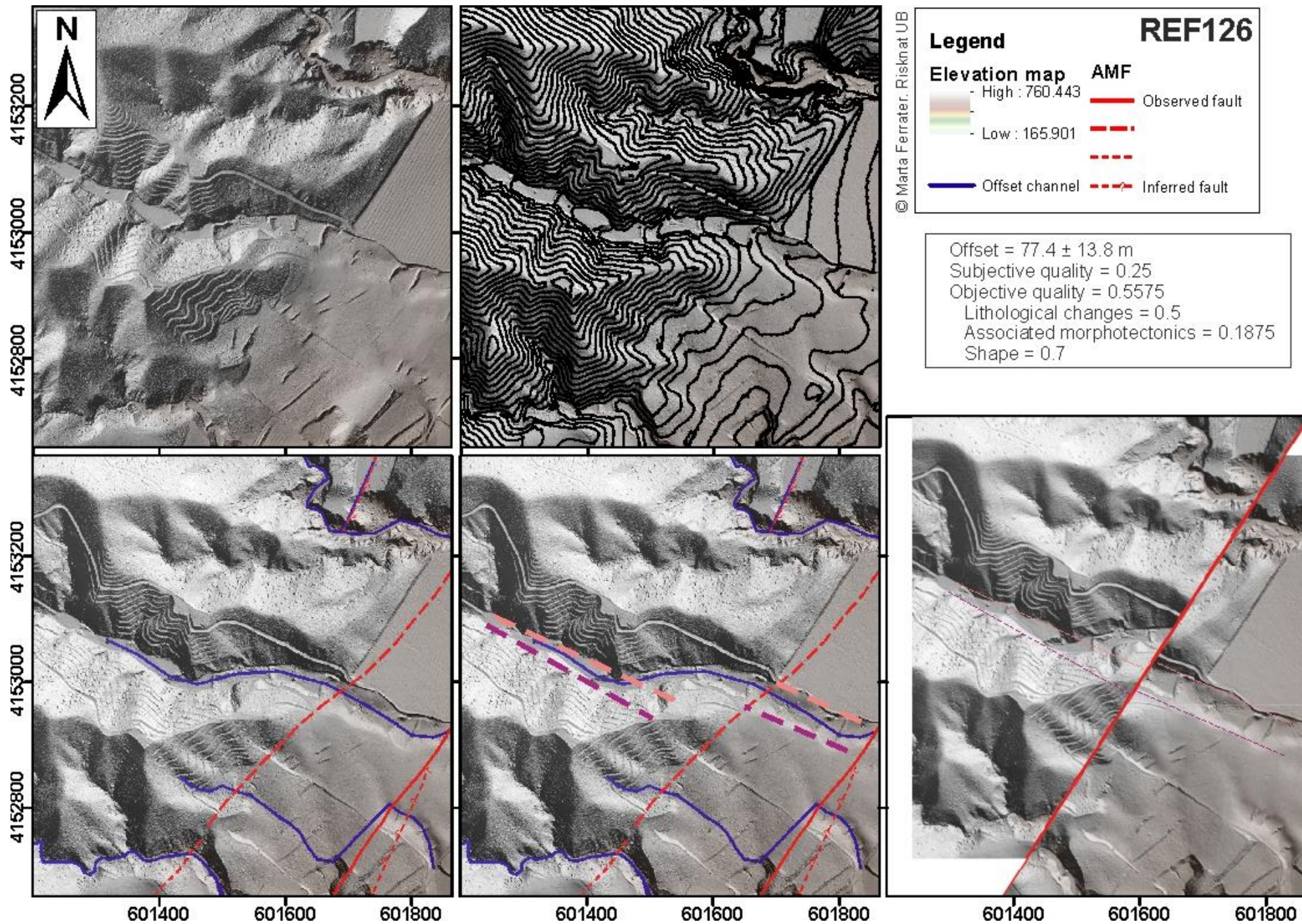


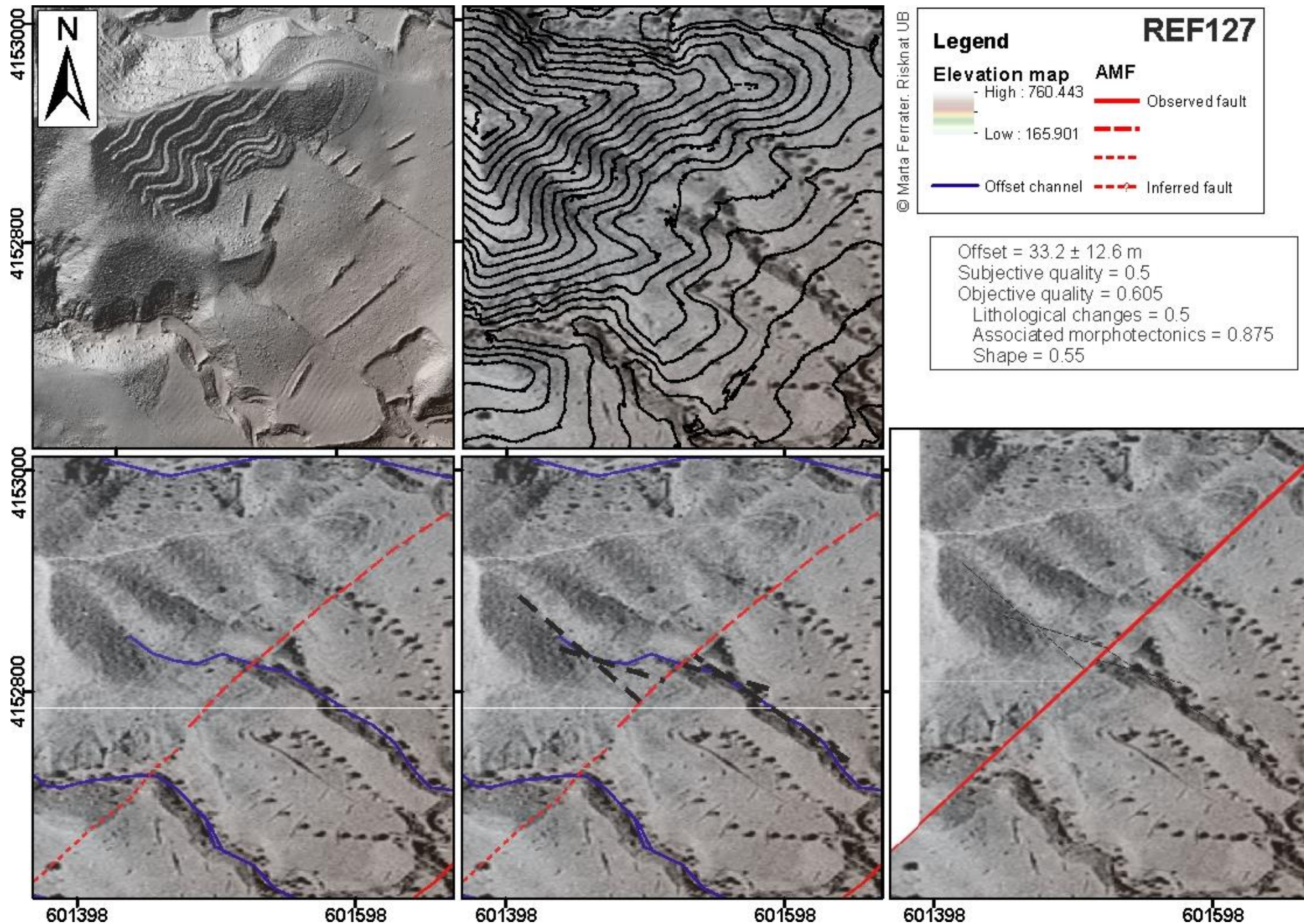


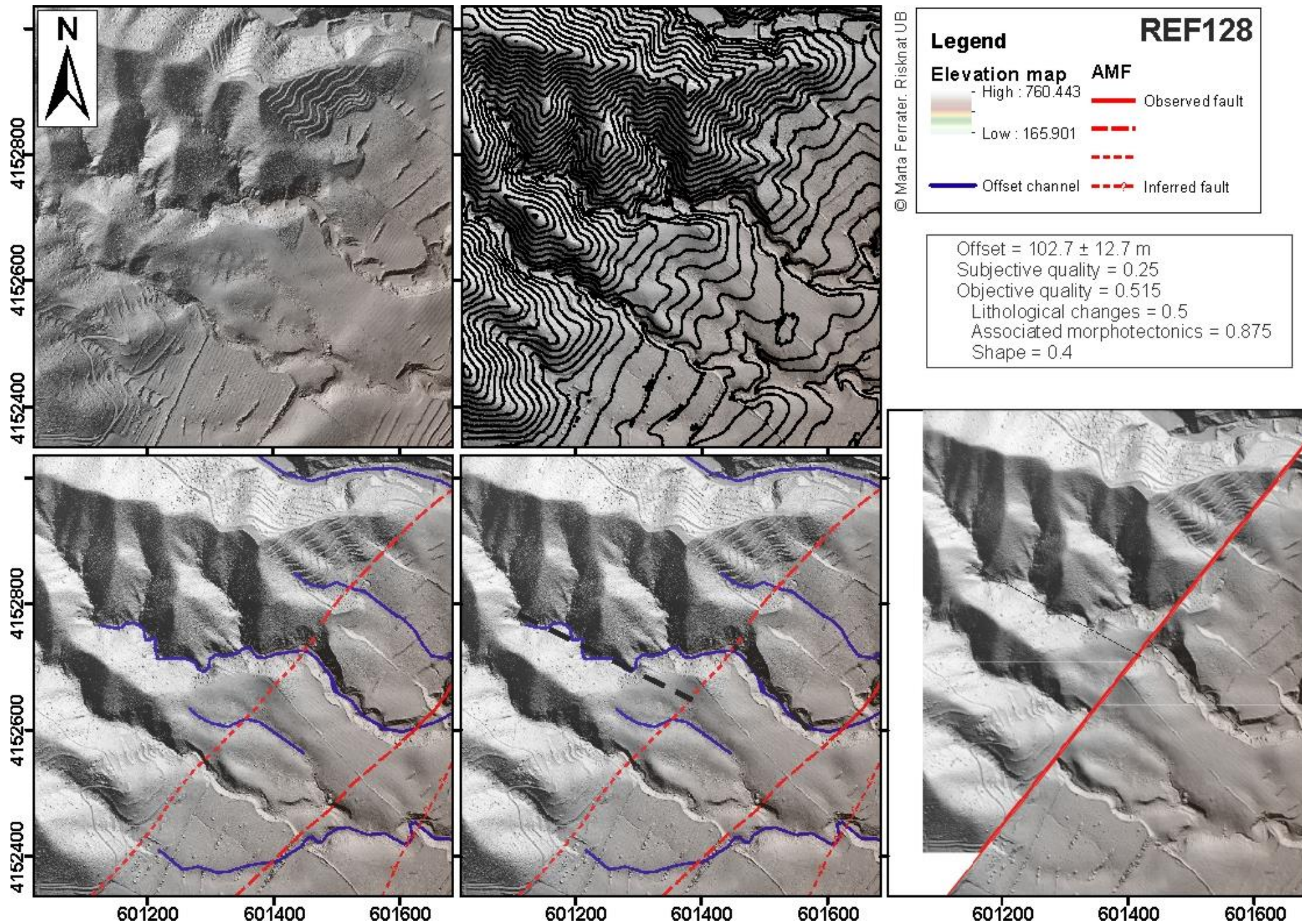


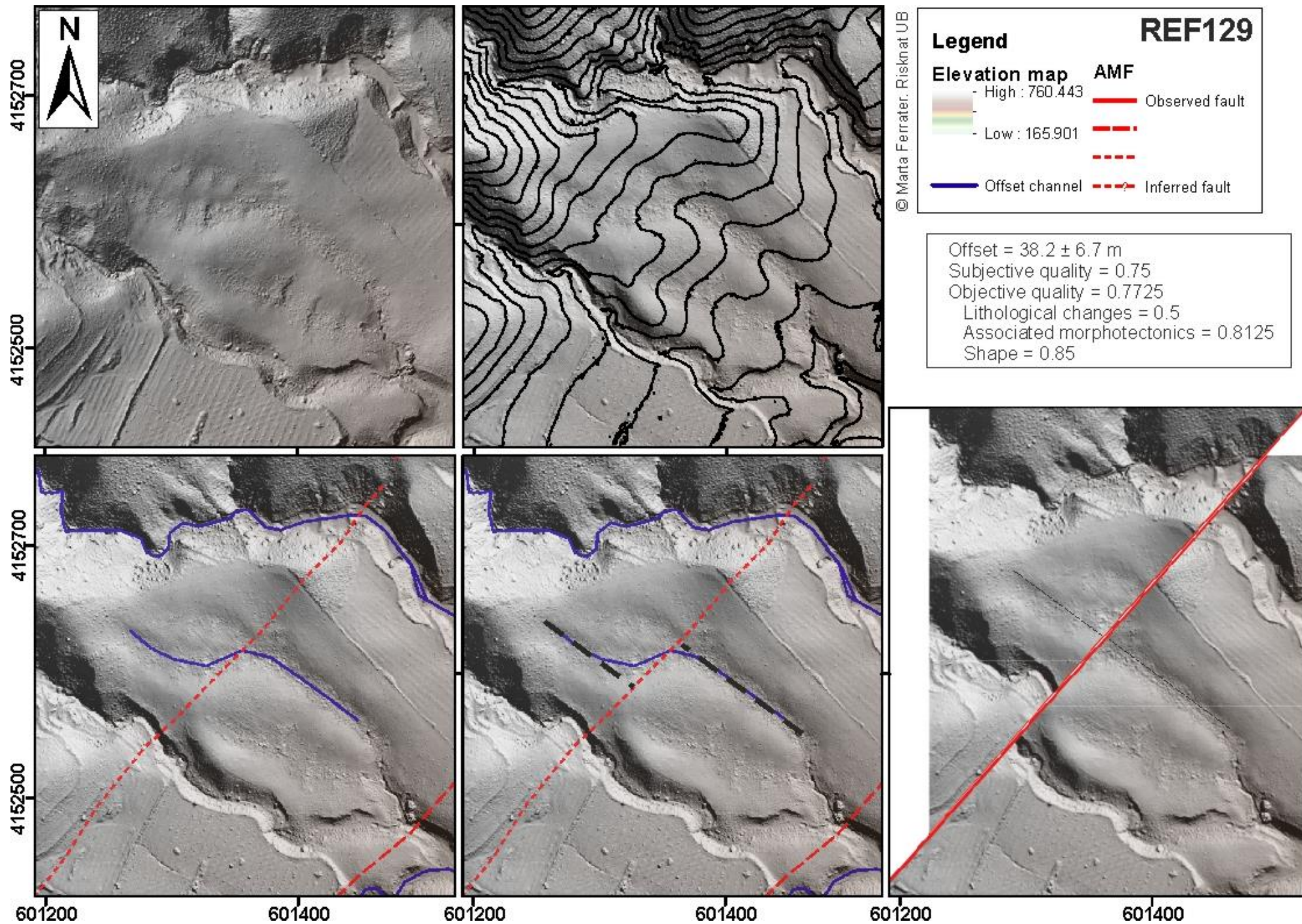


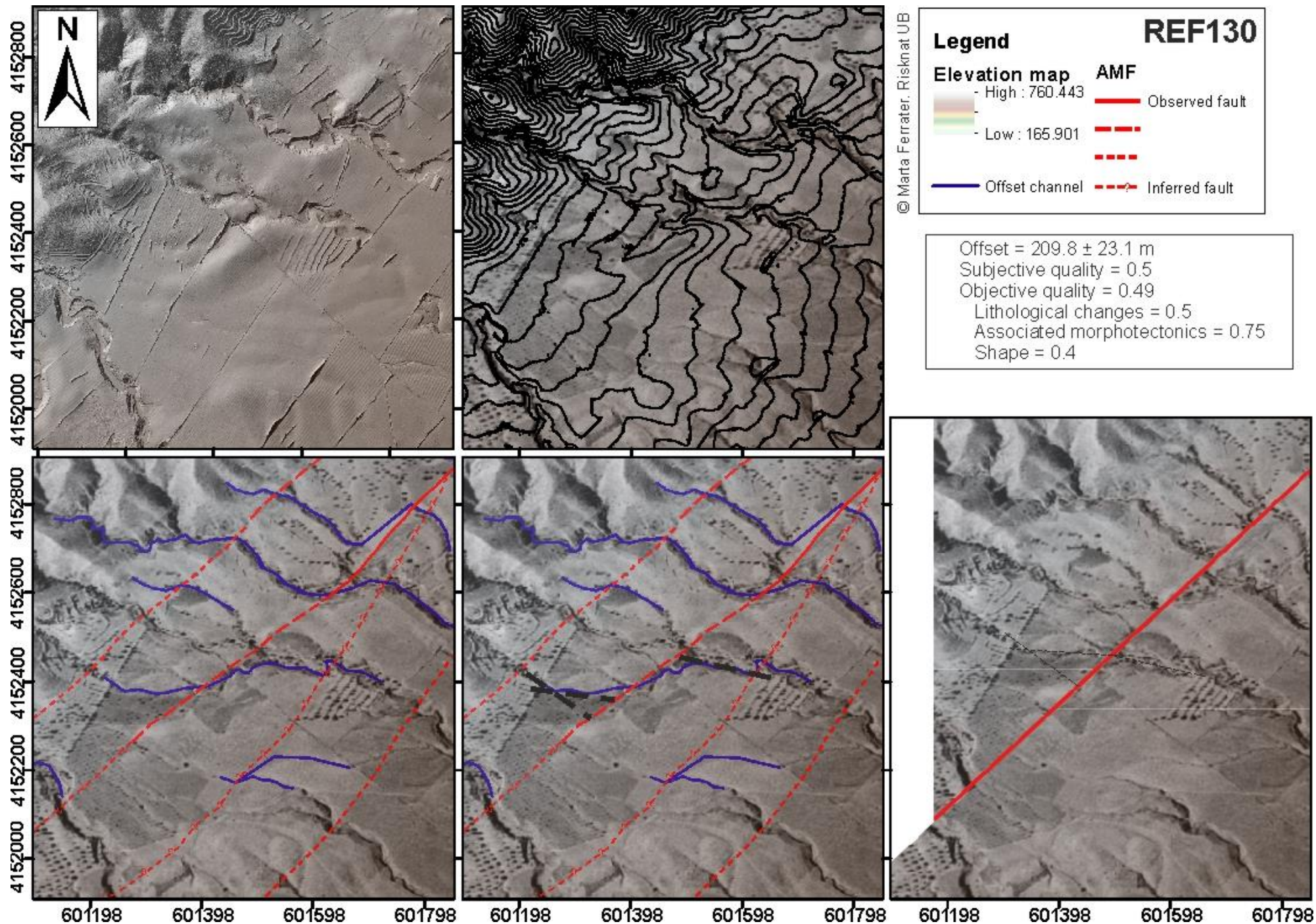


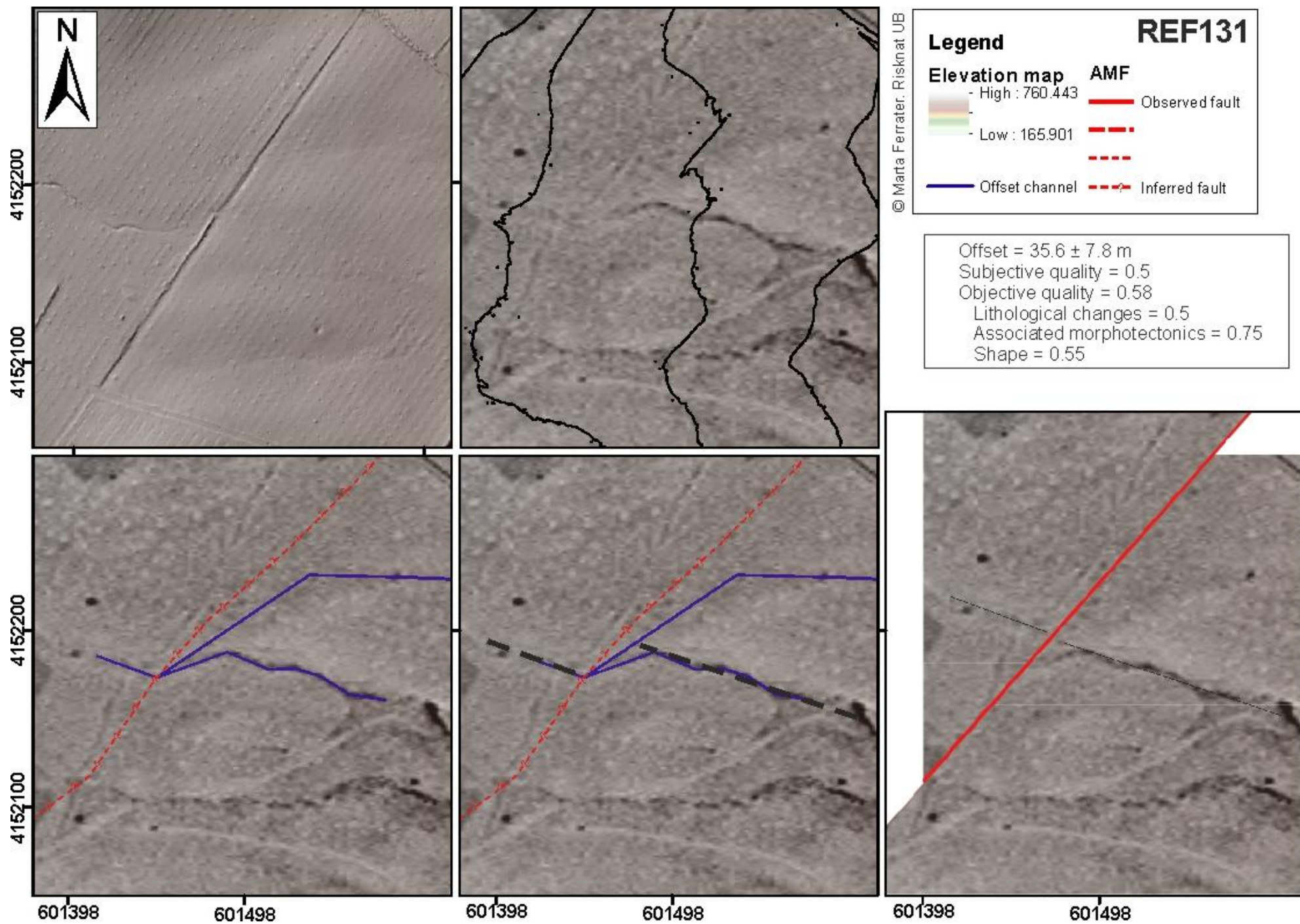


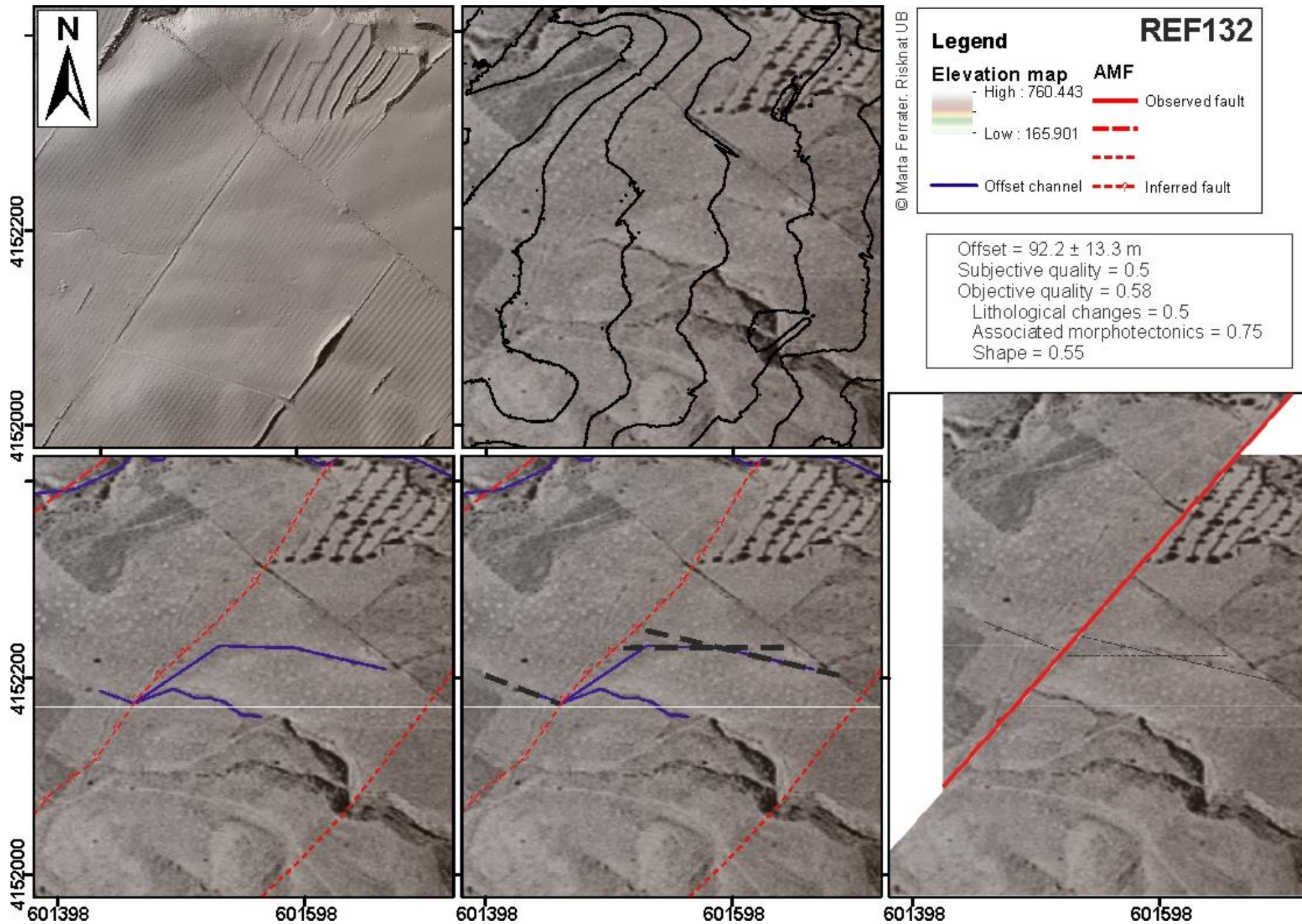


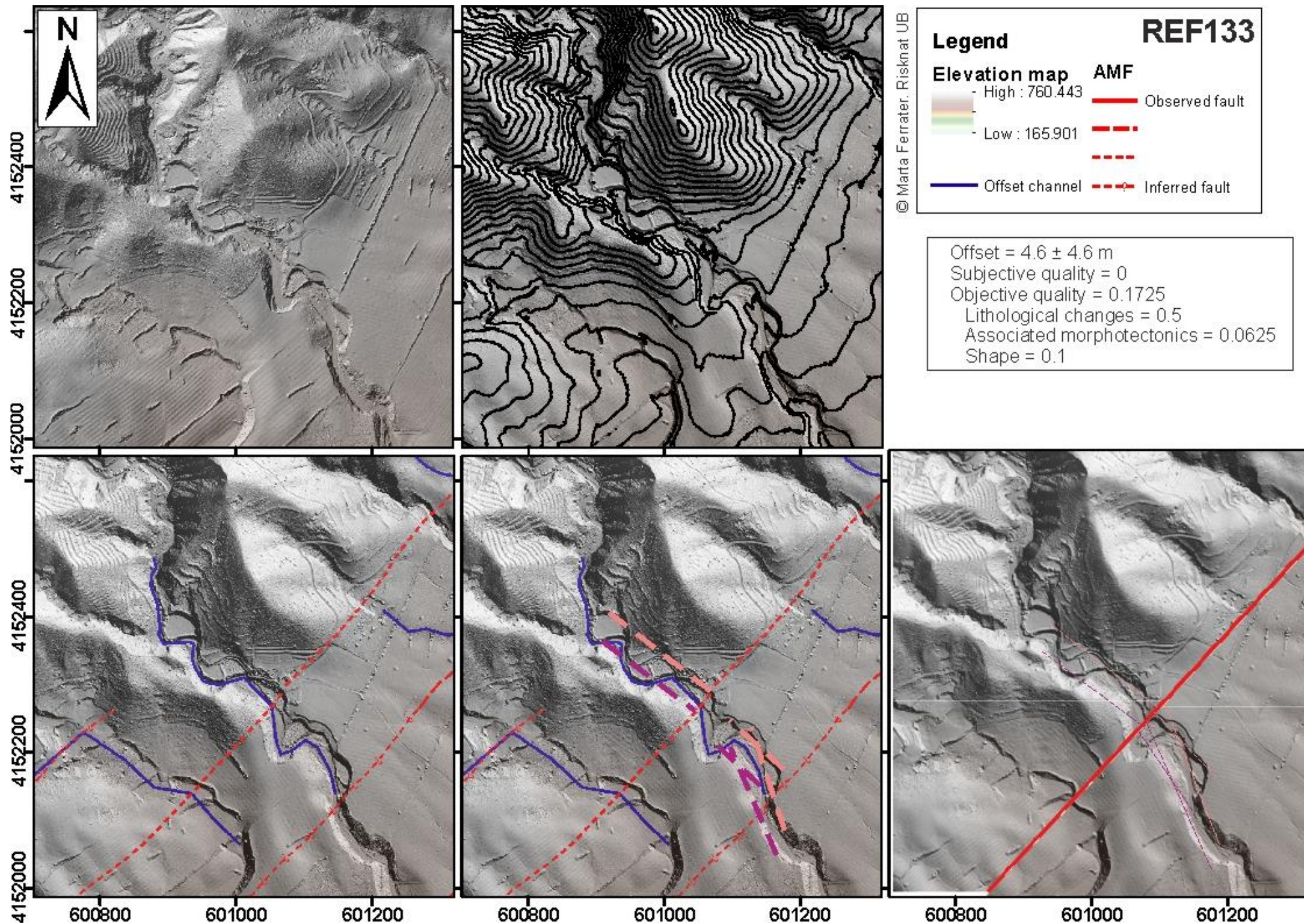


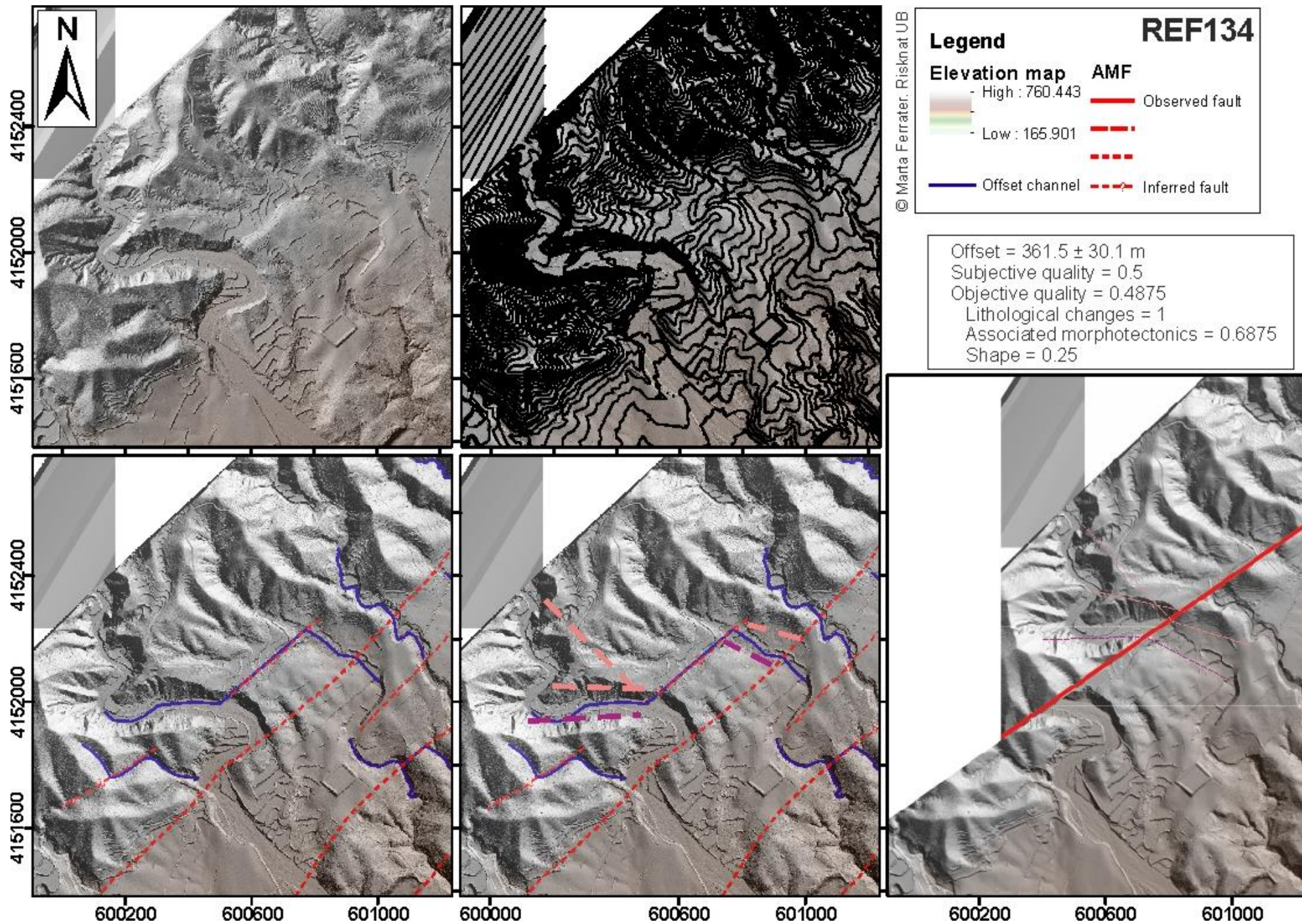


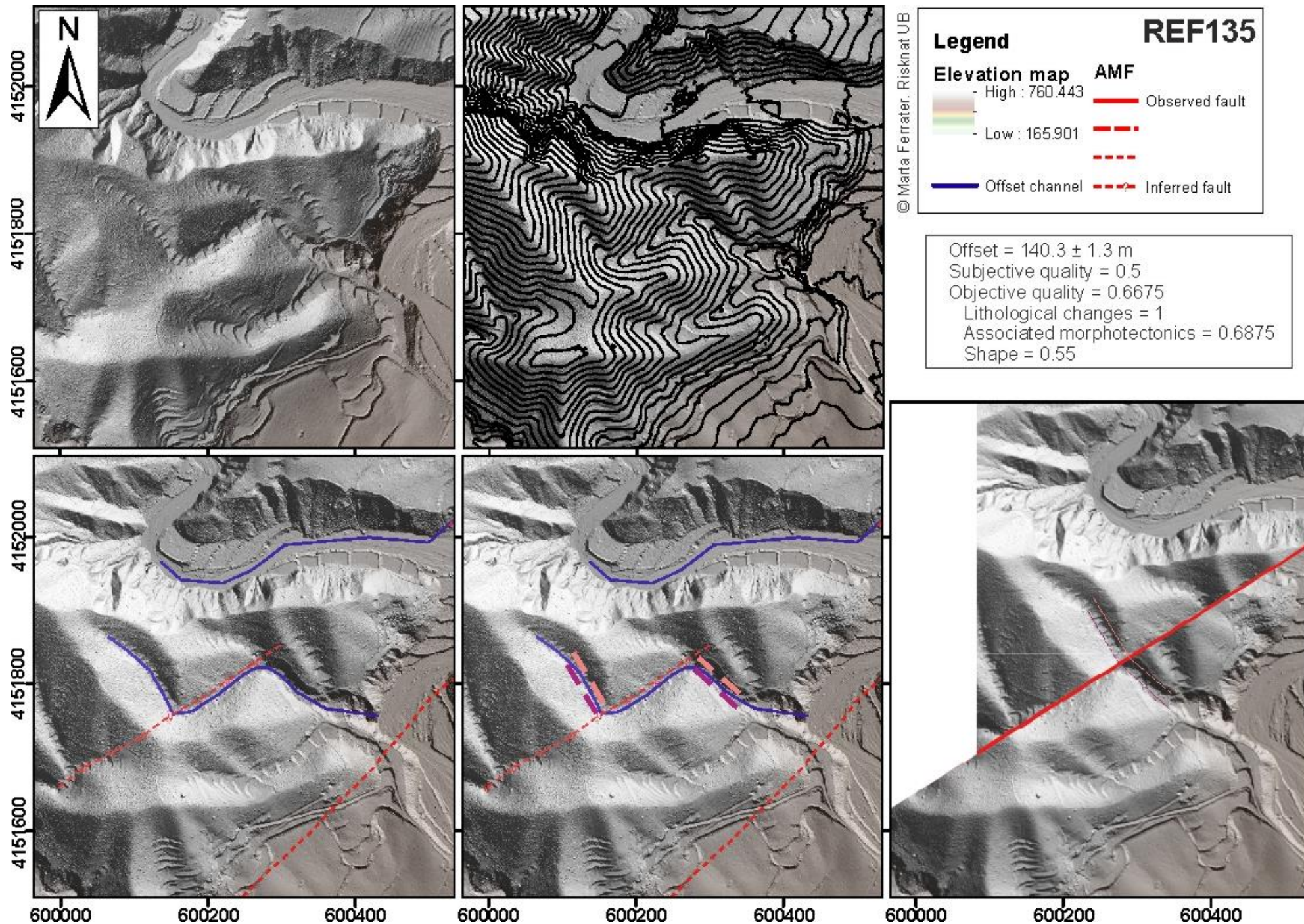


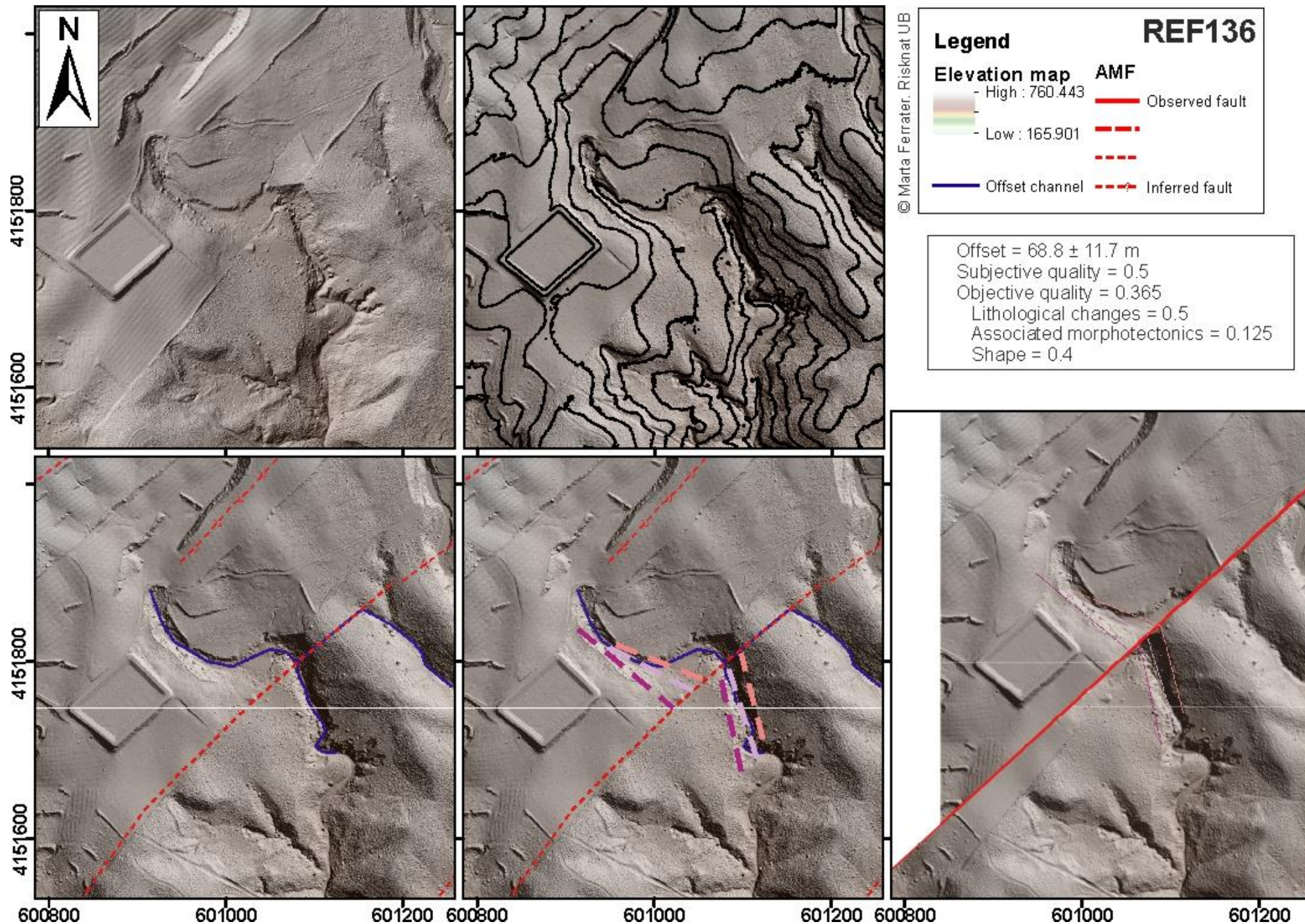


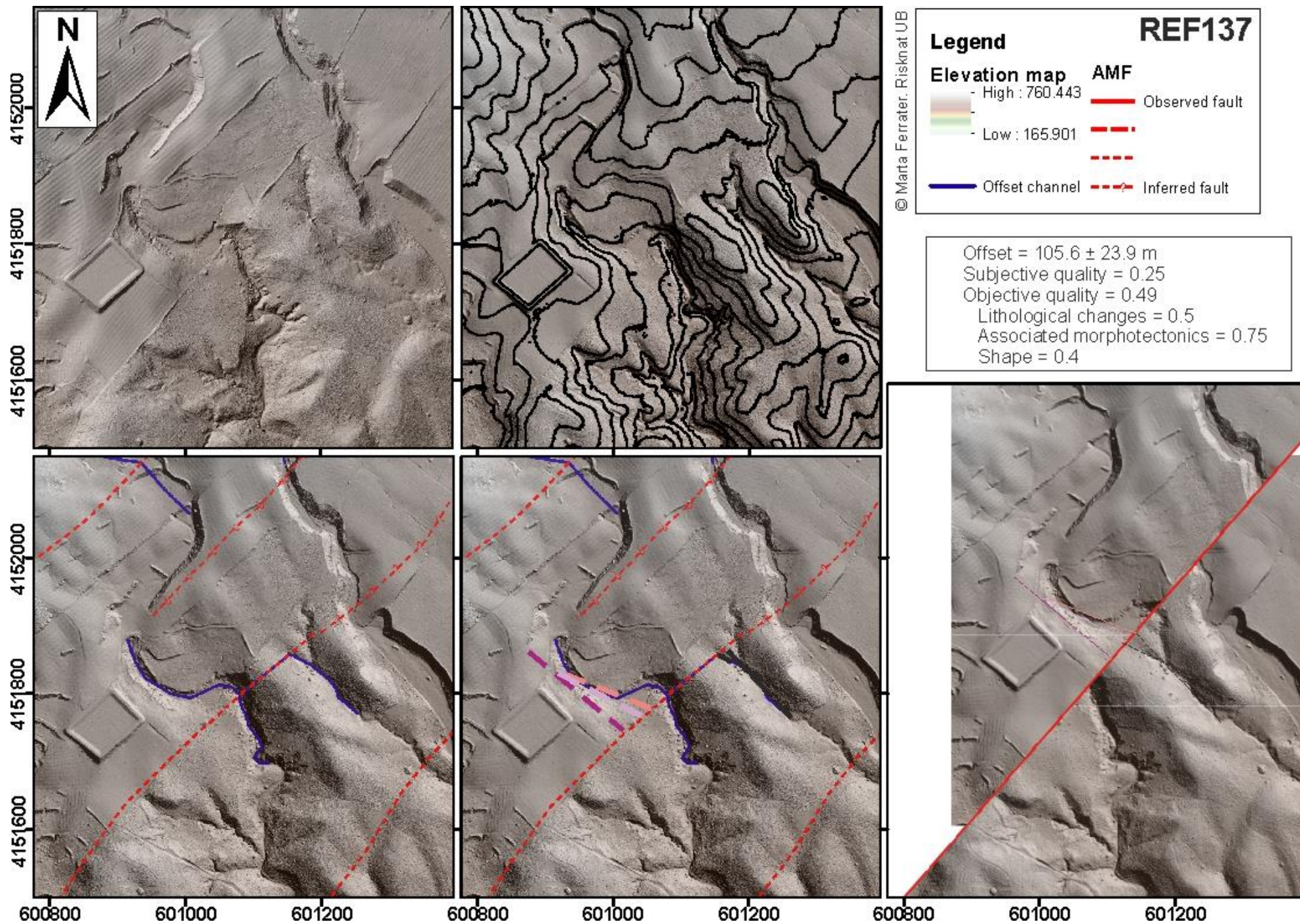












**Annex 5. Característiques de les
dislocacions tectòniques identificades
en la falla d'Alhama de Murcia**

Nom:REF	Dislocació	Incertesa aleatòria	Qualitat subjectiva	Element	Preservació	Edat coneguda	Canvis litològics	Elements morfològics associats	Forma	Qualitat objectiva
0	13,92	8,04	0,25	Ventall	NO	REL	1	0,125	0,55	0,555
1	33,02	17,01	0,25	Ventall	SI	REL	1	0,125	0,55	0,555
2	29,25	14,96	0,25	Ventall	SI	REL	1	0,75	0,7	0,77
3	10,54	0,92	0,5	Encaixat	SI	NO	0,5	0,6875	0,7	0,6575
4	27,19	1,96	0,5	Encaixat	SI	NO	0,5	0,6875	0,25	0,3875
5	49,9	5,5	0,25	Encaixat	NO	NO	0,5	0,625	0,7	0,645
6	90,94	43,83	0,25	Encaixat	NO	NO	0,5	0,625	0,25	0,375
7	291,56	37,96	0,5	Encaixat	SI	REL	0,5	0,6875	0,4	0,4775
8	43,08	3,86	0,5	Ventall	NO	REL	1	0,6875	0,7	0,7575
9	82,44	4,86	0,25	Ventall	NO	REL	1	0,125	0,55	0,555
10	41,99	13,44	0,25	Ventall	NO	NO	0,5	0,6875	0,4	0,4775
11	187,33	30,45	0,5	Encaixat	NO	NO	0,5	0,625	0,7	0,645
12	253,45	37,8	0,25	Encaixat	SI	NO	0,5	0,6875	0,25	0,3875
13	17,25	0,76	0,75	Encaixat	SI	REL	0,5	0,6875	0,85	0,7475
14	40,99	7,17	0,25	Encaixat	SI	NO	0,5	0,625	0,4	0,465
15	85,22	14,82	0,25	Encaixat	SI	NO	0,5	0,625	0,4	0,465
16	102,85	42,53	0,25	Encaixat	SI	NO	0,5	0,6875	0,4	0,4775
17	358,13	15,11	0,25	Encaixat	SI	NO	0,5	0	0,25	0,25
18	101,24	16,76	0,25	Encaixat	SI	NO	1	0,75	0,4	0,59
19	70	21,93	0,25	Carena	SI	NO	1	0,75	0,55	0,68
20	70,88	24,78	0	Encaixat	SI	NO	0,5	0	0,25	0,25
21	95,69	4,26	0,25	Encaixat	SI	NO	0,5	0	0,55	0,43
22	135,49	14,24	0,25	Encaixat	SI	NO	0,5	0,125	0,25	0,275
23	28,26	20,34	0,25	Encaixat	SI	NO	0,5	0,125	0,4	0,365
24	45,45	3,31	0,5	Encaixat	SI	NO	0,5	0,6875	0,7	0,6575
25	35,06	4,05	0,75	Encaixat	SI	NO	0,5	0,6875	0,85	0,7475
26	31,61	3,38	0,5	Encaixat	SI	REL	1	0,3125	0,55	0,5925
27	46,25	19,09	0,5	Ventall	SI	REL	1	1	0,55	0,73
28	26,04	4,42	0,5	Ventall	NO	REL	1	0,9375	0,7	0,8075
29	10,69	1,49	0,5	Ventall	SI	REL	1	0,9375	0,7	0,8075
30	202,69	5,95	0,5	Encaixat	SI	REL	1	0,625	0,55	0,655
31	73,98	33,76	0,75	Encaixat	NO	NO	0,5	0,75	0,7	0,67
32	29,79	12,06	0,5	Encaixat	SI	NO	0,5	0,8125	0,4	0,5025
33	196,2	37,85	0,25	Encaixat	SI	NO	0,5	0,6875	0,25	0,3875
34	117,04	37,15	0,25	Encaixat	SI	REL	1	0,6875	0,25	0,4875
35	79,74	8,78	0,25	Encaixat	NO	NO	0,5	0,6875	0,25	0,3875
36	98,37	2,72	0	Encaixat	NO	NO	0,5	0,75	0,4	0,49

37	130,58	16,96	0,5	Encaixat	NO	NO	0,5	0,875	0,55	0,605
38	139,79	27,92	0,5	Encaixat	SI	NO	0,5	0,75	0,4	0,49
39	75,05	18,68	0,5	Encaixat	NO	REL	0,5	0,6875	0,55	0,5675
40	9,92	4,43	0,5	Ventall	NO	REL	1	0,6875	0,7	0,7575
41	19,16	4,76	0,5	Ventall	NO	REL	1	0,75	0,55	0,68
42	23,55	7,63	0,5	Ventall	SI	REL	1	1	0,7	0,82
43	98,8	18,88	0,5	Ventall	SI	REL	1	1	0,7	0,82
44	23,55	1,21	0,25	Encaixat	SI	NO	0,5	0,625	0,4	0,465
45	12,9	4,52	0,5	Ventall	SI	NO	1	0,6875	0,55	0,6675
46	40,1	4	0,75	Encaixat	SI	NO	0,5	0,75	0,55	0,58
47	9,73	4,02	0,75	Encaixat	SI	NO	0,5	0,75	0,7	0,67
48	6,7	1,69	0,5	Ventall	SI	REL	1	0,6875	0,55	0,6675
49	17,98	4,09	0,5	Ventall	NO	REL	1	0,6875	0,4	0,5775
50	40,88	4,65	0,75	Encaixat	SI	NO	0,5	0,6875	0,4	0,4775
51	46,27	4,94	0,5	Encaixat	SI	NO	0,5	0,6875	0,55	0,5675
52	34,17	13,62	0,25	Encaixat	SI	NO	0,5	0,625	0,25	0,375
53	40,82	6,98	0,25	Encaixat	SI	NO	0,5	0,6875	0,25	0,3875
54	36,47	5,02	0,25	Encaixat	SI	REL	1	0,0625	0,55	0,5425
55	28,72	2,77	0,75	Ventall	SI	ABS	1	0,6875	1	0,9375
56	55,42	2,88	0,5	Encaixat	NO	REL	0,5	0,9375	0,7	0,7075
57	194,92	7,14	0,5	Encaixat	NO	NO	0,5	0,875	0,7	0,695
58	52,74	15,5	0,75	Encaixat	NO	REL	0,5	0,75	0,7	0,67
59	44,94	20,59	0,5	Ventall	NO	ABS	1	0,875	0,7	0,795
60	11,28	6,67	0,25	Ventall	NO	ABS	1	0,9375	0,55	0,7175
61	37,4	6,67	0,25	Ventall	NO	ABS	1	0,3125	0,55	0,5925
62	14,81	5,09	0,5	Ventall	NO	ABS	1	1	0,55	0,73
63	32,29	1,48	0,5	Ventall	NO	ABS	1	1	0,7	0,82
64	17,15	3,89	0,75	Ventall	NO	ABS	1	0,9375	0,55	0,7175
65	190,73	19	0,75	Encaixat	SI	NO	0,5	0,8125	0,7	0,6825
66	341,56	21,36	0,5	Encaixat	SI	NO	0,5	0,875	0,7	0,695
67	18,1	8,31	0,5	Encaixat	NO	REL	0,5	0,8125	0,7	0,6825
68	55,82	12,75	0,5	Encaixat	NO	REL	0,5	0,875	0,55	0,605
69	55,95	2,27	0,5	Encaixat	SI	NO	0,5	0,875	0,55	0,605
70	26,53	5,98	0,5	Encaixat	SI	REL	0,5	0,875	0,55	0,605
71	8,29	3,47	0,5	Encaixat	SI	REL	0,5	0,8125	0,55	0,5925
72	22,73	6,36	0,75	Encaixat	SI	NO	0,5	0,75	0,7	0,67
73	72,94	12,68	0,5	Encaixat	SI	REL	0,5	0,8125	0,7	0,6825
74	92,13	9,03	0,75	Encaixat	SI	NO	0,5	0,75	0,55	0,58
75	76,24	20,08	0,5	Encaixat	SI	NO	0,5	0,6875	0,4	0,4775
76	16,28	1,49	0,5	Encaixat	SI	NO	0,5	0,6875	0,7	0,6575
77	22,59	4,12	0,75	Encaixat	SI	NO	0,5	0,9375	0,7	0,7075
78	35,07	3,65	0,75	Carena	SI	NO	0,5	0,9375	0,7	0,7075
79	22,2	6,76	0,75	Encaixat	SI	NO	0,5	0,9375	0,7	0,7075
80	17,54	3,81	0,75	Carena	NO	NO	0,5	0,9375	0,7	0,7075
81	18,91	15,56	0,75	Encaixat	NO	NO	0,5	0,9375	0,7	0,7075

82	78,27	28,54	0	Encaixat	NO	REL	0,5	0,9375	0,4	0,5275
83	29,5	10,58	0,5	Encaixat	NO	NO	0,5	0,8125	0,55	0,5925
84	6,6	5	0,75	Encaixat	NO	NO	0,5	0,8125	0,85	0,7725
85	57,43	7,74	0,25	Encaixat	NO	NO	0,5	0,625	0,25	0,375
86	41,71	10,81	0,25	Encaixat	NO	NO	0,5	0,0625	0,55	0,4425
87	118,61	14,34	0,5	Encaixat	SI	NO	1	0,75	0,55	0,68
88	164,96	5,8	0,75	Encaixat	SI	NO	1	0,75	0,55	0,68
89	59,68	10,72	0,5	Encaixat	NO	NO	0,5	0,6875	0,85	0,7475
90	50,1	4,54	0,25	Encaixat	SI	NO	0,5	0	0,55	0,43
91	29,28	6,91	0,75	Encaixat	SI	NO	1	0,6875	0,55	0,6675
92	14,22	5,21	0,75	Encaixat	SI	NO	1	0,6875	0,55	0,6675
93	83,71	6,39	0,75	Encaixat	NO	REL	0,5	0,75	0,55	0,58
94	71,7	6,35	0,5	Encaixat	NO	REL	0,5	0,875	0,85	0,785
95	257,81	8,76	0,5	Encaixat	NO	REL	0,5	1	0,55	0,63
96	36,36	19,97	0	Encaixat	SI	NO	0,5	0,375	0,25	0,325
97	107,75	22,97	0	Encaixat	SI	NO	0,5	1	0,25	0,45
98	50,79	9,72	0,75	Encaixat	SI	REL	0,5	0,75	0,7	0,67
99	179,6	21,08	0,75	Encaixat	NO	REL	0,5	0,6875	0,7	0,6575
100	127,13	27,67	0,5	Encaixat	NO	REL	0,5	0,75	0,7	0,67
101	298,62	10,17	0,5	Encaixat	SI	NO	0,5	0,6875	0,4	0,4775
102	259,85	26,9	0,5	Encaixat	SI	NO	0,5	0,875	0,55	0,605
103	9,89	3,83	0,25	Encaixat	NO	REL	0,5	0,625	0,55	0,555
104	11,04	2,63	0,25	Encaixat	NO	REL	0,5	0,0625	0,55	0,4425
105	4,45	2,16	0,25	Encaixat	NO	REL	0,5	0,6875	0,55	0,5675
106	644,31	88,99	0,25	Encaixat	SI	NO	0,5	0,6875	0,55	0,5675
107	136,5	15,92	0,25	Encaixat	SI	NO	0,5	0,0625	0,85	0,6225
108	56,83	4,68	0,25	Encaixat	NO	NO	0,5	0,6875	0,85	0,7475
109	85,12	33,56	0,5	Encaixat	NO	REL	0,5	0,125	0,25	0,275
110	42,06	29,68	0,5	Encaixat	NO	REL	0,5	0,75	0,25	0,4
111	99,39	7,38	0,25	Encaixat	SI	NO	1	0,0625	0,4	0,4525
112	181,67	9,18	0,25	Encaixat	SI	NO	1	0,6875	0,4	0,5775
113	73,02	3,86	0,5	Encaixat	NO	NO	1	0,75	0,55	0,68
114	26,24	4,58	0,5	Encaixat	SI	NO	1	0,75	0,7	0,77
115	42,75	2,97	0,75	Encaixat	NO	NO	1	0,8125	0,7	0,7825
116	71,98	4,9	0,75	Encaixat	NO	NO	1	0,8125	0,7	0,7825
117	64,71	24,11	0,5	Encaixat	NO	REL	1	0,75	0,55	0,68
118	455,16	21,73	0,5	Encaixat	NO	REL	1	0,8125	0,55	0,6925
119	54,73	10,37	0,5	Ventall	NO	NO	1	0,6875	0,4	0,5775
120	15,52	2,15	0,75	Ventall	NO	REL	1	0,625	0,7	0,745
121	60,25	6,28	0,25	Encaixat	SI	NO	1	0,125	0,25	0,375
122	28,7	3,11	0,75	Encaixat	SI	ABS	1	0,8125	0,7	0,7825
123	160,21	12,8	0,5	Encaixat	NO	ABS	0,5	0,875	0,55	0,605
124	109,72	5,88	0,75	Encaixat	SI	ABS	0,5	0,8125	0,7	0,6825
125	104,03	5,09	0,5	Encaixat	NO	REL	0,5	0,6875	0,55	0,5675
126	77,43	13,76	0,25	Encaixat	SI	REL	0,5	0,1875	0,7	0,5575

127	33,21	12,63	0,5	Ventall	NO	REL	0,5	0,875	0,55	0,605
128	102,74	12,66	0,25	Encaixat	SI	REL	0,5	0,875	0,4	0,515
129	38,24	6,65	0,75	Encaixat	SI	REL	0,5	0,8125	0,85	0,7725
130	209,77	23,14	0,5	Encaixat	NO	REL	0,5	0,75	0,4	0,49
131	35,61	7,78	0,5	Ventall	NO	REL	0,5	0,75	0,55	0,58
132	92,17	13,3	0,5	Ventall	NO	REL	0,5	0,75	0,55	0,58
133	4,56	4,56	0	Encaixat	SI	NO	0,5	0,0625	0,1	0,1725
134	361,51	30,08	0,5	Encaixat	SI	ABS	1	0,6875	0,25	0,4875
135	140,3	1,28	0,5	Encaixat	SI	NO	1	0,6875	0,55	0,6675
136	68,83	11,68	0,5	Encaixat	SI	REL	0,5	0,125	0,4	0,365
137	105,62	23,86	0,25	Encaixat	SI	REL	0,5	0,75	0,4	0,49

Taula i. Característiques dels elements dislocats per l'activitat de la falla d'Alhama de Murcia. Llegendat:

Carena, l'element dislocat és una carena; Encaixat, el riu està encaixat en el basament; Ventall, el canal dislocat està sobre la superfície d'un ventall al·luvial; REL, l'edat coneguda per a aquell element és relativa; ABS, l'edat de l'element és coneguda numèricament.

**Annex 6. Codi per a calcular la
dislocació de paleocanals rectilinis
identificats en trinxeres
paleosísmiques**


```

clear all
close all

%% 1 ____ PIERCING POINT CALCULATION
% IMPORT dataset

Channelfeature = importdata('Emargin_blockSE.txt');
x = Channelfeature(:,1);
y = Channelfeature(:,2);
z = Channelfeature(:,3);
dx = Channelfeature(:,4);
dy = Channelfeature(:,5);
dz = Channelfeature(:,6);

% 3D straight line adjustment

[n,mx] = size(x); [ny,my] = size(y); [nz,mz] = size(z);
m = [mean(x),mean(y),mean(z)];
w = [x-m(1),y-m(2),z-m(3)]; % Use "mean" point as base
a = (1/n)*w'*w; % 'a' is a positive definite matrix
[u,d,v] = svd(a); % 'eig' & 'svd' get same eigenvalues for this matrix
p = u(:,1)'; % Get eigenvector for largest eigenvalue
s = d(2,2)+d(3,3); % Sum the other two eigenvalues

% Import fault

Faultplane = importdata('FaultPlane.txt');
A = Faultplane (1,1);
B = Faultplane (1,2);
C = Faultplane (1,3);
D = Faultplane (1,4);
k = (D-A*m(1,1)-B*m(1,2)-C*m(1,3))/(A*p(1,1)+B*p(1,2)+C*p(1,3));

% Piercing point

for i=1:3

PiercingPoint(1,i) = m(1,i)+k*p(1,i);

end

%% 2 ____ UNCERTAINTIES CALCULATION
% Create random points (x, y and z with a Gaussian distribution)
within the reference points uncertainty acquisition

nx=length(x);
rnd_values_x = randn(500,nx);
for i=1:500
    for j=1:nx
        values_x(j,i) = 0.35*rnd_values_x(i,j)*dx(j)+x(j);
    end
end

rnd_values_y = randn(500,nx);
for i=1:500
    for j=1:nx
        values_y(j,i) = 0.35*rnd_values_y(i,j)*dy(j)+y(j);
    end
end
end

```



```

rnd_values_z = randn(500,nx);
for i=1:500
    for j=1:nx
        values_z(j,i) = 0.35*rnd_values_z(i,j)*dz(j)+z(j);
    end
end

% Adjust 3D random piercing line

[n,mx] = size(values_x); [ny,my] = size(values_y); [nz,mz] =
size(values_z);
for l=1:mx
    m((l+1),:) =
[mean(values_x(:,l)),mean(values_y(:,l)),mean(values_z(:,l))];
    for s=1:nx
        w(s,1)= values_x(s,l)-m((l+1),1);
        w(s,2)= values_y(s,l)-m((l+1),2);
        w(s,3)= values_z(s,l)-m((l+1),3);
    %    w = [(values_x)-m((l+1),1);(values_y)-m((l+1),2);(values_z)-
m((l+1),3)]; % Use "mean" point as base
    end
    a = (1/n)*w'*w; % 'a' is a positive definite matrix
    [u,d,v] = svd(a); % 'eig' & 'svd' get same eigenvalues for this
matrix
    p((l+1),:) = u(:,1)'; % Get eigenvector for largest eigenvalue
    s((l+1),:) = d(2,2)+d(3,3); % Sum the other two eigenvalues

end

% Calculate random piercing point

for g=2:(mx+1)
    k = (D-A*m(g,1)-B*m(g,2)-C*m(g,3))/(A*p(g,1)+B*p(g,2)+C*p(g,3));
    PiercingPoint(g,:) = m(g,:)+k*p(g,:);
end

%% 3 ____ PIERCING POINT AND UNCERTAINTIES
% FINAL RESULTS
% The significant results are the piercing points and their
uncertainties

PiercingPointx = PiercingPoint(:,1);
PiercingPointy = PiercingPoint(:,2);
PiercingPointz = PiercingPoint(:,3);
Uncertainty_x = std (PiercingPointx);
Uncertainty_y = std (PiercingPointy);
Uncertainty_z = std (PiercingPointz);

Point_Error(1,:) =
[PiercingPoint(1,:),Uncertainty_x,Uncertainty_y,Uncertainty_z];

% Save
save('Emargin_blockSE_PP.txt','Point_Error','-ascii','-tabs');

%% 4 ____ INDIVIDUAL CHANNEL FEATURES (MARGINS OR THALWEG) OFFSET
MEASUREMENT
% To measure the distance between piercing point pairs, the three
previous

```

```

% steps should be done for the two segments of the channel

% IMPORT dataset
NWSegment = importdata('Emargin_blockNW_PP.txt');
SESegment = importdata('Emargin_blockSE_PP.txt');

% Offset measurement
Offset = sqrt ((SESegment(1,1)-NWSegment(1,1))^2+(SESegment(1,2)-
NWSegment(1,2))^2+(SESegment(1,3)-NWSegment(1,3))^2);
LateralOffset = sqrt ((SESegment(1,1)-
NWSegment(1,1))^2+(SESegment(1,2)-NWSegment(1,2))^2);
VerticalOffset = SESegment(1,3)-NWSegment(1,3); %Negative values
indicate that NW block is uplifted
Uncertainty_Offset = sqrt ((SESegment(1,4)-
NWSegment(1,4))^2+(SESegment(1,5)-NWSegment(1,5))^2+(SESegment(1,6)-
NWSegment(1,6))^2);
Uncertainty_LateralOffset = sqrt ((SESegment(1,4)-
NWSegment(1,4))^2+(SESegment(1,5)-NWSegment(1,5))^2);
Uncertainty_VerticalOffset = SESegment(1,6)-NWSegment(1,6);

% Save
ChannelOffset=[Offset, LateralOffset, VerticalOffset,
Uncertainty_Offset,
Uncertainty_LateralOffset,Uncertainty_VerticalOffset];
save('Emargin.txt','ChannelOffset','-ascii','-tabs');

%% 5 ____ CHANNEL OFFSET MEAN AND UNCERTAINTY
% To calculate the mean and the uncertainty of the three channel
features considered (two margins and the thalweg), we apply the Zechar
and frankel (2009) displacement functions

```


Annex 7. Calibratge de les datacions realitzades amb radiocarboni

Programa: Calib7.0

Corba: IntCal13

Especificacions: IntCal13 calibration is limited to 0-46,400 14C years BP. This data set is recommended for most non-marine samples. From 0-12.5ka cal BP it is based on tree-ring 14C measurements. Beyond 12.5ka it is based on marine coral and varve data. Details of the data set construction are given in Radiocarbon vol.55, 2013, pp xxxx-yyyyy

Bibliografia:

Reimer PJ, Bard E, Bayliss A, Beck JW, Blackwell PG, Bronk Ramsey C, Buck CE, Cheng H, Edwards RL, Friedrich M, Grootes PM, Guilderson TP, Hafflidason H, Hajdas I, HattÃ© C, Heaton TJ, Hogg AG, Hughen KA, Kaiser KF, Kromer B, Manning SW, Niu M, Reimer RW, Richards DA, Scott EM, Southon JR, Turney CSM, van der Plicht J. IntCal13 and MARINE13 radiocarbon age calibration curves 0-50000 years calBP Radiocarbon 55(4). DOI: 10.2458/azu_js_rc.55.16947. 2013

Alan G Hogg, Quan Hua, Paul G Blackwell, Caitlin E Buck, Thomas P Guilderson, Timothy J Heaton, Mu Niu, Jonathan G Palmer, Paula J Reimer, Ron W Reimer, Christian S M Turney, Susan R H Zimmerman. Radiocarbon 55(4). DOI: 10.2458/azu_js_rc.55.16783. 2013

Comentaris:

* This standard deviation (error) includes a lab error multiplier.

** 1 sigma = square root of (sample std. dev.^2 + curve std. dev.^2)

** 2 sigma = 2 x square root of (sample std. dev.^2 + curve std. dev.^2) where ^2 = quantity squared.

[] = calibrated range impinges on end of calibration data set

0* = cannot calibrate due to nuclear testing C-14.

1955* or 1960* denote influence of nuclear testing C-14

NOTE: Cal ages and ranges are rounded to the nearest year which may be too precise in many instances. Users are advised to results to the nearest 10 yr for samples with standard deviation in the radiocarbon age greater than 50 yr.

RADIOCARBON CALIBRATION PROGRAM*

CALIB REV7.0.1

Copyright 1986-2014 M Stuiver and PJ Reimer

*To be used in conjunction with:

Stuiver, M., and Reimer, P.J., 1993, Radiocarbon, 35, 215-

230.

Annotated results (text) - -

Export file - cl4res.csv

SAL-1
 Lab Code
 Cargol-Carbó. 14C
 Radiocarbon Age BP 3335 +/- 35
 Calibration data set: intcal13.14c # Reimer et al.
 2013
 % area enclosed cal AD age ranges relative area
 under
 probability
 distribution
 68.3 (1 sigma) cal BC 1682- 1674 0.059
 1666- 1606 0.673
 1583- 1558 0.210
 1553- 1546 0.058
 95.4 (2 sigma) cal BC 1733- 1718 0.025
 1693- 1526 0.975

SAL-2
 Lab Code
 Carbó. 14C
 Radiocarbon Age BP 21210 +/- 140
 Calibration data set: intcal13.14c # Reimer et al.
 2013
 % area enclosed cal AD age ranges relative area
 under
 probability
 distribution
 68.3 (1 sigma) cal BC 23769- 23452 1.000
 95.4 (2 sigma) cal BC 23883- 23279 1.000

SAL-3
 Lab Code
 Cargol-Carbó. 14C
 Radiocarbon Age BP 1410 +/- 30
 Calibration data set: intcal13.14c # Reimer et al.
 2013
 % area enclosed cal AD age ranges relative area
 under
 probability
 distribution
 68.3 (1 sigma) cal AD 618- 654 1.000
 95.4 (2 sigma) cal AD 591- 665 1.000

SAL-5
 Lab Code
 Cargol-Carbó. 14C
 Radiocarbon Age BP 525 +/- 35

Calibration data set: intcal13.14c # Reimer et al.
 2013
 % area enclosed cal AD age ranges relative area
 under
 probability
 distribution
 68.3 (1 sigma) cal AD 1334- 1336 0.027
 1398- 1436 0.973
 95.4 (2 sigma) cal AD 1318- 1352 0.207
 1390- 1443 0.793

SAL-6
 Lab Code
 Cargol-Carbó. 14C
 Radiocarbon Age BP 415 +/- 35
 Calibration data set: intcal13.14c # Reimer et al.
 2013
 % area enclosed cal AD age ranges relative area
 under
 probability
 distribution
 68.3 (1 sigma) cal AD 1437- 1488 0.947
 1604- 1608 0.053
 95.4 (2 sigma) cal AD 1426- 1521 0.850
 1575- 1585 0.014
 1590- 1624 0.137

SAL-16
 Lab Code
 Carbó. 14C
 Radiocarbon Age BP 1985 +/- 30
 Calibration data set: shcal13.14c # Hogg et al. 2013
 % area enclosed cal AD age ranges relative area
 under
 probability
 distribution
 68.3 (1 sigma) cal AD 23- 83 0.827
 96- 112 0.173
 95.4 (2 sigma) cal BC 47- 3 0.139
 cal AD 13- 123 0.861

SAL-20
 Lab Code
 Sample Description
 Radiocarbon Age BP 18210 +/- 45
 Calibration data set: intcal13.14c # Reimer et al.
 2013
 % area enclosed cal BP age ranges relative area
 under
 probability
 distribution
 68.3 (1 sigma) cal BP 21952 - 22176 1.000
 95.4 (2 sigma) cal BP 21870 - 22266 1.000
 Median Probability: 22071

Annex 8. Plantilla utilitzada per a realitzar les descripcions edàfiques

Información general del sitio, registro y ubicación:

- Número de perfil
- Fecha de la descripción
- Autores
- Ubicación
- Elevación

Factores de formación del suelo

- Condiciones atmosfericas del clima y tiempo
- Regimenes climáticos del suelo
- Geoforma y topografía (relieve)
 - Geoforma principal
 - Posición
 - Forma de la pendiente
 - Gradiente y orientación de la pendiente

Uso de la tierra y vegetación

- Uso de la tierra
- Cultivos
- Influencia humana
- Vegetación

- Material parental
- Edad de la superficie de la tierra

CUADRO 2

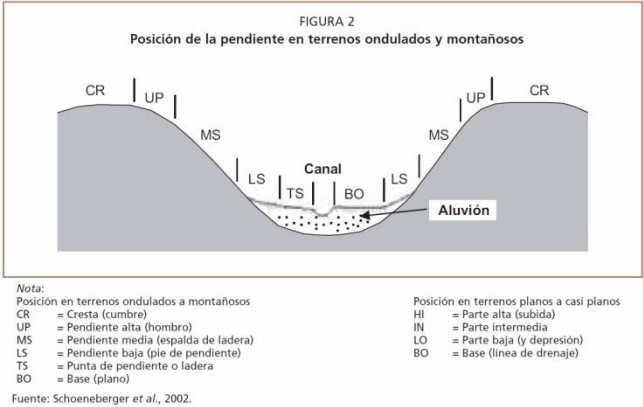
Códigos de las condiciones climáticas

Condiciones climáticas actuales (Schoeneberger et al., 2002)	
SU	Soleado / despejado
PC	Parcialmente nublado
OV	Nublado
RA	Lluvioso
SL	Granizo
SN	Nieve

Condiciones climáticas pasadas (Ad-hoc-AG-boden, 2005)

WC 1	Sin lluvia en el último mes
WC 2	Sin lluvia en la última semana
WC 3	Sin lluvia en las últimas 24 horas
WC 4	Lluvia ligera en las últimas 24 horas
WC 5	Lluvia torrencial por algunos días o tormenta en las últimas 24 horas
WC 6	Periodo extremadamente lluvioso o de deshielo

Nota: Por ejemplo: SU, 25°C; WC2 (=soleado, temperatura de 25°C; sin lluvia en la última semana).

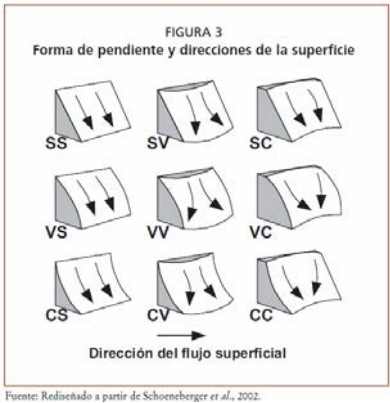


CUADRO 7

Clases de gradiente de la pendiente

Clase	Descripción	%
01	Plano	0-0,2
02	Nivel	0,2-0,5
03	Cercano al nivel	0,5-1,0
04	Muy ligeramente inclinado	1,0-2,0
05	Ligeramente inclinado	2-5
06	Inclinado	5-10
07	Fuertemente inclinado	10-15
08	Moderadamente escarpado	15-30
09	Escarpado	30-60
10	Muy escarpado	> 60

U	Rocas sedimentarias (no consolidadas)	UR	residuo intemperizado	UR1	bauxita, laterita
		UF	fluvial	UF1	arena y grava
				UF2	Limo, arcilla, franco
		UL	lacustrino	UL1	arena
				UL2	limo y arcilla
		UM	marino, estuarina	UM1	arena
				UM2	arcilla y limo
		UC	coluvial	UC1	depósitos de pendiente
				UC2	lahar
		UE	edólico	UE1	loes
				UE2	arena
		UG	glacial	UG1	morrena
				UG2	arena fluvio-glacial
				UG3	grava fluvio-glacial
		UK	* Criogénico	UK1	roca peri glacial derrumbe
				UK2	capa peri glacial de solifluxión



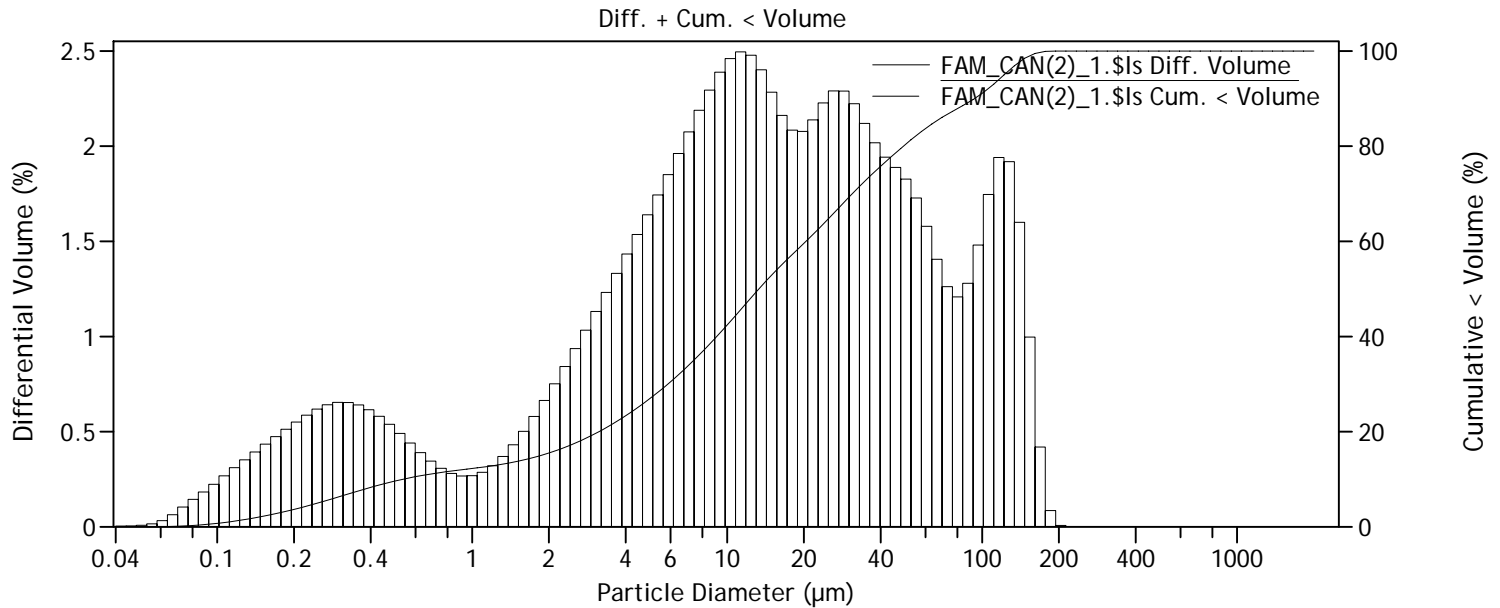
Número	Horitzó	Profund.	Límit		Color		Textura		Estructura			Consistència				Clav films	Estadis	carbonat
			Distinció	Topografia	Sec	Mullat	Fragments rocosos (Mida/Forma/Naturalesa/abundància)	Fracció fina	Grau	Tipus	Mida	Sec	Mullat	Adhesivitat	Plasticitat			
1			A C G D	S W I B					WE MO ST	RS SG MA PM BL PR WE CO GR WC PL CL LU	FF VM FM FC MC MV VC	LO SO SHA HA VHA EHA	LO VFR FR FI VFI EFI	NST SST ST VST	NPL SPL PL VPL		I II III IV	
2			A C G D	S W I B					WE MO ST	RS SG MA PM BL PR WE CO GR WC PL CL LU	FF VM FM FC MC MV VC	LO SO SHA HA VHA EHA	LO VFR FR FI VFI EFI	NST SST ST VST	NPL SPL PL VPL		I II III IV	
3			A C G D	S W I B					WE MO ST	RS SG MA PM BL PR WE CO GR WC PL CL LU	FF VM FM FC MC MV VC	LO SO SHA HA VHA EHA	LO VFR FR FI VFI EFI	NST SST ST VST	NPL SPL PL VPL		I II III IV	
4			A C G D	S W I B					WE MO ST	RS SG MA PM BL PR WE CO GR WC PL CL LU	FF VM FM FC MC MV VC	LO SO SHA HA VHA EHA	LO VFR FR FI VFI EFI	NST SST ST VST	NPL SPL PL VPL		I II III IV	
5			A C G D	S W I B					WE MO ST	RS SG MA PM BL PR WE CO GR WC PL CL LU	FF VM FM FC MC MV VC	LO SO SHA HA VHA EHA	LO VFR FR FI VFI EFI	NST SST ST VST	NPL SPL PL VPL		I II III IV	
6			A C G D	S W I B					WE MO ST	RS SG MA PM BL PR WE CO GR WC PL CL LU	FF VM FM FC MC MV VC	LO SO SHA HA VHA EHA	LO VFR FR FI VFI EFI	NST SST ST VST	NPL SPL PL VPL		I II III IV	
7			A C G D	S W I B					WE MO ST	RS SG MA PM BL PR WE CO GR WC PL CL LU	FF VM FM FC MC MV VC	LO SO SHA HA VHA EHA	LO VFR FR FI VFI EFI	NST SST ST VST	NPL SPL PL VPL		I II III IV	
8			A C G D	S W I B					WE MO ST	RS SG MA PM BL PR WE CO GR WC PL CL LU	FF VM FM FC MC MV VC	LO SO SHA HA VHA EHA	LO VFR FR FI VFI EFI	NST SST ST VST	NPL SPL PL VPL		I II III IV	

Figura ii. Plantilla per a la descripció dels sòls creada a partir de la guia de la FAO (2009). Distinció: A, abrupte; C, clar; G, gradual; D, difús. Topografia: S, suau; W, ondulat; I, irregular; B, fracturat. Grau: WE, dèbil; MO, moderat; ST, fort. Tipus: RS, estructura rociosa; SG, gra simple; MA, massiva; PM, massiva porosa; BL, bloc; PR, prismàtica; WE, forma de cunya; CO, columnar; GR, granular; WC, motlles de cucs; PL, laminar; CL, a terrossos; LU, grumolls. Mida: FF, molt fina a fina; VM, de molt fina a mitjana; FM, de fina a mitjana; FC, de fina a grollera; MC, mitjana a grollera, MV, de mitjana a molt grollera; VC, de grollera a molt grollera. Consistència: LO, solta; SO, suau; SHA, lleugerament dura; HA, dura; VHA, molt dura; EVA, extremadament dura; VRF, molt friable; FR, friable; FI, ferma; VFI, molt ferma; EFI, extremadament ferma. Adhesivitat: NST, no adherent; SST, lleugerament adherent; ST, adherent; VST, molt adherent. Plasticitat: NPL, no plàstica; SPL, lleugerament plàstica; PL, plàstica; VPL, molt plàstica.

Annex 9. Resultats de l'anàlisi dels sòls en el laboratori

- 9.1. Granulometria amb l'analitzador de partícules Coulter LS 230
- 9.2. Quantitat de carbonat de calci per calcimetria
- 9.3. Quantitat de carboni orgànic (matèria orgànica) i de carbonat de calci per ignició

File name: C:\GRANULOMETRIES COULTER\Marta Ferrater\FAM_CAN(2)_1.\$ls
 FAM_CAN(2)_1.\$ls
 File ID: FAM_CAN(2)_1
 Sample ID: FAM_CAN(2)_1
 Comment 1: Trinxera del Saltador
 Comment 2: Perfil de sols bloc enfonsat columna 5
 Optical model: Mediterraneo.rf780d PIDS included
 Start time: 11:33 8 Jul 2015



Volume Statistics (Arithmetic)

FAM_CAN(2)_1.\$ls

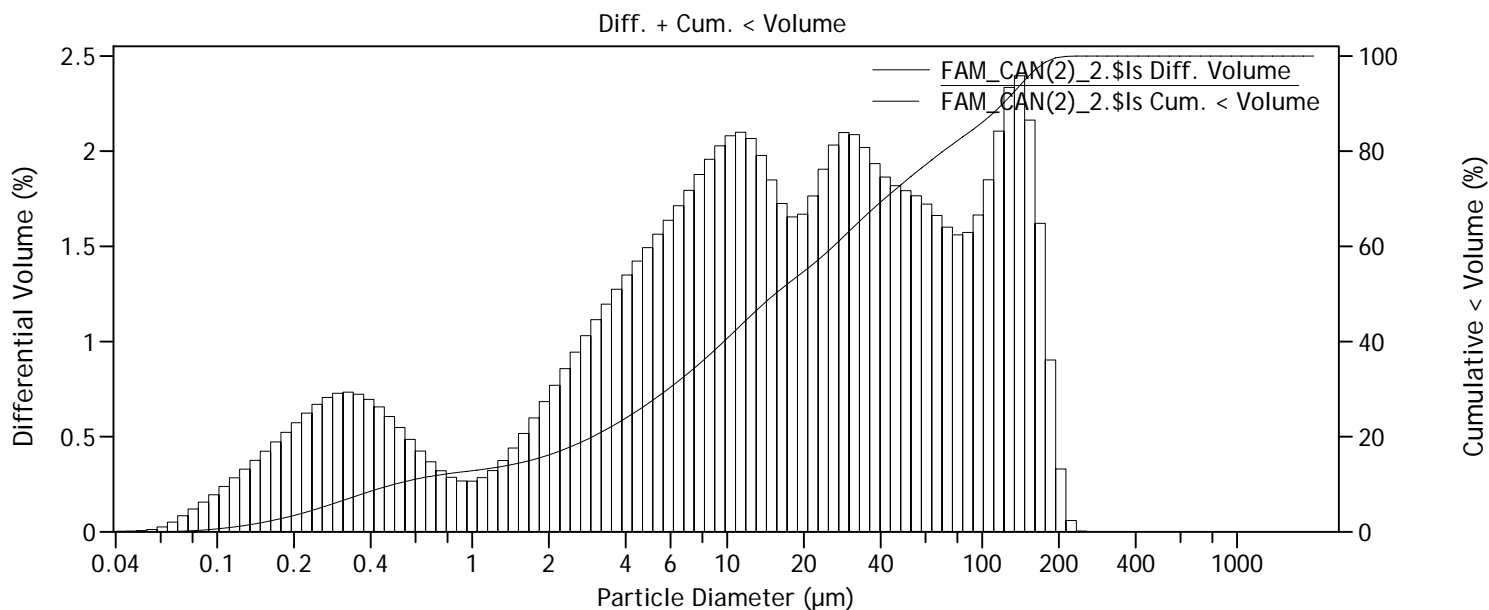
Calculations from 0.040 µm to 2000 µm

Volume:	100%	S.D.:	37.99 µm
Mean:	29.77 µm	Variance:	1444 µm ²
Median:	13.32 µm	C.V.:	128%
Mean/Median ratio:	2.234	Skewness:	1.759 Right skewed
Mode:	11.29 µm	Kurtosis:	2.347 Leptokurtic

d₁₀: 0.534 µm d₅₀: 13.32 µm d₉₀: 93.29 µm

Particle Diameter µm	FAM_CAN(2) _1.\$ls Volume % <
2	15.5
4	23.3
63	84.5
125	95.5
250	100
500	100
1000	100
2000	100

File name: C:\GRANULOMETRIES COULTER\Marta Ferrater\FAM_CAN(2)_2.\$ls
 FAM_CAN(2)_2.\$ls
 File ID: FAM_CAN(2)_2
 Sample ID: FAM_CAN(2)_2
 Comment 1: Trinxera del Saltador
 Comment 2: Perfil de sols bloc enfonsat columna 5
 Optical model: Mediterraneo.rf780d PIDS included
 Start time: 11:44 8 Jul 2015



Volume Statistics (Arithmetic)

FAM_CAN(2)_2.\$ls

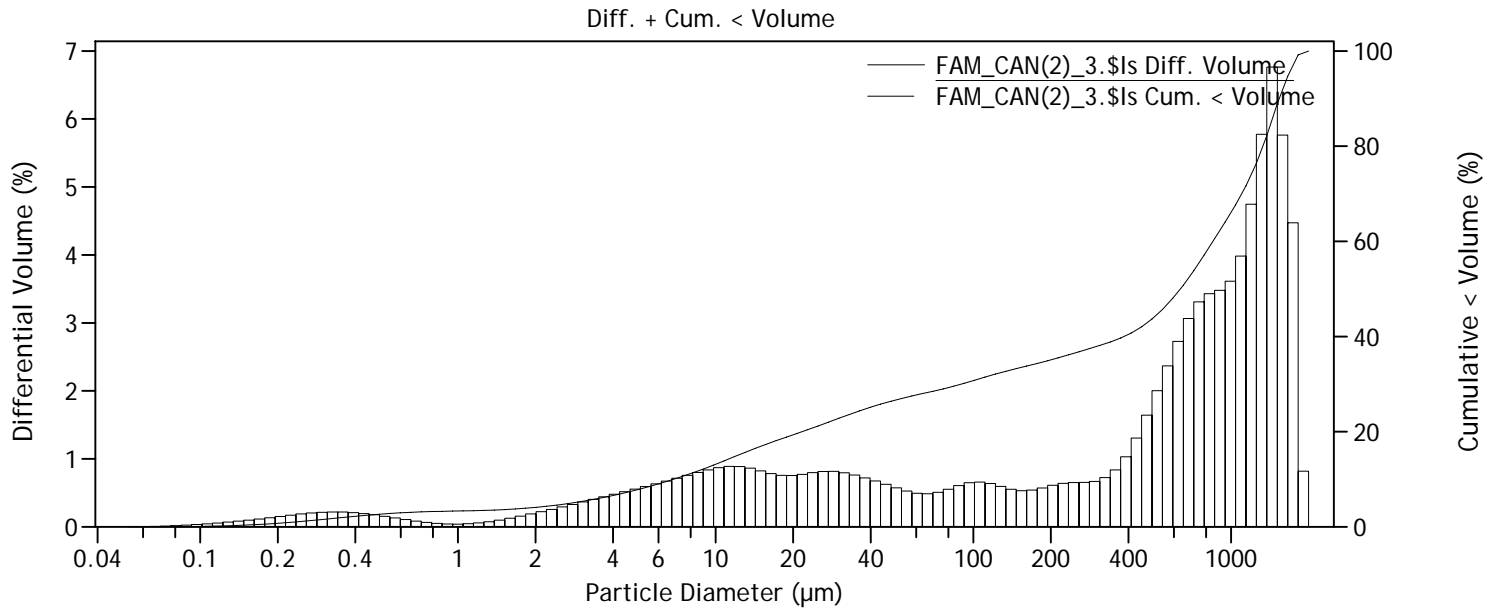
Calculations from 0.040 µm to 2000 µm

Volume:	100%	S.D.:	47.81 µm
Mean:	37.98 µm	Variance:	2286 µm ²
Median:	15.41 µm	C.V.:	126%
Mean/Median ratio:	2.464	Skewness:	1.511 Right skewed
Mode:	140.1 µm	Kurtosis:	1.308 Leptokurtic

d₁₀: 0.494 µm d₅₀: 15.41 µm d₉₀: 120.9 µm

Particle Diameter µm	FAM_CAN(2) _2.\$ls Volume % <
2	16.2
4	23.9
63	78.0
125	90.8
250	99.999
500	100
1000	100
2000	100

File name: C:\GRANULOMETRIES COULTER\Marta Ferrater\FAM_CAN(2)_3.\$ls
 FAM_CAN(2)_3.\$ls
 File ID: FAM_CAN(2)_3
 Sample ID: FAM_CAN(2)_3
 Comment 1: Trinxera del Saltador
 Comment 2: Perfil de sols bloc enfonsat columna 5
 Optical model: Mediterraneo.rf780d PIDS included
 Start time: 11:53 8 Jul 2015



Volume Statistics (Arithmetic)

FAM_CAN(2)_3.\$ls

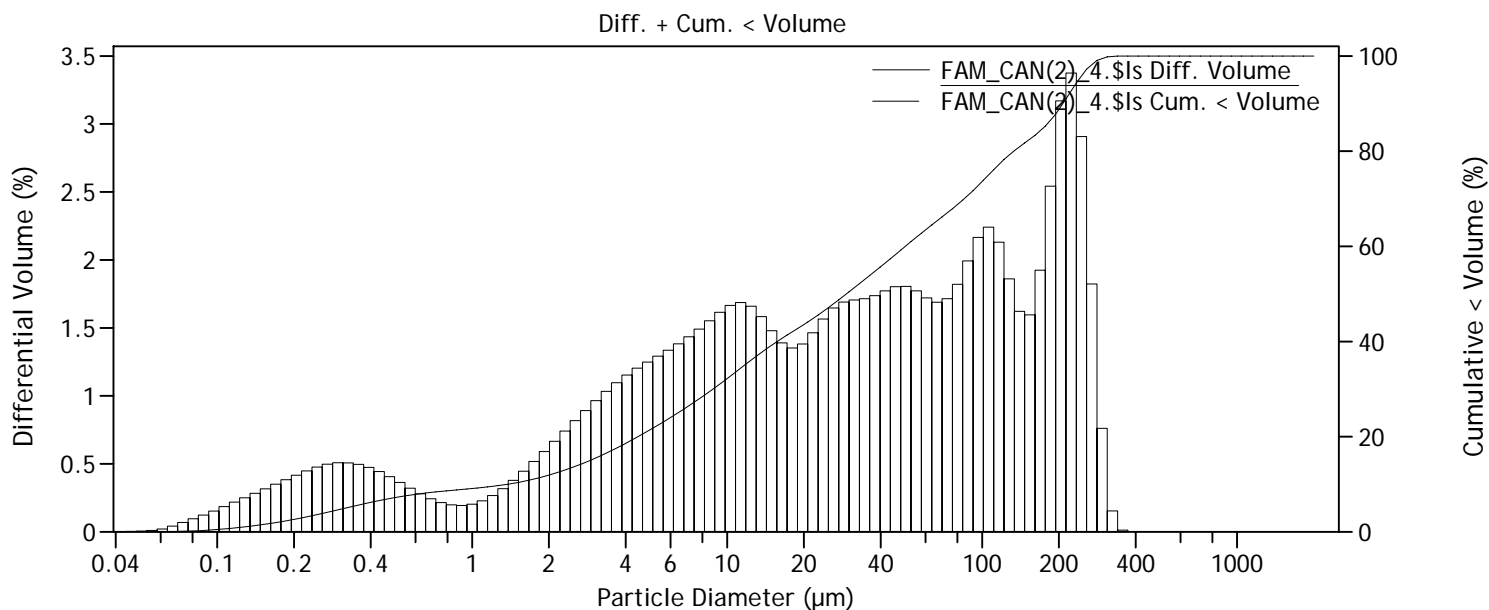
Calculations from 0.040 µm to 2000 µm

Volume:	100%	S.D.:	595.3 µm
Mean:	684.1 µm	Variance:	354.4e3 µm ²
Median:	636.4 µm	C.V.:	87.0%
Mean/Median ratio:	1.075	Skewness:	0.302 Right skewed
Mode:	1443 µm	Kurtosis:	-1.306 Platykurtic

d₁₀: 6.867 µm d₅₀: 636.4 µm d₉₀: 1539 µm

Particle Diameter µm	FAM_CAN(2) _3.\$ls Volume % <
2	4.10
4	6.60
63	28.0
125	32.3
250	36.6
500	43.9
1000	66.1
2000	100

File name: C:\GRANULOMETRIES COULTER\Marta Ferrater\FAM_CAN(2)_4.\$ls
 FAM_CAN(2)_4.\$ls
 File ID: FAM_CAN(2)_4
 Sample ID: FAM_CAN(2)_4
 Comment 1: Trinxera del Saltador
 Comment 2: Perfil de sols bloc enfonsat columna 5
 Optical model: Mediterraneo.rf780d PIDS included
 Start time: 12:00 8 Jul 2015



Volume Statistics (Arithmetic)

FAM_CAN(2)_4.\$ls

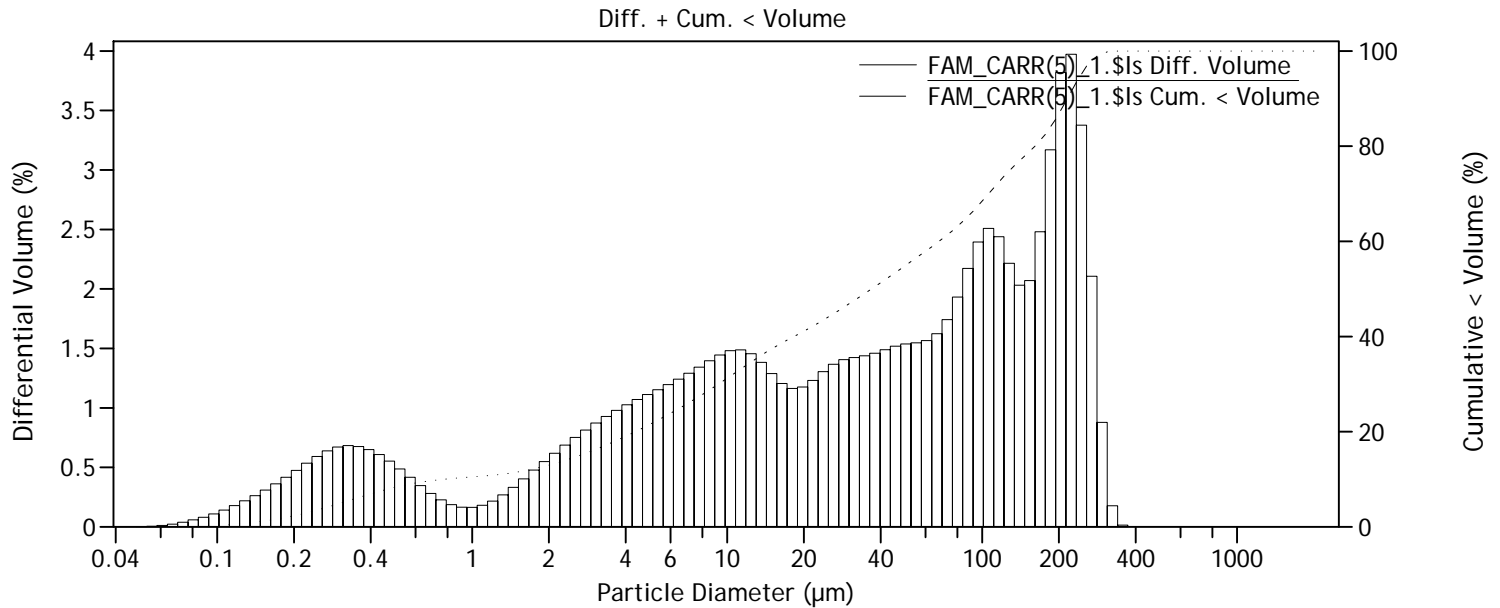
Calculations from 0.040 µm to 2000 µm

Volume:	100%	S.D.:	79.75 µm
Mean:	67.21 µm	Variance:	6361 µm ²
Median:	29.34 µm	C.V.:	119%
Mean/Median ratio:	2.291	Skewness:	1.228 Right skewed
Mode:	223.4 µm	Kurtosis:	0.318 Leptokurtic

d₁₀: 1.373 µm d₅₀: 29.34 µm d₉₀: 207.4 µm

Particle Diameter µm	FAM_CAN(2) _4.\$ls Volume % <
2	11.9
4	18.6
63	64.4
125	78.7
250	96.4
500	100
1000	100
2000	100

File name: C:\GRANULOMETRIES COULTER\Marta Ferrater\FAM_CARR(5)_1.\$ls
 FAM_CARR(5)_1.\$ls
 File ID: FAM_CARR(5)_1
 Sample ID: FAM_CARR(5)_1
 Comment 1: Trinxera de carrascoy
 Comment 2: Perfil de sols bloc enfonsat (NW)
 Optical model: Mediterraneo.rf780d PIDS included
 Start time: 12:45 8 Jul 2015



Volume Statistics (Arithmetic)

FAM_CARR(5)_1.\$ls

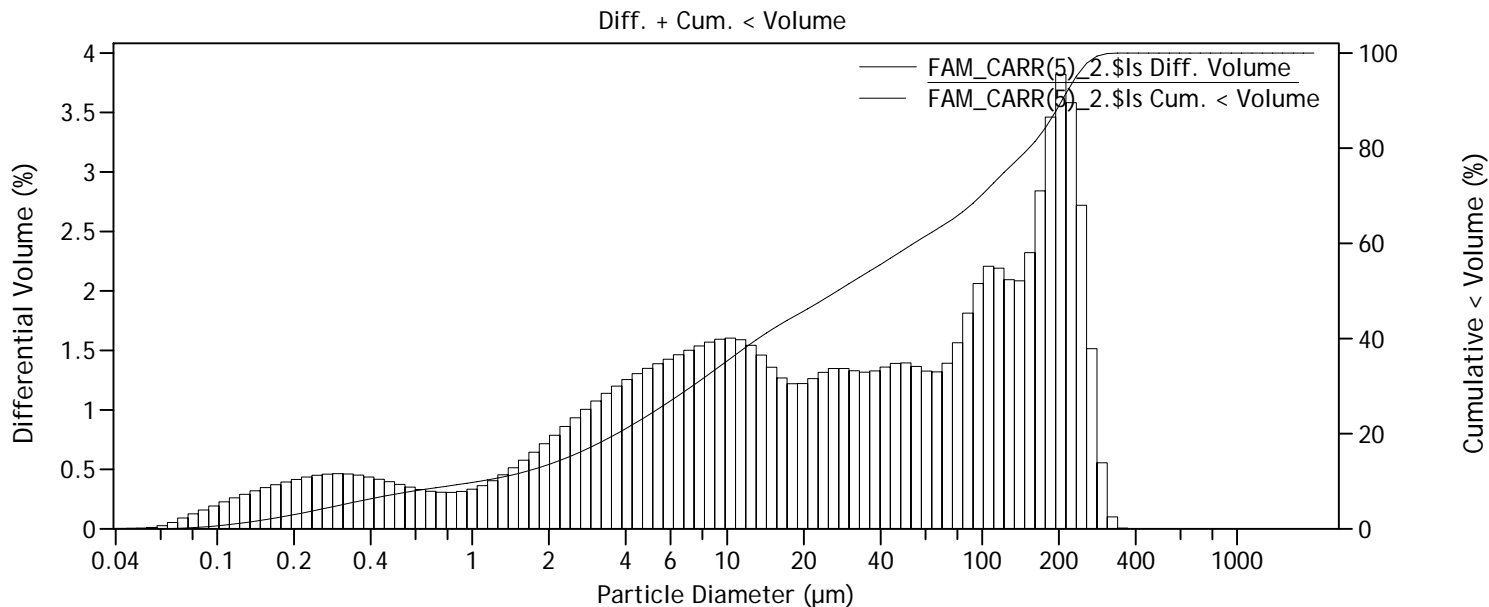
Calculations from 0.040 µm to 2000 µm

Volume:	100%	S.D.:	83.81 µm
Mean:	75.66 µm	Variance:	7024 µm ²
Median:	36.84 µm	C.V.:	111%
Mean/Median ratio:	2.054	Skewness:	0.983 Right skewed
Mode:	223.4 µm	Kurtosis:	-0.299 Platykurtic

d₁₀: 0.772 µm d₅₀: 36.84 µm d₉₀: 216.0 µm

Particle Diameter µm	FAM_CARR(5) _1.\$ls Volume % <
2	13.0
4	19.0
63	58.8
125	74.3
250	95.8
500	100
1000	100
2000	100

File name: C:\GRANULOMETRIES COULTER\Marta Ferrater\FAM_CARR(5)_2.\$ls
 FAM_CARR(5)_2.\$ls
 File ID: FAM_CARR(5)_2
 Sample ID: FAM_CARR(5)_2
 Comment 1: Trinxera de carrascoy
 Comment 2: Perfil de sols bloc enfonsat (NW)
 Optical model: Mediterraneo.rf780d PIDS included
 Start time: 12:52 8 Jul 2015



Volume Statistics (Arithmetic)

FAM_CARR(5)_2.\$ls

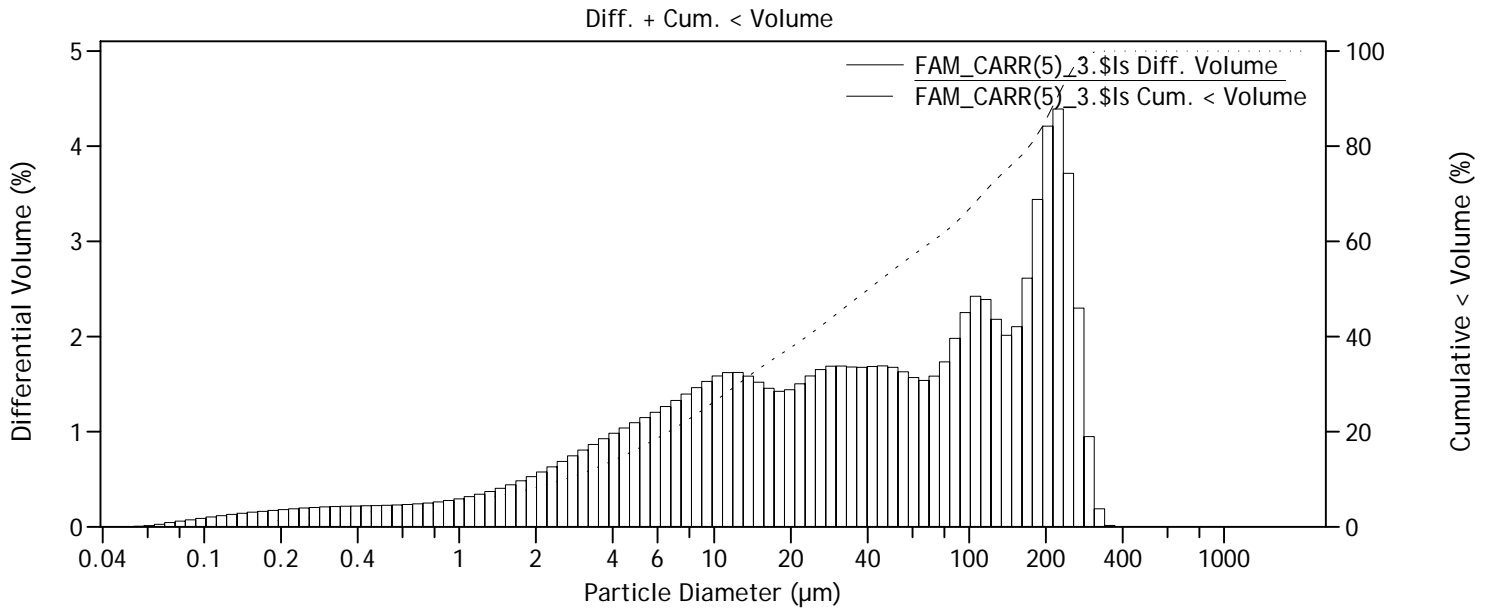
Calculations from 0.040 µm to 2000 µm

Volume:	100%	S.D.:	81.06 µm
Mean:	69.53 µm	Variance:	6570 µm ²
Median:	27.07 µm	C.V.:	117%
Mean/Median ratio:	2.568	Skewness:	1.045 Right skewed
Mode:	203.5 µm	Kurtosis:	-0.202 Platykurtic

d₁₀: 1.070 µm d₅₀: 27.07 µm d₉₀: 205.7 µm

Particle Diameter µm	FAM_CARR(5) _2.\$ls Volume % <
2	13.5
4	21.0
63	62.2
125	75.4
250	97.0
500	100
1000	100
2000	100

File name: C:\GRANULOMETRIES COULTER\Marta Ferrater\FAM_CARR(5)_3.\$Is
 FAM_CARR(5)_3.\$Is
 File ID: FAM_CARR(5)_3
 Sample ID: FAM_CARR(5)_3
 Comment 1: Trinxera de carrascoy
 Comment 2: Perfil de sols bloc enfonsat (NW)
 Optical model: Mediterraneo.rf780d PIDS included
 Start time: 12:59 8 Jul 2015



Volume Statistics (Arithmetic)

FAM_CARR(5)_3.\$Is

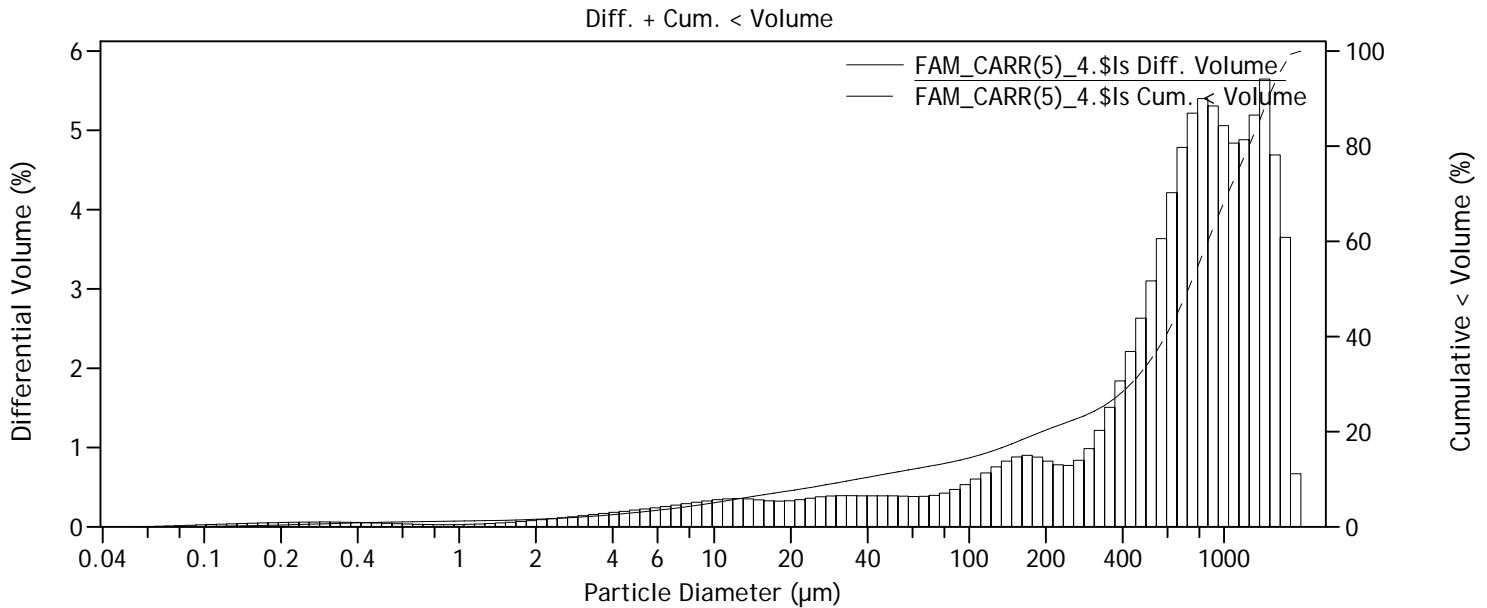
Calculations from 0.040 µm to 2000 µm

Volume:	100%	S.D.:	85.07 µm
Mean:	79.96 µm	Variance:	7236 µm ²
Median:	40.41 µm	C.V.:	106%
Mean/Median ratio:	1.979	Skewness:	0.922 Right skewed
Mode:	223.4 µm	Kurtosis:	-0.467 Platykurtic

d₁₀: 2.592 µm d₅₀: 40.41 µm d₉₀: 220.6 µm

Particle Diameter µm	FAM_CARR(5) _3.\$Is Volume % <
2	8.27
4	13.9
63	57.9
125	72.5
250	95.4
500	100
1000	100
2000	100

File name: C:\GRANULOMETRIES COULTER\Marta Ferrater\FAM_CARR(5)_4.\$ls
 FAM_CARR(5)_4.\$ls
 File ID: FAM_CARR(5)_4
 Sample ID: FAM_CARR(5)_4
 Comment 1: Trinxera de carrascoy
 Comment 2: Perfil de sols bloc enfonsat (NW)
 Optical model: Mediterraneo.rf780d PIDS included
 Start time: 13:05 8 Jul 2015



Volume Statistics (Arithmetic)

FAM_CARR(5)_4.\$ls

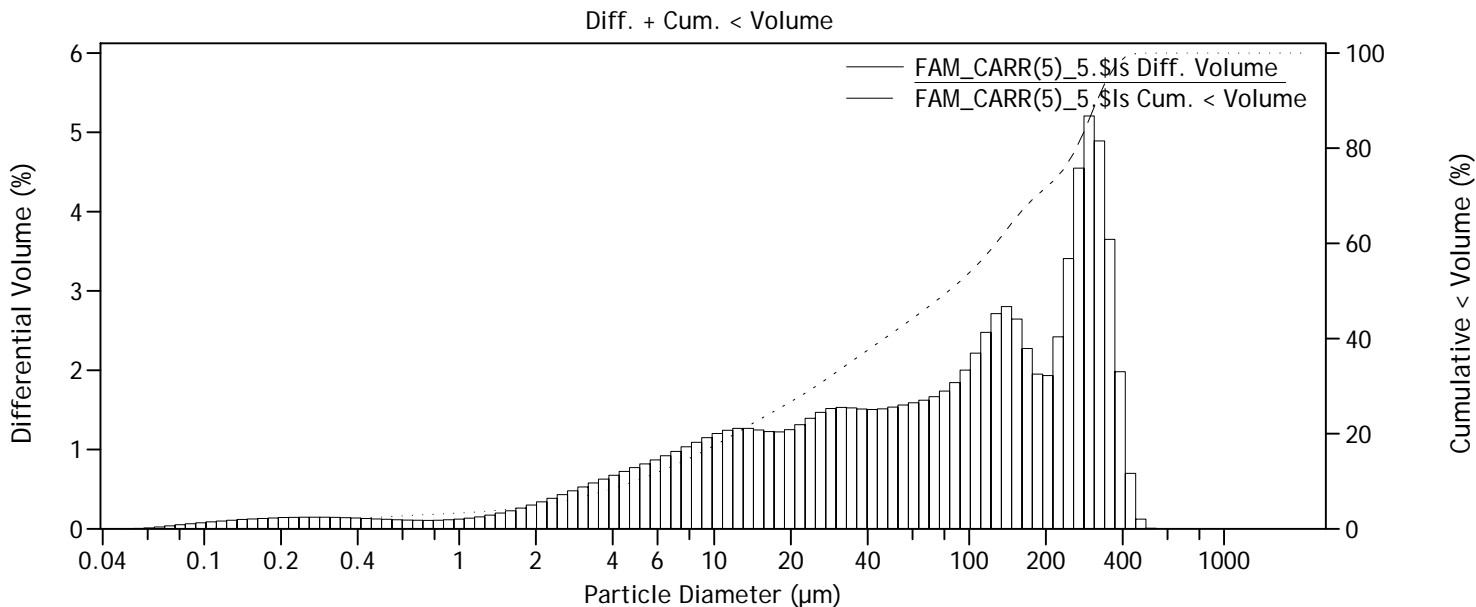
Calculations from 0.040 µm to 2000 µm

Volume:	100%	S.D.:	512.5 µm
Mean:	750.3 µm	Variance:	262.6e3 µm ²
Median:	724.2 µm	C.V.:	68.3%
Mean/Median ratio:	1.036	Skewness:	0.229 Right skewed
Mode:	1443 µm	Kurtosis:	-0.938 Platykurtic

d₁₀: 36.17 µm d₅₀: 724.2 µm d₉₀: 1488 µm

Particle Diameter µm	FAM_CARR(5) _4.\$ls Volume % <
2	1.59
4	2.56
63	12.3
125	16.0
250	22.2
500	34.1
1000	68.2
2000	100

File name: C:\GRANULOMETRIES COULTER\Marta Ferrater\FAM_CARR(5)_5.\$ls
 FAM_CARR(5)_5.\$ls
 File ID: FAM_CARR(5)_5
 Sample ID: FAM_CARR(5)_5
 Comment 1: Trinxera de carrascoy
 Comment 2: Perfil de sols bloc enfonsat (NW)
 Optical model: Mediterraneo.rf780d PIDS included
 Start time: 13:12 8 Jul 2015



Volume Statistics (Arithmetic)

FAM_CARR(5)_5.\$ls

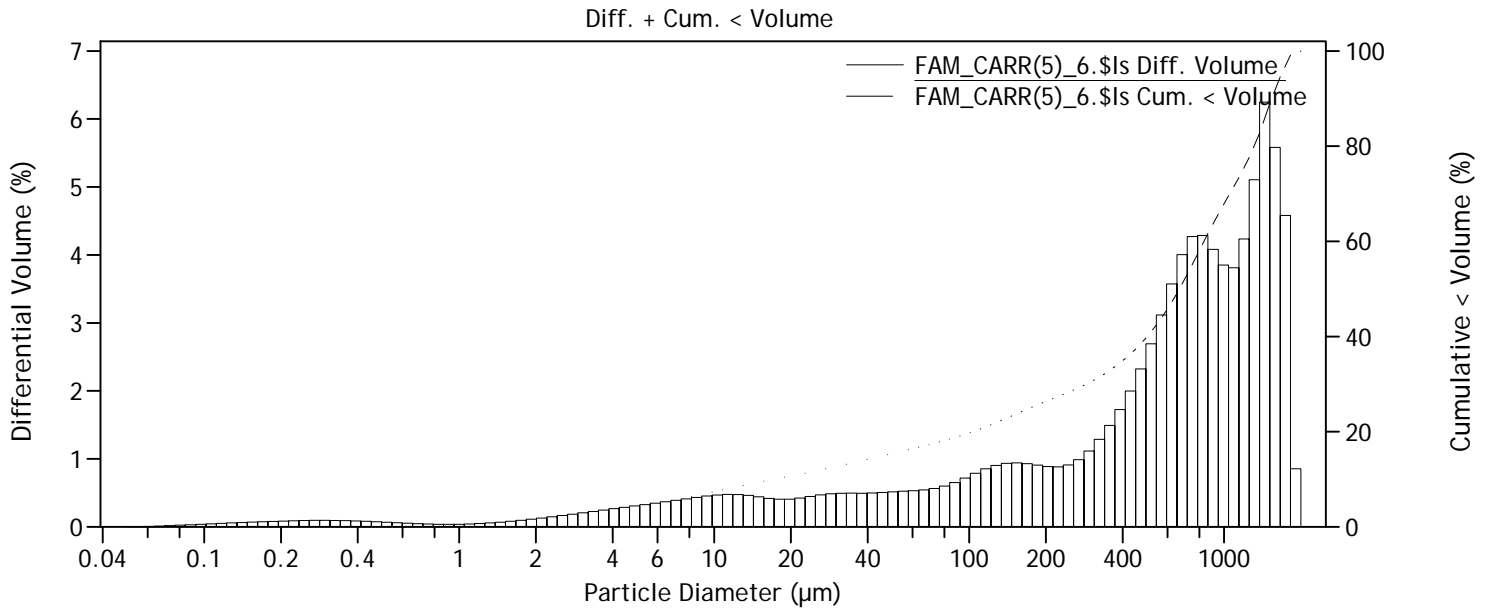
Calculations from 0.040 µm to 2000 µm

Volume:	100%	S.D.:	121.8 µm
Mean:	126.1 µm	Variance:	14840 µm ²
Median:	83.05 µm	C.V.:	96.6%
Mean/Median ratio:	1.518	Skewness:	0.741 Right skewed
Mode:	295.5 µm	Kurtosis:	-0.767 Platykurtic

d₁₀: 4.870 µm d₅₀: 83.05 µm d₉₀: 318.0 µm

Particle Diameter µm	FAM_CARR(5) _5.\$ls Volume % <
2	4.85
4	8.48
63	45.1
125	59.5
250	77.9
500	99.99
1000	100
2000	100

File name: C:\GRANULOMETRIES COULTER\Marta Ferrater\FAM_CARR(5)_6.\$ls
 FAM_CARR(5)_6.\$ls
 File ID: FAM_CARR(5)_6
 Sample ID: FAM_CARR(5)_6
 Comment 1: Trinxera de carrascoy
 Comment 2: Perfil de sols bloc enfonsat (NW)
 Optical model: Mediterraneo.rf780d PIDS included
 Start time: 13:19 8 Jul 2015



Volume Statistics (Arithmetic)

FAM_CARR(5)_6.\$ls

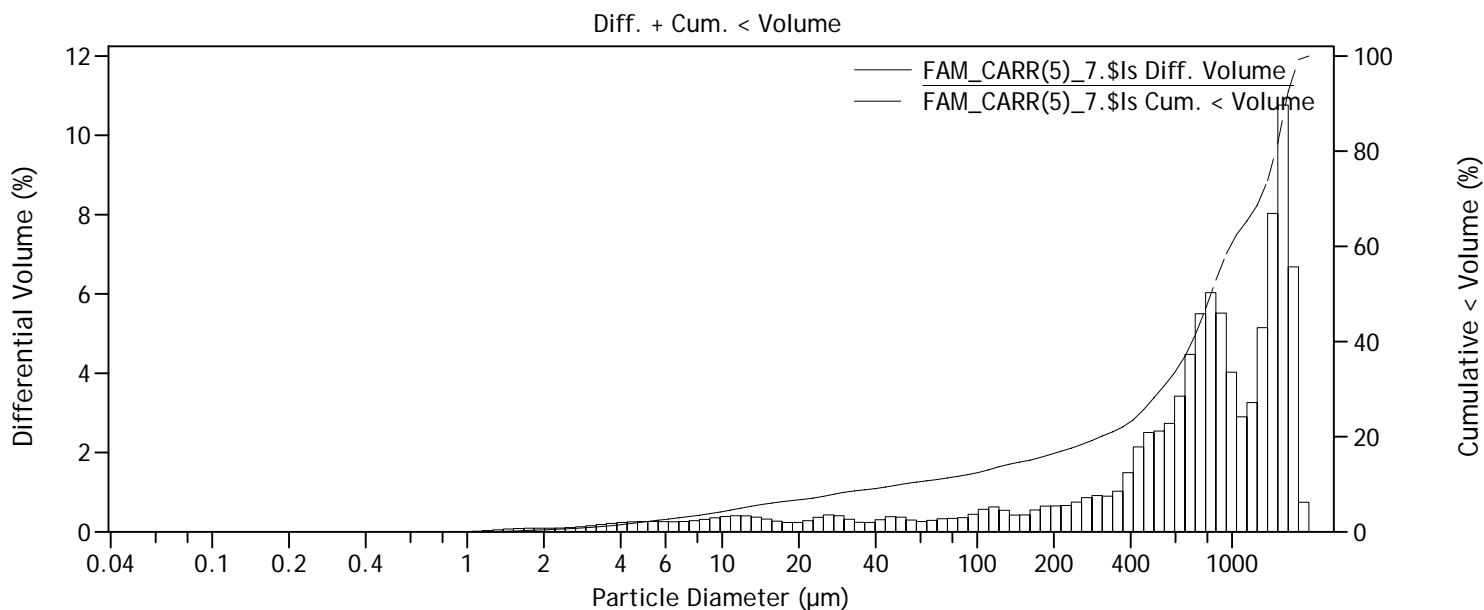
Calculations from 0.040 µm to 2000 µm

Volume:	100%	S.D.:	556.2 µm
Mean:	720.3 µm	Variance:	309.4e3 µm ²
Median:	667.6 µm	C.V.:	77.2%
Mean/Median ratio:	1.079	Skewness:	0.315 Right skewed
Mode:	1443 µm	Kurtosis:	-1.115 Platykurtic

d₁₀: 17.04 µm d₅₀: 667.6 µm d₉₀: 1539 µm

Particle Diameter µm	FAM_CARR(5) _6.\$ls Volume % <
2	2.37
4	3.79
63	16.7
125	21.7
250	28.5
500	40.1
1000	67.9
2000	100

File name: C:\GRANULOMETRIES COULTER\Marta Ferrater\FAM_CARR(5)_7.\$ls
 FAM_CARR(5)_7.\$ls
 File ID: FAM_CARR(5)_7
 Sample ID: FAM_CARR(5)_7
 Comment 1: Trinxera de carrascoy
 Comment 2: Perfil de sols bloc enfonsat (NW)
 Optical model: Mediterraneo.rf780d PIDS included
 Start time: 13:25 8 Jul 2015



Volume Statistics (Arithmetic)

FAM_CARR(5)_7.\$ls

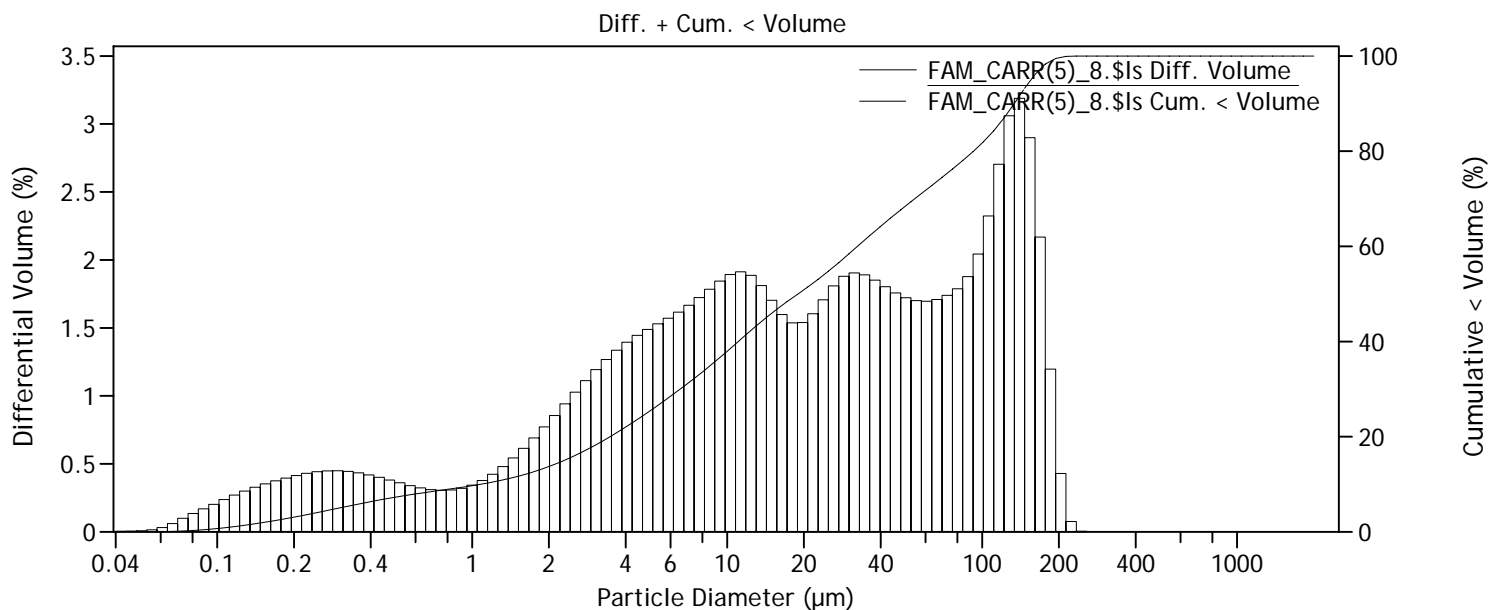
Calculations from 0.040 µm to 2000 µm

Volume:	100%	S.D.:	553.3 µm
Mean:	869.0 µm	Variance:	306.1e3 µm ²
Median:	826.7 µm	C.V.:	63.7%
Mean/Median ratio:	1.051	Skewness:	0.025 Right skewed
Mode:	1584 µm	Kurtosis:	-1.186 Platykurtic

d₁₀: 50.60 µm d₅₀: 826.7 µm d₉₀: 1624 µm

Particle Diameter µm	FAM_CARR(5) _7.\$ls Volume % <
2	0.44
4	1.52
63	10.7
125	13.8
250	18.1
500	28.5
1000	60.7
2000	100

File name: C:\GRANULOMETRIES COULTER\Marta Ferrater\FAM_CARR(5)_8.\$ls
 FAM_CARR(5)_8.\$ls
 File ID: FAM_CARR(5)_8
 Sample ID: FAM_CARR(5)_8
 Comment 1: Trinxera de carrascoy
 Comment 2: Perfil de sols bloc enfonsat (NW)
 Optical model: Mediterraneo.rf780d PIDS included
 Start time: 13:32 8 Jul 2015



Volume Statistics (Arithmetic)

FAM_CARR(5)_8.\$ls

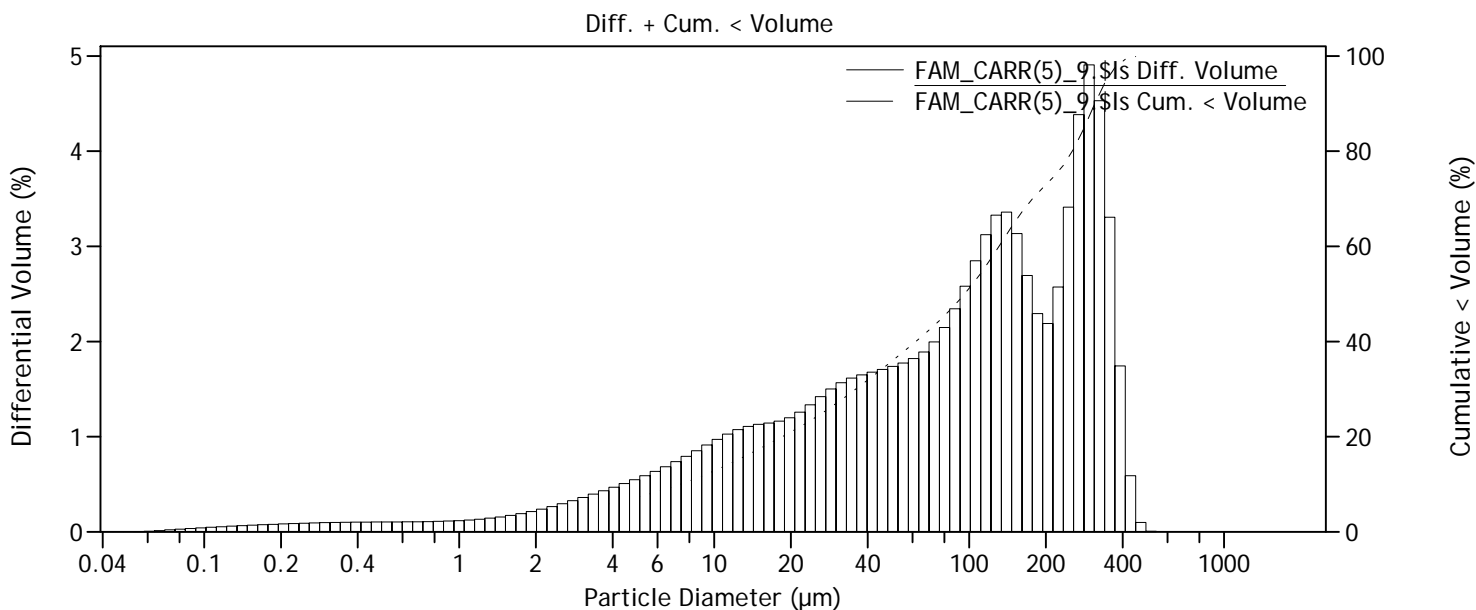
Calculations from 0.040 µm to 2000 µm

Volume:	100%	S.D.:	52.13 µm
Mean:	44.30 µm	Variance:	2718 µm ²
Median:	18.95 µm	C.V.:	118%
Mean/Median ratio:	2.337	Skewness:	1.221 Right skewed
Mode:	140.1 µm	Kurtosis:	0.310 Leptokurtic

d₁₀: 1.080 µm d₅₀: 18.95 µm d₉₀: 133.6 µm

Particle Diameter µm	FAM_CARR(5) _8.\$ls Volume % <
2	13.7
4	22.0
63	72.7
125	87.8
250	99.998
500	100
1000	100
2000	100

File name: C:\GRANULOMETRIES COULTER\Marta Ferrater\FAM_CARR(5)_9.\$ls
 FAM_CARR(5)_9.\$ls
 File ID: FAM_CARR(5)_9
 Sample ID: FAM_CARR(5)_9
 Comment 1: Trinxera de carrascoy
 Comment 2: Perfil de sols bloc enfonsat (NW)
 Optical model: Mediterraneo.rf780d PIDS included
 Start time: 13:42 8 Jul 2015



Volume Statistics (Arithmetic)

FAM_CARR(5)_9.\$ls

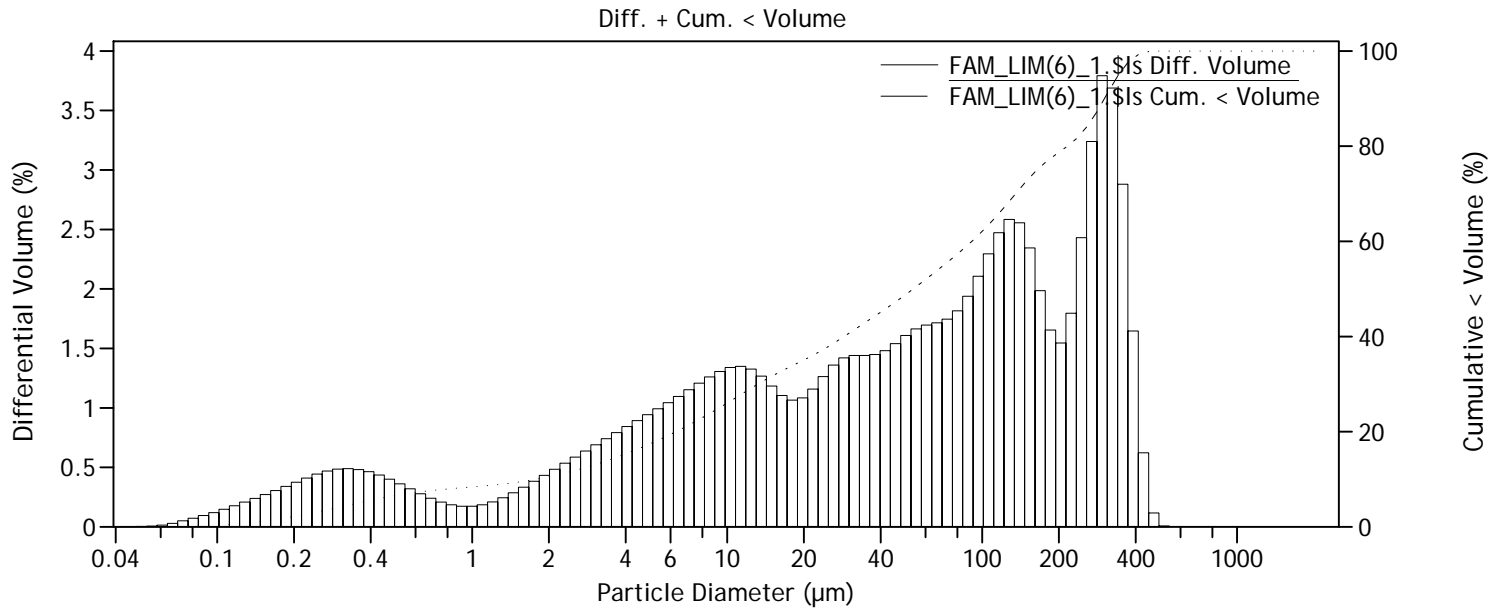
Calculations from 0.040 µm to 2000 µm

Volume:	100%	S.D.:	115.8 µm
Mean:	128.8 µm	Variance:	13412 µm ²
Median:	95.93 µm	C.V.:	89.9%
Mean/Median ratio:	1.342	Skewness:	0.743 Right skewed
Mode:	295.5 µm	Kurtosis:	-0.643 Platykurtic

d₁₀: 7.357 µm d₅₀: 95.93 µm d₉₀: 311.5 µm

Particle Diameter µm	FAM_CARR(5) _9.\$ls Volume % <
2	3.57
4	6.07
63	40.4
125	58.3
250	79.4
500	99.99
1000	100
2000	100

File name: C:\GRANULOMETRIES COULTER\Marta Ferrater\FAM_LIM(6)_1.\$Is
 FAM_LIM(6)_1.\$Is
 File ID: FAM_LIM(6)_1
 Sample ID: FAM_LIM(6)_1
 Comment 1: Límite 1
 Comment 2: Perfil de sols a la carretera que va cap a Goñar
 Optical model: Mediterraneo.rf780d PIDS included
 Start time: 9:32 10 Jul 2015



Volume Statistics (Arithmetic)

FAM_LIM(6)_1.\$Is

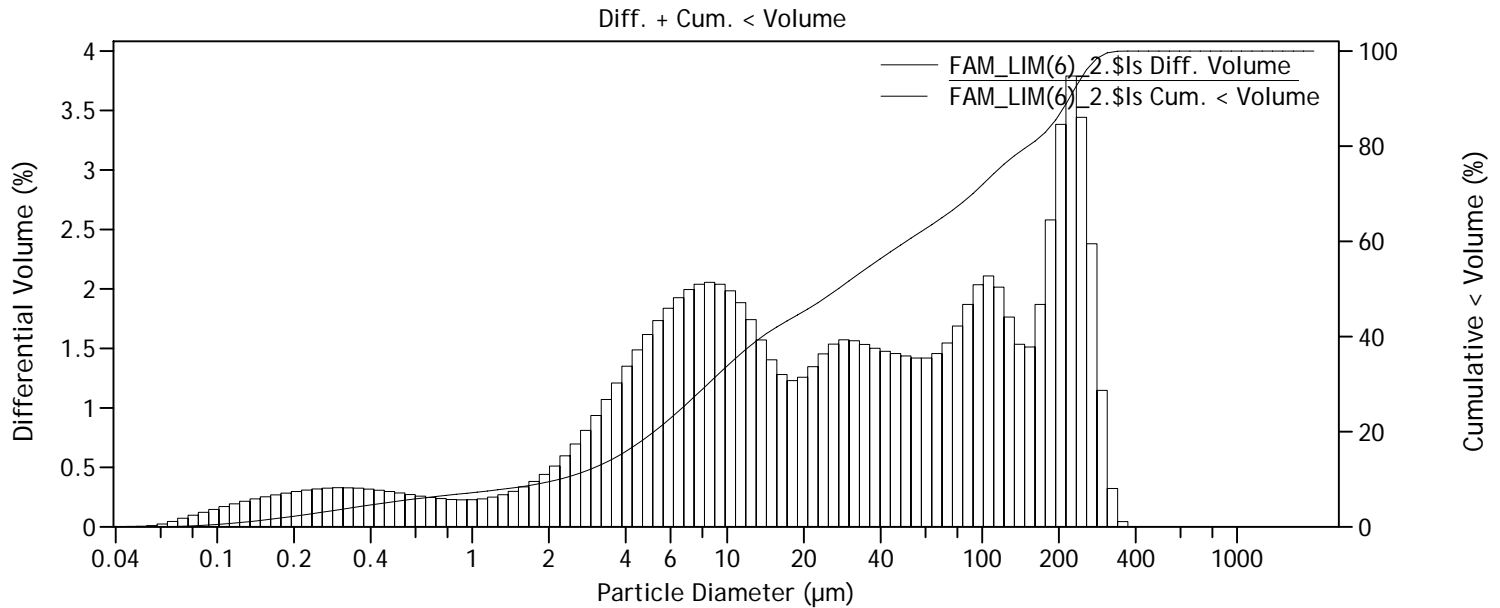
Calculations from 0.040 µm to 2000 µm

Volume:	100%	S.D.:	116.1 µm
Mean:	104.0 µm	Variance:	13486 µm ²
Median:	53.68 µm	C.V.:	112%
Mean/Median ratio:	1.937	Skewness:	1.075 Right skewed
Mode:	295.5 µm	Kurtosis:	-0.051 Platykurtic

d₁₀: 1.776 µm d₅₀: 53.68 µm d₉₀: 302.1 µm

Particle Diameter µm	FAM_LIM(6) _1.\$Is Volume % <
2	10.5
4	15.3
63	52.9
125	67.8
250	83.3
500	99.99
1000	100
2000	100

File name: C:\GRANULOMETRIES COULTER\Marta Ferrater\FAM_LIM(6)_2.\$Is
 FAM_LIM(6)_2.\$Is
 File ID: FAM_LIM(6)_2
 Sample ID: FAM_LIM(6)_2
 Comment 1: Límite 1
 Comment 2: Perfil de sols a la carretera que va cap a Goñar
 Optical model: Mediterraneo.rf780d PIDS included
 Start time: 9:38 10 Jul 2015



Volume Statistics (Arithmetic)

FAM_LIM(6)_2.\$Is

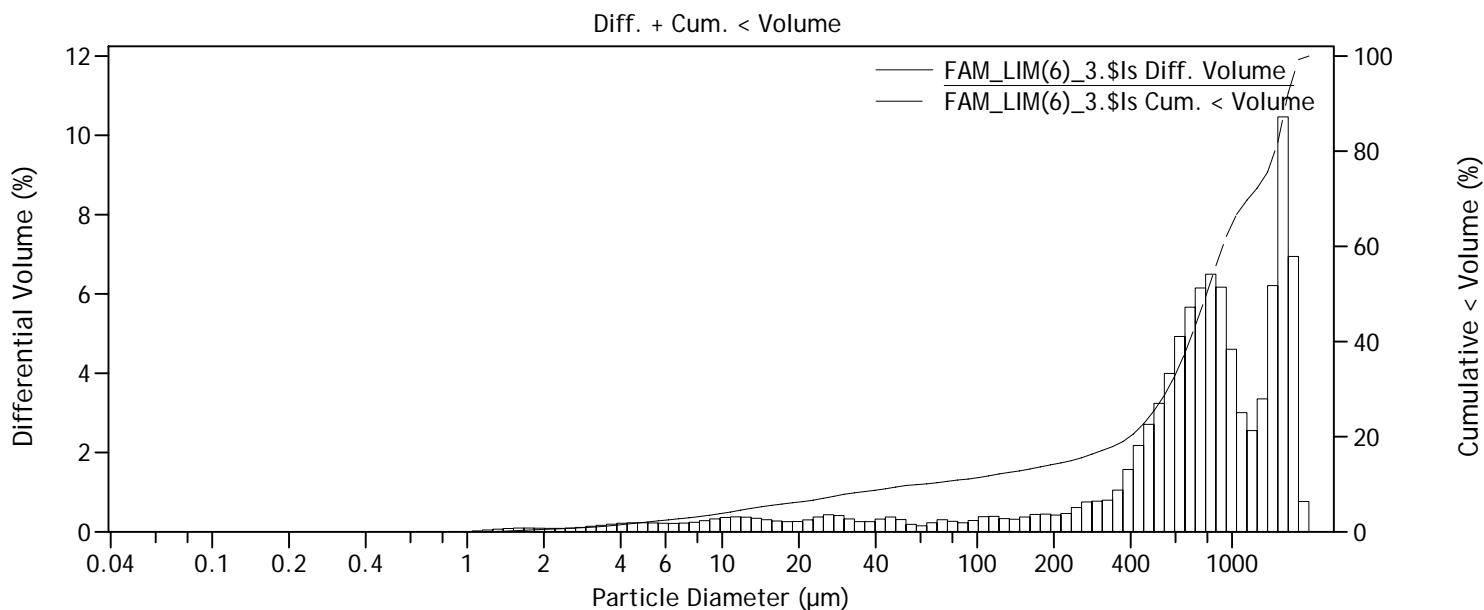
Calculations from 0.040 µm to 2000 µm

Volume:	100%	S.D.:	85.01 µm
Mean:	71.00 µm	Variance:	7227 µm ²
Median:	27.19 µm	C.V.:	120%
Mean/Median ratio:	2.611	Skewness:	1.169 Right skewed
Mode:	223.4 µm	Kurtosis:	0.078 Leptokurtic

d₁₀: 2.196 µm d₅₀: 27.19 µm d₉₀: 219.4 µm

Particle Diameter µm	FAM_LIM(6) _2.\$Is Volume % <
2	9.49
4	15.8
63	63.4
125	76.7
250	95.1
500	100
1000	100
2000	100

File name: C:\GRANULOMETRIES COULTER\Marta Ferrater\FAM_LIM(6)_3.\$Is
 FAM_LIM(6)_3.\$Is
 File ID: FAM_LIM(6)_3
 Sample ID: FAM_LIM(6)_3
 Comment 1: Límite 1
 Comment 2: Perfil de sols a la carretera que va cap a Goñar
 Optical model: Mediterraneo.rf780d PIDS included
 Start time: 9:45 10 Jul 2015



Volume Statistics (Arithmetic)

FAM_LIM(6)_3.\$Is

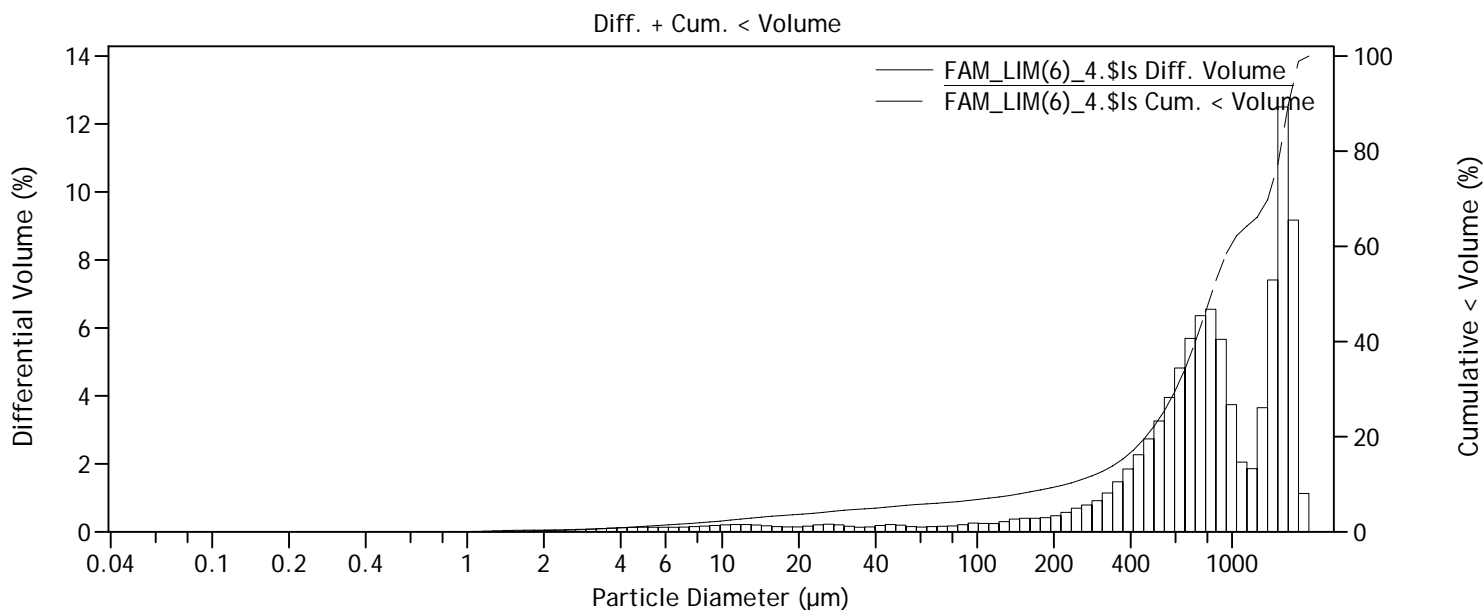
Calculations from 0.040 µm to 2000 µm

Volume:	100%	S.D.:	532.8 µm
Mean:	857.8 µm	Variance:	283.8e3 µm ²
Median:	793.8 µm	C.V.:	62.1%
Mean/Median ratio:	1.081	Skewness:	0.136 Right skewed
Mode:	1584 µm	Kurtosis:	-1.016 Platykurtic

d₁₀: 60.48 µm d₅₀: 793.8 µm d₉₀: 1627 µm

Particle Diameter µm	FAM_LIM(6) _3.\$Is Volume % <
2	0.52
4	1.50
63	10.1
125	12.3
250	15.4
500	25.9
1000	64.7
2000	100

File name: C:\GRANULOMETRIES COULTER\Marta Ferrater\FAM_LIM(6)_4.\$Is
 FAM_LIM(6)_4.\$Is
 File ID: FAM_LIM(6)_4
 Sample ID: FAM_LIM(6)_4
 Comment 1: Límite 1
 Comment 2: Perfil de sols a la carretera que va cap a Goñar
 Optical model: Mediterraneo.rf780d PIDS included
 Start time: 9:53 10 Jul 2015



Volume Statistics (Arithmetic)

FAM_LIM(6)_4.\$Is

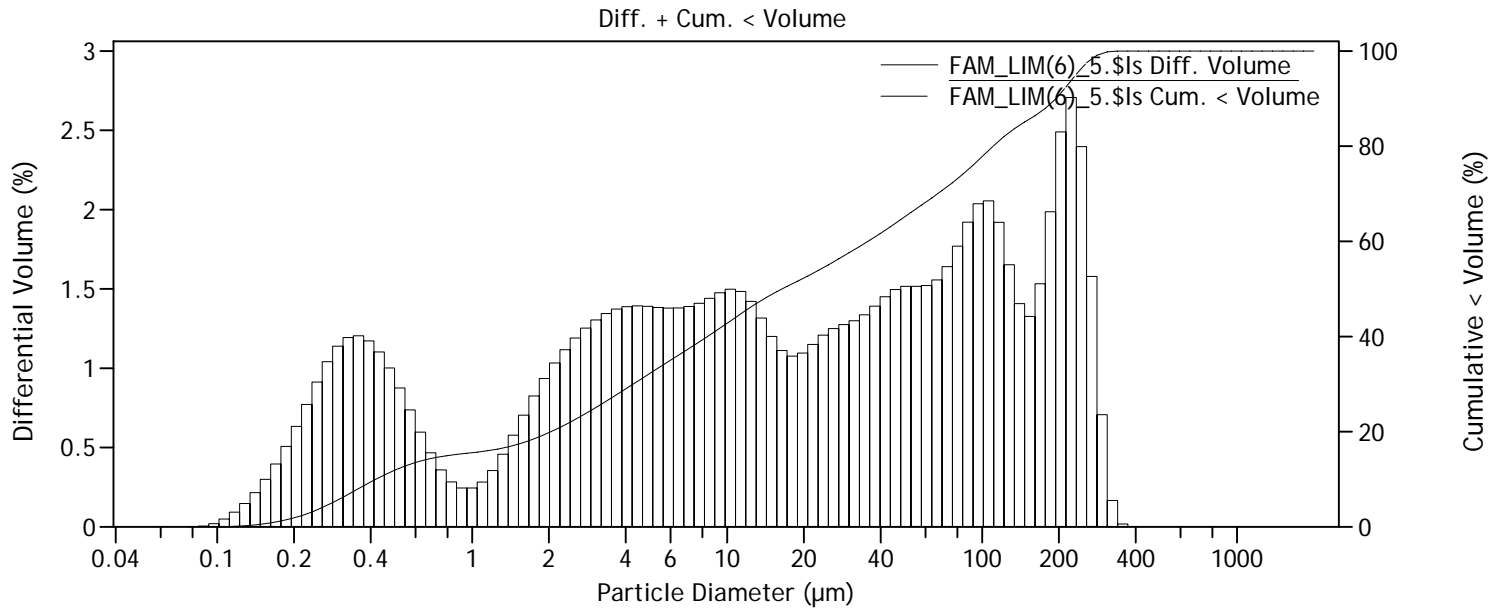
Calculations from 0.040 µm to 2000 µm

Volume:	100%	S.D.:	533.7 µm
Mean:	930.3 µm	Variance:	284.8e3 µm ²
Median:	830.8 µm	C.V.:	57.4%
Mean/Median ratio:	1.120	Skewness:	0.087 Right skewed
Mode:	1584 µm	Kurtosis:	-1.150 Platykurtic

d₁₀: 223.6 µm d₅₀: 830.8 µm d₉₀: 1665 µm

Particle Diameter µm	FAM_LIM(6) _4.\$Is Volume % <
2	0.27
4	0.86
63	5.87
125	7.42
250	10.8
500	22.6
1000	60.6
2000	100

File name: C:\GRANULOMETRIES COULTER\Marta Ferrater\FAM_LIM(6)_5.\$Is
 FAM_LIM(6)_5.\$Is
 File ID: FAM_LIM(6)_5
 Sample ID: FAM_LIM(6)_5
 Comment 1: Límite 1
 Comment 2: Perfil de sols a la carretera que va cap a Goñar
 Optical model: Mediterraneo.rf780d PIDS included
 Start time: 10:02 10 Jul 2015



Volume Statistics (Arithmetic)

FAM_LIM(6)_5.\$Is

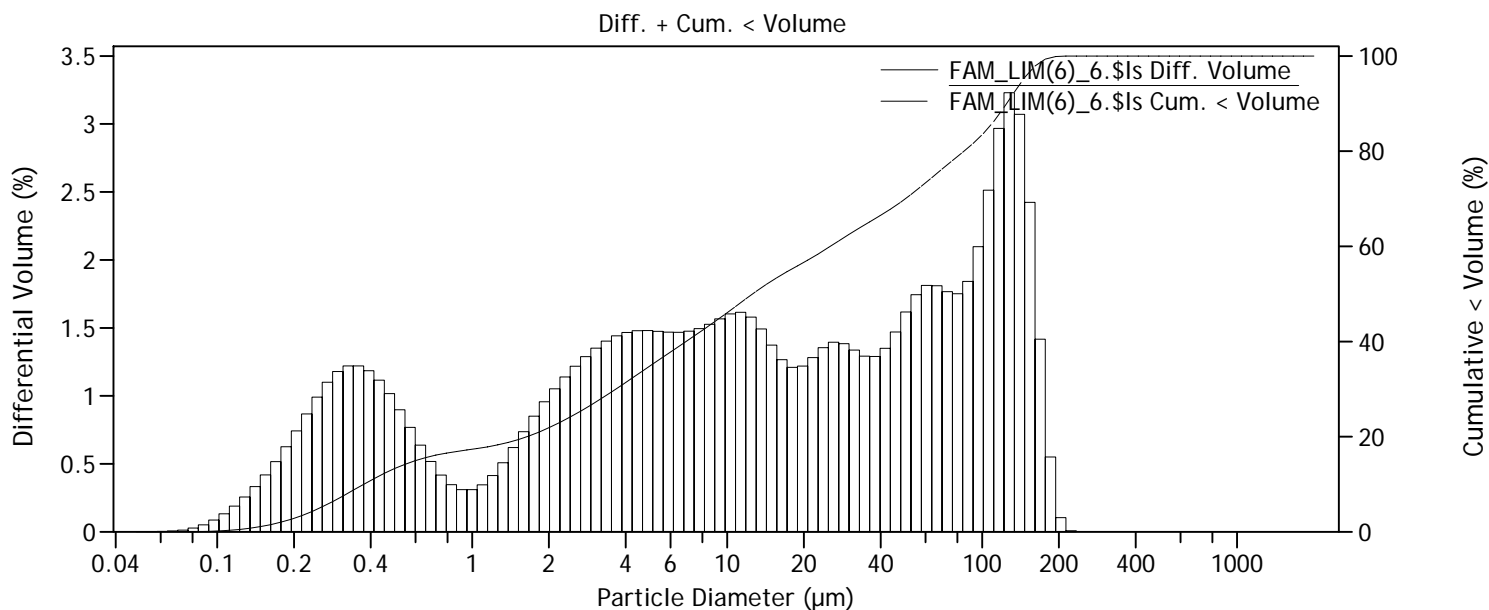
Calculations from 0.040 µm to 2000 µm

Volume:	100%	S.D.:	76.77 µm
Mean:	57.21 µm	Variance:	5894 µm ²
Median:	16.44 µm	C.V.:	134%
Mean/Median ratio:	3.480	Skewness:	1.465 Right skewed
Mode:	223.4 µm	Kurtosis:	1.065 Leptokurtic

d₁₀: 0.419 µm d₅₀: 16.44 µm d₉₀: 194.7 µm

Particle Diameter µm	FAM_LIM(6) _5.\$Is Volume % <
2	19.8
4	29.0
63	69.0
125	82.5
250	96.8
500	100
1000	100
2000	100

File name: C:\GRANULOMETRIES COULTER\Marta Ferrater\FAM_LIM(6)_6.\$Is
 FAM_LIM(6)_6.\$Is
 File ID: FAM_LIM(6)_6
 Sample ID: FAM_LIM(6)_6
 Comment 1: Límite 1
 Comment 2: Perfil de sols a la carretera que va cap a Goñar
 Optical model: Mediterraneo.rf780d PIDS included
 Start time: 10:09 10 Jul 2015



Volume Statistics (Arithmetic)

FAM_LIM(6)_6.\$Is

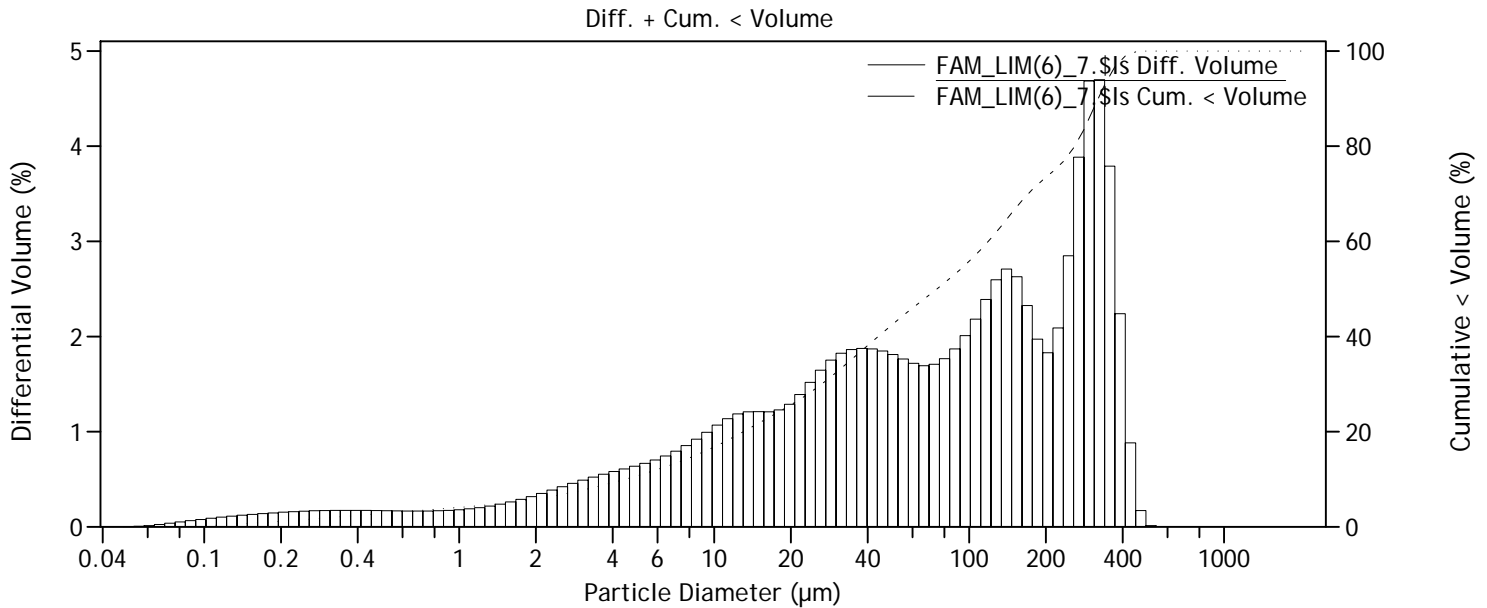
Calculations from 0.040 µm to 2000 µm

Volume:	100%	S.D.:	49.38 µm
Mean:	39.25 µm	Variance:	2439 µm ²
Median:	12.58 µm	C.V.:	126%
Mean/Median ratio:	3.119	Skewness:	1.236 Right skewed
Mode:	127.6 µm	Kurtosis:	0.284 Leptokurtic

d₁₀: 0.375 µm d₅₀: 12.58 µm d₉₀: 124.8 µm

Particle Diameter µm	FAM_LIM(6) _6.\$Is Volume % <
2	21.9
4	31.4
63	74.3
125	90.1
250	100
500	100
1000	100
2000	100

File name: C:\GRANULOMETRIES COULTER\Marta Ferrater\FAM_LIM(6)_7.\$Is
 FAM_LIM(6)_7.\$Is
 File ID: FAM_LIM(6)_7
 Sample ID: FAM_LIM(6)_7
 Comment 1: Límite 1
 Comment 2: Perfil de sols a la carretera que va cap a Goñar
 Optical model: Mediterraneo.rf780d PIDS included
 Start time: 10:15 10 Jul 2015



Volume Statistics (Arithmetic)

FAM_LIM(6)_7.\$Is

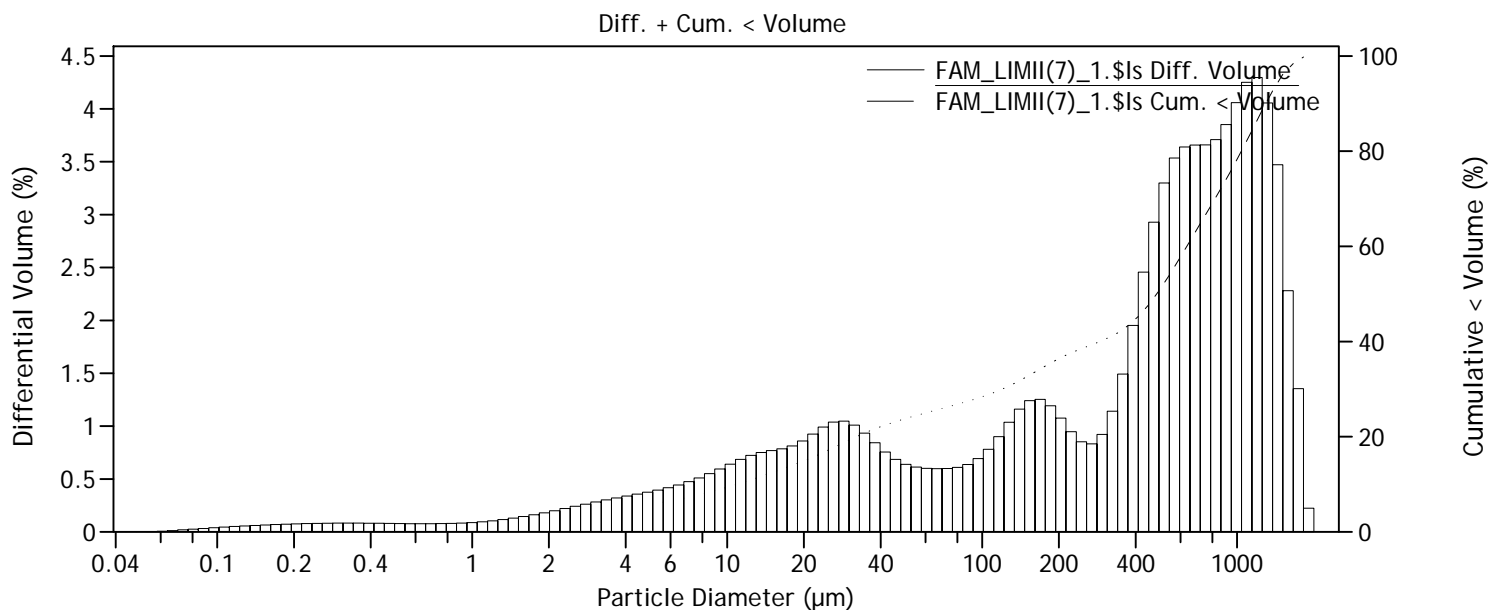
Calculations from 0.040 µm to 2000 µm

Volume:	100%	S.D.:	122.2 µm
Mean:	123.2 µm	Variance:	14934 µm ²
Median:	74.77 µm	C.V.:	99.2%
Mean/Median ratio:	1.647	Skewness:	0.839 Right skewed
Mode:	324.4 µm	Kurtosis:	-0.589 Platykurtic

d₁₀: 4.472 µm d₅₀: 74.77 µm d₉₀: 321.2 µm

Particle Diameter µm	FAM_LIM(6) _7.\$Is Volume % <
2	5.88
4	9.29
63	46.9
125	61.3
250	78.8
500	99.99
1000	100
2000	100

File name: C:\GRANULOMETRIES COULTER\Marta Ferrater\FAM_LIMII(7)_1.\$Is
 FAM_LIMII(7)_1.\$Is
 File ID: FAM_LIMII(7)_1
 Sample ID: FAM_LIMII(7)_1
 Comment 1: Límite 2
 Comment 2: Perfil de sols a la rambla que baixa de Goñar. Paleosol enterrat
 Optical model: Mediterraneo.rf780d PIDS included
 Start time: 10:26 10 Jul 2015



Volume Statistics (Arithmetic)

FAM_LIMII(7)_1.\$Is

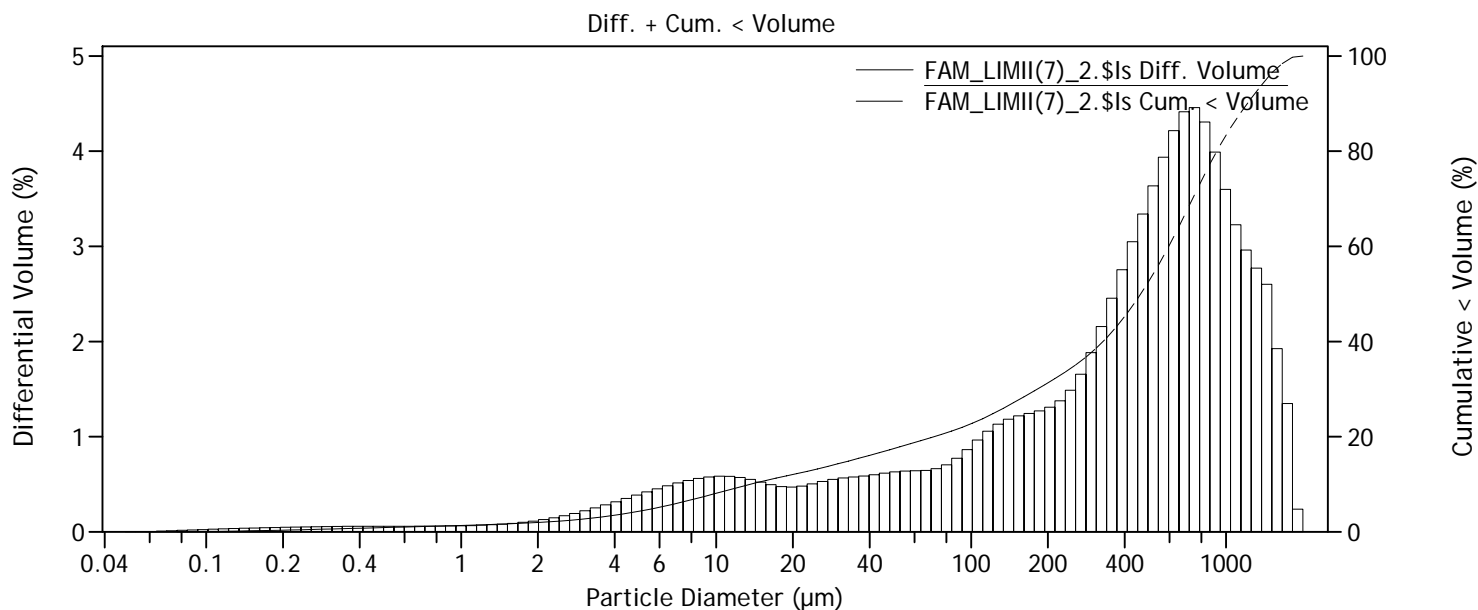
Calculations from 0.040 µm to 2000 µm

Volume:	100%	S.D.:	494.7 µm
Mean:	554.1 µm	Variance:	244.7e3 µm ²
Median:	483.8 µm	C.V.:	89.3%
Mean/Median ratio:	1.145	Skewness:	0.580 Right skewed
Mode:	1197 µm	Kurtosis:	-0.773 Platykurtic

d₁₀: 10.96 µm d₅₀: 483.8 µm d₉₀: 1296 µm

Particle Diameter µm	FAM_LIMII(7) _1.\$Is Volume % <
2	2.94
4	4.90
63	25.3
125	30.4
250	38.7
500	51.1
1000	78.3
2000	100

File name: C:\GRANULOMETRIES COULTER\Marta Ferrater\FAM_LIMII(7)_2.\$Is
 File ID: FAM_LIMII(7)_2
 Sample ID: FAM_LIMII(7)_2
 Comment 1: Límite 2
 Comment 2: Perfil de sols a la rambla que baixa de Goñar. Paleosol enterrat
 Optical model: Mediterraneo.rf780d PIDS included
 Start time: 10:32 10 Jul 2015



Volume Statistics (Arithmetic)

FAM_LIMII(7)_2.\$Is

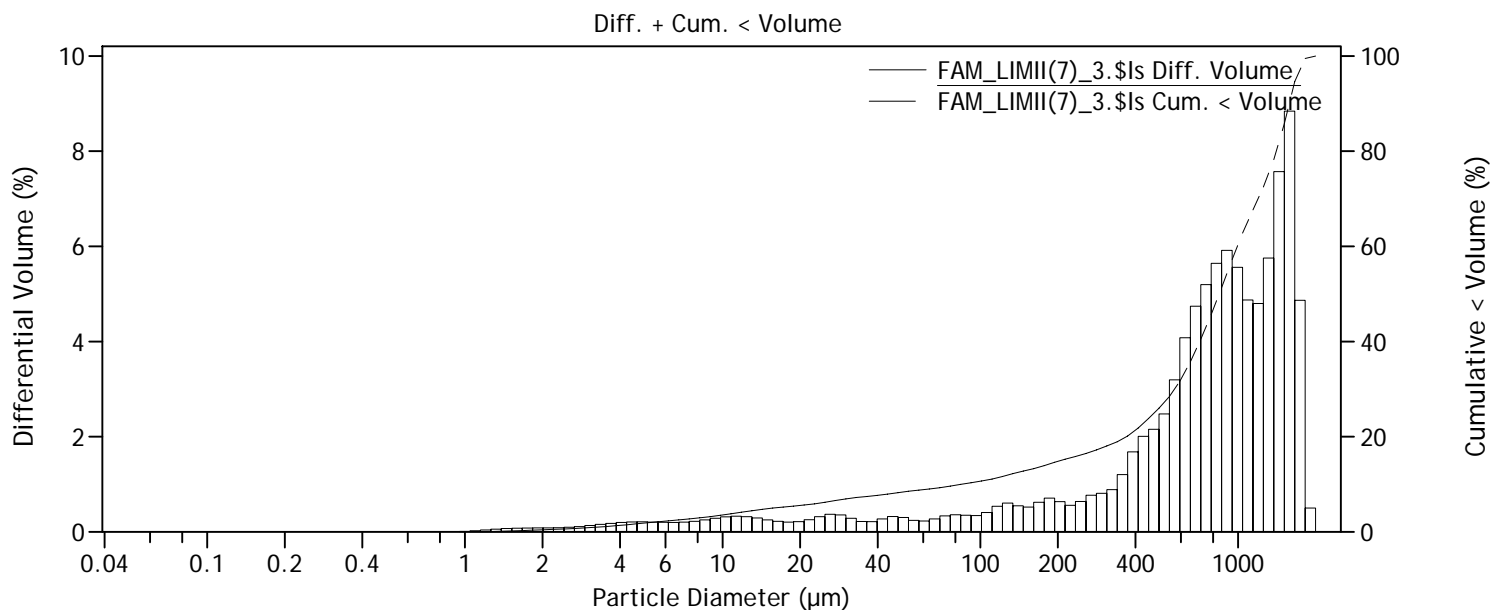
Calculations from 0.040 µm to 2000 µm

Volume:	100%	S.D.:	454.5 µm
Mean:	534.7 µm	Variance:	206.5e3 µm ²
Median:	462.4 µm	C.V.:	85.0%
Mean/Median ratio:	1.156	Skewness:	0.736 Right skewed
Mode:	751.1 µm	Kurtosis:	-0.248 Platykurtic

d₁₀: 13.61 µm d₅₀: 462.4 µm d₉₀: 1212 µm

Particle Diameter µm	FAM_LIMII(7) _2.\$Is Volume % <
2	1.98
4	3.50
63	19.1
125	25.1
250	34.6
500	52.9
1000	83.3
2000	100

File name: C:\GRANULOMETRIES COULTER\Marta Ferrater\FAM_LIMII(7)_3.\$Is
 FAM_LIMII(7)_3.\$Is
 File ID: FAM_LIMII(7)_3
 Sample ID: FAM_LIMII(7)_3
 Comment 1: Límite 2
 Comment 2: Perfil de sols a la rambla que baixa de Goñar. Paleosol enterrat
 Optical model: Mediterraneo.rf780d PIDS included
 Start time: 10:38 10 Jul 2015



Volume Statistics (Arithmetic)

FAM_LIMII(7)_3.\$Is

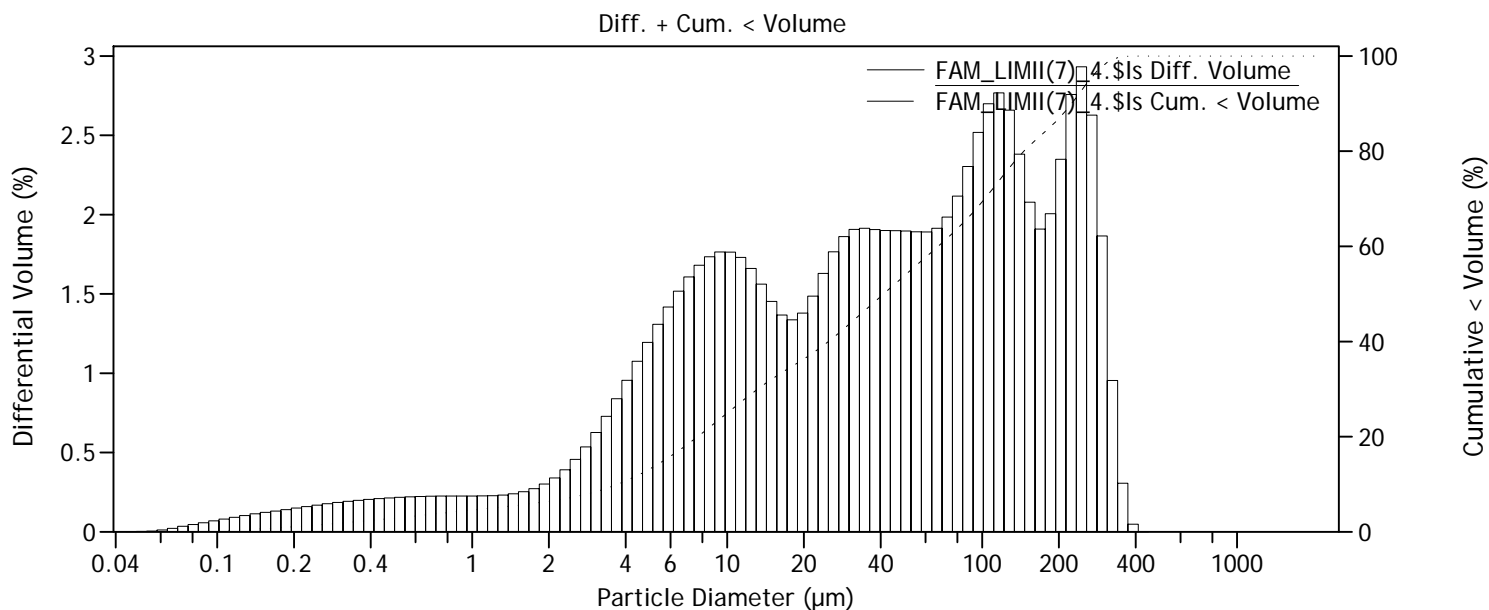
Calculations from 0.040 µm to 2000 µm

Volume:	100%	S.D.:	518.9 µm
Mean:	862.8 µm	Variance:	269.3e3 µm ²
Median:	845.9 µm	C.V.:	60.1%
Mean/Median ratio:	1.020	Skewness:	-0.0060 Left skewed
Mode:	1584 µm	Kurtosis:	-1.042 Platykurtic

d₁₀: 84.08 µm d₅₀: 845.9 µm d₉₀: 1582 µm

Particle Diameter µm	FAM_LIMII(7) _3.\$Is Volume % <
2	0.44
4	1.37
63	9.01
125	11.8
250	16.3
500	26.3
1000	60.3
2000	100

File name: C:\GRANULOMETRIES COULTER\Marta Ferrater\FAM_LIMII(7)_4.\$Is
 FAM_LIMII(7)_4.\$Is
 File ID: FAM_LIMII(7)_4
 Sample ID: FAM_LIMII(7)_4
 Comment 1: Límite 2
 Comment 2: Perfil de sols a la rambla que baixa de Goñar. Paleosol enterrat
 Optical model: Mediterraneo.rf780d PIDS included
 Start time: 10:45 10 Jul 2015



Volume Statistics (Arithmetic)

FAM_LIMII(7)_4.\$Is

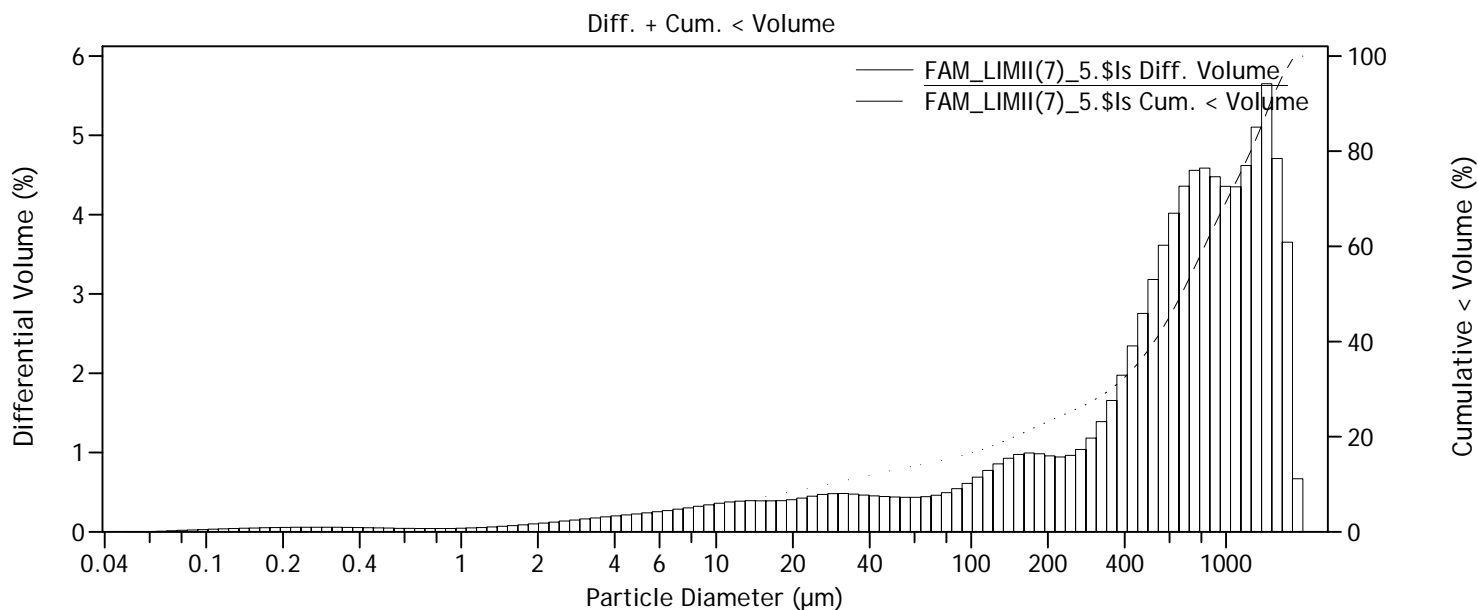
Calculations from 0.040 µm to 2000 µm

Volume:	100%	S.D.:	86.17 µm
Mean:	78.28 µm	Variance:	7425 µm ²
Median:	41.12 µm	C.V.:	110%
Mean/Median ratio:	1.904	Skewness:	1.212 Right skewed
Mode:	245.2 µm	Kurtosis:	0.465 Leptokurtic

d₁₀: 3.714 µm d₅₀: 41.12 µm d₉₀: 224.5 µm

Particle Diameter µm	FAM_LIMII(7) _4.\$Is Volume % <
2	6.43
4	10.7
63	58.7
125	75.8
250	93.3
500	100
1000	100
2000	100

File name: C:\GRANULOMETRIES COULTER\Marta Ferrater\FAM_LIMII(7)_5.\$Is
 FAM_LIMII(7)_5.\$Is
 File ID: FAM_LIMII(7)_5
 Sample ID: FAM_LIMII(7)_5
 Comment 1: Límite 2
 Comment 2: Perfil de sols a la rambla que baixa de Goñar. Paleosol enterrat
 Optical model: Mediterraneo.rf780d PIDS included
 Start time: 10:51 10 Jul 2015



Volume Statistics (Arithmetic)

FAM_LIMII(7)_5.\$Is

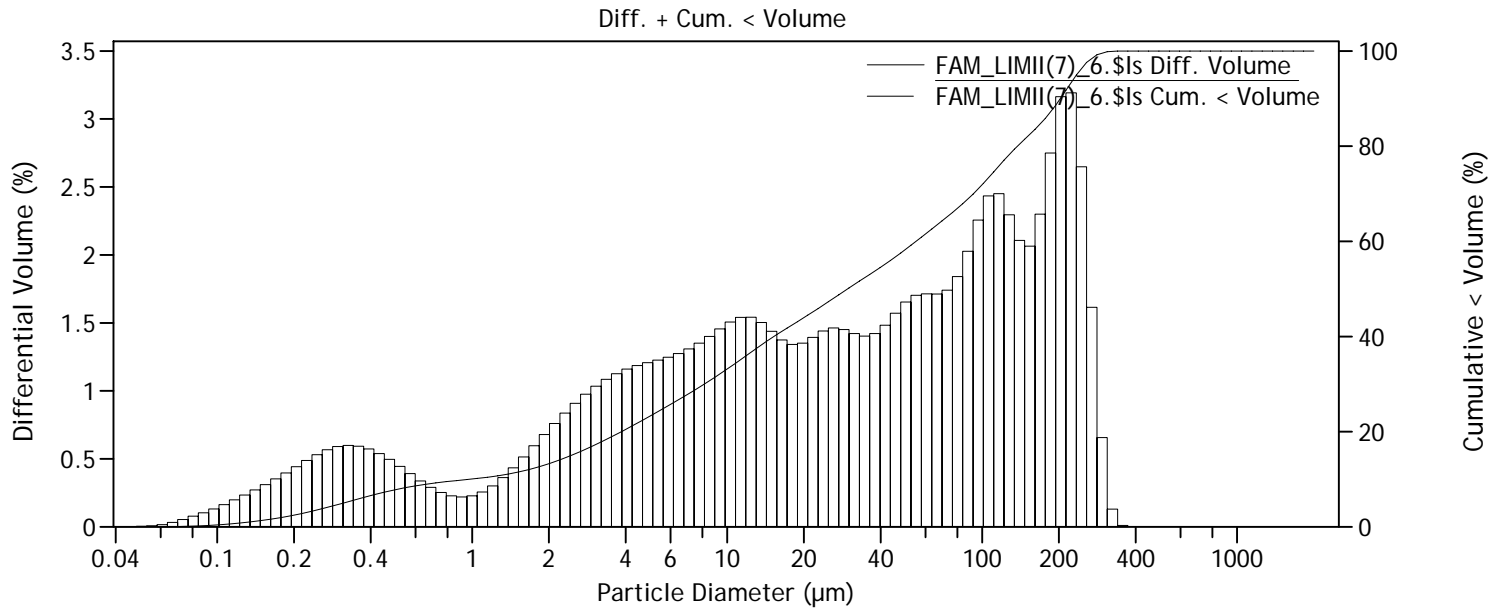
Calculations from 0.040 µm to 2000 µm

Volume:	100%	S.D.:	525.6 µm
Mean:	717.8 µm	Variance:	276.3e3 µm ²
Median:	669.0 µm	C.V.:	73.2%
Mean/Median ratio:	1.073	Skewness:	0.320 Right skewed
Mode:	1443 µm	Kurtosis:	-0.986 Platykurtic

d₁₀: 27.41 µm d₅₀: 669.0 µm d₉₀: 1489 µm

Particle Diameter µm	FAM_LIMII(7) _5.\$Is Volume % <
2	1.83
4	2.96
63	14.1
125	18.4
250	25.5
500	38.5
1000	69.3
2000	100

File name: C:\GRANULOMETRIES COULTER\Marta Ferrater\FAM_LIMII(7)_6.\$Is
 FAM_LIMII(7)_6.\$Is
 File ID: FAM_LIMII(7)_6
 Sample ID: FAM_LIMII(7)_6
 Comment 1: Límite 2
 Comment 2: Perfil de sols a la rambla que baixa de Goñar. Paleosol enterrat
 Optical model: Mediterraneo.rf780d PIDS included
 Start time: 10:57 10 Jul 2015



Volume Statistics (Arithmetic)

FAM_LIMII(7)_6.\$Is

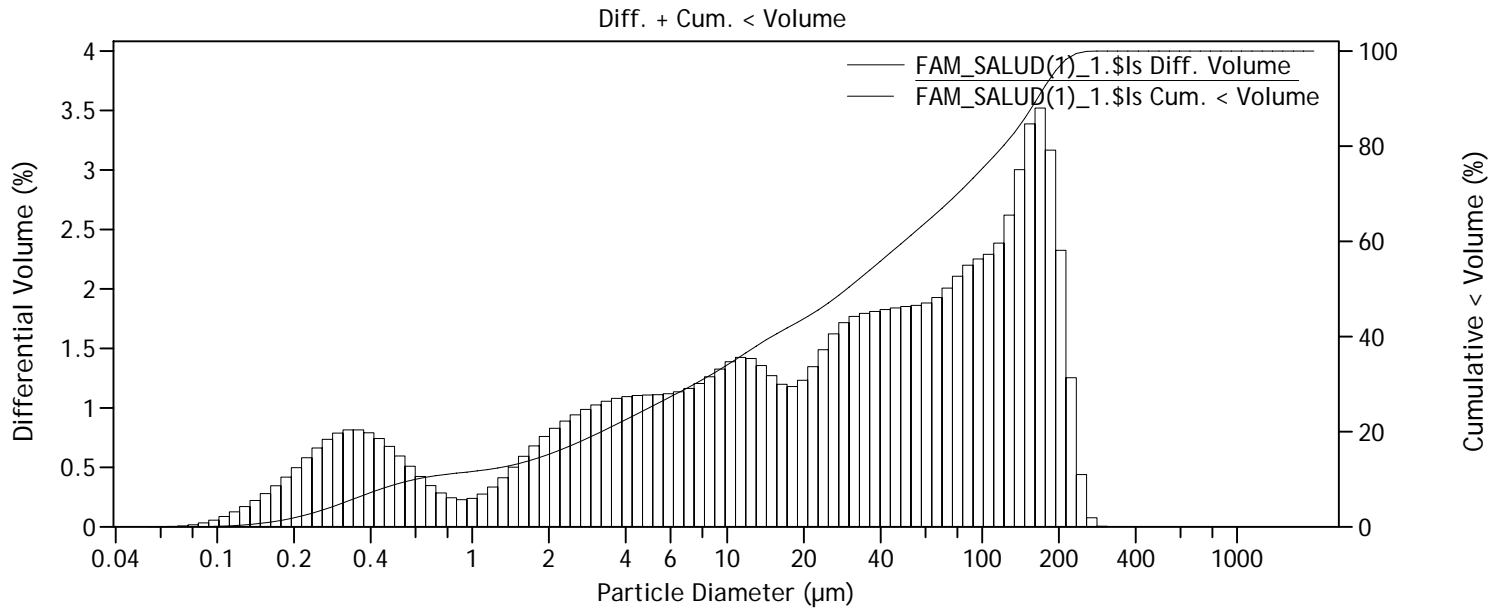
Calculations from 0.040 µm to 2000 µm

Volume:	100%	S.D.:	78.99 µm
Mean:	67.98 µm	Variance:	6239 µm ²
Median:	29.65 µm	C.V.:	116%
Mean/Median ratio:	2.293	Skewness:	1.145 Right skewed
Mode:	223.4 µm	Kurtosis:	0.152 Leptokurtic

d₁₀: 0.973 µm d₅₀: 29.65 µm d₉₀: 202.7 µm

Particle Diameter µm	FAM_LIMII(7) _6.\$Is Volume % <
2	13.3
4	20.5
63	62.5
125	77.7
250	96.8
500	100
1000	100
2000	100

File name: C:\GRANULOMETRIES COULTER\Marta Ferrater\FAM_SALUD(1)_1.\$ls
 File ID: FAM_SALUD(1)_1
 Sample ID: FAM_SALUD(1)_1
 Comment 1: Trinxera de la Salud
 Comment 2: Perfil de sols bloc aixecat
 Optical model: Mediterraneo.rf780d PIDS included
 Start time: 10:32 8 Jul 2015



Volume Statistics (Arithmetic)

FAM_SALUD(1)_1.\$ls

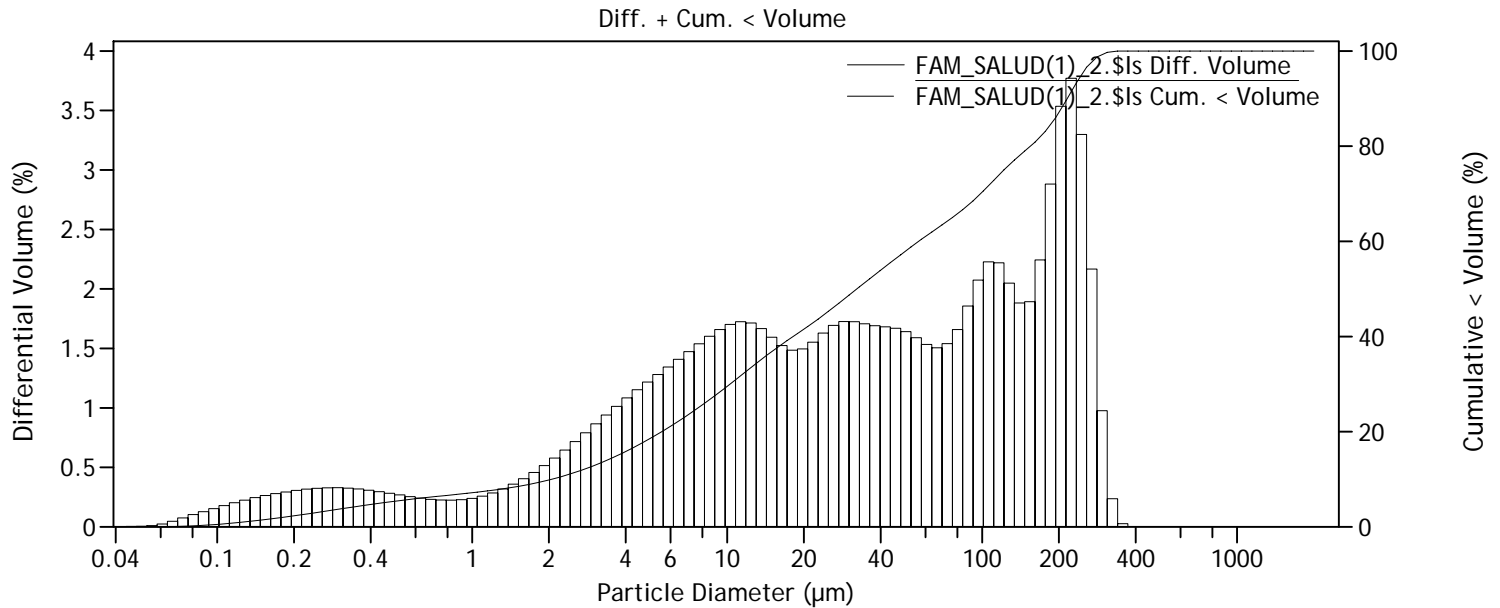
Calculations from 0.040 µm to 2000 µm

Volume:	100%	S.D.:	64.34 µm
Mean:	57.83 µm	Variance:	4140 µm ²
Median:	29.45 µm	C.V.:	111%
Mean/Median ratio:	1.964	Skewness:	1.040 Right skewed
Mode:	168.9 µm	Kurtosis:	-0.106 Platykurtic

d₁₀: 0.600 µm d₅₀: 29.45 µm d₉₀: 164.7 µm

Particle Diameter µm	FAM_SALUD(1) _1.\$ls Volume % <
2	15.3
4	22.5
63	64.9
125	80.9
250	99.8
500	100
1000	100
2000	100

File name: C:\GRANULOMETRIES COULTER\Marta Ferrater\FAM_SALUD(1)_2.\$Is
 FAM_SALUD(1)_2.\$Is
 File ID: FAM_SALUD(1)_2
 Sample ID: FAM_SALUD(1)_2
 Comment 1: Trinxera de la Salud
 Comment 2: Perfil de sols bloc aixecat
 Optical model: Mediterraneo.rf780d PIDS included
 Start time: 10:43 8 Jul 2015



Volume Statistics (Arithmetic)

FAM_SALUD(1)_2.\$Is

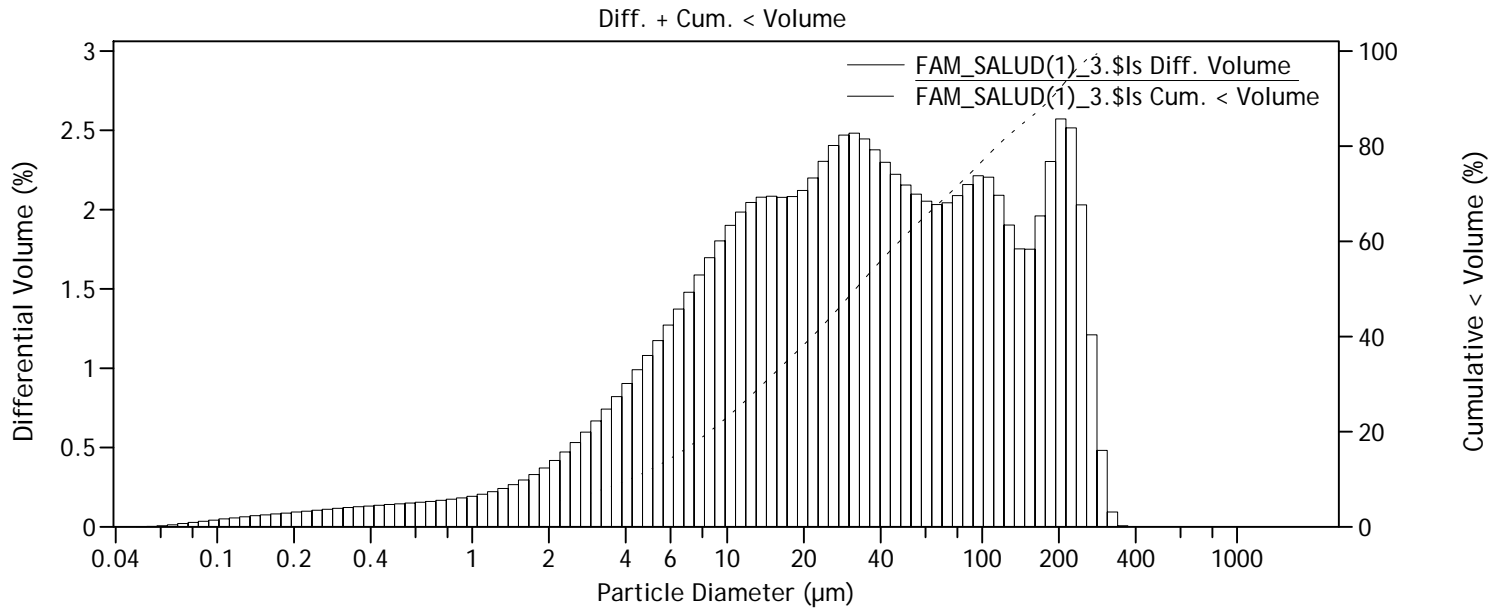
Calculations from 0.040 µm to 2000 µm

Volume:	100%	S.D.:	83.42 µm
Mean:	73.15 µm	Variance:	6959 µm ²
Median:	32.26 µm	C.V.:	114%
Mean/Median ratio:	2.268	Skewness:	1.095 Right skewed
Mode:	223.4 µm	Kurtosis:	-0.063 Platykurtic

d₁₀: 2.047 µm d₅₀: 32.26 µm d₉₀: 215.9 µm

Particle Diameter µm	FAM_SALUD(1) _2.\$Is Volume % <
2	9.86
4	15.8
63	61.8
125	75.6
250	95.6
500	100
1000	100
2000	100

File name: C:\GRANULOMETRIES COULTER\Marta Ferrater\FAM_SALUD(1)_3.\$ls
 FAM_SALUD(1)_3.\$ls
 File ID: FAM_SALUD(1)_3
 Sample ID: FAM_SALUD(1)_3
 Comment 1: Trinxera de la Salud
 Comment 2: Perfil de sols bloc aixecat
 Optical model: Mediterraneo.rf780d PIDS included
 Start time: 9:23 10 Jul 2015



Volume Statistics (Arithmetic)

FAM_SALUD(1)_3.\$ls

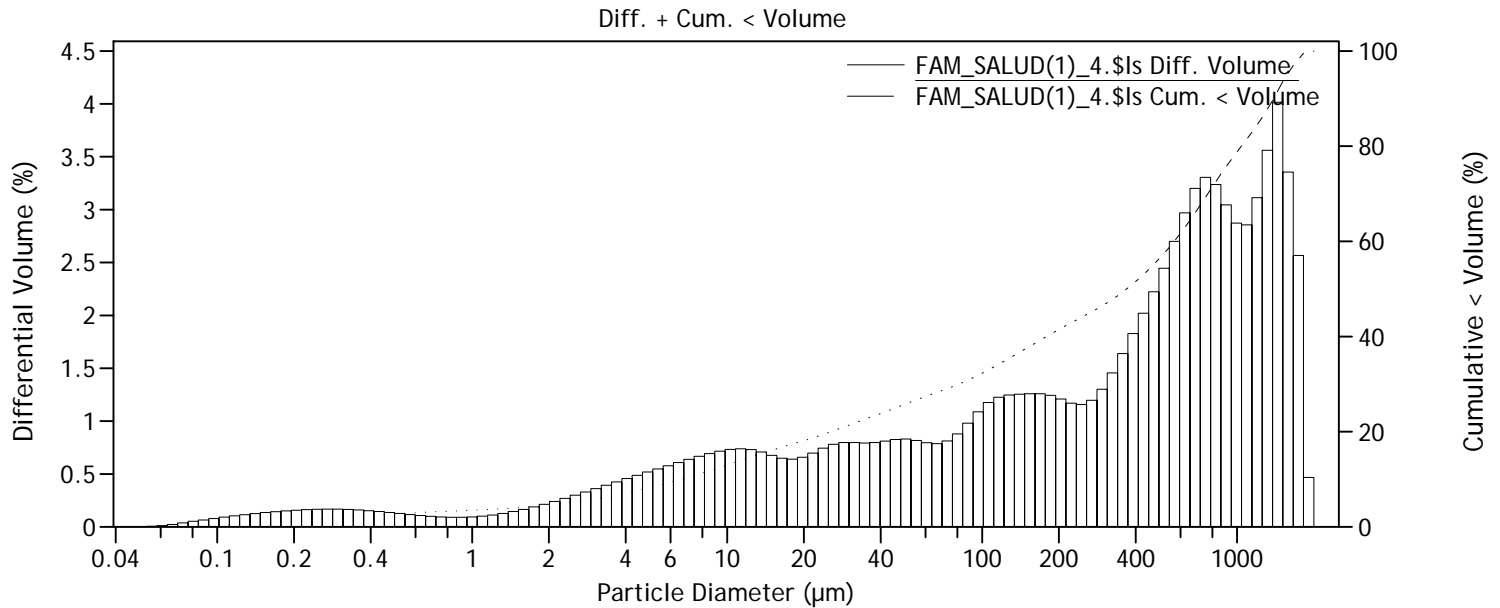
Calculations from 0.040 µm to 2000 µm

Volume:	100%	S.D.:	71.32 µm
Mean:	63.14 µm	Variance:	5087 µm ²
Median:	31.90 µm	C.V.:	113%
Mean/Median ratio:	1.979	Skewness:	1.400 Right skewed
Mode:	203.5 µm	Kurtosis:	1.002 Leptokurtic

d₁₀: 4.140 µm d₅₀: 31.90 µm d₉₀: 186.0 µm

Particle Diameter µm	FAM_SALUD(1) _3.\$ls Volume % <
2	5.06
4	9.66
63	66.4
125	81.9
250	97.6
500	100
1000	100
2000	100

File name: C:\GRANULOMETRIES COULTER\Marta Ferrater\FAM_SALUD(1)_4.\$ls
 FAM_SALUD(1)_4.\$ls
 File ID: FAM_SALUD(1)_4
 Sample ID: FAM_SALUD(1)_4
 Comment 1: Trinxera de la Salud
 Comment 2: Perfil de sols bloc aixecat
 Optical model: Mediterraneo.rf780d PIDS included
 Start time: 11:04 10 Jul 2015



Volume Statistics (Arithmetic)

FAM_SALUD(1)_4.\$ls

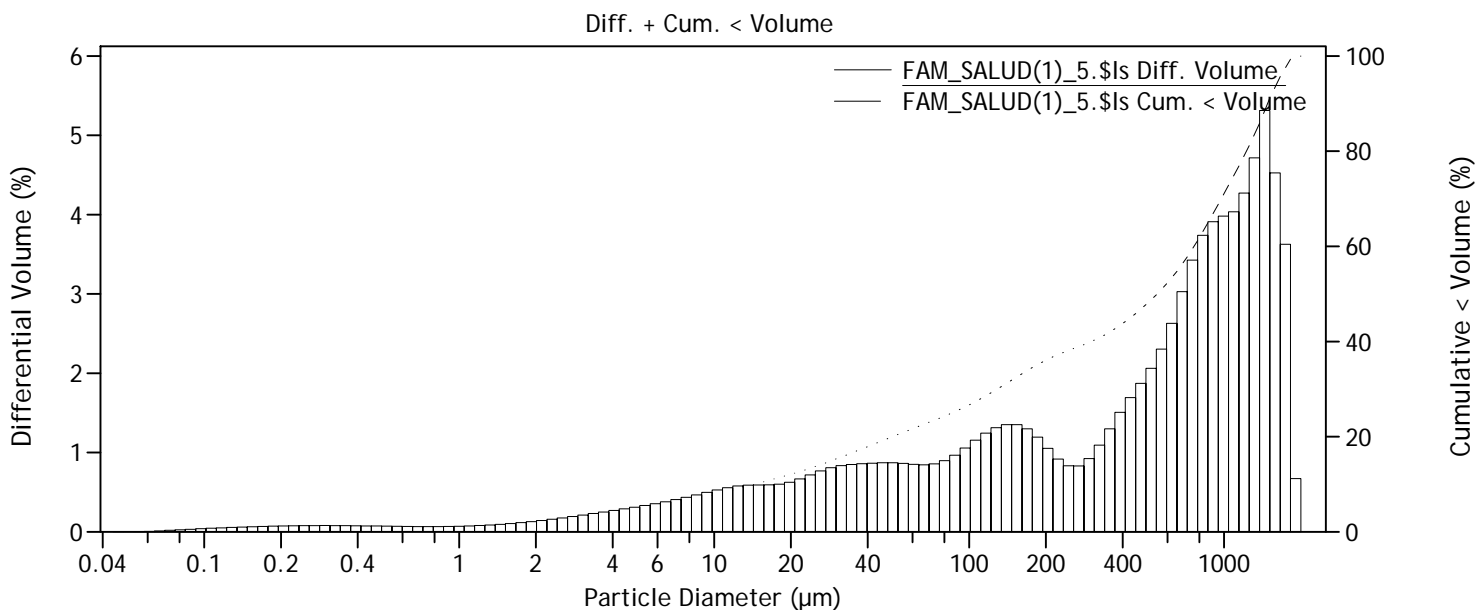
Calculations from 0.040 µm to 2000 µm

Volume:	100%	S.D.:	529.0 µm
Mean:	528.8 µm	Variance:	279.8e3 µm ²
Median:	368.8 µm	C.V.:	100%
Mean/Median ratio:	1.434	Skewness:	0.792 Right skewed
Mode:	1443 µm	Kurtosis:	-0.574 Platykurtic

d₁₀: 6.637 µm d₅₀: 368.8 µm d₉₀: 1391 µm

Particle Diameter µm	FAM_SALUD(1) _4.\$ls Volume % <
2	4.59
4	7.09
63	27.8
125	35.2
250	44.3
500	56.6
1000	78.8
2000	100

File name: C:\GRANULOMETRIES COULTER\Marta Ferrater\FAM_SALUD(1)_5.\$Is
 File ID: FAM_SALUD(1)_5
 Sample ID: FAM_SALUD(1)_5
 Comment 1: Trinxera de la Salud
 Comment 2: Perfil de sols bloc aixecat
 Optical model: Mediterraneo.rf780d PIDS included
 Start time: 10:57 8 Jul 2015



Volume Statistics (Arithmetic)

FAM_SALUD(1)_5.\$Is

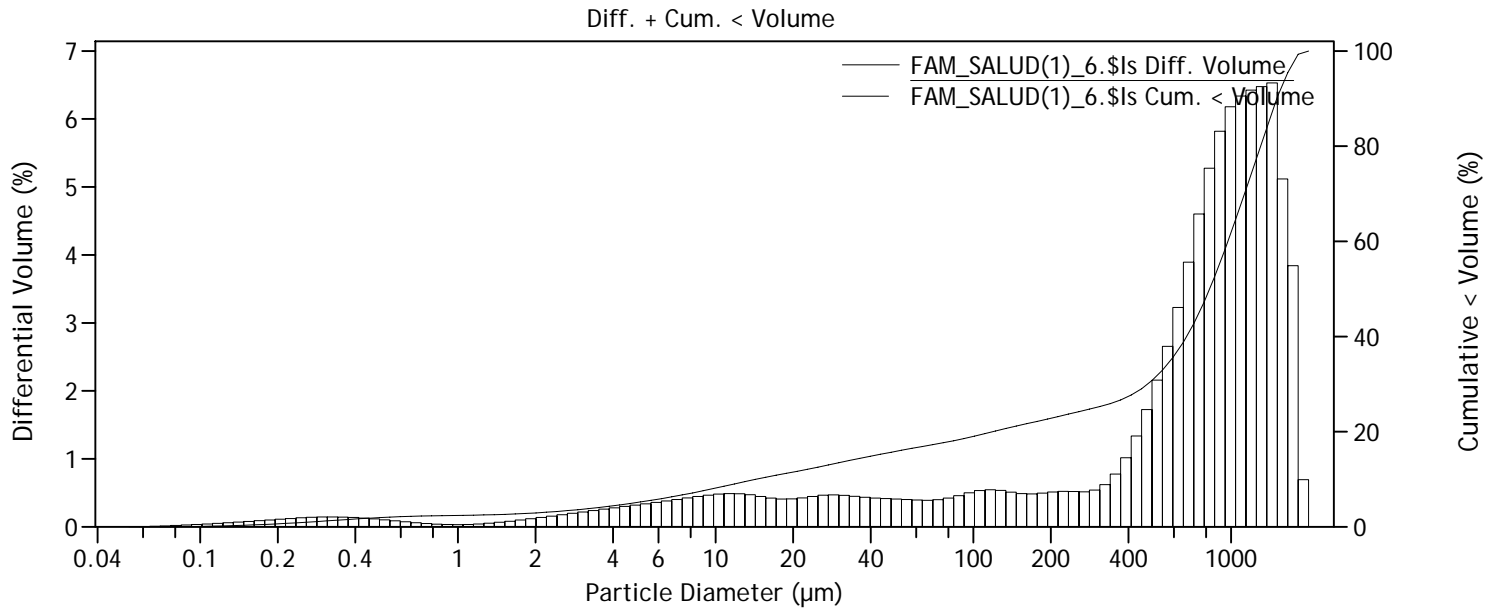
Calculations from 0.040 µm to 2000 µm

Volume:	100%	S.D.:	561.2 µm
Mean:	636.5 µm	Variance:	314.9e3 µm ²
Median:	546.1 µm	C.V.:	88.2%
Mean/Median ratio:	1.166	Skewness:	0.472 Right skewed
Mode:	1443 µm	Kurtosis:	-1.085 Platykurtic

d₁₀: 14.39 µm d₅₀: 546.1 µm d₉₀: 1482 µm

Particle Diameter µm	FAM_SALUD(1) _5.\$Is Volume % <
2	2.57
4	4.04
63	22.1
125	29.6
250	38.3
500	48.0
1000	71.1
2000	100

File name: C:\GRANULOMETRIES COULTER\Marta Ferrater\FAM_SALUD(1)_6.\$Is
 FAM_SALUD(1)_6.\$Is
 File ID: FAM_SALUD(1)_6
 Sample ID: FAM_SALUD(1)_6
 Comment 1: Trinxera de la Salud
 Comment 2: Perfil de sols bloc aixecat
 Optical model: Mediterraneo.rf780d PIDS included
 Start time: 11:06 8 Jul 2015



Volume Statistics (Arithmetic)

FAM_SALUD(1)_6.\$Is

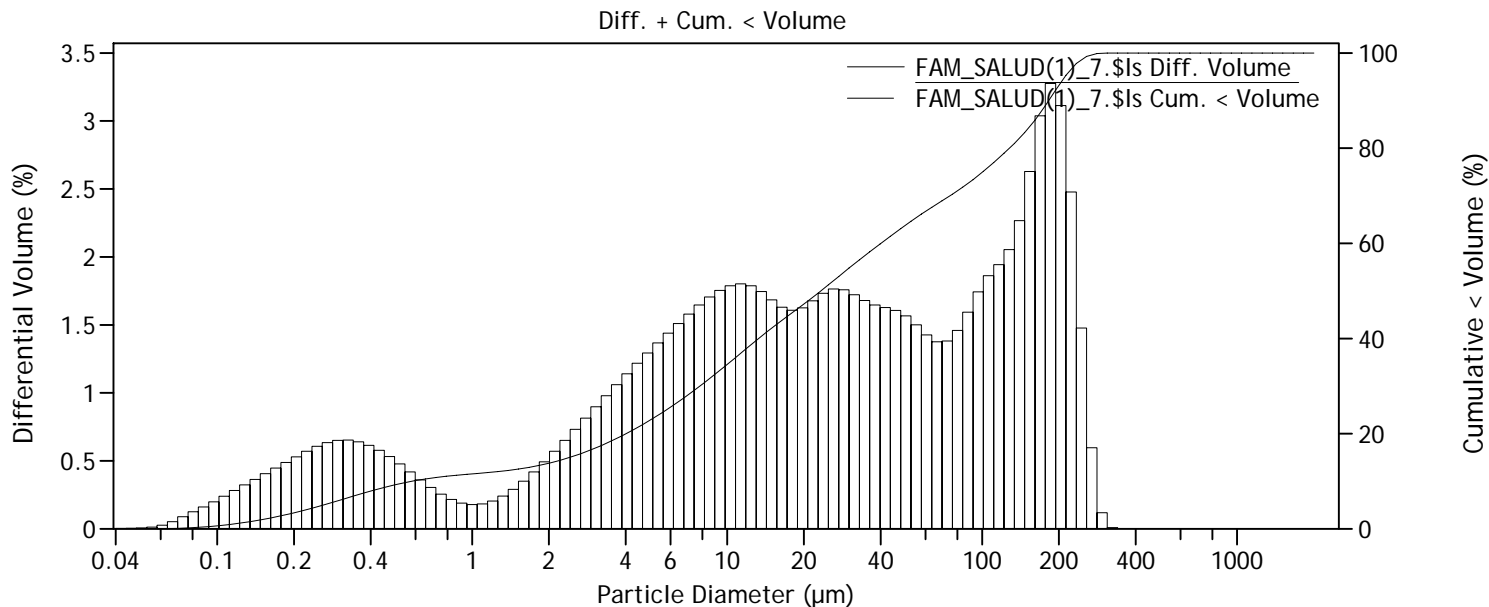
Calculations from 0.040 µm to 2000 µm

Volume:	100%	S.D.:	536.8 µm
Mean:	790.5 µm	Variance:	288.2e3 µm ²
Median:	826.3 µm	C.V.:	67.9%
Mean/Median ratio:	0.957	Skewness:	-0.014 Left skewed
Mode:	1443 µm	Kurtosis:	-1.099 Platykurtic

d₁₀: 14.29 µm d₅₀: 826.3 µm d₉₀: 1505 µm

Particle Diameter µm	FAM_SALUD(1) _6.\$Is Volume % <
2	2.93
4	4.44
63	16.9
125	20.3
250	24.1
500	31.0
1000	61.8
2000	100

File name: C:\GRANULOMETRIES COULTER\Marta Ferrater\FAM_SALUD(1)_7.\$Is
 FAM_SALUD(1)_7.\$Is
 File ID: FAM_SALUD(1)_7
 Sample ID: FAM_SALUD(1)_7
 Comment 1: Trinxera de la Salud
 Comment 2: Perfil de sols bloc aixecat
 Optical model: Mediterraneo.rf780d PIDS included
 Start time: 11:14 8 Jul 2015



Volume Statistics (Arithmetic)

FAM_SALUD(1)_7.\$Is

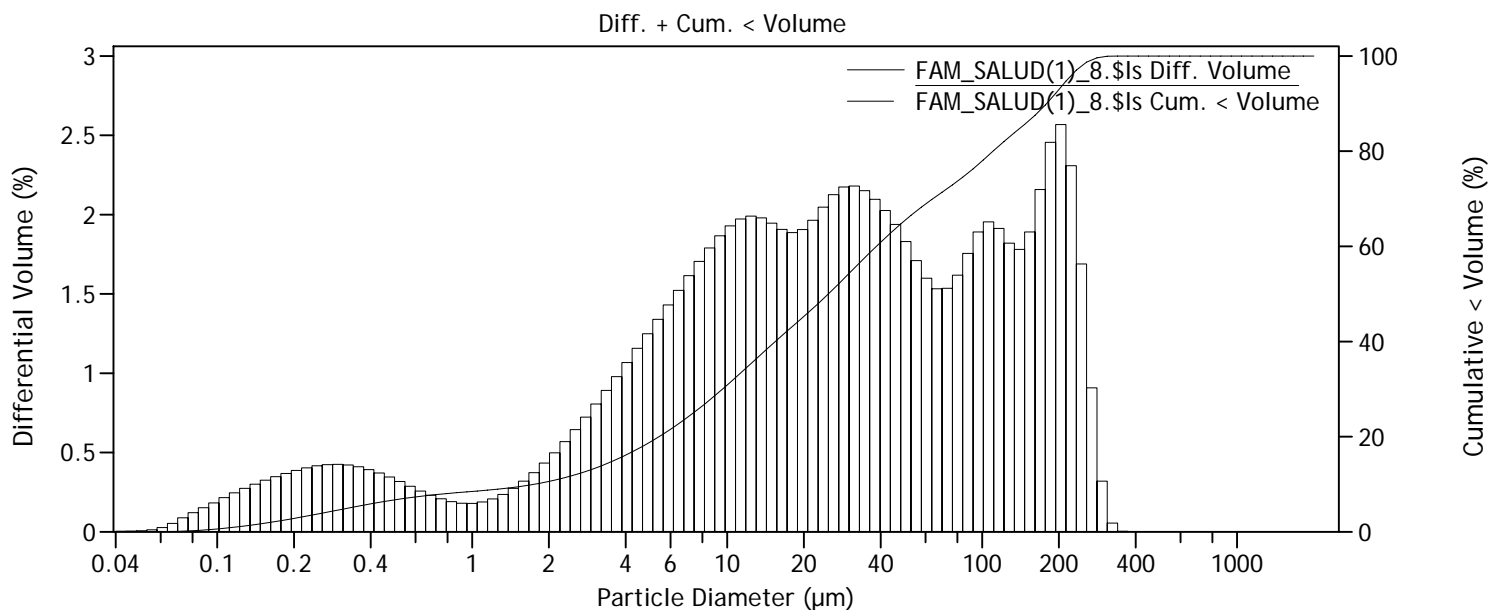
Calculations from 0.040 µm to 2000 µm

Volume:	100%	S.D.:	71.70 µm
Mean:	59.50 µm	Variance:	5140 µm ²
Median:	23.31 µm	C.V.:	120%
Mean/Median ratio:	2.553	Skewness:	1.206 Right skewed
Mode:	185.4 µm	Kurtosis:	0.218 Leptokurtic

d₁₀: 0.580 µm d₅₀: 23.31 µm d₉₀: 182.6 µm

Particle Diameter µm	FAM_SALUD(1) _7.\$Is Volume % <
2	13.8
4	20.0
63	67.5
125	79.5
250	98.8
500	100
1000	100
2000	100

File name: C:\GRANULOMETRIES COULTER\Marta Ferrater\FAM_SALUD(1)_8.\$Is
 FAM_SALUD(1)_8.\$Is
 File ID: FAM_SALUD(1)_8
 Sample ID: FAM_SALUD(1)_8
 Comment 1: Trinxera de la Salud
 Comment 2: Perfil de sols bloc aixecat
 Optical model: Mediterraneo.rf780d PIDS included
 Start time: 11:21 8 Jul 2015



Volume Statistics (Arithmetic)

FAM_SALUD(1)_8.\$Is

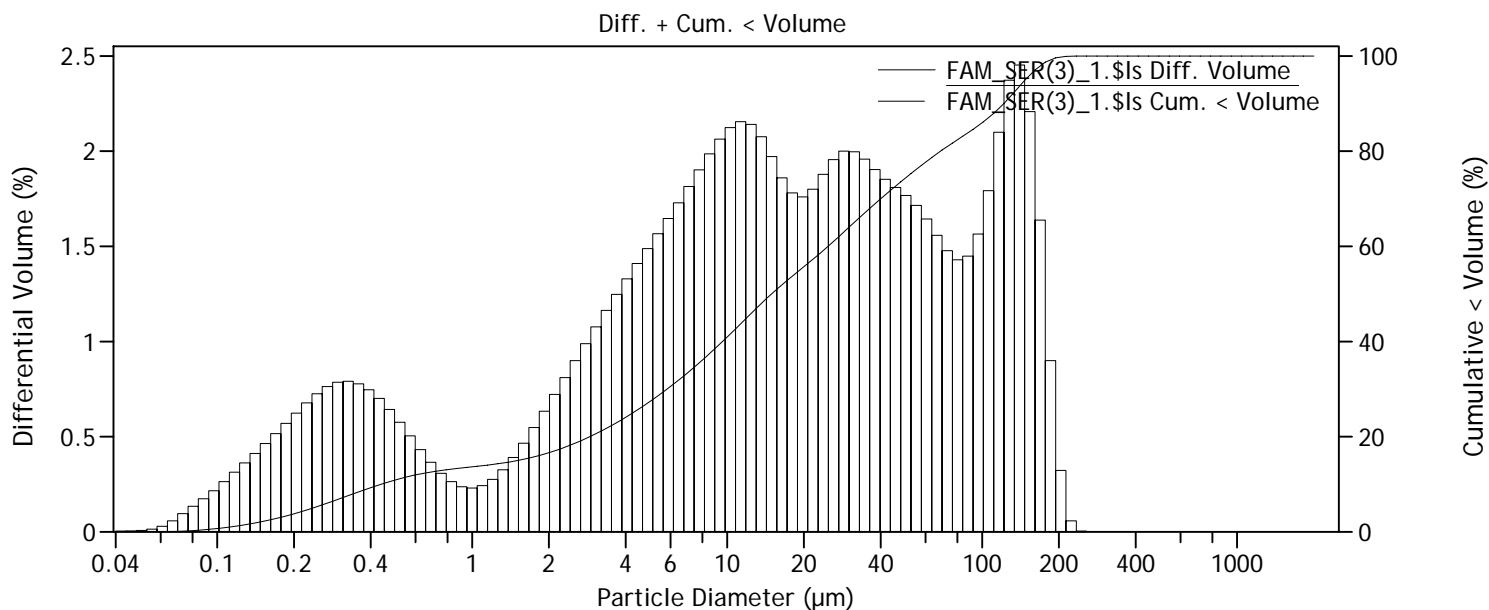
Calculations from 0.040 µm to 2000 µm

Volume:	100%	S.D.:	70.21 µm
Mean:	57.46 µm	Variance:	4930 µm ²
Median:	24.94 µm	C.V.:	122%
Mean/Median ratio:	2.304	Skewness:	1.436 Right skewed
Mode:	203.5 µm	Kurtosis:	1.041 Leptokurtic

d₁₀: 1.750 µm d₅₀: 24.94 µm d₉₀: 179.1 µm

Particle Diameter µm	FAM_SALUD(1) _8.\$Is Volume % <
2	10.6
4	16.1
63	69.7
125	82.5
250	98.2
500	100
1000	100
2000	100

File name: C:\GRANULOMETRIES COULTER\Marta Ferrater\FAM_SER(3)_1.\$ls
 FAM_SER(3)_1.\$ls
 File ID: FAM_SER(3)_1
 Sample ID: FAM_SER(3)_1
 Comment 1: Trinxera del Saltador
 Comment 2: Perfil de sols bloc enfonsat columna 5
 Optical model: Mediterraneo.rf780d PIDS included
 Start time: 12:07 8 Jul 2015



Volume Statistics (Arithmetic)

FAM_SER(3)_1.\$ls

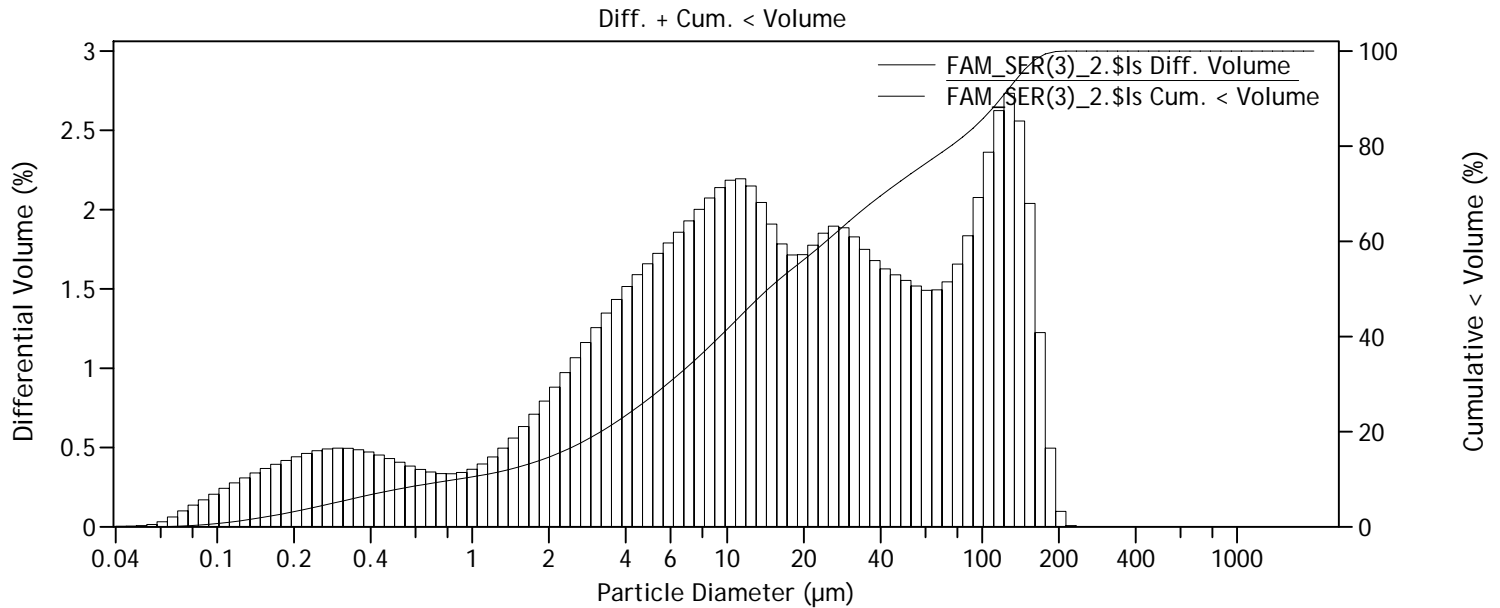
Calculations from 0.040 µm to 2000 µm

Volume:	100%	S.D.:	47.89 µm
Mean:	37.55 µm	Variance:	2293 µm ²
Median:	14.95 µm	C.V.:	128%
Mean/Median ratio:	2.512	Skewness:	1.534 Right skewed
Mode:	140.1 µm	Kurtosis:	1.352 Leptokurtic

d₁₀: 0.439 µm d₅₀: 14.95 µm d₉₀: 121.6 µm

Particle Diameter µm	FAM_SER(3) _1.\$ls Volume % <
2	16.6
4	24.1
63	78.6
125	90.7
250	99.999
500	100
1000	100
2000	100

File name: C:\GRANULOMETRIES COULTER\Marta Ferrater\FAM_SER(3)_2.\$ls
 FAM_SER(3)_2.\$ls
 File ID: FAM_SER(3)_2
 Sample ID: FAM_SER(3)_2
 Comment 1: Trinxera del Saltador
 Comment 2: Perfil de sols bloc enfonsat columna 30
 Optical model: Mediterraneo.rf780d PIDS included
 Start time: 12:15 8 Jul 2015



Volume Statistics (Arithmetic)

FAM_SER(3)_2.\$ls

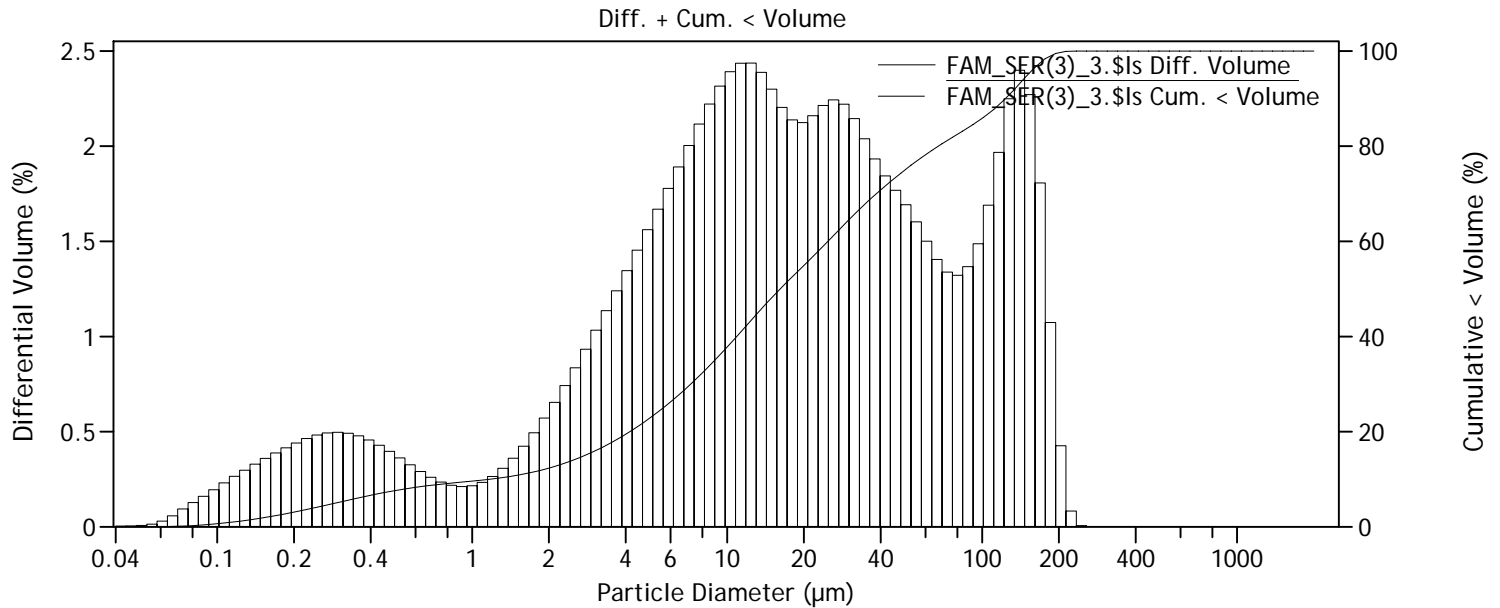
Calculations from 0.040 µm to 2000 µm

Volume:	100%	S.D.:	46.46 µm
Mean:	37.42 µm	Variance:	2159 µm ²
Median:	14.49 µm	C.V.:	124%
Mean/Median ratio:	2.583	Skewness:	1.400 Right skewed
Mode:	127.6 µm	Kurtosis:	0.839 Leptokurtic

d₁₀: 0.875 µm d₅₀: 14.49 µm d₉₀: 118.4 µm

Particle Diameter µm	FAM_SER(3) _2.\$ls Volume % <
2	14.7
4	23.4
63	77.1
125	91.6
250	100
500	100
1000	100
2000	100

File name: C:\GRANULOMETRIES COULTER\Marta Ferrater\FAM_SER(3)_3.\$ls
 FAM_SER(3)_3.\$ls
 File ID: FAM_SER(3)_3
 Sample ID: FAM_SER(3)_3
 Comment 1: Trinxera del Saltador
 Comment 2: Perfil de sols bloc enfonsat columna 30
 Optical model: Mediterraneo.rf780d PIDS included
 Start time: 12:22 8 Jul 2015



Volume Statistics (Arithmetic)

FAM_SER(3)_3.\$ls

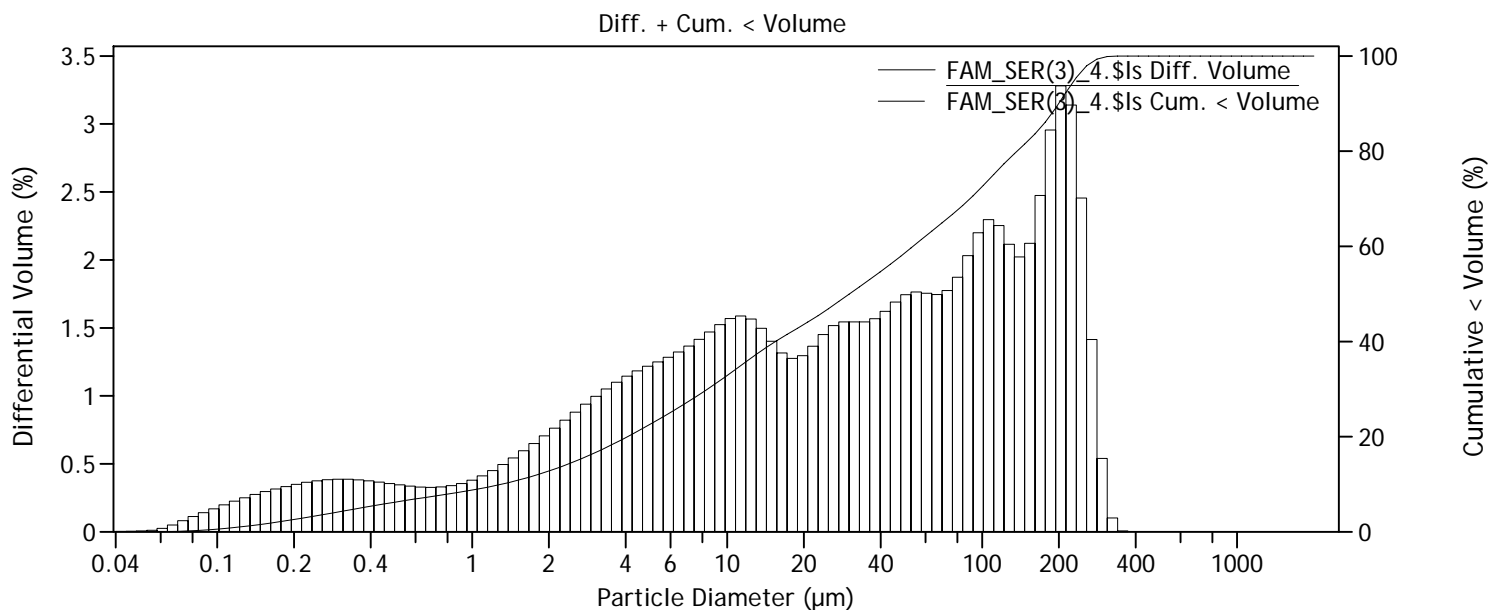
Calculations from 0.040 µm to 2000 µm

Volume:	100%	S.D.:	48.29 µm
Mean:	38.22 µm	Variance:	2332 µm ²
Median:	16.15 µm	C.V.:	126%
Mean/Median ratio:	2.366	Skewness:	1.592 Right skewed
Mode:	12.40 µm	Kurtosis:	1.535 Leptokurtic

d₁₀: 1.161 µm d₅₀: 16.15 µm d₉₀: 123.5 µm

Particle Diameter µm	FAM_SER(3) _3.\$ls Volume % <
2	12.4
4	19.5
63	79.0
125	90.3
250	99.998
500	100
1000	100
2000	100

File name: C:\GRANULOMETRIES COULTER\Marta Ferrater\FAM_SER(3)_4.\$ls
 FAM_SER(3)_4.\$ls
 File ID: FAM_SER(3)_4
 Sample ID: FAM_SER(3)_4
 Comment 1: Trinxera del Saltador
 Comment 2: Perfil de sols bloc enfonsat columna 30
 Optical model: Mediterraneo.rf780d PIDS included
 Start time: 12:29 8 Jul 2015



Volume Statistics (Arithmetic)

FAM_SER(3)_4.\$ls

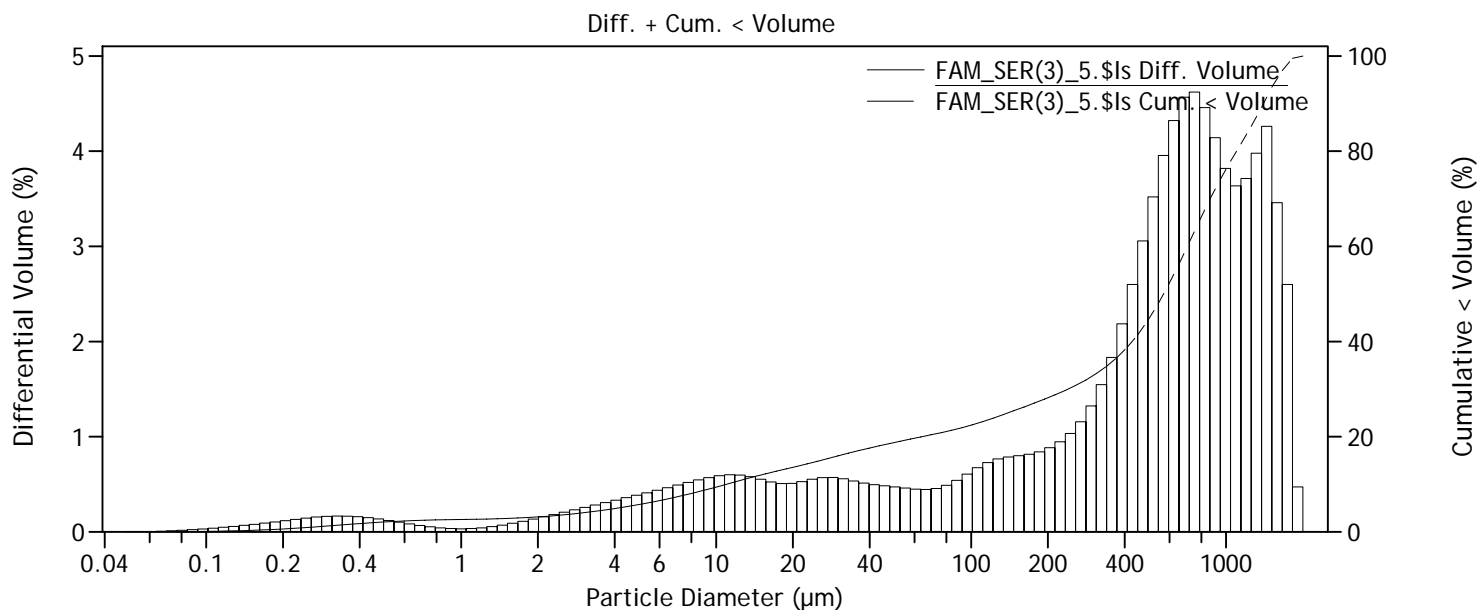
Calculations from 0.040 µm to 2000 µm

Volume:	100%	S.D.:	77.75 µm
Mean:	67.10 µm	Variance:	6046 µm ²
Median:	30.14 µm	C.V.:	116%
Mean/Median ratio:	2.226	Skewness:	1.150 Right skewed
Mode:	203.5 µm	Kurtosis:	0.157 Leptokurtic

d₁₀: 1.300 µm d₅₀: 30.14 µm d₉₀: 199.7 µm

Particle Diameter µm	FAM_SER(3) _4.\$ls Volume % <
2	12.8
4	19.8
63	63.1
125	77.9
250	97.2
500	100
1000	100
2000	100

File name: C:\GRANULOMETRIES COULTER\Marta Ferrater\FAM_SER(3)_5.\$ls
 FAM_SER(3)_5.\$ls
 File ID: FAM_SER(3)_5
 Sample ID: FAM_SER(3)_5
 Comment 1: Trinxera del Saltador
 Comment 2: Perfil de sols bloc enfonsat columna 30
 Optical model: Mediterraneo.rf780d PIDS included
 Start time: 12:38 8 Jul 2015



Volume Statistics (Arithmetic)

FAM_SER(3)_5.\$ls

Calculations from 0.040 µm to 2000 µm

Volume:	100%	S.D.:	508.0 µm
Mean:	625.0 µm	Variance:	258.0e3 µm ²
Median:	568.7 µm	C.V.:	81.3%
Mean/Median ratio:	1.099	Skewness:	0.513 Right skewed
Mode:	751.1 µm	Kurtosis:	-0.733 Platykurtic

d₁₀: 10.97 µm d₅₀: 568.7 µm d₉₀: 1402 µm

Particle Diameter µm	FAM_SER(3) _5.\$ls Volume % <
2	3.15
4	4.90
63	19.9
125	24.1
250	30.5
500	44.9
1000	76.2
2000	100

9.2. Quantitat de carbonat de calci per calcimetria

	V (ml)	
blanc 1	54,4	
blanc 2	50,2	
blanc 3	61,2	V' = 55,26666667

ERLENMEYER	MOSTRA	V (ml)	%CaCO ₃
1	SALUD(1)1	3	5,43
2	SALUD(1)2	10,4	18,82
3	SALUD(1)3	19,2	34,74
4	SALUD(1)4	14	25,33
5	SALUD(1)5	21	38,00
6	SALUD(1)6	21	38,00
7	SALUD(1)7	15,8	28,59
8	SALUD(1)8	10,4	18,82
9	CAN(2)1	6,4	11,58
10	CAN(2)2	6	10,86
11	CAN(2)3	9,6	17,37
12	CAN(2)4	12,5	22,62
13	SER(3)1	7,6	13,75
14	SER(3)2	13,4	24,25
15	SER(3)3	7,6	13,75
16	SER(3)4	12,3	22,26

	V (ml)	
blanc 1	54,4	
blanc 2	50,2	V' = 52,3

ERLENMEYER	MOSTRA	V (ml)	%CaCO ₃
1	SER(3)5	10,4	19,89
2	CARR(5)1	5,6	10,71
3	CARR(5)2	14,6	27,92
4	CARR(5)3	14,8	28,30
5	CARR(5)4	10,6	20,27
6	CARR(5)5	9	17,21
7	CARR(5)6	8,4	16,06

8	CARR(5)7	10	19,12
9	CARR(5)8	14,2	27,15
10	CARR(5)9	28	53,54
11	LIM(6)1	3,2	6,12
12	LIM(6)2	15,8	30,21
13	LIM(6)3	9,4	17,97
14	LIM(6)4	6,4	12,24
15	LIM(6)5	7	13,38
16	LIM(6)6	8,4	16,06
17	LIM(6)7	24,4	46,65

	V (ml)	
blanc 1	53,6	
blanc 2	54,2	V' = 53,9

ERLENMEYER	MOSTRA	V (ml)	%CaCO ₃
1	LIMII(7)1	18,3	33,95
2	LIMII(7)2	9	16,70
3	LIMII(7)3	7	12,99
4	LIMII(7)4	22	40,82
5	LIMII(7)5	10,2	18,92
6	LIMII(7)6	6,3	11,69

Taula ii. Resultats de la calcimetria amb el calcímetre de Bernard

9.3. Quantitat de carboni orgànic (matèria orgànica) i de carbonat de calci per ignició

MOSTRA	CRISOL	PES CRISOL	PES CRISOL + MOSTRA 105°C	PES CRISOL + CENDRES 560°C	PES MOSTRA	PES CENDRES 560°	PES M.O.	% LOI 560- MO
SALUD(1)1	1	16,6423	23,1238	22,8048	6,4815	6,1625	0,319	4,921700224
SALUD(1)2	2	16,9064	24,2142	23,8442	7,3078	6,9378	0,37	5,063083281
SALUD(1)3	3	16,336	21,1466	20,925	4,8106	4,589	0,2216	4,606493992
SALUD(1)4	4	16,5744	22,8784	22,7119	6,304	6,1375	0,1665	2,641180203
SALUD(1)5	5	16,9854	26,6349	26,2484	9,6495	9,263	0,3865	4,00538888
SALUD(1)6	6	17,7658	25,7121	25,4496	7,9463	7,6838	0,2625	3,303424235
SALUD(1)7	7	16,0151	22,8572	22,606	6,8421	6,5909	0,2512	3,67138744
SALUD(1)8	8	16,0504	27,9432	27,5335	11,8928	11,4831	0,4097	3,444941477
CAN(2)1	9	18,0776	27,4678	26,7586	9,3902	8,681	0,7092	7,552554791
CAN(2)2	10	16,081	26,4559	26,0236	10,3749	9,9426	0,4323	4,16678715
CAN(2)3	11	15,8309	26,7341	26,3843	10,9032	10,5534	0,3498	3,208232446
CAN(2)4	12	16,0987	25,802	25,4028	9,7033	9,3041	0,3992	4,114064287
SER(3)1	13	16,441	24,6557	24,3811	8,2147	7,9401	0,2746	3,342787929
SER(3)2	14	17,0219	26,1471	25,8473	9,1252	8,8254	0,2998	3,285407443
SER(3)3	15	17,6353	26,2201	25,932	8,5848	8,2967	0,2881	3,355931414
SER(3)4	16	16,9556	23,4203	23,0476	6,4647	6,092	0,3727	5,765155382
SER(3)5	17	15,389	21,9899	21,705	6,6009	6,316	0,2849	4,316078111
CARR(5)1	18	17,7807	26,1711	25,8612	8,3904	8,0805	0,3099	3,693506865
CARR(5)2	19	17,782	24,4361	24,1092	6,6541	6,3272	0,3269	4,912760554
CARR(5)3	20	16,0892	24,7565	24,4745	8,6673	8,3853	0,282	3,25360839
CARR(5)4	21	17,0724	23,3862	23,2556	6,3138	6,1832	0,1306	2,068484906
CARR(5)5	22	17,7606	24,6377	24,4681	6,8771	6,7075	0,1696	2,466155792
CARR(5)6	23	16,5757	24,0487	23,8808	7,473	7,3051	0,1679	2,246754985
CARR(5)7	24	16,0151	22,5098	22,3983	6,4947	6,3832	0,1115	1,716784455
CARR(5)8	25	18,0779	24,1465	23,9349	6,0686	5,857	0,2116	3,48680091
CARR(5)9	26	16,3359	21,2135	21,0985	4,8776	4,7626	0,115	2,35771691
LIM(6)1	27	16,9856	22,9422	22,772	5,9566	5,7864	0,1702	2,857334721

LIM(6)2	28	16,907	22,4032	22,1875	5,4962	5,2805	0,2157	3,924529675
LIM(6)3	29	16,0504	21,7887	21,6636	5,7383	5,6132	0,1251	2,180088179
LIM(6)4	30	15,8298	23,8922	23,749	8,0624	7,9192	0,1432	1,776146061
LIM(6)5	31	17,7684	24,5838	24,2509	6,8154	6,4825	0,3329	4,88452622
LIM(6)6	32	16,0981	23,035	22,664	6,9369	6,5659	0,371	5,348210296
LIM(6)7	33	16,0803	21,7946	21,5496	5,7143	5,4693	0,245	4,287489281
LIMII(7)1	34	10,2129	13,1248	12,9927	2,9119	2,7798	0,1321	4,536556887
LIMII(7)2	35	15,6157	23,9619	23,8084	8,3462	8,1927	0,1535	1,839160336
LIMII(7)3	36	12,278	19,7404	19,6244	7,4624	7,3464	0,116	1,554459691
LIMII(7)4	37	12,1492	18,5776	18,375	6,4284	6,2258	0,2026	3,151639599
LIMII(7)5	38	16,7597	23,9077	23,7753	7,148	7,0156	0,1324	1,852266368
LIMII(7)6	39	17,6285	24,5173	24,2623	6,8888	6,6338	0,255	3,701660667

Taula iii. Resultats de l'anàlisi de la quantitat de matèria orgànica (mufla - 560°C / 4 hores).

MOSTRA	CRISOL	PES CRISOL + CENDRES 950°C	PES CENDRES 950°	PES CARBONATS	% LOI 925 - C.inorg	% LOI 925 - C.inorg * 1,36
SALUD(1)1	1	22,3065	5,6642	0,4983	7,688035177	10,45572784
SALUD(1)2	2	22,7913	5,8849	1,0529	14,40789294	19,59473439
SALUD(1)3	3	20,0314	3,6954	0,8936	18,57564545	25,26287781
SALUD(1)4	4	21,9194	5,345	0,7925	12,57138325	17,09708122
SALUD(1)5	5	24,3699	7,3845	1,8785	19,46732991	26,47556868
SALUD(1)6	6	24,0115	6,2457	1,4381	18,09773102	24,61291419
SALUD(1)7	7	21,7903	5,7752	0,8157	11,9217784	16,21361863
SALUD(1)8	8	25,9192	9,8688	1,6143	13,57375891	18,46031212
CAN(2)1	9	26,3836	8,306	0,375	3,993525165	5,431194224
CAN(2)2	10	25,5684	9,4874	0,4552	4,387512169	5,96701655
CAN(2)3	11	25,7257	9,8948	0,6586	6,040428498	8,214982757
CAN(2)4	12	24,6417	8,543	0,7611	7,843723269	10,66746365
SER(3)1	13	23,9497	7,5087	0,4314	5,251561226	7,142123267
SER(3)2	14	24,8935	7,8716	0,9538	10,45237365	14,21522816
SER(3)3	15	25,1998	7,5645	0,7322	8,52902805	11,59947815
SER(3)4	16	22,3558	5,4002	0,6918	10,70119263	14,55362198

SER(3)5	17	21,4048	6,0158	0,3002	4,547864685	6,185095972
CARR(5)1	18	25,6296	7,8489	0,2316	2,760297483	3,754004577
CARR(5)2	19	23,5638	5,7818	0,5454	8,196450309	11,14717242
CARR(5)3	20	23,5624	7,4732	0,9121	10,52346175	14,31190798
CARR(5)4	21	22,8484	5,776	0,4072	6,449364883	8,771136241
CARR(5)5	22	24,021	6,2604	0,4471	6,50128688	8,841750156
CARR(5)6	23	23,5038	6,9281	0,377	5,044828048	6,860966145
CARR(5)7	24	21,9667	5,9516	0,4316	6,645418572	9,037769258
CARR(5)8	25	23,3875	5,3096	0,5474	9,020202353	12,2674752
CARR(5)9	26	20,1638	3,8279	0,9347	19,16311301	26,06183369
LIM(6)1	27	22,7016	5,716	0,0704	1,181882282	1,607359903
LIM(6)2	28	21,6857	4,7787	0,5018	9,129944325	12,41672428
LIM(6)3	29	21,3584	5,308	0,3052	5,31864838	7,233361797
LIM(6)4	30	23,3775	7,5477	0,3715	4,607809089	6,266620361
LIM(6)5	31	24,0637	6,2953	0,1872	2,746720662	3,7355401
LIM(6)6	32	22,378	6,2799	0,286	4,122879096	5,60711557
LIM(6)7	33	20,7125	4,6322	0,8371	14,64921338	19,92293019
LIMII(7)1	34	12,7134	2,5005	0,2793	9,591675538	13,04467873
LIMII(7)2	35	23,323	7,7073	0,4854	5,815820373	7,909515708
LIMII(7)3	36	19,293	7,015	0,3314	4,440930532	6,039665523
LIMII(7)4	37	17,3844	5,2352	0,9906	15,40974426	20,95725219
LIMII(7)5	38	23,3542	6,5945	0,4211	5,891158366	8,011975378
LIMII(7)6	39	24,0567	6,4282	0,2056	2,984554639	4,05899431

Taula iv. Resultats de l'anàlisi de la quantitat de carbonats (mufla - 950°C / 2 hores).